FAILURE ANALYSIS OF QUASI-BRITTLE MEDIA USING THE MICROPOLAR CONTINUUM THEORY, ELASTIC-DEGRADING CONSTITUTIVE MODELS, AND SMOOTHED POINT INTERPOLATION METHODS

by

Lapo Gori

FEDERAL UNIVERSITY OF MINAS GERAIS (UFMG)
SCHOOL OF ENGINEERING
DEPARTMENT OF STRUCTURAL ENGINEERING
GRADUATE PROGRAM IN STRUCTURAL ENGINEERING (PROPEES)

FAILURE ANALYSIS OF QUASI-BRITTLE MEDIA USING THE MICROPOLAR CONTINUUM THEORY, ELASTIC-DEGRADING CONSTITUTIVE MODELS, AND SMOOTHED POINT INTERPOLATION METHODS

Lapo Gori

Thesis submitted to the Graduate Program in Structural Engineering (PROPEES) of the School of Engineering at the FEDERAL UNIVERSITY OF MINAS GERAIS (UFMG), in partial fulfillment of the requirements for the degree of "Doctor of Philosophy in Structural Engineering"

Examining board:

Prof. Dr. Roque Luiz da Silva Pitangueira
DEES - UFMG (Supervisor)

Prof. Dr. Samuel Silva Penna
DEES - UFMG (Co-Supervisor)

Prof. Dr. Felício Bruzzi Barros
DEES - UFMG

Prof. Dr. Rodrigo Peluci de Figueiredo
UFOP

Prof. Dr. Jamile Salim Fuina
FUMEC

Prof. Dr. Renato Cardoso Mesquita
DEE - UFMG

Belo Horizonte, Brazil
15th June, 2018

Alla mamma e al babbo. A Larissa.

Acknowledgments

Alla mamma e al babbo per tutto.

A Larissa per tutto il resto.

Ao Roque, orientador e amigo, pela sugestão do tema dessa tese, pela orientação, pelas aulas de gramática portuguesa, pela confiança, e por me motivar a ir sempre além dos meus limites.

Ao Samuel, pela co-orientação, e pela disponibilidade e paciência em compartilhar o seu conhecimento sobre o **INSANE** e sobre a modelagem.

Aos demais professores do Departamento de Engenharia de Estruturas da UFMG pela recepção desde a minha chegada, especialmente para os professores Gabriel e Fernando pelo apoio na minha primeira experiência como professor.

Aos colegas do grupo **INSANE** e do Departamento de Engenharia de Estruturas, pelos congressos, pelas festas, e pela amizade ao longo desses anos.

Às funcionárias do Departamento de Engenharia de Estruturas, especialmente à Fátima, pelo carinho e atenção.

Ao Luciano, exemplo de vida que nunca deixa de surpreender, pelos papos, pelos trabalhos juntos, pelos congressos, pelos almoços frente ao Colosseo.

À Marcella, pela amizade desde a minha chegada no departamento.

À família Altemar, que sempre me recebeu com muito carinho.

La filosofia è scritta in questo grandissimo libro che continuamente ci sta aperto innanzi a gli occhi (io dico l'universo), ma non si può intendere se prima non s'impara a intender la lingua, e conoscer i caratteri, ne' quali è scritto. Egli è scritto in lingua matematica, e i caratteri son triangoli, cerchi, ed altre figure geometriche, senza i quali mezzi è impossibile a intenderne umanamente parola; senza questi è un aggirarsi vanamente per un oscuro laberinto.

Galileo Galilei
Il Saggiatore (1623)

Car je me trouvois embarrassé de tant de doutes et d'erreurs, qu'il me sembloit n'avoir fait autre profit, en tâchant de m'instruire, sinon que j'avois découvert de plus en plus mon ignorance.

René Descartes
Discours de la méthode (1637)

Resumo

Esta tese trata do problema de localização de deformações em materiais parcialmente frágeis, modelados como meios com degradação elástica, utilizando duas diferentes estratégias de regularização, aplicadas quer individualmente quer em combinação: uma regularização no nível da formulação através da teoria de contínuo micropolar, e uma regularização no nível numérico utilizando métodos sem malha do tipo *smoothed point interpolation*. Com o objetivo de permitir a representação de meios parcialmente frágeis com o modelo de contínuo micropolar, foi proposta uma formulação unificada monodissipativa para degradação elástica em meios micropolares, definida em termos de tensores secantes, funções de carregamento e regras de degradação, e dentro desse esquema geral foram obtidos diferentes modelos de dano escalar. Foi também introduzida uma especifica forma compacta para a representação de meios micropolares, com o objetivo de obter uma compatibilidade formal entre modelos constitutivos clássicos e micropolares. Aproveitando dessa compatibilidade, os modelos micropolares foram implementados em uma estrutura existente para meios clássicos, baseada no paradigma de orientação a objetos, caracterizada pela independência entre os modelos constitutivos e os métodos numericos e modelos de análise adotados durante a análise. Conceitos sobre a propagação de ondas de aceleração, como a condição de compatibilidade de Maxwell e a condição de propagação de Fresnel-Hadamard, foram derivados para a formulação micropolar proposta, com o objetivo de obter um indicador de localização, para ser utilizado como uma ferramenta analítica e numerica para a avaliação dos efeitos de regularização induzidos pelos parâmetros do material micropolar. Modelos existentes de tipo *smoothed point interpolation*, desenvolvidos originalmente para a elasticidade e elastoplasticidade clássicas, foram estendidos ao caso de degradação elástica em meios clássicos. A peculiar forma fraca de tipo *weakened-weak* na qual esses métodos são baseados, foi estendida também para o contínuo micropolar, considerando seja elasticidade que degradação elástica. Tais métodos foram implementados no mesmo projeto orientado a objetos no qual foram implementados os models constitutivos para o contínuo micropolar. Diferentes simulações numéricas relativas a problems de localização numérica e induzida, permitiram de destacar os efeitos de regularização da teoria micropolar em análises com o método dos elementos finitos, bem como os efeitos de regularização dos métodos de tipo *smoothed point interpolation* em modelos clássicos de degradação elástica. As duas estratégias se

mostraram capazes the regularizar, individualmente, a resposta em diferentes análises. Além disso, a combinação das duas permitiu de melhorar os resultados dos casos onde a aplicação individual delas não era suficiente. Os mesmos resultados foram obtidos com outras simulações, feitas utilizando dois testes esperimentais reais como base para a definição dos modelos discretos. Nesse caso foi possivel observar, além da regularização das instabilidades materiais, também uma certa capacidade dos métodos de tipo *smoothed point interpolation* de fornecer, durante as análises, resultados independentes da malha.

Palavras-chave: Localização de deformações; Contínuo micropolar; Mecânica do dano contínuo; Métodos sem malha; Smoothed point interpolation methods (S-PIM); Programação Orientada a Objetos (POO)

Abstract

The present thesis address the issue of localization (or discontinuous failure) in quasi-brittle materials modelled as elastic-degrading media, using two different regularization strategies, applied individually as well as in a combined form: a regularization at the formulation level with the micropolar continuum theory, and a regularization at the numerical level using smoothed point interpolation meshfree methods. In order to allow the representation of quasi-brittle media with the micropolar continuum model, a unified monodissipative formulation for elastic degradation in micropolar media, defined in terms of secant tensors, loading functions and degradation rules, has been proposed, also deriving a number of scalar damage models within its general scheme. A peculiar compact representation for micropolar media has been introduced, in order to guarantee a formal compatibility between classic and micropolar constitutive models. Taking advantage of this compatibility, the micropolar models have been implemented within an existing object-oriented constitutive models framework originally conceived for classic media, characterized by its independence on the underlying numerical method and analysis model adopted during an analysis. Well-known concepts of acceleration waves propagation, such as the Maxwell compatibility condition and the Fresnel–Hadamard propagation condition, have been derived for the proposed micropolar formulation, in order to obtain a proper localization indicator as a both analytical and numerical tool for the evaluation of the regularization effects induced by the micropolar material parameters. Existent smoothed point interpolation methods, originally developed for classic elasticity and elasto-plasticity, have been extended to the case of elastic degradation in classic media. The peculiar weakened-weak form which they are based on, has been also extended to the micropolar continuum, considering both elasticity and elastic degradation. These methods have been implemented within the same object-oriented project of the micropolar constitutive models framework. A number of simulations regarding problems of numerical and induced localization in damage models, allowed to point out the regularization effects of the micropolar theory in finite element analyses, as well as the regularization effects of smoothed point interpolation methods in classic elastic-degrading models. Both these strategies were capable to individually regularize the behaviour of a number of analyses. Furthermore, their combination allowed to improve the results in the cases where the use of just one of them wasn't sufficient. The same results were

obtained with another set of simulations performed using two different real experimental tests as a basis for the discrete models. In this case, beside the regularization of material instabilities, is was also possible to observe a certain capability of the smoothed point interpolation methods to provide mesh-objective results during the analyses.

Key-words: Strain localization; Micropolar continuum theory; Continuum damage mechanics; Meshfree methods; Smoothed point interpolation methods (S-PIM); Object-Oriented Programming (OOP)

Table of contents

List of tables

List of figures

List of symbols

$\mathbf{E}$	environment space
$\bar{\mathbf{E}}$	vector space associated to the environment space
$\mathbb{R}^N$	N-dimensional Euclidean space
$SO(3)$	space of the rotation tensors
$\mathbf{D}$	domain of a body
$\mathbf{D}_t$	domain of a body at the time instant t
$\partial\mathbf{D}$	boundary of a body
$\partial\mathbf{D}_e^u$	essential boundary for prescribed displacements
$\partial\mathbf{D}_e^\varphi$	essential boundary for prescribed microrotations
$\partial\mathbf{D}_n^u$	natural boundary for the prescribed stresses
$\partial\mathbf{D}_n^\varphi$	natural boundary for the prescribed couple-stresses
$\mathbf{D}_k^S$	k-th smoothing domain
$\partial\mathbf{D}_k^S$	boundary of the k-th smoothing domain
$\bar{u}$	displacement field
$\bar{\varphi}$	microrotation field
U	generalized micropolar displacement field
$\bar{w}$	displacement test function
$\bar{\omega}$	microrotation test function
W	generalized micropolar trial function
c	motion of the material points
$\underline{R}$	rotation tensor
ρ	density
$\rho\theta$	rotation inertia of the continuum particles
e	standard Levi-Civita operator with three indexes
$\bar{\eta}$	unit normal vector field to the body boundary $\partial\mathbf{D}$
$\bar{n}^{(k)}$	unit normal vector field to k-th smoothing domain $\mathbf{D}_k^S$
$\bar{t}_A$	prescribed surface forces
$\bar{t}_C$	prescribed surface couples
$\bar{b}_V$	prescribed volume forces
$\bar{l}_V$	prescribed volume couples

$\underline{\sigma}$	stess tensor
$\underline{\dot{\sigma}}$	stess rate tensor
$\underline{\dot{\sigma}}^e$	elastic part of the stess rate tensor
$\underline{\dot{\sigma}}^d$	degrading part of the stess rate tensor
$\underline{\mu}$	couple-stress tensor
$\underline{\dot{\mu}}$	couple-stress rate tensor
$\underline{\dot{\mu}}^e$	elastic part of the couple-stress rate tensor
$\underline{\dot{\mu}}^d$	degrading part of the couple-stress rate tensor
$\underline{\Sigma}$	generalized stress tensor (micropolar medium)
$\underline{\dot{\Sigma}}$	generalized stress rate tensor (micropolar medium)
$\underline{\varepsilon}$	strain tensor (classic medium)
$\underline{\dot{\varepsilon}}$	strain rate tensor (classic medium)
$\underline{\dot{\varepsilon}}^e$	elastic part of the strain rate tensor (classic medium)
$\underline{\dot{\varepsilon}}^d$	degrading part of the strain rate tensor (classic medium)
$\underline{\gamma}$	strain tensor (micropolar medium)
$\underline{\dot{\gamma}}$	strain rate tensor (micropolar medium)
$\underline{\dot{\gamma}}^e$	elastic part of the strain rate tensor (micropolar medium)
$\underline{\dot{\gamma}}^d$	degrading part of the strain rate tensor (micropolar medium)
$\underline{\kappa}$	microcurvature tensor
$\underline{\dot{\kappa}}$	microcurvature rate tensor
$\underline{\dot{\kappa}}^e$	elastic part of the microcurvature rate tensor
$\underline{\dot{\kappa}}^d$	degrading part of the microcurvature rate tensor
$\underline{\Gamma}$	generalized strain tensor (micropolar medium)
$\underline{\dot{\Gamma}}$	generalized strain rate tensor (micropolar medium)
$\underline{\tilde{\sigma}}$	smoothed stess tensor
$\underline{\tilde{\mu}}$	smoothed couple-stess tensor
$\underline{\tilde{\varepsilon}}$	smoothed strain tensor (classic medium)
$\underline{\tilde{\gamma}}$	smoothed strain tensor (micropolar medium)
$\underline{\tilde{\kappa}}$	smoothed microcurvature tensor
$\hat{\mathbf{E}}$	constitutive operator (classic stress/strain relation)
$\hat{\mathbf{E}}^S$	secant constitutive operator (classic stress/strain relation)
$\hat{\mathbf{E}}^t$	tangent constitutive operator (classic stress/strain relation)
$\hat{\mathbf{A}}$	constitutive operator (micropolar stress/strain relation)
$\hat{\mathbf{A}}^S$	secant constitutive operator (micropolar stress/strain relation)
$\hat{\mathbf{A}}^t$	tangent constitutive operator (micropolar stress/strain relation)
$\hat{\mathbf{C}}$	constitutive operator (micropolar couple-stress/microcurvature relation)
$\hat{\mathbf{C}}^S$	secant constitutive operator (micropolar couple-stress/microcurvature relation)
$\hat{\mathbf{C}}^t$	tangent constitutive operator (micropolar couple-stress/microcurvature relation)
$\hat{\mathcal{E}}$	generalized constitutive operator (micropolar generalized stress/strain relation)

$\hat{\mathcal{E}}^S$	generalized secant constitutive operator (micropolar generalized stress/strain relation)
$\hat{\mathcal{E}}^t$	generalized tangent constitutive operator (micropolar generalized stress/strain relation)
$\underline{id}$	second-order identity tensor
$\mathbf{I\hat{D}}$	fourth-order identity tensor
$\mathbf{I\hat{D}}^T$	transposed fourth-order identity tensor
$\mathbf{I\hat{D}}^{sym}$	symmetric fourth-order identity tensor
$\mathbf{I\hat{D}}^{skw}$	skew-symmetric fourth-order identity tensor
E	Young's modulus
ν	Poisson's ratio
G	shear modulus
G_c	Cosserat's shear modulus
L_b	internal bending length
ψ	Helmholtz's free energy density
$\mathbf{G}$	Gibbs's free energy density
$\dot{\lambda}$	inelastic multiplier
$\underline{m}_A$	direction of degradation of the strain degrading rate
$\underline{m}_C$	direction of degradation of the microcurvature degrading rate
$\underline{m}_A^*$	direction of degradation of the stress degrading rate
$\underline{m}_C^*$	direction of degradation of the couple-stress degrading rate
f	loading function
$\underline{n}_A$	gradient of the loading function w.r.t. the stress tensor
$\underline{n}_C$	gradient of the loading function w.r.t. the couple-stress tensor
$\underline{n}_A^*$	gradient of the loading function w.r.t. the strain tensor
$\underline{n}_C^*$	gradient of the loading function w.r.t. the microcurvature tensor
H, H^*	stress- and strain-based inelastic moduli
D	scalar damage variable
ε_{eq}	equivalent deformation
Γ_{eq}	equivalent generalized deformation
$a(\bar{w}, \bar{u})$	bilinear form
$\widetilde{a}(\bar{w}, \bar{u})$	smoothed bilinear form
$A(W, U)$	micropolar bilinear form
$\widetilde{A}(W, U)$	smoothed micropolar bilinear form
$f(\bar{w})$	linear functional of the weak form
$f(W)$	linear functional of the micropolar weak form
$G(\bar{w}, \bar{u})$	equilibrium functional of the weak form
$G(W, U)$	equilibrium functional of the micropolar weak form
$\mathcal{V}(\mathbf{D})$	space of trial functions (or admissible configurations) over $\mathbf{D}$

$\delta\mathcal{V}(\mathbf{D})$	space of admissible variations $\mathbf{D}$
$\mathcal{V}^0(\mathbf{D})$	space of test functions over $\mathbf{D}$
$\mathcal{V}_h(\mathbf{D})$	discretized space of trial functions (or admissible configurations) over $\mathbf{D}$
$\delta\mathcal{V}_h(\mathbf{D})$	discretized space of admissible variations $\mathbf{D}$
$\mathcal{V}_h^0(\mathbf{D})$	discretized space of test functions over $\mathbf{D}$
$(\mathcal{H}^1(\mathbf{D}))^k$	space of square integrable k-dimensional vector fields with square integrable first derivatives over $\mathbf{D}$
$\mathcal{H}^*(\mathbf{D})$	space of square integrable micropolar vector fields with square integrable first derivatives over $\mathbf{D}$
$(\mathcal{H}_h^1(\mathbf{D}))^k$	discretized space of square integrable k-dimensional vector fields with square integrable first derivatives over $\mathbf{D}$
$\mathcal{H}_h^*(\mathbf{D})$	discretized space of square integrable micropolar vector fields with square integrable first derivatives over $\mathbf{D}$
$(\mathcal{G}_h^1(\mathbf{D}))^k$	G-space for k-dimensional vector fields over $\mathbf{D}$
$\mathcal{G}_h^*(\mathbf{D})$	G-space for micropolar vector fields over $\mathbf{D}$
$\bar{n}$	normal direction to the localization surface
$\bar{p}_A, \bar{p}_C$	micropolar polarization vectors
$\bar{a}, \bar{b}$	localization traction vectors
q	localization indicator
$\underline{Q}$	acoustic tensor
$\underline{Q}_{AA}$	sub-tensor of the micropolar acoustic tensor
$\underline{Q}_{AC}$	sub-tensor of the micropolar acoustic tensor
$\underline{Q}_{CA}$	sub-tensor of the micropolar acoustic tensor
$\underline{Q}_{CC}$	sub-tensor of the micropolar acoustic tensor
$\underline{Q}^S$	secant acoustic tensor
$\underline{Q}_{AA}^S$	sub-tensor of the micropolar secant acoustic tensor
$\underline{Q}_{AC}^S$	sub-tensor of the micropolar secant acoustic tensor
$\underline{Q}_{CA}^S$	sub-tensor of the micropolar secant acoustic tensor
$\underline{Q}_{CC}^S$	sub-tensor of the micropolar secant acoustic tensor
$\underline{Q}^t$	tangent acoustic tensor
$\underline{Q}_{AA}^t$	sub-tensor of the micropolar tangent acoustic tensor
$\underline{Q}_{AC}^t$	sub-tensor of the micropolar tangent acoustic tensor
$\underline{Q}_{CA}^t$	sub-tensor of the micropolar tangent acoustic tensor
$\underline{Q}_{CC}^t$	sub-tensor of the micropolar tangent acoustic tensor
$[\![\cdot]\!]$	jump of a quantity across a discontinuity surface
$<\cdot,\cdot>_X$	inner product in the generic space X
$\|\cdot\|_X$	norm in the generic space X
$|\cdot|_X$	semi-norm in the generic space X

List of abbreviations and acronyms

RVE	Representative Volume Element
FEM	Finite Element Method
S-PIM	Smoothed Point Interpolation Methods
PIM	Point Interpolation Method
RPIM	Radial Point Interpolation Method (with polynomial reproduction)
NS-PIM	Node-Based Point Interpolation Method
NS-RPIM	Node-Based Radial Point Interpolation Method
ES-PIM	Edge-Based Point Interpolation Method
ES-RPIM	Edge-Based Radial Point Interpolation Method
MLS	Moving Least Square
EFG	Element-Free Galerkin
MLPG	Meshless Local Petrov-Galerkin
SPH	Smoothed Particle Hydrodynamics
RKPM	Reproducing Kernel Particle Method
W^2	Weakened-Weak form
INSANE	INteractive Structural ANalysis Environment
UML	Unified Modelling Language
XML	eXtensible Markup Language
OOP	Object-Oriented Programming
CSV	Comma-Separated Values

Chapter 1

Introduction

1.1 Motivations

The class of *quasi-brittle* media comprehends a large number of materials which are of interest in various engineering applications, such as concrete, rocks, coarse-grained ceramics, and most fibre-reinforced materials. Hence, a proper characterization of their behaviour is of fundamental importance. Among the different methods and techniques, *continuum damage mechanics* has been shown to be a valid approach for the representation of the physically non-linear phenomena characterizing the behaviour of quasi-brittle media. Briefly, it consists in the representation of the degradation (or damaging) of a material during a loading process in terms of a set of *state variables* (or *damage variables*), which are functions defined at every point of the domain representing the body under analysis. This continuous approach to degradation has been the objective of a large number of investigations, which led to the formalization of different independent constitutive approaches into *unified* frameworks. The continuous nature of this strategy is also appealing from the computational point of view since, in general, requires less efforts to be implemented within the finite element method or other discretization techniques. Numerous studies have also been devoted to questions regarding numerical and coding aspects of the aforementioned unified frameworks. The aim of these studies was the optimization of the implementations, especially regarding the issue of *independence* between the constitutive modelling aspects and the underlying numerical methods, which is important to guarantee the use of an implemented constitutive model independently on the peculiar numerical methods that is being used to perform the analysis.

Despite the advantages offered by this continuous approach to damage, finite element discretizations based on models defined within continuum damage mechanics may suffer for a number of issues, because of the *softening* behaviour of such models. Quasi-brittle media indeed, are characterized by a reduction of their load-carrying capacity, which manifests when a certain deformation threshold is attained, resulting in typical de-

scending branches in load-displacement plots. During this softening phase the degrading phenomena tend to concentrate in limited parts of the body under analysis, resulting in the so-called *strain localization*, which is a precursor of the failure of a sample. When this phenomenon occours, the numerical simulations may be affected by a number of pathological behaviours such that, for example, *strong mesh dependency*, *premature crack initiation*, and *instantaneous perfectly-brittle fracture*, which significantly alter the quality of the results.

The problem of strain localization has been investigated by many authors, considering both elasto-plastic and damage (or elastic-degrading) models. It has been pointed out that the pathological behaviours exhibited in numerical simulations where localization occours are due to the *local* description offered by the classic continuum theory, in contrast with the *non-local* nature of phenomena like plasticity and damage. The solutions that have been proposed over the years aimed to recover this non-locality introducing a sort of *internal length*, in order to *regularize* the behaviour of a model.

A common approach that has been followed by many authors in the past consists in the regularization of a model with the introduction of an internal length at the *formulation* level, i.e., directly in the continuum description, using *gradient-enhanced* models and *multifield* (or *generalized*) continuum descriptions. Among the latter, the Cosserat (or micropolar) continuum theory has been widely adopted to regularize problems with strain-softening elasto-plasticity, with limited applications also to damage models. Its popularity among the researchers is mainly due to the fact that, with respect to other generalized continuum strategies, it has a simple formulation and is easy to be implemented in standard FEM codes; furthermore, its parameters can be connected with the microstructural properties of a material. However, when dealing with the micropolar theory, as well as other multifield continuum theories, the main issue consists in a lack of generality of the physically non-linear models based on them. While for classic media, as commented before, great efforts have been made to attain comprehensive theoretical and computational frameworks for constitutive models, the same level of development is not currently available in the aforementioned gradient-enhanced and multifield continuum theories.

The other path that can be followed for the regularization of localization problems consists instead on the introduction of an internal length at the *numerical* level, i.e., within the discretization method. Different solutions have been proposed in the past in the field of the finite element method, like as embedded discontinuities or embedded localization zones. Recently, it has been shown that some classes of *meshfree* methods, like *moving least square*, *reproducing kernel* approximations, and methods based on *strain smoothing* techniques, are able to bring regularization effects on localization problems, due to the intrinsic non-local properties that are embedded in their formulation.

Regarding these two approaches to regularization, at the formulation and at the numer-

ical level, the existent literature points out that, often, a single strategy is not sufficient to regularize a wide range of problems, and better results can be obtained combining different methods.

1.2   Objectives

Taking into account the premises discussed in the previous Section 1.1, this thesis was developed with the aim to investigate localization problems occourring in quasi-brittle media using two different regularization strategies: the *micropolar continuum theory* at the formulation level, and *smoothed point interpolation methods* at the numerical level.

Due to the limited number of constitutive models based on the micropolar theory available in the literature and to their lack of generality, it was first necessary to develop a *unified formulation for elastic degradation* based on this continuum description, analogous to the existent one based on the classic theory. Peculiar efforts were also devoted to the implementation aspects of such formulation, aiming to obtain a computational framework for constitutive models independent on both the peculiar numerical method and analysis models adopted in an analysis, and compatible with an existent implementation for classic media[1].

The proposed constitutive models for elastic degradation in micropolar media were then investigated within the theory of *acceleration waves propagation*, a common approach to study localization phenomena. This investigation led to the definition of a *localization indicator* for the micropolar continuum, which was used to evaluate the role of the micropolar material parameters on the onset of localization.

Smoothed point interpolation methods allow for a more simple treatment of the essential boundary conditions with respect to other common meshfree methods. In the existent literature, they have been applied only to classic elasticity and elasto-plasticity, hence it was necessary to extend their application to elastic-degrading models based on both the classic and the micropolar continuum theories.

1.3   Outline

This treatise is organized in 7 chapters and 3 appendices. After this introduction (Chapter 1), Chapter 2 presents a survey on the literature concerning some aspects of the modelling of quasi-brittle media. It contains some basic informations on the physics of quasi-brittle media, on the modelling approach within continuum damage mechanics, and

---

[1] The implementation of such framework have been performed in the open-source software **INSANE**, taking advantage of its existent framework for constitutive models based on the classic continuum theory (Appendix C).

on a unified formulation for multidissipative elastic-degrading models. It also discusses about localization issues and possible regularization strategies.

The micropolar continuum is treated in Chapter 3. After a brief survey on physical and modelling aspects of materials with microstructure, the basic expressions of the micropolar formulation in linear elasticity are briefly recalled. The chapter then focuses on a novel unified formulation for micropolar elastic-degrading models proposed by the author.

Chapter 4 is devoted to the class of smoothed point interpolation methods. In the first part, after a brief review on general meshfree methods, the main concepts regarding smoothed point interpolation methods are recalled, focusing on two specific methods. Novel applications of such models to the case of elastic degradation in classic media, and to the case of elasticity and elastic degradation in micropolar media are then presented.

In Chapter 5 the localization analysis of the proposed constitutive models is performed. A proper localization indicator, which allows to perform both analytical and numerical localization analyses in micropolar media, is derived. Two analytical investigations are then performed in order to point out the role of the micropolar material parameters on the onset of localization.

A set of numerical simulations dealing with problems characterized by numerical and induced localization are presented in Chapter 6, which were performed with both the finite element method and meshfree methods, and considering both classic and micropolar theories.

Also Chapter 7 presents some numerical simulations, that in this case were performed using real experimental tests as a basis.

Finally, Chapter 8 close this treatise, summing up the main contributions of this thesis and discussing possible future developments in this research field.

This text is followed by a set of 3 appendices, containing other important informations which have been left out from the main text in order to ease the reading. The content of Appendix C is of fundamental importance as a support for this text, since it contains informations on the coding structure adopted for the implementations of micropolar constitutive models and of meshfree methods.

1.4   Notations

Some standard notations used in the body of the manuscript are summarized here. With the symbols $\mathbf{E}$, $\bar{\mathbf{E}}$ and $\mathbb{R}^N$, the *environment space* (a three-dimensional Euclidean space), its associated *vector space* and the *N-dimensional Euclidean space* are indicated. The symbols $(\bar{e}_i)$ and $(\bar{r}_\alpha)$ indicate, respectively, a basis of $\mathbf{E}$ and a basis of $\mathbb{R}^N$. The symbol $\mathbf{D} \subseteq \mathbf{E}$ indicates the domain of a body. In the following of the manuscript, if not differently specified, spaces will be assumed to be three-dimensional with latin indexes running from 1 to 3; an exception is represented by *generalized* quantities defined in six-dimensional

spaces, for which the indices will run from 1 to 6. *Vectors* are indicated as $\bar{x} \in \bar{\mathbf{E}}$, with $\bar{x} = x_i\,\bar{e}_i$, while *second-order* and *fourth-order* tensors respectively by $\underline{x} \in \bar{\mathbf{E}} \otimes \bar{\mathbf{E}}$, with $\underline{x} = x_{ij}\,\bar{e}_i \otimes \bar{e}_j$, and by $\hat{\mathbf{x}} \in \bar{\mathbf{E}} \otimes \bar{\mathbf{E}} \otimes \bar{\mathbf{E}} \otimes \bar{\mathbf{E}}$, with $\hat{\mathbf{x}} = x_{ijk\ell}\,\bar{e}_i \otimes \bar{e}_j \otimes \bar{e}_k \otimes \bar{e}_\ell$. The tensors of *third-* and *fifth-order* used in this manuscript are of mixed type, and are represented respectively by $\check{\mathbf{x}} \in \mathbb{R}^N \otimes \bar{\mathbf{E}} \otimes \bar{\mathbf{E}}$, with $\check{\mathbf{x}} = x_{\alpha ij}\,\bar{r}_\alpha \otimes \bar{e}_i \otimes \bar{e}_j$, and by $\check{\mathbf{x}} \in \mathbb{R}^N \otimes \bar{\mathbf{E}} \otimes \bar{\mathbf{E}} \otimes \bar{\mathbf{E}} \otimes \bar{\mathbf{E}}$, with $\check{\mathbf{x}} = x_{\alpha ijk\ell}\,\bar{r}_\alpha \otimes \bar{e}_i \otimes \bar{e}_j \otimes \bar{e}_k \otimes \bar{e}_\ell$. The symbol $\cdot$ denotes both the standard dot product between vectors and the total contraction between tensors like, for example, $\bar{x} \cdot \bar{y} = x_i\,y_i$, $\underline{x} \cdot \bar{y} = x_{ij}\,y_j\,\bar{e}_i$, $\hat{\mathbf{x}} \cdot \underline{y} = x_{ijk\ell}\,y_{k\ell}\,\bar{e}_i \otimes \bar{e}_j$ and the other possible combinations. The same symbol is used, with a slight abuse of notation, also for contractions with mixed order tensor, like $\underline{x} \cdot \check{\mathbf{y}} = x_{ij}\,y_{\alpha ij}\,\bar{r}_\alpha$, since there is no risk of confusion between the different indexes. With the symbol $\otimes$, the standard tensorial product, as $\bar{x} \otimes \bar{y} = x_i\,y_j\,\bar{e}_i \otimes \bar{e}_j$ or $\underline{x} \otimes \underline{y} = x_{ij}\,y_{k\ell}\,\bar{e}_i \otimes \bar{e}_j \otimes \bar{e}_k \otimes \bar{e}_\ell$, is indicated. In case of mixed tensors, combinations are given, for example, by $\check{\mathbf{x}} \otimes \check{\mathbf{y}} = x_{\alpha ij}\,y_{\beta k\ell}\,\bar{r}_\alpha \otimes \bar{e}_i \otimes \bar{e}_j \otimes \bar{r}_\beta \otimes \bar{e}_k \otimes \bar{e}_\ell$. In some applications the Voigt notation will be used to represent second-order and fourth-order tensors; once a certain coordinates system has been fixed, a generic second-order tensor with dimension three $\underline{x}$ can be represented by means of an *array* with nine components, indicated with the symbol $\{\underline{x}\}$. In an analogus way, a fourth-order tensor with dimension three $\hat{\mathbf{x}}$ can be represented by means of a 9×9 matrix, indicated as $[\hat{\mathbf{x}}]$. It should be noted that the provided dimensions refer to a general three-dimensional case; in different situations (e.g., plane-strain or plane-stress states, or peculiar symmetries), the size of arrays and matrices in Voigt representation is minor, in general. Such dimensions will be also different for the Voigt representation of generalized quantities. The same symbols $\{\cdot\}$ and $[\cdot]$ are also used to indicate, respectively, arrays and matrices in numerical equations. In this manuscript, second-order and fourth-order *identity tensors* are expressed as

$$\underline{id} := \delta_{ij}\,\bar{e}_i \otimes \bar{e}_j, \quad \underline{id} \cdot \bar{a} = \bar{a} \tag{1.1}$$

$$\mathbf{I\hat{D}} := \delta_{ik}\,\delta_{j\ell}\ \ \bar{e}_i \otimes \bar{e}_j \otimes \bar{e}_k \otimes \bar{e}_\ell, \quad \mathbf{I\hat{D}} \cdot \underline{a} = \underline{a} \tag{1.2}$$

$$\mathbf{I\hat{D}}^T := \delta_{i\ell}\,\delta_{jk}\ \ \bar{e}_i \otimes \bar{e}_j \otimes \bar{e}_k \otimes \bar{e}_\ell, \quad \mathbf{I\hat{D}}^T \cdot \underline{a} = \underline{a}^T \tag{1.3}$$

$$\mathbf{I\hat{D}}^{sym} := \frac{1}{2}\left(\delta_{ik}\delta_{j\ell} + \delta_{i\ell}\delta_{jk}\right)\ \bar{e}_i \otimes \bar{e}_j \otimes \bar{e}_k \otimes \bar{e}_\ell, \quad \mathbf{I\hat{D}}^{sym} \cdot \underline{a} = \underline{a}^{sym} \tag{1.4}$$

$$\mathbf{I\hat{D}}^{skw} := \frac{1}{2}\left(\delta_{ik}\delta_{j\ell} - \delta_{i\ell}\delta_{jk}\right)\ \bar{e}_i \otimes \bar{e}_j \otimes \bar{e}_k \otimes \bar{e}_\ell, \quad \mathbf{I\hat{D}}^{skw} \cdot \underline{a} = \underline{a}^{skw} \tag{1.5}$$

The symbol $[\![\cdot]\!]$ indicates the jump of a certain quantity across a discontinuity surface, while the symbols $<\cdot,\cdot>_X$, $\|\cdot\|_X$, and $|\cdot|_X$ indicate, respectively, an inner product, a norm, and a seminorm, in a generic space X.

1.5   Tools

Different tools have been of fundamental importance for the realization of this thesis. The numerical simulations presented in Chapters 6 and 7, as well as the implementation exposed in Appendix C, have been realized in the **INSANE**[2] software (*INSANE - INteractive Structural ANalysis Environment*, n.d.), an open source project based on the Object-Oriented Paradigm (OOP), and written in **Java**. The figures representing finite element meshes and the corresponding contour plots presented in Chapters 6 and 7 have been extracted from the post-processor of the software **INSANE**, except for the contour plots of the localization indicators in the finite element models, which have been generated with the **Python** library **Matplotlib** (Hunter, 2007). The triangular background cells used for the construction of meshfree discretizations in Chapters 6 and 7, as well as the contour plots for the meshfree models in Chapters 6 and 7, have been generated with the software **Gmsh** (Geuzaine and Remacle, 2009). The conversion of input/output files between the software **INSANE** and **Gmsh**, as well as the numerical localization analyses exposed in Chapter 6, have been performed with author's own applications, available at his Git repository (`https://github.com/grLapo`). This text has been prepared in LaTeX, using the editor **Kile** (*Kile*, n.d.). Large part of the figures and plots have been generated with the **Tikz** (Tantau, 2013) and **Pgfplots** (*Pgfplots*, n.d.) libraries. Other figures have been prepared and edited with **Inkscape** (*Inkscape*, n.d.) and **Gimp** (*Gimp*, n.d.).

---

[2] More informations on the project can be found at `https://www.insane.dees.ufmg.br/`, while the development code is freely available at the Git repository `http://git.insane.dees.ufmg.br/insane/insane.git`.

Chapter 2

Modelling of quasi-brittle media

The main concepts and issues related to the modelling of quasi-brittle media are exposed. After a brief survey on the physical aspects of such media, some concepts of continuum damage mechanics are presented, focusing on the notion of damage variables and on a unified formulation for elastic-degrading constitutive models. The issue of localization is then recalled, together with discussions on different regularization techniques.

2.1   Physical aspects

The different behaviours that a material may exhibit at a *macro* scale (i.e., the scale at which a solid is idealized as a *continuous body*) can be collected in three main ideal categories:

- ductile;
- brittle;
- quasi-brittle.

A specimen of a *ductile* material, loaded in an uniaxial state, after an initial linear elastic phase presents a non-linear load-displacement relation; if the cause of the deformation is removed, the specimen unloads following a path that presents the same slope as the initial linear elastic phase. Once at the stress-free state, the specimen presents a *residual strain*, that constitutes the history of the deformation process; a new loading phase will start from that residual deformation following a path parallel to the initial elastic one (Fig. 2.1(a)).

If a material has a *brittle* response, it presents a limited (or absent) non-linear branch, with a sudden failure once a certain load level is reached (Fig. 2.1(b)). A *quasi-brittle* material may present a wide non-linear branch as a ductile one; it differs however from a ductile material for its unloading path, that at a stress-free state is characterized by *no residual strains* (Fig. 2.1(c)). In other words, according to Lemaitre and Desmorat:

(a) Ductile   (b) Brittle   (c) Quasi-brittle
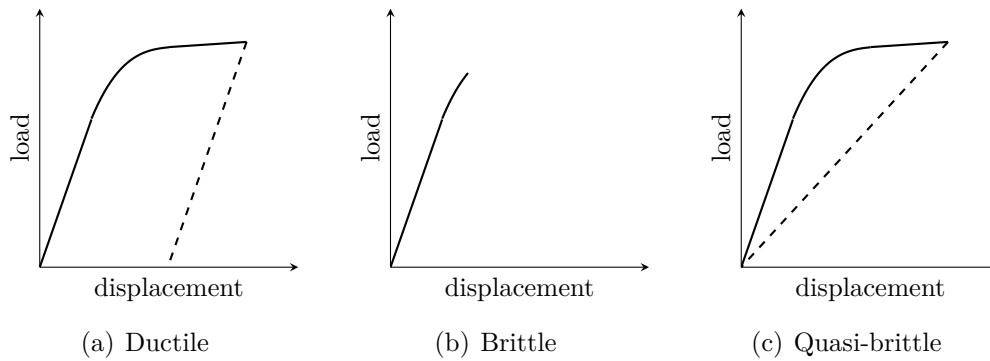
Figure 2.1: Material behaviours

> "A material is considered brittle when it brakes without any irreversible
> strains and without any dissipation prior to cracking [...]. It is consid-
> ered quasi-brittle when a dissipation prior to cracking exists with no or
> negligible permanent strains [...]."(Lemaitre and Desmorat, 2005, pag.
> 321)

In this case, the history of the deformation process is represented by the deterioration of the specimen stiffness, and a new loading branch starting from the stress-free configuration will follow a path different (with a less pronounced slope) from the initial elastic one.

The fact that a material belongs to one of the aforementioned categories is closely related to its characteristics at the *atomic* and the *micro* scales, and to the defects that it may present at such scales. At the atomic scale a solid is characterized by the geometry, topology and type of bonding of its atomic lattices (aggregates of atoms or molecules), and its defects are, among the others, atomic vacancies, dislocations, and disinclinations (Krajcinovic, 1996). The micro scale, in the words of Krajcinovic:

> "[...]refers to the range of lengths within which the solid is heteroge-
> neous and piece-wise continuous. Individual geometrical features of the
> microstructure (grains, chain-folded lamellae, fibers, etc.) are clearly
> recognizable. The deformation patterns are affected by grain and phase
> boundaries, inclusions, individual fibers, pores, grain size microcracks,
> and dislocation bands."(Krajcinovic, 1996, pag. 11)

At the macro scale, described before, the defects are constituted by macrocracks, notches, large perforations and shear bands, for example.

A ductile response is tipical of polycrystalline solids (e.g., metals and alloys[1]), that exhibit *plastic* deformations due to material flows through the lattices, like as grain sliding on crystallographic planes or dislocations flow, for example (Asaro (1983), Havner (1992)

---

[1] It is remarked that not all metals and alloys present a ductile behaviour. Furthermore, their be-
haviour may be influenced by factors that are not intrinsic to the material, like as temperature and
loading conditions, for example.

and Lubliner (2008)). The residual strains represent a measure of the effects of mutations at atomic and micro scales on the deformation at the macro scale of the body. If during the plastic process the number of bonds between the materials particles is *unaltered* (i.e., if the plastic mutations don't alter the connections among the particles of the body), also the elastic moduli of the material remain unaltered, resulting in an unloading-reloading path parallel to the initial elastic one (Fig. 2.1(a)). Ductile materials may fail because of *ductile fracture* (Fig. 2.2). In this case, the rupture of bonds between material particles may be caused by atomic decohesion due to dislocations piling in metals or by nucleation, growth and coalescence of microvoids (i.e., cavities of microscopic size) near inclusions and second-phase particles in metal alloys, which may lead to the formation of a macrocrack (Puttick (1959), Benzerga and Leblond (2010), Lemaitre and Desmorat (2005) and Chen and Butcher (2013)). The ductile behaviour is due to the fact that the crack tip, in this case, is blunted by dislocations emitting from the crack tip itself, and requires a large amount of energy to propagate (Rice (1992) and Rice and Thomson (1974)).
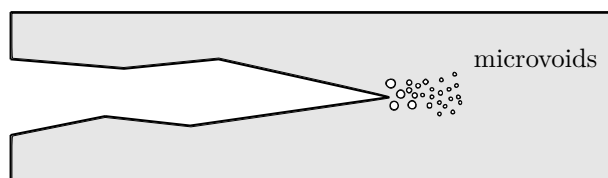
Figure 2.2: Fracture by microvoids nucleation

Rather than to material flow and microvoids nucleation, the non-linear behaviour of brittle and quasi-brittle media "is associated with the loss of interatomic bonds which is manifested on the micro scale as the nucleation and growth of microcracks" (Krajcinovic, 1996, pag. 17). Microcracks are the typical defects of brittle and quasi-brittle media, and differ from microvoids for their geometrical characteristics. While the latter can be described as cavities in the crystal structure of a metal, with no singular points, the former can be defined as "flat defects with an atomically sharp tip" (Krajcinovic, 1996, pag. 19), i.e., surfaces that form in a material, across which the continuity is lost.
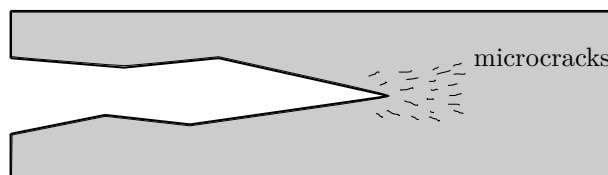
Figure 2.3: Fracture by microcracks nucleation

Most ceramics, glasses, and steels at low temperature belong to the class of brittle materials. The deformation process in this case is dominated by the propagation of a

small number of macrocracks, that may initiate in correspondence to existing defects, like as notches or pre-existing cracks, that is, at stress concentrations, in general (Fig. 2.3). Such materials present a limited non-linear deformation branch and an abrupt rupture (Fig. 2.1(b)), due to the fact that all the energy imparted by external loads is dissipated with the formation of microcracks in the direction of propagation of the macrocracks, leading to a rapid failure (the so-called crack growth-dominated process).

In quasi-brittle media, instead, the deformation process is dominated by the formation of microcracks that nucleate randomly over large parts of a specimen (the so-called nucleation-dominated process). Rather than because of stress concentrations, microcracks initiate due to the rupture of weak material bonds scattered across a specimen. Only part of them will assemble into a cluster, leading eventually to the formation of a macrocrack, and most of the imparted energy will be dissipated by micro defects nucleation across large parts of the specimen. The fact that in such materials microcracks may form without gathering into a macrocrack is due to their *heterogeneity* at the micro scale. When the material is heterogeneous at the micro scale, a microcrack may initiate and its growth be arrested by a material particle with higher fracture strength. In this case a large number of microcracks may nucleate, inducing a non-linear behaviour with dissipation of energy, without necessarily form a macrocrack that may lead to an abrupt failure. Brittle materials, on the contrary, are characterized by an homogeneous micro scale; when microcracks initiate due to stress concentrations they find no obstacles and are free to gather into one or more macrocracks. Heterogeneity at the micro scale is a characteristic of materials like concrete (Fig. 2.4), rocks, coarse-grained ceramics and most fibre-reinforced materials.
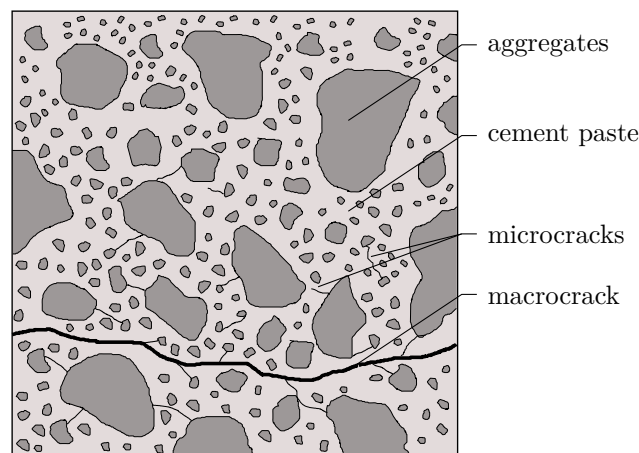
Figure 2.4: Concrete microstructure

The following sections will be devoted specifically to the class of quasi-brittle materials, considering both modelling aspects and common issues related to their numerical analysis. Before proceeding further, it should be remarked that the material models recalled in this section represent *idealized* material behaviours. If submitted to an experimental test, a

real specimen will be neither purely ductile nor purely brittle (or quasi-brittle) and will present, in general, a mixed behaviour. Moreover, in some cases, a certain behaviour could be not only an intrinsic property of a material but it could also depend on other factors (see, e.g., Nemat-Nasser and Chang (1990)) such as the stress state and the loading rate, for example (see, e.g., the so-called *brittle-to-ductile* transition phenomenom).

2.2   Continuum damage approach

As discussed in the previous section, the degradation of a quasi-brittle medium is a complex phenomenom which strongly depends on the heterogeneous character of the medium microstructure. Among the different strategies for the modelling of such materials this work focuses on *continuum damage mechanics*[2] [3]. Within this approach a quasi-brittle medium is modelled at the macro scale as a *continuum* body for the whole loading process[4]. As it will be specified in Section 2.2.1, here the term *damage* refers to the defects of a material at the micro scale, that is, microvoids and microcracks, that are responsible for the deterioration of its elastic properties. The discontinuous effect of these defects is taken into account by means of continuous field variables, the so-called *damage variables.* As it will be discussed in Section 2.2.2, these damage variables will be considered as *state variables* in the treatment of quasi-brittle media within the thermodynamics of irreversible processes.

A fundamental concept for the transition from the heterogeneous representation of the micro scale of a material to the continuous description at its macro scale is the one of *representative volume element* (RVE). In a material the RVE can be defined as

> "[...]a sample[, of that material,] that (a) is structurally entirely typical of the whole mixture on average, and (b) contains a sufficient number of inclusions for the apparent overall moduli to be effectively independent of the surface values of traction and displacement, so long as these values are 'macroscopically uniform.' That is, they fluctuate about a mean with a wavelength small compared with the dimensions of the sample, and the effects of such fluctuations become insignificant within a few wavelengths of the surface. The contribution of this surface layer to any average can

---

[2] For an exhaustive treatment on continuum damage mechanics and other modelling strategies like, for example, statistical models, lattice models, and micromechanical models, the reader may refer to the book by Krajcinovic (Krajcinovic, 1996).

[3] The first applications of the concept of continuum damage mechanics in concrete started in the 1980s with the works of Mazars (Mazars and Lemaitre, 1984, Mazars and Pijaudier-Cabot, 1989), devoted to its simplest *scalar* form.

[4] Eventually, a transition to a *discrete damage model* could be considered in order to take into account the formation of a macrocrack, as a discontinuity in the smooth fields describing the kinematics of the body (see, e.g., de Borst and Abellan (2002), de Borst, Remmers, Needleman and Abellan (2004)). However, this approach is not considered in the present work.

> be made negligible by taking the sample large enough."(Hill, 1963, pag.
> 359)

More concisely, the RVE can be identified also as

> "[...]the smallest volume on which a density may represent a field of
> discontinuous properties."(Lemaitre and Dufailly, 1987, pag. 644)

The heterogeneous material properties and the scattered defects at the micro scale are averaged in order to obtain an *effective continuum* approximation, where each point of the continuum model is characterized by such averaged quantities. The size of an RVE depends both on the material microstructure and on the defects at the micro scale; its linear size may vary from 0.05 to 0.5 mm for metals, and from 10 to 100 mm for concrete, for example.

As it will be discussed in Section 2.2.2, the degradation of a quasi-brittle material due to defects at the micro scale is represented mathematically as the evolution of its elastic properties. In an uniaxial state, for example, the Young's modulus passes from an initial value one E, to a *secant* value E^S, which evolves during the loading process (Fig. 2.5). In a more general case the degradation will be represented in terms of the whole constitutive operator that, in a loading process, will pass from an intial value $\hat{\mathbf{E}}$ to a secant one $\hat{\mathbf{E}}^S$. This strategy for the representation of the behaviour of quasi-brittle media is usually referred to as *elastic degradation*, since it aims to describe the evolution of the elastic properties of a material; a damage model is obtained when such evolution is represented in terms of *damage variables.*
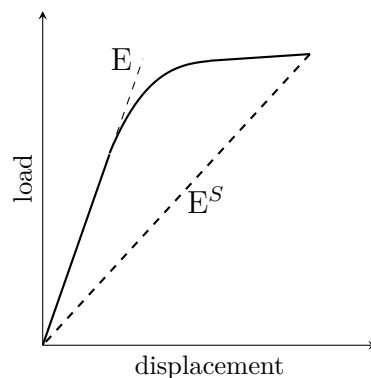
Figure 2.5: Elastic properties degradation

Remark 2.1: Computational approaches to damage

Besides continuum damage mechanics, two other approaches widely applied to the computational modelling of quasi-brittle media, and specifically of concrete, are the *discrete* and *smeared* crack models.

A first application of the *discrete* approach to concrete can be found in the work of Ngo and Scordelis (1967), where the crack was introduced as a geometric entity, allowed to grow in correspondence of a certain tensile strength criterion attained at the crack tip. Departing from the initial applications based on the concepts of *linear elastic fracture mechanics* (Griffith, 1921), important results in the analysis of quasi-brittle materials were obtained with the introduction of the *cohesive discontinuity* method (Dugdale, 1960, Barenblatt, 1962, Hillerborg et al., 1976, Needleman, 1987). Further improvements of the method aimed to solve one of its main drawbacks, i.e., the strong dependency of the crack path on the topology of the mesh, requiring the use of re-meshing procedures (Ingraffea and Saouma, 1987) or the application of *meshfree* methods (Belytschko and Black, 1999, Moes et al., 1999, Rabczuk and Belytschko, 2004, 2007).

An initial version of the *smeared* approach applied to concrete analysis was proposed by Rashid (1968), and later developed by Suidan and Schnobrich (1973), Bažant and Oh (1983) and Rots et al. (1985). Differently from the discrete approach, in this case the cracks are not explicitly represented, but are introduced as a degradation of the elements stiffness. Analogies between the smeared crack approach and continuum damage mechanics were pointed out by de Borst and Gutiérrez (1999) and de Borst (2002).

Both discrete and continuous approaches to fracture have a consistent physical basis in the field of quasi-brittle materials failure. Indeed, while the geometrical discontinuity proper of the discrete approach appears to be the most natural way to represent the final phases of failure process, where the microcracks tend to coalesce into one or more macrocracks, the continuous concept is a practical resource for the representation of the complex phenomena involved in the microcracks nucleation process, i.e., microcracks initiation, growth and coalesces (Rots and Blaauwendraad, 1989). Based on these considerations, the combination of the two approaches has been recently investigated in a number of works (see, e.g., de Borst and Abellan (2002) and de Borst, Remmers, Needleman and Abellan (2004)).

2.2.1   Damage variables

As discussed in the previous section, the damage variables represent a way to quantify the presence of microdefects in terms of continuous field variables. From a physical point of view, the damage can be defined as the surface density of microcracks and intersection of microvoids lying on a plane cutting a certain RVE (Lemaitre and Dufailly, 1987). Such density, that is a function of the plane orientation represented by its normal $\bar{n}$, is expressed as

$$D(\bar{n}) := \frac{S_D}{S} \tag{2.1}$$

where S is the cross-section of the cutted RVE and S_D the area of the defects at the cutting plane (Fig. 2.6). As it has been defined, this density represents a damage variable that goes from 0 (undamaged material) to 1 (completely damaged material); alternatively, an integrity variable, defined as $i(\bar{n}) := 1 - D(\bar{n})$, can be considered.
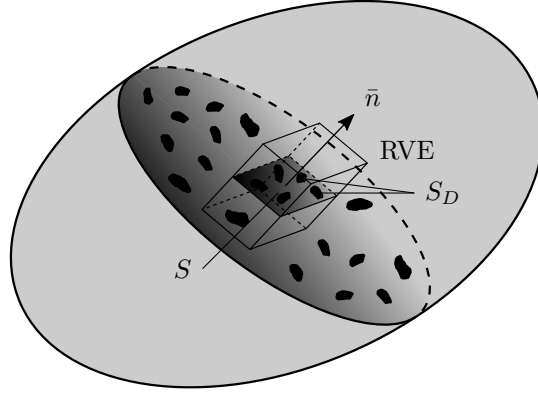
Figure 2.6: Damage representation on a RVE

Alongside the *nominal*[5] stresses and strains, i.e., the ones defined on the idealized continuum body, in the context of damage mechanics the concept of *effective* stresses and strains is usually introduced (see, e.g., Rabotnov (1968), Simo and Ju (1987), Rizzi (1995) and Lemaitre and Desmorat (2005)). Such quantities are defined as the stress and the strain which the undamaged material between the microdefects is subjected to. The relation between effective stresses and strains is assumed to be described by the same constitutive law of the *undamaged* material, considered as linear elastic (see, e.g., Carol et al. (2001*a*))

$$\underline{\sigma}^{eff} = \hat{\mathbf{E}} \cdot \underline{\varepsilon}^{eff} \rightarrow \sigma_{ij}^{eff} = E_{ijkl}\, \varepsilon_{kl}^{eff} \tag{2.2}$$

The passage from effective to nominal quantities involves the use of damage variables. First, the rule defining the passage from effective to nominal of one of the quantities, the stress or the strain, should be fixed in terms of damage variables. Then, the transformation of the remaining quantity may be perfomed through one of the following *equivalence conditions*:

- strain equivalence;
- stress equivalence;
- energy equivalence.

In the first case, the nominal and effective strains are assumed to be coincident, while the nominal stress depends on the effective one by mean of a fourth-order tensor $\hat{\alpha}$ measuring the average effect of distributed defects, resulting in the following secant constitutive

---

[5] The nominal stresses and strains are the ones that can be measured *externally* using, for example, the initial cross-section and length of a specimen during a test, without taking into account their evolution. Mathematically, they are the one that satisfy equilibrium and compatibility conditions at the macro scale.

operator

$$\underline{\varepsilon} = \underline{\varepsilon}^{eff}, \qquad \underline{\sigma} = \hat{\alpha} \cdot \underline{\sigma}^{eff}, \qquad E^S_{ijkl} = \alpha_{ijmn} E_{mnkl} \tag{2.3}$$

On the contrary, the stress equivalence assumes the nominal and effective stresses to be coincident, with the nominal strain depending again on a fourth-order tensor $\hat{\alpha}$; this results in the expressions

$$\underline{\sigma} = \underline{\sigma}^{eff}, \qquad \underline{\varepsilon}^{eff} = \hat{\alpha} \cdot \underline{\varepsilon}, \qquad E^S_{ijkl} = E_{ijmn} \alpha_{mnkl} \tag{2.4}$$

It is emphasized that both the aforementioned approaches don't transmit to $\hat{\mathbf{E}}^S$, in general, the major symmetry of $\hat{\mathbf{E}}$, that instead are maintained by the energy equivalence method, expressed by $\underline{\sigma} \cdot \underline{\varepsilon} = \underline{\sigma}^{eff} \cdot \underline{\varepsilon}^{eff}$. In this case two different approaches are possible, resulting in the following sets of equations

$$\underline{\sigma} = \hat{\alpha}^* \cdot \underline{\sigma}^{eff}, \quad \underline{\varepsilon}^{eff} = \hat{\alpha}^* \cdot \underline{\varepsilon}, \quad E^S_{ijkl} = \alpha^*_{ijpq} E_{pqrs} \alpha^*_{klrs} \tag{2.5}$$

$$\underline{\sigma}^{eff} = \hat{\alpha} \cdot \underline{\sigma}, \quad \underline{\varepsilon} = \hat{\alpha} \cdot \underline{\varepsilon}^{eff}, \quad E^S_{ijkl} = \alpha_{pqij} E_{pqrs} \alpha_{rskl} \tag{2.6}$$

where the tensors $\hat{\alpha}^*$ and $\hat{\alpha}$ are such that $\alpha^*_{ijpq} \alpha_{pqkl} = \alpha_{ijpq} \alpha^*_{pqkl} = ID^{sym}_{ijkl}$.

Once one of the previous methods is adopted, damage variables can be introduced in a model in different ways. The most common approach is the one of *scalar-isotropic*[6] damage, where the damage is described in terms of a single *scalar* variable, while more complex models consider the effects of the material degradation in terms of *second-order* or *fourth-order* tensors.

2.2.1.1 Scalar damage

The simplest approach to material degradation in terms of scalar variables is represented by the *scalar-isotropic* damage model. There, a single damage variable independent on the direction (i.e., isotropic) is considered (Kachanov, 1958). Recalling the representation within the strain equivalence condition, such model can be obtained by setting $\hat{\alpha} = i\,\hat{\mathbf{id}}$, where i is an integrity variable varying from 1 (virgin material) to 0 (fully damaged material). From Eq. (2.3), considering the damage variable D such that $i = 1 - D$, the well-known form of scalar-isotropic damage is recovered

$$\hat{\mathbf{E}}^S = (1 - D)\,\hat{\mathbf{E}} \tag{2.7}$$

---

[6] In the literature such form of damage is usually referred to simply as *isotropic* damage or as *scalar* damage. The term *scalar* refers to the nature of the scalar variable, while the term *isotropic* indicates the effect on the secant constitutive operator. However, it should be noted that such nomenclatures, when adopted independently may be ambiguous since, as recalled in this section, there are scalar models that are not isotropic, and isotropic models that are not described in terms of a single damage variable. In order to avoid confusion, in the following the classic damage expression $\hat{\mathbf{E}}^S = (1 - D)\,\hat{\mathbf{E}}$ will be referred to as *scalar-isotropic*.

Such model is labelled as isotropic since it affects in the same way all the components of the initial constitutive operator $\hat{\mathbf{E}}$; an eventual isotropy of such tensor is not destroyed by the damage variable.

This form of damage can be generalized in such a way to obtain a scalar damage format where the components of the initial constitutive operator are modified with different weights; the following expression can be adopted (see, e.g., Ortiz (1985))

$$\hat{\mathbf{E}}^S = \hat{\mathbf{E}} + \lambda(D)\,\hat{\mathbf{M}}^* \tag{2.8}$$

where $\hat{\mathbf{M}}^*$ is a fourth-order tensor defining the directions where damage takes place, and $\lambda(D)$ is a function depending on the damage variable and eventually on the elastic material parameters. If $\hat{\mathbf{M}}^*$ is isotropic the damage model is also referred to as isotropic; on the contrary, if $\hat{\mathbf{M}}^*$ is anisotropic, also the damage model is referred to as anisotropic. In the latter case, the scalar damage creates an anisotropic effect on the secant operator.

Other common forms of scalar damage include orthotropic models based on a single damage variable (de Borst and Gutiérrez, 1999), unilateral damage models that use two scalar variables in order to distinguish between damage in tension and compression (see, e.g., Ladevèze (1983), Mazars and Pijaudier-Cabot (1989), Mazars et al. (1990), Comi and Perego (2001) and Cervera and Tesei (2017)), and models that use more than one damage variable in order to describe the different damage mechanisms that may verify in a material (see, e.g., Ladevèze (1983) and Lemaitre and Desmorat (2005) where different variables are used to represent the damage mechanisms in composite materials).

2.2.1.2 Tensorial damage

When the dependence of the damage on the considered direction cannot be neglected, more complex representations must be adopted. In order to obtain a natural representation of the anistropy of the material degradation, the damage is usually represented in terms of second-order and fourth-order tensors (Krajcinovic, 1996, Lemaitre and Desmorat, 2005). Despite the importance of such representations they are not recalled here since this work, as it will be shown in Section 3.3, focuses on the degradation of micropolar media described in terms of scalar-isotropic damage models.

2.2.2 Unified formulation for constitutive models

As discussed before, the models of continuum damage mechanics that will be adopted here belong to the general class of *elastic-degrading* models, that is, models where the degradation of a material is represented in terms of the evolution of its elastic properties. While the theory of *elasto-plasticity* has a long tradition in the scientific and the engineering communities, with both theoretical and numerical aspects well-established

in the literature (see, e.g., Hill (1998), Simo and Hughes (1998), and Lubliner (2008)), the development of the theory of *elastic degradation* has been less uniform, with numerous mutually independent contributions (see, e.g., Carol et al. (1994) for some historical comments).

In the last years a lot of efforts have been made in order to collect the various independent contributions to the field of elastic degradation in a unified theoretical framework. One of the first comprehensive attempts of unification can be found in Carol et al. (1994), where the authors proposed a framework for the representation of different elastic-degrading models in terms of secant constitutive operators, a single loading function (i.e., monodissipative models), and degradation/flow rules, as in the case of elasto-plasticity. The inclusion of existent scalar damage models in the same framework was also explicitly illustrated. Subsequent contributions (see, e.g., de Borst (1987), Carol et al. (1994), Rizzi (1995), Carol and Willam (1996), Carol (1996), de Borst and Gutiérrez (1999), Armero and Oller (2000*a*,*b*), Carol et al. (2001*a*,*b*), and Hansen et al. (2001)) resulted in a multi-dissipative unified formulation where, in analogy to multisurface plasticity (see, e.g., Simo and Hughes (1998)), the different constitutive models can be represented in terms of secant constitutive operators, loading functions, and degradation/flow rules. At the heart of such formulation there is a tensorial formalism that guarantees the generality of the formulation (Rizzi and Carol, 2001), allowing to represent the main theoretical concepts independently on the peculiar constitutive models. Such generality also allows to perform various investigations on different constitutive models using as a basis their tensor-based general equations. An example is constituted by the studies by Rizzi and his co-authors on localization in mono and multidissipative elastic-degrading models (Rizzi et al., 1995, 1996), performed on the general tensor-based equations, without having to deal with the specificities of each peculiar model; the same approach was followed by the author in Gori et al. (2017*b*), as discussed in Chapter 5. As it will be discussed in Appendix C, this unified formulation, with its tensorial formalism, offers benefits also from a computational point of view, since it eases the implementation efforts for a large class of constitutive models, as shown by the *object-oriented* implementation presented in Penna (2011) and Gori et al. (2017*a*). In the following, the main aspects of this multidissipative formulation are briefly recalled[7], since they will be used in Section 3.3 to define an analogous theoretical framework for elastic-degrading micropolar media. Before proceeding further it is remarked that despite it is possible to couple elastic degradation with plastic effects in the same multidissipative representation, here the presence of plastic dissipation mechanisms is excluded.

In a geometrically linear context, an elastic-degrading medium is characterized by the

---

[7] The paragraphs that follow are mainly an excerpt of the treatment on the same subject contained in the paper by Gori et al. (2017*a*).

following *total* stress-strain relations

$$\underline{\sigma} = \hat{\mathbf{E}}^S \cdot \underline{\varepsilon}, \qquad \underline{\varepsilon} = (\hat{\mathbf{E}}^S)^{-1} \cdot \underline{\sigma} \tag{2.9}$$

where $\hat{\mathbf{E}}^S$ is the *secant* constitutive operator. These equations correspond to the assumption of an *unloading-reloading* process where the stiffness remains equal to the current secant one; in this case, a full unload leads to zero permanent strains. The rate form of the expressions in Eq. (2.9) results in the equations

$$\underline{\dot{\sigma}} = \hat{\mathbf{E}}^S \cdot \underline{\dot{\varepsilon}} + \dot{\hat{\mathbf{E}}}^S \cdot \underline{\varepsilon} = \underline{\dot{\sigma}}^e + \underline{\dot{\sigma}}^d, \qquad \underline{\dot{\varepsilon}} = (\hat{\mathbf{E}}^S)^{-1} \cdot \underline{\dot{\sigma}} + (\dot{\hat{\mathbf{E}}}^S)^{-1} \cdot \underline{\sigma} = \underline{\dot{\varepsilon}}^e + \underline{\dot{\varepsilon}}^d \tag{2.10}$$

where the superscripts e and d indicate, respectively, the *elastic* and the *degrading* parts of a quantity[8]. The previous expressions can be resumed in the tangent relations

$$\underline{\dot{\sigma}} = \hat{\mathbf{E}}^t \cdot \underline{\dot{\varepsilon}}, \qquad \underline{\dot{\varepsilon}} = (\hat{\mathbf{E}}^t)^{-1} \cdot \underline{\dot{\sigma}} \tag{2.11}$$

where the *tangent* constitutive operator $\hat{\mathbf{E}}^t$ has the following general representation

$$\hat{\mathbf{E}}^t = \hat{\mathbf{E}}^S - \underline{z}^{-1} \cdot (\check{\mathbf{x}} \otimes \check{\mathbf{y}}) = (E^S_{ijk\ell} - (z_{\alpha\beta})^{-1} \, x_{\beta ij} \, y_{\alpha k\ell}) \, \bar{e}_i \otimes \bar{e}_j \otimes \bar{e}_k \otimes \bar{e}_\ell \tag{2.12}$$

which specific expression depends on the chosen approach.

Remark 2.2

In analogy to multisurface plasticity, multidissipative elastic-degrading models consider a generic number N of dissipation mechanisms. Such number reduces to one in the case of monopotential models (see, e.g., Carol et al. (1994)), resulting in

$$\hat{\mathbf{E}}^t = \hat{\mathbf{E}}^S - \frac{1}{z} \cdot \left(\underline{x} \otimes \underline{y} \right) = \left(E^S_{ijk\ell} - \frac{1}{z} \, x_{ij} \, y_{k\ell} \right) \, \bar{e}_i \otimes \bar{e}_j \otimes \bar{e}_k \otimes \bar{e}_\ell \tag{2.13}$$

In the previous Eq. (2.12), the indices α and β refer to such dissipation mechanisms and run from 1 to N.

A first approach, referred to as *stress-based* approach, relies on the additive decomposition of the strain rate, $\underline{\dot{\varepsilon}} = \underline{\dot{\varepsilon}}^e + \underline{\dot{\varepsilon}}^d$. Within this approach, the inelastic rate $\underline{\dot{\varepsilon}}^d$ and the rate of the inverse of the secant constitutive operator are defined in terms of the

---

[8] In the decompositions expressed by Eq. (2.10), the same notations introduced in Carol et al. (1994) for the classic continuum theory have been adopted. At this point, an analogy with the concept of coupled-media (elasto-plastic coupling, i.e., dependence of the elastic moduli on the plastic deformation Maier and Hueckel (1979)) can be made. The *elastic* and *degrading* components defined here can be identified as the *reversible* and *irreversible* components defined in Collins and Houlsby (1997). However, differently from the elasto-plastic coupling, in the present work the elastic properties depend only on the elastic degradation of the material and no plastic behaviour is accounted for.

degradation rules

$$\dot{\underline{\varepsilon}}^d = \sum_{\beta=1}^{N} \dot{\lambda}_\beta \, \underline{m}^{(\beta)} = \dot{\bar{\lambda}} \cdot \check{\mathbf{m}}, \qquad (\dot{\hat{\mathbf{E}}^S})^{-1} = \sum_{\beta=1}^{N} \dot{\lambda}_\beta \, \hat{\mathbf{M}}^{(\beta)} = \dot{\bar{\lambda}} \cdot \check{\mathbf{M}} \qquad (2.14)$$

where $\dot{\bar{\lambda}} \in \mathbb{R}^N$ is the vector containing the N *inelastic multipliers*, $\check{\mathbf{m}}$ the third-order tensor containing the N *directions of degradation* $\underline{m}^{(\beta)}$ of the strain degrading rate, each one represented as a second-order tensor, and $\check{\mathbf{M}}$ the fifth-order tensor containing the N directions of degradation $\hat{\mathbf{M}}^{(\beta)}$ of the inverse of the secant constitutive operator, each one represented by a fourth-order tensor. It can be easily shown that the relation $\check{\mathbf{m}} = \check{\mathbf{M}} \cdot \underline{\sigma}$ holds. The different phases of the loading process are described in terms of N *loading functions* $f_\alpha(\underline{\sigma}, \pi)$, that can be collected in a vector $\bar{f} \in \mathbb{R}^N$, each one depending on the stress state $\underline{\sigma}$ and on a generic set of internal variables π, that in a thermodynamical context are referred to as *thermodynamical forces*. Like the inelastic strain rate, also the thermodynamical forces rate can be expressed in terms of a degradation rule as

$$\dot{\pi} = \sum_{\beta=1}^{N} \dot{\lambda}_\beta \, h^{(\beta)} \qquad (2.15)$$

where the terms $\dot{\lambda}_\beta$ are inelastic multipliers, and the terms $h^{(\beta)}$ are the directions of degradation of the set π. Within this approach, the operators appearing in Eq. (2.12) are represented by

$$\check{\mathbf{x}} := \hat{\mathbf{E}}^S \cdot \check{\mathbf{m}} = (E^S_{ijpq} \, m_{\beta pq}) \, \bar{r}_\beta \otimes \bar{e}_i \otimes \bar{e}_j \qquad (2.16)$$

$$\check{\mathbf{y}} := \check{\mathbf{n}} \cdot \hat{\mathbf{E}}^S = (n_{\alpha vz} \, E^S_{vzk\ell}) \, \bar{r}_\alpha \otimes \bar{e}_k \otimes \bar{e}_\ell \qquad (2.17)$$

$$\underline{z} := \underline{H} + \check{\mathbf{n}} \cdot (\hat{\mathbf{E}}^S \cdot \check{\mathbf{m}}) = (H_{\alpha\beta} + n_{\alpha mn} \, E^S_{mnrs} \, m_{\beta rs}) \, \bar{r}_\alpha \otimes \bar{r}_\beta \qquad (2.18)$$

where the terms $\check{\mathbf{n}}$ and $\underline{H}$ are the gradients of the loading functions, defined by

$$\check{\mathbf{n}} := \frac{\partial f_\alpha}{\partial \sigma_{vz}} \, \bar{r}_\alpha \otimes \bar{e}_v \otimes \bar{e}_z, \qquad \underline{H} := -\frac{\partial f_\alpha}{\partial \pi} h^{(\beta)} \, \bar{r}_\alpha \otimes \bar{r}_\beta = -\frac{\partial f_\alpha}{\partial \lambda_\beta} \, \bar{r}_\alpha \otimes \bar{r}_\beta \qquad (2.19)$$

The so-called *strain-based* approach, on the contrary, relies on the additive decomposition for the stress rate, $\dot{\underline{\sigma}} = \dot{\underline{\sigma}}^e + \dot{\underline{\sigma}}^d$. In this case, the inelastic rate $\dot{\underline{\sigma}}^d$ and the rate of the secant constitutive operator are defined in terms of the *degradation rules*

$$\dot{\underline{\sigma}}^d = \sum_{\beta=1}^{N} \dot{\lambda}_\beta \, \underline{m}^{*(\beta)} = \dot{\bar{\lambda}} \cdot \check{\mathbf{m}}^*, \qquad \dot{\hat{\mathbf{E}}^S} = \sum_{\beta=1}^{N} \dot{\lambda}_\beta \, \hat{\mathbf{M}}^{*(\beta)} = \dot{\bar{\lambda}} \cdot \check{\mathbf{M}}^* \qquad (2.20)$$

where $\dot{\bar{\lambda}} \in \mathbb{R}^N$ is again a vector containing the N *inelastic multipliers*, $\check{\mathbf{m}}^*$ the third-order tensor containing the N *directions of degradation* $\underline{m}^{*(\beta)}$ of the stress degrading rate, each one represented as a second-order tensor, and $\check{\mathbf{M}}^*$ the fifth-order tensor containing the N

directions of degradation $\hat{\mathbf{M}}^{*(\beta)}$ of the secant constitutive operator, each one represented by a fourth-order tensor. It can be easily shown that the relation $\check{\mathbf{m}}^* = \check{\mathbf{M}}^* \cdot \underline{\varepsilon}$ holds. As for the stress-based approach, a set of N *loading functions* $f_\alpha(\underline{\varepsilon}, \pi^*)$ describes the different phases of the loading process. In this case, each loading function depends on the strain state $\underline{\varepsilon}$ and on a generic set of internal variables π^*. Like the inelastic stress rate, also the thermodynamical forces rate $\dot{\pi}^*$ can be expressed in terms of a degradation rule as

$$\dot{\pi}^* = \sum_{\beta=1}^{N} \dot{\lambda}_\beta \ h^{*(\beta)} \tag{2.21}$$

where the terms $\dot{\lambda}_\beta$ are inelastic multipliers, and the terms $h^{*(\beta)}$ are the directions of degradation for the set π^*. Within this approach, the operators appearing in Eq. (2.12) are represented by

$$\check{\mathbf{x}} := -\check{\mathbf{m}}^* = m_{\beta ij} \ \bar{r}_\beta \ \otimes \bar{e}_i \otimes \bar{e}_j \tag{2.22}$$

$$\check{\mathbf{y}} := \check{\mathbf{n}}^* = n^*_{\alpha k\ell} \ \bar{r}_\alpha \otimes \bar{e}_k \otimes \bar{e}_\ell \tag{2.23}$$

$$\underline{z} := \underline{H}^* = H^*_{\alpha\beta} \ \bar{r}_\alpha \otimes \bar{r}_\beta \tag{2.24}$$

where the terms $\check{\mathbf{n}}^*$ and $\underline{H}^*$ are the gradients of the loading functions, defined by

$$\check{\mathbf{n}}^* := \frac{\partial f_\alpha}{\partial \varepsilon_{k\ell}} \ \bar{r}_\alpha \otimes \bar{e}_k \otimes \bar{e}_\ell, \qquad \underline{H}^* := -\frac{\partial f_\alpha}{\partial \pi^*} h^{*(\beta)} \ \bar{r}_\alpha \otimes \bar{r}_\beta = -\frac{\partial f_\alpha}{\partial \lambda_\beta} \ \bar{r}_\alpha \otimes \bar{r}_\beta \tag{2.25}$$

Within this general framework for elastic degradation, damage models can be obtained once the secant material properties are assumed to depend on a reduced set of parameters, the *damage variables*, as $(\hat{\mathbf{E}}^S)^{-1}((\hat{\mathbf{E}})^{-1}, \mathcal{D})$ for the stress-based approach, and $\hat{\mathbf{E}}^S(\hat{\mathbf{E}}, \mathcal{D}^*)$ for the strain-based approach. The symbols $\mathcal{D}$ and $\mathcal{D}^*$, representing the sets of damage variables for the stress- and the strain-based approaches, may indicate, in general, scalar, vectorial or tensorial damage variables (Rizzi, 1995, Ju, 1990). For a damage model, the rate of the secant constitutive operator can be expressed as

$$(\dot{\hat{\mathbf{E}}}^S)^{-1} = \frac{\partial (\hat{\mathbf{E}}^S)^{-1}}{\partial \mathcal{D}} * \dot{\mathcal{D}}, \qquad \dot{\hat{\mathbf{E}}}^S = \frac{\partial \hat{\mathbf{E}}^S}{\partial \mathcal{D}^*} * \dot{\mathcal{D}}^* \tag{2.26}$$

where with the symbol $*$, a contraction operation compatible with the peculiar nature of the damage variables sets is indicated. The rates of the damage variables sets can be expressed in terms of the following degradation rules

$$\dot{\mathcal{D}} = \sum_{\beta=1}^{N} \dot{\lambda}_\beta \ \mathcal{M}^{(\beta)} = \dot{\bar{\lambda}} \cdot \mathcal{M}, \qquad \dot{\mathcal{D}}^* = \sum_{\beta=1}^{N} \dot{\lambda}_\beta \ \mathcal{M}^{*(\beta)} = \dot{\bar{\lambda}} \cdot \mathcal{M}^* \tag{2.27}$$

where $\dot{\bar{\lambda}} \in \mathbb{R}^N$ is the vector of inelastic multipliers while $\mathcal{M}$ and $\mathcal{M}^*$ contain, respectively,

the N directions of degradation $\mathcal{M}^{(\beta)}$ and $\mathcal{M}^{*(\beta)}$ of the sets of damage variables $\mathcal{D}$ and $\mathcal{D}^*$. The directions of degradation of the damage variables sets and the ones of the secant constitutive operator are linked by the relations

$$\breve{\mathbf{M}} = \frac{\partial(\hat{\mathbf{E}}^S)^{-1}}{\partial \mathcal{D}} * \mathcal{M}, \qquad \breve{\mathbf{M}}^* = \frac{\partial \hat{\mathbf{E}}^S}{\partial \mathcal{D}^*} * \mathcal{M}^* \tag{2.28}$$

2.2.2.1 Scalar-isotropic damage models

As shown in Eq. (2.7), scalar-isotropic damage models are characterized by a secant constitutive operator that depends on the initial elastic one and on a single scalar damage variable, $\hat{\mathbf{E}}^S(D, \hat{\mathbf{E}}) = (1 - D)\,\hat{\mathbf{E}}$. Considering the contents of the previous section, scalar-isotropic models can be considered as strain-based monodissipative models. From Eq. (2.26), the rate of the secant constitutive operator reduces to

$$\dot{\hat{\mathbf{E}}}^S(D) = \frac{\partial \hat{\mathbf{E}}^S}{\partial D}\,\dot{D} = -\hat{\mathbf{E}}\,\dot{D} \tag{2.29}$$

Hence, it can be deduced that the operator defined in the previous section assume the expressions

$$\dot{\lambda} = \dot{D}, \qquad \hat{\mathbf{M}}^* = -\hat{\mathbf{E}}, \qquad \mathcal{M}^* = 1, \qquad \underline{m}^* = -\hat{\mathbf{E}} \cdot \underline{\varepsilon} = -\underline{\sigma}^0 \tag{2.30}$$

For a scalar damage model, a common choice for the loading function is represented by the following additive decomposition

$$f(\underline{\varepsilon}, D) = \varepsilon_{eq}(\underline{\varepsilon}) - K(D) \leq 0 \tag{2.31}$$

where $\varepsilon_{eq}(\underline{\varepsilon})$ is a function depending only on the strain tensor, usually indicated as *equivalent deformation*, that represents the loading condition of the continuum, while $K(D)$ is an *historical parameter* that depends only on the damage variable and that is representative of the maximum level of deformation reached during the loading process. Such a loading function results in the tangent constitutive operator

$$\hat{\mathbf{E}}^t = (1 - D)\,\hat{\mathbf{E}} - \frac{1}{H^*}\left(\underline{\sigma}^0 \otimes \underline{n}^*\right), \qquad \underline{n}^* = \frac{\partial \varepsilon_{eq}}{\partial \underline{\varepsilon}}, \qquad H^* = \frac{\partial K(D)}{\partial D} = \left(\frac{\partial D(\varepsilon_{eq})}{\partial \varepsilon_{eq}}\right)^{-1} \tag{2.32}$$

where $D(K)$ is a prescribed evolution law for the damage like, for example, the following exponential damage law

$$D(\varepsilon_{eq}) = 1 - \frac{K_0}{\varepsilon_{eq}}\left(1 - \alpha + \alpha e^{-\beta(\varepsilon_{eq} - K_0)}\right) \tag{2.33}$$

where K_0 is a threshold value for the equivalent deformation, representing the onset of damage, and where α and β are parameters that define, respectively, the maximum allowed damage level and the damage evolution intensity. Different scalar damage models can be obtained choosing a peculiar equivalent deformation; the classic damage models of *Mazars-Lemaitre* (Mazars and Lemaitre, 1984), *Simo-Ju* (Simo and Ju, 1987), *Marigo* (Marigo, 1985, Lemaitre and Desmorat, 2005) and *Mazars* (Mazars, 1984, de Borst and Gutiérrez, 1999) are defined by the equivalent deformations

$$\varepsilon_{eq} = \begin{cases} \sqrt{\underline{\varepsilon} \cdot \underline{\varepsilon}} & \text{(Mazars-Lemaitre)} \\ \sqrt{2\psi^0} & \text{(Simo-Ju)} \\ \sqrt{2\psi^0/E} & \text{(Marigo)} \\ \sqrt{\left[\sum_{k=1}^3 \left(<\varepsilon^{(k)}>_+ \right)^2 \right]} & \text{(Mazars)} \end{cases} \tag{2.34}$$

where $2\psi^0 = \underline{\varepsilon} \cdot (\hat{\mathbf{E}} \cdot \underline{\varepsilon})$ is the internal energy, E the initial Young's modulus, $\varepsilon^{(k)}$ the k-th eigenvalue of the strain tensor, and $<\varepsilon^{(k)}>_+= (\varepsilon^{(k)} + |\varepsilon^{(k)}|)/2$ its positive part.

2.3 Localization issues

The collapse of a whole body is triggered, in general, by a localized failure, i.e., a loss in the material continuity that interests a small portion of the body (Rizzi, 1995). As observed in experimental tests with metals (Nadai, 1931), geo-materials (Ord et al., 1991, Di Prisco et al., 1992) and concrete (Kupfer et al., 1969, Cedolin et al., 1987), such a localized failure is preceeded by the so-called *localization of deformations*, consisting in the concentration of irreversible phenomena, like plasticization and cracking, in a reduced region of a body; from a kinematical point of view, it results in high gradients of the displacement field, preceeding the material decohesion. Localization is a characteristic of elasto-plastic and quasi-brittle media, i.e., materials that can be described in terms of *strain-softening* models.

It is clear that the *localization analysis*, intended here in the sense given by Rudnicki and Rice (1975) as an investigation of material instabilities at the constitutive level (i.e., in a pointwise sense), is a fundamental issue, since it represents an important warning for the imminent failure of a system. It is remarked that the phenomenon of localization is strongly influenced by the boundary conditions of a body and, in a discrete model, by the mesh density and alignment; however, a pointwise analysis is still able to provide useful informations on the material failure.

Traditionally, the localization of deformations is analyzed within the theory of *acceleration waves propagation* (Hadamard, 1903, Hill, 1962), i.e., waves that carry a *weak discontinuity* in the velocity field. Localization, in this case, corresponds to a stationarity condition of the wavefront (Fresnel-Hadamard propagation condition). Similar results can

be derived also in a quasi-static context, where the localization is represented as a jump in the strain rate at a certain discontinuity surface (Maxell compatibility condition), at which the static equilibrium is imposed (Thomas, 1961, Rudnicki and Rice, 1975). Both the approaches lead to localization conditions that rely on the spectral properties of the *acoustic* (or localization) tensor, represented by the projection of the tangent constitutive operator along a certain direction

$$\underline{Q} := \bar{n} \cdot \left(\hat{\mathbf{E}}^t \cdot \bar{n} \right) \tag{2.35}$$

where $\bar{n}$ is the local normal to the discontinuity surface. One is the weak localization condition (det $\left(\underline{Q} \right) = 0$), corresponding to the *loss of ellipticity* of the equilibrium equations, that depends directly on the acoustic tensor, while the other is the strong localization condition (det $\left(\mathrm{Sym} \left[\underline{Q} \right] \right) = 0$), also known as *loss of strong ellipticity*, which depends instead on the symmetric part of the acoustic tensor.

Localization problems in the field of elasto-plasticity have been investigated by a lot of authors in the past, with a number of works devoted to the analysis of the spectral properties of the acoustic tensor for the loss of ellipticity (Rice, 1976, Rice and Rudnicki, 1980, Ortiz, 1987, Borré and Maier, 1989, Bigoni and Hueckel, 1991*a*, Ottosen and Runesson, 1991*a,b*, Bigoni and Zaccaria, 1994), and of its symmetric part for the loss of strong ellipticity (Ottosen and Runesson, 1991*a*, Bigoni and Hueckel, 1991*a*, Bigoni and Zaccaria, 1992, Neilsen and Schreyer, 1993, Szabó, 2000).

Localization analysis, usually indicated also as *discontinuous failure*, enriches the set of failure indicators, traditionally represented by the *loss of material stability* ($\dot{\underline{\varepsilon}} \cdot \dot{\underline{\sigma}} = 0$, $\forall \dot{\underline{\varepsilon}} \neq \underline{0}$) and *loss of uniqueness* ($\dot{\underline{\sigma}} = \underline{0}$), also known as *continuous failures* (Hill, 1958, Drucker, 1964, Maier and Hueckel, 1979, Runesson and Mróz, 1989). The different failure indicators have been studied by Neilsen and Schreyer (1993) and de Borst et al. (1993), that have established the relations between the various indicators and the necessary conditions for the different kinds of bifurcation. A summarization of the different contributes to the eigenvalues analysis of the constitutive operators and of the acoustic tensor for elasto-plastic models has been proposed by Szabó (1998). Despite the large amount of analytical developments for the localization analysis by the acoustic tensor, the computational aspects are still an active field of research (Xue and Belytschko, 2010, Arriaga et al., 2015).

Regarding the field of elastic degradation and damage models, only a few analytical investigations on localization phenomena have been performed (Desoyer and Cormery, 1994, Rizzi et al., 1995, Jirásek, 2007*a*), mainly focused on *scalar-isotropic* damage models, with some works devoted to elastic degradation coupled with plasticity (Maier and Hueckel, 1979, Bigoni and Hueckel, 1991*b*). However, taking advantage of a unified formulation (Carol et al., 1994, Rizzi et al., 1996, Rizzi and Carol, 2001), the theoretical and

the numerical resources developed in elasto-plasticity can be easily extended to damage models. An extensive treatise on the topic can be found in Rizzi (1995), where different localization conditions, as well as the further failure indicators, are investigated for elastic-degrading models based on the classic continuum theory, with peculiar attention on scalar damage models.

It is well known that numerical analyses where localization occours are characterized by a number of pathological behaviours, such as *strong mesh-dependency*, *premature fracture initiation* and *instantaneous perfectly-brittle fracture* (de Borst et al., 1993, Peerlings et al., 2002). These pathological effects are due to the fact that, when strain-softening material models are adopted, at a certain load level the continuum boundary value problem may become *ill-posed* (loss of ellipticity of the equilibrium equations, corresponding to a singular strain rate). The ill-posedness of the problem corresponds to an infinite set of solutions (discontinuous bifurcation), from which the numerical method selects the one corresponding to the smallest energy dissipation. This approximated solution strongly depends on the mesh; at mesh refinement it tends to a failure with zero energy dissipation, and then to a *non-physical* behaviour.

2.3.1 Regularization techniques

The problem of strain localization has been investigated by many authors in the past, with peculiar attention on elasto-plastic models. It has been pointed out that the pathological behaviours that may affect the numerical simulations where localization occours are due to the *local* representation offered by the classic continuum theory, in contrast with the *non-local* nature of phenomena like damage and plasticity (Bažant, 1991). The main aim of the proposed solutions to this problem (the so-called regularization techniques) is the introduction of an intrinsic (or internal) length in the continuum model, allowing to recover the non-local character of the phenomenon; an interesting overview on the different regularization methods can be found in de Borst et al. (1993) and Bažant and Jirásek (2002). Among the different alternatives there are: *non-local* and *gradient-enhanced* models (Bažant and Lin, 1988, Pijaudier-Cabot and Bažant, 1987, de Borst and Mühlhaus, 1992, Peerlings et al., 1996, Peerlings, 1999, Peerlings et al., 2001, 2002, Badnava et al., 2016), *viscous* models (Needleman, 1988), *cohesive zone* models (Dugdale, 1960, Barenblatt, 1962), methods based on the *fracture energy approach* (Bažant and Oh, 1983), and the *multifield continua* approach (see, e.g., Frémond and Nedjar (1996), Miehe et al. (2010, 2016) and Remark 3.1).

A valid alternative is also represented by the *micropolar* theory (Cosserat and Cosserat, 1909), that has been widely used in the past as a regularization method in strain-softening elasto-plasticity. In this case, the intrinsic length is due to an additional field that enriches the continuum kinematics with effects connected to the sub-structural level of the

material. The works of de Borst (1991), de Borst and Sluys (1991) and Sluys (1992), for example, investigated numerically the regularization properties of the micropolar theory on elasto-plastic models. The works of Dietsche et al. (1993) and Iordache and Willam (1998) instead, proposed an extension to the micropolar theory of the classic *Maxwell compatibility condition*; both analytical and numerical analyses are performed in order to evaluate the effects of the additional material parameters on the discontinuous failure of elasto-plastic models. Furthermore, the authors pointed out the presence of an additional localization condition (the so-called *second localization condition*), due to the asymmetry of the stress tensor. An extension of the *Fresnel-Hadamard propagation condition* can be found in Grioli (1980), for the visco-elastic case, and Eremeyev (2005), for the geometrically exact elastic case.

To the author knowledge, the only works that focus on the regularization properties of the micropolar theory combined with damage models are the one of Xotta et al. (2016) and a paper of the author himself (Gori et al. (2017*b*)). In the former the authors performed numerical evaluations on the localization conditions of a micropolar medium, in terms of the *Maxwell compatibility condition* and of the *second localization condition*. The micropolar medium considered by the authors is characterized by an elasto-plastic behaviour, coupled with scalar damage, where the damage variable is applied only to the Cauchy-like part of the elastic tensor, without affecting the couple-stresses. Furthermore, the considerations on bifurcation analysis are limited to the influence of the *Cosserat's shear modulus*, one of the additional material parameters of the micropolar theory. The paper by the author instead, provided a general investigation on the phenomenom of localization in generic elastic-degrading micropolar media, which will be discussed in detail in Chapter 5.

While the regularization strategies described up to this point are all based on the introduction of an intrinsic length at the *formulation level* (i.e., at the level of the continuum formulation), there are a class of numerical methods which allow to introduce an internal length at the *numerical level*. Among the various solutions based on the finite element method there are, for example, the use of elements with embedded discontinuities (Ortiz et al., 1987), able to represent various kind of weak and strong discontinuities, or element with embedded localization zones (Pietruszczak and Mróz, 1981, Belytschko et al., 1988). Recently it has been shown that some classes of *meshfree* methods, like *moving least square*, *reproducing kernel* approximations, and methods based on *strain smoothing* techniques, are able to bring regularization effects on localization problems (Liu et al., 1999, Chen et al., 2000, Li et al., 2000*a*,*b*, Chen et al., 2004, 2007, Wang and Li, 2012, Pozo et al., 2014), due to their intrinsic non-local properties. Their approximation functions indeed, are not constructed locally, as in the finite element method, because of the use of basis and weighting functions which support size is greater than the nodes spacing. Moreover, the use of a meshfree method allows, in general, to overcome the problem

of mesh orientation bias. Aspects on the regularization properties of meshfree methods will be discussed in Chapter 4 and in the examples of Chapter 6, with specific focus on *smoothed point interpolation methods*.

Chapter 3

Micropolar media

The present chapter deals with micropolar media in a physically non-linear context. After a brief survey on the physical aspects and the modelling issues regarding the class of materials with microstruture, the main aspects of the micropolar formulation in linear elasticity are recalled. Then, a novel unified formulation for elastic-degrading micropolar models proposed by the author is discussed in details. The weak form of the micropolar boundary value problem is also recalled, together with its linearization in the context of elastic degradation.

3.1 Materials with microstructure: physical aspects and modelling issues

In the previous chapter it has been pointed out that the quasi-brittle character of a material is due to its *heterogeneity at the micro scale*, where, according to Krajcinovic, the micro scale "refers to the range of lengths within which [...] individual geometrical features of the microstructure (grains, chain-folded lamellae, fibers, etc.) are clearly recognizable" (Krajcinovic, 1996, pag. 11). Materials "in which events developing at very small spatial scales with respect to the size of the body have influence on the macroscopic mechanical behaviour, exerted through interactions barely representable in terms of standard stresses" (Mariano, 2016, pag. 7), are referred to as *complex materials* (or *materials with microstructure*). According to these quotes, a large number of materials of interest in the field of structural engineering, such as concrete, geo-materials, coarse-grained ceramics, and most fibre-reinforced materials, for example, can be considered as *complex*, posing different issues regarding their analytical and computational modelling.

In the standard approach to continuum mechanics (the so-called *Cauchy's* or *classic* continuum theory) a real body is idealized, from a geometrical point of view, simply as a certain region in space, an open subset $\mathbf{D}$ of the three-dimensional Euclidean space

E, composed by a set of *particles*, or *material elements* (see, e.g., Noll (1958) or Marsden and Hughes (1994)). Each particle is characterized only by its position in space, and interactions between two particles are transmitted only by a *force vector*. Within this minimalistic approach, details on the nature of the material elements are purposely skipped, since such classic representation describes "the macroscopic configuration of a body and its changes, without furnishing *direct* information on the microscopic shape of the pertinent material at a certain scale, the one involved in the possible phenomena characterizing a peculiar behaviour of the body under analysis" (Mariano, 2016, pag. 9). As observed in Section 2.2, when modelling a body as a classic continuum, the influence of the microstructure on its gross behaviour (i.e., the set of details below the resolution level of the continuum model) is taken into account by means of *constitutive relations*, which parameters are averaged over a finite extension of the microstructure, the *representative volume element.*

While this approach allows to cover a large class of materials, in some situations the influence of the substructure may be so prominent that a representation through an homogenized classic continuum may not be sufficient to capture all the involved phenomena. Continuum theories in which the standard description is enriched by the introduction of additional variables able to carry informations on the material substructure go under the name of *multifield continuum theories* (see, e.g., Mariano (2002)), which initiated from the works of Voigt (1887) and Cosserat and Cosserat (1909)[1]. Alongside the standard *motion* of the body particles, multifield theories consider at each point of the body also a *morphological descriptor*, an object belonging to a generic differentiable manifold, which nature depends on the specific complex material under analysis. The micropolar continuum model considered in this treatise belongs to the more general class of *micromorphic continua*, which are themselves a specific class of multifield models. Briefly, a micromorphic continuum is represented as a classic continuum (referred to as *macrocontinuum* in this context) with *deformable particles*, i.e., each point of the continuum is endowed with a further deformable continuum structure, the *microcontinuum* (Eringen, 1999). In this case the morphological operator is a simple linear operator describing the uniform deformation of each microcontinuum; proper constraints on this operator allow to obtain the classes of *microstretch* and *micropolar* continua. This chapter focuses on the case of geometrically linear micropolar media, which will be formulated in the contex of continuum damage mechanics.

Remark 3.1: Multifield continua and material degradation

The multifield formulation have been shown to be an interesting approach to the

---

[1] The reader may refers to the introduction of the papers by Mariano (2002) and Mariano and Stazi (2005) for historical notes on the origin and evolution of multifield theories.

modelling of material degradation, allowing a direct representation of degrading phenomena in terms of additional field variables, alongside the motion of the material particles, instead of the standard representation within the context of thermodynamics with internal state variables (Coleman and Gurtin, 1967). Markov (1995) represented the deterioration of a solid in terms of a scalar damage variable, interpreted in the context of microstretch elasticity as a measure of the independent volume change of each material particle due to degradation. In Frémond and Nedjar (1996) the authors recasted the standard continuum damage mechanics in the perspective of a multifield approach, adding the classic scalar damage variable (Kachanov, 1958) to the field variables of the problem. Mariano (1999) represented microcracked bodies enriching the classic continuum description with an additional *microdisplacement* field, representing a perturbation to the standard displacement field of the material particles (see also, e.g., Mariano et al. (2002, 2004)). In a comprehensive paper, Forest (2009) showed how several gradient elastoviscoplasticity and damage models previously proposed in the literature can be represented within a same *micromorphic approach* (where the term "micromorphic" is used in a broader sense than in Eringen (1999), more like a synonymous of "multifield"). In Miehe et al. (2010, 2016) the authors considered the problem of fracture within the context of multifield continua, introducing an auxiliary field variable able to describe cracks topology. As a final example, in Oliver et al. (2012) the authors investigated the modelling of steel fiber reinforced concrete introducing an additional field variable representing the bond slip mechanism, i.e., the relative displacement between fibers and matrix. The examples described in this remark are not intended to be a comprehensive survey on the topic, and are provided only to expose some possibilities regarding the use of multifield continua. Concerning the approach adopted in the following sections for the physically non-linear micropolar modelling proposed by the author, it is important to emphasize that it differs from the ones discussed in this remark. As it will be shown, there the multifield approach is due to the additional kinematical desciptor associated to the material particles, while the degradation phenomena are represented at the constitutive level within the standard approach of thermodynamics with internal state variables.

3.2 Micropolar continuum theory

The micropolar continuum first appeared in the work of the Cosserat's brothers (Cosserat and Cosserat (1909)), based on some previous ideas formulated by Voigt (1887). Their point of view consisted in considering each material element of a body as a *small rigid body*, able to rotate independently of the neighboring particles. Such rotation (represented by an orthogonal tensor in a geometrically exact context, or by an axial vector assuming

a linear hypothesis for the geometry) constitutes an additional field variable that enriches the standard continuum description, which consider only the motion of the particles. As it will be discussed in the following sections, interactions between particles in a micropolar medium are represented not only in terms of the standard stress tensor, but also with an additional *couple-stress tensor*, which components are couples per unit of area. As it will be shown, the additional kinematical field endows the continuum with a set of *internal lengths*, responsible for its regularization properties in strain-softening problems (Section 2.3.1), which have been investigated by a number of authors in case of elasto-plasticity (see, e.g., de Borst and Sluys (1991), de Borst (1991, 1993), Sluys (1992), Dietsche et al. (1993), Iordache and Willam (1998)), with a few contributions in case of damage models (Xotta et al. (2016), Gori et al. (2017b)). Before proceeding to the presentation of the micropolar formulation for elastic degradation proposed by the author (Section 3.3), the basic equations defining the behaviour of a linear elastic micropolar medium will be briefly recalled[2].

3.2.1   Kinematics and equilibrium equations

The configuration $\mathbf{D}_t$ of a micropolar medium at a certain time instant t is characterized by the couple $(c(p,t), \underline{R}(p,t))$. As illustrated in Fig. 3.1, $c(p,t)$ is the standard *motion*, mapping the points of the continuum from a certain reference configuration $\mathbf{D}$ to the deformed configuration $\mathbf{D}_t$, with associated *displacement field* $\bar{u}(p,t) := c(p,t) - p$. The operator $\underline{R}(p,t) \in \mathrm{SO}(3)$ is an orthogonal tensor, measuring the *rigid rotation* of the particles of the micropolar medium, represented by the transformation of the rigid directors $\left(\bar{\bar{\Xi}}_1, \bar{\bar{\Xi}}_2, \bar{\bar{\Xi}}_3\right)$ into $\left(\bar{\xi}_1, \bar{\xi}_2, \bar{\xi}_3\right)$, where $\bar{\xi}_i = \underline{R} \cdot \bar{\bar{\Xi}}_i$.
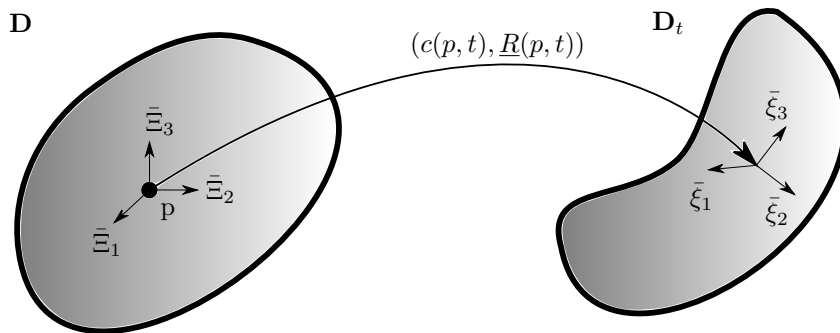
Figure 3.1: Configuration of a micropolar medium

In a geometrically linear context the distinction between the reference and the deformed configurations is dropped, and the linearization of the kinematical quantities

---

[2] For a comprehensive understanding on the subject the reader may refer to the existing literature on the topic. See, e.g., the books by Eringen (1999) and Eremeyev et al. (2013) for a generic treatment, and the papers cited in Section 2.3.1 for applications to physically non-linear problems.

allows to replace the rotation operator with a *rotation vector* (the *axial vector* of a skew-symmetric tensor obtained as a linearization of $\underline{R}$). Within this assumption, the configuration of a micropolar continuum is characterized, at each point $p \in \mathbf{D}$, by a *displacement field* $\bar{u}$ and a *microrotation vector* $\bar{\varphi}$[3]. The choice of such field variables for the representation of the kinematics of the body leads to the strain measures

$$\underline{\gamma} = \mathrm{grad}^{\mathrm{T}}(\bar{u}) - \mathsf{e} \cdot \bar{\varphi} = (u_{j,i} - \mathsf{e}_{ijk}\,\varphi_k)\,\bar{e}_i \otimes \bar{e}_j \tag{3.1}$$

$$\underline{\kappa} = \mathrm{grad}^{\mathrm{T}}(\bar{\varphi}) = \varphi_{j,i}\,\bar{e}_i \otimes \bar{e}_j \tag{3.2}$$

which are referred to as *strain tensor* and *microcurvature tensor*, respectively, and where the symbol e indicates the standard *Levi-Civita* operator with three indexes. To these strain measures correspond, respectively, the *stress tensor* $\underline{\sigma}$ and the *couple-stress tensor* $\underline{\mu}$ which must satisfy the local equilibrium equations[4] for forces and moments in the domain $\mathbf{D}$

$$\mathrm{div}^{\mathrm{T}}(\underline{\sigma}) + \bar{b}_V = \rho\ddot{\bar{u}} \longrightarrow \sigma_{ij,i} + b_{Vj} = \rho\ddot{u}_j \tag{3.3}$$

$$\mathrm{div}^{\mathrm{T}}\left(\underline{\mu}\right) + \mathsf{e} \cdot \underline{\sigma} + \bar{l}_V = \rho\theta\ddot{\bar{\varphi}} \longrightarrow \mu_{ij,i} + \mathsf{e}_{jkl}\,\sigma_{kl} + l_{Vj} = \rho\theta\ddot{\varphi}_j \tag{3.4}$$

where $\bar{b}_V$ and $\bar{l}_V$ represent, respectively, volume forces and volume couples acting in the body domain, ρ is the density of the medium, and $\rho\theta$ is the scalar measure of the rotation inertia of continuum particles (see, e.g., Eremeyev (2005)). To the previous equations, the following *natural* and *essential* boundary conditions are associated

$$\bar{\eta} \cdot \underline{\sigma} = \bar{t}_A \text{ at } \partial\mathbf{D}_n^u, \quad \bar{\eta} \cdot \underline{\mu} = \bar{t}_C \text{ at } \partial\mathbf{D}_n^\varphi \tag{3.5}$$

$$\bar{u} = \bar{u}^* \text{ at } \partial\mathbf{D}_e^u, \quad \bar{\varphi} = \bar{\varphi}^* \text{ at } \partial\mathbf{D}_e^\varphi \tag{3.6}$$

where $\bar{\eta}$ is the *unit normal vector field* defined at the boundary $\partial\mathbf{D}$ of the body.

3.2.2 Linear isotropic elasticity

In linear elasticity, disregarding the direct coupling between the Cauchy-type and Cosserat-type effects (i.e., the *chirality* effect), stress and deformation measures are linked by the following constitutive equations

$$\underline{\sigma} = \hat{\mathbf{A}} \cdot \underline{\gamma} \tag{3.7}$$

$$\underline{\mu} = \hat{\mathbf{C}} \cdot \underline{\kappa} \tag{3.8}$$

---

[3] The explicit dependence on the point p and on the time t of both $\bar{u}$ and $\bar{\varphi}$ is dropped in order to simplify the notation.

[4] Though in the following attention will be focused on *quasi-static* problems, the *inertial terms* are explicitly represented in the equilibrium equations since they will be used in Chapter 5 in the discussions regarding micropolar acceleration waves.

where $\hat{\mathbf{A}}$ and $\hat{\mathbf{C}}$ are the initial constitutive operators for the micropolar model that, assuming an initially *isotropic* material, are expressed in terms of six material parameters as

$$\hat{\mathbf{A}} = A_1 \, \underline{id} \otimes \underline{id} + (A_2 + A_3) \, \mathbf{I}\hat{\mathbf{D}}^{sym} + (A_2 - A_3) \, \mathbf{I}\hat{\mathbf{D}}^{skw} \tag{3.9}$$

$$\hat{\mathbf{C}} = C_1 \, \underline{id} \otimes \underline{id} + (C_2 + C_3) \, \mathbf{I}\hat{\mathbf{D}}^{sym} + (C_2 - C_3) \, \mathbf{I}\hat{\mathbf{D}}^{skw} \tag{3.10}$$

or alternatively as

$$\hat{\mathbf{A}} = A_1 \, \underline{id} \otimes \underline{id} + A_2 \, \mathbf{I}\hat{\mathbf{D}} + A_3 \, \mathbf{I}\hat{\mathbf{D}}^{T} \tag{3.11}$$

$$\hat{\mathbf{C}} = C_1 \, \underline{id} \otimes \underline{id} + C_2 \, \mathbf{I}\hat{\mathbf{D}} + C_3 \, \mathbf{I}\hat{\mathbf{D}}^{T} \tag{3.12}$$

It should be noted that the components of the microcurvature tensor $\underline{\kappa}$ and of the couple-stress tensor $\underline{\mu}$ are not characterized by the same units of measure of, respectively, the strain tensor $\underline{\gamma}$ and the stress tensor $\underline{\sigma}$. In a number of applications it is convenient to scale such operators in order to obtain a dimensional compatibility. The microcurvature and couple-stress tensors can be replaced by the scaled operators $\underline{\kappa}^*$ and $\underline{\mu}^*$ defined as $\underline{\kappa}^* = \hat{\mathbf{L}} \cdot \underline{\kappa}$ and $\underline{\mu}^* = \hat{\mathbf{L}}^{-1} \cdot \underline{\mu}$, where $\hat{\mathbf{L}}$ is a fourth-order tensor containing the characteristic lengths of the micropolar medium. The constitutive relation for the scaled operators, analogous to the one of Eq. (3.8) is expressed as $\underline{\mu}^* = \hat{\mathbf{C}}^* \cdot \underline{\kappa}^*$, with $\hat{\mathbf{C}}^* = \hat{\mathbf{L}}^{-1} \cdot \hat{\mathbf{C}} \cdot \hat{\mathbf{L}}^{-1}$.

Remark 3.2: Chirality effect

The problem of *chirality* (or *non-centrosymmetry*) in a three-dimensional micropolar medium was first treated by Nowacki (1986), and consists in considering a coupling between the constitutive equations of Eqs. (3.7) and (3.8), in the form

$$\underline{\sigma} = \hat{\mathbf{A}} \cdot \underline{\gamma} + \hat{\mathbf{B}} \cdot \underline{\kappa} \tag{3.13}$$

$$\underline{\mu} = \hat{\mathbf{C}} \cdot \underline{\kappa} + \hat{\mathbf{B}} \cdot \underline{\gamma} \tag{3.14}$$

with the introduction of the additional constitutive tensor $\hat{\mathbf{B}}$. It is worth to note that such representation, in an hyperelastic context, is the most general one, and correspond to the choice of an *Helmholtz free energy density* of the form

$$\psi \left(\underline{\gamma}, \underline{\kappa} \right) = \frac{1}{2} \, \underline{\gamma} \cdot \left(\hat{\mathbf{A}} \cdot \underline{\gamma} \right) + \frac{1}{2} \, \underline{\kappa} \cdot \left(\hat{\mathbf{C}} \cdot \underline{\kappa} \right) + \underline{\gamma} \cdot \left(\hat{\mathbf{B}} \cdot \underline{\kappa} \right) \tag{3.15}$$

Despite being usually disregarded, this effect may be relevant, depending on the microstructure of the material under analysis (see, e.g., Joumaa and Ostoja-Starzewski (2011) and Rezakhani and Cusatis (2014)). Regarding the formulation discussed in

Section 3.3, it is emphasized that the inclusion of chirality shouldn't require peculiar efforts, except for the presence of additional material parameters to be defined.

3.2.3   Micropolar material parameters

When dealing with generalized continuum theories one of the main drawbacks is the presence of additional material parameters, with respect to the two of a classic isotropic continuum. Two problems must be worked out, in general: the first is the definition of proper "engineering" parameters with clear physical, meaning like the classic Young's modulus and Poisson's ratio, the second is their calibration. A recent contribution on these issues is represented by Hassanpour and Heppler (2015), where the authors presented a survey on both notations and experimental aspects related to the linear isotropic micropolar model. Due to its completeness, it will be used as a basis for the following discussions[5].

3.2.3.1   Parameters redefinition

Regarding the definition of proper material parameters, different conventions have been adopted in the past, often leading to errors and a certain confusion when comparing the different contributions available in the literature, as pointed out in Hassanpour and Heppler (2015). Some of the discussions presented in Hassanpour and Heppler (2015) are recalled in the following, in order to introduce the "engineering" parameters adopted throughout this treatise. In order to simplify the comparison with the cited work, the elastic parameters appearing in Eqs. (3.9) and (3.10) are recalled in Table 3.1 alongside the corresponding ones adopted in Hassanpour and Heppler (2015).

Current	Hassanpour and Heppler (2015)
A_1	λ
A_2	$\mu + \kappa$
A_3	$\mu - \kappa$
C_1	α
C_2	$\gamma + \beta$
C_3	$\gamma - \beta$

Table 3.1: Micropolar parameters

First it is interesting to observe that applying the constitutive operator expressed in Eq. (3.9), the stress tensor $\underline{\sigma}$ appearing in Eq. (3.7) is naturally decomposed into a

---

[5] Though they have not been taken into account in the present treatise, interesting investigations on the micropolar material parameters can be found in the works of Neff and his co-authors (see, e.g., Neff (2006), Neff and Jeong (2009), Neff et al. (2010) and Jeong and Neff (2015)).

symmetric and a *skew-symmetric* parts as

$$\underline{\sigma} = \underbrace{A_1 \text{tr}(\underline{\gamma})\ \underline{id} + (A_2 + A_3)\ \underline{\gamma}^{sym}}_{\text{symmetric}} + \underbrace{(A_2 - A_3)\ \underline{\gamma}^{skew}}_{\text{skew-symmetric}} \tag{3.16}$$

Since the symmetric part of the strain tensor $\underline{\gamma}$ coincides with the classic strain tensor $(\underline{\gamma}^{sym} = (\text{grad}(\bar{u}) + \text{grad}^{\mathrm{T}}(\bar{u}))/2)$, the parameters A_1, A_2 and A_3 can be associated to the Lamé's parameters λ and μ (or G) as

$$A_1 = \lambda, \quad A_2 + A_3 = 2\mu = 2G \tag{3.17}$$

Furthermore, considering an uniaxial stress state $\sigma_{11} \neq 0$, with associated strain components γ_{11}, γ_{22} and γ_{33}, the classic Young's modulus and Poisson's ratio can be introduced as

$$E := \frac{\sigma_{11}}{\gamma_{11}}, \quad \nu := -\frac{\gamma_{22}}{\gamma_{11}} = -\frac{\gamma_{33}}{\gamma_{11}}, \quad G = \frac{E}{2(1+\nu)}, \quad \lambda = \frac{E\nu}{(1-2\nu)(1+\nu)} \tag{3.18}$$

The skew-symmetric part of the stress tensor is usually recast in terms of an additional material parameter, the *Cosserat's shear modulus* G_c, defined as $2G_c = A_2 - A_3$. Taking into account that the skew-symmetric part of the strain tensor corresponds to the difference between the micro and the macrorotation of the continuum

$$\underline{\gamma}^{skew} = \left(\underbrace{(-\mathsf{e}_{ijk}\ \varphi_k)}_{\text{microrotation}} - \underbrace{\frac{1}{2}\left(u_{i,j} - u_{j,i}\right)}_{\text{macrorotation}} \right)\ \bar{e}_i \otimes \bar{e}_j \tag{3.19}$$

it can be observed that the Cosserat's shear modulus controls the contribution of the microrotation to the macro stress; hence, it can be interpreted as a parameter that controls the effect of the microstructure of a material on its gross behaviour. As it will be pointed out in Chapter 5, such parameter also exhibits a prominent influence on the regularization properties of the micropolar model.

As already done in Eq. (3.16) for the stress tensor, also the couple-stress tensor can be naturally decomposed into a symmetric and a skew-symmetric parts, as

$$\underline{\mu} = \underbrace{C_1 \text{tr}(\underline{\kappa})\ \underline{id} + (C_2 + C_3)\ \underline{\kappa}^{sym}}_{\text{symmetric}} + \underbrace{(C_2 - C_3)\ \underline{\kappa}^{skew}}_{\text{skew-symmetric}} \tag{3.20}$$

As pointed out in Hassanpour and Heppler (2015), considering an uniaxial couple-stress state $\mu_{11} \neq 0$, with the associated microcurvature components κ_{11}, κ_{22} and κ_{33}, the material moduli $\mathcal{E}$ and ξ, analogous to the Young's modulus and the Poisson's ratio, can

be defined as

$$\mathcal{E} := \frac{\mu_{11}}{\kappa_{11}} = \frac{(3C_1 + C_2 + C_3)(C_2 + C_3)}{2C_1 + C_2 + C_3} \tag{3.21}$$

$$\xi := -\frac{\kappa_{22}}{\kappa_{11}} = -\frac{\kappa_{33}}{\kappa_{11}} = \frac{C_1}{2C_1 + C_2 + C_3} \tag{3.22}$$

Furthermore, the material modulus η, such that $2\eta = C_2 - C_3$, can be introduced as the parameter relating the skew-symmetric parts of the couple-stress and the microcurvature tensors.

With the aforementioned material parameters, the stress and the couple-stress tensors of an isotropic micropolar medium can be expressed as

$$\underline{\sigma} = \frac{E\nu}{(1 - 2\nu)(1 + \nu)} \ \mathrm{tr}(\underline{\gamma}) \ \underline{id} + 2G \ \underline{\gamma}^{sym} + 2G_c \ \underline{\gamma}^{skew} \tag{3.23}$$

$$\underline{\mu} = \frac{\mathcal{E}\xi}{(1 - 2\xi)(1 + \xi)} \ \mathrm{tr}(\underline{\kappa}) \ \underline{id} + \frac{\mathcal{E}}{1 + \xi} \ \underline{\kappa}^{sym} + 2\eta \ \underline{\kappa}^{skew} \tag{3.24}$$

The material moduli $\mathcal{E}$ and ξ are usually replaced by two or more *characteristic lengths*, with a more significative physical meaning. It is worth to note that there isn't a common agreement on the definition of such lengths, and different expressions may be found in the literature (see, e.g., Gauthier and Jahsman (1975), Reddys and Venkatasubramaniano (1979), Mühlhaus and Vardoulakis (1987), Park and Lakes (1987), de Borst (1991), Lakes (1995), Liu and Hu (2005), and Huang and Xu (2015)). While some of the characteristic lengths defined in the literature are of general validity, other assume a precise physical meaning only for peculiar stress/strain states. In a plane-stress state, like the one considered in the numerical analyses performed in the present treatise (Chapters 6 and 7), a common choice (see, e.g., de Borst (1991)) consists in the use of a single *intrinsic bending length* (or simply, *internal length*) L_b such that

$$\mu_{13} = 2GL_b^2 \ \kappa_{13}, \quad \mu_{23} = 2GL_b^2 \ \kappa_{23} \tag{3.25}$$

which can be associated to the characteristics of the microstructure of a material (see, e.g., de Borst and Sluys (1991)). From Eq. (3.12), it can be observed that the characteristic length L_b satisfies the equality $2GL_b^2 = C_2$. It is also interesting to observe that in a plane-stress state, the six material parameters of the micropolar continuum reduces to four independent parameters, the classic Young's modulus and Poisson's ratio, the Cosserat's shear modulus, and the internal bending length.

3.2.3.2   Parameters characterization

This treatise doesn't deal with the characterization of the additional material parameters of the micropolar theory, but rather with their regularization effects in elastic-degrading

problems where localization occours. However, since this is an important task for future practical applications, a brief review of the main contributions on the topic is here presented. In order to characterize the micropolar material moduli, two different approaches can be followed: *experimental tests*, aiming to evaluate the material parameters through a fitting procedure with experimental measures, and *homogenization techniques*, aiming to replace a microstructured material with an effective *generalized* continuum model.

Regarding the experimental investigations on the micropolar parameters, a large number of works is available in the literature, which mainly focus on bio-materials like bones, and on polymeric and metallic foams. A quite complete survey can be found in Hassanpour and Heppler (2015) and won't be repeated here.

Homogenization techniques can be divided into analytical and numerical methods. The former consist in the evaluation of the micropolar moduli through the comparison of the response of lattice structures able to represent the substructure of a certain material; such an approach is well suited for periodic substructures (e.g., crystals). In the numerical approach the homogenization is performed by calibrating the material moduli through numerical simulations of representative volume elements (RVE). In this case, random microstructures can be easily accounted for. Regarding the existing literature on the topic:

> "Adomeit (1968) considered a three-dimensional honeycomb structure built of cubical cells and calculated the elastic coefficients of its equivalent couple-stress continuum from a structural view point. Employing the couple-stress theory to describe the dynamics of a composite with a laminated structure, Herrmann and Achenbach (1968) obtained the non-classical material constants as functions of the geometry and the classical material constants of the composite's constituents. Banks and Sokolowski (1968) showed an analogy between the equations governing the behaviour of a planar lattice structure built up from elastic beams and the equations of the two-dimensional couple-stress theory and related the elastic moduli of the couple-stress continuum to the elastic properties of the beam elements in the lattice structure. In a similar work, Askar and Cakmak (1968) proposed an equivalent micropolar continuum model for a two-dimensional lattice structure composed of orientable mass points joined by massless beam elements and represented the micropolar elastic moduli of the equivalent continuum in terms of the properties of the connecting beams. In these works, the characteristic length (of the couple-stress or micropolar elasticity theory) was found to be related to the size of the structural elements.
>
> There have been many other scholars trying to theoretically (usually based on an equivalent continuum approach) calculate the material coefficients from structural considerations (Bažant and Christensen,

1972, Kanatani, 1979, Noor and Nemeth, 1980*a,b*, Berglund, 1982, Wang and Stronge, 1999, Ostoja-Starzewski et al., 1999, Ostoja-Starzewski, 2002, Mora and Waas, 2007, TekogLu, 2007, Tekoglu and Onck, 2008, Salehian, 2008, Chung and Waas, 2009, Tekoglu et al., 2011, Seppecher et al., 2011). Recently, Ganghoffer et al. (Dos Reis and Ganghoffer, 2011, 2012, Goda, Assidi, Belouettar and Ganghoffer, 2012, Goda, Assidi and Ganghoffer, 2012, Goda et al., 2014) have put a lot of effort into using the homogenization techniques to establish non-classical constitutive equations and determine the elastic moduli corresponding to repetitive lattices and trabecular structures (e.g. bone)."(Hassanpour and Heppler, 2015, pag. 9)

The existing literature cited in Hassanpour and Heppler (2015) can be complemented with the works by Chang et al. devoted to granular materials (Chang and Liao, 1990, Chang and Ma, 1991, 1992), and other focused on regular and random composites (Bigoni and Drugan, 2007, Suiker et al., 2001, Willoughby et al., 2012, De Bellis and Addessi, 2014, Trovalusci et al., 2015, Addessi et al., 2016), and Trovalusci et al. (2017).

3.3 A unified formulation for elastic degradation in micropolar continua

Section 2.2.2 has been devoted to the description of the so-called *unified formulation for constitutive models*, a theoretical resource able to represent, in a common framework, a large number of *multidissipative* elasto-plastic and elastic-degrading models with a tensorial formalism, in terms of constitutive operators, loading functions, and degradation/flow rules, which has been object of investigation by a number of authors (see, e.g., de Borst (1987), Carol et al. (1994), Rizzi (1995), Carol and Willam (1996), Carol (1996), de Borst and Gutiérrez (1999), Armero and Oller (2000*a,b*), Carol et al. (2001*a,b*), and Hansen et al. (2001)). As it will be commented in Appendix C, such approach to constitutive modelling have been also shown to be particularly useful as a basis for computational implementations (Penna, 2011, Gori et al., 2017*a*).

Taking into account the advantages offered by a unified formulation for constitutive models based on a tensorial formalism, and considering the lack of generality regarding the constitutive aspects of existent elasto-plastic and damage micropolar models (see, e.g., de Borst and Sluys (1991), de Borst (1991, 1993), Sluys (1992), Dietsche et al. (1993), Iordache and Willam (1998), Steinmann (1995), and Xotta et al. (2016)), the author proposed an extension of such concept to constitutive models based on the micropolar continuum theory. This attempt resulted in a both theoretical and computational framework inspired on the *single-criterion Cosserat's plasticity* approach discussed in Forest

and Sievert (2003), able to represent a large number of elasto-plastic and elastic-degrading micropolar models (Gori et al., 2015*a*, 2017*c*), that has been successfully applied to the analysis of localization phenomena in problems with scalar-isotropic damage (Gori et al., 2017*b*). As it will be shown, the key for the realization of such a framework has been a *compact tensorial representation* of the micropolar constitutive equations, inspired by the symbolism adopted by Eremeyev in his paper on acceleration waves in micropolar elastic media (Eremeyev, 2005). The theoretical aspects of this approach to constitutive modelling, which are mainly drawn from Gori et al. (2017*c*), will be discussed in the following sections, while the computational aspects will be discussed in details in Appendix C.

3.3.1   Elastic degradation in micropolar media

The starting point for the derivation of an *elastic-degrading* constitutive model within the context of the micropolar theory is the extension of the *Clausius-Duhem inequality* to the micropolar case (Steinmann, 1995)

$$\dot{\psi} - \underline{\sigma} \cdot \dot{\underline{\gamma}} - \underline{\mu} \cdot \dot{\underline{\kappa}} \leq 0 \quad \forall \dot{\underline{\gamma}}, \dot{\underline{\kappa}} \tag{3.26}$$

where ψ is the *Helmholtz free energy density*, depending on the current state of the material. Alternatively, the Clausius-Duhem inequality can be rewritten in terms of the *Gibbs free energy* $\mathbf{G}$, obtained from the Helmholtz free energy with a *Legendre transformation* (Collins and Houlsby, 1997), and characterized by $\psi + \mathbf{G} = \underline{\sigma} \cdot \underline{\gamma} + \underline{\mu} \cdot \underline{\kappa}$, resulting in

$$\dot{\mathbf{G}} - \underline{\gamma} \cdot \dot{\underline{\sigma}} - \underline{\kappa} \cdot \dot{\underline{\mu}} \geq 0 \quad \forall \dot{\underline{\sigma}}, \dot{\underline{\mu}} \tag{3.27}$$

The choice of a peculiar expression for the Helmholtz or the Gibbs free energy densities should be based on the material under analysis. Regarding the Helmholtz free energy density, in general, a common choice is to make it dependent on the measures of deformation, which indicates the current state of a body, and on a set of parameters indicating the state of elastic or plastic degradation of the material[6] (see, e.g., Coleman and Gurtin (1967)). In this context, the degradation of the material properties is assumed to be elastic, i.e., not induced by any plastic mechanism[7]. Furthermore, no microcracks closure-reopening effect is accounted for. Hence, the Helmholtz and the Gibbs free energies can be expressed

---

[6] Of course, since it is a *density*, it also depends on the considered position inside the body. However, such dependence is not made explicit here in order to contain the notation.

[7] Though, as it will be shown, the case of *perfect plasticity* can be easily included within the same framework discussed here.

as[8]

$$\psi\left(\underline{\gamma},\underline{\kappa},\hat{\mathbf{A}}^S,\hat{\mathbf{C}}^S\right) = \frac{1}{2}\,\underline{\gamma}\cdot\left(\hat{\mathbf{A}}^S\cdot\underline{\gamma}\right) + \frac{1}{2}\,\underline{\kappa}\cdot\left(\hat{\mathbf{C}}^S\cdot\underline{\kappa}\right) \tag{3.28}$$

$$\mathbf{G}\left(\underline{\sigma},\underline{\mu},(\hat{\mathbf{A}}^S)^{-1},(\hat{\mathbf{C}}^S)^{-1}\right) = \frac{1}{2}\,\underline{\sigma}\cdot\left((\hat{\mathbf{A}}^S)^{-1}\cdot\underline{\sigma}\right) + \frac{1}{2}\,\underline{\mu}\cdot\left((\hat{\mathbf{C}}^S)^{-1}\cdot\underline{\mu}\right) \tag{3.29}$$

where $\hat{\mathbf{A}}^S$ and $\hat{\mathbf{C}}^S$ are the current *secant* constitutive operators. It is worth to note that in a more complex case, with microcracks closure-reopening effects or plastic damage, the current constitutive operators wouldn't be secant, and residual deformations could appear at a zero stress state. The inequalities expressed in Eqs. (3.26) and (3.27) can then be rewritten as

$$\left(\frac{\partial\psi}{\partial\underline{\gamma}} - \underline{\sigma}\right)\cdot\dot{\underline{\gamma}} + \left(\frac{\partial\psi}{\partial\underline{\kappa}} - \underline{\mu}\right)\cdot\dot{\underline{\kappa}} - \dot{\mathfrak{D}}^* \leq 0 \quad \forall\dot{\underline{\gamma}},\dot{\underline{\kappa}} \tag{3.30}$$

$$\left(\frac{\partial\mathbf{G}}{\partial\underline{\sigma}} - \underline{\gamma}\right)\cdot\dot{\underline{\sigma}} + \left(\frac{\partial\mathbf{G}}{\partial\underline{\mu}} - \underline{\kappa}\right)\cdot\dot{\underline{\mu}} + \dot{\mathfrak{D}} \geq 0 \quad \forall\dot{\underline{\sigma}},\dot{\underline{\mu}} \tag{3.31}$$

where the *dissipation* functions $\dot{\mathfrak{D}}^*$ and $\dot{\mathfrak{D}}$ are expressed as

$$\dot{\mathfrak{D}}^* := -\hat{\boldsymbol{\Pi}}_A^* \cdot \dot{\hat{\mathbf{A}}}^S - \hat{\boldsymbol{\Pi}}_C^* \cdot \dot{\hat{\mathbf{C}}}^S, \qquad \dot{\mathfrak{D}} := -\hat{\boldsymbol{\Pi}}_A \cdot (\dot{\hat{\mathbf{A}}}^S)^{-1} - \hat{\boldsymbol{\Pi}}_C \cdot (\dot{\hat{\mathbf{C}}}^S)^{-1} \tag{3.32}$$

in terms of the *thermodynamical forces*

$$\hat{\boldsymbol{\Pi}}_A^* := \frac{\partial\psi}{\partial\hat{\mathbf{A}}^S} = \frac{1}{2}\left(\underline{\gamma}\otimes\underline{\gamma}\right), \qquad \hat{\boldsymbol{\Pi}}_C^* := \frac{\partial\psi}{\partial\hat{\mathbf{C}}^S} = \frac{1}{2}\left(\underline{\kappa}\otimes\underline{\kappa}\right) \tag{3.33}$$

$$\hat{\boldsymbol{\Pi}}_A := -\frac{\partial G}{\partial(\hat{\mathbf{A}}^S)^{-1}} = -\frac{1}{2}\left(\underline{\sigma}\otimes\underline{\sigma}\right), \qquad \hat{\boldsymbol{\Pi}}_C := -\frac{\partial\psi}{\partial(\hat{\mathbf{C}}^S)^{-1}} = \frac{1}{2}\left(\underline{\mu}\otimes\underline{\mu}\right) \tag{3.34}$$

From Eqs. (3.30) and (3.31), due to the arbitrariness of the quantities $\dot{\underline{\gamma}}$, $\dot{\underline{\kappa}}$, $\dot{\underline{\sigma}}$, and $\dot{\underline{\mu}}$, the following relations hold

$$\underline{\sigma} = \frac{\partial\psi}{\partial\underline{\gamma}} = \hat{\mathbf{A}}^S\cdot\underline{\gamma}, \qquad \underline{\mu} = \frac{\partial\psi}{\partial\underline{\kappa}} = \hat{\mathbf{C}}^S\cdot\underline{\kappa}, \qquad \dot{\mathfrak{D}}^* \geq 0 \tag{3.35}$$

$$\underline{\gamma} = \frac{\partial G}{\partial\underline{\sigma}} = (\hat{\mathbf{A}}^S)^{-1}\cdot\underline{\sigma}, \qquad \underline{\kappa} = \frac{\partial G}{\partial\underline{\mu}} = (\hat{\mathbf{C}}^S)^{-1}\cdot\underline{\mu}, \qquad \dot{\mathfrak{D}} \geq 0 \tag{3.36}$$

where the *non-negativeness* of the dissipation terms is related to the *irreversibility* of the degradation process. The previous equations emphasize that, for a micropolar elastic-degrading material, total relations between stress and deformation measures exist, and are expressed in terms of the current secant material properties.

Deriving Eq. (3.35), the expressions of the stress and the couple-stress rate tensors

---

[8] These expressions can be viewed as a generalization to a micropolar medium of the ones proposed in Carol et al. (1994) for the classic continuum.

can be obtained as

$$\dot{\underline{\sigma}} = \frac{\partial^2 \psi}{\partial \underline{\gamma} \partial \underline{\gamma}} \cdot \dot{\underline{\gamma}} + \frac{\partial^2 \psi}{\partial \underline{\gamma} \partial \hat{\mathbf{A}}^S} \cdot \dot{\hat{\mathbf{A}}}^S = \hat{\mathbf{A}}^S \cdot \dot{\underline{\gamma}} + \dot{\hat{\mathbf{A}}}^S \cdot \underline{\gamma} \tag{3.37}$$

$$\dot{\underline{\mu}} = \frac{\partial^2 \psi}{\partial \underline{\kappa} \partial \underline{\kappa}} \cdot \dot{\underline{\kappa}} + \frac{\partial^2 \psi}{\partial \underline{\kappa} \partial \hat{\mathbf{C}}^S} \cdot \dot{\hat{\mathbf{C}}}^S = \hat{\mathbf{C}}^S \cdot \dot{\underline{\kappa}} + \dot{\hat{\mathbf{C}}}^S \cdot \underline{\kappa} \tag{3.38}$$

These equations (see also Fig. 3.2, where the stress and the strain rates have been replaced with their infinitesimal increments) show that both the stress and the couple-stress rates can be decomposed into two contributions: an *elastic* contribution due to deformation increments at fixed secant stiffness, and a *degrading* one induced by stiffness degradation at constant deformation

$$\dot{\underline{\sigma}} = \dot{\underline{\sigma}}^e + \dot{\underline{\sigma}}^d, \qquad \dot{\underline{\sigma}}^e := \hat{\mathbf{A}}^S \cdot \dot{\underline{\gamma}}, \qquad \dot{\underline{\sigma}}^d := \dot{\hat{\mathbf{A}}}^S \cdot \underline{\gamma} \tag{3.39}$$

$$\dot{\underline{\mu}} = \dot{\underline{\mu}}^e + \dot{\underline{\mu}}^d, \qquad \dot{\underline{\mu}}^e := \hat{\mathbf{C}}^S \cdot \dot{\underline{\kappa}}, \qquad \dot{\underline{\mu}}^d := \dot{\hat{\mathbf{C}}}^S \cdot \underline{\kappa} \tag{3.40}$$
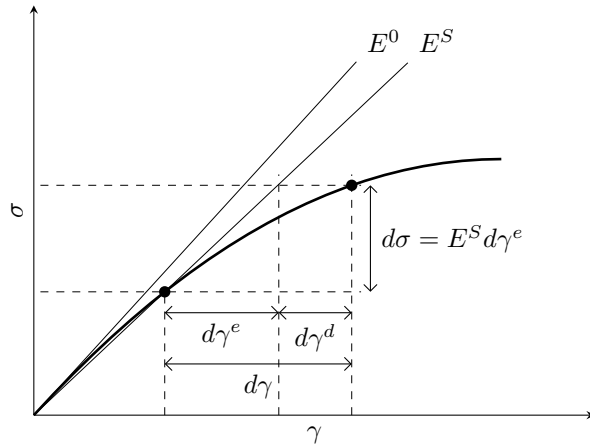
Figure 3.2: Additive decomposition of the strain rate

In an analogous way, from Eq. (3.36), the strain and the microcurvature rate tensors can be expressed as

$$\dot{\underline{\gamma}} = \frac{\partial^2 \mathbf{G}}{\partial \underline{\sigma} \partial \underline{\sigma}} \cdot \dot{\underline{\sigma}} + \frac{\partial^2 \mathbf{G}}{\partial \underline{\sigma} \partial (\hat{\mathbf{A}}^S)^{-1}} \cdot (\dot{\hat{\mathbf{A}}}^S)^{-1} = (\hat{\mathbf{A}}^S)^{-1} \cdot \dot{\underline{\sigma}} + (\dot{\hat{\mathbf{A}}}^S)^{-1} \cdot \underline{\sigma} \tag{3.41}$$

$$\dot{\underline{\kappa}} = \frac{\partial^2 \mathbf{G}}{\partial \underline{\mu} \partial \underline{\mu}} \cdot \dot{\underline{\mu}} + \frac{\partial^2 \mathbf{G}}{\partial \underline{\mu} \partial (\hat{\mathbf{C}}^S)^{-1}} \cdot (\dot{\hat{\mathbf{C}}}^S)^{-1} = (\hat{\mathbf{C}}^S)^{-1} \cdot \dot{\underline{\mu}} + (\dot{\hat{\mathbf{C}}}^S)^{-1} \cdot \underline{\mu} \tag{3.42}$$

A decomposition similar to the one adopted in Eqs. (3.39) and (3.40) can be introduced, resulting in the following *elastic* and *degrading* contributions

$$\dot{\underline{\gamma}} = \dot{\underline{\gamma}}^e + \dot{\underline{\gamma}}^d, \qquad \dot{\underline{\gamma}}^e := (\hat{\mathbf{A}}^S)^{-1} \cdot \dot{\underline{\sigma}}, \qquad \dot{\underline{\gamma}}^d := (\dot{\hat{\mathbf{A}}}^S)^{-1} \cdot \underline{\sigma} \tag{3.43}$$

$$\dot{\underline{\kappa}} = \dot{\underline{\kappa}}^e + \dot{\underline{\kappa}}^d, \qquad \dot{\underline{\kappa}}^e := (\hat{\mathbf{C}}^S)^{-1} \cdot \dot{\underline{\mu}}, \qquad \dot{\underline{\kappa}}^d := (\dot{\hat{\mathbf{C}}}^S)^{-1} \cdot \underline{\mu} \tag{3.44}$$

where the degrading deformation measures are related to the degrading parts of the stress and the couple-stress rate tensors by

$$\underline{\dot{\sigma}}^d = -\hat{\mathbf{A}}^S \cdot \underline{\dot{\gamma}}^d, \qquad \underline{\dot{\mu}}^d = -\hat{\mathbf{C}}^S \cdot \underline{\dot{\kappa}}^d \tag{3.45}$$

Making use of the aforementioned decompositions, the dissipation terms (Eq. (3.32)) can be expressed as

$$\dot{\mathfrak{D}}^* = -\frac{1}{2}\,\underline{\gamma} \cdot \underline{\dot{\sigma}}^d - \frac{1}{2}\,\underline{\kappa} \cdot \underline{\dot{\mu}}^d, \qquad \dot{\mathfrak{D}} = \frac{1}{2}\,\underline{\sigma} \cdot \underline{\dot{\gamma}}^d + \frac{1}{2}\,\underline{\mu} \cdot \underline{\dot{\kappa}}^d \tag{3.46}$$

Furthermore, considering the relations in Eq. (3.45), it can be easily shown that the equality $\dot{\mathfrak{D}} = \dot{\mathfrak{D}}^*$ holds.

Remark 3.3: Coupled media

In the decompositions expressed by Eqs. (3.39), (3.40), (3.43) and (3.44), the same notations introduced in Carol et al. (1994) for the classic continuum theory have been adopted. At this point, an analogy with the concept of *coupled media* (elasto-plastic coupling, i.e., dependence of the elastic moduli on the plastic deformation (Maier and Hueckel, 1979)) can be made. The *elastic* and the *degrading* components defined here can be identified as the *reversible* and the *irreversible* components defined in Collins and Houlsby (1997). However, differently from elasto-plastic coupling, in the present work the elastic properties depend only on the elastic degradation of the material and no plastic behaviour is accounted for.

3.3.1.1 Stress-based formulation

The stress-based formulation relies on the additive decomposition of the strain and the microcurvature rate tensors of Eqs. (3.43) and (3.44). Like in micropolar elasto-plasticity, two *degradation rules* are introduced to represent the degrading parts of the strain and the microcurvature rate tensors

$$\underline{\dot{\gamma}}^d = \dot{\lambda}\,\underline{m}_A \tag{3.47}$$

$$\underline{\dot{\kappa}}^d = \dot{\lambda}\,\underline{m}_C \tag{3.48}$$

where the term $\dot{\lambda}$ is the *inelastic multiplier*, defining the magnitude of the inelastic rates, while the operators $\underline{m}_A$ and $\underline{m}_C$ represent the *directions of degradation* of the strain and the microcurvature degrading rates, respectively. The degradation rules, together with Eqs. (3.43) and (3.44), allow to obtain the following expressions for the stress and the

couple-stress rate tensors

$$\dot{\underline{\sigma}} = \hat{\mathbf{A}}^S \cdot \dot{\underline{\gamma}} - \dot{\lambda}\,\hat{\mathbf{A}}^S \cdot \underline{m}_A \tag{3.49}$$

$$\dot{\underline{\mu}} = \hat{\mathbf{C}}^S \cdot \dot{\underline{\kappa}} - \dot{\lambda}\,\hat{\mathbf{C}}^S \cdot \underline{m}_C \tag{3.50}$$

It should be noted that the aforementioned degradation rules are not sufficient to completely define the evolution of the material properties during the degradation process, i.e., to represent univocally the evolution of the secant constitutive operators (see, e.g., Carol et al. (1994) for the same consideration in the classic continuum case). Indeed, it can be observed that each one of the expressions of the strain and the microcurvature degrading parts, here recalled for simplicity,

$$\dot{\underline{\gamma}}^d = (\dot{\hat{\mathbf{A}}}^S)^{-1} \cdot \underline{\sigma}, \qquad \dot{\underline{\kappa}}^d = (\dot{\hat{\mathbf{C}}}^S)^{-1} \cdot \underline{\mu} \tag{3.51}$$

represents, for a known stress-strain state, a system of 9 equations in 45 unknowns (the independent components of each one of the constitutive operators). Hence, proper degradation rules for the secant constitutive operators must be introduced in order to completely define the evolution of the model; for the considered stress-based approach these are represented by

$$(\dot{\hat{\mathbf{A}}}^S)^{-1} = \dot{\lambda}\,\hat{\mathbf{M}}_A \tag{3.52}$$

$$(\dot{\hat{\mathbf{C}}}^S)^{-1} = \dot{\lambda}\,\hat{\mathbf{M}}_C \tag{3.53}$$

where $\dot{\lambda}$ is an inelastic multiplier, defining the magnitude of the rates, and $\hat{\mathbf{M}}_A$ and $\hat{\mathbf{M}}_C$ represent, the directions of degradation of the inverse of the secant constitutive operators. It can be easily shown that the following relations between the different directions of degradation hold

$$\underline{m}_A = \hat{\mathbf{M}}_A \cdot \underline{\sigma} \tag{3.54}$$

$$\underline{m}_C = \hat{\mathbf{M}}_C \cdot \underline{\mu} \tag{3.55}$$

The different phases of the loading process are described in terms of the loading function[9] $f(\underline{\sigma}, \underline{\mu}, \hat{\mathbf{\Pi}}_A, \hat{\mathbf{\Pi}}_C)$, characterized by the classic Kuhn-Tucker conditions

$$\dot{\lambda} \geq 0, \qquad f \leq 0, \qquad \dot{\lambda} f = 0 \tag{3.56}$$

---

[9] This approach, consisting in a single loading function describing the loading process of both the Cauchy-like and the Cosserat-like parts of the formulation, is analogous to the *single-criterion* approach described by Forest and Sievert (2003) in micropolar elasto-plasticity. As it will be shown, this approach leads to a *coupling* between the non-linear constitutive equations, which will be addressed in Section 3.3.3.

When damage occours, the following *consistency condition* holds

$$\dot{f} = \frac{\partial f}{\partial \underline{\sigma}} \cdot \dot{\underline{\sigma}} + \frac{\partial f}{\partial \underline{\mu}} \cdot \dot{\underline{\mu}} + \frac{\partial f}{\partial \hat{\mathbf{\Pi}}_A} \cdot \dot{\hat{\mathbf{\Pi}}}_A + \frac{\partial f}{\partial \hat{\mathbf{\Pi}}_C} \cdot \dot{\hat{\mathbf{\Pi}}}_C = 0 \qquad (3.57)$$

Taking into account that degradation rules can be introduced also for the rates of the thermodynamic forces as

$$\dot{\hat{\mathbf{\Pi}}}_A = \dot{\lambda}\, \hat{\mathbf{h}}_A, \qquad \dot{\hat{\mathbf{\Pi}}}_C = \dot{\lambda}\, \hat{\mathbf{h}}_C \qquad (3.58)$$

the consistency condition can be rewritten as

$$\dot{f} = \underline{n}_A \cdot \dot{\underline{\sigma}} + \underline{n}_C \cdot \dot{\underline{\mu}} - H\, \dot{\lambda} = 0 \qquad (3.59)$$

where the following partial derivatives of the loading function have been introduced

$$\underline{n}_A := \frac{\partial f}{\partial \underline{\sigma}}, \quad \underline{n}_C := \frac{\partial f}{\partial \underline{\mu}}, \quad \hat{\mathbf{N}}_A := -\frac{\partial f}{\partial \hat{\mathbf{\Pi}}_A}, \quad \hat{\mathbf{N}}_C := -\frac{\partial f}{\partial \hat{\mathbf{\Pi}}_C} \qquad (3.60)$$

$$H := \hat{\mathbf{N}}_A \cdot \hat{\mathbf{h}}_A + \hat{\mathbf{N}}_C \cdot \hat{\mathbf{h}}_C = -\frac{\partial f}{\partial \lambda} \qquad (3.61)$$

It can be easily shown that the following relations between the partial derivatives of the loading function hold

$$\underline{n}_A = \hat{\mathbf{N}}_A \cdot \underline{\sigma}, \qquad \underline{n}_C = \hat{\mathbf{N}}_C \cdot \underline{\mu} \qquad (3.62)$$

Introducing the rate expressions for the stress and the couple-stress tensors of Eqs. (3.49) and (3.50) into the consistency condition, the following *strain-driven* expression for the inelastic multiplier can be obtained

$$\dot{\lambda} = \frac{\underline{n}_A \cdot (\hat{\mathbf{A}}^S \cdot \dot{\underline{\gamma}}) + \underline{n}_C \cdot (\hat{\mathbf{C}}^S \cdot \dot{\underline{\kappa}})}{H + \underline{n}_A \cdot (\hat{\mathbf{A}}^S \cdot \underline{m}_A) + \underline{n}_C \cdot (\hat{\mathbf{C}}^S \cdot \underline{m}_C)} \qquad (3.63)$$

Finally, introducing such equation into Eqs. (3.49) and (3.50), the following expressions for the stress and the couple-stress rate tensors can be obtained

$$\dot{\underline{\sigma}} = \left(\hat{\mathbf{A}}^S - \frac{(\hat{\mathbf{A}}^S \cdot \underline{m}_A) \otimes (\underline{n}_A \cdot \hat{\mathbf{A}}^S)}{H + \underline{n}_A \cdot (\hat{\mathbf{A}}^S \cdot \underline{m}_A) + \underline{n}_C \cdot (\hat{\mathbf{C}}^S \cdot \underline{m}_C)} \right) \cdot \dot{\underline{\gamma}}$$

$$- \frac{(\hat{\mathbf{A}}^S \cdot \underline{m}_A) \otimes (\underline{n}_C \cdot \hat{\mathbf{C}}^S)}{H + \underline{n}_A \cdot (\hat{\mathbf{A}}^S \cdot \underline{m}_A) + \underline{n}_C \cdot (\hat{\mathbf{C}}^S \cdot \underline{m}_C)} \cdot \dot{\underline{\kappa}} \qquad (3.64)$$

$$\dot{\underline{\mu}} = \left(\hat{\mathbf{C}}^S - \frac{(\hat{\mathbf{C}}^S \cdot \underline{m}_C) \otimes (\underline{n}_C \cdot \hat{\mathbf{C}}^S)}{H + \underline{n}_A \cdot (\hat{\mathbf{A}}^S \cdot \underline{m}_A) + \underline{n}_C \cdot (\hat{\mathbf{C}}^S \cdot \underline{m}_C)} \right) \cdot \dot{\underline{\kappa}}$$

$$- \frac{(\hat{\mathbf{C}}^S \cdot \underline{m}_C) \otimes (\underline{n}_A \cdot \hat{\mathbf{A}}^S)}{H + \underline{n}_A \cdot (\hat{\mathbf{A}}^S \cdot \underline{m}_A) + \underline{n}_C \cdot (\hat{\mathbf{C}}^S \cdot \underline{m}_C)} \cdot \dot{\underline{\gamma}} \qquad (3.65)$$

3.3.1.2 Strain-based formulation

The concepts developed in the previous section for the stress-based formulation are here repeated in a dual way, in order to obtain a *strain-based* formulation for micropolar elastic-degrading media. In this case, the additive decomposition of the stress and the couple-stress rate tensors (Eqs. (3.39) and (3.40)) is considered.

The degrading parts of the stress and the couple-stress rate tensors are defined in terms of the following degradation rules

$$\dot{\underline{\sigma}}^d = \dot{\lambda}\ \underline{m}_A^* \tag{3.66}$$

$$\dot{\underline{\mu}}^d = \dot{\lambda}\ \underline{m}_C^* \tag{3.67}$$

where $\dot{\lambda}$ is the *inelastic multiplier*, defining the magnitude of the inelastic rates, while the operators $\underline{m}_A^*$ and $\underline{m}_C^*$ represent, respectively, the *directions of degradations* of the stress and the couple-stress degrading rates. The degradation rules, together with Eqs. (3.39) and (3.40), allow to obtain the following expressions for the stress and the couple-stress rate tensors

$$\dot{\underline{\sigma}} = \hat{\mathbf{A}}^S \cdot \dot{\underline{\gamma}} + \dot{\lambda}\ \underline{m}_A^* \tag{3.68}$$

$$\dot{\underline{\mu}} = \hat{\mathbf{C}}^S \cdot \dot{\underline{\kappa}} + \dot{\lambda}\ \underline{m}_C^* \tag{3.69}$$

Due to the same considerations already made for the stress-based approach, degradation rules for the rates of the secant constitutive operators must be introduced as

$$\dot{\hat{\mathbf{A}}}^S = \dot{\lambda}\ \hat{\mathbf{M}}_A^* \tag{3.70}$$

$$\dot{\hat{\mathbf{C}}}^S = \dot{\lambda}\ \hat{\mathbf{M}}_C^* \tag{3.71}$$

where $\dot{\lambda}$ is an inelastic multiplier, defining the magnitude of the rates, and $\hat{\mathbf{M}}_A^*$ and $\hat{\mathbf{M}}_C^*$ represents, respectively, the directions of degradation of the secant constitutive operators. It can be easily shown that the following relations between the different directions of degradation hold

$$\underline{m}_A^* = \hat{\mathbf{M}}_A^* \cdot \underline{\gamma} \tag{3.72}$$

$$\underline{m}_C^* = \hat{\mathbf{M}}_C^* \cdot \underline{\kappa} \tag{3.73}$$

In an analogous way as in the stress-based approach, a single loading function $f(\underline{\gamma}, \underline{\kappa}, \hat{\mathbf{\Pi}}_A^*, \hat{\mathbf{\Pi}}_C^*)$ defines the different phases of the loading process; for such a function, the classic Kuhn-Tucker conditions hold

$$\dot{\lambda} \geq 0, \qquad f \leq 0, \qquad \dot{\lambda}f = 0 \tag{3.74}$$

In this case, the *consistency condition*, verified when damage occours, is represented by

$$\dot{f} = \frac{\partial f}{\partial \underline{\gamma}} \cdot \dot{\underline{\gamma}} + \frac{\partial f}{\partial \underline{\kappa}} \cdot \dot{\underline{\kappa}} + \frac{\partial f}{\partial \hat{\mathbf{\Pi}}_A^*} \cdot \dot{\hat{\mathbf{\Pi}}}_A^* + \frac{\partial f}{\partial \hat{\mathbf{\Pi}}_C^*} \cdot \dot{\hat{\mathbf{\Pi}}}_C^* = 0 \tag{3.75}$$

Defining the degradation rules for the rates of the thermodynamical forces as

$$\dot{\hat{\mathbf{\Pi}}}_A^* = \dot{\lambda}\, \hat{\mathbf{h}}_A^*, \qquad \dot{\hat{\mathbf{\Pi}}}_C^* = \dot{\lambda}\, \hat{\mathbf{h}}_C^* \tag{3.76}$$

the consistency condition can be rewritten as

$$\dot{f} = \underline{n}_A^* \cdot \dot{\underline{\gamma}} + \underline{n}_C^* \cdot \dot{\underline{\kappa}} - H^* \dot{\lambda} = 0 \tag{3.77}$$

where the following partial derivatives of the loading function have been introduced

$$\underline{n}_A^* := \frac{\partial f}{\partial \underline{\gamma}}, \quad \underline{n}_C^* := \frac{\partial f}{\partial \underline{\kappa}}, \quad \hat{\mathbf{N}}_A^* := \frac{\partial f}{\partial \hat{\mathbf{\Pi}}_A^*}, \quad \hat{\mathbf{N}}_C^* := \frac{\partial f}{\partial \hat{\mathbf{\Pi}}_C^*} \tag{3.78}$$

$$H^* := -\hat{\mathbf{N}}_A^* \cdot \hat{\mathbf{h}}_A^* - \hat{\mathbf{N}}_C^* \cdot \hat{\mathbf{h}}_C^* = -\frac{\partial f}{\partial \lambda} \tag{3.79}$$

It can be easily shown that the partial derivatives of the loading function are related by

$$\underline{n}_A^* = \hat{\mathbf{N}}_A^* \cdot \underline{\gamma}, \qquad \underline{n}_C^* = \hat{\mathbf{N}}_C^* \cdot \underline{\kappa} \tag{3.80}$$

The consistency condition leads to the following strain-driven expression for the inelastic multiplier

$$\dot{\lambda} = \frac{1}{H^*} \left(\underline{n}_A^* \cdot \dot{\underline{\gamma}} + \underline{n}_C^* \cdot \dot{\underline{\kappa}} \right) \tag{3.81}$$

that, when introduced into Eqs. (3.68) and (3.69), allows to obtain the following expressions for the stress and the couple-stress rate tensors

$$\dot{\underline{\sigma}} = \left(\hat{\mathbf{A}}^S + \frac{1}{H^*}(\underline{m}_A^* \otimes \underline{n}_A^*) \right) \cdot \dot{\underline{\gamma}} + \frac{1}{H^*}(\underline{m}_A^* \otimes \underline{n}_C^*) \cdot \dot{\underline{\kappa}} \tag{3.82}$$

$$\dot{\underline{\mu}} = \left(\hat{\mathbf{C}}^S + \frac{1}{H^*}(\underline{m}_C^* \otimes \underline{n}_C^*) \right) \cdot \dot{\underline{\kappa}} + \frac{1}{H^*}(\underline{m}_C^* \otimes \underline{n}_A^*) \cdot \dot{\underline{\gamma}} \tag{3.83}$$

Remark 3.4: General expressions of the constitutive equations

The unified formulation for classic constitutive models has been presented in Section 2.2.2 using an expression of the tangent constitutive operator (Eq. (2.12)) of general character, able to describe both the stress- and the strain-based approaches. An analogous expression can be obtained also for the rate equations of the micropolar

models discussed here, and is represented by (Gori et al., 2018)

$$\dot{\underline{\sigma}} = \left(\hat{\mathbf{A}}^S - \frac{1}{z} \left(\underline{x}_A \otimes \underline{y}_A \right) \right) \cdot \dot{\underline{\gamma}} - \frac{1}{z} \left(\underline{x}_A \otimes \underline{y}_C \right) \cdot \dot{\underline{\kappa}} \tag{3.84}$$

$$\dot{\underline{\mu}} = \left(\hat{\mathbf{C}}^S - \frac{1}{z} \left(\underline{x}_C \otimes \underline{y}_C \right) \right) \cdot \dot{\underline{\kappa}} - \frac{1}{z} \left(\underline{x}_C \otimes \underline{y}_A \right) \cdot \dot{\underline{\gamma}} \tag{3.85}$$

The expressions of the stress-based approach (Eqs. (3.64) and (3.65)) can be obtained assuming

$$z := H + \underline{n}_A \cdot \left(\hat{\mathbf{A}}^S \cdot \underline{m}_A \right) + \underline{n}_C \cdot \left(\hat{\mathbf{C}}^S \cdot \underline{m}_C \right) \tag{3.86}$$

$$\underline{x}_A := \hat{\mathbf{A}}^S \cdot \underline{m}_A, \quad \underline{x}_C := \hat{\mathbf{C}}^S \cdot \underline{m}_C \tag{3.87}$$

$$\underline{y}_A := \underline{n}_A \cdot \hat{\mathbf{A}}^S, \quad \underline{y}_C := \underline{n}_C \cdot \hat{\mathbf{C}}^S \tag{3.88}$$

while the ones of the strain-based approach (Eqs. (3.82) and (3.83)) are characterized by

$$z := H^* \tag{3.89}$$

$$\underline{x}_A := -\underline{m}_A^*, \quad \underline{x}_C := -\underline{m}_C^* \tag{3.90}$$

$$\underline{y}_A := \underline{n}_A^*, \quad \underline{y}_C := \underline{n}_C^* \tag{3.91}$$

3.3.1.3 Duality of the representations

The main operators characterizing the two different formulations of elastic degradation are resumed in Table 3.2. Peculiar duality relations between such operators can be obtained.

	Stress-based formulation	Strain-based formulation
Additive decompositions	$\dot{\underline{\gamma}} = \dot{\underline{\gamma}}^e + \dot{\underline{\gamma}}^d \rightarrow \dot{\underline{\sigma}} = \hat{\mathbf{A}}^S \cdot \dot{\underline{\gamma}}^e$ $\dot{\underline{\kappa}} = \dot{\underline{\kappa}}^e + \dot{\underline{\kappa}}^d \rightarrow \dot{\underline{\mu}} = \hat{\mathbf{C}}^S \cdot \dot{\underline{\kappa}}^e$	$\dot{\underline{\sigma}} = \dot{\underline{\sigma}}^e + \dot{\underline{\sigma}}^d \rightarrow \dot{\underline{\gamma}} = (\hat{\mathbf{A}}^S)^{-1} \cdot \dot{\underline{\sigma}}^e$ $\dot{\underline{\mu}} = \dot{\underline{\mu}}^e + \dot{\underline{\mu}}^d \rightarrow \dot{\underline{\kappa}} = (\hat{\mathbf{C}}^S)^{-1} \cdot \dot{\underline{\mu}}^e$
Degradation rules	$\dot{\underline{\gamma}}^d = \dot{\lambda}\, \underline{m}_A$ $\dot{\underline{\kappa}}^d = \dot{\lambda}\, \underline{m}_C$ $(\hat{\dot{\mathbf{A}}}^S)^{-1} = \dot{\lambda}\, \hat{\mathbf{M}}_A$ $(\hat{\dot{\mathbf{C}}}^S)^{-1} = \dot{\lambda}\, \hat{\mathbf{M}}_C$	$\dot{\underline{\sigma}}^d = \dot{\lambda}\, \underline{m}_A^*$ $\dot{\underline{\mu}}^d = \dot{\lambda}\, \underline{m}_C^*$ $\hat{\dot{\mathbf{A}}}^S = \dot{\lambda}\, \hat{\mathbf{M}}_A^*$ $\hat{\dot{\mathbf{C}}}^S = \dot{\lambda}\, \hat{\mathbf{M}}_C^*$
Loading function gradient	$f = f(\underline{\sigma}, \underline{\mu}, \hat{\mathbf{\Pi}}_A, \hat{\mathbf{\Pi}}_C)$ $\underline{n}_A = \frac{\partial f}{\partial \underline{\sigma}}$ $\underline{n}_C = \frac{\partial f}{\partial \underline{\mu}}$ $H = -\frac{\partial f}{\partial \lambda}$	$f = f(\underline{\gamma}, \underline{\kappa}, \hat{\mathbf{\Pi}}_A^*, \hat{\mathbf{\Pi}}_C^*)$ $\underline{n}_A^* = \frac{\partial f}{\partial \underline{\gamma}}$ $\underline{n}_C^* = \frac{\partial f}{\partial \underline{\kappa}}$ $H^* = -\frac{\partial f}{\partial \lambda}$
Inelastic multiplier	$\dot{\lambda} = \frac{\underline{n}_A \cdot (\hat{\mathbf{A}}^S \cdot \dot{\underline{\gamma}}) + \underline{n}_C \cdot (\hat{\mathbf{C}}^S \cdot \dot{\underline{\kappa}})}{H + \underline{n}_A \cdot (\hat{\mathbf{A}}^S \cdot \underline{m}_A) + \underline{n}_C \cdot (\hat{\mathbf{C}}^S \cdot \underline{m}_C)}$	$\dot{\lambda} = \frac{1}{H^*} \left(\underline{n}_A^* \cdot \dot{\underline{\gamma}} + \underline{n}_C^* \cdot \dot{\underline{\kappa}} \right)$

Table 3.2: Stress- and strain-based formulations

Comparing the expressions of the stress and the couple-stress rate tensors of the stress-

based formulation (Eqs. (3.49) and (3.50)) with the ones of the strain-based formulation (Eqs. (3.68) and (3.69)), it can be easily shown that the following relations between the directions of degradation hold

$$\underline{m}_A^* = -\hat{\mathbf{A}}^S \cdot \underline{m}_A \tag{3.92}$$

$$\underline{m}_C^* = -\hat{\mathbf{C}}^S \cdot \underline{m}_C \tag{3.93}$$

A relation between the gradients of the loading function can be obtained considering the chain rule for derivation, resulting in

$$\underline{n}_A^* = \frac{\partial f}{\partial \underline{\gamma}} = \frac{\partial f}{\partial \underline{\sigma}} \cdot \frac{\partial \underline{\sigma}}{\partial \underline{\gamma}} = \underline{n}_A \cdot \hat{\mathbf{A}}^S \tag{3.94}$$

$$\underline{n}_C^* = \frac{\partial f}{\partial \underline{\kappa}} = \frac{\partial f}{\partial \underline{\mu}} \cdot \frac{\partial \underline{\mu}}{\partial \underline{\kappa}} = \underline{n}_C \cdot \hat{\mathbf{C}}^S \tag{3.95}$$

Finally, a relation between the terms H and H^* can be obtained by equating the expressions of Eqs. (3.63) and (3.81) for the inelastic multiplier

$$H^* = H + \underline{n}_A \cdot (\hat{\mathbf{A}}^S \cdot \underline{m}_A) + \underline{n}_C \cdot (\hat{\mathbf{C}}^S \cdot \underline{m}_C) \tag{3.96}$$

It can be observed that the relations between the operators of the two formulations presented in this section are completely analogous to the ones that characterize the elastic-degading formulation based on the classic continuum theory (see, e.g., Carol et al. (1994) and Penna (2011) for a comparison).

3.3.2   Damage variables

In the previous sections, a generic elastic-degrading model for micropolar media has been developed. From this generic framework, a *damage model* is obtained once the secant constitutive operators are assumed to depend on a set of reduced parameters, the set of *damage variables*, that completely defines the state of degradation, or damage, of a material during a loading process. The main advantage of this approach is that a reduced number of parameters can be used instead of the 45 independents components of each one of the secant constitutive operators, allowing for a reduction in the complexity of the problem.

In a general case, two different sets of damage variables can be introduced: one representing the degradation of the stress-strain relation and the other the degradation of the relation between the couple-stress and the microcurvature. For a stress-based formulation the two sets of variables are indicated, respectively, as $\mathcal{D}_A$ and $\mathcal{D}_C$, while for a strain-based one, the symbols $\mathcal{D}_A^*$ and $\mathcal{D}_C^*$ are used. It should be noted that both the sets $\mathcal{D}_A$ and $\mathcal{D}_C$ and $\mathcal{D}_A^*$ and $\mathcal{D}_C^*$ represent the same physical phenomenon; however, a distinction

is maintained since the former are used to define the degradation of *compliance* tensors, while the latter define the degradation of *stiffness* tensors. In this general introduction, the peculiar nature of the operators defining the damage variables for the micropolar theory is not specified. Indeed, the previous symbols may be used to indicate, in general, scalar, vectorial or tensorial damage variables.

3.3.2.1   Stress-based formulation

In the stress-based approach, as already stated, the degradation process is represented in terms of the evolution of *compliance* constitutive operators. Introducing proper sets of damage variables, such operators can be expressed as

$$(\hat{\mathbf{A}}^S)^{-1} = (\hat{\mathbf{A}}^S)^{-1}\left((\hat{\mathbf{A}})^{-1}, \mathcal{D}_A\right) \tag{3.97}$$

$$(\hat{\mathbf{C}}^S)^{-1} = (\hat{\mathbf{C}}^S)^{-1}\left((\hat{\mathbf{C}})^{-1}, \mathcal{D}_C\right) \tag{3.98}$$

Hence, their time derivatives are represented by

$$(\dot{\hat{\mathbf{A}}}^S)^{-1} = \frac{\partial(\hat{\mathbf{A}}^S)^{-1}}{\partial \mathcal{D}_A} * \dot{\mathcal{D}}_A \tag{3.99}$$

$$(\dot{\hat{\mathbf{C}}}^S)^{-1} = \frac{\partial(\hat{\mathbf{C}}^S)^{-1}}{\partial \mathcal{D}_C} * \dot{\mathcal{D}}_C \tag{3.100}$$

where with the symbol $*$, a contraction operation compatible with the peculiar nature of the damage variables sets is indicated.

At this point it is observed that, similarly to the degradation rules introduced in Eqs. (3.52) and (3.53), analogous rules can be defined for the evolution of the damage variables as

$$\dot{\mathcal{D}}_A = \dot{\lambda}\,\mathcal{M}_A \tag{3.101}$$

$$\dot{\mathcal{D}}_C = \dot{\lambda}\,\mathcal{M}_C \tag{3.102}$$

where $\dot{\lambda}$ represents the *inelastic multiplier*, defining the magnitude of the damage evolution, while the operators $\mathcal{M}_A$ and $\mathcal{M}_C$ represent, respectively, the *directions of degradation* of the damage variables sets. Such operators present the same scalar, vectorial or tensorial nature of the sets of damage variables. Replacing these degradation rules in Eqs. (3.99) and (3.100), and comparing with the degradation rules of Eqs. (3.52)

and (3.53), it can be shown that the following relations hold

$$\hat{\mathbf{M}}_A = \frac{\partial (\hat{\mathbf{A}}^S)^{-1}}{\partial \mathcal{D}_A} * \mathcal{M}_A \tag{3.103}$$

$$\hat{\mathbf{M}}_C = \frac{\partial (\hat{\mathbf{C}}^S)^{-1}}{\partial \mathcal{D}_C} * \mathcal{M}_C \tag{3.104}$$

3.3.2.2 Strain-based formulation

Proceeding in a dual way, in the strain-based approach the degradation process is represented by means of the evolution of *stiffness* constitutive operators. Assuming their dependence on the sets of damage variables they can be expressed as

$$\hat{\mathbf{A}}^S = \hat{\mathbf{A}}^S \left(\hat{\mathbf{A}}, \mathcal{D}_A^* \right) \tag{3.105}$$

$$\hat{\mathbf{C}}^S = \hat{\mathbf{C}}^S \left(\hat{\mathbf{C}}, \mathcal{D}_C^* \right) \tag{3.106}$$

with time derivatives

$$\dot{\hat{\mathbf{A}}}^S = \frac{\partial \hat{\mathbf{A}}^S}{\partial \mathcal{D}_A^*} * \dot{\mathcal{D}}_A^* \tag{3.107}$$

$$\dot{\hat{\mathbf{C}}}^S = \frac{\partial \hat{\mathbf{C}}^S}{\partial \mathcal{D}_C^*} * \dot{\mathcal{D}}_C^* \tag{3.108}$$

Like for the stress-based formulation, proper degradation rules are introduced for the evolution of the damage variables

$$\dot{\mathcal{D}}_A^* = \dot{\lambda} \, \mathcal{M}_A^* \tag{3.109}$$

$$\dot{\mathcal{D}}_C^* = \dot{\lambda} \, \mathcal{M}_C^* \tag{3.110}$$

for which the following relations hold

$$\hat{\mathbf{M}}_A^* = \frac{\partial \hat{\mathbf{A}}^S}{\partial \mathcal{D}_A^*} * \mathcal{M}_A^* \tag{3.111}$$

$$\hat{\mathbf{M}}_C^* = \frac{\partial \hat{\mathbf{C}}^S}{\partial \mathcal{D}_C^*} * \mathcal{M}_C^* \tag{3.112}$$

3.3.3 Compact tensorial formulation for micropolar continua

The purpose of this section is to address the problem of *consistency* (or *compatibility*) between the proposed formulation for elastic degradation in micropolar model discussed above, and the existing analogous formulation for classic media discussed in Section 2.2.2. As pointed out in Section 2.2.2 and in the references therein, a unified formulation is useful for three reasons, since it allows to:

- represent different constitutive models within the same general equations;
- analyze different models at the same time performing the investigations directly on their common equations;
- reduce the implementation efforts, especially in case of an object-oriented approach.

Despite these points could be easily satisfied also by the formulation for micropolar media discussed previously, it is worth to note that they have been already addressed in case of classic media by an extensive literature (see, e.g., the localization analyses by Rizzi (1995) and Rizzi et al. (1996), the object-oriented implementations for elasto-plasticity by Jeremić and his co-authors (Jeremić and Sture, 1998, Jeremić et al., 1999, Jeremić and Yang, 2002), and for elastic degradation and elasto-plasticity by Penna and his co-authors (Penna, 2011, Gori et al., 2017a)); hence, it would be interesting for the micropolar models to take advantage of these theoretical and computational resources already defined for classic continuum models.

The main issue is constituted by the difference between the general equations of the classic and the micropolar formulations. Indeed, the formulation for classic media consists in the single rate expression $\dot{\underline{\sigma}} = \hat{\mathbf{E}}^t \cdot \dot{\underline{\varepsilon}}$, represented by the tangent constitutive operator expressed in Eq. (2.12), which for a monodissipative medium reduces to

$$\hat{\mathbf{E}}^t = \hat{\mathbf{E}}^S - \frac{1}{z}\left(\underline{x} \otimes \underline{y}\right) = (E_{ijk\ell}^S - \frac{1}{z}\, x_{ij}\, y_{k\ell})\, \bar{e}_i \otimes \bar{e}_j \otimes \bar{e}_k \otimes \bar{e}_\ell \qquad (3.113)$$

while a micropolar medium is represented in terms of the two rate expressions of Eqs. (3.84) and (3.85), here repeated for simplicity

$$\dot{\underline{\sigma}} = \left(\hat{\mathbf{A}}^S - \frac{1}{z}\left(\underline{x}_A \otimes \underline{y}_A\right)\right) \cdot \dot{\underline{\gamma}} - \frac{1}{z}\left(\underline{x}_A \otimes \underline{y}_C\right) \cdot \dot{\underline{\kappa}} \qquad (3.114)$$

$$\dot{\underline{\mu}} = \left(\hat{\mathbf{C}}^S - \frac{1}{z}\left(\underline{x}_C \otimes \underline{y}_C\right)\right) \cdot \dot{\underline{\kappa}} - \frac{1}{z}\left(\underline{x}_C \otimes \underline{y}_A\right) \cdot \dot{\underline{\gamma}} \qquad (3.115)$$

The solution of the problem of compatibility between the two formulations was proposed by the author in Gori et al. (2017c), using a compact tensorial formulation, originally adopted by Eremeyev (2005) for the problem of elastic waves propagation in micropolar media. Within this approach, the aforementioned micropolar rate equations can be condensed in a single *generalized tangent relation*

$$\dot{\underline{\underline{\Sigma}}} = \hat{\mathcal{E}}^t \cdot \dot{\underline{\underline{\Gamma}}} \qquad (3.116)$$

where the *generalized stress rate operator* $\dot{\underline{\underline{\Sigma}}}$ and the *generalized strain rate operator* $\dot{\underline{\underline{\Gamma}}}$, both represented by second-order tensors with dimension six, are defined by

$$\dot{\underline{\underline{\Sigma}}} = \begin{pmatrix} \dot{\underline{\sigma}} & \underline{0} \\ \underline{0} & \dot{\underline{\mu}} \end{pmatrix}, \qquad \dot{\underline{\underline{\Gamma}}} = \begin{pmatrix} \dot{\underline{\gamma}} & \underline{0} \\ \underline{0} & \dot{\underline{\kappa}} \end{pmatrix} \qquad (3.117)$$

The *generalized tangent operator* $\hat{\mathcal{E}}^t$ is instead represented by a fourth-order tensor with dimension six, and assumes the expression

$$\hat{\mathcal{E}}^t = \hat{\mathcal{E}}^S - \frac{1}{z}\left(\underline{X} \otimes \underline{Y}\right) \tag{3.118}$$

where $\underline{X}$ and $\underline{Y}$ are defined by

$$\underline{X} = \begin{pmatrix} \underline{x}_A & \underline{0} \\ \underline{0} & \underline{x}_C \end{pmatrix}, \qquad \underline{Y} = \begin{pmatrix} \underline{y}_A & \underline{0} \\ \underline{0} & \underline{y}_C \end{pmatrix} \tag{3.119}$$

The *generalized secant operator* is represented by a fourth-order tensor with dimension six, such that

$$\underline{\Sigma} = \hat{\mathcal{E}}^S \cdot \underline{\Gamma} \longrightarrow \begin{pmatrix} \underline{\sigma} & \underline{0} \\ \underline{0} & \underline{\mu} \end{pmatrix} = \hat{\mathcal{E}}^S \cdot \begin{pmatrix} \underline{\gamma} & \underline{0} \\ \underline{0} & \underline{\kappa} \end{pmatrix} \tag{3.120}$$

containing the elements of both the operators $\hat{\mathbf{A}}^S$ and $\hat{\mathbf{C}}^S$, as illustrated in the following scheme

$$(\hat{\mathcal{E}}^S)_{\beta\nu\delta\psi} = \begin{cases} \begin{pmatrix} A^S_{\beta\nu 11} & A^S_{\beta\nu 12} & A^S_{\beta\nu 13} & 0 & 0 & 0 \\ A^S_{\beta\nu 21} & A^S_{\beta\nu 22} & A^S_{\beta\nu 23} & 0 & 0 & 0 \\ A^S_{\beta\nu 31} & A^S_{\beta\nu 32} & A^S_{\beta\nu 33} & 0 & 0 & 0 \\ \hline 0 & 0 & 0 & 0 & 0 & 0 \\ 0 & 0 & 0 & 0 & 0 & 0 \\ 0 & 0 & 0 & 0 & 0 & 0 \end{pmatrix}, \text{ for } \beta, \nu = 1, 2, 3 \\[2em] \begin{pmatrix} 0 & 0 & 0 & 0 & 0 & 0 \\ 0 & 0 & 0 & 0 & 0 & 0 \\ 0 & 0 & 0 & 0 & 0 & 0 \\ \hline 0 & 0 & 0 & C^S_{(\beta-3)(\nu-3)11} & C^S_{(\beta-3)(\nu-3)12} & C^S_{(\beta-3)(\nu-3)13} \\ 0 & 0 & 0 & C^S_{(\beta-3)(\nu-3)21} & C^S_{(\beta-3)(\nu-3)22} & C^S_{(\beta-3)(\nu-3)23} \\ 0 & 0 & 0 & C^S_{(\beta-3)(\nu-3)31} & C^S_{(\beta-3)(\nu-3)32} & C^S_{(\beta-3)(\nu-3)33} \end{pmatrix}, \text{ for } \beta, \nu = 4, 5, 6 \end{cases} \tag{3.121}$$

At this point it should be noted how the generalized tangent operator depicted in Eq. (3.118) presents a tensorial expression that is formally identical to the one of the tangent operator for classic media (Eq. (3.113)), except for the dimension of the involved operators, hence solving the problem of compatibility between the two formulations. The compact tensorial formulation presented in Gori et al. (2017*c*) and discussed in this section, was adopted by the author in Gori et al. (2017*b*) to extend to micropolar elastic-degrading models concepts of localization and discontinuous failure previously formulated for classic media (Chapter 5), and in Gori et al. (2018) to represent micropolar constitutive models within the same computational framework of classic elastic-degrading models (discussed in details in Appendix C).

3.3.3.1 Stress-based formulation

In the stress-based approach the generalized tangent operator (Eq. (3.118)) is expressed by

$$\hat{\mathcal{E}}^t = \hat{\mathcal{E}}^S - \frac{(\hat{\mathcal{E}}^S \cdot \underline{m}) \otimes (\underline{n} \cdot \hat{\mathcal{E}}^S)}{H + \underline{n} \cdot (\hat{\mathcal{E}}^S \cdot \underline{m})} \tag{3.122}$$

The directions of degradation and the partial derivatives of the loading function are represented in a generalized form as

$$\underline{m} = \begin{pmatrix} m_A & 0 \\ 0 & m_C \end{pmatrix}, \qquad \underline{n} = \frac{\partial f}{\partial \underline{\Sigma}} = \begin{pmatrix} n_A & 0 \\ 0 & n_C \end{pmatrix} \tag{3.123}$$

Regarding the directions of degradation for the evolution of the secant constitutive operators, a generalized operator $\hat{\mathbf{M}}$ can be introduced in a way to include the components of both $\hat{\mathbf{M}}_A$ and $\hat{\mathbf{M}}_C$, following the same scheme adopted in Eq. (3.121). With this generalized operator, the rate of variation of the generalized secant constitutive operator is represented by

$$(\dot{\hat{\mathcal{E}}}^S)^{-1} = \dot{\lambda}\,\hat{\mathbf{M}} \tag{3.124}$$

It should be noted that this compact tensorial formulation can be extended also to the operators defining the damage variables, that can be represented by means of a generalized set of damage variables $\mathcal{D}$, containing both the operators $\mathcal{D}_A$ and $\mathcal{D}_C$, which explicit expression depends on the peculiar nature of the sets of damage variables. For the generalized set of damage variables the degradation rule is

$$\dot{\mathcal{D}} = \dot{\lambda}\,\mathcal{M} \tag{3.125}$$

where $\mathcal{M}$ is a generalized operator containing the directions of degradation $\mathcal{M}_A$ and $\mathcal{M}_C$.

3.3.3.2 Strain-based formulation

The strain-based approach is characterized by the following generalized tangent operator

$$\hat{\mathcal{E}}^t = \hat{\mathcal{E}}^S + \frac{1}{H^*}(\underline{m}^* \otimes \underline{n}^*) \tag{3.126}$$

where the generalized operators $\underline{m}^*$ and $\underline{n}^*$ are represented by

$$\underline{m}^* = \begin{pmatrix} m_A^* & 0 \\ 0 & m_C^* \end{pmatrix}, \qquad \underline{n}^* = \frac{\partial f}{\partial \underline{\Gamma}} = \begin{pmatrix} n_A^* & 0 \\ 0 & n_C^* \end{pmatrix} \tag{3.127}$$

Proceeding in a dual way to the stress-based case, a generalized operator $\hat{\mathbf{M}}^*$, containing the components of both $\hat{\mathbf{M}}_A^*$ and $\hat{\mathbf{M}}_C^*$ can be introduced, allowing the representation

of the evolution of the generalized secant constitutive operator as

$$\dot{\hat{\mathcal{E}}}^S = \dot{\lambda} \, \hat{\mathbf{M}}^* \tag{3.128}$$

Regarding the damage variables and their evolution, the same considerations already made for the stress-based formulation hold. Hence, the generalized set of damage variable $\mathcal{D}^*$, containing both the operators $\mathcal{D}_A^*$ and $\mathcal{D}_C^*$, can be introduced, together with its evolution rule

$$\dot{\mathcal{D}}^* = \dot{\lambda} \, \mathcal{M}^* \tag{3.129}$$

where $\mathcal{M}^*$ is the generalized operator containing the directions of degradation $\mathcal{M}_A^*$ and $\mathcal{M}_C^*$.

3.3.4 Scalar-isotropic damage models

Scalar damage models can be derived within the general formulation discussed in Section 3.3.1 by reducing the set of damage variables to a single scalar value, like in a classic medium. If damage is assumed to be also isotropic, the resulting generalized constitutive operator can be expressed as

$$\hat{\mathcal{E}}^S(\hat{\mathcal{E}}, D) = (1 - D) \, \hat{\mathcal{E}} \tag{3.130}$$

where the damage variable D is assumed to vary from 0 (undamaged material) to 1 (completely damaged material), and where $\hat{\mathcal{E}}$ represents the initial elastic operator. The evolution of the secant material properties depends on the rate of the damage variable as

$$\dot{\hat{\mathcal{E}}}^S(\hat{\mathcal{E}}, D) = \frac{\partial \hat{\mathcal{E}}^S}{\partial D} \, \dot{D} = -\hat{\mathcal{E}} \, \dot{D} \tag{3.131}$$

Focusing on the strain-based approach, the comparison of the previous equation with Eq. (3.128) shows that the following relations hold

$$\dot{\lambda} = \dot{D}, \quad \hat{\mathbf{M}}^* = -\hat{\mathcal{E}}, \quad \hat{\mathbf{M}}_A^* = -\hat{\mathbf{A}}, \quad \hat{\mathbf{M}}_C^* = -\hat{\mathbf{C}} \tag{3.132}$$

$$\mathcal{M} = \mathcal{M}_A^* = \mathcal{M}_C^* = 1 \tag{3.133}$$

Hence, the directions of degradation for the inelastic rates are represented by

$$\left. \begin{array}{l} \underline{m}_A^* = -\hat{\mathbf{A}} \cdot \underline{\gamma} = -\underline{\sigma}^0 \\ \underline{m}_C^* = -\hat{\mathbf{C}} \cdot \underline{\kappa} = -\underline{\mu}^0 \end{array} \right\} \longrightarrow \underline{m}^* = -\underline{\Sigma}^0 := - \begin{pmatrix} \underline{\sigma}^0 & \underline{0} \\ \underline{0} & \underline{\mu}^0 \end{pmatrix} \tag{3.134}$$

A common choice for the loading function $f(\underline{\gamma}, \underline{\kappa}, D) = f(\underline{\Gamma}, D)$ in the case of scalar

damage is represented by the following additive decomposition

$$f(\underline{\gamma}, \underline{\kappa}, D) = \Gamma_{eq}(\underline{\gamma}, \underline{\kappa}) - K(D) \leq 0 \qquad (3.135)$$

where $\Gamma_{eq}(\underline{\gamma}, \underline{\kappa}) = \Gamma_{eq}(\underline{\Gamma})$ is a function depending only on the deformation operators, usually referred to as *equivalent deformation*, that represents the loading condition of the continuum, while $K(D)$ is an *historical parameter* that depends only on the damage variable. The historical parameter is representative of the maximum level of deformation reached during the loading process. With this assumption it follows that

$$\underline{n}_A^* = \frac{\partial \Gamma_{eq}}{\partial \underline{\gamma}}, \quad \underline{n}_C^* = \frac{\partial \Gamma_{eq}}{\partial \underline{\kappa}}, \quad H = \frac{\partial K}{\partial D} = \left(\frac{\partial D(\Gamma_{eq})}{\partial \Gamma_{eq}} \right)^{-1} \qquad (3.136)$$

where $D(\Gamma_{eq})$ is a prescribed evolution law for the damage variable.

At this point, it can be easily shown that, for a scalar-isotropic damage model, the stress and the couple-stress rates (Eqs. (3.82) and (3.83)) can be rewritten as

$$\dot{\underline{\sigma}} = \left((1 - D) \, \hat{\mathbf{A}} - \frac{\partial D(\Gamma_{eq})}{\partial \Gamma_{eq}} \, \left(\underline{\sigma}^0 \otimes \frac{\partial \Gamma_{eq}}{\partial \underline{\gamma}} \right) \right) \cdot \dot{\underline{\gamma}}$$
$$- \frac{\partial D(\Gamma_{eq})}{\partial \Gamma_{eq}} \left(\underline{\sigma}^0 \otimes \frac{\partial \Gamma_{eq}}{\partial \underline{\kappa}} \right) \cdot \dot{\underline{\kappa}} \qquad (3.137)$$

$$\dot{\underline{\mu}} = \left((1 - D) \, \hat{\mathbf{C}} - \frac{\partial D(\Gamma_{eq})}{\partial \Gamma_{eq}} \, \left(\underline{\mu}^0 \otimes \frac{\partial \Gamma_{eq}}{\partial \underline{\kappa}} \right) \right) \cdot \dot{\underline{\kappa}}$$
$$- \frac{\partial D(\Gamma_{eq})}{\partial \Gamma_{eq}} \left(\underline{\mu}^0 \otimes \frac{\partial \Gamma_{eq}}{\partial \underline{\gamma}} \right) \cdot \dot{\underline{\gamma}} \qquad (3.138)$$

or in terms of the generalized tangent operator

$$\hat{\mathcal{E}}^t = (1 - D) \, \hat{\mathcal{E}} - \frac{\partial D(\Gamma_{eq})}{\partial \Gamma_{eq}} \, \left(\underline{\Sigma}^0 \otimes \frac{\partial \Gamma_{eq}}{\partial \underline{\Gamma}} \right) \qquad (3.139)$$

Within this general framework different damage models can be obtained, once peculiar equivalent deformations and damage law are choosen. In the following, the two damage models used in the numerical simulations of Chapters 6 and 7 will be presented; further models proposed by the author in other pubblications will be presented in Appendix A. Before proceeding to the presentation of these models, a brief discussion on the special case of *associated* models is reported, since it will be used in Section 5.4.

3.3.4.1 Associated models in strain space

A peculiar class of scalar-isotropic damage models is represented by the ones that are *associated in the strain-space*, i.e., damage models for which the gradient of the loading function $\underline{n}$ (or $\underline{n}^*$) has the same direction of the degradation rule $\underline{m}$ (or $\underline{m}^*$). Such models

can be expressed as $\underline{n}^* = \tau \, \underline{\Sigma}^0$, where the parameter τ depends on the peculiar damage model. In this case, the generalized tangent operator assumes the expression

$$\hat{\mathcal{E}}^t = (1 - D) \, \hat{\mathcal{E}} - \tau \frac{\partial D(\Gamma_{eq})}{\partial \Gamma_{eq}} \, \left(\underline{\Sigma}^0 \otimes \underline{\Sigma}^0 \right) \tag{3.140}$$

3.3.4.2   Marigo's micropolar damage model

The so-called *Marigo's micropolar scalar damage model* has been adopted by the author in Gori et al. (2017*b*), where it was used to perform analytical and numerical localization analyses. It is an associated model, obtained as an extension to the micropolar theory of the classic damage model based on strain energy proposed by Marigo (1985), and is characterized by the following equivalent deformation

$$\Gamma_{eq} = \sqrt{\frac{2\psi^0}{E}}, \quad \psi^0 = \frac{1}{2} \, \underline{\gamma} \cdot \left(\hat{\mathbf{A}} \cdot \underline{\gamma} \right) + \frac{1}{2} \, \underline{\kappa} \cdot \left(\hat{\mathbf{C}} \cdot \underline{\kappa} \right), \quad \tau = \frac{1}{E \, \Gamma_{eq}} \tag{3.141}$$

In the numerical simulations of Chapter 6, it was associated to the following exponential damage law

$$D(\Gamma_{eq}) = 1 - \frac{K_0}{\Gamma_{eq}} \left(1 - \alpha + \alpha e^{-\beta(\Gamma_{eq} - K_0)} \right) \tag{3.142}$$

where, like in the analogous law for the classic continuum depicted in Eq. (2.33), K_0 is a threshold value for the equivalent deformation, representing the onset of damage, and where α and β are parameters that allow to control, the maximum value of the scalar damage variable and the damage evolution intensity, respectively.

3.3.4.3   Mazars micropolar damage model

This model was proposed by the author in Gori et al. (2017*c*), and it is an extension of the classic Mazar damage model (Mazars, 1984). It is represented by the following equivalent deformation[10]

$$\Gamma_{eq}(\underline{\gamma}, \underline{\kappa}) = \sqrt{\left[\sum_{k=1}^{3} \left(< \varepsilon^{(k)} >_+ \right)^2 \right] + \underline{\kappa}^* \cdot \underline{\kappa}^*}, \quad < \varepsilon^{(k)} >_+ = \frac{\varepsilon^{(k)} + |\varepsilon^{(k)}|}{2} \tag{3.143}$$

where $\varepsilon^{(k)}$ is the k-th eigenvalue of the symmetric part of the strain tensor ($\underline{\varepsilon} = \underline{\gamma}^{sym}$), while the operator $< \cdot >_+$ indicates the positive part of a quantity. With this choice for the equivalent deformation, the gradients of the loading function, represented in Voigt

---

[10] It should be noted that, for dimensionality reasons, the scaled microcurvature tensor $\underline{\kappa}^*$ defined in Section 3.2.2 has been used in Eq. (3.143).

notation, are expressed as

$$\left\{\frac{\partial f}{\partial \underline{\gamma}}\right\}_g = \frac{1}{\Gamma_{eq}}\ [T_\varepsilon]^T < \{\underline{\varepsilon}\}_\ell >_+ \tag{3.144}$$

$$\left\{\frac{\partial f}{\partial \underline{\kappa}^*}\right\}_g = \frac{1}{\Gamma_{eq}}\ \{\underline{\kappa}^*\}_g \tag{3.145}$$

where with the subscripts g and ℓ are indicated, respectively, a *global* coordinate system, and the *local principal* system of the tensor $\underline{\varepsilon}$, and where the matrix $[T_\varepsilon]$ represents the transformation matrix of the symmetric part of the strain tensor between these two systems, $\{\underline{\varepsilon}\}_\ell = [T_\varepsilon]\ \{\underline{\varepsilon}\}_g$.

An alternative version of the model, used in the numerical examples of Chapter 7, can be obtained by removing the dependence of the equivalent deformation on the microcurvature tensor

$$\Gamma_{eq}(\underline{\gamma}, \underline{\kappa}) = \Gamma_{eq}(\underline{\gamma}) = \sqrt{\left[\sum_{k=1}^{3} \left(< \varepsilon^{(k)} >_+\right)^2\right]} \tag{3.146}$$

which makes the term $\{\partial f/\partial \underline{\kappa}^*\}_g$ to vanish.

In the original work by Mazars a specific treatment for the evolution of the scalar damage variable was adopted, which extension to the micropolar formulation have been discussed in Gori et al. (2017*c*) and will be recalled in Appendix A. In the numerical simulations presented in Chapter 7, the approach suggested in de Borst and Gutiérrez (1999) was followed. This is a simplified version of the Mazar's model, where the exponential damage law of Eq. (3.142) replace the original treatment of the damage variable proposed by Mazars.

3.4   Weak form and FEM representation

3.4.1   Weak form of the micropolar boundary values problem

The weak form of the coupled boundary values problem that governs a micropolar medium described in Section 3.2, can be obtained in a straightforward manner using the weighted residual method, for example. Once obtained, the problem resumes in: find the set $U = (\bar{u}, \bar{\varphi}) \in \mathcal{V}(\mathbf{D})$ such that

$$A(W, U) = f(W), \quad \forall\ W = (\bar{w}, \bar{\omega}) \in \mathcal{V}^0(\mathbf{D}) \tag{3.147}$$

where $\mathcal{V}(\mathbf{D})$ is the space of *trial functions* (or *admissible configurations*), and $\mathcal{V}^0(\mathbf{D})$ the space of *test functions*, defined as

$$\mathcal{V}(\mathbf{D}) := \{U \equiv (\bar{u}, \bar{\varphi}) \in \mathcal{H}^*(\mathbf{D}) \mid \bar{u} = \bar{u}^* \text{ at } \partial\mathbf{D}_e^u, \bar{\varphi} = \bar{\varphi}^* \text{ at } \partial\mathbf{D}_e^\varphi\} \qquad (3.148)$$

$$\mathcal{V}^0(\mathbf{D}) := \left\{W \equiv (\bar{w}, \bar{\omega}) \in \mathcal{H}^*(\mathbf{D}) \mid \bar{w} = \bar{0} \text{ at } \partial\mathbf{D}_e^u, \bar{\omega} = \bar{0} \text{ at } \partial\mathbf{D}_e^\varphi\right\} \qquad (3.149)$$

where $\mathcal{H}^*(\mathbf{D}) = (\mathcal{H}^1(\mathbf{D}))^n \times (\mathcal{H}^1(\mathbf{D}))^m$, with $(\mathcal{H}^1(\mathbf{D}))^k$ the space of square integrable k-dimensional vector fields with square integrable first derivatives over the domain $\mathbf{D}$. The *bilinear form* $A(W, U) = A((\bar{w}, \bar{\omega}), (\bar{u}, \bar{\varphi}))$ is expressed as

$$\begin{aligned} A(W, U) &:= \int_{\mathbf{D}} \left(\text{grad}^{\mathrm{T}}(\bar{w}) - \mathsf{e} \cdot \bar{\omega}\right) \cdot \left(\hat{\mathbf{A}} \cdot \left(\text{grad}^{\mathrm{T}}(\bar{u}) - \mathsf{e} \cdot \bar{\varphi}\right)\right) \, \mathrm{d}\mathcal{V} \\ &\quad + \int_{\mathbf{D}} \text{grad}^{\mathrm{T}}(\bar{\omega}) \cdot \left(\hat{\mathbf{C}} \cdot \text{grad}^{\mathrm{T}}(\bar{\varphi})\right) \, \mathrm{d}\mathcal{V} \end{aligned} \qquad (3.150)$$

and the *linear functional* $f(W) = f(\bar{w}, \bar{\omega})$ as

$$f(W) := \int_{\partial\mathbf{D}_n^u} \bar{w} \cdot \bar{t}_A \, \mathrm{d}\mathcal{S} + \int_{\mathbf{D}} \bar{w} \cdot \bar{b}_V \, \mathrm{d}\mathcal{V} + \int_{\partial\mathbf{D}_n^\varphi} \bar{\omega} \cdot \bar{t}_C \, \mathrm{d}\mathcal{S} + \int_{\mathbf{D}} \bar{\omega} \cdot \bar{l}_V \, \mathrm{d}\mathcal{V} \qquad (3.151)$$

The existence and uniqueness of the solution of the problem of Eq. (3.147) have been proven in Hlaváček and Hlaváček (1969).

Recalling the definition of the strain and the microcurvature tensors given in Eqs. (3.1) and (3.2), the bilinear form can be rewritten as

$$\begin{aligned} A(W, U) &= \int_{\mathbf{D}} \underline{\gamma}(W) \cdot \left(\hat{\mathbf{A}} \cdot \underline{\gamma}(U)\right) \, \mathrm{d}\mathcal{V} + \int_{\mathbf{D}} \underline{\kappa}(W) \cdot \left(\hat{\mathbf{C}} \cdot \underline{\kappa}(U)\right) \, \mathrm{d}\mathcal{V} \\ &= \int_{\mathbf{D}} \underline{\Gamma}(W) \cdot \left(\hat{\mathcal{E}} \cdot \underline{\Gamma}(U)\right) \, \mathrm{d}\mathcal{V} \end{aligned} \qquad (3.152)$$

3.4.1.1   Linearization of the weak form

In order to treat the presence of physical non-linearities, the weak form defined in Eq. (3.147) must be *linearized*. This procedure is briefly recalled in the following; the aspects concerning the discretization of such linearized weak form are skipped, since they will be addressed in more details in the following Sections 4.3 and 4.4.

The linearization is performed introducing the space of *admissible variations* $\delta\mathcal{V}(\mathbf{D})$, defined by

$$\delta\mathcal{V}(\mathbf{D}) := \left\{\delta U \equiv (\delta\bar{u}, \delta\bar{\varphi}) \in \mathcal{H}^*(\mathbf{D}) \mid \delta\bar{u} = \bar{0} \text{ at } \partial\mathbf{D}_e^u, \delta\bar{\varphi} = \bar{0} \text{ at } \partial\mathbf{D}_e^\varphi\right\} \qquad (3.153)$$

which allows to obtain a set of *perturbed* configurations $\mathcal{V}_\varepsilon(\mathbf{D})$, characterized by elements $U_\varepsilon = U + \delta U$ satisfying the kinematical boundary conditions of the problem. Recasting

the weak form of Eq. (3.147) for a known equilibrium configuration U as

$$G(W, U) := A(W, U) - f(W) = 0, \quad \forall W \in \mathcal{V}^0(\mathbf{D}) \tag{3.154}$$

with the introduction of the functional $G(W, U)$, a perturbed configuration near the equilibrium one, which still satisfies the equilibrium condition of the body, can be expressed in terms of the elements of the space of admissible variations as

$$G(W, U_\varepsilon) := A(W, U_\varepsilon) - f(W) = 0, \quad \forall W \in \mathcal{V}^0(\mathbf{D}) \tag{3.155}$$

The variation δU which allows to reach the new equilibrium configuration can be evaluated approximating the functional G with its linearization $G(W, U_\varepsilon) \simeq L\left[G(W, U_\varepsilon)\right]$, resulting in

$$L\left[G(W, U_\varepsilon)\right] = G(W, U) + DG(W, U) \cdot \delta U = 0, \quad \forall W \in \mathcal{V}^0(\mathbf{D}) \tag{3.156}$$

where the term $DG(W, U_\varepsilon) \cdot \delta U$ is the following *directional* (or *Fréchet*) derivative

$$DG(W, U) \cdot \delta \bar{u} = \left. \frac{\partial G(W, U_\varepsilon)}{\partial \varepsilon} \right|_{\varepsilon=0} \tag{3.157}$$

The linearized weakened-weak form can then be recasted into: find the *increment* $\delta U \in \delta \mathcal{V}(\mathbf{D})$ such that

$$DG(W, U) \cdot \delta U = -G(W, U), \quad \forall W \in \mathcal{V}^0(\mathbf{D}) \tag{3.158}$$

It can be easily shown (see, Section 3.4.1) that the term $DG(W, U) \cdot \delta U$ appearing in the linearized weak form of Eq. (3.158) is expressed by

$$DG(W, U) \cdot \delta U = \int_{\mathbf{D}} \underline{\Gamma}(W) \cdot \left(\hat{\mathcal{E}}^t \cdot \delta \underline{\Gamma}(U) \right) \, \mathrm{d}\mathcal{V} \tag{3.159}$$

where $\hat{\mathcal{E}}^t$ is the generalized *tangent* constitutive operator as defined in Section 3.3, and where the variation $\delta \underline{\Gamma}(U)$ can be interpreted as the *rate* of the generalized deformation tensors $\dot{\underline{\Gamma}}$ appearing in Section 3.3.

3.4.2 Voigt notation

The weak form illustrated above can be rewritten in Voigt notation, a form that is more suitable for the numerical implementation discussed in Appendix C, exposed briefly here for a plane-stress problem. In this case, the only components of the displacement and the microrotation fields that characterize the problem are u_x, u_y, and φ_z, while stress and

deformation measures are expressed by

$$\{\underline{\sigma}\} = (\sigma_{xx} \ \sigma_{xy} \ \sigma_{yx} \ \sigma_{yy})^T, \qquad \{\underline{\gamma}\} = (\gamma_{xx} \ \gamma_{xy} \ \gamma_{yx} \ \gamma_{yy})^T \qquad (3.160)$$

$$\{\underline{\mu}^*\} = (\mu_{xz}/L_b \ \mu_{yz}/L_b)^T, \qquad \{\underline{\kappa}^*\} = (\kappa_{xz}L_b \ \kappa_{yz}L_b)^T \qquad (3.161)$$

where the scaled couple-stresses and microcurvatures are being used, since, as shown in de Borst (1991), they lead to a more convenient numerical representation.

The expressions of the strain and the microcurvature tensors (Eqs. (3.1) and (3.2)) can be rewritten in Voigt notation as

$$\{\underline{\gamma}\} = [L_A]\{\bar{u}\} - [\mathsf{e}]\{\bar{\varphi}\} = \begin{pmatrix} \partial_x & 0 \\ 0 & \partial_x \\ \partial_y & 0 \\ 0 & \partial_y \end{pmatrix} \begin{pmatrix} u_x \\ u_y \end{pmatrix} - \begin{pmatrix} 0 \\ 1 \\ -1 \\ 0 \end{pmatrix} \varphi_z \qquad (3.162)$$

$$\{\underline{\kappa}^*\} = [L_C^*]\{\bar{\varphi}\} = \begin{pmatrix} L_b \ \partial_x \\ L_b \ \partial_y \end{pmatrix} \varphi_z \qquad (3.163)$$

where the derivative operator $[L_C^*]$ already embeds the characteristic bending length L_b. From Eq. (3.150), the bilinear form $A(W, U)$ can be expressed as

$$A(W, U) = \int_{\mathbf{D}} ([L_A]\{\bar{w}\} - [\mathsf{e}]\{\bar{\omega}\})^T [\hat{\mathbf{A}}] ([L_A]\{\bar{u}\} - [\mathsf{e}]\{\bar{\varphi}\}) \ \mathrm{d}\mathcal{V}$$
$$+ \int_{\mathbf{D}} ([L_C^*]\{\bar{\omega}\})^T [\hat{\mathbf{C}}^*] ([L_C^*]\{\bar{\varphi}\}) \ \mathrm{d}\mathcal{V} \qquad (3.164)$$

where the matricial expressions of the constitutive operators $[\hat{\mathbf{A}}]$ and $[\hat{\mathbf{C}}^*]$ are

$$[\hat{\mathbf{A}}] = \begin{pmatrix} \frac{E}{1-\nu^2} & 0 & 0 & \frac{\nu E}{1-\nu^2} \\ 0 & G + G_c & G - G_c & 0 \\ 0 & G - G_c & G + G_c & 0 \\ \frac{\nu E}{1-\nu^2} & 0 & 0 & \frac{E}{1-\nu^2} \end{pmatrix}, \quad [\hat{\mathbf{C}}^*] = \begin{pmatrix} 2G & 0 \\ 0 & 2G \end{pmatrix} \qquad (3.165)$$

while from Eq. (3.151) the linear functional $f(W)$ can be expressed as

$$f(W) = \int_{\partial\mathbf{D}_n^u} \{\bar{w}\}^T \{\bar{t}_A\} \ \mathrm{d}\mathcal{S} + \int_{\mathbf{D}} \{\bar{w}\}^T \{\bar{b}_V\} \ \mathrm{d}\mathcal{V}$$
$$+ \int_{\partial\mathbf{D}_n^\varphi} \{\bar{\omega}\}^T \{\bar{t}_C\} \ \mathrm{d}\mathcal{S} + \int_{\mathbf{D}} \{\bar{\omega}\}^T \{\bar{l}_V\} \ \mathrm{d}\mathcal{V} \qquad (3.166)$$

It is worth to note that, in general, when a micropolar medium is investigated numerically with the finite element method or with other discretization methods, the field variables and the stress and the deformation measures are not represented separately with different objects as in the equations above. The field variables u_x, u_y, and φ_z, for example,

are usually collected in a single array $(u_x \; u_y \; \varphi_z)^T$ that is indicated here with the symbol $\{U\}$, while the symbol $\{W\}$ will indicate the array of test functions $(w_x \; w_y \; \omega_z)^T$; stress and deformation measures are usually represented in terms of their generalized forms as (see, e.g., de Borst (1991))

$$\{\underline{\Sigma}\} = (\sigma_{xx} \; \sigma_{xy} \; \sigma_{yx} \; \sigma_{yy} \; \mu_{xz}/L_b \; \mu_{yz}/L_b)^T \tag{3.167}$$

$$\{\underline{\Gamma}\} = (\gamma_{xx} \; \gamma_{xy} \; \gamma_{yx} \; \gamma_{yy} \; \kappa_{xz}L_b \; \kappa_{yz}L_b)^T \tag{3.168}$$

These two arrays are linked by the equation $\{\underline{\Sigma}\} = [\hat{\mathcal{E}}] \, \{\underline{\Gamma}\}$, where $[\hat{\mathcal{E}}]$ is the matricial representation of the generalized constitutive operator $\hat{\mathcal{E}}$, expressed in a plane-stress state by

$$[\hat{\mathcal{E}}] = \begin{pmatrix} [\hat{\mathbf{A}}] & [0] \\ [0] & [\hat{\mathbf{C}}^*] \end{pmatrix} = \begin{pmatrix} \frac{E}{1-\nu^2} & 0 & 0 & \frac{\nu E}{1-\nu^2} & 0 & 0 \\ 0 & G+G_C & G-G_C & 0 & 0 & 0 \\ 0 & G-G_C & G+G_C & 0 & 0 & 0 \\ \frac{\nu E}{1-\nu^2} & 0 & 0 & \frac{E}{1-\nu^2} & 0 & 0 \\ 0 & 0 & 0 & 0 & 2G & 0 \\ 0 & 0 & 0 & 0 & 0 & 2G \end{pmatrix} \tag{3.169}$$

The array $\{\underline{\Gamma}\}$ can be expressed in terms of $\{U\}$ as

$$\{\underline{\Gamma}\} = [L]\{U\} = \begin{pmatrix} [L_A] & [-\mathsf{e}] \\ [0] & [L_C^*] \end{pmatrix} \begin{pmatrix} u_x \\ u_y \\ \varphi_z \end{pmatrix} = \begin{pmatrix} \partial_x & 0 & 0 \\ 0 & \partial_x & 1 \\ \partial_y & 0 & -1 \\ 0 & \partial_y & 0 \\ 0 & 0 & L_b\,\partial_x \\ 0 & 0 & L_b\,\partial_y \end{pmatrix} \begin{pmatrix} u_x \\ u_y \\ \varphi_z \end{pmatrix} \tag{3.170}$$

resulting in the following expressions for the bilinear form and the linear functional

$$A(W,U) = \int_{\mathbf{D}} ([L]\{W\})^T [\hat{\mathcal{E}}] \, ([L]\{U\}) \; \mathrm{d}\mathcal{V} \tag{3.171}$$

$$f(W) = \int_{\partial \mathbf{D}_n^u} \{W\}^T \{t\} \; \mathrm{d}\mathcal{S} + \int_{\mathbf{D}} \{W\}^T \{b_V\} \; \mathrm{d}\mathcal{V} \tag{3.172}$$

where the symbols $\{t\}$ and $\{b_V\}$ indicate the arrays $(t_{Ax} \; t_{Ay} \; t_{Cz})^T$ and $(b_{Vx} \; b_{Vy} \; l_z)^T$, respectively.

3.4.3 FEM representation: Bubnov-Galerkin discretization

After the introduction of the generalized terms, the weak form expressed by the bilinear form and the linear functional of Eqs. (3.171) and (3.172) is completely analogous to the standard weak form of classic elasticity (see, e.g., Eqs. (4.27) and (4.28)). It then follows that also the discretization procedure that allow to obtain a finite element representation

is the same as in classic elasticity, widely discussed in any FEM book (see, e.g., Bathe (1996) or Zienkiewicz and Taylor (2000)). Taking into account this premise, the present section will provide some basic informations on the discretization procedure for the micropolar formulation discussed above. Attention will be focused on the aspects that may be different with respect to the analogous approach in classic elasticity, and many details will be skipped since they can be easily found in the mentioned literature on FEM.

In the discretization of a model, the sets of trial and test functions U and W are replaced by the approximations $U^h \in \mathcal{V}_h(\mathbf{D})$ and $W^h \in \mathcal{V}_h^0(\mathbf{D})$, where the discretized spaces $\mathcal{V}_h(\mathbf{D})$ and $\mathcal{V}_h^0(\mathbf{D})$ are defined as

$$\mathcal{V}_h(\mathbf{D}) := \left\{ U^h \equiv (\bar{u}^h, \bar{\varphi}^h) \in \mathcal{H}_h^*(\mathbf{D}) \mid \bar{u}^h = \bar{u}^* \text{ at } \partial\mathbf{D}_e^u, \bar{\varphi}^h = \bar{\varphi}^* \text{ at } \partial\mathbf{D}_e^\varphi \right\} \qquad (3.173)$$

$$\mathcal{V}_h^0(\mathbf{D}) := \left\{ W^h \equiv (\bar{w}^h, \bar{\omega}^h) \in \mathcal{H}_h^*(\mathbf{D}) \mid \bar{w}^h = \bar{0} \text{ at } \partial\mathbf{D}_e^u, \bar{\omega}^h = \bar{0} \text{ at } \partial\mathbf{D}_e^\varphi \right\} \qquad (3.174)$$

where $\mathcal{H}_h^*(\mathbf{D}) = (\mathcal{H}_h^1(\mathbf{D}))^n \times (\mathcal{H}_h^1(\mathbf{D}))^m$, with $(\mathcal{H}_h^1(\mathbf{D}))^k$ the space of *discretized* square integrable k-dimensional vector fields with square integrable first derivatives over the domain $\mathbf{D}$. Within the Bubnov-Galerkin approach, these approximations are both expressed in terms of the same *shape functions* $N_i(p)$, and of the *nodal parameters* d_i and d_i^W, which are the nodal values of the trial and the test functions at each node i of the discretized model, in the following way[11] (for the trial functions)

$$\{U(p)\} \simeq \{U^h(p)\} = \sum_{i=1}^N [N_i(p)]\{d_i\} = \sum_{i=1}^N \begin{pmatrix} [N_{Ai}(p)] & [0] \\ [0] & [N_{Ci}(p)] \end{pmatrix} \begin{pmatrix} \{d_{Ai}\} \\ \{d_{Ci}\} \end{pmatrix} \qquad (3.175)$$

where N is the number of nodes of the element which the point p belongs to, $[N_i(p)]$ is the shape functions matrix, and $\{d_i\}$ the array collecting the nodal parameters at the node i. The subscripts A and C, as already done before, are used to distinguish between Cauchy-like and Cosserat-like terms. In a plane problem, for which the state variables reduce to the components u_x, u_y, and φ_z, the approximation (of the trial functions) is expressed by

$$\begin{pmatrix} u_x(p) \\ u_y(p) \\ \varphi_z(p) \end{pmatrix} \simeq \begin{pmatrix} u_x^h(p) \\ u_y^h(p) \\ \varphi_z^h(p) \end{pmatrix} = \sum_{i=1}^N \begin{pmatrix} N_i(p) & 0 & 0 \\ 0 & N_i(p) & 0 \\ 0 & 0 & N_i(p) \end{pmatrix} \begin{pmatrix} d_{xi}^u \\ d_{yi}^u \\ d_{zi}^\varphi \end{pmatrix} \qquad (3.176)$$

---

[11] In the present approach, the same approximation functions are used to discretize both the displacement field and the microrotation field of the micropolar medium. From the following Eq. (3.181) it can be seen that, differently from a classic medium, in this case also the approximation functions must be integrated together with their spatial derivatives, hence requiring a larger number of integration points with respect to a classic continuum model. In order to overcome this issue a possible solution suggested in de Borst (1991) is to use a different order of interpolation for the two state variables. For example, in a six-nodes triangular element, a number of integration points equal to three is sufficient if the microrotation are linearly interpolated, using their nodal values at only three nodes.

Once replaced into the weak form of the problem (Eqs. (3.171) and (3.172)), the discretized trial and test functions allow to obtain a matricial system representing the behaviour of the discrete model

$$[K]\,\{X\} = \{R\} \tag{3.177}$$

where $[K]$ is the global stiffness matrix of the system, $\{X\}$ the nodal parameters vector collecting all the nodal parameters $\{d_i\}$, and $\{R\}$ the vector of nodal dual parameters. Performing the integration over the domain $\mathbf{D}$ appearing in Eq. (3.171) in an element-wise manner, the assembly of the stiffness matrix result in the superposition of the contributions of each element composing the model

$$[K]_{el} = \int_{\mathbf{D}_{el}} [B(p)]^T [\hat{\mathcal{E}}(p)][B(p)]\ \mathrm{d}\mathcal{V} \tag{3.178}$$

where the symbol $\int_{\mathbf{D}_{el}}$ indicates the integral over an element. The matrix $[B(p)]$ is composed by the submatrices $[B_i(p)]$ as $[B(p)] = ([B_1(p)]\dots[B_i(p)]\dots[B_N(p)])$, such that

$$\{\underline{\Gamma}(p)\} = \sum_{i=1}^{N}[B_i(p)]\{d_i\} \tag{3.179}$$

each one given by

$$[B_i(p)] = \begin{pmatrix} [L_A][N_{Ai}(p)] & [-\mathsf{e}][N_{Ci}(p)] \\ [0] & [L_C^*][N_{Ci}(p)] \end{pmatrix} \tag{3.180}$$

Focusing again on a plane stress problem, the matrix $[B_i(p)]$ of Eq. (3.180) can be expressed as

$$[B_i(p)] = \begin{pmatrix} \partial_x N_i(p) & 0 & 0 \\ 0 & \partial_x N_i(p) & N_i(p) \\ \partial_y N_i(p) & 0 & -N_i(p) \\ 0 & \partial_y N_i(p) & 0 \\ 0 & 0 & L_b\,\partial_x N_i(p) \\ 0 & 0 & L_b\,\partial_y N_i(p) \end{pmatrix} \tag{3.181}$$

Chapter 4

Smoothed point interpolation methods

This chapter is devoted to the class of meshfree smoothed point interpolation methods. After a brief general review on meshfree methods, the main concepts of smoothed point interpolation methods applied to the case of linear elastic classic media are recalled. The novel applications to elastic-degrading constitutive models and to elastic and elastic-degrading micropolar media are then discussed.

4.1   Meshfree methods: a brief review

In order to solve the system of partial differential equations (PDEs) governing a problem of continuum mechanics (or any other continuum problem representable in terms of PDEs), the finite element method (see, e.g., Bathe (1996) or Zienkiewicz and Taylor (2000)) *discretizes* the problem domain with a *mesh*, in the following manner:

> "
>
> 1. The continuum is separated by imaginary lines or surfaces into a number of "finite elements".
> 2. The elements are assumed to be interconnected at a discrete number of nodal points situated on their boundaries and occasionally in their interior.
>
> "(Zienkiewicz and Taylor, 2000, pag. 18)

The unknown parameters of the problem are then represented by the nodal values of the field variable (e.g., the displacement field in a solid mechanics problem). The choice of proper approximation functions within each element allows to mount a system of linear equations for the solution of the problem. On the other hand:

"The meshfree method is used to establish a system of algebraic equations for the whole problem domain without the use of a predefined mesh, or uses easily generable meshes in a much more flexible or "freer" manner. Meshfree methods essentially use a set of nodes scattered within the problem domain as well as on the boundaries to represent the problem domain and its boundaries. The field functions are then approximated locally using these nodes."(Liu, 2009, pag. 14)

As pointed out by Liu in his book (Liu, 2009), the standard finite element method suffers for a number of limitations; among them there are:

- the need for a quality mesh, that reduces the automation in mesh generation;
- the "overly stiff" behaviour, resulting from the full compatibility in the assumed displacement field, and leading to locking and poor solutions in gradient/derivatives;
- the loss of accuracy due to element distorsions in problems with large deformations;
- the mesh bias in problems like crack growth and phase transformations;
- the difficult simulation of breakage and fragmentation problems;
- the costly adaptive and remeshing approaches;
- the availability of solely a "lower bound" to the exact solution.

An examination of this list reveals that most of the mentioned issues are due to the "heavy and rigid reliance on the use of quality elements that are the building blocks of FEM " (Liu, 2009, pag. 17), and to the predefined connectivity required by such elements.

The basic idea of meshfree methods is then to mitigate these issues by eliminating or reducing the reliance on a mesh[1]. Among the most common meshfree methods there are the *smoothed particle hydrodynamics* (SPH) method (Gingold and Monaghan, 1977), the *element-free Galerkin*[2] (EFG) method (Belytschko et al., 1994), the *reproducing kernel particle method* (RKPM) (Liu et al., 1995), the family of *point interpolation methods* (discussed in the following section), and the *meshless local Petrov-Galerkin* (MLPG) method (Atluri and Zhu, 1998). Despite a computational cost that is, in general, higher than in the standard FEM, meshfree methods exhibit a number of important features; among them, the following can be highlighted (Liu, 2009):

- easy automatic mesh generation using triangulation strategies;
- absent or limited mesh alignment sensitivity;
- no need for remeshing operations, especially in problems with large deformations or moving discontinuities;
- construction of shape functions of any desired order of continuity.

Regarding physically non-linear problems, meshfree methods, due to their characteristics, have been shown to be well suited for discrete fracture and continuum damage

---

[1] Though meshfree discretizations are not based on a conventional mesh as intended in the standard FEM, the term "mesh" will still be used in the following to indicate such discretizations.

[2] Based on the *diffuse elements method* (DEM) originated by Nayroles et al. (1992).

mechanics problems (see, e.g., Rabczuk (2013) and Daxini and Prajapati (2014) for an extensive survey on the topic), for example. However, as pointed out in Section 2.3.1, in this treatise the interest on such numerical methods is because of the *regularization* properties that they are able to introduce in strain localization problems, as emphasized in a number of contributions (Liu et al., 1999, Chen et al., 2000, Li et al., 2000*a*,*b*, Chen et al., 2004, 2007, Wang and Li, 2012, Pozo et al., 2014).

The following Section 4.2 will focus on the class of *smoothing point interpolation methods*, recalling their basic aspects with specific attention on the *node-based smoothed point interpolation method* (NS-PIM) (Liu et al., 2005, Zhang et al., 2007) and the *edge-based smoothed point interpolation method* (ES-PIM) (Liu and Zhang, 2008). Sections 4.3 and 4.4, instead, will be devoted to original contributions by the author. The former will deal with the extension of these methods to the field of continuum damage mechanics, while the latter will focus on the application to the micropolar continuum theory.

4.2 Smoothed point interpolation methods

Smoothed point interpolation methods, like other meshfree methods, rely on a set of nodes scattered in the problem domain, usually obtained through a triangulation operation. At each integration point $p \in \mathbf{D}$, the approximation $u^h(p)$ of a certain field variable $u(p)$ is represented in terms of a set of approximation (or shape) functions $\phi_i(p)$ and nodal parameters $u_i := u(p_i)$ as

$$u(p) \simeq u^h(p) = \sum_{i \in S_d} \phi_i(p) u_i \tag{4.1}$$

where the approximation functions are constructed considering a set of nodes in the neighbourhood of the point itself, the so-called *support domain*[3] S_d (composed by *support nodes*). Support domains vary from point to point and they are, in general, overlapping.

In these methods the shape functions may be generated with the *point interpolation method*, the *radial point interpolation method*, and the *radial point interpolation method with polynomial reproduction*. The first meshfree methods based on these shape functions were proposed by Liu and his co-authors in Liu and Gu (2001) and Wang and Liu (2002*a*), as an alternative to existent meshfree methods. Indeed, due to their *delta Kronecker* property they allowed a more simple imposition of essential boundary conditions, with respect to other meshfree methods.

Despite the advantage of the delta Kronecker property, point interpolation approximations, in general, are *incompatible*, since such shape functions may present *discontinuities* when passing from a support domain to another. This fact poses a limit on the application of the standard weak form of solid mechanics problems, which is based on the hypothesis

---

[3] Making an analogy with the FEM, one can think about the nodes of a finite element as the *support nodes* of the integration points belonging to that element.

of *continuity* of the approximation functions. In order to overcome this issue, Liu and his co-authors proposed the use of a *smoothing operation*[4] of the gradients involved in the formulation, in order to reduce the continuity requirement of the shape functions. The combination of the smoothing technique with point interpolation functions allowed to obtain different smoothed meshfree methods[5,6], like the *node-based smoothed point interpolation* (NS-PIM) method (Liu et al., 2005, Zhang et al., 2007), the *edge-based smoothed point interpolation* (ES-PIM) method (Liu and Zhang, 2008), and the *cell-based smoothed point interpolation method* (Liu and Zhang, 2009). In order to deal with the presence of incompatible shape functions and smoothing operations, Liu developed a new theoretical framework, establishing two novel concepts: the *G-space theory* and the *weakened-weak form* (W^2) formulation (see, e.g., Liu (2010*a,b*), Liu and Zhang (2013)).

In the following of the present section, the basic concepts of point interpolation shape functions, G-space theory, and weakened-weak form will be discussed, since they will serve as a basis for the novel developments presented in Sections 4.3 and 4.4. The numerical implementation of these methods in the software **INSANE** will be discussed in Appendix C.

4.2.1 Shape functions

Two kind of shape functions will be presented in this section: the ones obtained with the *point interpolation method* (PIM) and the ones by the *radial point interpolation method with polynomial reproduction* (RPIM). Both these strategies have been implemented in the **INSANE** software (Appendix C) and adopted in the simulations of Chapters 6 and 7. Due to its lack of consistency, the simple radial point interpolation method has not been considered.

---

[4] As mentioned by Liu (see, e.g., the introduction of Liu (2010*a*)) such smoothing technique (Liu, 2008) is analogous to the one adopted in other contextes like non-local continuum mechanics (Zhang et al., 2006, Eringen and Edelen, 1972), SPH methods (Liu and Liu, 2003, Lucy, 1977, Liu et al., 2008, Monaghan, 1982), hybrid FEM (Quarteroni and Valli, 1994), for the regularization of spatial instabilities in nodal integrated meshfree methods Chen et al. (2001), and, as mentioned in Section 2.3.1, for the regularization of material instabilities (Chen et al., 2000).

[5] The smoothing technique has been also applied by Liu and his co-authors to the standard FEM, obtaining the so-called *smoothed finite element method* (see, e.g., Liu, Dai and Nguyen (2007) and Liu et al. (2009)).

[6] As pointed out in Liu and Zhang (2013), the smoothed point interpolation methods belong to the more general class of *strain constructed* methods, which still relies on point interpolation function, but with a different strategy for the treatement of the gradients.

4.2.1.1   Point interpolation method

In the point interpolation method (Liu and Gu, 2001), the approximation $u^h(q)$ of a certain field variable $u(q)$ is represented at each point $q \in \mathbf{D}$ as the following series representation

$$u(q) \simeq u^h(q) = \sum_{i=1}^{n} p_i(q)a_i = \{p(q)\}^T\{a\} \tag{4.2}$$

where the terms $p_i(q)$ are a set of monomials evaluated at q, constituting a polynomial basis, n is the number of support nodes in the local support domain at the point q, a_i are the coefficients corresponding to the monomials $p_i(q)$, which must be evaluated in order to define the approximation functions.

Remark 4.1: Polynomial basis functions

The monomials, in general, are chosen in a top-down approach from the Pascal triangle. Focusing on a two-dimensional domain, the polynomial basis at a point p of coordinates (x, y) is represented by

$$\{p(q)\} = \begin{pmatrix} 1 & x & y \end{pmatrix}^T \tag{4.3}$$

when three support nodes are accounted for (like in the T3-scheme discussed in Section 4.2.1.3), and by

$$\{p(q)\} = \begin{pmatrix} 1 & x & y & xy & x^2 & y^2 \end{pmatrix}^T \tag{4.4}$$

for six support nodes (as in the case of the T6/3-scheme presented in Section 4.2.1.3). The presence of the constant term in the basis is fundamental to guarantee the *partition of unity* property of the resulting shape functions, while the constant term and the first order monomial together allow to obtain the *linear consistency* of the shape functions (i.e., the *exact* reproduction of at least a linear function).

The unknown coefficients a_i can be evaluated by imposing the following interpolation condition for each node of the support domain

$$u_j = \sum_{i=1}^{n} p_i(q_j)a_i, \quad j = 1, \dots, n \tag{4.5}$$

that can be recasted in the compact form

$$\{U\} = [P_q]\{a\} \tag{4.6}$$

where $\{U\} = (u_1, \dots, u_n)^T$ is the vector of the nodal parameters of the field variable, while $[P_q]$ is the *moment matrix*, each line of which is composed by the basis function

evaluated at a support nodes

$$[P_q] = \begin{pmatrix} \{p(q_1)\}^T \\ \vdots \\ \{p(q_n)\}^T \end{pmatrix} \tag{4.7}$$

Assuming the moment matrix to be invertible, from Eq. (4.6) the coefficients can be calculated as $\{a\} = [P_q]^{-1}\{U\}$, that replaced into Eq. (4.2) lead to

$$u^h(q) = \{p(q)\}^T [P_q]^{-1}\{U\} = \{\phi(q)\}^T\{U\} \tag{4.8}$$

where each *shape function* $\phi_i(q)$ is given by

$$\phi_i(q) = p_j(q)[P_q]^{-1}_{ji} \tag{4.9}$$

As long as the moment matrix is invertible and linear terms are included in the basis, such PIM shape function are characterized by the following properties (Liu, 2009):

- they are linearly independent;
- they posses the delta Kronecker property;
- they form a partition of unity;
- they posses the linear reproducing property[7];
- they present compact support (as long as the support domain is compact);
- they are not compatible, in general.

Remark 4.2: Incompatibility of the PIM shape functions

As already pointed out PIM shape functions, in general, are not compatible, since they may present discontinuities over the domain. According to Liu (2009), these discontinuities are due to the absence of a *smooth transition* between support domains. When passing from an integration point to another, with different support domains, the shape function for a node changes suddenly, resulting in a discontinuity at that point. This doesn't happen, for example, in the *moving least square* (MLS) method (Liu, 2009), where the presence of weight functions allows for a smooth transition between support domains; MLS shape functions indeed, are compatible, in general. As it will be discussed in Section 4.2.2, a special treatement is required in order to properly deal with this incompatibility.

Remark 4.3: Singularity of the moment matrix

---

[7] Furthermore, each function included in the basis can be exactly reproduced.

The evaluation of the unknown coefficients a_i requires the invertibility of the moment matrix. However, such matrix may be singular, for example in presence of peculiar nodes alignments (Liu, 2009). As pointed by Liu (2009), among the possible strategies able to avoid the singularity of the moment matrix there is the use of *radial basis functions* and the use of *T-schemes* for support nodes selection.

4.2.1.2   Radial point interpolation method with polynomial reproduction

The radial point interpolation method (RPIM) is similar to the PIM, with the difference that *radial basis functions* are used instead of polynomial ones. As mentioned in Remark 4.3, the use of a radial basis is sufficient to guarantee the invertibility of the moment matrix (Liu, 2009). The main drawback of shape function constructed with the RPIM is the lack of consistency, in the sense that they don't exhibit polynomial reproduction of any order. As pointed out by Liu (2009), though the approximations of any continuous function using radial basis functions can be shown to converge, the main issue is related to the impossibility of passing the standard *patch test*. The solution proposed in Wang and Liu (2002*a*) was to enrich the approximation adding polynomial terms (up to the linear order, in general) to the radial basis, obtaining the so-called *radial point interpolation method with polynomial reproduction*. Another important reason to add polynomial terms to the radial basis is that in this way the dependence of the quality of the solution on the parameters of the radial functions is reduced.

The approximation in the RPIM with polynomial reproduction is expressed by

$$u(q) \simeq u^h(q) = \sum_{i=1}^{n} R_i(q)a_i + \sum_{j=1}^{m} p_j(q)b_j = \{R(q)\}^T\{a\} + \{p(q)\}^T\{b\} \qquad (4.10)$$

where the terms $R_i(q)$ are a set of radial functions evaluated at q, constituting a radial basis, n is the number of support nodes in the local support domain at the point q, the terms $p_j(q)$ constitutes a polynomial basis as in the PIM, and m is the number of monomials composing the polynomial basis. The number of monomials should be sufficient to guarantee, at least, the linear reproduction (e.g., in a two-dimensional domain three monomials are sufficient to pass the standard patch test, the constant term and the two linear terms in the coordinates x and y). The approximation of Eq. (4.10) is characterized by two sets of unknown coefficients

$$\{a\} = \Big(a_1, \dots, a_n\Big)^T, \quad \{b\} = \Big(b_1, \dots, b_m\Big)^T \qquad (4.11)$$

which can be evaluated imposing the interpolation condition

$$u_k = \sum_{i=1}^{n} R_i(q_k)a_i + \sum_{j=1}^{m} p_j(q_k)b_j, \quad k = 1, \dots, n \qquad (4.12)$$

and the additional condition (Golberg et al., 1999)

$$\sum_{i=1}^{n} p_j(q_i)a_i = 0, \quad j = 1, \ldots, m \tag{4.13}$$

that can be recast in the following compact form

$$\begin{cases} \{U\} &= [R_q]\{a\} + [P_m]\{b\} \\ \{0\} &= [P_m]^T\{a\} \end{cases} \rightarrow \begin{pmatrix} [R_q] & [P_m] \\ [P_m]^T & [0] \end{pmatrix} \begin{pmatrix} \{a\} \\ \{b\} \end{pmatrix} = \begin{pmatrix} \{U\} \\ \{0\} \end{pmatrix} \tag{4.14}$$

where the matrix $[R_q]$ with dimension $n \times n$ is the *moment matrix*, each line of which is composed by the radial basis function evaluated at a support node, while the matrix $[P_m]$ with dimension $n \times m$ has its lines formed by the polynomial basis evaluated at the support nodes

$$[R_q] = \begin{pmatrix} \{R(q_1)\}^T \\ \vdots \\ \{R(q_n)\}^T \end{pmatrix}, \quad [P_m] = \begin{pmatrix} \{p(q_1)\}^T \\ \vdots \\ \{p(q_n)\}^T \end{pmatrix} \tag{4.15}$$

After some manipulations of the involved equations (see, e.g., Liu (2009)), the unknown coefficients can be evaluated as

$$\{a\} = [S_a]\{U\}, \quad \{b\} = [S_b]\{U\} \tag{4.16}$$

where the matrices $[S_a]$ and $[S_b]$ are represented by

$$[S_a] := [R_q]^{-1} - [R_q]^{-1}[P_m][S_b] \tag{4.17}$$

$$[S_b] := \left([P_m]^T[R_q]^{-1}[P_m]\right)^{-1} [P_m]^T[R_q]^{-1} \tag{4.18}$$

resulting in the approximation

$$u^h(q) = \left(\{R(q)\}^T[S_a] + \{p(q)\}^T[S_b]\right)\{U\} = \{\phi(q)\}^T\{U\} \tag{4.19}$$

where each *shape function* $\phi_i(q)$ is given by

$$\phi_i(q) = R_j(q)[S_a]_{ji} + p_j(q)[S_b]_{ji} \tag{4.20}$$

As pointed out by Liu (2009), the construction of such approximation is possible as long as the matrix $[P_m]^T[R_q]^{-1}[P_m]$ is invertible; the invertibility of such matrix is guaranteed, in general, as long as $n \geq m$. Shape functions constructed with the RPIM posses the same properties mentioned for the ones obtained with the PIM, including the linear reproduction property, as long as linear polynomial terms are taken into account.

Remark 4.4: Radial basis functions

The *radial functions* $R_i(p)$ appearing in Eq. (4.10) defined for each node i in the support domain, depend only on the distance r_i between the point $p \in \mathbf{D}$ at which they must be evaluated and the node i. In the numerical simulations presented in Chapters 6 and 7 only two kind of radial functions have been used, the *multiquadric* (MQ) function

$$R_i(r_i) = \left(r_i^2 + C^2 \right)^q \tag{4.21}$$

depending on the shape parameters C and q, and the *Gaussian*, or *exponential* (EXP) function

$$R_i(r_i) = \exp\left(-c r_i^2 \right) \tag{4.22}$$

depending on the shape parameter c, both of them adopted in Wang and Liu (2002*a*). Investigations on the choice of optimal shape parameters for the accuracy of the approximation can be found in Wang and Liu (2002*a*) and Wang and Liu (2002*b*), for example. However, as pointed out in Liu (2009), in presence of polynomial terms as in the RPIM with polynomial reproduction, and when smoothing techniques are adopted, the reliance of the accuracy on the shape parameters is significantly reduced.

4.2.1.3   Support nodes selection schemes

In order to construct PIM (Eq. (4.2)) and RPIM (Eq. (4.10)) approximations at a certain point q of the problem domain it is necessary to use a number of n *support nodes*, composing the so-called *support domain* at the point q. In order to compose the support domain selecting proper nodes in the neighbourhood of the point q, two different strategies have been adopted in this work: the selection via *influence domains* and via *T-schemes*[8].

The selection of support nodes via *influence domains* is a standard approach adopted in a number of meshfree methods. Each node is endowed with an *influence domain*, characterized by a *shape* and its *dimensions*. For example, in Fig. 4.1, each node posseses a *circular* influence domain, characterized by a certain radius which may vary from node to node. For each integration point, the corresponding support domain is generated adding all the nodes which influence domains contain the selected integration point. In the example depicted in Fig. 4.1, the support domain at the selected integration have been

---

[8] Another strategy, that hasn't been considered in this treatise but that could improve the performances of this class of meshfree methods, especially in case of large models, is the support nodes selection via *K-Nearest Neighbor* (KNN) algorithms, that could also be useful as an alternative to the methods considered in this treatise for the investigation of the regularization properties related to the non-locality of PIM and RPIM approximations. As pointed out in Remark 4.6, the use of the influence domains strategy tends to affect the sparseness of the stiffness matrix in a negative way; in this case, KNN strategies should introduce a non-locality analogous to the one of the influence domains strategy, with a reduced effect on the sparseness of the stiffness matrix.

marked with an hollow circle. The number of nodes in each support domain is controlled by the ratio between the size of the influence domains and the mean nodal distance. While this method works well for MLS and RPIM shape functions, when applied to PIM shape functions it may lead to a singular moment matrix, in case of peculiar nodal alignments.
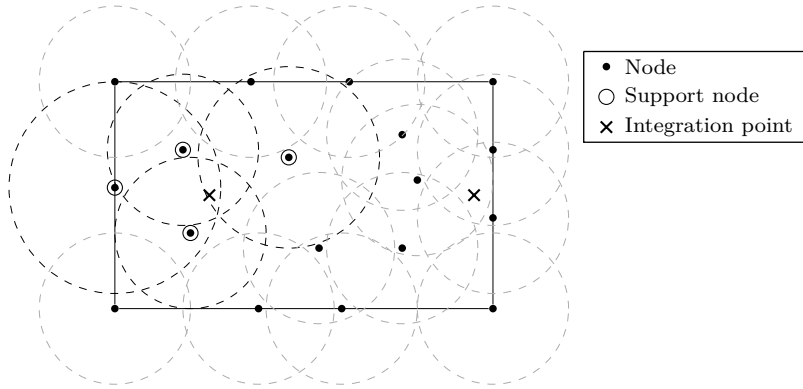
Figure 4.1: Support nodes selection via influence domains

An alternative is represented by the so-called *T-schemes* (Liu, 2009). Such methods perform the support nodes selection making use of *background triangular cells*, constructed as a triangulation of the scattered nodes of the discrete model. In general, there is no need to construct such set of cells specifically for the application of the T-schemes. A triangulation indeed, could have been already constructed during the discretization of the domain, at the moment of the nodes generation. Furthermore, in smoothed point interpolation methods, like the ones considered in this treatise, a set of background cells is necessary for the construction of the *smoothing domains* (Section 4.2.2); hence, the triangular cells are already available for nodes selection. In the examples presented in Chapters 6 and 7, two kind of T-schemes have been considered: the *T3-scheme* and the *T6/3-scheme*, which, as pointed out by Liu (Liu, 2009), allow to obtain invertible moment matrices with both PIM and RPIM shape functions[9]. For an integration point belonging to a certain cell, the T3-scheme selects as support nodes the three nodes at the vertices of the cell (Fig. 4.2(a)). The T6/3-scheme distinguishes between *interior* and *boundary* cells. The former are cells which have no one of their edges on the boundary of the problem, while the latter are cells with at least an edge on the boundary of the domain. For a boundary cell, the three nodes at the vertices of the cell are selected as support nodes, like in the T3-scheme. On the other hand, in case of an interior cell, a total number of six nodes is selected: the three nodes located at the vertices of the cell, and three nodes located at the remote vertices of the three neighboring cells (Fig. 4.2(b)).

---

[9] As pointed out in Liu (2009), two further methods based on triangular background cells are available, the so-called T6 and T2L schemes, which selects, in general, a larger number of nodes with respect to the T-schemes already mentioned in this section. However, the example discussed in Chapters 6 and 7, and the implementation proposed by the author in Appendix C, focused only on the two T-schemes discussed in this section.

(a) T3-scheme

(b) T6/3-scheme
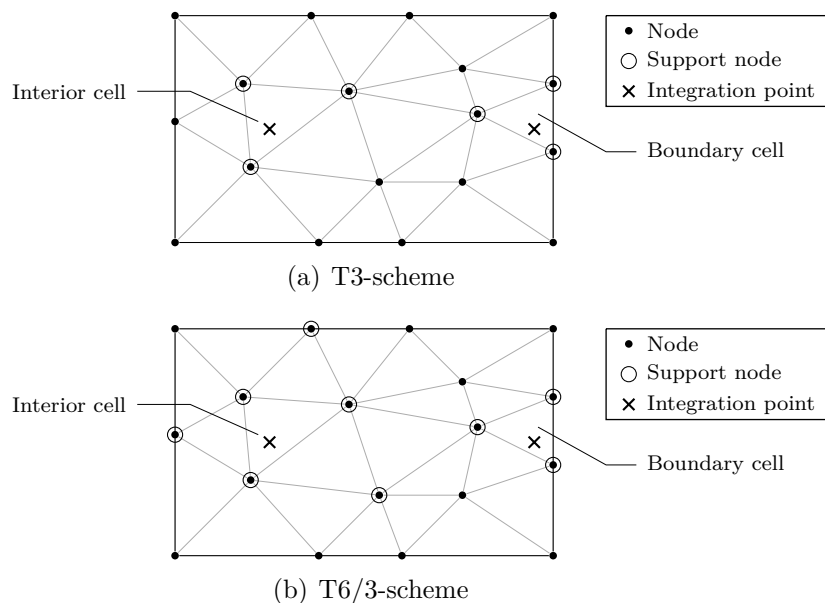
Figure 4.2: Support nodes selection via T-schemes

Remark 4.5: Quadrilateral background cells

Though the standard procedure in smoothed point interpolation methods is to use triangular background cells, since they don't require peculiar meshing efforts, it is possible to use also different geometries for the background cells. In the simulations discussed in Section 6.4, for example, quadrilateral cells were used, since the idea of the presented example was to compare the results obtained with the adopted meshfree methods with the ones of an FEM mesh of quadrilateral elements. In order to select the support nodes of quadrilateral cells, the same T-scheme concepts for triangular cells can be adopted. For the example of Section 6.4, two strategies were introduced, that were named *T4-scheme* and *T12/4-scheme*. For an integration point belonging to an interior or boundary cell, the former selects as support nodes the four nodes corresponding to the vertices of the cell (Fig. 4.3(a)). The latter instead, considers again four nodes for boundary cells, and twelve nodes for interior cells, selected as in the following: four nodes corresponding to the vertices of the interior cell, and eight nodes located at the remote vertices of the four neighboring cells (Fig. 4.3(b)). These two strategies have been used only with the RPIM.

(a) T4-scheme

(b) T12/4-scheme
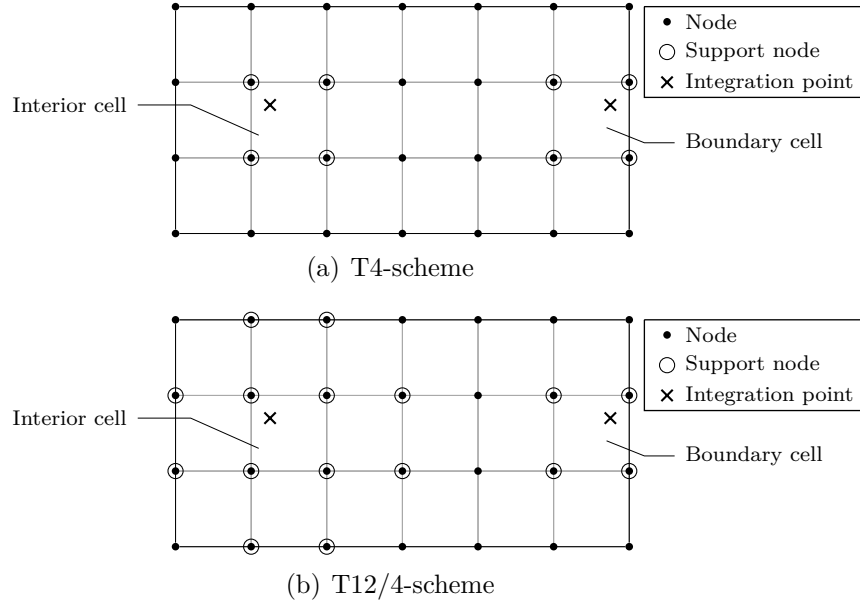
Figure 4.3: Support nodes selection via T-schemes on quadrilateral cells

---

Remark 4.6: T-schemes vs influence domains

It has been mentioned that T-schemes are useful to guarantee the invertibility of the moment matrix in the PIM strategy. As pointed out by Liu (2009), they are also important to obtain a *sparse* stiffness matrix, which eases the solution of the linear system of equations. The sparseness of the stiffness matrix results from the *compact* character of the support domains generated with the T-schemes. Another interesting feature is that they also allow to know *a priori* the parts of the domain where the approximation functions may exhibit discontinuities, which is important for the node- and edge-based methods presented in Sections 4.2.3 and 4.2.4.

The influence domains strategy on the contrary, depending on the size of the influence domains, tends to destroy the sparseness of the stiffness matrix. Furthermore, when using the influence domains strategy, the positions of the shape functions discontinuities is not known *a priori*. Despite these disadvantages, this strategy was adopted in the simulations of Section 7.3 in order to investigate the non-local effects of the PIM and RPIM meshfree methods.

4.2.2   G-space theory and weakened-weak form

As pointed out in the previous sections, the use of *incompatible* approximation functions led Liu and his co-authors to the introduction of a novel theoretical structure, constituted by the *G-space theory* and the *weakened-weak form* (W^2) formulation (see, e.g., Liu (2010a,b) and Liu and Zhang (2013)), which will be briefly recalled here, since they will

be used in the following Section 4.4 for the application of PIM and RPIM approximation methods to the analysis of micropolar media. First, the concept of weak form in classic elasticity is briefly recalled. Then, the novel formulation introduced by Liu and his co-authors is recalled, focusing on the following points:

- smoothing domains generation;
- smoothing operation;
- G-spaces;
- weakened-weak form.

4.2.2.1 Weak form in classic elasticity

For a problem of classic elasticity, characterized by the unknown field variable $\bar{u}$ defined over the problem domain $\mathbf{D}$, by the essential boundary condition $\bar{u} = \bar{u}^*$ at $\partial\mathbf{D}_e$, by the natural boundary condition $\bar{n} \cdot \underline{\sigma} = \bar{t}$ at $\partial\mathbf{D}_n$, and subjected to volume forces $\bar{b}_V$ defined over the whole domain $\mathbf{D}$, the weak form of the problem can be expressed as in the following: find the field $\bar{u} \in \mathcal{V}(\mathbf{D})$ such that

$$\int_{\mathbf{D}} \underline{\varepsilon}(\bar{w}) \cdot \left(\hat{\mathbf{E}} \cdot \underline{\varepsilon}(\bar{u})\right) \, \mathrm{d}\mathcal{V} - \int_{\partial\mathbf{D}_n} \bar{w} \cdot \bar{t} \, \mathrm{d}\mathcal{S} - \int_{\mathbf{D}} \bar{w} \cdot \bar{b}_V \, \mathrm{d}\mathcal{V} = 0, \quad \forall \bar{w} \in \mathcal{V}^0(\mathbf{D}) \qquad (4.23)$$

where $\underline{\varepsilon}(\bar{u}) = (u_{i,j} + u_{j,i})/2 \, \bar{e}_i \otimes \bar{e}_j$, and where $\mathcal{V}(\mathbf{D})$ and $\mathcal{V}^0(\mathbf{D})$ are, respectively, the spaces of *trial* and *test* functions, defined as

$$\mathcal{V}(\mathbf{D}) := \left\{\bar{u} \in \left(\mathcal{H}^1(\mathbf{D})\right)^n \mid \bar{u} = \bar{u}^* \text{ at } \partial\mathbf{D}_e^u\right\} \qquad (4.24)$$

$$\mathcal{V}^0(\mathbf{D}) := \left\{\bar{w} \in \left(\mathcal{H}^1(\mathbf{D})\right)^n \mid \bar{w} = 0 \text{ at } \partial\mathbf{D}_e^u\right\} \qquad (4.25)$$

where $\left(\mathcal{H}^1(\mathbf{D})\right)^n$ is the space of square integrable n-dimensional vector fields with square integrable first derivatives over the domain $\mathbf{D}$. The weak form of Eq. (4.23) can be recasted in a compact for as

$$a(\bar{w}, \bar{u}) = f(\bar{w}), \quad \forall \bar{w} \in \mathcal{V}^0(\mathbf{D}) \qquad (4.26)$$

where the *bilinear form* $a(\bar{w}, \bar{u})$ and the *linear functional* $f(\bar{w})$ have been introduced, defined as

$$a(\bar{w}, \bar{u}) := \int_{\mathbf{D}} \underline{\varepsilon}(\bar{w}) \cdot \left(\hat{\mathbf{E}} \cdot \underline{\varepsilon}(\bar{u})\right) \, \mathrm{d}\mathcal{V} \qquad (4.27)$$

$$f(\bar{w}) := \int_{\partial\mathbf{D}_n} \bar{w} \cdot \bar{t} \, \mathrm{d}\mathcal{S} + \int_{\mathbf{D}} \bar{w} \cdot \bar{b}_V \, \mathrm{d}\mathcal{V} \qquad (4.28)$$

It is worth to note that the requirement $\bar{u}, \bar{w} \in (\mathcal{H}^1(\mathbf{D}))^n$ is necessary to bound from above the value of the bilinear form[10].

Introducing the Voigt notation for a plane stress case, as done in Section 3.4.2 for the micropolar medium, the components of the weak form of Eq. (4.26) can be recasted as

$$a(\bar{w}, \bar{u}) := \int_{\mathbf{D}} ([L]\{\bar{w}\})^T [\hat{\mathbf{E}}] ([L]\{\bar{u}\}) \ \mathrm{d}\mathcal{V} \tag{4.29}$$

$$f(\bar{w}) := \int_{\partial \mathbf{D}_n} \{\bar{w}\}^T \{\bar{t}\} \ \mathrm{d}\mathcal{S} + \int_{\mathbf{D}} \{\bar{w}\}\{\bar{b}_V\} \ \mathrm{d}\mathcal{V} \tag{4.30}$$

where the derivative operator $[L]$ is such that

$$\{\underline{\varepsilon}(\bar{u})\} = [L]\{\bar{u}\} \rightarrow \begin{pmatrix} \varepsilon_{xx} \\ \varepsilon_{yy} \\ \varepsilon_{xy} \end{pmatrix} = \begin{pmatrix} \partial_x & 0 \\ 0 & \partial_y \\ \partial_y & \partial_x \end{pmatrix} \begin{pmatrix} u_x \\ u_y \end{pmatrix} \tag{4.31}$$

Within the FEM approach the weak form of Eq. (4.26) is discretized by replacing the trial and test functions $\bar{u}$ and $\bar{w}$ with the approximations $\bar{u}^h \in \mathcal{V}_h(\mathbf{D})$ and $\bar{w}^h \in \mathcal{V}_h^0(\mathbf{D})$, where $\mathcal{V}_h(\mathbf{D})$ and $\mathcal{V}_h^0(\mathbf{D})$ are the *discretized* spaces of trial and test functions such that

$$\mathcal{V}_h(\mathbf{D}) := \left\{ \bar{u} \in \left(\mathcal{H}_h^1(\mathbf{D})\right)^n \mid \bar{u} = \bar{u}^* \text{ at } \partial \mathbf{D}_e^u \right\} \tag{4.32}$$

$$\mathcal{V}_h^0(\mathbf{D}) := \left\{ \bar{w} \in \left(\mathcal{H}_h^1(\mathbf{D})\right)^n \mid \bar{w} = 0 \text{ at } \partial \mathbf{D}_e^u \right\} \tag{4.33}$$

where $(\mathcal{H}_h^1(\mathbf{D}))^n$ is the space of square integrable n-dimensional *discretized* vector fields (i.e., constructed with approximation functions in terms of a set of nodal parameters) with square integrable first derivatives over the domain $\mathbf{D}$. As already discussed for the micropolar medium, the discretization results in a matricial system like the one of Eq. (3.177), where the stiffness matrix $[K]$ is evaluated through the contributions of the finite elements

$$[K]_{el} = \int_{\mathbf{D}_{el}} [B(p)]^T [\hat{\mathbf{E}}(p)] [B(p)] \ \mathrm{d}\mathcal{V} \tag{4.34}$$

where the symbol $\int_{\mathbf{D}_{el}}$ indicates the integral over an element. The matrix $[B(p)]$ is composed by the submatrices $[B_i(p)]$ as $[B(p)] = ([B_1(p)] \dots [B_i(p)] \dots [B_N(p)])$, such that

$$\{\underline{\varepsilon}(p)\} = \sum_{i=1}^{N} [B_i(p)]\{d_i\} = \begin{pmatrix} \partial_x N_i(p) & 0 \\ 0 & \partial_y N_i(p) \\ \partial_y N_i(p) & \partial_x N_i(p) \end{pmatrix} \begin{pmatrix} d_{xi}^u \\ d_{yi}^u \end{pmatrix} \tag{4.35}$$

The requirement of the approximated field variable to belong to the discretized space $(\mathcal{H}_h^1(\mathbf{D}))^n$ is satisfied when the approximation is constructed with FEM shape functions, which exhibit a piecewise continuous first derivative that is *bounded in an integral sense.*

---

[10] Taking into account the analogy between the bilinear form and the total strain energy of a body it is possible to emphasize that this requirement is necessary to bound from above the strain energy.

This requirement however, poses a limitation on the use of shape functions generated with the PIM and RPIM. Since such shape functions are, in general, *incompatible*, also the resulting approximation of the field variable will be *incompatible*, i.e., it will present *discontinuities*. Hence, if the trial and test functions $\bar{u}$ and $\bar{w}$ are replaced by the approximations $\bar{u}^h$ and $\bar{w}^h$ obtained with PIM or RPIM shape functions, the requirement on the square integrable first derivative won't be satisfied anymore.

4.2.2.2   Smoothing domains creation

G-spaces are defined for discrete models, where the field variables are expressed in terms of approximation functions and nodal parameters, like the space $(\mathcal{H}_h^1(\mathbf{D}))^n$ containing the approximated field variables of an FEM model as pointed out in the previous section. Before recalling the definition of G-spaces is then necessary to present the peculiar discretization strategy which they rely on.

As pointed out in Liu (2010*a*), the domain $\mathbf{D}$ is discretized with a set of N_e non-overlapping *background cells* $\mathbf{D}_i^C$, with $i = 1, \ldots, N_e$, which vertices correspond to a set of N_n scattered nodes. These cells are, in general, triangular; however, as pointed out also in Section 4.2.1.3, any polygonal shape can be adopted. It is worth to note that, if one of the T-schemes illustrated in Section 4.2.1.3 is adopted, the boundaries $\partial \mathbf{D}_i^C$ of the cells represent parts of the domain where the approximation functions may be discontinuous. A further tassellation of the domain is performed, introducing a set of N_S non-overlapping *smoothing domains* $\partial \mathbf{D}_k^S$, with $k = 1, \ldots, N_S$. When generating this second subdivision, the following *no-sharing rule* must be considered: the boundaries $\partial \mathbf{D}_k^S$ of the smoothing domains must not share any finite portion with the boundaries $\partial \mathbf{D}_i^C$ of the background cells, i.e., they may share at most a finite number of points with the parts of the domain where the approximation functions may be discontinuous. As it will be shown in the following Sections 4.2.3 and 4.2.4, where specific discretization strategies will be presented, the reason for this requirement is to guarantee the possibility to perform the integration of the approximation functions along the boundary of the smoothing domains.

4.2.2.3   Smoothing operation

The smoothing operation illustrated in this section was introduced by Liu (see, e.g., Liu (2008)) in order to reduce the requirement of continuity of the field variable appearing in the weak form expressed by Eq. (4.23). Such smoothing operation is based on the domain tassellation discussed in the previous section, assuming the tassellation to be *stationary*[11] during the analysis. Within this approach, the derivative $\text{grad}(\bar{u}) = u_{i,j} \, \bar{e}_i \otimes \bar{e}_j$ of the field variable $\bar{u}$ at a certain point $p \in \mathbf{D}_k^S$ is replaced inside the smoothing domain $\mathbf{D}_k^S$ by

---

[11] The stationarity requirement was originally adopted in Liu (2010*a*); however, other *smoothed* methods don't rely on this assumption (see, e.g., Liu and Zhang (2013)).

the *smoothed derivative* $\widetilde{\mathrm{grad}}(\bar{u}) = \widetilde{u_{i,j}}\,\bar{e}_i \otimes \bar{e}_j$, with

$$u_{i,j}(p) \simeq \widetilde{u_{i,j}}(p_k) := \int_{\mathbf{D}_k^S} u_{i,j}(\xi)\,\widetilde{W}(p_k - \xi)\,\mathrm{d}\mathcal{V}, \quad p \in \mathbf{D}_k^S \tag{4.36}$$

constant within a smoothing domain, where $\widetilde{W}$ is a *smoothing function*, and where p_k is the centre of the smoothing domain. If the field variable $\bar{u}$ is continuous, the Green's divergence theorem can be applied, resulting in

$$
\begin{aligned}
\widetilde{u_{i,j}}(p_k) = &\int_{\partial \mathbf{D}_k^S} \left(u_i(\xi) \otimes n_j^{(k)}(\xi) \right)\,\widetilde{W}(p_k - \xi)\,\mathrm{d}\mathcal{S} \\
&- \int_{\mathbf{D}_k^S} u_i(\xi) \otimes \widetilde{W}_{,j}(p_k - \xi)\,\mathrm{d}\mathcal{V}
\end{aligned}
\tag{4.37}
$$

where $\bar{n}^{(k)}$ is the unitary outward normal vector field on the boundary $\partial \mathbf{D}_k^S$. A common choice for the smoothing function $\widetilde{W}$ is the following Heaviside-type function

$$\widetilde{W}(p_k - \xi) := \begin{cases} 1/A_k & \xi \in \mathbf{D}_k^S \\ 0 & \xi \notin \mathbf{D}_k^S \end{cases} \tag{4.38}$$

where $A_k = \int_{\mathbf{D}_k^S} \mathrm{d}\mathcal{V}$, which results in

$$\widetilde{u_{i,j}}(p_k) = \frac{1}{A_k} \int_{\partial \mathbf{D}_k^S} u_i(\xi) \otimes n_j^{(k)}(\xi)\,\mathrm{d}\mathcal{S} \tag{4.39}$$

As pointed out by Liu and Zhang:

> "The "smoothed derivatives" defined in Equation (2.67) [Eq. (4.39)] is a generalized concept. It is NOT "the derivative obtained by smoothing the derivatives of the function", because such a gradient does not in general exist, as the function may not be continuous! Rigorously speaking, the "smoothed derivative" is the outward flux of the function across the smoothing domain boundary $\Gamma_\mathbf{x}^s$ [$\partial \mathbf{D}_k^S$]. The smoothed derivative of a function can be approximated using only the function values, and no differentiation is needed. Hence the consistency requirement on the function is reduced, if only the approximate derivative is required."(Liu and Zhang, 2013, pag. 67)

As emphasized in the quoted text, the smoothing operation consists into replace the derivative of the field variable with the smoothed derivative illustrated in Eq. (4.39). This substitution is assumed to be valid whether the field variable is continuous or not, i.e., whether the application of the Green's theorem in Eq. (4.37) is licit or not. As pointed out in Liu (2008), though not rigorous in theory, this operation is possible to implement, since Eq. (4.39) require no differentiation of the field variable, opening the possibility to use PIM and RPIM *incompatible* functions for the approximation of the field variable.

4.2.2.4   G-space theory

A general treatement on the G-space theory can be found in Liu (2010a) and Liu and Zhang (2013), and its application to classic elasticity in Liu (2010b). Briefly, the G-space[12] $\mathcal{G}_h^1(\mathbf{D})$ is defined as the following space of functions $u(p)$ *discretized* in terms of approximation functions $\phi_j(p)$ and nodal parameters d_j

$$
\begin{aligned}
\mathcal{G}_h^1(\mathbf{D}) := \Bigg\{ u \mid u(p) = \sum_{j=1}^{N_n} \phi_j(p)d_j, \ u \in \mathcal{L}^2(\mathbf{D}), \\
\sum_{k=1}^{N_S} \left(\int_{\partial \mathbf{D}_k^S} u(\xi)\, n_i^{(k)}(\xi)\, \mathrm{d}\mathcal{S} \right)^2 > 0 \Leftrightarrow u \neq c \in \mathbb{R}, \ i = 1,\ldots,d \Bigg\}
\end{aligned}
\tag{4.40}
$$

where $c \in \mathbb{R}$ is a constant, d the dimension of the space $\mathbf{D}$, and $\mathcal{L}^2(\mathbf{D})$ the *Lebesgue* space of square integrable functions. When n-dimensional vector fields are considered, the following space can be introduced

$$
\left(\mathcal{G}_h^1(\mathbf{D}) \right)^n := \left\{ \bar{u} = u_i\, \bar{e}_i \mid u_i \in \mathcal{G}_h^1(\mathbf{D}), \ i = 1,\ldots,n \right\}
\tag{4.41}
$$

This space is endowed with the following *inner product*

$$
< \bar{u}, \bar{w} >_{\mathcal{G}^1} = \underbrace{\int_{\mathbf{D}} (\bar{u} \cdot \bar{w})\, \mathrm{d}\mathcal{V}}_{< \bar{u}, \bar{w} >_{\mathcal{L}^2}} + \underbrace{\int_{\mathbf{D}} \left(\widetilde{\mathrm{grad}}(\bar{u}) \cdot \widetilde{\mathrm{grad}}(\bar{w}) \right) \mathrm{d}\mathcal{V}}_{< \widetilde{\mathrm{grad}}(\bar{u}), \widetilde{\mathrm{grad}}(\bar{w}) >_{\mathcal{L}^2}}, \quad \bar{u}, \bar{v} \in \left(\mathcal{G}_h^1(\mathbf{D}) \right)^n
\tag{4.42}
$$

with induced *norm* $\|\cdot\|_{\mathcal{G}^1}^2$ and *semi-norm* $|\cdot|_{\mathcal{G}^1}^2$ expressed as combination of norms in the Lebesgue space $\mathcal{L}^2(\mathbf{D})$

$$
\|\bar{u}\|_{\mathcal{G}^1}^2 = \|\bar{u}\|_{\mathcal{L}^2}^2 + |\bar{u}|_{\mathcal{G}^1}^2, \quad \bar{u} \in \left(\mathcal{G}_h^1(\mathbf{D}) \right)^n
\tag{4.43}
$$

$$
|\bar{u}|_{\mathcal{G}^1}^2 = \left\| \widetilde{\mathrm{grad}}(\bar{u}) \right\|_{\mathcal{L}^2}^2, \quad \bar{u} \in \left(\mathcal{G}_h^1(\mathbf{D}) \right)^n
\tag{4.44}
$$

As it can be observed in Eq. (4.40), the shape functions must be (i) *linearly independent*, in order to form a basis, (ii) *bounded*, i.e., square integrable, and (iii) must verify the *positivity condition* $\sum_{k=1}^{N_S} \left(\int_{\partial \mathbf{D}_k^S} u(\xi)\, n_i^{(k)}(\xi)\, \mathrm{d}\mathcal{S} \right)^2 > 0$. The two last requirements, as pointed out by Liu (Liu, 2010a), are necessary to guarantee the stability and convergence of the numerical models built upon the weakened-weak formulation based on G-spaces.

The main difference between the space $\mathcal{G}_h^1(\mathbf{D})$ and the space $\mathcal{H}_h^1(\mathbf{D})$ usually adopted in FEM applications (i.e., the discretized space of square integrable functions with square integrable first derivative), is the fact that the latter requires both the function and its first derivative to be square integrable ($\|\bar{u}\|_{\mathcal{L}^2(\mathbf{D})}^2 < \infty$ and $\|\mathrm{grad}(\bar{u})\|_{\mathcal{L}^2(\mathbf{D})}^2 < \infty$) in order to ensure an upper bound to the strain energy (aka the bilinear form), while in the

---

[12] The more general case of spaces $\mathcal{G}_h^m(\mathbf{D})$ with $m > 1$ is not considered here.

former only the function is required to be square integrable since, as it will be discussed in the following section, the bilinear form of the weakened-weak form depends only on the function and not on its first derivative. While in the weakened-weak form the strain energy is automatically bounded from above once the functions are square integrable, a lower bound must be explicitly imposed, with the aforementioned positivity condition; in the standard weak form, as pointed out in Liu (2010a), an explicit lower bound is not necessary, since the condition $\|\mathrm{grad}(\bar{u})\|_{\mathcal{L}^2(\mathbf{D})}^2 = 0$ is attained only if the function is zero everywhere, due to the Poincare-Friedrichs inequality[13] (Liu, 2009). The reduced order of continuity required by the space $\mathcal{G}_h^1(\mathbf{D})$ opens the possibility to use PIM and RPIM shape functions as a basis to generate its elements. The main characteristics of G-spaces needed to guarantee the existence and uniqueness of the solution of the weakened-weak formulation discussed in the following Section 4.2.2.5 have been widely discussed by Liu and his co-authors in a number of papers and books (see, e.g., Liu (2010a,b, 2009) and Liu and Zhang (2013)) and won't be recalled here; part of them will be presented in Section 4.4 in a version adapted for micropolar media.

4.2.2.5 Weakened-weak form of the classic elasticity problem

The weakened-weak form in classic elasticity have been presented in Liu (2010b). As discussed in the mentioned paper, such formulation can be obtained by replacing the strain tensor $\underline{\varepsilon}$ appearing in the bilinear form of Eq. (4.27) with its *smoothed* version $\widetilde{\underline{\varepsilon}}$, resulting in the *smoothed bilinear form*

$$\widetilde{a}(\bar{w}, \bar{u}) = \int_{\mathbf{D}} \widetilde{\underline{\varepsilon}}(\bar{w}(p_k)) \cdot \left(\hat{\mathbf{E}} \cdot \widetilde{\underline{\varepsilon}}(\bar{u}(p_k)) \right) \ \mathrm{d}\mathcal{V} \tag{4.45}$$

where the smoothed strain tensor $\widetilde{\underline{\varepsilon}}$ is obtained considering the smoothing derivatives of Eq. (4.39)

$$\widetilde{\varepsilon}_{ij} = \frac{1}{2} \left(\widetilde{u_{i,j}} + \widetilde{u_{j,i}} \right) \tag{4.46}$$

In plane stress case, it assumes the matricial expression

$$\{\widetilde{\underline{\varepsilon}}(\bar{u}(p_k))\} = \frac{1}{A_k} \int_{\partial \mathbf{D}_k^S} [\widetilde{L_n}(\xi)] \{\bar{u}(\xi)\} \ \mathrm{d}\mathcal{S} \tag{4.47}$$

$$\begin{pmatrix} \widetilde{\varepsilon}_{xx} \\ \widetilde{\varepsilon}_{yy} \\ \widetilde{\varepsilon}_{xy} \end{pmatrix} = \frac{1}{A_k} \int_{\partial \mathbf{D}_k^S} \begin{pmatrix} n_x^{(k)}(\xi) & 0 \\ 0 & n_y^{(k)}(\xi) \\ n_y^{(k)}(\xi) & n_x^{(k)}(\xi) \end{pmatrix} \begin{pmatrix} u_x(\xi) \\ u_y(\xi) \end{pmatrix} \mathrm{d}\mathcal{S} \tag{4.48}$$

---

[13] As pointed out in Liu (2009), the Poincare-Friedrichs inequality is represented by $c\|\bar{w}\|_{\mathcal{H}^1}^2 \leq |\bar{w}|_{\mathcal{H}^1}^2$, $\forall \, \bar{w} \in \left(\mathcal{H}_0^1(\mathbf{D}) \right)^k$, with $c \in \mathbb{R}$ and $c > 0$, and expresses an equivalence between the norm and the seminorm for k-dimensional vector fields in the space $\mathcal{H}_0^1(\mathbf{D})$ of square integrable k-dimensional vector fields with square integrable first derivative with prevented *rigid-body* motions.

Recalling that the smoothed derivatives are *constant* within each smoothing domain defined in Section 4.2.2.2, and also assuming the constitutive operator $\hat{\mathbf{E}}$ to be constant within each smoothing domain, the integral $\int_{\mathbf{D}}$ may be replaced with a summation over the smoothing domains, resulting in

$$\widetilde{a}(\bar{w}, \bar{u}) = \sum_{k=1}^{N_S} A_k \left(\widetilde{\underline{\varepsilon}}(\bar{w}(p_k)) \cdot \left(\hat{\mathbf{E}} \cdot \widetilde{\underline{\varepsilon}}(\bar{u}(p_k)) \right) \right) \tag{4.49}$$

The *weakened-weak form* of the classic elasticity problem recalled in Section 4.2.2.1 consists then into find the field $\bar{u} \in \mathcal{V}(\mathbf{D})$ such that

$$\widetilde{a}(\bar{w}, \bar{u}) = f(\bar{w}), \quad \forall \bar{w} \in \mathcal{V}^0(\mathbf{D}) \tag{4.50}$$

where $\mathcal{V}(\mathbf{D})$ and $\mathcal{V}^0(\mathbf{D})$ are, respectively, the spaces of *trial* and *test* functions, defined as

$$\mathcal{V}(\mathbf{D}) := \left\{ \bar{u} \in \left(\mathcal{G}_h^1(\mathbf{D}) \right)^n \mid \bar{u} = \bar{u}^* \text{ at } \partial \mathbf{D}_e^u \right\} \tag{4.51}$$

$$\mathcal{V}^0(\mathbf{D}) := \left\{ \bar{w} \in \left(\mathcal{G}_h^1(\mathbf{D}) \right)^n \mid \bar{w} = 0 \text{ at } \partial \mathbf{D}_e^u \right\} \tag{4.52}$$

Discussions on the properties of the weakened-weak form of Eq. (4.50), as well as on the conditions that ensure the existence and uniqueness of the solution $\bar{u} \in \mathcal{V}(\mathbf{D})$ can be found in Liu and Zhang (2008) and Liu (2010*b*).

The absence of derivatives in the smoothed bilinear form (Eq. (4.49)) allows to express both the trial and the test functions in terms of PIM and RPIM shape functions $\phi_i(p)$, since they are well suited to form a basis for the space $\left(\mathcal{G}_h^1(\mathbf{D}) \right)^n$, resulting (for the trial functions) in

$$\{\bar{u}(p)\} = \sum_{i \in S_d} [\phi_i(p)]\{d_i\} \tag{4.53}$$

where $\{d_i\}$ is the array collecting the nodal parameters at the node i, and where S_d is the support domain of the point $p \in \mathbf{D}$. The smoothed strains can be expressed in terms of the smoothed strain-displacement matrix $[\widetilde{B}_i(p_k)]$ as

$$\{\widetilde{\underline{\varepsilon}}(\bar{u}(p_k))\} = \sum_{i \in S_d} [\widetilde{B}_i(p_k)]\{d_i\} \tag{4.54}$$

where $[\widetilde{B}_i(p_k)]$, in a plane stress state, is represented by

$$
\begin{aligned}
[\widetilde{B}_i(p_k)] &= \frac{1}{A_k} \int_{\partial \mathbf{D}_k^S} [\widetilde{L_n}(\xi)][\phi_i(\xi)] \, \mathrm{d}\mathcal{S} \\
&= \frac{1}{A_k} \int_{\partial \mathbf{D}_k^S} \begin{pmatrix} n_x^{(k)}(\xi)\,\phi_i(\xi) & 0 \\ 0 & n_y^{(k)}(\xi)\,\phi_i(\xi) \\ n_y^{(k)}(\xi)\,\phi_i(\xi) & n_x^{(k)}(\xi)\,\phi_i(\xi) \end{pmatrix} \, \mathrm{d}\mathcal{S} \\
&= \begin{pmatrix} \widetilde{\phi}_{i,x}(p_k) & 0 \\ 0 & \widetilde{\phi}_{i,y}(p_k) \\ \widetilde{\phi}_{i,y}(p_k) & \widetilde{\phi}_{i,x}(p_k) \end{pmatrix}
\end{aligned}
\tag{4.55}
$$

where the terms $\widetilde{\phi}_{i,l}(p_k)$ are the *smoothed* derivatives of the shape functions, expressed by

$$
\widetilde{\phi}_{i,l}(p_k) := \frac{1}{A_k} \int_{\partial \mathbf{D}_k^S} n_l^{(k)}(\xi)\,\phi_i(\xi) \, \mathrm{d}\mathcal{S}, \quad l = x, y
\tag{4.56}
$$

The discretization results in the same algebraic system expressed in Eq. (3.177), where now the stiffness matrix $[K]$ is evaluated through the contribution of each *smoothing domain*

$$
[K(p_k)]_{Sd} = A_k [\widetilde{B}(p_k)]^T [\hat{\mathbf{E}}(p_k)][\widetilde{B}(p_k)]
\tag{4.57}
$$

where as in the FEM, the matrix $[\widetilde{B}(p_k)]$ is composed by the submatrices $[\widetilde{B}_i(p_k)]$ as $[\widetilde{B}(p_k)] = \left([\widetilde{B}_1(p_k)] \dots [\widetilde{B}_i(p_k)] \dots [\widetilde{B}_N(p_k)] \right)$, where N is the number of nodes in the support domain S_d at the point p_k.

Remark 4.7: Softening effects

In Liu and Zhang (2007) and Liu (2008), the authors pointed out that the smoothed bilinear form is capable to provide *softer* results with respect to the standard weak form, when the same approximation functions are used ($\tilde{a}(\bar{w}, \bar{w}) \leq a(\bar{w}, \bar{w}), \bar{w} \in \mathcal{V}_h^0(\mathbf{D})$). They also showed that it is also capable to provide an *upper bound* approximation to the exact solution. This last characteristic however, depends on both the kind of approximation functions that are being adopted, and on the peculiar strategy used for the generation of the smoothing domains. As shown in Remark 7.2, the NS-PIM is capable to provide such upper bound approximation, while the ES-PIM provides, in general, a lower bound approximation as the standard FEM, though with a solution that is still softer than the one of the standard FEM.

4.2.3   Node-based smoothed point interpolation method

The *node-based smoothed point interpolation method* (NS-PIM) was originally proposed by Liu and his co-authors in Liu et al. (2005), Liu and Zhang (2007), and Zhang et al. (2007) as a meshfree method based on *point interpolation* shape functions with a *nodal integration procedure*[14], and was later shown to belong to the more general class of methods obtained with a *gradient smoothing technique* (Liu, 2008). Such method relies on the weakened-weak form presented in Section 4.2.2.5 and, as anticipated by its name, on smoothing domains based on the scattered nodes of the discrete model. Despite it could be used also for one- and three-dimensional problems, in the following attention is focused on the two-dimensional case. The generation of smoothing domains with the *equally-shared smoothing domains strategy*[15] (see, e.g., Liu and Zhang (2013)) is depicted in Fig. 4.4, for an *internal* and a *boundary* domains. The generic smoothing domain $\mathbf{D}_k^S$ at the node k is generated using the surrounding triangular cells, by connecting sequentially, the midpoints of the cells edges containing the node k with the centroids of the cells. With this strategy, the number of smoothing domains is equal to the number of nodes ($N_S = N_n$), which satifies the minimum number requirement discussed in Liu (2008). From Fig. 4.4 it can be observed that these domains also satisfy the requirements presented in Section 4.2.2.2, since they are *non-overlapping* and they respect the *no-sharing rule*; indeed, the boundary $\partial\mathbf{D}_k^S$ of a generic smoothing domain doesn't share any finite portion with the edges of the surrounding cells, where the approximation functions may be discontinuous, but share only the midpoint of their edges.
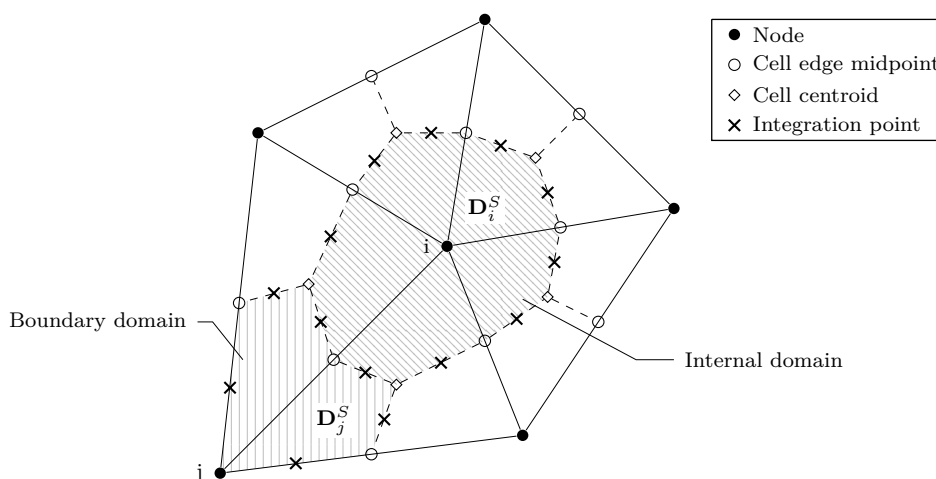
Figure 4.4: Node-based smoothing domain

When regular quadrilateral cells are used, as in the simulations of Section 6.4, the

---

[14] In the cited papers the method was originally called *linearly conforming point interpolation method* (LC-PIM).

[15] The equally-shared smoothing domain strategy is the most common in the NS-PIM. However, as pointed out in Liu and Zhang (2013), for example, also Voronoi cells can be used as smoothing domains, as done in Chen et al. (2001) for the nodal integration strategy in the EFG method.

strategy for the generation of the smoothing domains is the same as the one described above, and is depicted in Fig. 4.5.
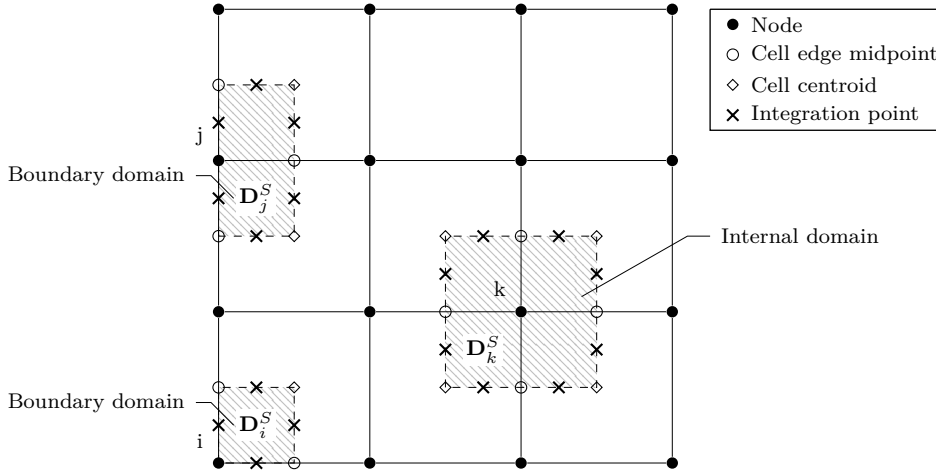
Figure 4.5: Node-based smoothing domain - Quadrilateral cells

The smoothed shape functions appearing in Eq. (4.56), which allow to evaluate the smoothed bilinear form, are calculated performing a numerical integration along the boundary $\partial \mathbf{D}_k^S$ of each smoothing domain. Since the boundary of each smoothing domain is composed by a set of linear segments, the integration can be expressed as a sum of Gaussian quadratures over each segment, resulting in

$$\widetilde{\phi}_{i,l}(p_k) = \frac{1}{A_k} \sum_{m=1}^{n_{seg}} \frac{L_m}{2} \left(\sum_{n=1}^{n_{gp}} W_n^{gp} \, \phi_i(p_{m,n}) \, n_{l,m}^{(k)} \right), \quad l = x, y \tag{4.58}$$

where n_{seg} is the number of segments, L_m the length of the m-th segment, n_{gp} the number of integration points of each segment, $p_{m,n}$ the n-th integration point of the m-th segment with associated weight W_n^{gp}, and $n_{l,m}^{(k)}$ the component in the direction l of the unit normal to the m-th segment of the k-th smoothing domain.

4.2.4   Edge-based smoothed point interpolation method

The *edge-based smoothed point interpolation method* (ES-PIM) was introduced by Liu and his co-authors in Liu and Zhang (2008) in order to correct the excessive *softnening* effect of the NS-PIM, which resulted in temporally unstable dynamic problems. As pointed out in Liu and Zhang (2013), the ES-PIM exhibits a stiffer behaviour with respect to the NS-PIM, is both spatially and temporally stable, and is capable to produce much more accurate results compared to the NS-PIM and the standard FEM.

The difference between the NS-PIM and the ES-PIM relies in the strategy for the generation of the smoothing domains, which in the latter, as anticipated by the name of the method, is based on the *edges* of the background cells instead of the nodes. As illustrated in Fig. 4.6, the smoothing domain associated to the generic internal edge j is

constructed by connecting the two nodes at the ends of the edge with the centroids of
the two triangular cells that share the edge j. For a boundary edge the procedure is the
same, except for the fact that also the edge belongs to the boundary of the smoothing
domain. As pointed out in Liu (2009), also this strategy satisfies the requirement on the
minimum number of smoothing domains, is *non-overlapping*, and respect the *no-sharing*
rule.
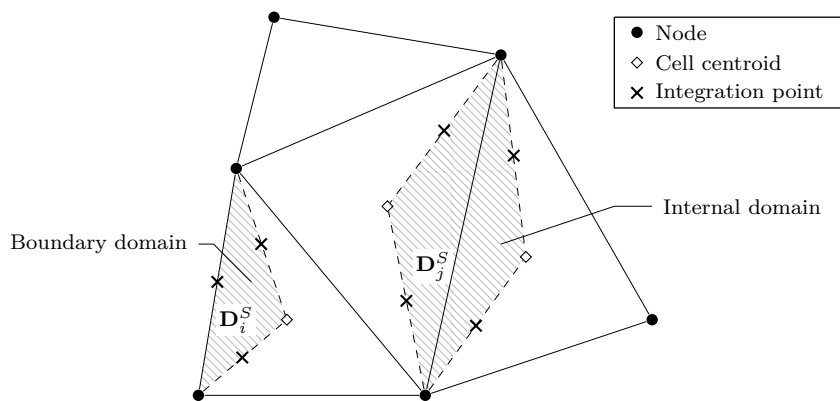
Figure 4.6: Edge-based smoothing domain

In presence of quadrilateral background cells, as in the example of Section 6.4, the
same strategy applies, resulting in the smoothing domains depicted in Fig. 4.7.
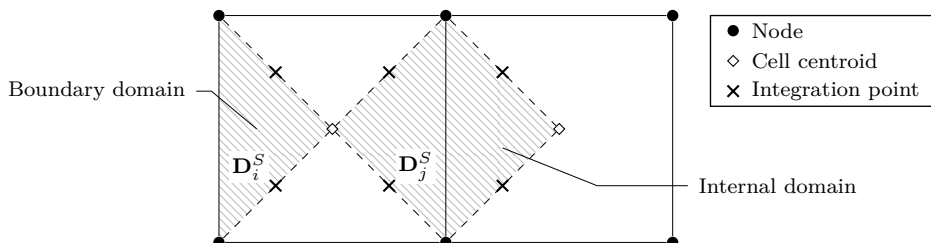
Figure 4.7: Edge-based smoothing domain - Quadrilateral cells

Also with the edge-based strategy the boundary of each smoothing domain is composed
by linear segments; in this case the number is fixed, and is equal to four segments for
an internal edge, and three for a boundary edge, while in the NS-PIM it depends on the
number of cells surrounding the node. The numerical integration of the smoothed shape
functions is the same as the one expressed in Eq. (4.58).

4.2.5   Non-local character of smoothed point interpolation approximations

As already stated, the reason for using smoothed meshfree methods in this treatise is
to take advantage of their *intrinsic non-local* character, and to the corresponding regu-
larization effects in strain-softening problems. In one of the first works devoted to the
investigation of the regularization properties of meshfree methods (Chen et al., 2000),

the authors, focusing on *moving least square* (MLS) and *reproducing kernel* (RK) approximations, pointed out that these methods posses an *intrinsic non-locality* due to the presence of weight functions which support size is greater than the nodal spacing. They also emphasized that a further non-local effect can be introduced when a *nodal integration* strategy is adopted.

To the author knowledge, analogous investigations on the class of smoothed point interpolation methods have not been performed yet. The NS-PIM strategy has been applied to strain-softening elasto-plasticity in Zhang et al. (2015), though with no explicit discussions on eventual regularization effects. It is the author opinion (supported by the results presented in Chapters 6 and 7) that also this class of meshfree methods is capable to regularize the behaviour of numerical simulations of strain-softening problems, due to intrinsic non-local properties. In smoothed point interpolation methods these non-local properties can be ascribed to two of the concepts which these methods are based on. The first is the generation of state variables approximations via PIM and RPIM with T-schemes. Despite the absence of weight functions (which are present in MLS approximations), also the PIM and RPIM approximations embed a certain non-locality. Indeed, while the T3-scheme generates the support domain at an integration point using the three nodes of the triangular cells which the point belongs to (Fig. 4.2(a)), resulting in a situation similar to the one of a triangular finite element, the T6/3-scheme (Fig. 4.2(b)) allows to obtain support domains that are larger than the nodal spacing. The second concept capable to introduce a certain degree of non-locality is the use of *smoothed strains*, resulting in a procedure that is analogous to the nodal integration scheme adopted in Chen et al. (2000).

4.3   Application to continuum damage mechanics

To the author knowledge, the only application of a smoothed point interpolation method to a physically non-linear problem is the one of Zhang et al. (2015), where the NS-PIM was used to investigate elasto-plastic models. However, the nodal integration strategy which the NS-PIM is based on, had already been applied to non-linear elasticity and elasto-plasticity (Chen et al., 2002) and to scalar damage (Chen et al., 2000). In this treatise attention is focused on the application of both the NS-PIM and ES-PIM to problems of *continuum damage mechanics*, represented in terms of the *elastic-degrading* constitutive models discussed in Section 2.2.

In Section 4.2.2.5, the passage from Eq. (4.45) to Eq. (4.49), that is, the passage from a smoothed bilinear form expressed in terms of the domain integral $\int_{\mathbf{D}}$ to a smoothed bilinear form expressed as a summation over the number of smoothing domains, is made possible with the assumption of a linear elastic constitutive operator $\hat{\mathbf{E}}$ *constant* over the smoothing domain. In a physically linear problem, since the material properties

are independent on the state of the body, this assumption is verified both in case of homogeneous and heterogeneous materials; an eventual heterogeneous distribution of the material properties indeed, could be easily considered with the attribution of different material properties at each smoothing domain, constant over the same smoothing domain.

When dealing with elastic-degrading models, the initial elastic constitutive operator $\hat{\mathbf{E}}$ appearing in Eq. (4.45) must be replaced with a *secant* operator $\hat{\mathbf{E}}^S$ which depends on the state of the body, and which varies during the loading process

$$\tilde{a}(\bar{w}, \bar{u}) = \int_{\mathbf{D}} \tilde{\underline{\varepsilon}}(\bar{w}(p_k)) \cdot \left(\hat{\mathbf{E}}^S(\underline{\varepsilon}(\bar{u})) \cdot \tilde{\underline{\varepsilon}}(\bar{u}(p_k)) \right) \, \mathrm{d}\mathcal{V} \tag{4.59}$$

In order to obtain an expression similar to the one of Eq. (4.49), a *smoothed* constitutive operator $\widetilde{\hat{\mathbf{E}}^S}(p_k)$, *constant* over the smoothing domain $\mathbf{D}_k^S$, can be introduced as

$$\widetilde{\hat{\mathbf{E}}^S}(p_k) := \frac{1}{A_k} \int_{\mathbf{D}_k^S} \hat{\mathbf{E}}^S(\xi) \, \mathrm{d}\mathcal{V} \tag{4.60}$$

resulting in

$$\tilde{a}(\bar{w}, \bar{u}) = \sum_{k=1}^{N_S} A_k \left(\tilde{\underline{\varepsilon}}(\bar{w}(p_k)) \cdot \left(\widetilde{\hat{\mathbf{E}}^S}(p_k) \cdot \tilde{\underline{\varepsilon}}(\bar{u}(p_k)) \right) \right) \tag{4.61}$$

The integration appearing in Eq. (4.60) can be avoided, in general, taking into account the following considerations. First, it can be observed that the secant operator depends on the state of the body at each point $\xi \in \mathbf{D}_k^S$, for example, on the current strain $\underline{\varepsilon}(\bar{u}(\xi))$ which depends on the state variable. In NS-PIM and ES-PIM procedures, the state variable is calculated at the point p_k of each smoothing domain $\mathbf{D}_k^S$, resulting in a smoothed strain tensor $\tilde{\underline{\varepsilon}}(\bar{u}(p_k))$ (Eq. (4.46)) which is constant over the smoothing domain. The smoothed constitutive operator can then be assumed to be equal to the secant operator generated using the smoothed strain as

$$\hat{\mathbf{E}}(\underline{\varepsilon}(\bar{u})) \to \widetilde{\hat{\mathbf{E}}^S}(p_k) \equiv \hat{\mathbf{E}}^S(\tilde{\underline{\varepsilon}}(\bar{u}(p_k)) \tag{4.62}$$

In case of a scalar-isotropic damage model, for example, the secant constitutive operator depends on the initial constitutive operator $\hat{\mathbf{E}}$ and on the scalar damage variable D as $\hat{\mathbf{E}}^S = (1 - D) \, \hat{\mathbf{E}}$ (Eq. (2.7)), where the variable D depends on the current strain state of the body through an equivalent strain measure (Eq. (2.34)), $D = D(\varepsilon_{eq})$ with $\varepsilon_{eq} = \varepsilon_{eq}(\underline{\varepsilon}(\bar{u}(p)))$. In this case, the smoothed constitutive operator will depend on a smoothed damage variable $\widetilde{D}(p_k)$ as

$$\widetilde{\hat{\mathbf{E}}^S}(p_k) = (1 - \widetilde{D}(p_k)) \, \hat{\mathbf{E}}, \quad \widetilde{D}(p_k) = D(\tilde{\varepsilon}_{eq}), \quad \tilde{\varepsilon}_{eq} = \varepsilon_{eq}(\tilde{\underline{\varepsilon}}(\bar{u}(p_k)) \tag{4.63}$$

4.3.1   Linearization of the weakened-weak form

The introduction of PIM or RPIM approximation functions in the smoothed bilinear form of Eq. (4.61), and in the linear functional of Eq. (4.28), leads to an algebraic system analogous to the one of Eq. (3.177), where the stiffness matrix $[K]$ is replaced by the *secant stiffness matrix* $[K^S]$, which components depend on the current state of the body

$$[K^S]\,\{X\} = \{R\} \tag{4.64}$$

The solution of this non-linear system allows to find the evolution, during the loading process, of the state variable $\bar{u}(p,t)$, which now depends both on the position $p \in \mathbf{D}$ and on a parameter t, usually called *pseudo-time* in a quasi-static context as the one considered here. The non-linear system can be solved with an incremental-iterative strategy (Remark 4.8) based on the *Newton-Rhapson* method, which requires a *linearization* of Eq. (4.64), as in the standard non-linear FEM (see, e.g., Wriggers (2008)).

The first step for the linearization within the Newton-Rhapson method consists in the introduction of a space of *admissible variations* $\delta\mathcal{V}(\mathbf{D})$, associated to the space of trial functions $\mathcal{V}(\mathbf{D})$[16], defined as

$$\delta\mathcal{V}(\mathbf{D}) := \left\{ \delta\bar{u} \in \left(\mathcal{G}_h^1(\mathbf{D})\right)^n \mid \delta\bar{u} = \bar{0} \text{ at } \partial\mathbf{D}_e^u \right\} \tag{4.65}$$

The admissible variations $\delta\bar{u}$ allow to obtain a set of *perturbed* configurations $\mathcal{V}_\varepsilon(\mathbf{D})$, which elements $\bar{u}_\varepsilon = \bar{u} + \varepsilon\,\delta\bar{u}$ satisfy the kinematical boundary conditions of the problem. The weakened-weak form of Eq. (4.50) can be recast as

$$G(\bar{w}, \bar{u}) := \widetilde{a}(\bar{w}, \bar{u}) - f(\bar{w}) = 0, \quad \forall \bar{w} \in \mathcal{V}^0(\mathbf{D}) \tag{4.66}$$

with the introduction of the functional $G(\bar{w}, \bar{u})$. The basic idea of this approach is to find a *perturbed* configuration $G(\bar{w}, \bar{u}_\varepsilon)$ near the *known* equilibrium configuration $G(\bar{w}, \bar{u})$ (which satisfies Eq. (4.66)), such that it satisfies the condition

$$G(\bar{w}, \bar{u}_\varepsilon) = \widetilde{a}(\bar{w}, \bar{u}_\varepsilon) - f(\bar{w}) = 0, \quad \forall \bar{w} \in \mathcal{V}^0(\mathbf{D}) \tag{4.67}$$

The vector field $\delta\bar{u}$ which allows to reach the new equilibrium configuration can be calculated with the linearization $G(\bar{w}, \bar{u}_\varepsilon) \simeq L\left[G(\bar{w}, \bar{u}_\varepsilon)\right]$, resulting in

$$L\left[G(\bar{w}, \bar{u}_\varepsilon)\right] = G(\bar{w}, \bar{u}) + DG(\bar{w}, \bar{u}) \cdot \delta\bar{u} = 0, \quad \forall \bar{w} \in \mathcal{V}^0(\mathbf{D}) \tag{4.68}$$

---

[16] In this case the space of trial functions is also known as space of *admissible configurations* of the body.

where the terms $DG(\bar{w}, \bar{u}_\varepsilon) \cdot \delta\bar{u}$ is the following *directional* (or *Fréchet*) derivative

$$DG(\bar{w}, \bar{u}) \cdot \delta\bar{u} = \left.\frac{\partial G(\bar{w}, \bar{u}_\varepsilon)}{\partial \varepsilon}\right|_{\varepsilon=0} \tag{4.69}$$

The linearized weakened-weak form can then be recast into: find the *increments* $\delta\bar{u} \in \delta\mathcal{V}(\mathbf{D})$ such that

$$DG(\bar{w}, \bar{u}) \cdot \delta\bar{u} = -G(\bar{w}, \bar{u}), \quad \forall \bar{w} \in \mathcal{V}^0(\mathbf{D}) \tag{4.70}$$

Proposition 4.1. In case of elastic-degrading constitutive models in a geometrically linear context, the directional derivative of Eq. (4.69) is expressed by

$$
\begin{aligned}
DG(\bar{w}, \bar{u}) \cdot \delta\bar{u} &= \sum_{k=1}^{N_S} A_k \left(\widetilde{\underline{\varepsilon}}(\bar{w}(p_k)) \cdot \left(\widetilde{\hat{\mathbf{E}}^t}(p_k) \cdot \delta\widetilde{\underline{\varepsilon}}(\bar{u}(p_k)) \right) \right) \\
&= \sum_{k=1}^{N_S} A_k \left(\widetilde{\underline{\varepsilon}}(\bar{w}(p_k)) \cdot \left(\widetilde{\hat{\mathbf{E}}^t}(p_k) \cdot \dot{\widetilde{\underline{\varepsilon}}}(\bar{u}(p_k)) \right) \right)
\end{aligned}
\tag{4.71}
$$

where $\dot{\widetilde{\underline{\varepsilon}}} \equiv \delta\widetilde{\underline{\varepsilon}}$ is the *rate* of the smoothed strain tensor, analogous to the one defined in Section 2.2.2 for the strain tensor.

Proof. *First, since in a geometrically linear context the linear functional $f(\bar{w})$ doesn't depend on $\bar{u}$, the directional derivative of $G(\bar{w}, \bar{u})$ reduces to the directional derivative of the bilinear form*

$$DG(\bar{w}, \bar{u}) \cdot \delta\bar{u} = \left.\frac{\partial \widetilde{a}(\bar{w}, \bar{u}_\varepsilon)}{\partial \varepsilon}\right|_{\varepsilon=0}$$

From Eq. (4.61) the bilinear form can be expressed as

$$\widetilde{a}(\bar{w}, \bar{u}) = \sum_{k=1}^{N_S} A_k \left(\widetilde{\underline{\varepsilon}}(\bar{w}(p_k)) \cdot \widetilde{\underline{\sigma}}(\bar{u}_\varepsilon(p_k)) \right)$$

where the smoothed stress tensor $\widetilde{\underline{\sigma}}(\bar{u}_\varepsilon(p_k)) = \hat{\mathbf{E}}^S(\widetilde{\underline{\varepsilon}}(\bar{u}_\varepsilon(p_k)) \cdot \widetilde{\underline{\varepsilon}}(\bar{u}_\varepsilon(p_k))$ has been introduced, resulting in

$$DG(\bar{w}, \bar{u}) \cdot \delta\bar{u} = \sum_{k=1}^{N_S} A_k \left(\widetilde{\underline{\varepsilon}}(\bar{w}(p_k)) \cdot \left.\frac{\partial \widetilde{\underline{\sigma}}(\bar{u}_\varepsilon(p_k))}{\partial \varepsilon}\right|_{\varepsilon=0} \right)$$

The directional derivative of the smoothed stress tensor can be expressed as

$$
\begin{aligned}
\delta\widetilde{\underline{\sigma}}(\bar{u}(p_k)) :&= \left.\frac{\partial \widetilde{\underline{\sigma}}(\bar{u}_\varepsilon(p_k))}{\partial \varepsilon}\right|_{\varepsilon=0} \\
&= \left.\frac{\partial}{\partial \varepsilon} \left(\hat{\mathbf{E}}^S(\widetilde{\underline{\varepsilon}}(\bar{u}_\varepsilon(p_k)) \cdot \widetilde{\underline{\varepsilon}}(\bar{u}_\varepsilon(p_k))) \right)\right|_{\varepsilon=0} \\
&= \hat{\mathbf{E}}^S(\widetilde{\underline{\varepsilon}}(\bar{u}(p_k)) \cdot \left.\frac{\partial \widetilde{\underline{\varepsilon}}(\bar{u}_\varepsilon(p_k))}{\partial \varepsilon}\right|_{\varepsilon=0} + \left.\frac{\partial \hat{\mathbf{E}}^S(\widetilde{\underline{\varepsilon}}(\bar{u}_\varepsilon(p_k)))}{\partial \varepsilon}\right|_{\varepsilon=0} \cdot \widetilde{\underline{\varepsilon}}(\bar{u}(p_k)) \\
&= \hat{\mathbf{E}}^S(\widetilde{\underline{\varepsilon}}(\bar{u}(p_k)) \cdot \delta\widetilde{\underline{\varepsilon}}(\bar{u}(p_k)) + \delta\hat{\mathbf{E}}^S(\widetilde{\underline{\varepsilon}}(\bar{u}(p_k)) \cdot \widetilde{\underline{\varepsilon}}(\bar{u}(p_k))
\end{aligned}
$$

The directional derivatives of the smoothed stress and strain tensors and of the secant constitutive

operator can be identified with their rates

$$\delta\underline{\widetilde{\sigma}} \equiv \dot{\underline{\widetilde{\sigma}}}, \quad \delta\underline{\widetilde{\varepsilon}} \equiv \dot{\underline{\widetilde{\varepsilon}}}, \quad \delta\hat{\mathbf{E}}^S \equiv \dot{\hat{\mathbf{E}}}^S$$

hence, the expression of $\delta\underline{\widetilde{\sigma}}(\bar{u}(p_k))$ is the same as the one of Eq. (2.10) ($\dot{\underline{\sigma}} = \hat{\mathbf{E}}^S\cdot\dot{\underline{\varepsilon}}+\dot{\hat{\mathbf{E}}}^S\cdot\underline{\varepsilon}$), except for the presence of the smoothed terms. Taking into account the discussions in Section 2.2.2, the directional derivative of the smoothed stress can be expressed in terms of the tangent constitutive operator $\hat{\mathbf{E}}^t(\underline{\widetilde{\varepsilon}}(\bar{u}(p_k)) \equiv \widetilde{\hat{\mathbf{E}}^t}(p_k)$ as

$$\delta\underline{\widetilde{\sigma}}(\bar{u}(p_k)) = \hat{\mathbf{E}}^t(\underline{\widetilde{\varepsilon}}(\bar{u}(p_k)) \cdot \delta\underline{\widetilde{\varepsilon}}(\bar{u}(p_k)) \equiv \hat{\mathbf{E}}^t(\underline{\widetilde{\varepsilon}}(\bar{u}(p_k)) \cdot \dot{\underline{\widetilde{\varepsilon}}}(\bar{u}(p_k)) = \dot{\underline{\sigma}}(\bar{u}(p_k))$$

leading to the expressions in proposition 4.1. □

The right hand side of Eq. (4.70) is known, since it depends on the displacement field $\bar{u}$ of a known equilibrium configuration, and is expressed as

$$\begin{aligned} G(\bar{w}, \bar{u}) &= \widetilde{a}(\bar{w}, \bar{u}) - f(\bar{w}) \\ &= \sum_{k=1}^{N_S} A_k \left(\underline{\widetilde{\varepsilon}}(\bar{w}(p_k)) \cdot \underline{\widetilde{\sigma}}(\bar{u}_\varepsilon(p_k))\right) - f(\bar{w}) \end{aligned} \tag{4.72}$$

Introducing the PIM or RPIM approximation functions into Eq. (4.70), for both the test functions $\bar{w}(p)$ and the increments $\delta\bar{u}(p)$

$$\{\bar{w}(p)\} = \sum_{i\in S_d} [\phi_i(p)]\{d_i^w\}, \quad \{\delta\bar{u}(p)\} = \sum_{i\in S_d} [\phi_i(p)]\{\delta d_i\} \tag{4.73}$$

and taking into account proposition 4.1, the following algebraic system can be obtained

$$[K^t]\{\Delta X\} = \{N\} \tag{4.74}$$

where $[K^t]$ is the global *tangent* stiffness matrix of the system, $\{\Delta X\}$ the nodal parameters vector collecting all the nodal parameters $\{\delta d_i\}$, and $\{N\}$ an array containing the discretization of the right hand side of Eq. (4.70).

Remark 4.8: Solution of the tangent system

The tangent system of Eq. (4.74) can be solved using an incremental-iterative method for which the pseudo-time is replaced by a finite discretization, by means of a set of *increments* (or *steps*); inside each step an iterative procedure is performed (predictor-corrector method). The incremental equilibrium equation at the iteration n of the step k is then represented by

$$[K^t]_{n-1}^k \{\Delta X\}_n^k = \Delta\lambda_n^k \{P\} + \{Q\}_{n-1}^k \tag{4.75}$$

where $[K^t]_{n-1}^k$ is the tangent stiffness matrix at the iteration $n-1$ of the step k, depending in general on the current values of the field variables, $\{\Delta X\}_n^k$ is the vector of incremental nodal parameters at the iteration n of the step k, $\Delta\lambda_n^k$ is the increment of the load multiplier at the iteration n of the step k, $\{P\}$ the vector of the nodal reference loads, and $\{Q\}_{n-1}^k$ the vector of the residual forces at the iteration $n-1$ of the step k, given by $\{Q\}_{n-1}^k = \lambda_{n-1}^k \{P\} - \{F\}_{n-1}^k$, where $\{F\}_{n-1}^k$ is the vector of nodal forces equivalent to internal stresses.

The stiffness matrix $[K^t]$ and the vector $\{F\}$ are assembled considering the contribution of each smoothing domain composing the discrete model

$$[K^t(p_k)]_{S_d} = A_k[\widetilde{B}(p_k)]^T[\widetilde{\hat{\mathbf{E}}^t(p_k)}][\widetilde{B}(p)] \tag{4.76}$$

$$\{F(p_k)\}_{S_d} = A_k[\widetilde{B}(p_k)]^T\{\widetilde{\underline{\sigma}}(p_k)\}\ \mathrm{d}\mathcal{V} \tag{4.77}$$

where the expression of the *tangent* stiffness matrix is analogous to the one of Eq. (4.57) with the initial constitutive operator $\hat{\mathbf{E}}$ replaced by the smoothed tangent one $\widetilde{\hat{\mathbf{E}}^t}(p_k) \equiv \hat{\mathbf{E}}^t(\widetilde{\underline{\varepsilon}}(\bar{u}(p_k)))$. It is worth to note that in Eq. (4.76) it is possible to use directly the tangent constitutive operator defined in Eq. (2.12), since no return mapping operation is involved in the evaluation of the stress tensor, which is calculated directly using the secant constitutive operator.

4.4 Application to micropolar media

The present section is devoted to the application of smoothed meshfree methods to the analysis of micropolar media. In Section 3.4, the standard weak form for micropolar media has been presented, together with the Petrov-Galerkin discretization for the FEM representation. As discussed in Section 4.2.2, standard weak forms rely on trial and test functions which must be *continuous*. As already stated, when using PIM or RPIM approximations, which may exhibit discontinuities, a special treatement is required, which resulted in the formulation of the G-space theory and the weakened-weak form by Liu and his co-authors (see, e.g., Liu (2010*a,b*) and Liu and Zhang (2013)), recalled in Section 4.2.2. The aim of this section is then to extend the theoretical framework developed by Liu and his co-authors to the case of micropolar media. First, the concept of *smoothing operation* is applied to the gradients appearing in the strain and microcurvature tensors, and a G-space theory for micropolar media is formulated. Then, a weakened-weak form for the micropolar problem is introduced, and the existence and uniqueness of its solution is proven. Finally, the discretization in terms of PIM and RPIM shape functions is presented, and a linearization procedure for physically non-linear problems is exposed.

4.4.1   Smoothing operation

Using a smoothing technique analogous to the one exposed in Section 4.2.2.3, the strain and microcurvature tensors $\underline{\gamma}$ (Eq. (3.1)) and $\underline{\kappa}$ (Eq. (3.2)) depending on the set $U(p) \equiv (\bar{u}(p), \bar{\varphi}(p))$ at each point p of a certain smoothing domain $\mathbf{D}_k^S$ generated as in Section 4.2.2.2, can be replaced by the *smoothed* strain and microcurvature tensors $\widetilde{\underline{\gamma}}(U(p_k))$ and $\widetilde{\underline{\kappa}}(U(p_k))$, depending on the set of field variables $U(p_k)$ at the centre p_k of the smoothing domain $\mathbf{D}_k^S$, defined as

$$\underline{\gamma}(p) \simeq \widetilde{\underline{\gamma}}(U(p_k)) := \int_{\mathbf{D}_k^S} \underline{\gamma}(\xi)\, \widetilde{W}(p_k - \xi)\, \mathrm{d}\mathcal{V}, \quad p \in \mathbf{D}_k^S \tag{4.78}$$

$$\underline{\kappa}(p) \simeq \widetilde{\underline{\kappa}}(U(p_k)) := \int_{\mathbf{D}_k^S} \underline{\kappa}(\xi)\, \widetilde{W}(p_k - \xi)\, \mathrm{d}\mathcal{V}, \quad p \in \mathbf{D}_k^S \tag{4.79}$$

where, as in Section 4.2.2.3, $\widetilde{W}$ is a smoothing function. Considering Eqs. (3.1) and (3.2), they can be expressed as

$$\widetilde{\underline{\gamma}}(U(p_k)) = \int_{\mathbf{D}_k^S} \left(\mathrm{grad}^{\mathrm{T}}(\bar{u}(\xi)) - \mathsf{e} \cdot \bar{\varphi}(\xi) \right)\, \widetilde{W}(p_k - \xi)\, \mathrm{d}\mathcal{V} \tag{4.80}$$

$$\widetilde{\underline{\kappa}}(U(p_k)) = \int_{\mathbf{D}_k^S} \mathrm{grad}^{\mathrm{T}}(\bar{\varphi}(\xi))\, \widetilde{W}(p_k - \xi)\, \mathrm{d}\mathcal{V} \tag{4.81}$$

If the fields $\bar{u}$ and $\bar{\varphi}$ are continuous (i.e., at least piecewise differentiable) the Green's divergence theorem can be applied to Eqs. (4.80) and (4.81), resulting in

$$\widetilde{\underline{\gamma}}(U(p_k)) = \int_{\partial \mathbf{D}_k^S} (\bar{n}(s) \otimes \bar{u}(s))\, \widetilde{W}(p_k - \xi)\, \mathrm{d}\mathcal{V} - \int_{\mathbf{D}_k^S} \bar{u}(\xi) \otimes \mathrm{grad}(\widetilde{W}(p_k - \xi))\, \mathrm{d}\mathcal{V}$$

$$- \int_{\mathbf{D}_k^S} (\mathsf{e} \cdot \bar{\varphi}(\xi))\, \widetilde{W}(p_k - \xi)\, \mathrm{d}\mathcal{V} \tag{4.82}$$

$$\widetilde{\underline{\kappa}}(U(p_k)) = \int_{\partial \mathbf{D}_k^S} (\bar{n}(s) \otimes \bar{\varphi}(s))\, \widetilde{W}(p_k - \xi)\, \mathrm{d}\mathcal{V} - \int_{\mathbf{D}_k^S} \bar{\varphi}(\xi) \otimes \mathrm{grad}(\widetilde{W}(p_k - \xi))\, \mathrm{d}\mathcal{V} \tag{4.83}$$

Assuming the same Heaviside-type smoothing function expressed in Eq. (4.38), Eqs. (4.82) and (4.83) reduce to

$$\widetilde{\underline{\gamma}}(U(p_k)) = \underbrace{\frac{1}{A_k} \int_{\partial \mathbf{D}_k^S} \bar{n}^{(k)}(s) \otimes \bar{u}(s)\, \mathrm{d}\mathcal{S}}_{\widetilde{\mathrm{grad}}^{\mathrm{T}}(\bar{u})} - \mathsf{e} \cdot \widetilde{\bar{\varphi}}(U(p_k)) \tag{4.84}$$

$$\widetilde{\underline{\kappa}}(U(p_k)) = \underbrace{\frac{1}{A_k} \int_{\partial \mathbf{D}_k^S} \bar{n}^{(k)}(s) \otimes \bar{\varphi}(s)\, \mathrm{d}\mathcal{S}}_{\widetilde{\mathrm{grad}}^{\mathrm{T}}(\bar{\varphi})} \tag{4.85}$$

where the *smoothed microrotation* $\widetilde{\bar{\varphi}}(U(p_k))$, constant over the smoothing domain $\mathbf{D}_k^S$, has been defined as

$$\widetilde{\bar{\varphi}}(U(p_k)) := \frac{1}{A_k} \int_{\mathbf{D}_k^S} \bar{\varphi}(\xi)\, \mathrm{d}\mathcal{V} \tag{4.86}$$

    With the application of the Green's divergence theorem, all the domain integrals where the field variables appeared in terms of their gradient have been transformed into boundary integrals. Due to the presence of the field variable $\bar{\varphi}$, the smoothed strain tensor $\widetilde{\underline{\gamma}}(U(p_k))$ (Eq. (4.84)) still contains a domain integral (Eq. (4.86)), which requires a special treatement for the construction of a micropolar weakened-weak form. It is worth to note that the problem of the presence of a field variable in a strain measure in terms of the variable itself and not in terms of its gradient is analogous to the case of an *axisymmetric* problem in classic elasticity. According to the available literature on smoothing methods and nodal integration strategies applied to axisymmetric problems two approaches can be followed. In Tootoonchi and Khoshghalb (2016) the authors focused on axisymmetric problems with the application of the cell-based smoothed point interpolation method. The strain terms depending on the field variable were treated by the authors considering a numerical integration of the domain integral, using integration points inside each smoothing domain. Within this approach, the expression in Eq. (4.86) should be directly used for the evaluation of the smoothed microrotation. In Chen et al. (2002) instead, the authors proposed a nodal integration strategy for Galerkin meshfree methods applied to geometrical non-linearities and elasto-plasticity. The case of axisymmetric problems was briefly mentioned, stating that the strain terms containing the field variable should be evaluated nodally. Within this approach the following approximation should be introduced

$$\widetilde{\bar{\varphi}}(p_k) \simeq \bar{\varphi}(p_k) \tag{4.87}$$

which consists into approximate the smoothed field variable appearing in Eq. (4.84) with its value at the point p_k[17]. In the present treatise the approach by Chen et al. (2002) has been preferred to the one by Tootoonchi and Khoshghalb (2016), since it led to a more simple treatement of the strain tensor, also from a computational point of view. Then, replacing Eq. (4.87) into Eq. (4.84), the smoothed strain tensor can be expressed as

$$\widetilde{\underline{\gamma}}(U(p_k)) = \frac{1}{A_k} \int_{\partial \mathbf{D}_k^S} \bar{n}^{(k)}(s) \otimes \bar{u}(s) \, \mathrm{d}\mathcal{S} - \bar{\varphi}(p_k) \tag{4.88}$$

4.4.2 G-space for micropolar field variables

The concept of G-space presented in Section 4.2.2.4 can be extended to the case of micropolar media following a procedure similar to the one adopted in Section 3.4, where the space $\mathcal{H}^*(\mathbf{D})$ was introduced to represent the micropolar trial and test functions. In a micropolar medium indeed, discretized trial and test functions, $U \equiv (\bar{u}, \bar{\varphi})$ and $W \equiv (\bar{w}, \bar{\omega})$,

---

[17] For the node-based strategy it would be the nodal value of $\bar{\varphi}$, like for the nodal integration approach adopted by Chen et al. (2002), while for the edge-based one it would be the interpolated value of $\bar{\varphi}$ at p_k.

can be considered as elements of the space

$$\mathcal{G}_h^*(\mathbf{D}) := \left(\mathcal{G}_h^1(\mathbf{D})\right)^n \times \left(\mathcal{G}_h^1(\mathbf{D})\right)^m \tag{4.89}$$

where the generic G-space $(\mathcal{G}_h^1\mathbf{D}))^k$ for k-dimensional vector fields has been defined in Eq. (4.41). Since it has been defined as the cartesian product of two Hilbert spaces, it follows that also $\mathcal{G}_h^*(\mathbf{D})$ is an Hilbert space, with natural (i.e., induced by the cartesian product, as in Hlaváček and Hlaváček (1969)) inner product $< \cdot, \cdot >'_{\mathcal{G}^*(\mathbf{D})}$ expressed as a combination of inner products in a standard G-space (Eq. (4.42))

$$< W, U >'_{\mathcal{G}^*} = < \bar{w}, \bar{u} >_{\mathcal{G}^1} + < \bar{\omega}, \bar{\varphi} >_{\mathcal{G}^1}, \quad W, U \in \mathcal{G}_h^*(\mathbf{D}) \tag{4.90}$$

with induced *norm* $\|\cdot\|'_{\mathcal{G}^*}$ and *semi-norm* $|\cdot|'_{\mathcal{G}^*}$ expressed as combinations of norms in the Lebesgue space $\mathcal{L}^2(\mathbf{D})$

$$\|W\|'^2_{\mathcal{G}^*} = \|W\|^2_{\mathcal{L}^2} + |W|^2_{\mathcal{G}^*} = \|\bar{w}\|^2_{\mathcal{L}^2} + \|\bar{\omega}\|^2_{\mathcal{L}^2} + |W|^2_{\mathcal{G}^*}, \quad W \in \mathcal{G}_h^*(\mathbf{D}) \tag{4.91}$$

$$|W|'^2_{\mathcal{G}^*} = \underbrace{\left\|\widetilde{\mathrm{grad}}(\bar{w})\right\|^2_{\mathcal{L}^2}}_{|\bar{w}|^2_{\mathcal{G}^1}} + \underbrace{\left\|\widetilde{\mathrm{grad}}(\bar{\omega})\right\|^2_{\mathcal{L}^2}}_{|\bar{\omega}|^2_{\mathcal{G}^1}}, \quad W \in \mathcal{G}_h^*(\mathbf{D}) \tag{4.92}$$

Aiming to prove the existence and uniqueness of the micropolar weakened-weak form discussed in Section 4.4.3, the author observed that the alternative inner product

$$< W, U >_{\mathcal{G}^*} = \underbrace{\underbrace{\int_{\mathbf{D}} \bar{w} \cdot \bar{u} \, \mathrm{d}\mathcal{V}}_{< \bar{w}, \bar{u} >_{\mathcal{L}^2}} + \underbrace{\int_{\mathbf{D}} \bar{\omega} \cdot \bar{\varphi} \, \mathrm{d}\mathcal{V}}_{< \bar{\omega}, \bar{\varphi} >_{\mathcal{L}^2}}}_{< W, U >_{\mathcal{L}^2}} + \underbrace{\int_{\mathbf{D}} \underline{\widetilde{\Gamma}}(W) \cdot \underline{\widetilde{\Gamma}}(U) \, \mathrm{d}\mathcal{V}}_{< \underline{\widetilde{\Gamma}}(W), \underline{\widetilde{\Gamma}}(U) >_{\mathcal{L}^2}}, \quad W, U \in \mathcal{G}_h^*(\mathbf{D}) \tag{4.93}$$

represents a more convenient choice. Taking into account the expression of the generalized deformation operator (Eq. (3.117)), the term $< \underline{\widetilde{\Gamma}}(W), \underline{\widetilde{\Gamma}}(U) >_{\mathcal{L}^2}$ can be recast as

$$< \underline{\widetilde{\Gamma}}(W), \underline{\widetilde{\Gamma}}(U) >_{\mathcal{L}^2} = \underbrace{\int_{\mathbf{D}} \underline{\widetilde{\gamma}}(W) \cdot \underline{\widetilde{\gamma}}(U) \, \mathrm{d}\mathcal{V}}_{< \underline{\widetilde{\gamma}}(W), \underline{\widetilde{\gamma}}(U) >_{\mathcal{L}^2}} + \underbrace{\int_{\mathbf{D}} \underline{\widetilde{\kappa}}(W) \cdot \underline{\widetilde{\kappa}}(U) \, \mathrm{d}\mathcal{V}}_{< \underline{\widetilde{\kappa}}(W), \underline{\widetilde{\kappa}}(U) >_{\mathcal{L}^2}} \tag{4.94}$$

Finally, considering that the smoothed operators are *constant* over each smoothing domain, the following expressions can be obtained

$$< \underline{\widetilde{\Gamma}}(W), \underline{\widetilde{\Gamma}}(U) >_{\mathcal{L}^2} = \sum_{k=1}^{N_S} A_k \left(\underline{\widetilde{\Gamma}}(W(p_k)) \cdot \underline{\widetilde{\Gamma}}(U(p_k)) \right) \tag{4.95}$$

$$= \sum_{k=1}^{N_S} A_k \left(\underline{\widetilde{\gamma}}(W(p_k)) \cdot \underline{\widetilde{\gamma}}(U(p_k)) \right) + \sum_{k=1}^{N_S} A_k \left(\underline{\widetilde{\kappa}}(W(p_k)) \cdot \underline{\widetilde{\kappa}}(U(p_k)) \right)$$

$$\tag{4.96}$$

This inner product results in the induced norm $\|\cdot\|_{\mathcal{G}^*}$

$$\|W\|_{\mathcal{G}^*}^2 = \|W\|_{\mathcal{L}^2}^2 + |W|_{\mathcal{G}^*}^2 = \|\bar{w}\|_{\mathcal{L}^2}^2 + \|\bar{\omega}\|_{\mathcal{L}^2}^2 + |W|_{\mathcal{G}^*}^2, \quad W \in \mathcal{G}_h^*(\mathbf{D}) \tag{4.97}$$

which is analogous to the one of Eq. (4.91) except for the different semi-norm $|\cdot|_{\mathcal{G}^*}$ expressed by

$$|W|_{\mathcal{G}^*}^2 = \left\|\widetilde{\underline{\Gamma}}(W)\right\|_{\mathcal{L}^2}^2 = \left\|\widetilde{\underline{\gamma}}(W)\right\|_{\mathcal{L}^2}^2 + \|\widetilde{\underline{\kappa}}(W)\|_{\mathcal{L}^2}^2 \tag{4.98}$$

The term $|W|_{\mathcal{G}^*}^2$ in Eq. (4.98) qualifies as a semi-norm since it may exist a function $W \in \mathcal{G}_h^*(\mathbf{D}), W \neq 0$ such that $|W|_{\mathcal{G}^*}^2 = 0$ (i.e., a *rigid body motion* for which $\widetilde{\underline{\Gamma}} = \underline{0}$).

The relation between the semi-norms $|\cdot|_{\mathcal{G}^*}^{\prime 2}$ and $|\cdot|_{\mathcal{G}^*}^2$, and between the norms $\|\cdot\|_{\mathcal{G}^*}^{\prime 2}$ and $\|\cdot\|_{\mathcal{G}^*}^2$, can be pointed out by introducing the expressions of the smoothed strain (Eq. (4.84)) and microcurvature (Eq. (4.85)) tensors in Eq. (4.97), resulting in

$$\left\|\widetilde{\underline{\gamma}}(W)\right\|_{\mathcal{L}^2}^2 = \underbrace{\left\|\widetilde{\mathrm{grad}}^{\mathrm{T}}(\bar{w})\right\|_{\mathcal{L}^2}^2}_{|\bar{w}|_{\mathcal{G}^1}^2} + \underbrace{2\left\|\widetilde{\bar{\omega}}\right\|_{\mathcal{L}^2}^2 - 2< \widetilde{\mathrm{grad}}^{\mathrm{T}}(\bar{w}), \mathsf{e}\cdot\widetilde{\bar{\omega}} >_{\mathcal{L}^2}}_{2h(W)} \tag{4.99}$$

$$\|\widetilde{\underline{\kappa}}(W)\|_{\mathcal{L}^2}^2 = \underbrace{\left\|\widetilde{\mathrm{grad}}^{\mathrm{T}}(\bar{\omega})\right\|_{\mathcal{L}^2}^2}_{|\bar{\omega}|_{\mathcal{G}^1}^2} \tag{4.100}$$

where in the first equation, the term

$$2h(W) := 2\left\|\widetilde{\bar{\omega}}\right\|_{\mathcal{L}^2}^2 - 2< \widetilde{\mathrm{grad}}^{\mathrm{T}}(\bar{w}), \mathsf{e}\cdot\widetilde{\bar{\omega}} >_{\mathcal{L}^2} \tag{4.101}$$

has been introduced. Comparing Eq. (4.92) with Eq. (4.98), the following relations hold

$$\|W\|_{\mathcal{G}^*}^{\prime 2} = \|W\|_{\mathcal{G}^*}^2 - 2h(W) \tag{4.102}$$

$$|W|_{\mathcal{G}^*}^{\prime 2} = |W|_{\mathcal{G}^*}^2 - 2h(W) \tag{4.103}$$

Proposition 4.2. The inner-product space $(\mathcal{G}_h^*(\mathbf{D}), < \cdot, \cdot >_{\mathcal{G}^*})$ is an *Hilbert* space.

Proof. *An inner-product space $(\mathcal{G}_h^*(\boldsymbol{D}), < \cdot, \cdot >_{\mathcal{G}^*})$ is an Hilbert space when the associated normed space $\left(\mathcal{G}_h^*(\boldsymbol{D}), \|\cdot\|_{\mathcal{G}^*}\right)$ is complete with respect to the metric induced by the norm, i.e., if it is a Banach space. Since, according to Eqs. (4.97) and (4.98), the norm $\|\cdot\|_{\mathcal{G}^*}$ is a composition of $\|\cdot\|_{\mathcal{L}^2}$ norms, this proof can be conducted following the same procedure adopted to prove that a Sobolev space is a Banach space (see, e.g., Brenner and Scott (2008)).*

Let $\{W_j\}$ be a Cauchy sequence with respect to the norm $\|\cdot\|_{\mathcal{G}^*}$. Since $\|\cdot\|_{\mathcal{G}^*}$ is a combination of norms $\|\cdot\|_{\mathcal{L}^2}$

$$\|W_j\|_{\mathcal{G}^*}^2 = \|W_j\|_{\mathcal{L}^2}^2 + \left\|\widetilde{\underline{\Gamma}}(W_j)\right\|_{\mathcal{L}^2}^2$$

it follows that $\{W_j\}$ itself and $\left\{\widetilde{\underline{\Gamma}}(W_j)\right\}$ are Cauchy sequences with respect to the norm $\|\cdot\|_{\mathcal{L}^2}$.

Since the Lebesgue space $\mathcal{L}^2(\boldsymbol{D})$ is also a Banach space (i.e., it is complete), it follows that

$$\exists V \in \mathcal{L}^2(\boldsymbol{D}) \mid \|W_j - V\|_{\mathcal{L}^2} \to 0 \quad as \ j \to \infty$$

$$\exists \widetilde{\underline{\Gamma}}^* \in \mathcal{L}^2(\boldsymbol{D}) \mid \left\|\widetilde{\underline{\Gamma}}(W_j) - \widetilde{\underline{\Gamma}}^*\right\|_{\mathcal{L}^2} \to 0 \quad as \ j \to \infty$$

In order to complete the proof it is necessary to show that $\widetilde{\underline{\Gamma}}(V)$ exists and is equal to $\widetilde{\underline{\Gamma}}^*$. First, it can be observed that

$$\lim_{j \to \infty} \widetilde{\underline{\Gamma}}(W_j) = \widetilde{\underline{\Gamma}}^*$$

Then, considering that $W_j \to V$ in $\mathcal{L}^2(\boldsymbol{D})$, it follows that

$$\lim_{j \to \infty} \widetilde{\underline{\Gamma}}(W_j) = \widetilde{\underline{\Gamma}}(V)$$

Hence, it follows that $\widetilde{\underline{\Gamma}}(V) = \widetilde{\underline{\Gamma}}^*$. □

The fact that the space $\mathcal{G}_h^*(\mathbf{D})$ is an Hilbert space also with respect to the new inner product (Eq. (4.93)), as stated in proposition 4.2, is fundamental for the discussions in the following Section 4.4.3. The proofs of existence and uniqueness of the micropolar weakened-weak form presented in Section 4.4.3 indeed, as in case of a standard weak form or a weakened weak form for a classic medium (see, e.g., Liu (2009)), are based on the *Lax-Milgram theorem* (see, e.g., Brenner and Scott (2008)), which requires the variational problem (i.e., the weak or weakened-weak form) to be formulated for functions belonging to Hilbert spaces.

Another important property that is necessary for the developments in the following Section 4.4.3 is the *equivalency* between the norm and semi-norm when peculiar constrained G-spaces are accounted for. This property, which involves the standard Korn's and Friedrichs-Poincaré's inequalities for standard media (Brenner and Scott, 2008), has been shown to be valid also for the classic G-space (Liu, 2010a), when functions are choosen to belong to a constrained space like the $\mathcal{V}^0(\mathbf{D})$ of Eq. (4.52), (i.e., a space where *rigid body motions* are prevented, making the semi-norm *full* positive). For the G-space $\mathcal{G}_h^*(\mathbf{D})$, this issue is addressed in the following propositions.

Proposition 4.3. For any function W belonging to the G-space $\mathcal{G}_h^*(\mathbf{D})$ the following inequality between the norm $\|\cdot\|_{\mathcal{G}^*}$ and semi-norm $|\cdot|_{\mathcal{G}^*}$ holds

$$\|W\|_{\mathcal{G}^*}^2 \geq |W|_{\mathcal{G}^*}^2, \quad \forall W \in \mathcal{G}_h^*(\mathbf{D}) \tag{4.104}$$

Proof. *The proof of the inequality of Eq. (4.104) is straightforward. Recalling the expressions of Eqs. (4.97) and (4.98)*

$$\|W\|_{\mathcal{G}^*}^2 = \|W\|_{\mathcal{L}^2}^2 + |W|_{\mathcal{G}^*}^2 = \|W\|_{\mathcal{L}^2}^2 + \left\|\widetilde{\underline{\Gamma}}(W)\right\|_{\mathcal{L}^2}^2$$

and taking into account the full positivity of the norm and the semi-positivity of the semi-norm, it is observed that it may exist a $W \in \mathcal{G}_h^*(\boldsymbol{D}), W \neq 0$ such that $\|W\|_{\mathcal{G}^*} \neq 0$ and $|W|_{\mathcal{G}^*} = 0$, which

leads to the inequality

$$\|W\|_{\mathcal{G}^*}^2 \geq |W|_{\mathcal{G}^*}^2, \quad \forall W \in \mathcal{G}_h^*(\boldsymbol{D})$$

$\square$

Proposition 4.4. For any function W belonging to the constrained space $\mathcal{V}_h^0(\mathbf{D}) \in \mathcal{G}_h^*(\mathbf{D})$ such that

$$\mathcal{V}_h^0(\mathbf{D}) := \left\{ W \equiv (\bar{w}, \bar{\omega}) \in \mathcal{G}_h^*(\mathbf{D}) \mid \bar{w} = \bar{0} \text{ at } \partial \mathbf{D}_e^u, \bar{\omega} = \bar{0} \text{ at } \partial \mathbf{D}_e^\varphi \right\} \tag{4.105}$$

the following inequality between the norm $\|\cdot\|_{\mathcal{G}^*}$ and semi-norm $|\cdot|_{\mathcal{G}^*}$ holds

$$\exists c_G \in \mathbb{R}, c_G > 0 \mid c_G \|W\|_{\mathcal{G}^*} \leq |W|_{\mathcal{G}^*}, \quad \forall W \in \mathcal{V}_h^0(\mathbf{D}) \tag{4.106}$$

Taking into account the expression of the semi-norm in Eq. (4.98), the inequality of Eq. (4.106) become[18]

$$c_G \|W\|_{\mathcal{G}^*} \leq \left\| \widetilde{\underline{\Gamma}}(W) \right\|_{\mathcal{L}^2}, \quad \forall W \in \mathcal{V}_h^0(\mathbf{D}) \tag{4.107}$$

which is equivalent to the second Korn's inequality in classic elasticity.

Proof. *This proof is based on a result by Liu, the so-called third inequality presented in Liu (2010a), which casts a relation between the norm and semi-norm in a constrained G-space, consisting in the following result*

$$\exists c_1 \in \mathbb{R}, c_1 > 0 \mid c_1 \|\bar{v}\|_{\mathcal{G}^1} \leq |\bar{v}|_{\mathcal{G}^1}, \quad \forall \bar{v} \in \left(\mathcal{G}_{h,0}^1(\boldsymbol{D}) \right)^n$$

where the space constrained $\left(\mathcal{G}_{h,0}^1(\boldsymbol{D}) \right)^n$ is a subspace of the G-space $\left(\mathcal{G}_h^1(\boldsymbol{D}) \right)^n$ such that

$$\left(\mathcal{G}_{h,0}^1(\boldsymbol{D}) \right)^n := \left\{ \bar{v} \in \left(\mathcal{G}_h^1(\boldsymbol{D}) \right)^n \mid \bar{v} = \bar{0} \text{ at } \partial \boldsymbol{D}_e \right\}$$

Introducing this result into the natural seminorm of Eq. (4.92) it follows that

$$|W|_{\mathcal{G}^*}^{'2} = |\bar{w}|_{\mathcal{G}^1}^2 + |\bar{\omega}|_{\mathcal{G}^1}^2 \geq c_1 \|\bar{w}\|_{\mathcal{G}^1}^2 + c_1 \|\bar{\omega}\|_{\mathcal{G}^1}^2 = c_1 \|W\|_{\mathcal{G}^1}^{'2}$$

and then

$$|W|_{\mathcal{G}^*}^{'2} \geq c_1 \|W\|_{\mathcal{G}^*}^{'2}$$

Taking into account the relation between the natural seminorm $|\cdot|_{\mathcal{G}^*}^{'}$ and the seminorm $|\cdot|_{\mathcal{G}^*}$ expressed in Eq. (4.103), it follows that

$$|W|_{\mathcal{G}^*}^2 = |W|_{\mathcal{G}^*}^{'2} + 2h(W) \geq c_1 \|W\|_{\mathcal{G}^*}^{'2} + 2h(W)$$

Due to the upper bound in Eq. (4.104), it follows that $c_1 \leq 1$ (see also Horgan (1995)), hence

---

[18] In the papers by Liu (see, e.g., Liu (2010a) and Liu (2010b)) the inequalities like the ones of Eq. (4.106) and Eq. (4.107) are indicated as *third* and *fourth* inequalities, respectively.

from the above equation

$$c_1\|W\|_{\mathcal{G}^*}'^2 + 2h(W) \geq c_1\left(\|W\|_{\mathcal{G}^*}'^2 + 2h(W)\right) = c_1\|W\|_{\mathcal{G}^*}^2$$

which results in Eq. (4.106)

$$|W|_{\mathcal{G}^*}^2 \geq c_1\|W\|_{\mathcal{G}^*}^2 \to |W|_{\mathcal{G}^*} \geq c_G\|W\|_{\mathcal{G}^*} \tag{4.108}$$

$\square$

Proposition 4.5. For any function W belonging to the constrained space $\mathcal{V}_h^0(\mathbf{D}) \in \mathcal{G}_h^*(\mathbf{D})$ defined in Eq. (4.105), the norm $\|\cdot\|_{\mathcal{G}^*}$ and *semi-norm* $|\cdot|_{\mathcal{G}^*}$ are *equivalent*, i.e.,

$$\exists c_G \in \mathbb{R}, c_G > 0 \mid c_G\|W\|_{\mathcal{G}^*} \leq |W|_{\mathcal{G}^*} \leq \|W\|_{\mathcal{G}^*}, \quad \forall\, W \in \mathcal{V}_{(}^0 \mathbf{D}) \tag{4.109}$$

Proof. *The proposition follows directly from proposition 4.3 and proposition 4.4.* $\square$

4.4.3   A weakened-weak form for the micropolar continuum

The weakened-weak form for the micropolar boundary value problem can be introduced in an analogous way as done in Section 4.2.2.5 for the classic elasticity problem, introducing the *smoothed bilinear form* $\widetilde{A}(W, U)$, obtained from Eq. (3.152) by replacing the strain and microcurvature tensors, $\underline{\gamma}$ and $\underline{\kappa}$, with the *smoothed* operators defined in Eqs. (4.84) and (4.85), resulting in

$$\widetilde{A}(W, U) = \int_{\mathbf{D}} \left(\widetilde{\underline{\gamma}}(W) \cdot \left(\hat{\mathbf{A}} \cdot \widetilde{\underline{\gamma}}(U)\right)\right)\, \mathrm{d}\mathcal{V} + \int_{\mathbf{D}} \left(\widetilde{\underline{\kappa}}(W) \cdot \left(\hat{\mathbf{C}} \cdot \widetilde{\underline{\kappa}}(U)\right)\right)\, \mathrm{d}\mathcal{V} \tag{4.110}$$

$$= \int_{\mathbf{D}} \left(\widetilde{\underline{\Gamma}}(W) \cdot \left(\hat{\mathcal{E}} \cdot \widetilde{\underline{\Gamma}}(U)\right)\right)\, \mathrm{d}\mathcal{V} \tag{4.111}$$

Recalling that the smoothed strain and microcurvature tensors defined in Section 4.4.1 are *constant* within each smoothing domain $\mathbf{D}_k^S$, and also assuming the constitutive operators $\hat{\mathbf{A}}$ and $\hat{\mathbf{C}}$ to be constant within each smoothing domain, the domain integral $\int_{\mathbf{D}}$ can be transformed in a summation over the N_S smoothing domains composing the discrete model, resulting in the following expressions for the smoothed bilinear form

$$\widetilde{A}(W, U) = \sum_{k=1}^{N_s} A_k \left(\widetilde{\underline{\gamma}}(W(p_k)) \cdot \left(\hat{\mathbf{A}} \cdot \widetilde{\underline{\gamma}}(U(p_k))\right)\right)$$

$$+ \sum_{k=1}^{N_s} A_k \left(\widetilde{\underline{\kappa}}(W(p_k)) \cdot \left(\hat{\mathbf{C}} \cdot \widetilde{\underline{\kappa}}(U(p_k))\right)\right) \tag{4.112}$$

$$= \sum_{k=1}^{N_s} A_k \left(\widetilde{\underline{\Gamma}}(W(p_k)) \cdot \left(\hat{\mathcal{E}} \cdot \widetilde{\underline{\Gamma}}(U(p_k))\right)\right) \tag{4.113}$$

Definition 4.6 (Micropolar weakened-weak form)**.** The *weakened-weak form* of the micropolar boundary value problem defined in Section 3.2 consists into: find the set $U \equiv (\bar{u}, \bar{\varphi}) \in \mathcal{V}_h(\mathbf{D})$ such that

$$\widetilde{A}(W, U) = f(W), \quad \forall\, W = (\bar{w}, \bar{\omega}) \in \mathcal{V}_h^0(\mathbf{D}) \tag{4.114}$$

where $\mathcal{V}_h(\mathbf{D})$ and $\mathcal{V}_h^0(\mathbf{D})$ are, respectively, the discretized spaces of *trial* and *test* functions, defined as

$$\mathcal{V}_h(\mathbf{D}) := \{U \equiv (\bar{u}, \bar{\varphi}) \in \mathcal{G}_h^*(\mathbf{D}) \mid \bar{u} = \bar{u}^* \text{ at } \partial \mathbf{D}_e^u, \bar{\varphi} = \bar{\varphi}^* \text{ at } \partial \mathbf{D}_e^\varphi\} \tag{4.115}$$

$$\mathcal{V}_h^0(\mathbf{D}) := \left\{W \equiv (\bar{w}, \bar{\omega}) \in \mathcal{G}_h^*(\mathbf{D}) \mid \bar{w} = \bar{0} \text{ at } \partial \mathbf{D}_e^u, \bar{\omega} = \bar{0} \text{ at } \partial \mathbf{D}_e^\varphi\right\} \tag{4.116}$$

where $\mathcal{G}_h^*(\mathbf{D})$ is the G-space for micropolar field variables introduced in Section 4.4.2.

4.4.3.1 Existence and uniqueness of the solution

Since, like it has been pointed out before, the space $\mathcal{G}_h^*(\mathbf{D})$ is an *Hilbert* space with the inner product defined in Eq. (4.93), the *existence* and *uniqueness* of the solution of the problem depicted in definition 4.6 is guaranteed by the well-known *Lax-Milgram* theorem (see, e.g., Brenner and Scott (2008)). In order to satisfy the conditions of the theorem it is necessary to verify if the bilinear form $\widetilde{A}(W, U)$ (Eq. (4.113)) is:

- coercive in $\mathcal{V}_h^0(\mathbf{D})$
- continuous in $\mathcal{V}_h(\mathbf{D})$

The proofs for coercivity and continuity of the bilinear form are collected in the following propositions, and are similar to the ones developed in Liu (2010*b*) for the smoothed bilinear form in classic elasticity.

Proposition 4.7 (Coercivity with respect to the semi-norm)**.** The smoothed bilinear form is *coercive* in $\mathcal{V}_h^0(\mathbf{D})$ with respect to the semi-norm $|\cdot|_{\mathcal{G}^*}$ defined in Eq. (4.98), that is

$$\exists c_1 \in \mathbb{R}, c_1 > 0 \mid \widetilde{A}(W, W) \geq c_1 |W|_{\mathcal{G}^*}^2, \quad \forall W \in \mathcal{V}_h^0(\mathbf{D}) \tag{4.117}$$

Proof. *Since the matrix $[\hat{\mathcal{E}}]$ representing the constitutive operator $\hat{\mathcal{E}}$ is symmetric positive definite, it can be decomposed as*

$$[\hat{\mathcal{E}}] = [\mathbf{U}]^T [\mathbf{\Lambda}][\mathbf{U}]$$

where $[\mathbf{\Lambda}]$ is a diagonal matrix containing all the positive eigenvalues of $[\hat{\mathcal{E}}]$, and where $[\mathbf{U}]$ is a unitary matrix (i.e., such that $[\mathbf{U}]^T[\mathbf{U}] = [\hat{\mathbf{ID}}]$) of eigenvectors. Replacing this decomposition

into Eq. (4.113) (or in the Voigt representation of the cited equation, Eq. (4.126)) leads to

$$
\widetilde{A}(W,W) = \sum_{k=1}^{N_s} A_k \left(\left([\mathbf{U}]\{\widetilde{\underline{\Gamma}}(W(p_k))\} \right)^T [\mathbf{\Lambda}] \left([\mathbf{U}]\{\widetilde{\underline{\Gamma}}(W(p_k))\} \right) \right)
$$

$$
\geq \lambda_{min} \sum_{k=1}^{N_s} A_k \left(\left([\mathbf{U}]\{\widetilde{\underline{\Gamma}}(W(p_k))\} \right)^T \left([\mathbf{U}]\{\widetilde{\underline{\Gamma}}(W(p_k))\} \right) \right)
$$

$$
= \lambda_{min} \sum_{k=1}^{N_s} A_k \left(\{\widetilde{\underline{\Gamma}}(W(p_k))\}^T [\mathbf{U}]^T [\mathbf{U}] \{\widetilde{\underline{\Gamma}}(Wp_k))\} \right)
$$

$$
= \lambda_{min} \sum_{k=1}^{N_s} A_k \left(\{\widetilde{\underline{\Gamma}}(W(p_k))\}^T \{\widetilde{\underline{\Gamma}}(W(p_k))\} \right)
$$

$$
= \lambda_{min} \sum_{k=1}^{N_s} A_k \left(\widetilde{\underline{\Gamma}}(W(p_k)) \cdot \widetilde{\underline{\Gamma}}(W(p_k)) \right)
$$

$$
= \lambda_{min} \left\| \widetilde{\underline{\Gamma}}(W) \right\|_{\mathcal{G}^*}^2 = \lambda_{min} |W|_{\mathcal{G}^*}^2
$$

where λ_{min} is the smallest eigenvalue of $[\hat{\mathcal{E}}]$. Assuming $c_1 = \lambda_{min}$ the proposition of Eq. (4.117) is proven.   □

Proposition 4.8 (Coercivity with respect to the norm)**.** The smoothed bilinear form is *coercive* in $\mathcal{V}_h^0(\mathbf{D})$ with respect to the norm $\|\cdot\|_{\mathcal{G}^*}$ defined in Eq. (4.97), that is

$$
\exists c_2 \in \mathbb{R}, c_2 > 0 \mid \widetilde{A}(W,W) \geq c_2 \|W\|_{\mathcal{G}^*}^2, \quad \forall W \in \mathcal{V}_h^0(\mathbf{D}) \tag{4.118}
$$

Proof. *This proof is straightforward, and consists in the introduction in the previous equation for coercivity with respect to the semi-norm (Eq. (4.117)) of the upper bound to the norm represented in Eq. (4.106), resulting in*

$$
\widetilde{A}(W,W) \geq c_1 |W|_{\mathcal{G}^*}^2 \geq \underbrace{c_1 \, c_G^2}_{c_2} \|W\|_{\mathcal{G}^*}^2
$$

□

Proposition 4.9 (Continuity with respect to the norm)**.** The smoothed bilinear form is *continuous* in $\mathcal{V}_h(\mathbf{D})$ with respect to the norm $\|\cdot\|_{\mathcal{G}^*}$ defined in Eq. (4.97), that is

$$
\exists c_3 \in \mathbb{R}, c_3 > 0 \mid \widetilde{A}(W,U) \leq c_3 \|W\|_{\mathcal{G}^*} \|U\|_{\mathcal{G}^*}, \quad \forall W, U \in \mathcal{V}_h(\mathbf{D}) \tag{4.119}
$$

Proof. *This proof is similar to the one of proposition 4.7, since it is based on the same decomposition $[\hat{\mathcal{E}}] = [\mathbf{U}]^T [\mathbf{\Lambda}][\mathbf{U}]$ of the symmetric positive definite matrix $[\hat{\mathcal{E}}]$, into a diagonal matrix $[\mathbf{\Lambda}]$ containing all the positive eigenvalues of $[\hat{\mathcal{E}}]$, and a unitary matrix $[\mathbf{U}]$ (i.e., such that $[\mathbf{U}]^T [\mathbf{U}] = [\mathbf{I}\hat{\mathbf{D}}]$) of eigenvectors. Replacing this decomposition into Eq. (4.113) (or in the*

Voigt representation of the cited equation, Eq. (4.126)) leads to

$$
\widetilde{A}(W,U) = \sum_{k=1}^{N_s} A_k \left(\left([\mathbf{U}]\{\widetilde{\underline{\Gamma}}(W(p_k))\} \right)^T [\mathbf{\Lambda}] \left([\mathbf{U}]\{\widetilde{\underline{\Gamma}}(U(p_k))\} \right) \right)
$$

$$
\leq \lambda_{max} \sum_{k=1}^{N_s} A_k \left(\left([\mathbf{U}]\{\widetilde{\underline{\Gamma}}(W(p_k))\} \right)^T \left([\mathbf{U}]\{\widetilde{\underline{\Gamma}}(U(p_k))\} \right) \right)
$$

$$
= \lambda_{max} \sum_{k=1}^{N_s} A_k \left(\{\widetilde{\underline{\Gamma}}(W(p_k))\}^T [\mathbf{U}]^T [\mathbf{U}]\{\widetilde{\underline{\Gamma}}(U(p_k))\} \right)
$$

$$
= \lambda_{max} \sum_{k=1}^{N_s} A_k \left(\{\widetilde{\underline{\Gamma}}(W(p_k))\}^T \{\widetilde{\underline{\Gamma}}(U(p_k))\} \right)
$$

$$
= \lambda_{max} \sum_{k=1}^{N_s} A_k \left(\widetilde{\underline{\Gamma}}(W(p_k)) \cdot \widetilde{\underline{\Gamma}}(U(p_k)) \right)
$$

$$
= \lambda_{max} < \widetilde{\underline{\Gamma}}(W), \widetilde{\underline{\Gamma}}(U) >_{\mathcal{L}^2}
$$

Considering the Schwarz inequality of the inner product it follows that

$$
\widetilde{A}(W,U) \leq \lambda_{max} \left\| \widetilde{\underline{\Gamma}}(W) \right\|_{\mathcal{L}^2} \left\| \widetilde{\underline{\Gamma}}(U) \right\|_{\mathcal{L}^2} = \lambda_{max} |W|_{\mathcal{G}^*} |U|_{\mathcal{G}^*}
$$

The proof of Eq. (4.119) follows directly by proposition 4.3, and by assuming $c_3 = \lambda_{max}$.   □

4.4.3.2   Voigt notation and discretization

The Voigt notation for the weakened-weak form of Eq. (4.111) is introduced as done for the case of the standar weak form (Section 3.4.2), focusing on a plane-stress case. The smoothed strain and microcurvature tensors can be represented in terms of the following arrays

$$
\{\widetilde{\underline{\gamma}}(U(p_k))\} = \left(\widetilde{\gamma}_{xx}(U(p_k)) \quad \widetilde{\gamma}_{xy}(U(p_k)) \quad \widetilde{\gamma}_{yx}(U(p_k)) \quad \widetilde{\gamma}_{yy}(U(p_k)) \right)^T \tag{4.120}
$$

$$
\{\widetilde{\underline{\kappa}}(U(p_k))\} = \left(\widetilde{\kappa}_{xz}(U(p_k))L_b \quad \widetilde{\kappa}_{yz}(U(p_k))L_b \right)^T \tag{4.121}
$$

which expressions in terms of the field variables is

$$
\{\widetilde{\underline{\gamma}}(U(p_k))\} = \frac{1}{A_k} \int_{\partial \mathbf{D}_k^S} [\widetilde{L}_{nA}(\xi)]\{\bar{u}(\xi)\} \, \mathrm{d}\mathcal{S} - [\mathrm{e}]\{\bar{\varphi}(p_k)\} \tag{4.122}
$$

$$
\{\widetilde{\underline{\kappa}}^*(U(p_k))\} = \frac{1}{A_k} \int_{\partial \mathbf{D}_k^S} [\widetilde{L}_{nC}^*(\xi)]\{\bar{\varphi}(\xi)\} \, \mathrm{d}\mathcal{S} \tag{4.123}
$$

where the operators containing the normal vector are expressed, in a plane-stress state, as

$$
[\widetilde{L}_{nA}] := \begin{pmatrix} n_x^{(k)} & 0 \\ 0 & n_x^{(k)} \\ n_y^{(k)} & 0 \\ 0 & n_y^{(k)} \end{pmatrix}, \quad [\widetilde{L}_{nC}^*] := \begin{pmatrix} L_b n_x^{(k)} \\ L_b n_y^{(k)} \end{pmatrix} \tag{4.124}
$$

This results in the following Voigt representation of the smoothed bilinear form

$$\widetilde{A}(W,U) = \sum_{k=1}^{N_s} A_k \left(\{\underline{\widetilde{\gamma}}(W(p_k))\}^T [\hat{\mathbf{A}}] \{\underline{\widetilde{\gamma}}(U(p_k))\} \right)$$

$$+ \sum_{k=1}^{N_s} A_k \left(\{\underline{\widetilde{\kappa}}^*(W(p_k))\}^T [\hat{\mathbf{C}}^*] \{\underline{\widetilde{\kappa}}^*(U(p_k))\} \right) \tag{4.125}$$

$$= \sum_{k=1}^{N_s} A_k \left(\{\underline{\widetilde{\Gamma}}(W(p_k))\}^T [\hat{\mathcal{E}}] \{\underline{\widetilde{\Gamma}}(U(p_k))\} \right) \tag{4.126}$$

The trial (and the test) functions belonging to the G-space $\mathcal{G}_h^*(\mathbf{D})$ can be expressed in terms of PIM or RPIM shape functions $\phi_i(p)$ and nodal parameters d_i as

$$\{U(p)\} = \sum_{i \in S_d} [\phi_i(p)]\{d_i\} = \sum_{i \in S_d} \begin{pmatrix} [\phi_{Ai}(p)] & [0] \\ [0] & [\phi_{Ci}(p)] \end{pmatrix} \begin{pmatrix} \{d_{Ai}\} \\ \{d_{Ci}\} \end{pmatrix} \tag{4.127}$$

where S_d is the support domain at the point p, $[\phi_i(p)]$ is the shape functions matrix, and $\{d_i\}$ the array collecting the nodal parameters at the node i. As before, the subscripts A and C are used to distinguish between Cauchy-like and Cosserat-like terms

$$\{\bar{u}(p)\} = \sum_{i \in S_d} [\phi_{Ai}(p)]\{d_{Ai}\}, \qquad \{\bar{\varphi}(p)\} = \sum_{i \in S_d} [\phi_{Ci}(p)]\{d_{Ci}\} \tag{4.128}$$

Introducing these expressions into Eqs. (4.122) and (4.123) results in

$$\{\underline{\widetilde{\gamma}}(U(p_k))\} = \sum_{i \in S_d} [\widetilde{B}_{AAi}]\{d_{Ai}\} + \sum_{i \in S_d} [\widetilde{B}_{ACi}]\{d_{Ci}\} \tag{4.129}$$

$$\{\underline{\widetilde{\kappa}}^*(U(p_k))\} = \sum_{i \in S_d} [\widetilde{B}_{CCi}]\{d_{Ci}\} \tag{4.130}$$

where the following operators, containing the smoothed derivatives of the shape functions defined in Eq. (4.56), have been introduced[19]

$$[\widetilde{B}_{AAi}(p_k)] := \frac{1}{A_k} \int_{\partial \mathbf{D}_k^S} [\widetilde{L}_{nA}(\xi)][\phi_{Ai}(\xi)] \, \mathrm{d}\mathcal{S} \tag{4.131}$$

$$[\widetilde{B}_{ACi}(p_k)] := -[\mathbf{e}][\phi_{Ci}(p_k)] \tag{4.132}$$

$$[\widetilde{B}_{CCi}(p_k)] := \frac{1}{A_k} \int_{\partial \mathbf{D}_k^S} [\widetilde{L}_{nC}(\xi)][\phi_{Ci}(\xi)] \, \mathrm{d}\mathcal{S} \tag{4.133}$$

When the compact representation is accounted for, the generalized deformation tensor $\underline{\widetilde{\Gamma}}$

---

[19] Due to the assumption of Eq. (4.87), no smoothing operation is applied to the microrotation vector appearing in the smoothed strain tensor.

can be expressed as

$$\{\underline{\widetilde{\Gamma}}(U(p_k))\} = \sum_{i \in S_d} [\widetilde{B}_i(p_k)]\{d_i\} = \sum_{i \in S_d} \begin{pmatrix} [\widetilde{B}_{AAi}(p_k)] & [\widetilde{B}_{ACi}(p_k)] \\ [0] & [\widetilde{B}_{CCi}(p_k)] \end{pmatrix} \begin{pmatrix} \{d_{Ai}\} \\ \{d_{Ci}\} \end{pmatrix} \quad (4.134)$$

The representation in terms of shape functions and nodal parameters results in an algebraic system like the one expressed in Eq. (3.177), where the stiffness matrix $[K]$ can be evaluated through the contribution of each *smoothing domain*

$$[K(p_k)]_{Sd} = A_k [\widetilde{B}(p_k)]^T [\hat{\mathcal{E}}(p_k)][\widetilde{B}(p)] \quad (4.135)$$

where as in the FEM, the matrix $[\widetilde{B}(p_k)]$ is composed by the submatrices $[\widetilde{B}_i(p_k)]$ as $[\widetilde{B}(p_k)] = \left([\widetilde{B}_1(p_k)] \ldots [\widetilde{B}_i(p_k)] \ldots [\widetilde{B}_N(p_k)]\right)$, where N is the number of nodes in the support domain S_d at the point p_k.

4.4.3.3 Linearization of the micropolar weakened-weak form

The linearization procedure is analogous to the one discussed in Section 3.4.1 for the micropolar standard weak form and in Section 4.3.1 for the weakened-weak form in classic media; the details of the derivation will be skipped, since they are the same that can be found in the mentioned sections.

Definition 4.10 (Micropolar linearized weakened-weak form)**.** The *linearized weakened-weak form* of the micropolar boundary value problem defined in Section 3.2 consists into: find the increment $\delta U \equiv (\delta \bar{u}, \delta \bar{\varphi}) \in \delta \mathcal{V}_h(\mathbf{D})$ such that

$$DG(W, U) \cdot \delta U = -G(W, U), \quad \forall W \in \mathcal{V}_h^0(\mathbf{D}) \quad (4.136)$$

where $\delta \mathcal{V}_h(\mathbf{D})$ and $\mathcal{V}_h^0(\mathbf{D})$ are, respectively, the spaces of *admissible variations* and *test functions*, defined as

$$\mathcal{V}_h(\mathbf{D}) := \left\{ \delta U \equiv (\delta \bar{u}, \delta \bar{\varphi}) \in \mathcal{G}_h^*(\mathbf{D}) \mid \delta \bar{u} = \bar{0} \text{ at } \partial \mathbf{D}_e^u, \delta \bar{\varphi} = \bar{0} \text{ at } \partial \mathbf{D}_e^\varphi \right\} \quad (4.137)$$

$$\mathcal{V}_h^0(\mathbf{D}) := \left\{ W \equiv (\bar{w}, \bar{\omega}) \in \mathcal{G}_h^*(\mathbf{D}) \mid \bar{w} = \bar{0} \text{ at } \partial \mathbf{D}_e^u, \bar{\omega} = \bar{0} \text{ at } \partial \mathbf{D}_e^\varphi \right\} \quad (4.138)$$

where $\mathcal{G}_h^*(\mathbf{D})$ is the G-space for micropolar field variables introduced in Section 4.4.2.

Proposition 4.11. In case of elastic-degrading constitutive models in a geometrically linear context, the directional derivative of Eq. (4.136) is expressed by

$$\begin{aligned} DG(\bar{w}, \bar{u}) \cdot \delta \bar{u} &= \sum_{k=1}^{N_S} A_k \left(\underline{\widetilde{\Gamma}}(\bar{w}(p_k)) \cdot \left(\hat{\mathcal{E}}^t(p_k) \cdot \delta \underline{\widetilde{\Gamma}}(\bar{u}(p_k)) \right) \right) \\ &= \sum_{k=1}^{N_S} A_k \left(\underline{\widetilde{\Gamma}}(\bar{w}(p_k)) \cdot \left(\hat{\mathcal{E}}^t(p_k) \cdot \dot{\underline{\widetilde{\Gamma}}}(\bar{u}(p_k)) \right) \right) \end{aligned} \quad (4.139)$$

where, in an analogous way as pointed out in Section 3.4.1.1, $\dot{\tilde{\underline{\Gamma}}} \equiv \delta\tilde{\underline{\Gamma}}$ is the *rate* of the smoothed generalized strain tensor, and $\hat{\mathcal{E}}^t$ is the generalized tangent constitutive operator.

Proof. *This proof follows the same procedure adopted in proposition 4.1. Observing that in a geometrically linear context the linear functional $f(W)$ doesn't depend on U, the directional derivative of $G(W,U)$ reduces to the directional derivative of the bilinear form*

$$DG(W,U) \cdot \delta U = \left.\frac{\partial \tilde{A}(W,U_\varepsilon)}{\partial \varepsilon}\right|_{\varepsilon=0}$$

From Eq. (4.113) the bilinear form can be expressed as

$$\tilde{A}(W,U) = \sum_{k=1}^{N_S} A_k \left(\tilde{\underline{\Gamma}}(W(p_k)) \cdot \tilde{\underline{\Sigma}}(U_\varepsilon(p_k)) \right)$$

where the smoothed generalized stress tensor $\tilde{\underline{\Sigma}}(U_\varepsilon(p_k)) = \hat{\mathcal{E}}^S(\tilde{\underline{\Gamma}}(U_\varepsilon(p_k)) \cdot \tilde{\underline{\Gamma}}(U_\varepsilon(p_k))$ has been introduced, resulting in

$$DG(W,U) \cdot \delta U = \sum_{k=1}^{N_S} A_k \left(\tilde{\underline{\Gamma}}(W(p_k)) \cdot \left.\frac{\partial \tilde{\underline{\Sigma}}(U_\varepsilon(p_k))}{\partial \varepsilon}\right|_{\varepsilon=0} \right)$$

The directional derivative of the smoothed generalized stress tensor can be expressed as

$$\begin{aligned}
\delta\tilde{\underline{\Sigma}}(U(p_k)) :&= \left.\frac{\partial \tilde{\underline{\Sigma}}(U_\varepsilon(p_k))}{\partial \varepsilon}\right|_{\varepsilon=0} \\
&= \frac{\partial}{\partial \varepsilon}\left(\hat{\mathcal{E}}^S(\tilde{\underline{\Gamma}}(U_\varepsilon(p_k)) \cdot \tilde{\underline{\Gamma}}(U_\varepsilon(p_k))) \right)\Big|_{\varepsilon=0} \\
&= \hat{\mathcal{E}}^S(\tilde{\underline{\Gamma}}(U(p_k)) \cdot \left.\frac{\partial \tilde{\underline{\Gamma}}(U_\varepsilon(p_k))}{\partial \varepsilon}\right|_{\varepsilon=0} + \left.\frac{\partial \hat{\mathcal{E}}^S(\tilde{\underline{\Gamma}}(U_\varepsilon(p_k))}{\partial \varepsilon}\right|_{\varepsilon=0} \cdot \tilde{\underline{\Gamma}}(U(p_k)) \\
&= \hat{\mathcal{E}}^S(\tilde{\underline{\Gamma}}(U(p_k)) \cdot \delta\tilde{\underline{\Gamma}}(U(p_k)) + \delta\hat{\mathcal{E}}^S(\tilde{\underline{\Gamma}}(U(p_k)) \cdot \tilde{\underline{\Gamma}}(U(p_k))
\end{aligned}$$

The directional derivatives of the smoothed generalized stress and deformation tensors and of the generalized secant constitutive operator can be identified with their rates

$$\delta\tilde{\underline{\Sigma}} \equiv \dot{\tilde{\underline{\Sigma}}}, \quad \delta\tilde{\underline{\Gamma}} \equiv \dot{\tilde{\underline{\Gamma}}}, \quad \delta\hat{\mathcal{E}}^S \equiv \dot{\hat{\mathcal{E}}}^S$$

hence, the expression of $\delta\tilde{\underline{\Sigma}}(U(p_k))$ is the same as the one of Eq. (2.10) ($\dot{\underline{\Sigma}} = \hat{\mathcal{E}}^S \cdot \dot{\underline{\Gamma}} + \dot{\hat{\mathcal{E}}}^S \cdot \underline{\Gamma}$), except for the presence of the smoothed terms. Taking into account the discussions in Section 3.4.1.1, the directional derivative of the smoothed stress can be expressed in terms of the smoothed tangent constitutive operator $\widetilde{\hat{\mathcal{E}}}^t(p_k) \equiv \hat{\mathcal{E}}^t(\tilde{\underline{\Gamma}}(U(p_k))$, constant over each smoothing domain, as

$$\delta\tilde{\underline{\Sigma}}(U(p_k)) = \hat{\mathcal{E}}^t(\tilde{\underline{\Gamma}}(U(p_k)) \cdot \delta\tilde{\underline{\Gamma}}(U(p_k)) \equiv \hat{\mathcal{E}}^t(\tilde{\underline{\Gamma}}(U(p_k)) \cdot \dot{\tilde{\underline{\Gamma}}}(U(p_k)) = \dot{\underline{\Sigma}}(U(p_k))$$

leading to the expressions in Eq. (4.139).   □

The right hand side of Eq. (4.136) is known, since it depends on the displacement field

U of a known equilibrium configuration, and is expressed as

$$G(W, U) = \widetilde{A}(W, U) - f(W)$$
$$= \sum_{k=1}^{N_S} A_k \left(\widetilde{\underline{\Gamma}}(W(p_k)) \cdot \widetilde{\underline{\Sigma}}(U_\varepsilon(p_k)) \right) - f(W) \tag{4.140}$$

Introducing PIM or RPIM approximation functions into Eq. (4.136), for both the test functions $W(p)$ and the increments $\delta U(p)$

$$\{W(p)\} = \sum_{i \in S_d} [\phi_i(p)]\{d_i^W\}, \quad \{\delta U(p)\} = \sum_{i \in S_d} [\phi_i(p)]\{\delta d_i\} \tag{4.141}$$

and taking into account proposition 4.11, the following algebraic system can be obtained

$$[K^t]\{\Delta X\} = \{N\} \tag{4.142}$$

where $[K^t]$ is the global *tangent* stiffness matrix of the system, $\{\Delta X\}$ the nodal parameters vector collecting all the nodal parameters $\{\delta d_i\}$, and $\{N\}$ an array containing the discretization of the right hand side of Eq. (4.70); the solution procedure for this system is the same recalled in Remark 4.8 for the weakened-weak formulation in classic media.

Chapter 5

Discontinuous failure in micropolar elastic-degrading media

The present chapter illustrates the phenomenon of discontinuous failure (or localization) in elastic-degrading micropolar media. The concept of acceleration waves propagation is applied to the elastic-degrading micropolar models proposed by the author, extending to these models the classic Maxwell compatibility condition and Fresnel-Hadamard propagation condition. A proper localization indicator is derived, and used to evaluate the effects of the micropolar additional material parameters on the onset of localization, through analytical investigations.

5.1 A preface

Section 2.3 provided a survey on the existent contributions on the topic of localization analysis in elasto-plastic and elastic-degrading classic and micropolar media. It pointed out that while the literature on localization in classic media is vast, with contributions on concepts like acceleration waves propagation, failure indicators for continuous (loss of material stability and loss of uniqueness) and discontinuous failure (loss of ellipticity and loss of strong ellipticity), and eigenvalue analysis of constitutive operators and acoustic tensors, the contributions regarding the micropolar theory are more limited. As discussed in Section 2.3, the main contributions to this topic identified by the author consist in:

- the numerical investigations on regularization effects in micropolar elasto-plasticity by de Borst (1991), de Borst and Sluys (1991) and Sluys (1992);
- the extension to micropolar elasto-plasticity of the classic *Maxwell compatibility condition* by Dietsche et al. (1993) and Iordache and Willam (1998), together with analytical and numerical analyses on the regularization effects of the additional material parameters;
- the extension of the classic *Fresnel-Hadamard propagation condition* to visco-elastic

107

micropolar media by Grioli (1980) and to geometrically exact elastic micropolar media by Eremeyev (2005);

- the evaluation of the effects of the Cosserat's shear modulus on localization with numerical investigations based on an extension of the *Maxwell compatibility condition* for micropolar media with scalar damage[1] by Xotta et al. (2016).

Taking into account these contributions the author, in a previous paper (Gori et al., 2017*b*), proposed an extension of the discontinuous failure concepts to elastic-degrading micropolar media, using as a basis the general formulation proposed in Gori et al. (2017*c*). Following a path analogous to the one of Grioli (1980) and Eremeyev (2005), the author investigated the problem of acceleration waves propagation within the elastic-degrading formulation of Gori et al. (2017*c*), deriving a proper extension of the classic *Maxwell compatibility condition* and *Fresnel-Hadamard propagation condition*, using these conditions as a basis for subsequent localization analyses. The main advantage of this approach consisted in the fact that since the different concepts were derived for the general expressions of the unified formulation for elastic-degrading micropolar media, they can be directly extended to all the peculiar models that can be derived within the aforementioned formulation. In the paper, specific attention was paid on an extension of the classic *weak* (or kinematically compatible) localization condition, relying on the analysis of a *generalized* acoustic tensor. Using this condition, a peculiar *localization indicator* was introduced as a quantity that allows to evaluate the onset of a *bifurcation* in a boundary value problem. Specific investigations were also proposed in order to investigates the effects of the additional material parameters, considering the peculiar case of an *associated scalar-isotropic damage model* in a *plane-stress state*. The theoretical content of the paper (Gori et al., 2017*b*), as well as its analytical investigations, are discussed in the present chapter, while the numerical simulations are collected in Chapter 6.

5.2 Acceleration waves in elastic-degrading micropolar media

A wave, in the sense of Hadamard (Hadamard, 1903), is an isolated, smooth and orientable geometric surface $\mathcal{S}(p,t)$ (the *wavefront*) parametrized by the time t, with $p \in \mathbf{D}$, not necessarily plane, that moves relatively to the material, and across which certain field variables are momentarily discontinuous (Hill, 1962). The wave propagates with velocity c in the normal direction $\bar{n}$. The unitary vectors $\bar{p}_A$ and $\bar{p}_C$ indicates the *directions of polarization*, i.e., the directions defining the motion of the material points on the surface in terms of displacement and microrotation, respectively. The body is divided into two parts

---

[1]In this case the authors applied the scalar damage only to the Cauchy-like part of the constitutive operator, without affecting the couple-stresses. Hence, only the effect of the Cosserat's shear modulus was evaluated.

by the wavefront; the symbols a^+ and a^- indicate the values of a certain field variable a at each one of the opposite sides of the wavefront, while the symbol $[\![a]\!] := a^+ - a^-$ indicates the *jump* of the same variable across the wavefront.

An *acceleration wave* in a micropolar medium is characterized by a second-order discontinuity in the displacement field $\bar{u}$ and in the microrotation field $\bar{\varphi}$ (Eremeyev, 2005). It is emphasized that, in general, in an elastic context, second-order discontinuities in the displacement and microrotation fields are transported by different waves (with different propagation velocities); a single wave transporting both the discontinuities is a peculiar case (Grioli, 1980). The acceleration fields $\ddot{\bar{u}}$ and $\ddot{\bar{\varphi}}$ and the gradients of the velocity fields $\dot{\bar{u}}$ and $\dot{\bar{\varphi}}$ are then discontinuous, while the displacement, microrotation, and velocities fields themselves remain continuous across the wavefront (see, e.g., Grioli (1980) and Eremeyev (2005))

$$[\![\bar{u}]\!] = 0, \quad [\![\dot{\bar{u}}]\!] = 0, \quad [\![\ddot{\bar{u}}]\!] \neq 0, \quad [\![\mathrm{grad}(\dot{\bar{u}})]\!] \neq 0 \tag{5.1}$$

$$[\![\bar{\varphi}]\!] = 0, \quad [\![\dot{\bar{\varphi}}]\!] = 0, \quad [\![\ddot{\bar{\varphi}}]\!] \neq 0, \quad [\![\mathrm{grad}(\dot{\bar{\varphi}})]\!] \neq 0 \tag{5.2}$$

From the previous conditions it can be easily shown that also the strain and microcurvature rate tensors $\dot{\underline{\gamma}}$ and $\dot{\underline{\kappa}}$, as well as the stress and couple-stress rate tensors $\dot{\underline{\sigma}}$ and $\dot{\underline{\mu}}$, are discontinuous across the wavefront.

In this context, the localization analysis consists in to verify the existence of acceleration waves with the aforementioned characteristics; as it will be shown in the following, localization arises when the conditions for the propagation of such waves are violated, i.e., when an acceleration wave become *stationary*.

5.2.1   Maxwell compatibility condition

An analogous version of the *Maxwell compatibility condition* for classic media (Rizzi, 1995), i.e., a condition for the jumps in the gradients appearing in Eqs. (5.1) and (5.2), is now derived for a micropolar medium (see, e.g., Dietsche et al. (1993) for the elasto-plastic case). First, it is observed that the continuity conditions $[\![\dot{\bar{u}}]\!] = 0$ and $[\![\dot{\bar{\varphi}}]\!] = 0$ impose a restriction on the derivatives of the fields $\dot{\bar{u}}$ and $\dot{\bar{\varphi}}$: in the directions $\bar{\tau} \perp \bar{n}$ the derivatives must vanish ($[\![\mathrm{grad}(\dot{\bar{u}})]\!] \cdot \bar{\tau} = 0$ and $[\![\mathrm{grad}(\dot{\bar{\varphi}})]\!] \cdot \bar{\tau} = 0$), while the same doesn't apply to the derivatives along $\bar{n}$. Hence, the jumps in the velocities gradients exhibit a component only in the normal direction

$$[\![\mathrm{grad}(\dot{\bar{u}})]\!] = \bar{g}_A \otimes \bar{n}, \qquad [\![\mathrm{grad}(\dot{\bar{\varphi}})]\!] = \bar{g}_C \otimes \bar{n} \tag{5.3}$$

Like for classic media (see, e.g., Jirásek (2007a)), the vectors $\bar{g}_A := [\![\mathrm{grad}(\dot{\bar{u}})]\!] \cdot \bar{n}$ and $\bar{g}_A := [\![\mathrm{grad}(\dot{\bar{u}})]\!] \cdot \bar{n}$, can be rewritten in the form

$$\bar{g}_A = \dot{\gamma}_A \, \bar{p}_A, \qquad \bar{g}_C = \dot{\gamma}_C \, \bar{p}_C \tag{5.4}$$

where $\dot{\gamma}_A := \|\bar{g}_A\|$ and $\dot{\gamma}_C := \|\bar{g}_C\|$ represents the magnitude of the jumps, while the unitary vectors $\bar{p}_A := \bar{g}_A/\|\bar{g}_A\|$ and $\bar{p}_C := \bar{g}_C/\|\bar{g}_C\|$ are the previously mentioned *polarization vectors*. The *Maxwell compatibility condition* for the micropolar medium is then expressed by

$$[\![\mathrm{grad}(\dot{\bar{u}})]\!] = \dot{\gamma}_A \, \bar{p}_A \otimes \bar{n}, \qquad [\![\mathrm{grad}(\dot{\bar{\varphi}})]\!] = \dot{\gamma}_C \, \bar{p}_C \otimes \bar{n} \tag{5.5}$$

resulting in the following jumps of the strain and microcurvature rate tensors

$$[\![\dot{\underline{\gamma}}]\!] = \bar{n} \otimes \bar{g}_A, \qquad [\![\dot{\underline{\kappa}}]\!] = \bar{n} \otimes \bar{g}_C \tag{5.6}$$

The previous quantities can be recast in terms of acceleration jumps $[\![\ddot{\bar{u}}]\!]$ and $[\![\ddot{\bar{\varphi}}]\!]$, and normal velocity c as follows. Considering an infinitesimal time interval dt, the differentials of the velocity fields can be expressed as $d\dot{\bar{u}} = \mathrm{grad}(\dot{\bar{u}}) \cdot d\bar{x} + \ddot{\bar{u}} \, dt$ and $d\dot{\bar{\varphi}} = \mathrm{grad}(\dot{\bar{\varphi}}) \cdot d\bar{x} + \ddot{\bar{\varphi}} \, dt$, where $d\bar{x} = c \, dt \, \bar{n}$ indicates the change of position of a point $p \in \mathbf{D}$ on the wavefront in the time interval dt. The continuity conditions $[\![\dot{\bar{u}}(p + d\bar{x}, t + dt)]\!] \simeq [\![\dot{\bar{u}}(p,t) + d\dot{\bar{u}}]\!] = 0$ and $[\![\dot{\bar{\varphi}}(p + d\bar{x}, t + dt)]\!] \simeq [\![\dot{\bar{\varphi}}(p,t) + d\dot{\bar{u}}]\!] = 0$, together with Eqs. (5.1) and (5.2), imply that $[\![d\dot{\bar{u}}]\!] = 0$ and $[\![d\dot{\bar{\varphi}}]\!] = 0$; hence

$$c[\![\mathrm{grad}(\dot{\bar{u}})]\!] \cdot \bar{n} + [\![\ddot{\bar{u}}]\!] = 0, \quad \bar{g}_A = -\frac{[\![\ddot{\bar{u}}]\!]}{c}, \quad \dot{\gamma}_A = -\frac{[\![\ddot{u}]\!]}{c}, \quad [\![\ddot{u}]\!] := \|[\![\ddot{\bar{u}}]\!]\| \tag{5.7}$$

$$c[\![\mathrm{grad}(\dot{\bar{\varphi}})]\!] \cdot \bar{n} + [\![\ddot{\bar{\varphi}}]\!] = 0, \quad \bar{g}_C = -\frac{[\![\ddot{\bar{\varphi}}]\!]}{c}, \quad \dot{\gamma}_C = -\frac{[\![\ddot{\varphi}]\!]}{c}, \quad [\![\ddot{\varphi}]\!] := \|[\![\ddot{\bar{\varphi}}]\!]\| \tag{5.8}$$

In Eremeyev (2005) the vectors $\bar{g}_A$ and $\bar{g}_C$ are referred to as *vector amplitudes for the jumps of linear and angular accelerations*; together with the normal velocity c, they allow to express the jumps in the accelerations as $[\![\ddot{\bar{u}}]\!] = -c \, \bar{g}_A$ and $[\![\ddot{\bar{\varphi}}]\!] = -c \, \bar{g}_C$.

5.2.2   Fresnel-Hadamard propagation condition

In an acceleration wave, the gradients of both the displacement and microrotation fields are assumed to be continuous[2] across the discontinuity surface, i.e., $[\![\mathrm{grad}(\bar{u})]\!] = 0$ and $[\![\mathrm{grad}(\bar{\varphi})]\!] = 0$ (Eqs. (5.1) and (5.2)). Hence, from Eqs. (3.1) and (3.2), it can be easily shown that the jumps in the strain and microcurvature tensors also vanish, $[\![\underline{\gamma}]\!] = 0$ and $[\![\underline{\kappa}]\!] = 0$. Since the secant constitutive operators depend on the state of deformation but not on its rate, it follows that they are continuous across the discontinuity surface and

---

[2] The acceleration waves theory considers discontinuities in the sole second-order terms. The gradient is a first-order term.

that also the stress and couple-stress tensor are continuous

$$[\![\underline{\sigma}]\!] = [\![\hat{\mathbf{A}}^S \cdot \underline{\gamma}]\!] = \hat{\mathbf{A}}^S \cdot [\![\underline{\gamma}]\!] = 0, \quad [\![\underline{\mu}]\!] = [\![\hat{\mathbf{C}}^S \cdot \underline{\kappa}]\!] = \hat{\mathbf{C}}^S \cdot [\![\underline{\kappa}]\!] = 0 \tag{5.9}$$

As discussed by Rice (1976), Bigoni (2014), since the conditions $[\![\underline{\sigma}]\!] = 0$ and $[\![\underline{\mu}]\!] = 0$ hold, the Maxwell compatibility condition can be applied in a straightforward manner to the vectors $\underline{\sigma} \cdot \bar{v}$ and $\underline{\mu} \cdot \bar{v}$, where $\bar{v}$ is an arbitrary constant vector, leading to (Appendix B.1)

$$[\![\mathrm{grad}(\underline{\sigma} \cdot \bar{v})]\!] = -\frac{1}{c}\left([\![\dot{\underline{\sigma}}]\!] \cdot \bar{v}\right) \otimes \bar{n}, \quad [\![\mathrm{grad}(\underline{\mu} \cdot \bar{v})]\!] = -\frac{1}{c}\left([\![\dot{\underline{\mu}}]\!] \cdot \bar{v}\right) \otimes \bar{n} \tag{5.10}$$

Taking the trace of both equations leads to (Appendix B.1)

$$[\![\mathrm{div}^{\mathrm{T}}(\underline{\sigma})]\!] = -\frac{1}{c}\,\bar{n} \cdot [\![\dot{\underline{\sigma}}]\!], \quad [\![\mathrm{div}^{\mathrm{T}}(\underline{\mu})]\!] = -\frac{1}{c}\,\bar{n} \cdot [\![\dot{\underline{\mu}}]\!] \tag{5.11}$$

From Eqs. (3.3) and (3.4), the jump of the local equilibrium equations can be expressed as $[\![\mathrm{div}^{\mathrm{T}}(\underline{\sigma})]\!] = \rho\,[\![\ddot{\bar{u}}]\!]$ and $[\![\mathrm{div}^{\mathrm{T}}(\underline{\mu})]\!] = \rho\theta\,[\![\ddot{\bar{\varphi}}]\!]$. Replacing the divergence of the stress and couple-stress tensors, and the expressions of $[\![\ddot{\bar{u}}]\!]$ and $[\![\ddot{\bar{\varphi}}]\!]$ in terms of the vectors $\bar{g}_A$ and $\bar{g}_C$, leads to the following generalization of the *Fresnel-Hadamard propagation condition*

$$\bar{n} \cdot [\![\dot{\underline{\sigma}}]\!] = \rho c^2\,\bar{g}_A, \qquad \bar{n} \cdot [\![\dot{\underline{\mu}}]\!] = \rho\theta c^2\,\bar{g}_C \tag{5.12}$$

defining the conditions for propagation of acceleration waves in a micropolar elastic-degrading medium.

5.2.3   Elastic waves

A wave is elastic when the material at both sides of the discontinuity surface is undamaged (i.e., $\hat{\mathbf{A}}^S = \hat{\mathbf{A}}$ and $\hat{\mathbf{C}}^S = \hat{\mathbf{C}}$). Taking into account that in this case $[\![\dot{\underline{\sigma}}]\!] = \hat{\mathbf{A}} \cdot [\![\dot{\underline{\gamma}}]\!]$ and $[\![\dot{\underline{\mu}}]\!] = \hat{\mathbf{C}} \cdot [\![\dot{\underline{\kappa}}]\!]$ (with $[\![\dot{\underline{\gamma}}]\!]$ and $[\![\dot{\underline{\kappa}}]\!]$ defined as in Eq. (5.6)), the Fresnel-Hadamard propagation condition (Eq. (5.12)) results in

$$\underline{Q}_{AA} \cdot \bar{g}_A = \rho c^2\,\bar{g}_A, \qquad \underline{Q}_{CC} \cdot \bar{g}_C = \rho\theta c^2\,\bar{g}_C \tag{5.13}$$

where

$$\underline{Q}_{AA} := (n_k A_{ki\ell j} n_\ell)\,\bar{e}_i \otimes \bar{e}_j, \quad \underline{Q}_{CC} := (n_k C_{ki\ell j} n_\ell)\,\bar{e}_i \otimes \bar{e}_j \tag{5.14}$$

are the *initial acoustic tensors*. The expressions in Eq. (5.13) can be recast in the following compact form

$$\underline{Q} \cdot \bar{g} = \rho c^2 \underline{V} \cdot \bar{g} \quad \rightarrow \quad \tilde{\underline{Q}} \cdot \bar{g} = \rho c^2\,\bar{g} \tag{5.15}$$

where the *generalized initial acoustic tensor* $\tilde{Q}$ is defined, together with $\bar{g}$ and $\underline{V}$, as

$$\tilde{Q} := \left(\underline{V}^{-1}\underline{Q}\right) = \begin{pmatrix} Q_{AA} & \underline{0} \\ \underline{0} & \underline{Q}_{CC}/\theta \end{pmatrix}, \qquad \bar{g} := \begin{pmatrix} \bar{g}_A \\ \bar{g}_C \end{pmatrix}, \qquad \underline{V} := \begin{pmatrix} \underline{id} & \underline{0} \\ \underline{0} & \theta\,\underline{id} \end{pmatrix} \qquad (5.16)$$

As discussed by Eremeyev (2005), the expressions in Eq. (5.13) represent a generalized version of the *Fresnel-Hadamard propagation condition* for micropolar elastic media, defining the conditions for propagation of elastic acceleration waves. Considering an initially isotropic material, both the initial acoustic tensors can be expressed as a *rank-one modification* of the identity tensor as

$$\underline{Q}_{AA} = A_2\,\underline{id} + (A_1 + A_3)\,\bar{n} \otimes \bar{n}, \qquad \underline{Q}_{CC} = C_2\,\underline{id} + (C_1 + C_3)\,\bar{n} \otimes \bar{n} \qquad (5.17)$$

The problem of elastic acceleration waves in micropolar media has been investigated by Grioli (1980), Eremeyev (2005); since some of these results are useful for the following analysis of damaging waves, they are briefly resumed in Appendix B.2.

5.2.4   Damaging waves

In a *damaging wave* both the sides of the discontinuity surface are in a damaged state[3] [4]. Recalling the general rate equations of a micropolar elastic-degrading medium expressed in Eqs. (3.84) and (3.85), the jump in the stress and couple-stress rates can be rewritten as

$$[\![\dot{\sigma}]\!] = \left(\hat{\mathbf{A}}^S - \frac{1}{z}\underline{x}_A \otimes \underline{y}_A\right) \cdot [\![\dot{\gamma}]\!] - \frac{1}{z}\left(\underline{x}_A \otimes \underline{y}_C\right) \cdot [\![\dot{\kappa}]\!] \qquad (5.18)$$

$$[\![\dot{\mu}]\!] = \left(\hat{\mathbf{C}}^S - \frac{1}{z}\underline{x}_C \otimes \underline{y}_C\right) \cdot [\![\dot{\kappa}]\!] - \frac{1}{z}\left(\underline{x}_C \otimes \underline{y}_A\right) \cdot [\![\dot{\gamma}]\!] \qquad (5.19)$$

---

[3] A more complex condition could be represented by a mixed damaged-undamaged state for the two constitutive relations, that is, for example, a damage state for the stress-strain relation and an elastic state for the couple-stress-microcurvature one. However, due to the assumption of a single loading function for the representation of the elastic domain, this condition is excluded, since both the constitutive relations enter in a damage state at the same time.

[4] In this work, the same degradation evolution is assumed at both the sides of the discontinuity surface, that is, the cases of *loading waves* and *unloading waves* (i.e., when one side of the discontinuity surface is in a damaged state while the other is still elastic) are not considered here. In classic media, such a choice is justified by the fact that a discontinuous bifurcation always verifies for the former condition before the latter one, as shown in Rice and Rudnicki (1980), Borré and Maier (1989) and Ottosen and Runesson (1991a) for the elasto-plastic case, and in Jirásek (2007a) for scalar damage. However, it is remarked that analogous results are not currently available for micropolar media, and should be object of further investigations.

Replacing these rates into Eq. (5.12) results in the propagation conditions

$$\bar{n} \cdot \left[\left(\hat{\mathbf{A}}^S - \frac{1}{z} \left(\underline{x}_A \otimes \underline{y}_A \right) \right) \cdot (\bar{n} \otimes \bar{g}_A) - \frac{1}{z} \left(\underline{x}_A \otimes \underline{y}_C \right) \cdot (\bar{n} \otimes \bar{g}_C) \right] = \rho c^2 \bar{g}_A \qquad (5.20)$$

$$\bar{n} \cdot \left[\left(\hat{\mathbf{C}}^S - \frac{1}{z} \left(\underline{x}_C \otimes \underline{y}_C \right) \right) \cdot (\bar{n} \otimes \bar{g}_C) - \frac{1}{z} \left(\underline{x}_C \otimes \underline{y}_A \right) \cdot (\bar{n} \otimes \bar{g}_A) \right] = \rho \theta c^2 \bar{g}_C \qquad (5.21)$$

Introducing the *tangent acoustic tensors*

$$\underline{Q}^t_{AA} := \underline{Q}^S_{AA} - \frac{1}{z} \, \bar{b}_A \otimes \bar{a}_A, \qquad \underline{Q}^t_{AC} := -\frac{1}{z} \, \bar{b}_A \otimes \bar{a}_C \qquad (5.22)$$

$$\underline{Q}^t_{CC} := \underline{Q}^S_{CC} - \frac{1}{z} \, \bar{b}_C \otimes \bar{a}_C, \qquad \underline{Q}^t_{CA} := -\frac{1}{z} \, \bar{b}_C \otimes \bar{a}_A \qquad (5.23)$$

with the *secant acoustic tensors* and the *traction vectors* (Hill, 1962) defined as

$$\underline{Q}^S_{AA} := \left(n_k A^S_{ki\ell j} n_\ell \right) \, \bar{e}_i \otimes \bar{e}_j, \quad \underline{Q}^S_{CC} := \left(n_k C^S_{ki\ell j} n_\ell \right) \, \bar{e}_i \otimes \bar{e}_j \qquad (5.24)$$

$$\bar{a}_A := \bar{n} \cdot \underline{y}_A, \quad \bar{b}_A := \bar{n} \cdot \underline{x}_A, \quad \bar{a}_C := \bar{n} \cdot \underline{y}_C, \quad \bar{b}_C := \bar{n} \cdot \underline{x}_C \qquad (5.25)$$

the expressions in Eqs. (5.20) and (5.21) can be rewritten as

$$\underline{Q}^t_{AA} \cdot \bar{g}_A + \underline{Q}^t_{AC} \cdot \bar{g}_C = \rho c^2 \bar{g}_A \qquad (5.26)$$

$$\underline{Q}^t_{CA} \cdot \bar{g}_A + \underline{Q}^t_{CC} \cdot \bar{g}_C = \rho \theta c^2 \bar{g}_C \qquad (5.27)$$

or in the compact form

$$\underline{Q}^t \cdot \bar{g} = \rho c^2 \underline{V} \cdot \bar{g}, \qquad \tilde{\underline{Q}}^t \cdot \bar{g} = \rho c^2 \, \bar{g} \qquad (5.28)$$

where the *generalized acoustic tensors* $\underline{Q}^t$ and $\tilde{\underline{Q}}^t$ are expressed by

$$\underline{Q}^t := \begin{pmatrix} \underline{Q}^t_{AA} & \underline{Q}^t_{AC} \\ \underline{Q}^t_{CA} & \underline{Q}^t_{CC} \end{pmatrix}, \qquad \tilde{\underline{Q}}^t := \left(\underline{V}^{-1} \underline{Q}^t \right) = \begin{pmatrix} \underline{Q}^t_{AA} & \underline{Q}^t_{AC} \\ \underline{Q}^t_{CA}/\theta & \underline{Q}^t_{CC}/\theta \end{pmatrix} \qquad (5.29)$$

In a compact form, the generalized acoustic tensor can be expressed in terms of the generalized secant acoustic tensor $\underline{Q}^S$ and of the generalized traction vectors $\bar{a}$ and $\bar{b}$ as

$$\underline{Q}^t = \underline{Q}^S - \frac{1}{z} \left(\bar{b} \otimes \bar{a} \right), \quad \underline{Q}^S := \begin{pmatrix} \underline{Q}^S_{AA} & \underline{0} \\ \underline{0} & \underline{Q}^S_{CC} \end{pmatrix}, \quad \bar{a} := \begin{pmatrix} \bar{a}_A \\ \bar{a}_C \end{pmatrix}, \quad \bar{b} := \begin{pmatrix} \bar{b}_A \\ \bar{b}_C \end{pmatrix} \qquad (5.30)$$

The expressions in Eqs. (5.26) and (5.27) represent a generalized version of the classic *Fresnel-Hadamard* propagation condition (already discussed in Eremeyev (2005) for non-linear micropolar elastic media), defining the conditions for propagation of acceleration waves in a micropolar elastic-degrading medium.

5.3 Localization analysis

Within the theory of acceleration waves, the onset of localization is represented by the *stationarity condition of the wavefront*: localization arises when the propagation condition for an acceleration wave is no more satisfied, i.e., when the wavefront became *stationary* ($c \to 0$) for certain normal and polarization directions

$$\tilde{\underline{Q}}^t \cdot \bar{g} = \bar{0} \tag{5.31}$$

Making use of the concepts exposed in the previous section, a generalization of the localization conditions traditionally defined in the classic continuum theory (see, e.g., Rizzi (1995) and Rizzi et al. (1995, 1996)) is here presented. In this work attention is focused on the so-called *weak localization condition* (also known as kinematically compatible failure[5]), based on the spectral properties of the acoustic tensor. The *strong localization condition* that, as discussed in the introduction, is based on the spectral properties of the symmetric part of the acoustic tensor, is not taken into account[6].

5.3.1 Localization condition

Regarding the localization in the context of damaging waves, the most general case is represented by the stationarity of a wavefront transporting a second-order discontinuity in both the fields $\bar{u}$ and $\bar{\varphi}$ (i.e., with $[\![\ddot{u}]\!] \neq 0$ and $[\![\ddot{\varphi}]\!] \neq 0$), resulting, from Eq. (5.31) in the condition

$$\det\left(\tilde{\underline{Q}}^t\right) = 0 \tag{5.32}$$

that, considering Eq. (5.29), is equivalent to $\det\left(\underline{Q}^t\right) = 0$ (as long as $\theta \neq 0$). From this one, two special cases can be obtained (for further details see Appendix B.3): (i) the stationarity of a wavefront transporting a second-order discontinuity in the field $\bar{u}$ ($[\![\ddot{u}]\!] \neq 0$ and $[\![\ddot{\varphi}]\!] = 0$), (ii) the stationarity of a wavefront transporting a second-order discontinuity in the field $\bar{\varphi}$ ($[\![\ddot{u}]\!] = 0$ and $[\![\ddot{\varphi}]\!] \neq 0$), resulting in the conditions

$$(i)\ \det\left(\underline{Q}^t_{AA}\right) = 0 \qquad (ii)\ \det\left(\underline{Q}^t_{CC}\right) = 0 \tag{5.33}$$

where the former is associated to $\bar{b}_C = \bar{0}$, while the latter to $\bar{b}_A = \bar{0}$.

---

[5] The name *kinematically compatible failure* originates from the fact that such condition can be also derived in a quasi-static context, independently on the theory of acceleration waves propagation, assuming the kinematical conditions of discontinuity expressed by the Maxwell equations (Eq. (5.5)). The quasi-static approach has been followed by Dietsche et al. (1993) and Iordache and Willam (1998), for the localization analysis in micropolar elasto-plasticity.

[6] It is remarked that in case of associated models, as the ones considered in Section 5.4, the two conditions coincide.

5.3.2   Localization indicator

A common procedure in localization analysis, usually adopted in the classic continuum theory, consists into simplify the localization problem replacing the aforementioned localization conditions with equivalent ones (see, e.g., Rizzi et al. (1996)). Considering for example the generalized tangent acoustic tensor $\underline{Q}^t$ (Eq. (5.30)), the following tensor can be introduced

$$\underline{D} := (\underline{Q}^S)^{-1}\underline{Q}^t = \begin{pmatrix} \underline{id} & 0 \\ 0 & \underline{id} \end{pmatrix} - \frac{1}{z}\left((\underline{Q}^S)^{-1}\cdot\bar{b}\right)\otimes\bar{a} \tag{5.34}$$

which determinant, from the matrix determinant lemma (see, e.g., Ding and Zhou (2007)), can be expressed as

$$\begin{aligned} \det\left(\underline{D}\right) &= \frac{\det\left(Q^t\right)}{\det\left(Q^S\right)} = 1 - \frac{1}{z}\left(\bar{a}\cdot\left((\underline{Q}^S)^{-1}\cdot\bar{b}\right)\right) \\ &= 1 - \frac{1}{z}\left[\bar{a}_A\cdot\left((\underline{Q}_{AA}^S)^{-1}\cdot\bar{b}_A\right) + \bar{a}_C\cdot\left((\underline{Q}_{CC}^S)^{-1}\cdot\bar{b}_C\right)\right] \end{aligned} \tag{5.35}$$

The general localization condition of Eq. (5.32) is equivalent to $\det\left(\underline{D}\right) = 0$; hence, introducing the *localization indicator* q as

$$q := \det\left(\underline{D}\right) = \frac{\det\left(Q^t\right)}{\det\left(Q^S\right)} \tag{5.36}$$

the condition for the onset of localization in a micropolar medium (Eq. (5.32)) can be expressed by $q = 0$. From Eq. (5.35), it can be shown that the localization indicator q vanishes at a certain direction $\bar{n}$ when the modulus z is equal to a certain limit value[7] $z_{df}(\bar{n})$

$$\begin{aligned} q = 0 \iff z = z_{df}(\bar{n}) :&= \bar{a}\cdot\left((\underline{Q}^S)^{-1}\cdot\bar{b}\right) \\ &= \bar{a}_A\cdot\left((\underline{Q}_{AA}^S)^{-1}\cdot\bar{b}_A\right) + \bar{a}_C\cdot\left((\underline{Q}_{CC}^S)^{-1}\cdot\bar{b}_C\right) \end{aligned} \tag{5.37}$$

Discontinuous failure is prevented as long as $z_{df}(\bar{n}) < z$. For the special cases corresponding to $\bar{b}_C = 0$ and $\bar{b}_A = 0$, the localization indicator reduces to

$$\begin{aligned} q &= 1 - \frac{1}{z}\,\bar{a}_A\cdot\left((\underline{Q}_{AA}^S)^{-1}\cdot\bar{b}_A\right), \quad \text{if } \bar{b}_C = 0 \\ q &= 1 - \frac{1}{z}\,\bar{a}_C\cdot\left((\underline{Q}_{CC}^S)^{-1}\cdot\bar{b}_C\right), \quad \text{if } \bar{b}_A = 0 \end{aligned} \tag{5.38}$$

---

[7] As in traditional works based on the classic continuum theory, the subscript *df* indicates the limit values corresponding to the onset of a *discontinuous failure*, i.e., a localization.

with the following limit values for the onset of localization

$$
\begin{aligned}
z_{df}(\bar{n}) &= \bar{a}_A \cdot \left((\underline{Q}^S_{AA})^{-1} \cdot \bar{b}_A \right), \quad \text{if } \bar{b}_C = 0 \\
z_{df}(\bar{n}) &= \bar{a}_C \cdot \left((\underline{Q}^S_{CC})^{-1} \cdot \bar{b}_C \right), \quad \text{if } \bar{b}_A = 0
\end{aligned}
\tag{5.39}
$$

Taking into account the expressions for the modulus z in the stress- and strain-based approaches defined in Remark 3.4, the following limit values for the inelastic moduli H and H^* can be obtained

$$
H_{df}(\bar{n}) = \bar{a} \cdot \left((\underline{Q}^S)^{-1} \cdot \bar{b} \right) - \underline{n}_A \cdot \left(\underline{A}^S \cdot \underline{m}_A \right) - \underline{n}_C \cdot \left(\underline{C}^S \cdot \underline{m}_C \right)
\tag{5.40}
$$

$$
H^*_{df}(\bar{n}) = \bar{a} \cdot \left((\underline{Q}^S)^{-1} \cdot \bar{b} \right)
\tag{5.41}
$$

As observed by Rizzi (1995) for classic media, the conditions $H_{df}(\bar{n}) < H$ and $H^*_{df}(\bar{n}) < H^*$ are equivalent, since the moduli H and H^* differ for the quantity $\underline{n}_A \cdot (\underline{A}^S \cdot \underline{m}_A) + \underline{n}_C \cdot (\underline{C}^S \cdot \underline{m}_C)$, which doesn't depend on the direction $\bar{n}$.

If the material is initially isotropic (as it will be assumed in the following section), the inverses of the secant acoustic tensors are expressed by

$$
\left(\underline{Q}^S_{AA} \right)^{-1} = \frac{1}{A_2} \, \underline{id} - \frac{A_1 + A_3}{A_1 + A_2 + A_3} \, \bar{n} \otimes \bar{n}
\tag{5.42}
$$

$$
\left(\underline{Q}^S_{CC} \right)^{-1} = \frac{1}{C_2} \, \underline{id} - \frac{C_1 + C_3}{C_1 + C_2 + C_3} \, \bar{n} \otimes \bar{n}
\tag{5.43}
$$

and then

$$
\bar{a}_A \cdot \left((\underline{Q}^S_{AA})^{-1} \cdot \bar{b}_A \right) = \frac{1}{A_2} \left[\bar{a}_A \cdot \bar{b}_A - \frac{A_1 + A_3}{A_1 + A_2 + A_3} \, (\bar{a}_A \cdot \bar{n})(\bar{n} \cdot \bar{b}_A) \right]
\tag{5.44}
$$

$$
\bar{a}_C \cdot \left((\underline{Q}^S_{CC})^{-1} \cdot \bar{b}_C \right) = \frac{1}{C_2} \left[\bar{a}_C \cdot \bar{b}_C - \frac{C_1 + C_3}{C_1 + C_2 + C_3} \, (\bar{a}_C \cdot \bar{n})(\bar{n} \cdot \bar{b}_C) \right]
\tag{5.45}
$$

5.4 Regularization effects of the micropolar parameters

While the previous sections provided a general approach to localization analysis in micropolar elastic-degrading media, the present section focuses on the case of associated scalar-isotropic damage models expressed in the strain-based approach, in a plane stress state, with specific attention on the Marigo model defined by Eq. (3.141). The objective of this section is to provide some quantitative results regarding the formulation presented in the previous sections, and to evaluate the effects on the onset of localization of the additional material parameters of the micropolar continuum theory. These evaluations were performed by the author in Gori et al. (2017b) considering two cases: a uniaxial stress state, able to provide informations on the effects of the Cosserat's shear modulus,

and a more complex stress state obtained with the analytical solution of a plate with a circular hole, influenced also by internal bending length.

5.4.1 Associated scalar-isotropic damage in plane stress

For an associated scalar-isotropic damage model, expressed by $\underline{n} = \tau \, \underline{\Sigma}^0$, it can be easily shown that the traction vectors appearing in Eq. (5.25) reduces to

$$\bar{a}_A = \tau \, \bar{b}_A, \quad \bar{b}_A = \bar{n} \cdot \underline{\sigma}^0, \quad \bar{a}_C = \tau \, \bar{b}_C, \quad \bar{b}_C = \bar{n} \cdot \underline{\mu}^0 \tag{5.46}$$

and, once replaced into Eqs. (5.22) and (5.23), lead to the following expression for the tangent acoustic tensors

$$\underline{Q}_{AA}^t := (1 - D) \, \underline{Q}_{AA} - \frac{\tau}{H^*} \, \bar{b}_A \otimes \bar{b}_A, \qquad \underline{Q}_{AC}^t := -\frac{\tau}{H^*} \, \bar{b}_A \otimes \bar{b}_C \tag{5.47}$$

$$\underline{Q}_{CC}^t := (1 - D) \, \underline{Q}_{CC} - \frac{\tau}{H^*} \, \bar{b}_C \otimes \bar{b}_C, \qquad \underline{Q}_{CA}^t := -\frac{\tau}{H^*} \, \bar{b}_C \otimes \bar{b}_A \tag{5.48}$$

Assuming a plane-stress state in the plane (x,y), the polarization vectors, and the direction of propagation reduce to

$$\bar{p}_A = \begin{pmatrix} p_{Ax} \\ p_{Ay} \end{pmatrix}, \quad \bar{p}_C = \begin{pmatrix} 1 \end{pmatrix}, \quad \bar{n} = \begin{pmatrix} n_x \\ n_y \end{pmatrix} \tag{5.49}$$

Taking into account the following elastic isotropic constitutive relations in Voigt notation

$$\begin{pmatrix} \sigma_{xx} \\ \sigma_{xy} \\ \sigma_{yx} \\ \sigma_{yy} \end{pmatrix} = \begin{pmatrix} \frac{E}{1-\nu^2} & 0 & 0 & \frac{\nu E}{1-\nu^2} \\ 0 & G + G_c & G - G_c & 0 \\ 0 & G - G_c & G + G_c & 0 \\ \frac{\nu E}{1-\nu^2} & 0 & 0 & \frac{E}{1-\nu^2} \end{pmatrix} \begin{pmatrix} \gamma_{xx} \\ \gamma_{xy} \\ \gamma_{yx} \\ \gamma_{yy} \end{pmatrix} \tag{5.50}$$

$$\begin{pmatrix} \mu_{xz} \\ \mu_{yz} \end{pmatrix} = \begin{pmatrix} 2GL_b^2 & 0 \\ 0 & 2GL_b^2 \end{pmatrix} \begin{pmatrix} \kappa_{xz} \\ \kappa_{yz} \end{pmatrix} \tag{5.51}$$

the following expressions for the initial acoustic tensors in plane stress can be obtained

$$\underline{Q}_{AA} = \begin{pmatrix} G + G_c & 0 \\ 0 & G + G_c \end{pmatrix} + \left(\frac{\nu E}{1 - \nu^2} + G - G_c \right) \begin{pmatrix} n_x^2 & n_x n_y \\ n_x n_y & n_y^2 \end{pmatrix} \tag{5.52}$$

$$\underline{Q}_{CC} = 2GL_b^2 \tag{5.53}$$

with their inverse

$$\left(\underline{Q}_{AA}\right)^{-1} = \begin{pmatrix} \frac{1}{G+G_c} & 0 \\ 0 & \frac{1}{G+G_c} \end{pmatrix} - \frac{\chi}{G+G_c}\begin{pmatrix} n_x^2 & n_x n_y \\ n_x n_y & n_y^2 \end{pmatrix} \tag{5.54}$$

$$\left(\underline{Q}_{CC}\right)^{-1} = \frac{1}{2GL_b^2} \tag{5.55}$$

where the material parameter

$$\chi := \left(\frac{\nu E}{1-\nu^2} + G - G_c\right)\frac{1-\nu^2}{E} \tag{5.56}$$

has been introduced. Replacing these values into Eq. (5.35), the limit value of the inelastic modulus is equal to

$$H_{df}^*(\bar{n}) = \frac{\tau}{1-D}\left[\frac{1}{G+G_c}\left(\bar{b}_A \cdot \bar{b}_A - \chi(\bar{n}\cdot\bar{b}_A)^2\right) + \frac{1}{2GL_b^2}\bar{b}_C\cdot\bar{b}_C\right] \tag{5.57}$$

Before exposing the analytical results discussed in Gori et al. (2017b), a comment should be made on the validity of these results. As already stated, the localization analysis treated in the present work is at the *material level*, i.e., a *pointwise* analysis that supposes an ideal stress state with no boundary effects. In a real system, the boundary conditions, as well as the mesh density and alignment, have an important influence on the solution of the problem and on the effects related to the localization. Despite this limitation, such pointwise analysis is still able to provide important informations on the material failure and on the influence of the different material parameters.

5.4.2   Uniaxial stress state

The first example presented in Gori et al. (2017b) considered a uniaxial stress state in absence of couple-stresses, assuming as only non-zero component of the stress tensor $\underline{\sigma}^0$ the term σ_{yy}^0. For the considered model of Eq. (3.141), this choice corresponds to the value $\Gamma_{eq} = \gamma_{yy}$ for the equivalent strain measure and to the value $\tau = 1/\sigma_{yy}^0$ for the factor characterizing the associated model. In absence of couple-stresses and microcurvatures, the only localization condition that has to be accounted for is the stationarity of a wavefront transporting a second-order discontinuity in the field $\bar{u}$, represented by $\det\left(\underline{Q}_{AA}^t\right) = 0$ (Eq. (5.33)). The localization analysis then relies on the evaluation of the localization indicator $q = 1 - H_{df}^*(\bar{n})/H^*$ for different directions of propagation, with $H_{df}^*(\bar{n})$ defined as in Eq. (5.57). Replacing the uniaxial stress state into the equations defined previously,

the limit values of the inelastic modulus can be expressed as

$$
\begin{aligned}
H_{df}^*(\bar{n}) &= \frac{\tau(\sigma_{yy}^0)^2}{(1-D)(G+G_c)}\left(n_y^2 - \chi\, n_y^4\right) \\
&= \frac{\sigma_{yy}^0}{(1-D)(G+G_c)}\left(n_y^2 - \chi\, n_y^4\right)
\end{aligned}
\tag{5.58}
$$

where n_y is the projection of the direction of propagation onto the y axis.

In order to perform the analysis, a specific material was considered, with Young's modulus E = 20000 N/mm^2, Poisson's ratio ν = 0.30 and shear modulus G = 7692.31 N/mm^2, with the following parameters for the exponential damage law, α = 0.999, β = 500 and K$_0$ = 5 × 10^{-5}. The regularization effects of the micropolar medium were evaluated considering three different values for the Cosserat's shear modulus: G$_c$ = 0 N/mm^2, in order to reproduce the limit case of a classic medium, G$_c$ = 500 N/mm^2 and G$_c$ = 2500 N/mm^2.

Figs. 5.1 and 5.2 present the results of the analysis for different values of the Cosserat's shear modulus in terms of the limit values of the inelastic modulus and of the localization indicator at the onset of damage (i.e., with D $\simeq$ 0), where the inelastic modulus $H^* = (\partial D(\Gamma_{eq})/\partial\Gamma_{eq})^{-1}$ (as defined in Eq. (3.136)) assumes the value $H^* = 4.8782 \times 10^{-5}$. In both of them, the results are plotted against the angle θ_n between the propagation direction and the y axis ($n_y = \cos(\theta_n)$). As it can be observed, the value of the Cosserat's shear modulus exhibited a certain influence on the onset of localization. For G$_c$ = 0 N/mm^2, the case corresponding to the classic medium behaviour, the condition for discontinuous failure $H_{df}^* > H^*$ was attained since damage initiation, for certain directions of propagation, as also for G$_c$ = 500 N/mm^2. Focusing on the state of damage initiation, it is observed that in this case the value G$_c$ = 2500 N/mm^2 was able to prevent the discontinuos failure, since the conditions $H_{df}^* < H^*$ and q > 0 were satisfied for each direction of propagation.
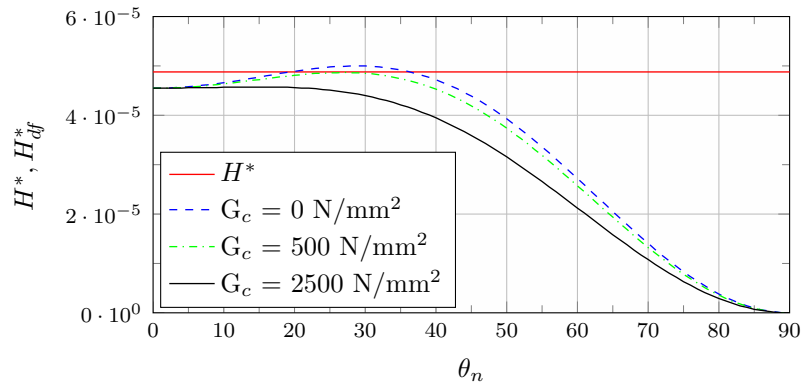
Figure 5.1: Uniaxial stress - Inelastic modulus limit values at damage initiation

It is interesting to observe that, in Fig. 5.1, while the values of H_{df}^* in the range $\theta_n \in$
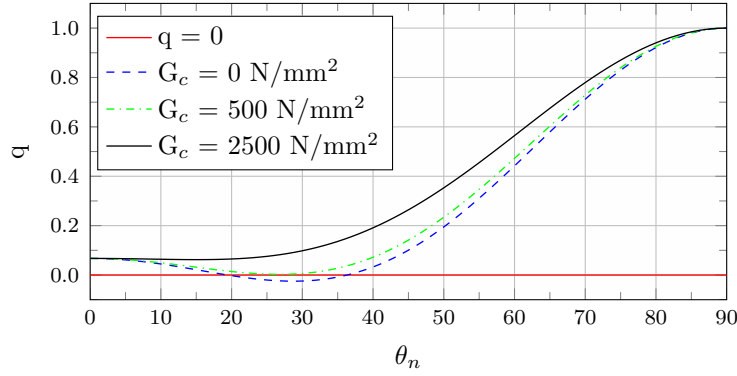
Figure 5.2: Uniaxial stress - Localization indicator at damage initiation

$(0, 90)$ were influenced by variations on the Cosserat's shear modulus, the value associated to a mode-I failure[8], corresponding in this example to the angle $\theta_n = 0$, wasn't influenced by the Cosserat's shear modulus; as it will be discussed in the following section, such value is influenced only by the internal length, in presence of couple-stresses. Furthermore, it is worth to note that for high values of the Cosserat's shear modulus, that mode tended to become the critical one. This is a well known deficiency of the micropolar model for problems where the contribution of the internal length is not activated. In that cases, in order to obtain a stronger regularization effect, different continuum formulations should be cosidered, such as the micromorphic model (see, e.g., Forest et al. (2005)), for example.

In Fig. 5.3, the results corresponding to states beyond damage initiation are illustrated. There, the values of the localization indicator are plotted against the discontinuity angle θ_n and the scalar damage variable. It is interesting to observe that in the case with $G_c = 2500$ N/mm^2, where the localization was prevented at the onset of damage, at a certain threshold value of the scalar damage variable the localization condition $q = 0$ was attained for a certain critical angle θ_n.

Remark 5.1: Numerical simulations

In Gori et al. (2017*b*), the uniaxial stress state discussed in the present section was also investigated numerically with the finite element method, with an example of *induced localization*. The aim of such an investigation was to confirm the analytical evaluations presented in this section, showing the presence of bifurcated solutions in the FEM models for the classic medium and for the micropolar medium with $G_c = 500$ N/mm^2, and regularized solutions for the value $G_c = 2500$ N/mm^2, for which the localization condition wasn't attained. The same example will be presented in Section 6.4, where also simulations with smoothed point interpolation methods will

---

[8] A *mode-I* localized deformation is characterized by a jump in the displacement gradient only in the normal direction to the discontinuity surface, $[\![\dot{\gamma}]\!] = \dot{\gamma}_A\,\bar{n}\otimes\bar{n}$, i.e., when the normal $\bar{n}$ and the polarization vector $\bar{p}_A$ coincides.

(a) $G_c = 0$ N/mm^2

(b) $G_c = 500$ N/mm^2

(c) $G_c = 2500$ N/mm^2
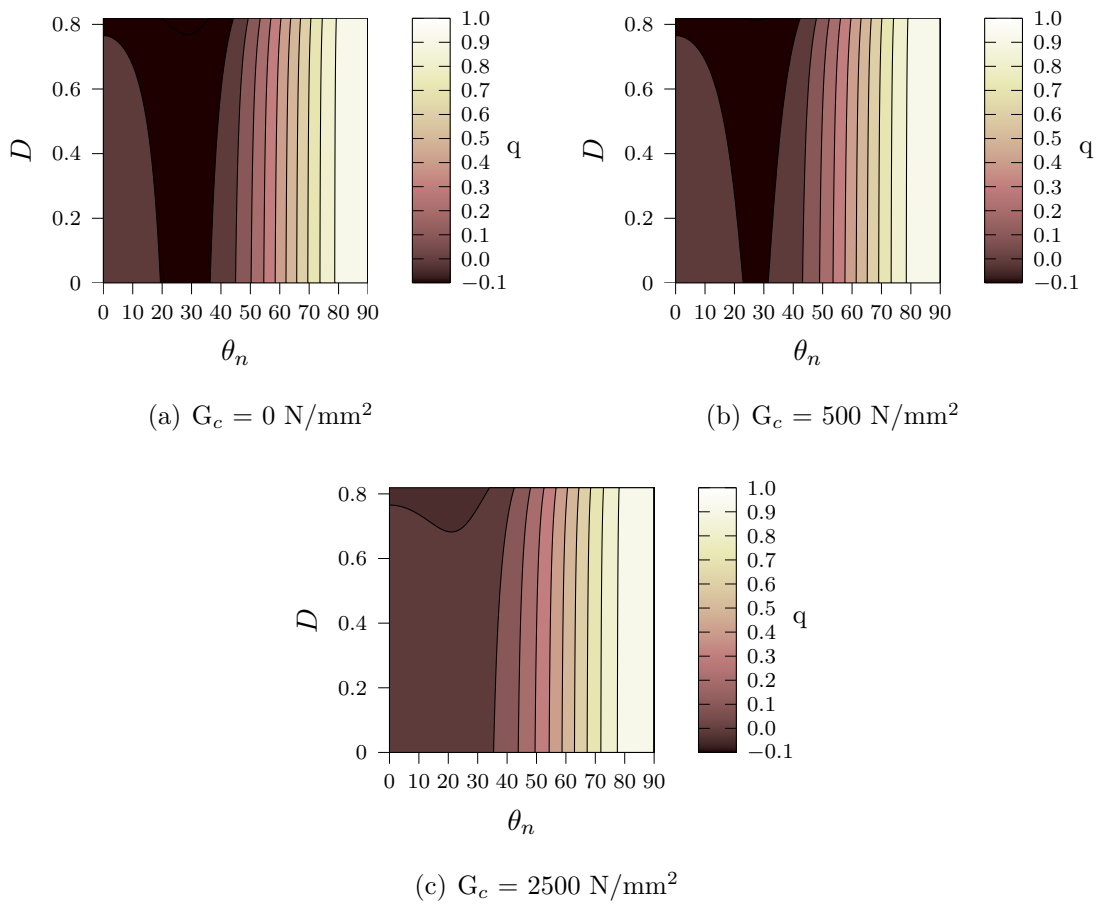
Figure 5.3: Uniaxial stress - Localization indicator beyond damage initiation

be shown, together with another example treating the case of *numerical localization* (Section 6.3).

5.4.3   Plate with circular hole

While the previous example allowed to emphasize the role of the Cosserat's shear modulus on the onset of localization, the second example presented in Gori et al. (2017*b*) allowed to evaluate also the effect of the internal bending length. As already stated, in order to evaluate the effect of the internal bending length, a more complex stress state is needed, with presence of couple-stresses. Though a generic stress state could have been adopted, in Gori et al. (2017*b*) the case of an infinite micropolar plate with a circular hole (Fig. 5.4) was choosen since an analytical solution is available. Such problem has been widely studied in the past, with the aim to derive proper stress intensity factors for the micropolar model. In the cited paper the analytical solution provided by Kaloni and Ariman (1967) was considered (for the explicit equations of the analytical solution the reader should refer to the cited work or to the book by Eringen (1999)), assuming a circular hole with a unitary radius.
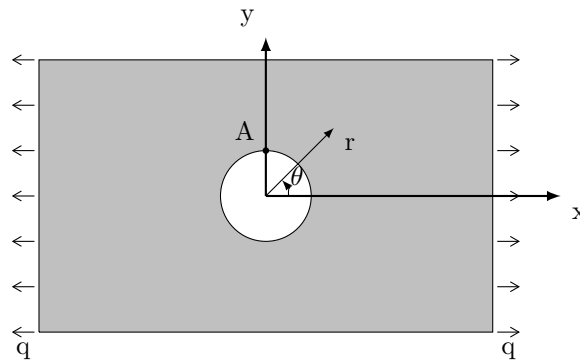
Figure 5.4: Plate with circular hole

The localization analysis discussed here was based on the point of coordinates (1, 90, 0) in the polar system (r, θ, z), the point A in Fig. 5.4. Furthermore, only the state at the onset of damage (i.e., for $D \simeq 0$) was taken into account. Different points or different damage states couldn't have been considered because of the limitation of the analytical solution; since A is the most stressed point, the damage initiates there, and as the behaviour is no more linear elastic the validity of the analytical solution is lost[9]. At the selected point, the stress state is characterized by the non-zero components σ_{rr}, $\sigma_{r\theta}$, $\sigma_{\theta r}$, $\sigma_{\theta\theta}$ and $\mu_{\theta z}$, where in general $\sigma_{r\theta} \neq \sigma_{\theta r}$.

---

[9] In order to extend the localization analysis to different points in the domain and to different damage states, a possible strategy is to mount the acoustic tensors not with values from analytical solutions but rather using data from finite element analyses, as done in Xotta et al. (2016) and Gori et al. (2017*d*) for example. This same approach, called numerical localization analysis, will be discussed in Chapter 6.

Due to the presence of couple-stresses, and since no one of the conditions $\bar{b}_C = \bar{0}$ or $\bar{b}_A = \bar{0}$ is verified for the selected solution, the general case of a second-order discontinuity in both the displacement and microrotation fields must be taken into account, resulting in a failure analysis relying on the evaluation of the localization indicator $q = 1 - H_{df}^*(\bar{n})/H^*$ for different directions of propagation, where the limit values of the inelastic modulus can be obtained from Eq. (5.57). As it can be observed in the cited equation, in this case also the internal bending length appears in the expression of H_{df}^*. In this case it is interesting to emphasize the values of H_{df}^* corresponding to the mode-I localized deformation state, since they are directly influenced by the value of the internal bending length. Since such condition corresponds to $\bar{p}_A = \bar{n}$, the limit value of the inelastic modulus of the mode-I failure can be found replacing the polarization vector $\bar{p}_A$ with the normal vector $\bar{n}$ into Eq. (5.31). It can be shown that the resulting system of equations is satisfied only for the direction $(n_r, n_\theta) = (0, 1)$ in the plane (r,θ), for a limit value of the inelastic modulus expressed by

$$H_{df}^*(0, 1) = \frac{\tau}{E\,(1 - D)} \left[\sigma_{\theta\theta}^2(1 - \nu^2) + \frac{E\mu_{\theta z}^2}{2GL_b^2} \right] \tag{5.59}$$

corresponding to the following ratio between $[\![\ddot{\varphi}]\!]$ and $[\![\ddot{u}]\!]$

$$\frac{[\![\ddot{\varphi}]\!]}{[\![\ddot{u}]\!]} = \frac{E\mu_{\theta z}}{(1 - \nu^2)2GL_b^2\sigma_{\theta\theta}} \tag{5.60}$$

In order to perform the analysis, a specific material was considered, with Young's modulus E = 20000 N/mm², Poisson's ratio $\nu = 0.30$ and shear modulus G = 7692.31 N/mm², with the following parameters for the exponential damage law, $\alpha = 0.999$, $\beta = 3000$ and $K_0 = 5 \times 10^{-5}$. The effect of the micropolar parameters was evaluated considering two different values for the Cosserat's shear modulus, $G_c = 500$ N/mm² and $G_c = 2500$ N/mm², as well as two different values of the internal bending length, $L_b = 0.05$ mm and $L_b = 0.25$ mm.

The results in terms of the inelastic modulus are illustrated in Fig. 5.5, at the onset of damage (i.e., with D ≃ 0) for the range of directions $\theta = [0, 90]$. There, the function H_{df} is plotted against the angle θ_n of the propagation direction with the r axis ($n_r = \cos\theta_n$), and compared with the limit value $H^* = (\partial D(\Gamma_{eq})/\partial\Gamma_{eq})^{-1}$ as defined in Eq. (3.136), equal to $H^* = 4.35 \times 10^{-5}$. Also the value $H_{df}(0, 1)$ associated to the mode-I failure is plotted, at the position $\theta_n = 90°$. As it can be observed, localization was prevented only for the condition "d" ($G_c = 2500$ N/mm² - $L_b = 0.25$ mm), which satisfied the inequality $H_{df}^* < H^*$ for each direction. Analogous conclusions can be drawn from the data contained in Fig. 5.6, where the localization indicator q (Eq. (5.36)) is illustrated.

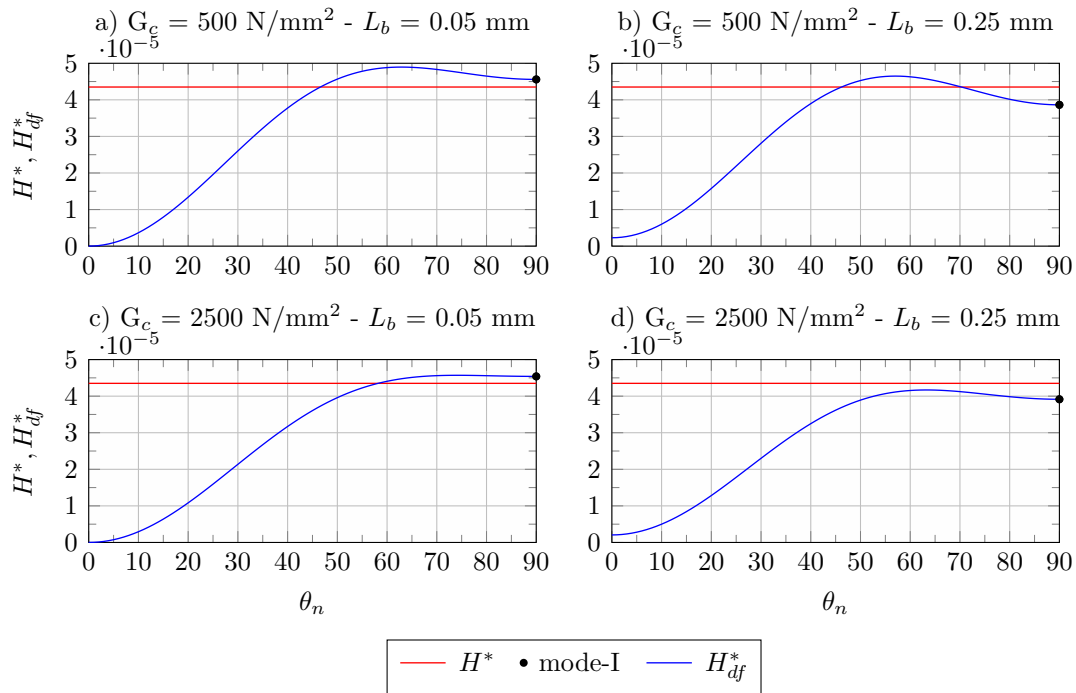**Remark 5.2: Effects of the micropolar parameters**

a) $G_c = 500$ N/mm^2 - $L_b = 0.05$ mm

b) $G_c = 500$ N/mm^2 - $L_b = 0.25$ mm

c) $G_c = 2500$ N/mm^2 - $L_b = 0.05$ mm

d) $G_c = 2500$ N/mm^2 - $L_b = 0.25$ mm

Figure 5.5: Inelastic modulus limit values

a) $G_c = 500$ N/mm^2 - $L_b = 0.05$ mm

b) $G_c = 500$ N/mm^2 - $L_b = 0.25$ mm

c) $G_c = 2500$ N/mm^2 - $L_b = 0.05$ mm

d) $G_c = 2500$ N/mm^2 - $L_b = 0.25$ mm
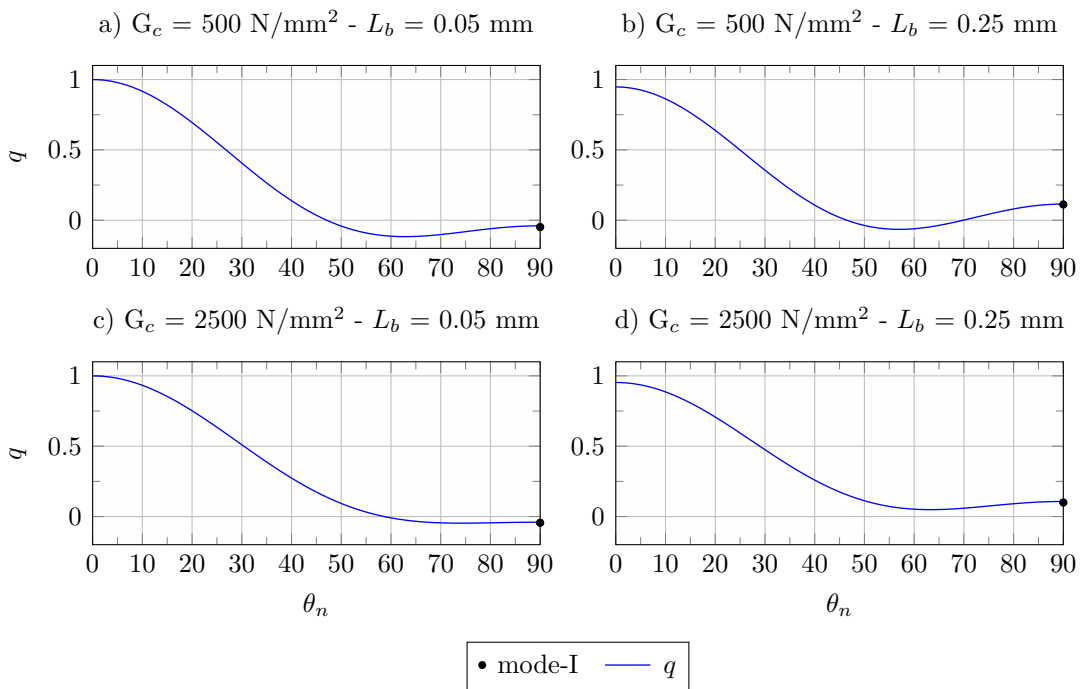
Figure 5.6: Localization indicator

Taking into account the results presented in this section and in the previous one, some considerations regarding the influence of the additional material parameters of the micropolar theory can be made. From Figs. 5.1 and 5.5 it can be observed that, in the considered examples, the Cosserat's shear modulus exhibited an influence on the limit value $H^*_{df}(\theta_n)$ in the range $\theta_n \in (0, 90)$, without affecting the values at $\theta_n = 0°$ and $\theta_n = 90°$ (this can be seen comparing the combination "a" with "c" in Fig. 5.5, for example). The internal bending length L_b, on the contrary, manifested an influence on the limit value $H^*_{df}(\theta_n)$ in the whole range $\theta_n \in [0, 90]$. For both of the Cosserat's moduli it can be observed that the greater their value, the smaller the limit value H^*_{df} was. Taking into account these considerations, it can be stated that:

- in absence of couple-stresses the onset of localization is ruled only by the Cosserat's shear modulus, and may verify at different directions depending on the relation between H^* and H^*_{df};

- in presence of couple-stresses the limit value H^*_{df} is ruled by both the Cosserat's shear modulus and the internal bending length, and localization may verify at different directions depending on the relation between H^* and H^*_{df};

- as the value of the Cosserat's shear modulus grows, the localization tends to be of a mode-I type;

- in that case, the onset of localization is ruled solely by the internal bending length.

Chapter 6

Numerical and induced localization examples

The present chapter collects a set of simulations involving problems of numerical and induced localization. The different examples aim to show the regularization effects induced by the micropolar continuum model and by smoothed meshfree methods in such kind of problems.

6.1   Numerical vs induced localization

As discussed in Section 2.3, the problem of localization is a fundamental issue in numerical simulations involving strain-softening constitutive models, like the damage models usually adopted for the modelling of quasi-brittle media, for example (Chapter 2), especially when *tangent* approximations of the constitutive operators are accounted for. The aforementioned section pointed out the physical aspects of localization, as an irreversible phenomenon corresponding to plasticization or cracks formation in certain parts of a real body. It also emphasized the mathematics behind this phenomenon. The condition for localization is usually associated to a certain state of the so-called *acoustic tensor* and, from a mathematical point of view, corresponds to the *loss of ellipticity* of the partial differential equations defining the elastic equilibrium problem. When trying to solve numerically a problem where localization occours, the main issue is that the numerical solution become *unstable*, i.e., highly sensitive to perturbations; once ellipticity is lost, the boundary value problem ceases to be well posed, and bifurcated solutions may appear.

Depending on the kind of perturbation that is being considered, one may distinguish between two different situations, called *numerical* and *induced* localization, respectively. The former can be conveniently explained basing the discussion on an hypothetical sample characterized by an initially uniform stress/strain state. As illustrated analytically in Section 5.4, a sample in a uniform state may attain a *localization condition* for a certain deformation level. If, hypothetically, all the variables calculated numerically during the

analysis of such a sample were uniformly distributed among its integration points (as indeed it should be expected for a sample in a uniform stress/strain state), the verification of the localization condition would not affect the current equilibrium path of the sample. However, due to the floating-point arithmetic, at each integration point of the discrete model the variables may assume values that are different from the expected uniform ones. Due to the high sensitiveness of the model as a consequence of the localization condition, such difference may be sufficient to trigger a *bifurcated solution*, divergent with respect to the expected one. Such bifurcated solution happen to depend on the size of the discretization; hence, convergence upon mesh refinement is lost. This phenomenon goes by the name of *numerical localization* due to the fact that it originates from an approximation error that is intrisic to discrete (aka numerical) models.

Remark 6.1: Initially non-uniform states

The problem of numerical localization discussed in the present section is based on an initially uniform stress/strain state. However, it is important to point out that such issue may also affect problems that don't present an initial uniform state. In that case, if a localization condition occours, the solution may still become unstable due to numerical perturbations, usually presenting an instantaneous brittle failure. Hence, it is important to rely on methods that allow to avoid such situations.

The phenomenon of *induced localization* is strictly related to the one of numerical localization. The necessary condition for both phenomena to manifest is the same, the verification of the localization condition (Section 5.3). What distinguishes them is the triggering event. In case of numerical localization, as discussed above, a bifurcated solution may be triggered by a numerical instability, able to provide a sufficient perturbation. On the other hand, the initiation of an induced localization is due to a physical characteristic of the considered model. This characteristic may be a certain geometric configuration or a local variation in the material properties, for example, i.e., any peculiarity able to induce a sufficient perturbation. Depending on the triggering event, the initial state may be uniform or not. In the examples discussed in Section 6.3, the initial state is uniform, since the triggering event is constituted by the introduction of *weakened elements*, i.e., elements characterized by a material with a reduced damage initiation threshold; in this case the problem is uniform until damage initiation. On the other hand, the case of the infinite shear layer with constrained microrotations (Section 6.2) presents an non-uniform solution since the beginning of the loading process.

The first example that will be presented is the analysis of an *infinite shear layer* (Section 6.2), a model that has been widely adopted in the past to illustrate the regularization properties of the micropolar medium in elasto-plasticity. Differently from existent investigations, in this case the infinite shear layer was analyzed considering a scalar damage

model in a plane-stress state, instead of an elasto-plastic one in a plane-strain state. It was investigated using only the FEM, and it has been included in this manuscript as a sort of benchmark test for the micropolar models proposed in Section 3.3, leaving the investigations on the regularization effects of both the micropolar and smoothed point interpolation strategies to the subsequent examples of Sections 6.3 and 6.4.

6.2　Infinite shear layer

The *infinite shear layer* problem has been widely adopted in the past to expose the regularization properties of the micropolar formulation in elasto-plastic models with strain softening. Among the different contributions there are the works by de Borst (1991, 1993) and de Borst and Sluys (1991), that focused on the regularization aspects in micropolar elasto-plastic models, the work by Huang and Bauer (2003), devoted to the analysis of cohesionless granular materials, and the work by Liu, Scarpas and Kasbergen (2007), devoted to the analysis of two-phase three-dimensional micropolar elasto-plastic models.

The problem, depicted in Fig. 6.1(a), consists in a sample of height H, which extends indefinitely in the x direction. The bottom of the layer is constrained in both the x and y directions, and each point of the layer is prevented from moving in the y direction. The load is represented by a shear force applied at the top, in the x direction. In virtue of the symmetry condition induced by the infinite extension assumption, the problem can be investigated focusing the attention on a thin strip of the layer (usually a single strip of finite elements in an FEM model); inside this strip, points with the same y coordinate are assumed to have the same horizontal displacement (and the same microrotation, in case of a micropolar medium).

(a) Geometry　　　　　　　(b) Constitutive behaviour
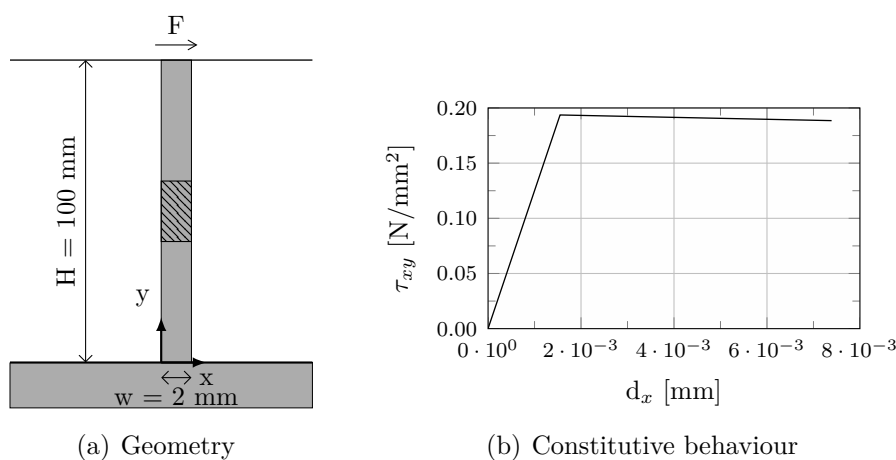
Figure 6.1: Infinite shear layer

In the investigation exposed in the present section, a layer characterized by an height H = 100 mm and a width w = 2 mm was considered. The layer was assumed to be in

a plane-stress state[1], with a unitary thickness. The material was modelled as a *Marigo* scalar damage model (Eq. (2.34)), assuming as elastic properties the Young's modulus E = 30000 N/mm², Poisson's ratio ν = 0.20, and shear modulus G = 12500 N/mm², and assuming an exponential damage law for the evolution of the scalar damage variable characterized by the parameters α = 0.950, β = 750 and K_0 = 1.0 $\times 10^{-5}$; these material properties correspond to the constitutive behaviour depicted in Fig. 6.1(b). Like in the examples discussed in the previous sections, also in the shear layer a perturbation is needed to trigger a localized solution once the localization condition is met[2]. To this scope, a weakened region was inserted in the middle of the layer (the hatched area in Fig. 6.1(a)), characterized by a slightly reduced value of the parameter K_0. The height of the weakened region was choosen accordingly to each discretization. Considering the FEM meshes illustrated in Fig. 6.2, in the coarser mesh the weakened zone occupied the central element of the layer, while in the other meshes it occupied the two middle elements; the meshes 1 and 2 were then characterized by the same heigh of the weakened zone, while the meshes 3 and 4 by a reduced height.

6.2.1   FEM simulations

The analyses with the finite element method were performed considering four discretizations, illustrated in Fig. 6.2, composed by 5, 10, 20, and 40 four-nodes finite elements, disposed in a single strip, that is, with just one element in the x direction. The resulting discretizations were characterized by elements with a fixed width of 2 mm and height equal to 20 mm, 10 mm, 5 mm, and 2.5 mm, respectively. As it can be observed, all the nodes were constrained in the vertical direction, in virtue of the aforementioned hypothesis that each point of the layer is prevented from moving in the y direction. Furthermore, the symmetry condition of the layer, stating that points with the same y coordinate have the same horizontal displacement, was imposed with a *master-slave* strategy.

The FEM analyses were performed adopting a loading process driven by the *displacement control* method, assuming a reference load F = 2 N, an initial loading factor increment of 1.0 $\times 10^{-5}$, and a tollerance for convergence in relative force of 1.0 $\times 10^{-4}$. All the simulations presented in this section were performed considering the tangent approximation of the constitutive operator.

The results of the analyses, in terms of horizontal displacement of the top section plotted against the load factor, are illustrated in Fig. 6.3. As it can be observed, the

---

[1] While the present investigation considered a plane-stress state, the shear layer problem is commonly treated as a plane-strain problem (see, e.g., de Borst (1991)). Since the objective of this investigation was just to point out the properties of the proposed micropolar damage models concerning the problem of localization, this discrepancy is not relevant.

[2] An exception is constituted by the analyses performed with the micropolar medium with constrained microrotations at the top and bottom sections of the layer, that will be discussed in the following Section 6.2.2.2.

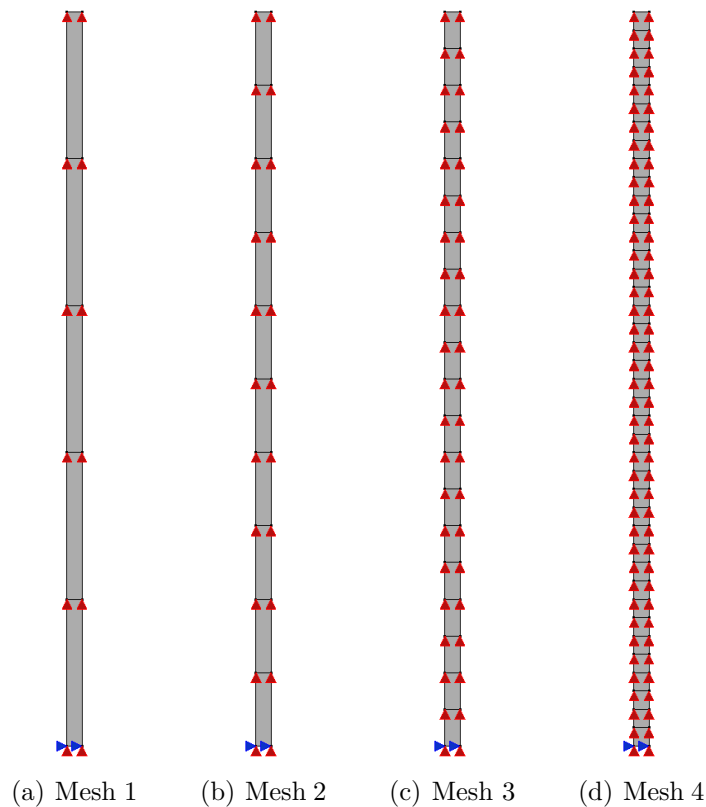(a) Mesh 1   (b) Mesh 2   (c) Mesh 3   (d) Mesh 4

Figure 6.2: Infinite shear layer - FEM meshes

results were strongly dependent on the discretization. The first two meshes, characterized by the same height of the weakened zone, presented the same equilibrium path, while the most refined meshes manifested a stronger softening in the post-peak branch. The effect of the different heigths of the weakened zone is also emphasized by the contour plots of the scalar damage variable illustrated in Fig. 6.4. There it can be observed that, at the onset of damage, the damaged zone of the layer was confined to the weakened elements; during the loading process such zone didn't expand, and tended to remain concentrated in the initially damaged elements (Fig. 6.5).
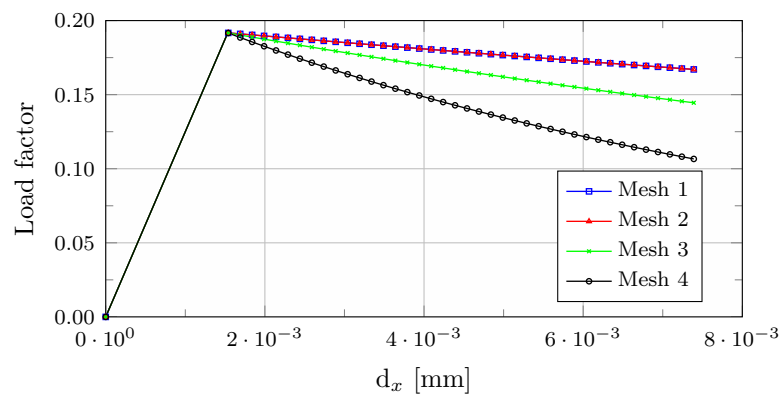
Figure 6.3: Infinite shear layer - FEM - Equilibrium paths

(a) Mesh 1   (b) Mesh 2   (c) Mesh 3   (d) Mesh 4
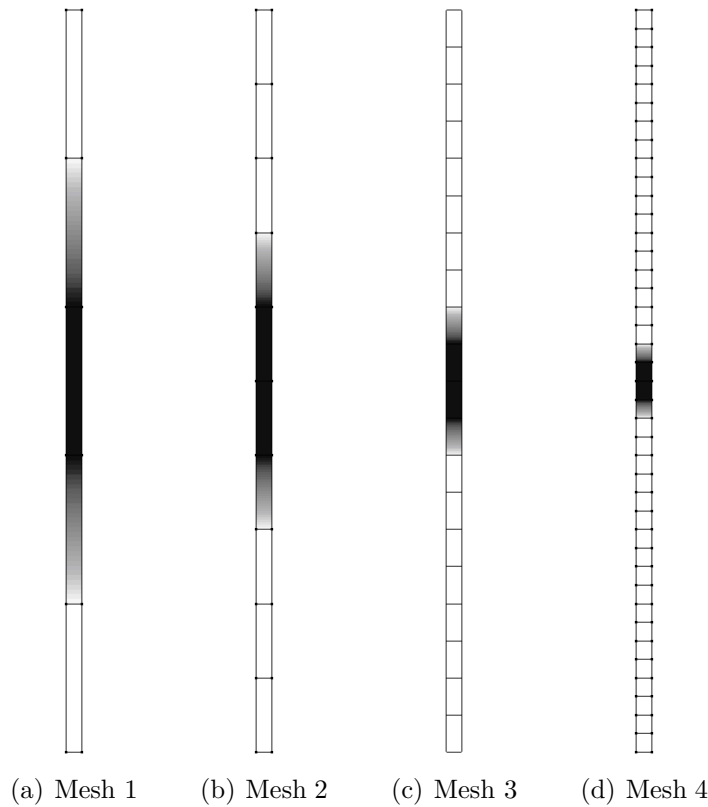
Figure 6.4: Infinite shear layer - FEM - Damage initiation

Fig. 6.5 illustrates the deformed and damaged configurations exhibited by the different discretizations of the layer at the final step of the analysis, corresponding to an horizontal displacement of the top of the layer equal to $d_x = 7.39 \times 10^{-3}$ m. As it can be observed, all the deformations of the layer tended to concentrate in the central elements (i.e., the weakened ones), while the other parts of the layer exhibited rigid displacements. These results are analogous to the ones found by other authors in case of elasto-plasticity, and allow to show how in a classic medium the width of the localization zone "is entirely governed by the spacing of the finite element mesh" (de Borst, 1991, pag. 326).

6.2.2   Regularization by micropolar formulation

As already commented, the analysis of the infinite shear layer problem has been carried out by a number of authors in the past, for the case of micropolar elasto-plasticity (see, e.g., de Borst (1991, 1993), de Borst and Sluys (1991), Huang and Bauer (2003), and Liu, Scarpas and Kasbergen (2007)). In the existent literature the authors usually considered two different conditions regarding the degree of constraint at the top and bottom sections of the layer: *free* and *constrained* microrotations. The former is characterized by an homogeneous strain state and, as in the case of a classic medium, the insertion of a weakened zone is needed to trigger a bifurcated solution once the localization condition is met. In the latter instead, an homogeneous strain state is not obtained since "already

(a) Mesh 1   (b) Mesh 2   (c) Mesh 3   (d) Mesh 4
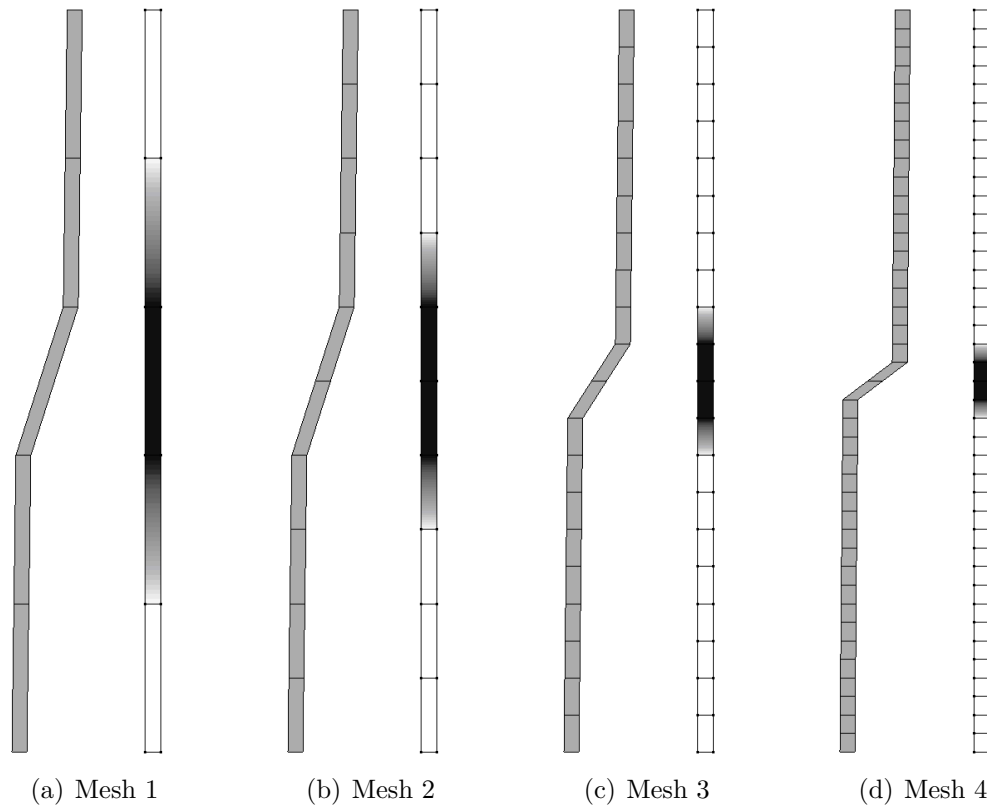
Figure 6.5: Infinite shear layer - FEM - Deformed and damaged configurations at $d_{x,max} = 7.39 \times 10^{-3}$ m

in the elastic regime a boundary layer of approximately a height l [the internal bending length L_b] develops at the upper and lower parts of the shear layer and the strains are not uniform over the height of the entire shear layer" (de Borst, 1991, pag. 326). As a consequence bifurcated solutions naturally arise, with no need of artificially introduced imperfections.

Remark 6.2: Constrained microrotations: physical interpretation

Large part of the investigations on the infinite shear layer problem performed in the past introduced the hypothesis of constrained microrotations just as a mean to obtain a naturally non-homogeneous strain state, in order to induce bifurcated solutions in the micropolar medium without introducing ad hoc perturbations. However, such hypothesis can be justified by physical motivations. In Huang and Bauer (2003) the authors analysed the infinite shear layer problem considering different degrees of constraint for the microrotations. They considered the shear layer as a sample placed between two bounding structures, at the top and bottom sections, respectively. Since they focused on the analysis of cohesionless granular materials, they introduced a correlation between the roughness of such bounding structures and the degree of

constraint on the microrotations.

> "The influence of the rotation resistance of particles in contact with a bounding structure in motion can be modeled with the Cosserat boundary conditions in a physically natural manner. Very rough walls can capture small grains so that a rotation of particles along the bounding surface is prevented."(Huang and Bauer, 2003, pag. 345)

Besides the case of fully constrained microrotations corresponding to very rough bounding structures, the authors believes that "for a smoother boundary it is conceivable to consider a certain coupling between the displacement of the boundary and the corresponding particle rotation" (Huang and Bauer, 2003, pag. 345). In order to evaluate this coupling they assumed an empirical equation, originally proposed by proposed by Tejchman (Tejchman, 1997), which takes into account both the mean grain diameter of the material particles and the roughness of the bounding surfaces. While, as found by other authors and also observed in Section 6.2.2.2, in case of fully constrained microrotations localization develops in the middle of the height layer, in case of intermediary degrees of constraint the authors found that localization may arise also in different parts of the sample.

6.2.2.1 Free microrotations

The analysis of the micropolar infinite shear layer with free microrotations was performed considering 9 different combinations of the material parameters, using the values 500, 1000, and 2000 N/mm² for the Cosserat's shear layer G_c and the values 0.1, 1.0 and 5.0 mm for the internal bending length L_b.

The results of the analyses for the various combinations of parameters in terms of equilibrium paths, are illustrated in Fig. 6.6. As it can be observed, for a fixed value of the bending length, to higher values of the Cosserat's shear modulus corresponded post-peak branches with reduced slope, which tendend to the one of the homogeneous case, that is, without weakening (Fig. 6.1(b)). For the smallest values of L_b this effect was clearly evident just in the coarsest mesh. In the other meshes it was noticeable only in the first part of the descending branch, and the behaviour of the remaining part of the post-peak branch was almost unchanged. For a sufficiently high value of the bending length (in this case $L_b = 5.0$ mm), the entire post-peak branch was affected also in the finer meshes, leading to mesh objective solutions for the combination $G_c = 2000$ N/mm² and $L_b = 5.0$ mm (Fig. 6.6(i)).

The effect of the different values of the Cosserat's material parameters can be observed also in Fig. 6.7. There, the damaged configurations exhibited by the most refined mesh at step 30 (a few steps after damage initiation), for the same combinations of parameters
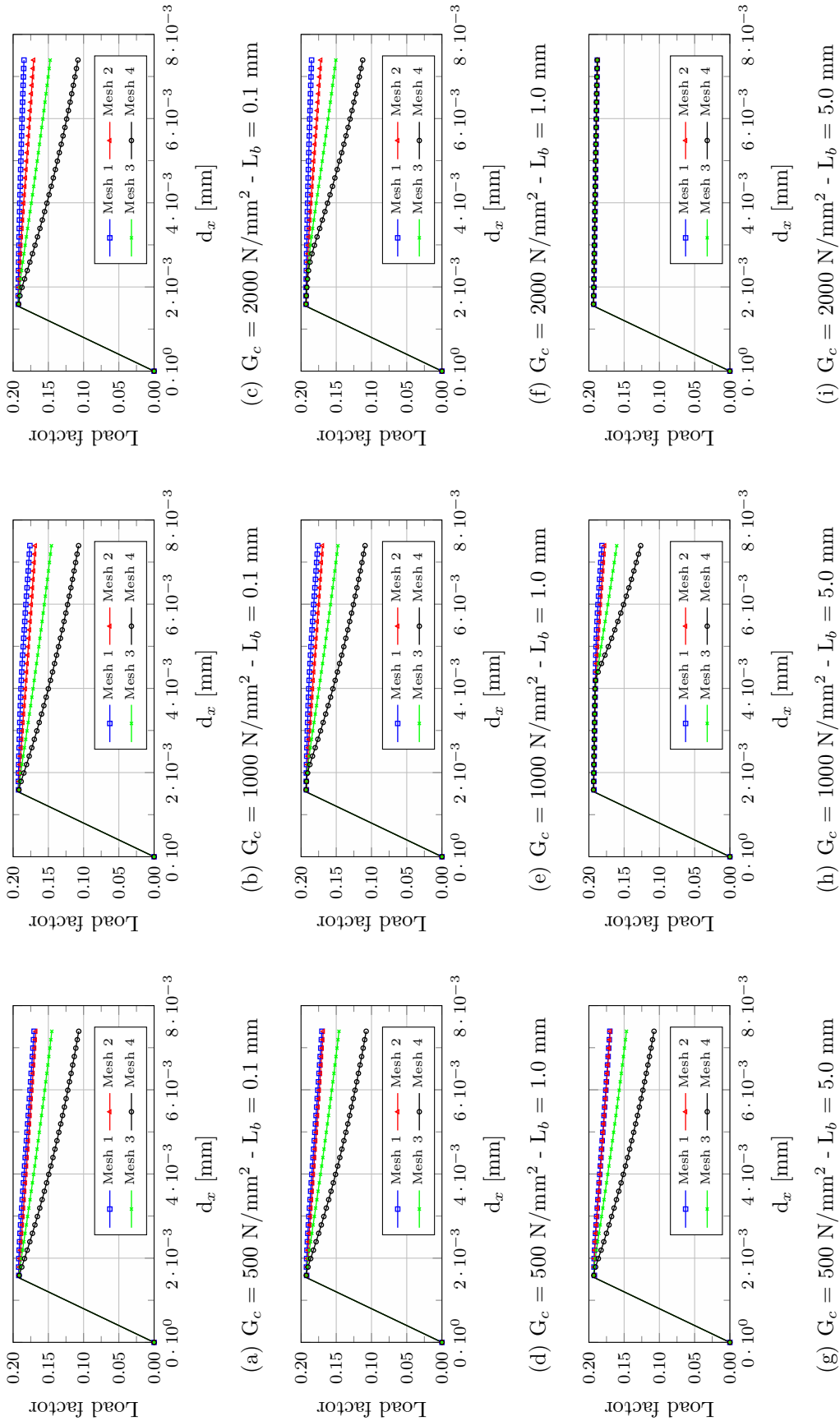
Figure 6.6: Infinite shear layer - Micropolar FEM - Free microrotations

used in Fig. 6.6, are illustrated. As it can be observed, to higher values of both G_c and L_b corresponded a wider damaged zone.

The fact that the combination of Cosserat's material parameters given by $G_c = 2000$ N/mm^2 and $L_b = 5.0$ mm was able to provide mesh objective solutions (as it can be observed in Fig. 6.6) can be emphasized comparing the results in terms of deformed and damaged configurations at the end of the loading process obtained with the classic medium (Fig. 6.5) with the ones obtained with the micropolar medium with $G_c = 2000$ N/mm^2 and $L_b = 5.0$ mm (Fig. 6.8). While for the classic medium each mesh exhibited a different behaviour, with deformations and damage concentrated in the two central elements, the analysis with the micropolar medium manifested the same deformed configuration in each one of the meshes. The same holds also for the damage variable , which distribution was almost the same among the different meshes.

6.2.2.2   Constrained microrotations

As stated above, in case of constrained microrotations there is no need of an artificial imperfection in order to trigger a bifurcated solution in the infinite shear layer. Taking into account this fact, the constrained micropolar model was investigated with two different conditions, one with the same weakened zones like in the previous case and the other with an homogeneous material all along the height of the layer. The analysis was performed considering 9 different combinations of the material parameters, using the values 1000, 2000, and 3000 N/mm^2 for the Cosserat's shear layer G_c and the values 0.1, 1.0 and 5.0 mm for the internal bending length L_b. The results in terms of equilibrium paths for both the weakened (Fig. 6.9) and the homogeneous (Fig. 6.10) materials were similar to the ones exhibited by the case with free microrotations (Fig. 6.6), regarding the effect of the Cosserat's material parameters. Indeed, also in these cases, to higher values of G_c and L_b corresponded post-peak branches with reduced slope. With the combination $G_c = 3000$ N/mm^2 and $L_b = 5.0$ mm it was possible to obtain mesh objective behaviours, except for the most refined mesh in the case with weakened material, which exhibited a divergence in the equilibrium path for the last steps of the loading process.

The same conclusions can be drawn from the observation of the results obtained with the combination $G_c = 3000$ N/mm^2 - $L_b = 5.0$ mm depicted in Figs. 6.11 and 6.12, in terms of deformed and damaged configurations. Regarding the case with weakened material Fig. 6.11, it can be observed that the results manifested a certain mesh objectivity except for the mesh 4 that, as already observed in the equilibrium paths, exhibited a localization of the deformations in the final steps of the analysis. On the other hand, the case with homogeneous material Fig. 6.12 manifested the same behaviour with the four meshes. Comparing these results with the one of the case with free microrotations (Fig. 6.8) it can be observed that the deformed configurations were slightly different: in the case with free microrotations the deformations were more evenly distributed along the height of the
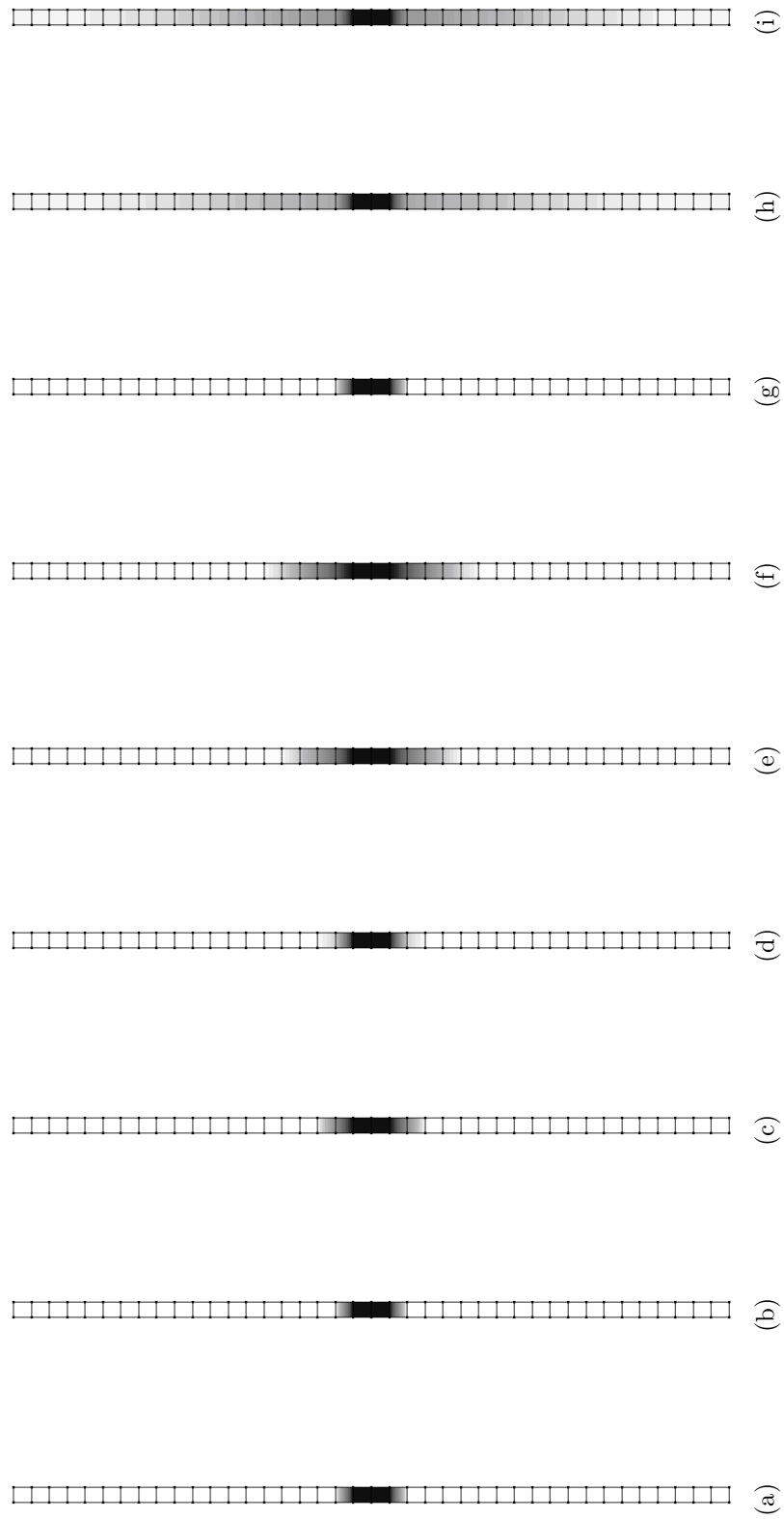
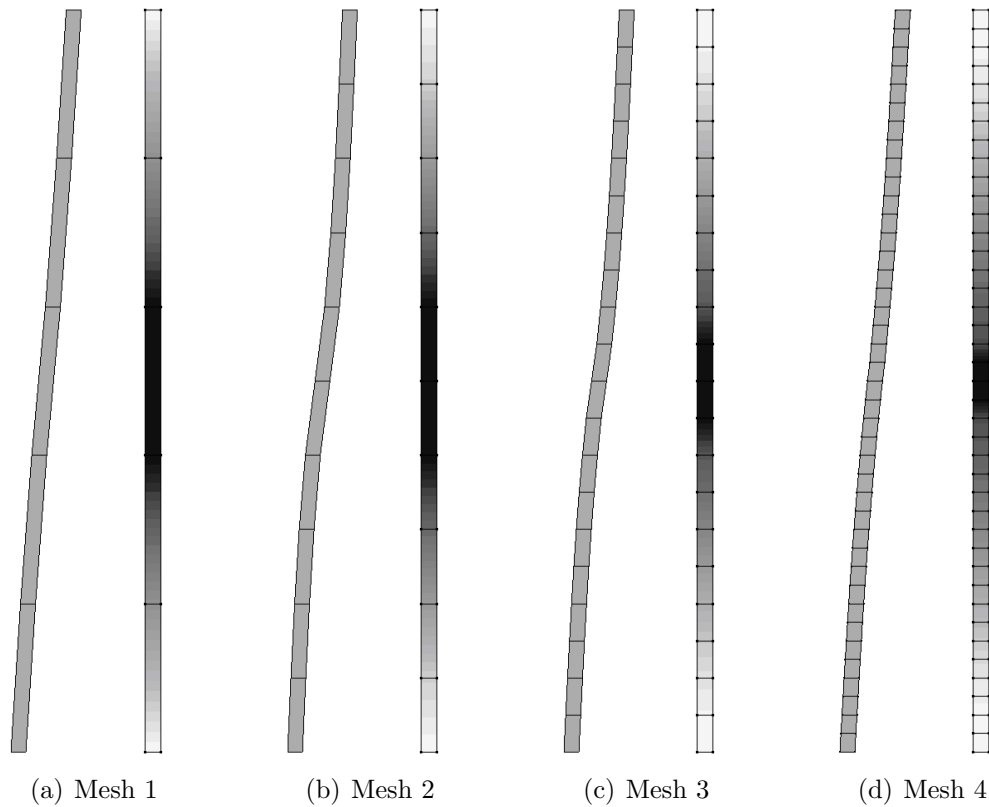Figure 6.7: Infinite shear layer – Micropolar FEM - Damaged configurations at step 30

(a) Mesh 1   (b) Mesh 2   (c) Mesh 3   (d) Mesh 4

Figure 6.8: Infinite shear layer - Micropolar FEM - $G_c = 2000$ N/mm^2 - $L_b = 5.0$ mm - Deformed and damaged configurations at $d_{x,max} = 7.39 \times 10^{-3}$ m

layer, while in the case with constrained microrotations they were concentrated in a zone in the middle of the layer.

As pointed out in previous investigations involving micropolar elasto-plastic models (see, e.g., de Borst (1991)), the infinite shear layer problem allows to point out the capability of the micropolar formulation to represent the size of localization zones independently on the size of the underlying discretization. In the case of scalar damage investigated in the present section this behaviour can be emphasized considering the distribution of the damage variable at the onset of damage. As it can be observed in the contour plots of Fig. 6.13, at the onset of damage the four meshes analysed with the combination G_c = 3000 N/mm^2 - $L_b = 5.0$ mm exhibited approximately the same damage distribution, independently on the discretization.
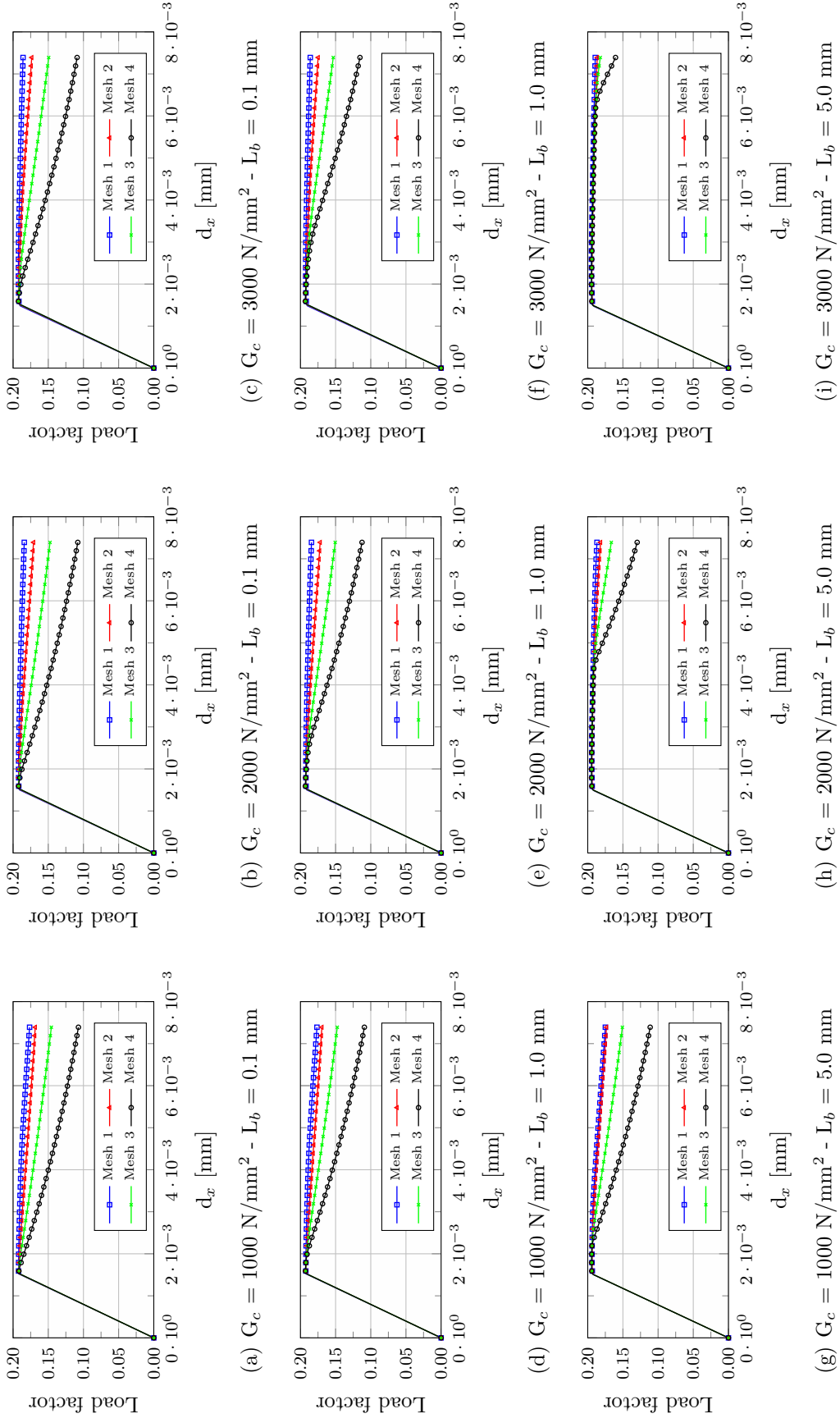
Figure 6.9: Infinite shear layer - Micropolar FEM - Constrained microrotations
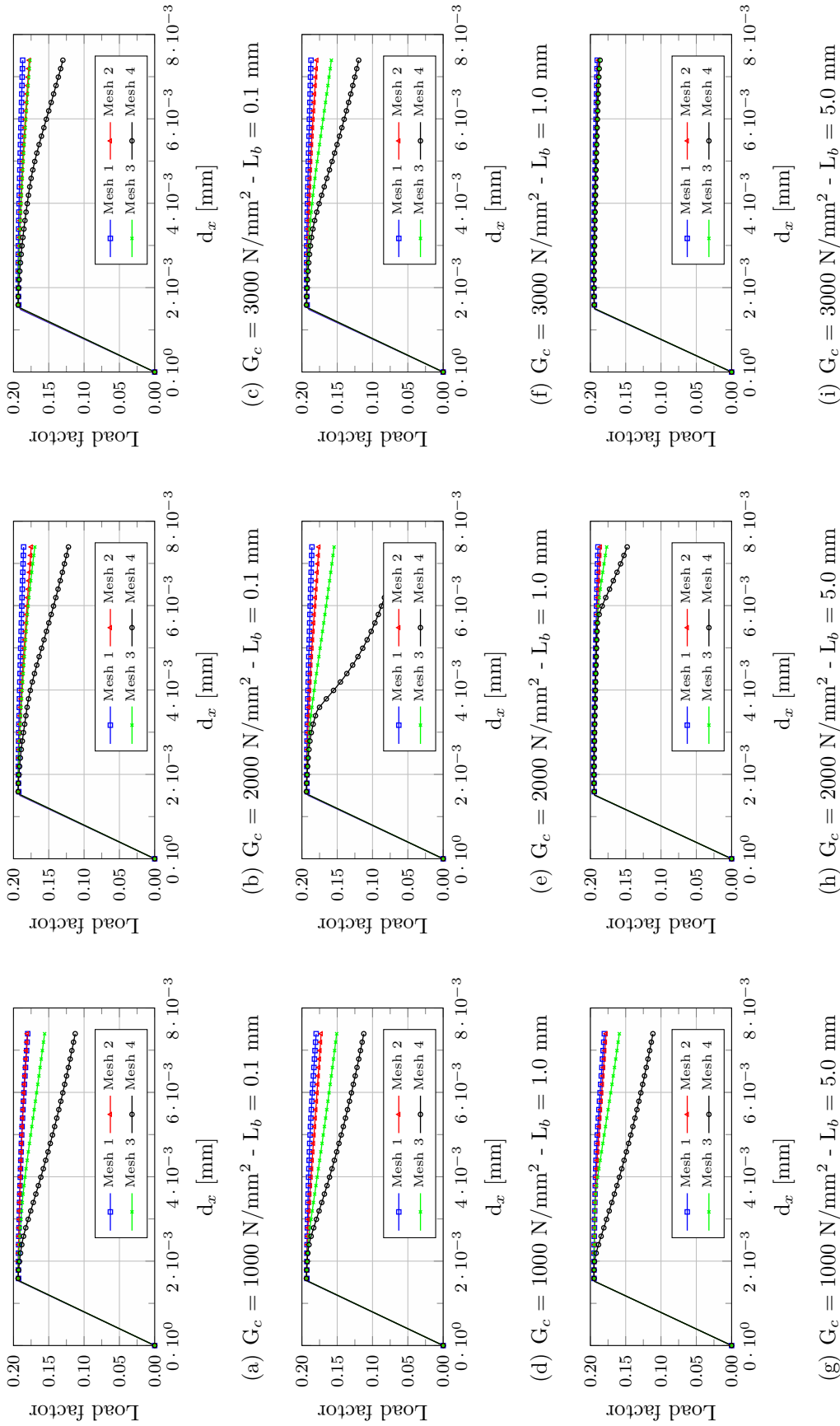
Figure 6.10: Infinite shear layer - Micropolar FEM - Constrained microrotations - Uniform material

(a) Mesh 1   (b) Mesh 2   (c) Mesh 3   (d) Mesh 4
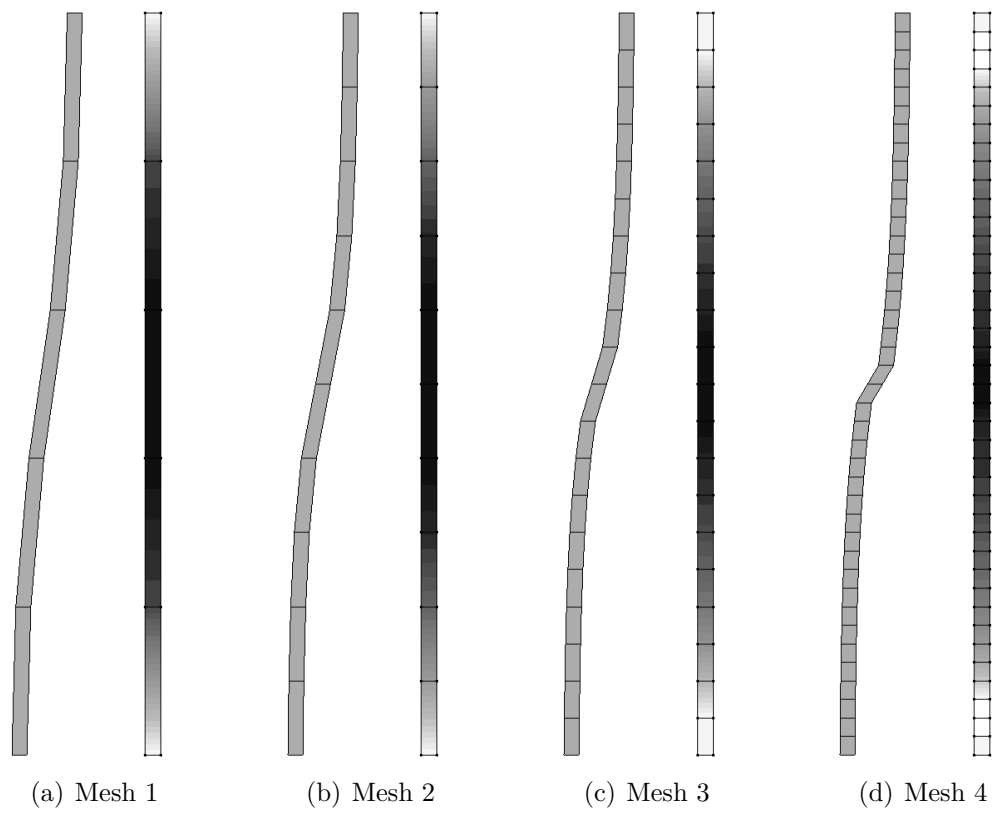
Figure 6.11: Infinite shear layer - Micropolar FEM with constrained microrotations - $G_c = 3000$ N/mm^2 - $L_b = 5.0$ mm - Deformed and damaged configurations at $d_{x,max} = 7.39 \times 10^{-3}$ m

(a) Mesh 1   (b) Mesh 2   (c) Mesh 3   (d) Mesh 4
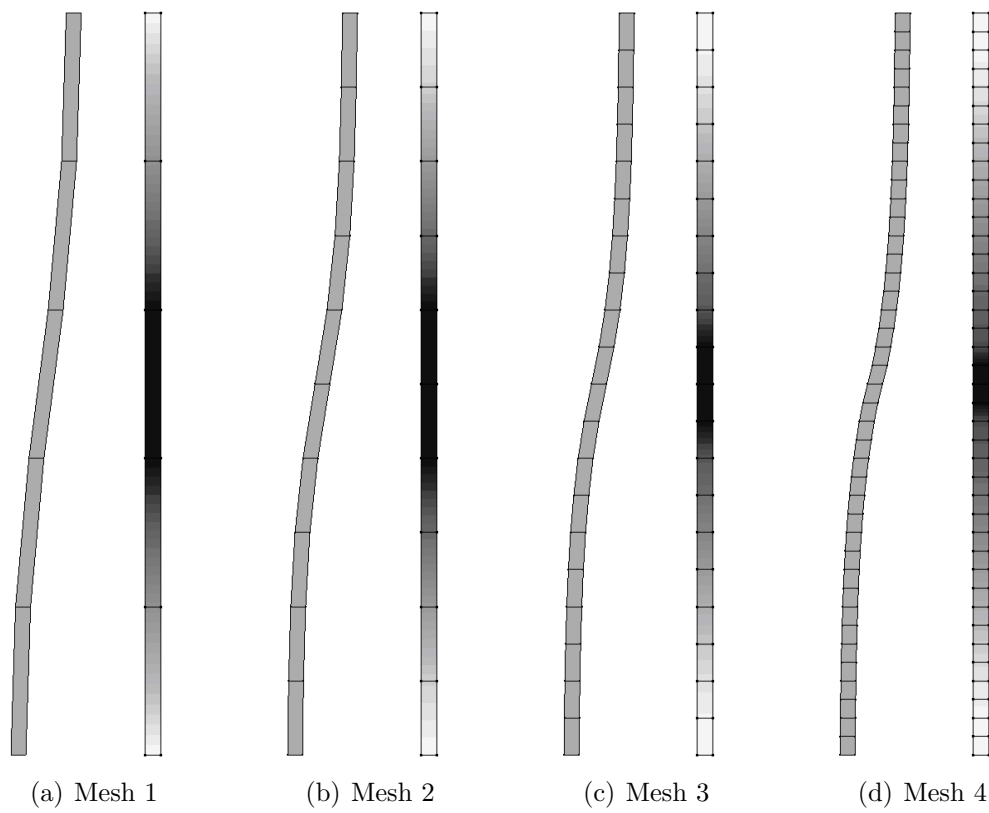
Figure 6.12: Infinite shear layer - Micropolar FEM with constrained microrotations and uniform material - $G_c = 3000$ N/mm^2 - $L_b = 5.0$ mm - Deformed and damaged configurations at $d_{x,max}$ = 7.39×10^{-3} m

(a) Mesh 1   (b) Mesh 2   (c) Mesh 3   (d) Mesh 4
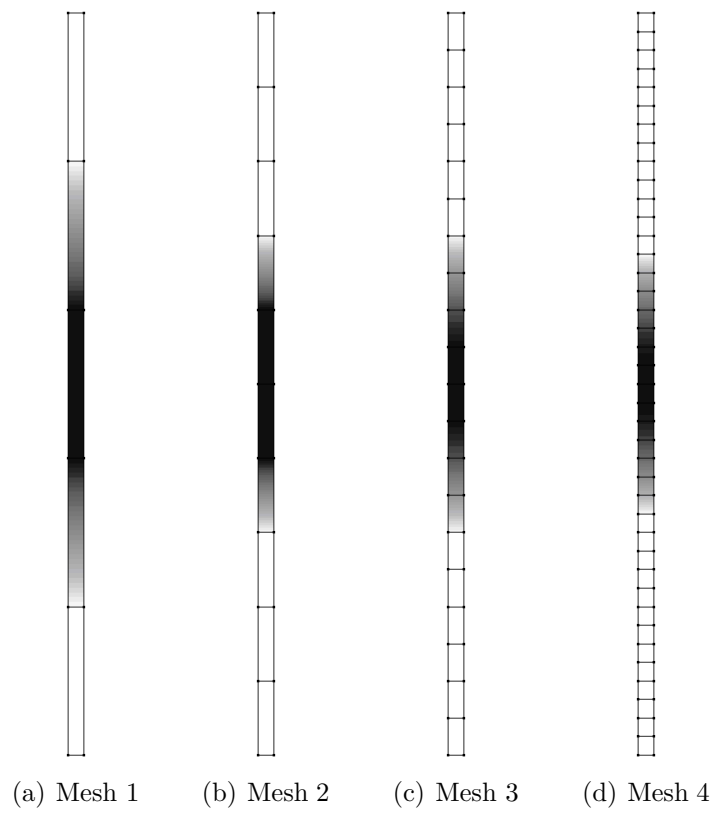
Figure 6.13: Infinite shear layer - Micropolar FEM with constrained microrotations and uniform material - $G_c = 3000$ N/mm^2 - $L_b = 5.0$ mm - Damage initiation

6.3 Uniaxial stress state: numerical localization

The problem of numerical localization was investigated considering the sample illustrated in Fig. 6.14(a), constituted by a square panel in a plane-stress state with unitary thickness, loaded in the x direction. The same material parameters of the uniaxial stress state investigated analytically in Chapter 5 were adopted, with Young's modulus E = 20000 N/mm^2, Poisson's ratio $\nu = 0.30$, and shear modulus G = 7692.31 N/mm^2. The *Marigo's* scalar damage model was adopted (Eq. (2.34)), with the following parameters for the exponential damage law, $\alpha = 0.999$, $\beta = 500$ and K$_0$ = 5 $\times 10^{-5}$, leading to the constitutive behaviour depicted in Fig. 6.14(b). As observed in Section 5.4.2, the classic continuum model in an uniaxial stress state with the aforementioned parameters attains the localization condition as soon as damage initiates (Fig. 5.1).

(a) Geometry   (b) Constitutive behaviour
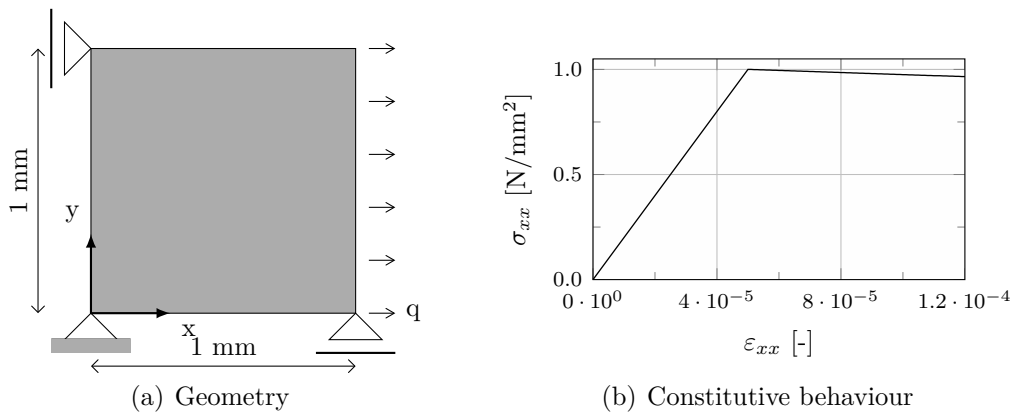
Figure 6.14: Numerical localization - Square panel

6.3.1 FEM simulations

In order to investigate the localization issues associated to the model of Fig. 6.14(a), the three finite element meshes of Fig. 6.15 were considered. They are composed by 8, 36, and 184 triangular elements, with mean element sizes of 0.5 mm, 0.25 mm, and 0.125 mm, respectively.

Remark 6.3

The basic idea of this kind of tests is that as the number of elements increases (and then the number of integration points), the probability to have a perturbation in a certain variable, able to trigger a bifurcated solution, increases.

The FEM analyses were performed adopting a loading process driven by the *generalized displacement control method* (Yang and Shieh, 1990), assuming a reference load q = 1

(a) Mesh 1   (b) Mesh 2   (c) Mesh 3
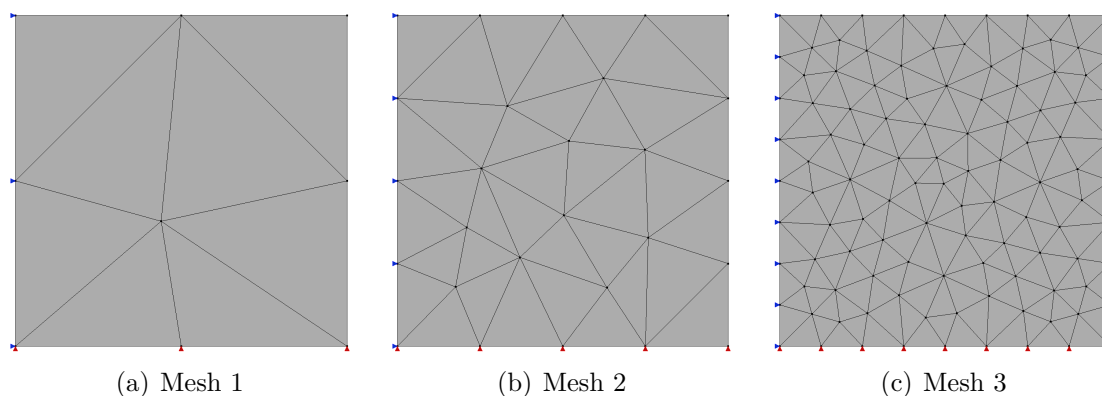
Figure 6.15: Numerical localization - FEM meshes

N/mm, an initial loading factor increment of 0.005, and a tollerance for convergence in relative displacement of 1×10^{-4}. All the simulations presented in this section were performed considering the tangent approximation of the constitutive operator. The results of the analyses, in terms of horizontal displacement plotted against the load factor, are illustrated in Fig. 6.16. As it can be observed, the coarsest meshes exhibited stable and convergent solutions, coherent with the expected constitutive behaviour (Fig. 6.14(b)), while the most refined one presented an instability as soon as the damage initiated, indicating the presence of a bifurcation due to numerical localization. The third mesh lost convergence as the peak value of the load factor was reached, and wasn't able to represent the post-peak branch. The prediction of the analytical investigation of Section 5.4.2 appears then to be correct, up to this point.

6.3.2   Regularization by micropolar formulation

The analytical investigation presented in Section 5.4.2 pointed out that the micropolar continuum theory, under certain values of its material parameters, should be able to prevent localization to occour. For a uniaxial stress state as the one considered here, with the same material parameters, it has been shown that the adoption of a Cosserat's shear modulus $G_c = 2500$ N/mm^2 is sufficient to guarantee a positive value of the localization indicator (Fig. 5.2). Hence, with the adoption of such continuum description it should be possible to regularize the behaviour of the otherwise unstable analyses illustrated in Fig. 6.16.

The finite element analyses of the meshes illustrated in Fig. 6.15 were repeated using the micropolar theory instead of the classic one, considering two different values of the Cosserat's shear modulus: $G_c = 2500$ N/mm^2, for which the localization condition is not verified at the onset of damage, and $G_c = 500$ N/mm^2, for which the localization condition is attained as soon as the damage initiates. The internal bending length was set to $L_b = 1$ mm; however, it is remarked that, as long as the solution is uniform, such parameter

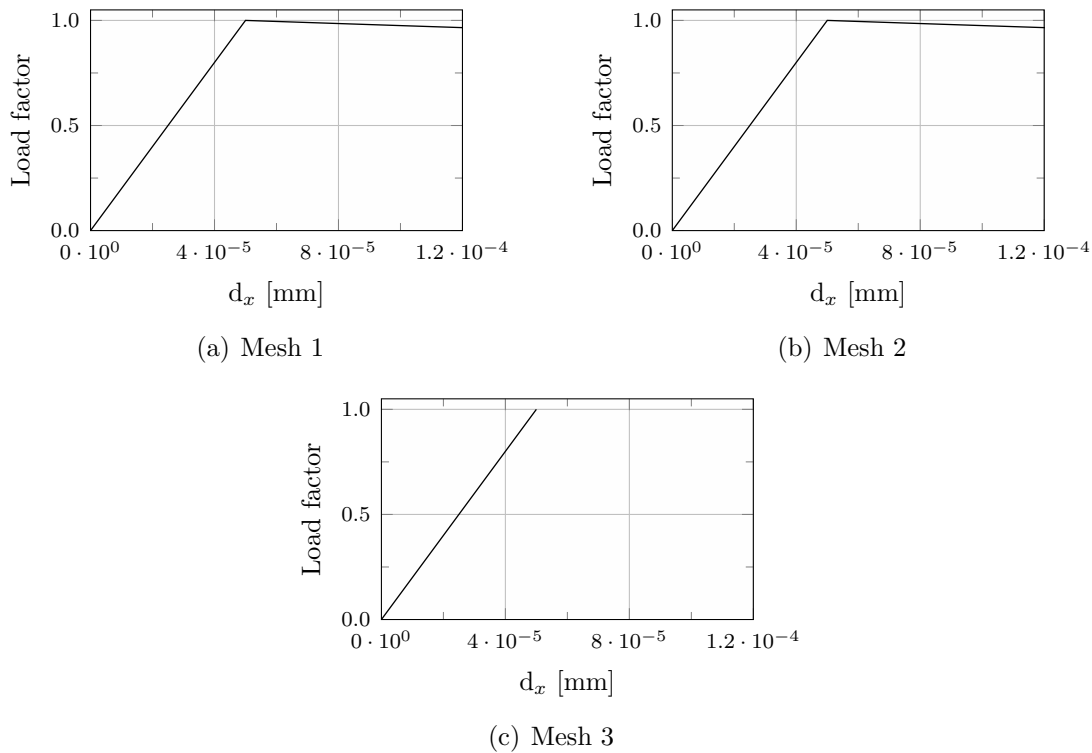(a) Mesh 1

(b) Mesh 2

(c) Mesh 3

Figure 6.16: Numerical localization - FEM - Equilibrium paths

has no influence on the onset of localization.

The results of these analyses are illustrated in Fig. 6.17. As predicted by the analytical investigation of Section 5.4.2, the value $G_c = 2500$ N/mm^2 resulted in the same solution for the three meshes (Fig. 6.17(a)), without loss of convergence due to the onset of localization. On the other hand, the case with $G_c = 500$ N/mm^2 was not able to regularize the analysis with the most refined mesh (Fig. 6.17(b)). As it can be observed in Fig. 6.17(b), the equilibrium path of the third mesh was different from the expected one, correspondent to the uniform solution. Though the solution wasn't convergent, there still was an improvement with respect to the analysis with the classic continuum model, which was not able to represent at all the post-peak equilibrium path.

(a) $G_c = 2500$ N/mm^2

(b) $G_c = 500$ N/mm^2
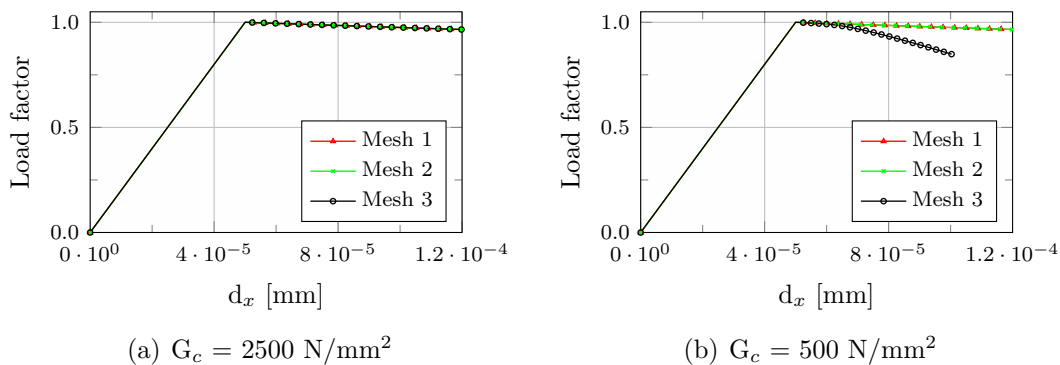
Figure 6.17: Numerical localization - Micropolar FEM - Equilibrium paths

Focusing on this divergent solution it is interesting to observe how the bifurcation due to numerical localization affected the distribution of the internal variables inside the analysed discrete model. For the scalar damage variable, for example, Fig. 6.18 shows how this variable tended to concentrate in specific parts of the model, and to go to zero elsewhere.
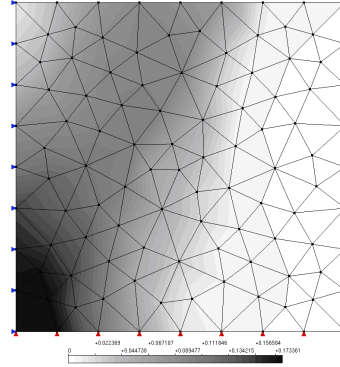
Figure 6.18: Numerical localization - Micropolar FEM- Scalar damage variable

6.3.2.1   Localization indicator: numerical evaluation

The results discussed up to this point allowed to emphasize the role of the Cosserat's shear modulus on the pathological effects that appear in simulations where numerical localization occours, confirming the analytical predictions presented in Chapter 5. Further informations on the relation between numerical localization, localization indicator, and Cosserat's shear modulus, can be drawn performing a *numerical evaluation* of the localization indicator. Following the same procedure presented by the author in Gori et al. (2017*d*), the sample of Fig. 6.14(a) was investigated performing the localization analysis discussed in Chapter 5 using the values of the state variables calculated during the loading process at each integration point of the finite element model, instead of the analytical values of the uniaxial stress state as in Section 5.4.2.

Fig. 6.19 illustrates the results of such analysis, in terms of localization indicator at damage initiation for the most refined mesh. As it can be observed, the simulations performed with the classic medium (Fig. 6.19(a)) and with the micropolar one with G_c = 500 N/mm^2 (Fig. 6.19(b)) exhibited negative values of the localization indicator since damage initiation. On the other hand, the micropolar medium with G_c = 2500 N/mm^2 (Fig. 6.19(c)) manifested positive values of the localization indicator at each integration point, as predicted in Fig. 5.2; the numerical value of the localization indicator is q = 0.06234460, corresponding to a critical angle $\theta_n = 15°$, and it is equal to the minimum value illustrated in Fig. 5.2.

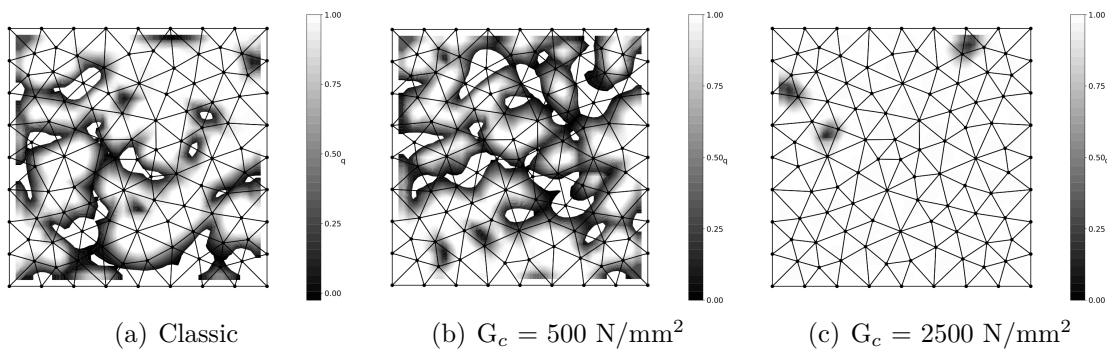(a) Classic   (b) G$_c$ = 500 N/mm^2 (c) G$_c$ = 2500 N/mm^2

Figure 6.19: Numerical localization - Numerical values of the localization indicator at damage initiation

---

Remark 6.4

In this case the numerical evaluation of the localization indicator has been presented only as a mean to confirm the analytical predictions discussed in Section 5.4.2. However, as it will be shown in Section 6.4.2.2, this procedure can be also useful to investigate different behaviours appearing in numerical simulations that cannot be predicted by analytical investigations.

6.3.3   Regularization by smoothed meshfree methods

In order to assert the behaviour of smoothed meshfree methods under conditions of numerical localization, the example depicted in Fig. 6.14(a) was investigated using both the NS-PIM and ES-PIM strategies discussed in Chapter 4. The adopted discretizations are illustrated in Fig. 6.20 for the NS-PIM method, and in Fig. 6.21 for the ES-PIM method; in these figures, nodes, smoothing domains, and underlying triangular cells are depicted. As it can be observed, node- and edge-based smoothing domains were constructed using as underlying triangular cells the finite elements depicted in Fig. 6.15.

(a) Mesh 1   (b) Mesh 2   (c) Mesh 3
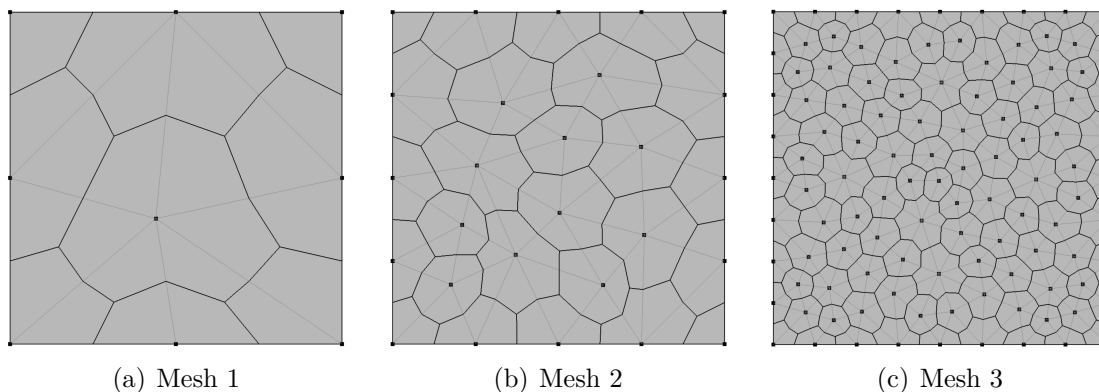
Figure 6.20: Numerical localization - NS-PIM discretizations

(a) Mesh 1 (b) Mesh 2 (c) Mesh 3
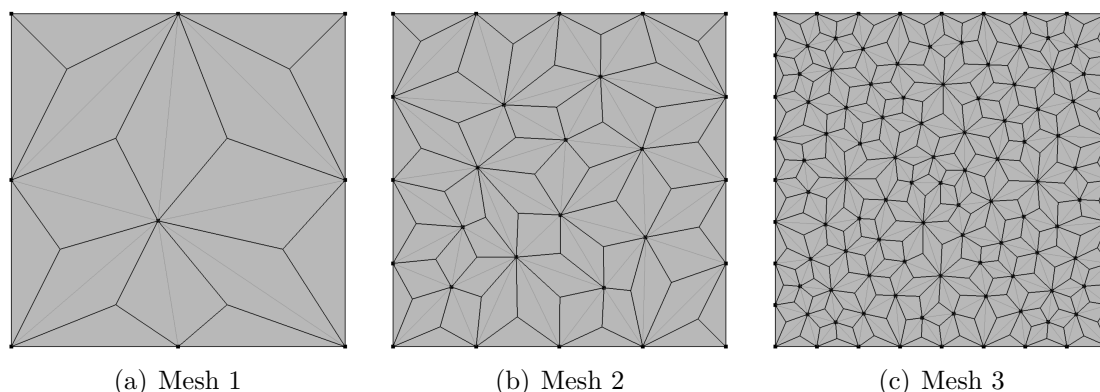
Figure 6.21: Numerical localization - ES-PIM discretizations

Regarding the generation of support domains, both the T3 and the T6/3 schemes were adopted. The shape functions were constructed with both the *point interpolation method* and *radial point interpolation method with polynomial reproduction*. For the latter, MQ radial basis functions were adopted (Eq. (4.21)), with C = 1.42 and q = 1.03, with a number of polynomial terms equal to 3. Like for the finite element method, the non-linear analyses were performed adopting a loading process driven by the *generalized displacement control method* (Yang and Shieh, 1990), assuming a reference load q = 1 N/mm, an initial loading factor increment of 0.005, and a tollerance for convergence in relative displacement of 1×10^{-4}, considering the tangent approximation of the constitutive operator.

Concerning the regularization of numerical instabilities due to localization, the plots of Fig. 6.22 illustrate that, in this specific situation, the NS-PIM didn't present any significative improvement with respect to the finite element method. The coarser mesh exhibited the same results for all the simulations, coherent with the expected constitutive behaviour (Fig. 6.14(b)), except for the case NS-RPIM T3, where a snap-back appeared in the post-peak branch. The intermediate mesh manifested an instability and a snap-back in the NS-PIM T3 and NS-PIM T6/3 analyses, respectively. The NS-RPIM T3 was able to represent the post-peak branch with the intermediate mesh, though divergent from the expected one. The NS-RPIM T6/3, instead, was able to correctly represent the post-peak phase with the intermediate mesh. Regarding the finer mesh only the NS-RPIM T6/3 was able to give a partial representation of the post-peak branch, though different from the expected one; with the other configurations the analyses arrested at damage initiation.

As highlighted by the plots of Fig. 6.23, the simulations performed with the ES-PIM clearly exhibited a better behaviour with respect to the ones with the NS-PIM, in the analysis of the example of Fig. 6.14(a). The analyses performed with the coarser mesh exhibited the same post-peak behaviour in all the considered cases, coherent with the adopted constitutive law (Fig. 6.14(b)). The behaviour of the intermediate mesh was represented correctly with the T6/3 scheme, while the combinations ES-PIM T3 and ES-RPIM T3 manifested instabilities at damage initiation. The cases ES-PIM T3, ES-PIM

(a) NS-PIM T3

(b) NS-PIM T6/3
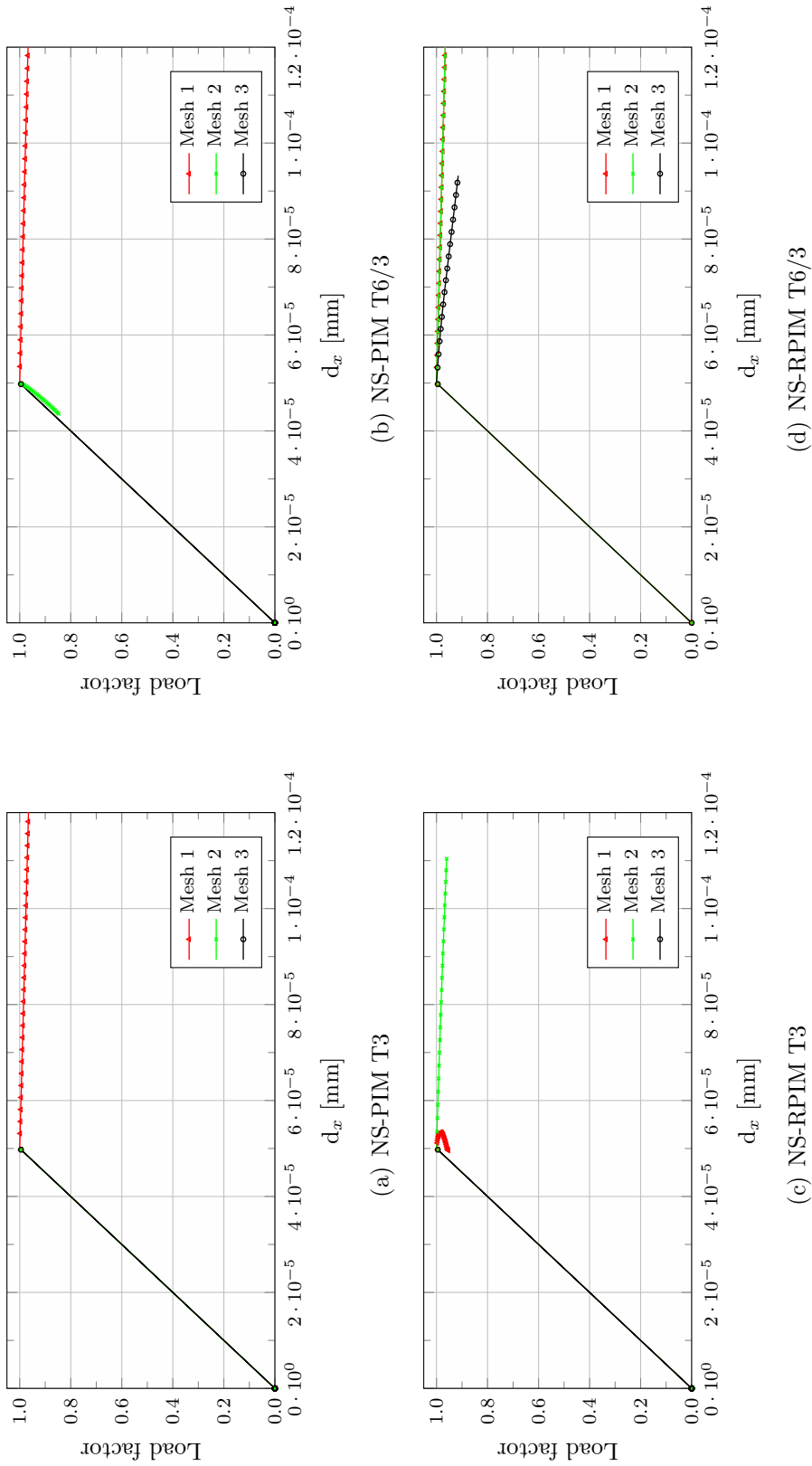
(c) NS-RPIM T3

(d) NS-RPIM T6/3

Figure 6.22: Numerical localization - NS-PIM - Equilibrium paths

T6/3 and ES-RPIM T3 with the most refined mesh presented a divergent equilibrium path, The analysis performed with the case ES-RPIM T6/3 was the only one able to correctly represent the post-peak branch with the most refined mesh, showing a result analogous to the one obtained with the finite element analysis of the micropolar model with $G_c = 2500$ N/mm^2 (Fig. 6.17(a)).

Remark 6.5

A first conclusion that can be drawn from the discussions above is that the ES-PIM, especially in its version with radial basis functions with polynomial reproduction and T6/3 selection scheme, appears to be better suited as a discretization strategy for problems where numerical localization may occour if compared to the NS-PIM and to the standard FEM, at least for the example discussed here. Focusing on the mesh-free approach, the radial basis functions with polynomial reproduction provided more stable solutions than the polynomial ones. Regarding the regularization of numerical instabilities due to localization, the results presented above clearly indicate that the T6/3 scheme was able to produce better results than the T3 scheme. This last conclusion seems to corroborate the hypothesis discussed in Section 4.2.5 that point interpolation methods, as other meshfree methods, should be able to regularize problems where localization occours due to their *intrinsic non-local nature* (as observed in Chen et al. (2000) for *reproducing kernel methods*). Regarding these considerations, it is important to emphasize that the results which they are based on were obtained using a single set of parameters for the MQ radial functions; though, as pointed out by Liu (Liu, 2009), in presence of polynomial reproduction the solution should be less dependent on variations in the shape parameters of the radial functions, it is worth to note that variations in such parameters could lead to different performances regarding the regularization effects.

Remark 6.6: ES-RPIM and localization indicator

As illustrated in Fig. 6.23(d), the configuration ES-RPIM T6/3 was able to perform correctly the non-linear analysis of the sample of Fig. 6.14(a) with all the discretizations of Fig. 6.21, presenting results analogous to the ones obtained with the finite element method combined with the micropolar theory. As already discussed, the regularization effects of the micropolar model are related to the value of the Cosserat's shear layer and of the localization indicator: the case with $G_c = 2500$ N/mm^2, corresponding to a positive localization indicator all along the analysis (see, e.g., Fig. 5.2), was able to provide a regularized solution, while the case with $G_c = 500$ N/mm^2,
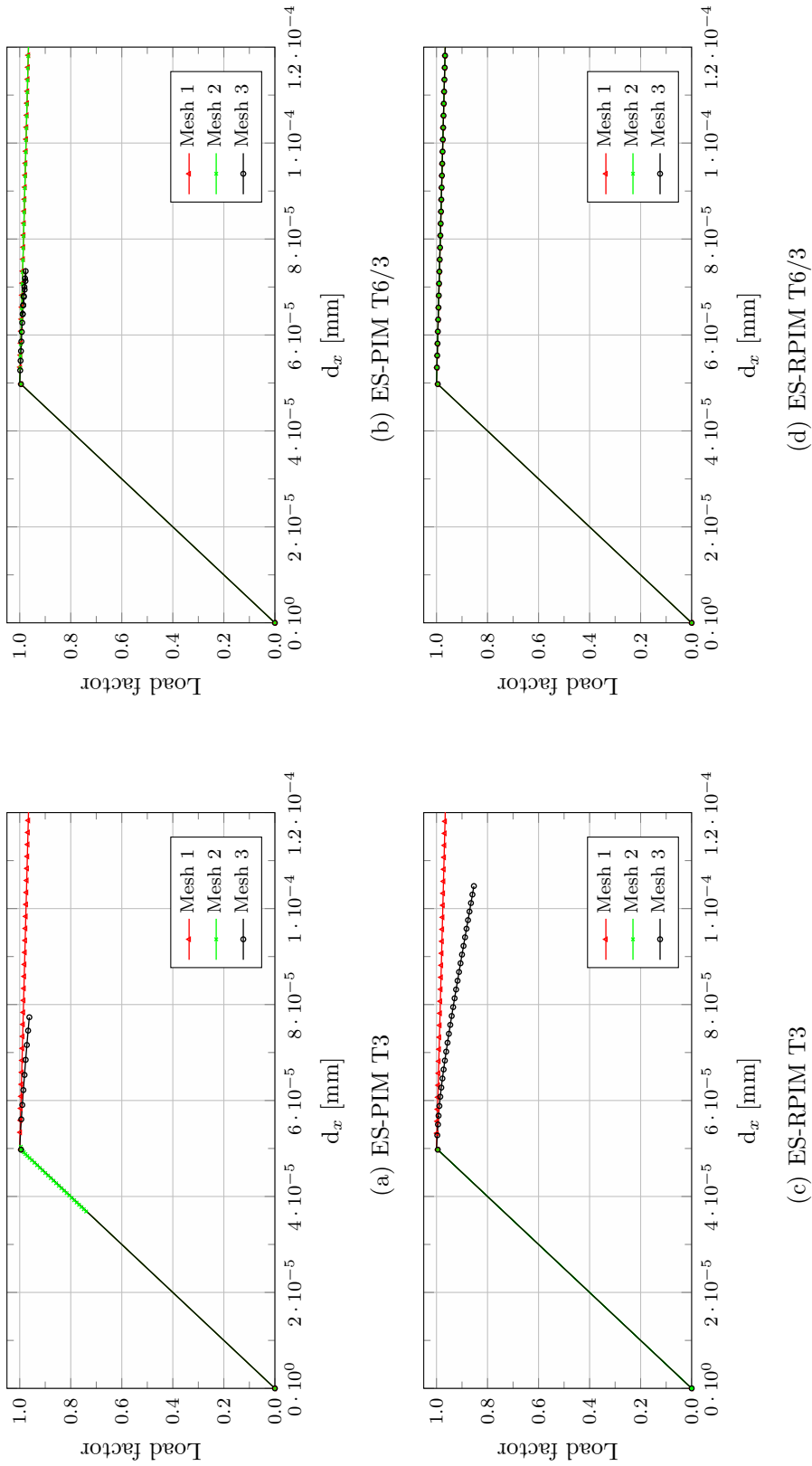
(a) ES-PIM T3

(b) ES-PIM T6/3

(c) ES-RPIM T3

(d) ES-RPIM T6/3

Figure 6.23: Numerical localization - ES-PIM - ES-PIM - Equilibrium paths

for which the localization indicator was negative (see, e.g., Fig. 5.2), wasn't able to provide a regularized solution. It is interesting to observe that the regularization effect provided by the ES-RPIM T6/3 for the examined problem is different in nature from the one of the micropolar model. Indeed, as it can be observed in Fig. 6.24, for example, though exhibiting regularization effects, the simulations performed with the ES-RPIM T6/3 still presented a negative localization indicator since damage initiation, like in the case of FEM simulation with the classic continuum theory.
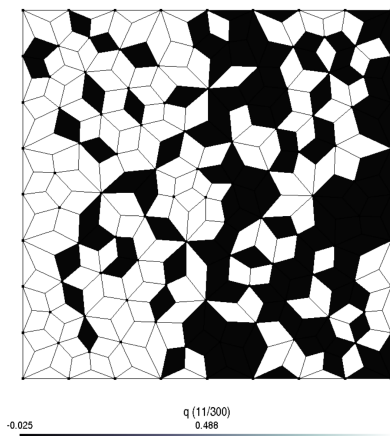
Figure 6.24: Numerical localization - ES-RPIM T6/3: localization indicator

6.3.4 Micropolar NS-PIM and ES-PIM

Once pointed out the regularization properties of both the micropolar formulation and smoothed meshfree methods, the analysis of the sample illustrated in Fig. 6.14(a) were repeated combining these two strategies. Comparing Fig. 6.22 with Fig. 6.25, it can be observed how the adoption of the micropolar model with $G_c = 2500$ N/mm^2 improved the results obtained with the NS-PIM; as for the classic formulation, the most accurate results were obtained with the combination NS-RPIM T6/3, which was able to correctly reproduce the equilibrium path of all the three meshes. Also the results obtained with the ES-PIM were enhanced by its combination with the micropolar formulation. In this case all the analyses exhibited convergent results, except the ones of the most refined mesh with the combinations ES-PIM T3 and ES-RPIM T3, as well as the one of the intermediate mesh with the ES-RPIM T3 which presented a snap-back (Fig. 6.26).

6.4 Uniaxial stress state: induced localization

The problem of induced localization was investigated considering the sample illustrated in Fig. 6.27(a), constituted by a square panel in a plane-stress state with unitary thickness, loaded in the y direction. The material parameters were choosen in order to match the ones adopted in Section 5.4.2 for the analytical localization investigation of the uniaxial
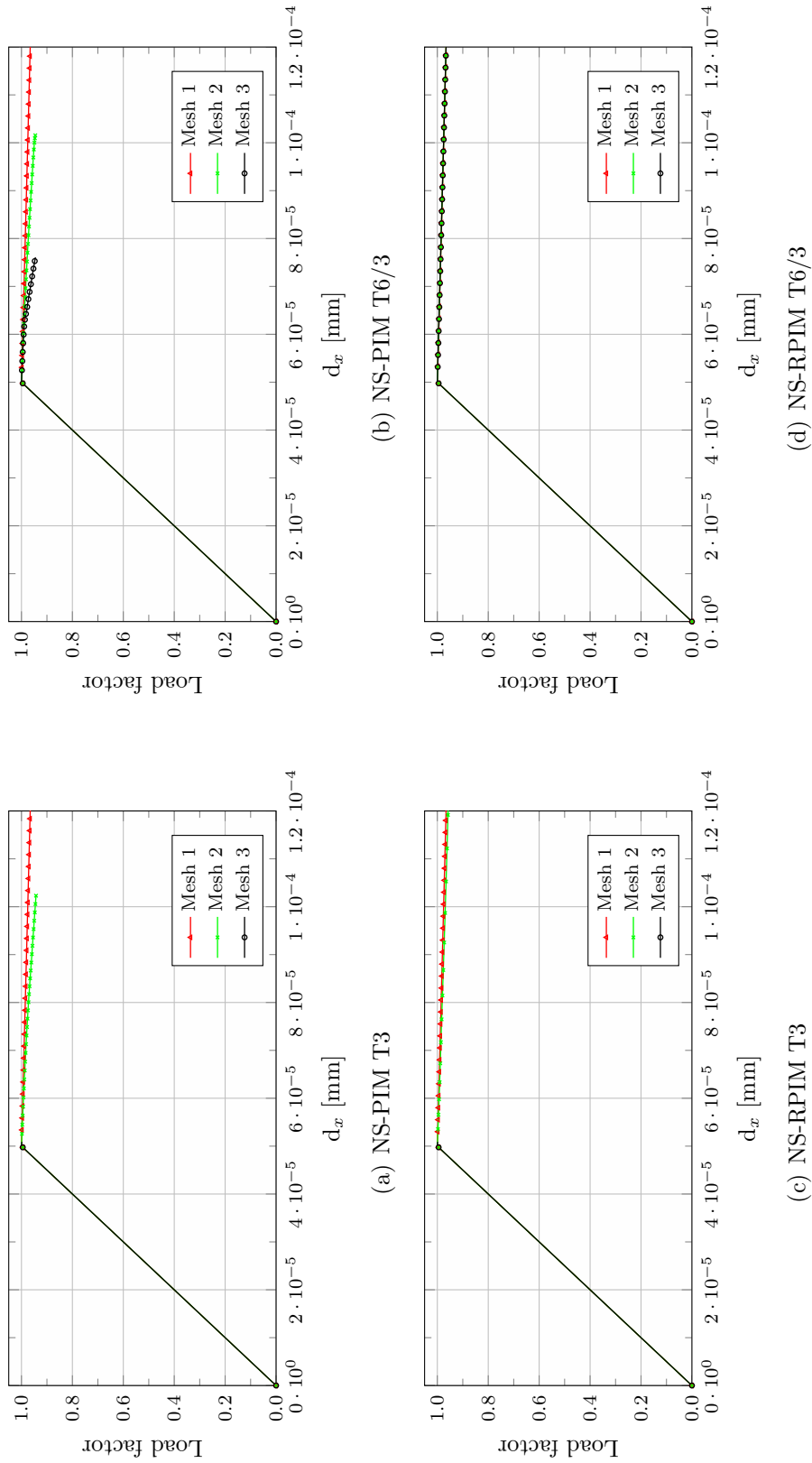
(a) NS-PIM T3

(b) NS-PIM T6/3

(c) NS-RPIM T3

(d) NS-RPIM T6/3

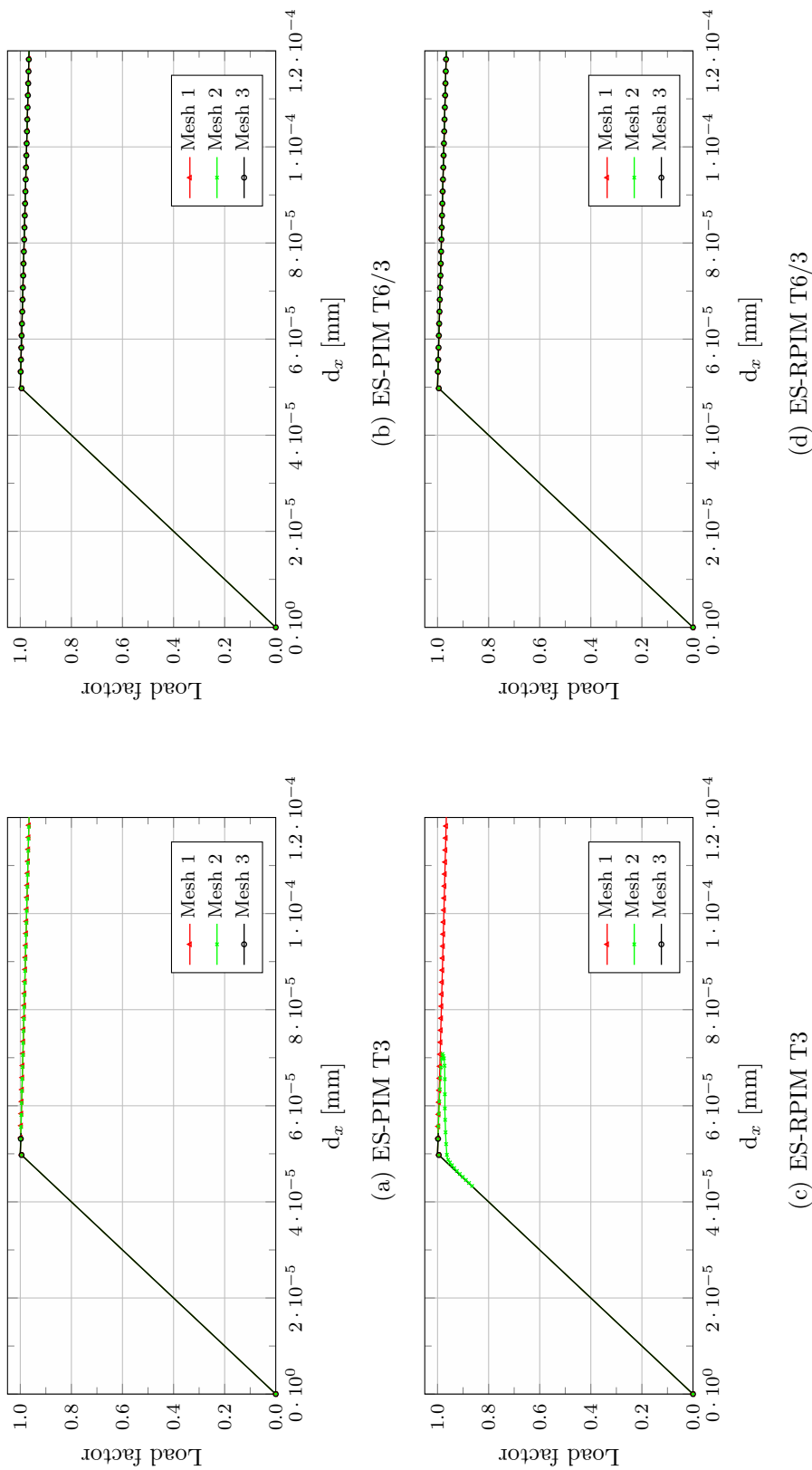Figure 6.25: Numerical localization - Micropolar NS-PIM - $G_c = 2500$ N/mm^2 - Equilibrium paths

Figure 6.26: Numerical localization - Micropolar ES-PIM - $G_c = 2500$ N/mm^2 - Equilibrium paths

stress state, with Young's modulus E = 20000 N/mm², Poisson's ratio ν = 0.30 and shear modulus G = 7692.31 N/mm². The *Marigo's* scalar damage model was adopted (Eq. (2.34)), with the following parameters for the exponential damage law, α = 0.999, β = 500 and K_0 = 5 ×10⁻⁵, corresponding to the constitutive behaviour depicted in Fig. 6.27(b). As for the previous example, these values of the material parameters and damage law are such that the condition for discontinuous failure is attained as soon as the damage initiates (Fig. 5.2). In order to trigger a bifurcated solution, two symmetric weakened zones were placed in the model (the hatched areas in Fig. 6.27(a)), characterized by a slightly reduced value of K_0, with size 0.1 mm × 0.2 mm, which was kept constant for all the FEM and meshfree discretizations.

(a) Geometry   (b) Constitutive behaviour
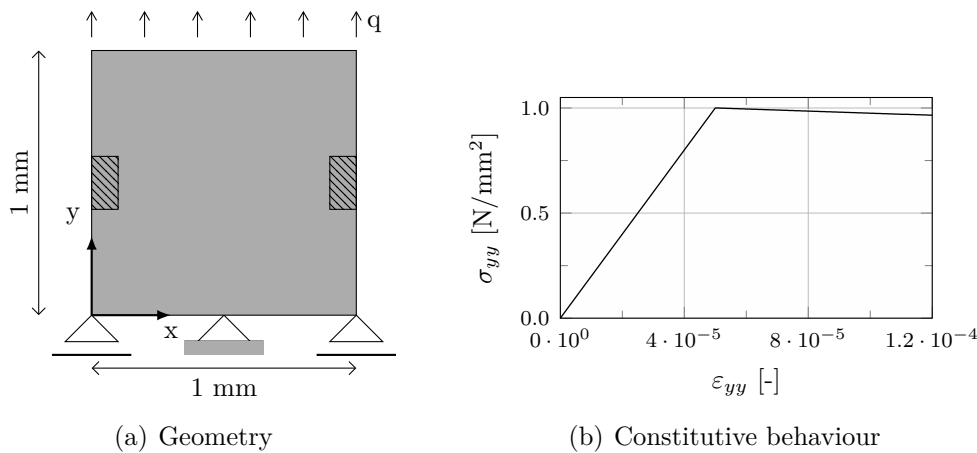
Figure 6.27: Induced localization - Square panel

6.4.1   FEM simulations

The effects of induced localization on the model of Fig. 6.27(a) were first investigated using three FEM meshes composed, respectively, by 100, 400, and 1600 four-nodes quadrilateral elements Fig. 6.28, with size 0.1 mm × 0.1 mm, 0.05 mm × 0.05 mm, and 0.025 mm × 0.025 mm. Since the localization is *induced*, the use of different discretizations is not related to the probability of numerical instability to manifest, it is a mean to illustrate the strong mesh dependency of the bifurcated solutions that may appear in the post-peak branch.

Remark 6.7: Gori et al. (2017*b*)

The results of this example had already been presented by the author in a paper devoted to the phenomenon of discontinuous failure (or localization) in elastic-degrading micropolar media (Gori et al., 2017*b*). There, the meshes depicted in Fig. 6.28 were analysed using both the classic and the micropolar continuum theories, as in the

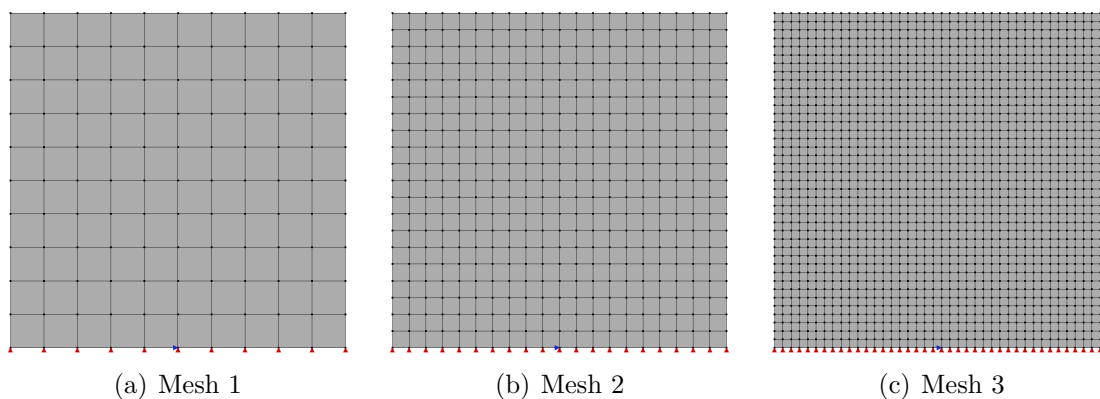(a) Mesh 1   (b) Mesh 2   (c) Mesh 3

Figure 6.28: Induced localization - FEM meshes

present section of this manuscript. The simulations investigated in the aforementioned paper have been performed again, before collecting their results in this manuscript. As the reader will notice, the results presented here are slightly different from the ones of the cited paper. For example, the contour plots of the damaged states in the paper present some asymmetric configurations that differs from the ones presented here, which are all symmetric. In the author opinion, these discrepancies are due to the fact that some of the simulations presented in (Gori et al., 2017*b*) were affected also by numerical localization, beside induced localization. Since, as already stated, the former is a rather *aleatory* phenomenon, it didn't manifested once the simulations were repeated. The symmetric defects depicted in Fig. 6.27(a) should always produce a symmetric damaged configuration; an asymmetric one can only be a consequence of a numerical instability of the discrete model.

The FEM analyses were performed adopting a loading process driven by the *generalized displacement control method* (Yang and Shieh, 1990), assuming a reference load q = 1 N/mm, an initial loading factor increment of 0.005, and a tollerance for convergence in relative displacement of 1×10^{-4}. The nodes at the top of each mesh were constrained to have the same vertical displacement, by means of the *master-slave* imposition method, assuming the node of coordinates (0.5, 1.0) as master. All the simulations were performed considering the tangent approximation of the constitutive operator. The results of the analyses, in terms of vertical displacement plotted against the load factor, are illustrated in Fig. 6.29. As it can be observed, the results produced by each mesh were different.

The fact that each analysis produced different results is emphasized by the contour plots of the scalar damage variable illustrated in Fig. 6.30. There, the distribution of the scalar damage variable across the discrete model is represented for the three meshes at the steps 11 (damage initiation), 15, 100, 200, and 300 of the analysis, the images at the left illustrating the step at damage initiation. These figures clearly illustrate how the solution in terms of damaged configuration changes upon mesh refinement.
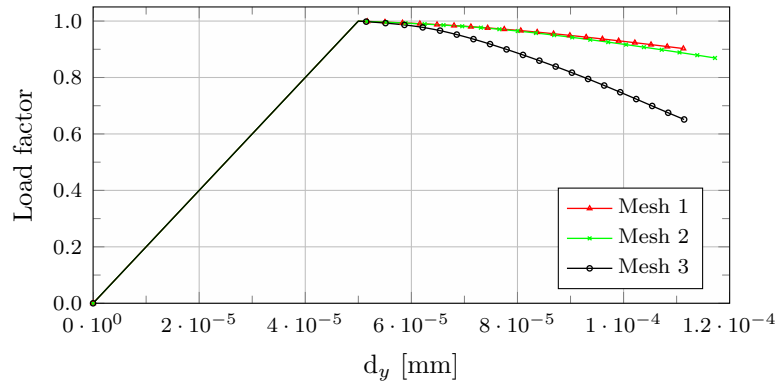
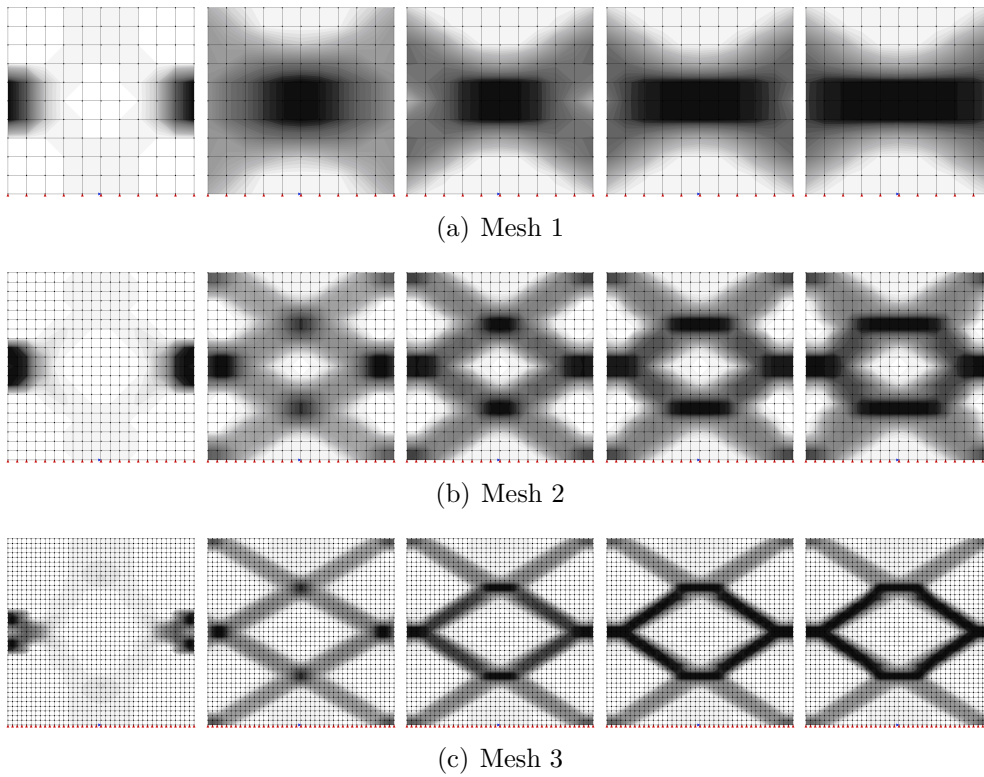Figure 6.29: Induced localization - FEM - Equilibrium paths

(a) Mesh 1

(b) Mesh 2

(c) Mesh 3

Figure 6.30: Induced localization - Damage distribution

6.4.2   Regularization by micropolar formulation

As already done for the case of numerical localization, the finite element simulations of the model illustrated in Fig. 6.27(a) were repeated, adopting the micropolar formulation instead of the classic one. Two values of the Cosserat's shear modulus were adopted, $G_c = 2500$ N/mm^2 and $G_c = 500$ N/mm^2, while the value of the internal bending length was set to $L_b = 1$ mm. As already discussed in Section 6.3, the first value of the Cosserat's shear modulus should be capable to avoid localized configurations since, according to Fig. 5.2, it should be able to maintain a positive value of the localization indicator. The role of the internal bending length is slightly different than in the case presented in Section 6.3, and will be discussed in detail in Section 6.4.2.2.

The results of these analyses are illustrated in Fig. 6.31. The case with $G_c = 500$ N/mm^2 (Fig. 6.31(a)) produced divergent solutions, as in the case of the classic continuum model. On the other hand, as predicted in Fig. 5.2, the case with $G_c = 2500$ N/mm^2 was able to regularize the analysis, and allowed to obtain equilibrium paths that were objective upon mesh refinement (Fig. 6.31(b)), until the last steps of the analysis where the paths started to diverge.

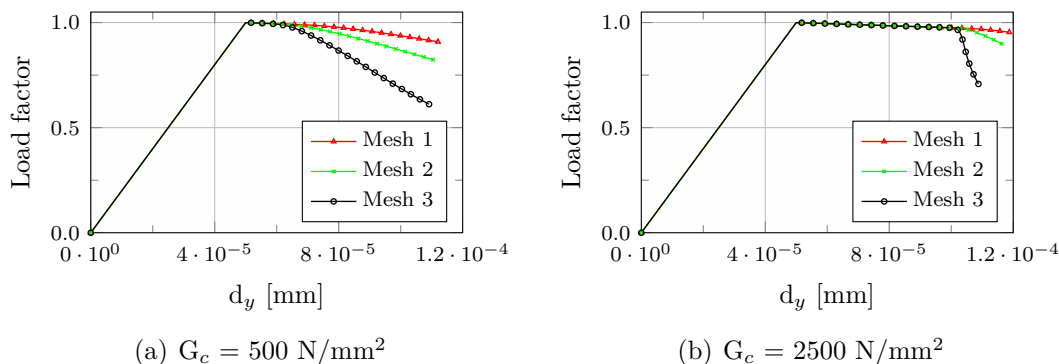(a) $G_c = 500$ N/mm^2 (b) $G_c = 2500$ N/mm^2

Figure 6.31: Induced localization - Micropolar FEM - Equilibrium paths

The regularization effects of the micropolar formulation are well emphasized also by the contour plots of the scalar damage variable illustrated in Figs. 6.32 and 6.33 for the steps 11, 15, 100, 200, and 300 of the analysis, the same steps adopted in Fig. 6.30. While the case with $G_c = 500$ N/mm^2 (Fig. 6.32) still showed mesh dependent damaged configurations as the classic model case, the analysis performed with $G_c = 2500$ N/mm^2 (Fig. 6.33) manifested a different behaviour. In the latter case indeed, the damaged zone was approximately the same for the three discretizations, except for the last steps of the simulations, where the damage was trapped in the central bands of elements, exhibiting a mode-I failure; this behaviour will be discussed in details in Section 6.4.2.2. Regarding the simulations performed with $G_c = 2500$ N/mm^2, the step 200 corresponds to a vertical displacement of the points at the top of the sample of $d_y = 9.78 \times 10^{-5}$ mm, right before the point of divergence in the plots of Fig. 6.31(b).

(a) Mesh 1
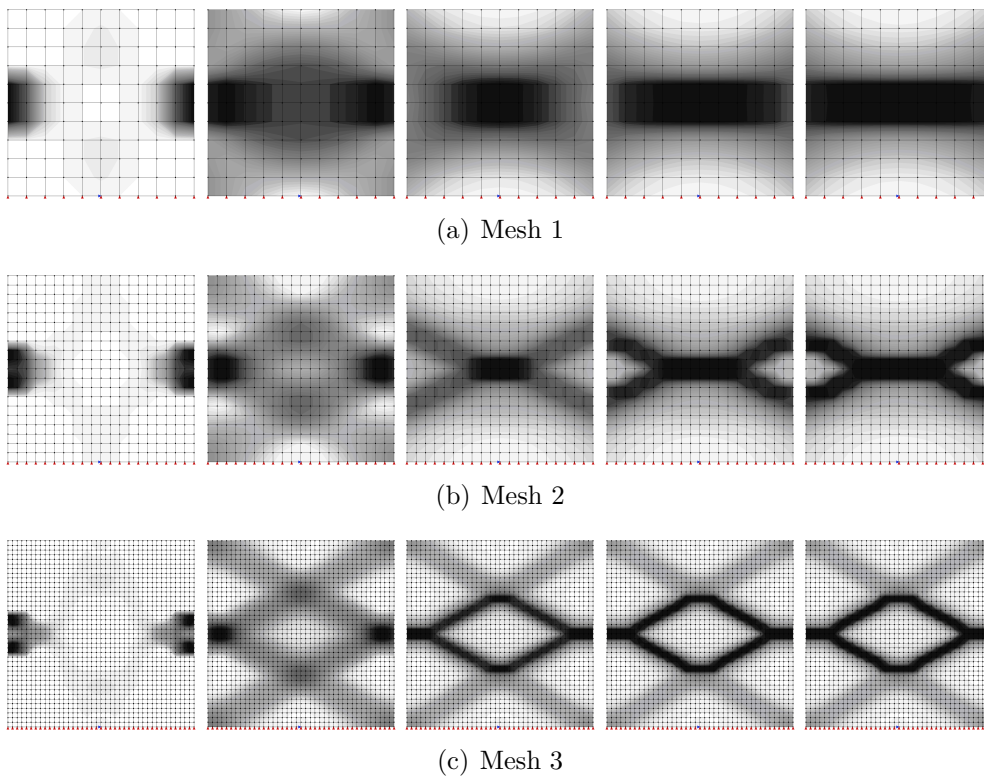
(b) Mesh 2

(c) Mesh 3

Figure 6.32: Induced localization - Damage distribution - $G_c = 500$ N/mm^2
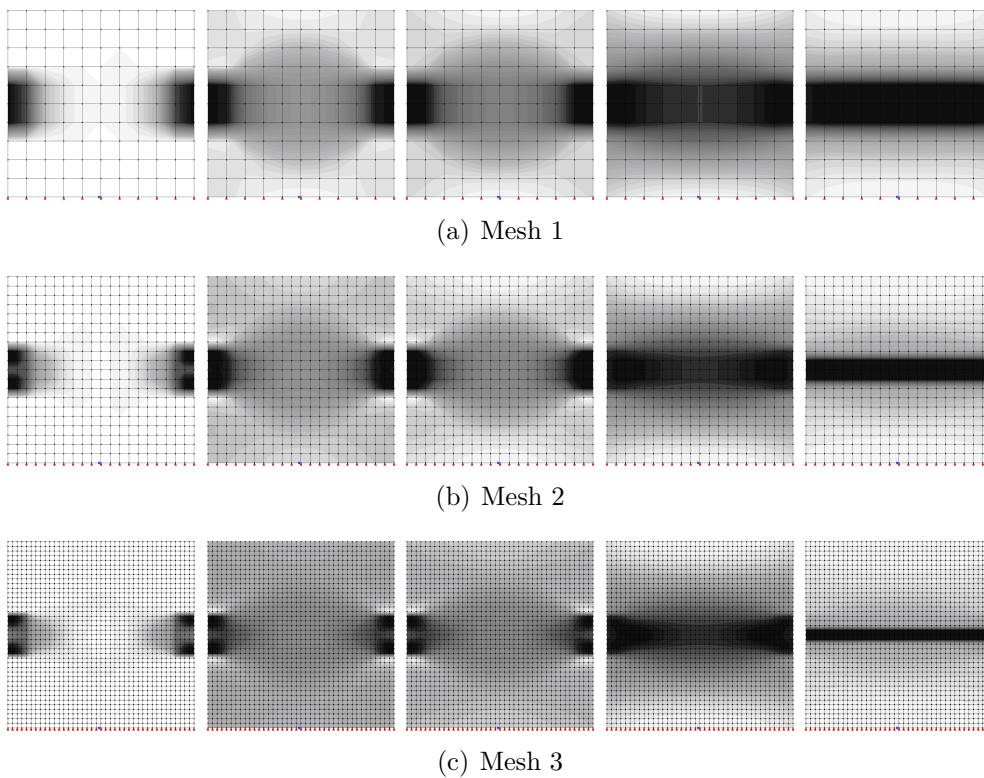

(a) Mesh 1

(b) Mesh 2

(c) Mesh 3

Figure 6.33: Induced localization - Damage distribution - $G_c = 2500$ N/mm^2

6.4.2.1   Localization indicator: numerical evaluation

As already done in Section 6.3.2.1 for the case of numerical localization, also the sample of Fig. 6.27(a) was investigated performing a numerical evaluation of the localization indicator, using the values of the state variables calculated during the loading process at each integration point[3]. The following Figs. 6.34 to 6.36 illustrate the results of this investigation for the most refined mesh, considering the same five steps of the previous figures.

<div style="border:1px solid black; padding:10px;">

Remark 6.8: Discrete localization analysis

The analytical investigations discussed in Section 5.4.2 were based on the hypothesis of uniaxial stress state; for the simulations presented in this section such hypothesis is valid only in the elastic phase and at damage initiation ($D \simeq 0$), and is lost as soon as damage grows ($D > 0$). This hypothesis clearly poses a limit to the applicability of such analytical investigations to discrete models. The discrete localization analysis, based on a numerical evaluation of the localization indicator, overcomes this limitation, and allow to investigates the discrete models for states beyond the onset of damage, for which the uniaxial stress state hypothesis is not rigorously applicable.

</div>

In Figs. 6.34 and 6.35 it can be observed that, as predicted analytically, the simulation with the classic medium and with the micropolar one with $G_c = 500$ N/mm^2 exhibited negative values of the localization indicator already at the step corresponding to damage initiation. In the subsequent steps, it can be observed how the values of the localization indicator follow the same patterns of the damage variable depicted in Figs. 6.30 and 6.32, presenting negative values all along the loading process.

As predicted by the analytical investigations, the simulation performed with the micropolar medium with $G_c = 2500$ N/mm^2 exhibited positive values of the localization indicator at the onset of damage (Fig. 6.36). The figures referring to steps 15 and 100 indicate that the localization indicator still presented positive values up to that point of the loading process, with the lower values in correspondence to the weakened zones of the sample. At step 200, right before the divergence point in the plots of Fig. 6.31(b), the distribution of the localization indicator is quite different from the one at the previous steps, with negative values appearing in some parts of the domain. The figure depicting the last step of the analysis emphasizes the presence of a *mode-I* localized deformation[4], with negative values of the localization indicator in correspondence to the central band of elements.

---

[3] The results of this investigation were presented by the author in Gori et al. (2017*d*).

[4] A *mode-I* localized deformation is characterized by a jump in the displacement gradient only in the normal direction to the discontinuity surface, $[\![\dot{\gamma}]\!] = \dot{\gamma}_A \, \bar{n} \otimes \bar{n}$, i.e., when the normal $\bar{n}$ and the polarization vector $\bar{p}_A$ coincide.
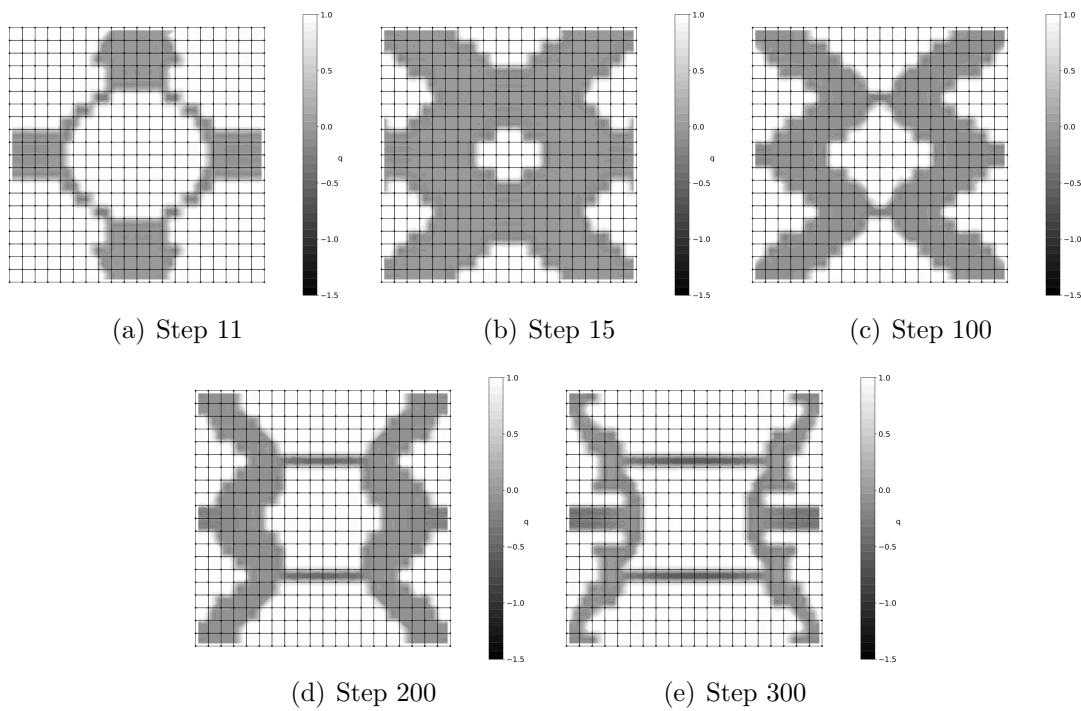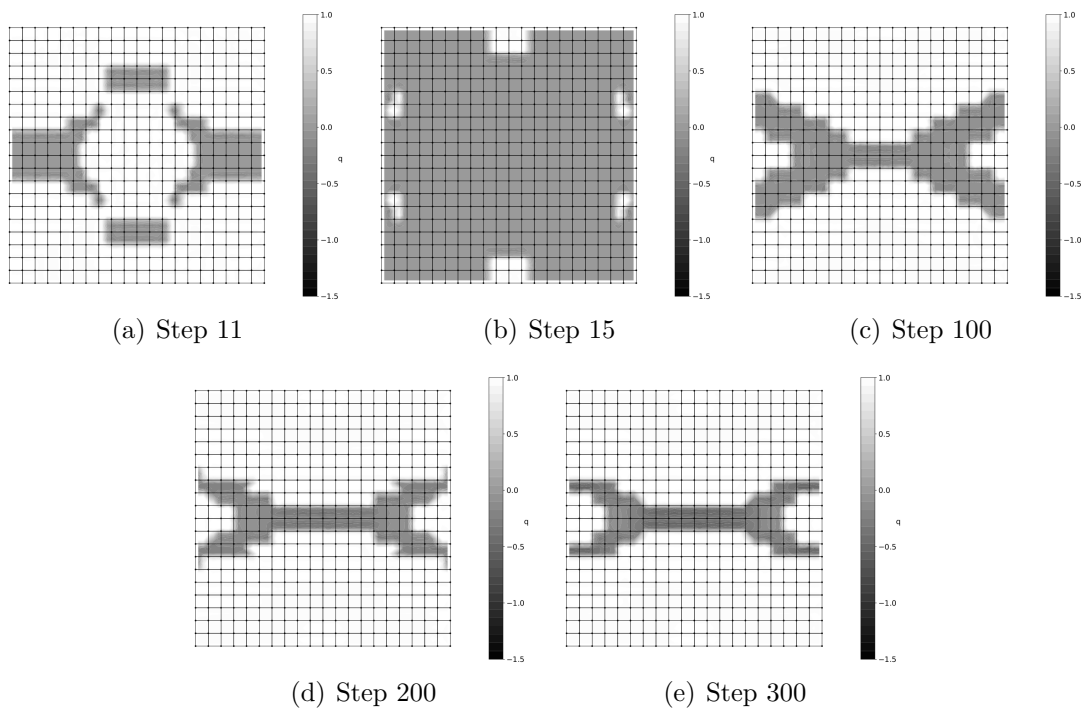
(a) Step 11   (b) Step 15   (c) Step 100

(d) Step 200   (e) Step 300

Figure 6.34: Induced localization - Localization indicator - Classic medium

(a) Step 11   (b) Step 15   (c) Step 100

(d) Step 200   (e) Step 300

Figure 6.35: Induced localization - Localization indicator - Micropolar medium - $G_c = 500$ N/mm^2

(a) Step 11   (b) Step 15   (c) Step 100

(d) Step 200   (e) Step 300
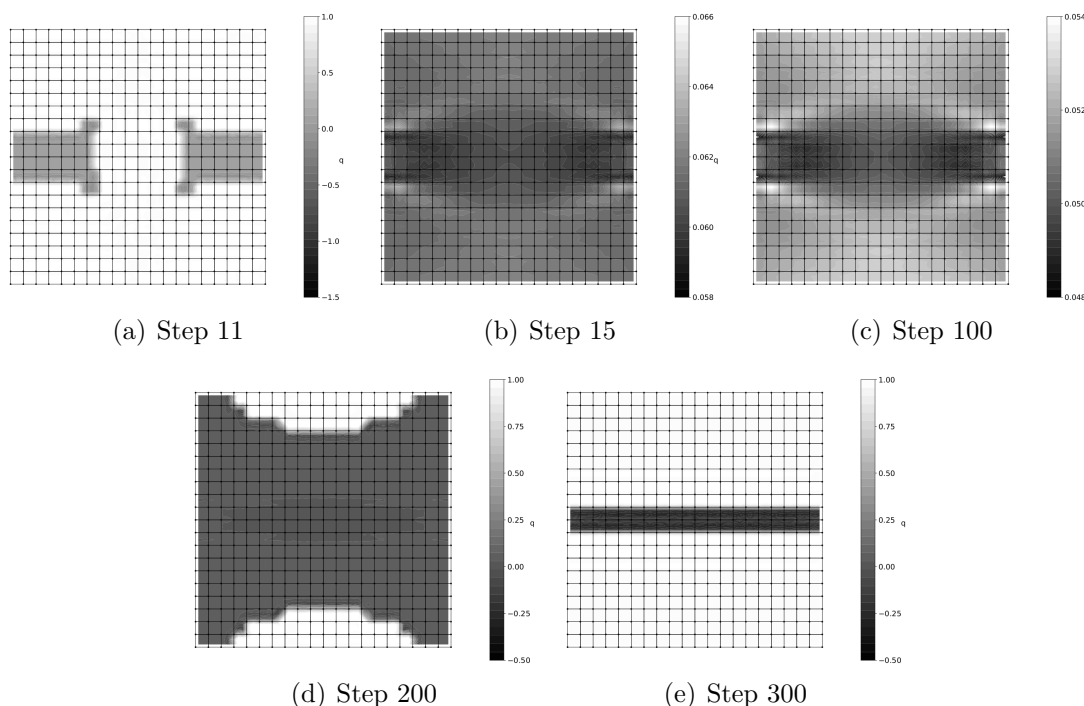
Figure 6.36: Induced localization - Localization indicator - Micropolar medium - $G_c = 2500$ N/mm^2

6.4.2.2   Mode-I failure and role of the internal bending length

The results discussed above allowed to emphasize the role of the Cosserat's shear modulus on the pathological effects that appear in numerical simulations where localization occours, confirming the analytical predictions of Section 5.4.2. Despite the regularization effects manifested in the simulations with the higher value of the Cosserat's shear modulus it is worth to note that, also for values of G_c such that the localization condition wasn't fulfilled at damage initiation, the problem wasn't fully independent on the mesh since, at a certain point of the loading process, the damage tended to be trapped in the central band of elements with a mode-I localized deformation; since the size of the central band of elements varied with the different discretizations, the numerical analyses became mesh-dependent after a certain damage threshold (Fig. 6.33).

The reason this mode-I localization in the final steps of the simulations passed undetected by the localization analysis of Section 5.4.2 has to be searched in the discrepancy between the analytical and the discrete models. Despite the fact that Fig. 5.3 indicates that also the case of uniaxial stress state with $G_c = 2500$ N/mm^2 attains the localization condition at a certain damage level, the associated critical angle doesn't match the mode-I failure manifested by the discrete model. Indeed, the values of the localization indicator in that figure had been obtained analytically under the hypothesis of an uniaxial stress state, hypothesis that is lost as soon as damage develops. Another difference is due to the fact that, as pointed out in Iordache and Willam (1998), since the stress state is no

more uniform after damage initiation, the limit values of H^*_{df} may become locally higher than the ones predicted analytically (i.e., with lower values of the localization indicator), in such a way as to attain the localization condition.

As pointed out by the author in a previous publication (Gori et al., 2017d), this mode-I failure is strictly related to the internal bending length of the micropolar model. In the analytical investigations of Section 5.4.2, because of the assumed uniaxial stress state in which couple-stresses were absent, only the Cosserat's shear modulus had an active role on the values of the localization indicator. However, in the discrete models discussed above, as soon as damage initiated at the weakened zones of the sample the stress state was no longer a pure uniaxial one; couple-stresses arised, activating the internal bending length. As pointed out by the analytical investigation of the plate with a circular hole (Section 5.4.3), for sufficiently high values of the Cosserat's shear modulus, the onset of localization is ruled solely by the internal bending length, and the failure tends to be of a mode-I type. The role of the internal bending length in the present example was pointed out repeating the finite element analysis with the micropolar formulation with $G_c = 2500$ N/mm^2 adopting the value $L_b = 0.1$ mm, instead of the value $L_b = 1.0$ mm used in the simulations discussed above. The results depicted in Fig. 6.37 show that both the simulations manifested a similar behaviour, presenting convergent solutions up to a certain point of the analysis, where the paths started to diverge due to a mode-I failure. The main difference was that the analysis with $L_b = 0.1$ mm manifested the mode-I failure for a minor value of the vertical displacement with respect to the case with $L_b = 1.0$ mm, confirming, for this example, the prediction of Section 5.4.3 that for higher values of the Cosserat's shear modulus the localization is ruled solely by the internal bending length.

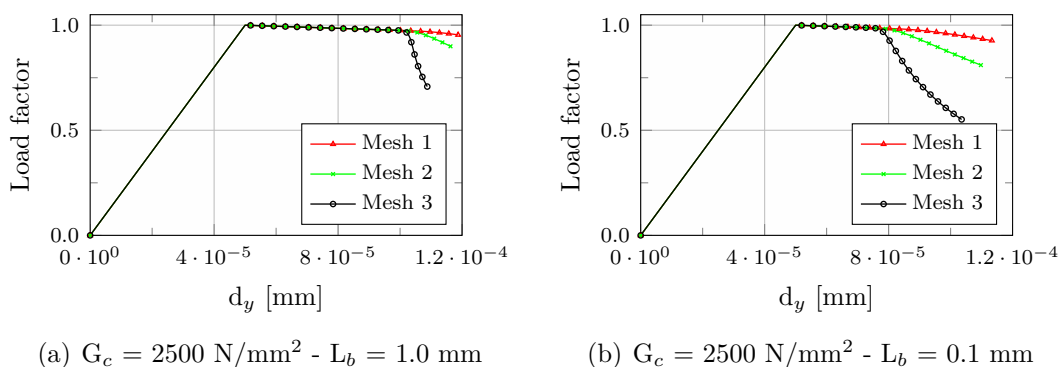(a) $G_c = 2500$ N/mm^2 - $L_b = 1.0$ mm   (b) $G_c = 2500$ N/mm^2 - $L_b = 0.1$ mm

Figure 6.37: Induced localization - Micropolar FEM - Equilibrium paths

The same conclusions can be drawn observing the results of the discrete localization analysis performed with the micropolar sample with $G_c = 2500$ N/mm^2 and $L_b = 0.1$ mm (Fig. 6.38). The first steps of the analysis exhibited results similar to the ones of the case with $L_b = 1.0$ mm (Fig. 6.36). However, it can be observed that the case with the reduced internal bending length already presented a mode-I localized deformation at

step 200, while at the same step the case with $L_b = 1.0$ mm was still presenting the first symptoms of localization.
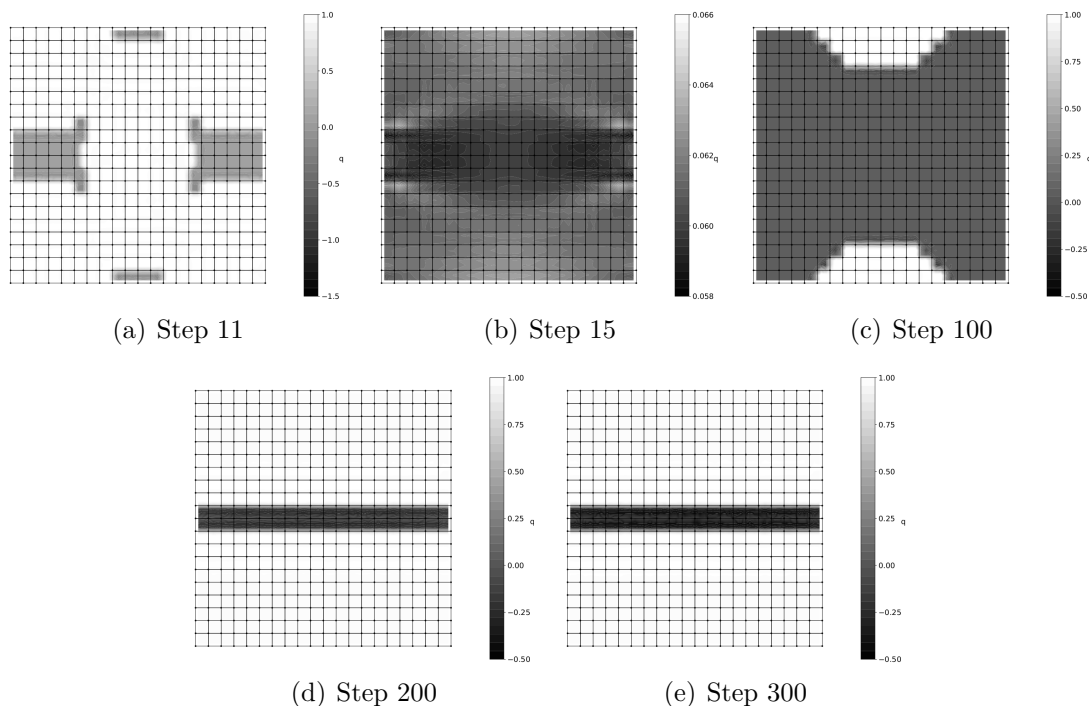

<div align="center">(a) Step 11   (b) Step 15   (c) Step 100</div>

<div align="center">(d) Step 200   (e) Step 300</div>

Figure 6.38: Induced localization - Localization indicator - Micropolar medium - $G_c = 2500$ N/mm^2 - $L_b = 0.1$ mm

6.4.3 Regularization by smoothed meshfree methods

The example of Fig. 6.27(a) was investigated also with the smoothed methods NS-PIM and ES-PIM, with the discretizations depicted in Figs. 6.39 and 6.40. As it can be observed, node- and edge-based smoothing domains were generated using as underlying cells the finite elements meshes depicted in Fig. 6.28, in order to maintain the same nodes distributions.
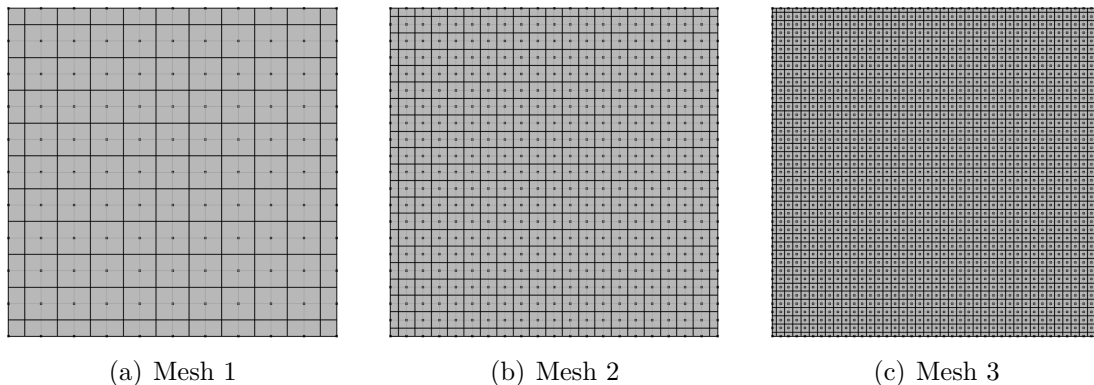

<div align="center">(a) Mesh 1   (b) Mesh 2   (c) Mesh 3</div>

Figure 6.39: Induced localization - NS-PIM discretizations

(a) Mesh 1   (b) Mesh 2   (c) Mesh 3
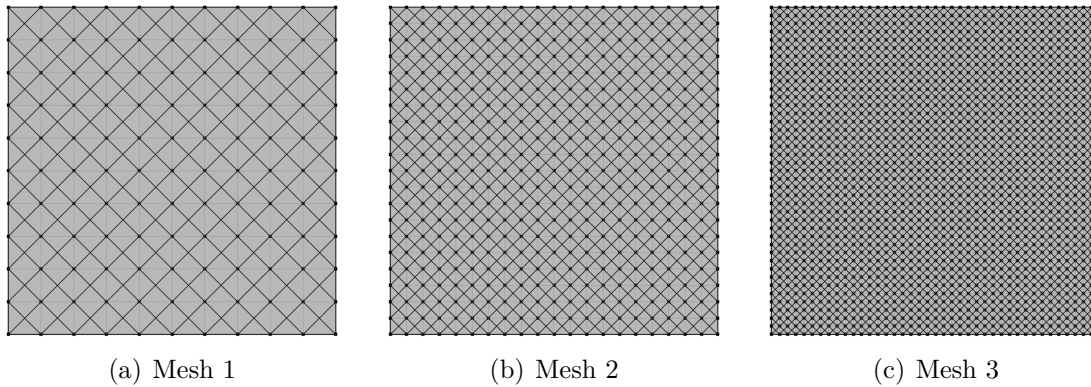
Figure 6.40: Induced localization - ES-PIM discretizations

The support domains were generated using both the T4 and the T12/4 schemes, the analogous for quadrilateral cells of the T3 and the T6/3 schemes (Remark 4.5). The shape functions were constructed with the *radial point interpolation method with polynomial reproduction*, with a number of polynomial terms equal to 3; the use of polynomial basis functions was avoided in this example, because with the T12/4 scheme they would have lead to singular moment matrices. The exponential radial basis function (Eq. (4.22)) was adopted, with c = -0.3635 for the mesh 1 and c = -1.4540 for the meshes 2 and 3. Like for the finite element method, the non-linear analyses were performed adopting a loading process driven by the *generalized displacement control method* (Yang and Shieh, 1990), assuming a reference load q = 1 N/mm, an initial loading factor increment of 0.005, and a tollerance for convergence in relative displacement of 1×10^{-4}, considering the tangent approximation of the constitutive operator.


Remark 6.9: Quadrilateral background cells

As discussed in Chapter 4, the smoothing domains of the NS-PIM and the ES-PIM are usually generated using triangular background cells, though a simulation performed with quadrilateral cells was presented in Zhang et al. (2015). Regarding the investigation of the sample of Fig. 6.27(a) with smoothed meshfree methods, in order to make a comparison with previously published FEM results based on quadrilateral elements (Gori et al., 2017b), quadrilateral background cells were used for the generation of the smoothing domains. It is worth to note that the regular nodal patterns depicted in Fig. 6.28 could have been easily reproduced also with triangular cells. However, the choice of quadrilateral cells was driven by the idea of having, for the T4 scheme at each integration point, the same number of support nodes as in the quadrilateral finite elements, since the extent of the support domain is an important factor in localization problems.

Despite the interesting results exhibited by the ES-PIM concerning localization is-

sues, as shown in the following paragraphs, it is necessary to emphasize that, at least for the example investigated in the present section, the use of quadrilateral background cells probably wasn't the optimal choice. Indeed, these simulations exhibited an high sensitivity to the choices regarding the radial basis functions; a wide preliminary investigation was necessary in order to find suitable parameters for the choosen function. This behaviour wasn't expected since smoothed point interpolation methods combined with radial basis functions with polynomial reproduction shouldn't be so sensitive to changes in the radial functions parameters (see, e.g., Liu (2009) and Wang and Liu (2002*b*)); hence, further investigations should be performed in the future in order to address this issue. In the author opinion this issue is almost certainly due to the use of quadrilateral background cells, since the smoothed methods have been shown to perform well with regular nodal patterns and T-schemes for support nodes selection (Liu, 2009).

Regarding the NS-RPIM, it was observed that both the T4 and the T12/4 schemes led to unstable analysis with the tangent approximation of the constitutive operator, which arrested as soon as damage started to develop. The ES-RPIM with T4 scheme was able to perform the analysis with the coarser mesh, though with results different from the expected ones in terms of equilibrium paths (Fig. 6.41(a)). The analysis with the intermediate mesh arrested a few steps after damage initiation, while the one with the finer mesh arrested at the onset of damage. Better results were obtained with the T12/4 scheme. As it can be observed in Fig. 6.41(b), the equilibrium paths obtained with the finer and intermediate meshes were stable and compatible with the expected one. The analyses with the coarser one instead, gave only a partial representation of the equilibrium path, since it exhibited slight perturbations at the final steps.
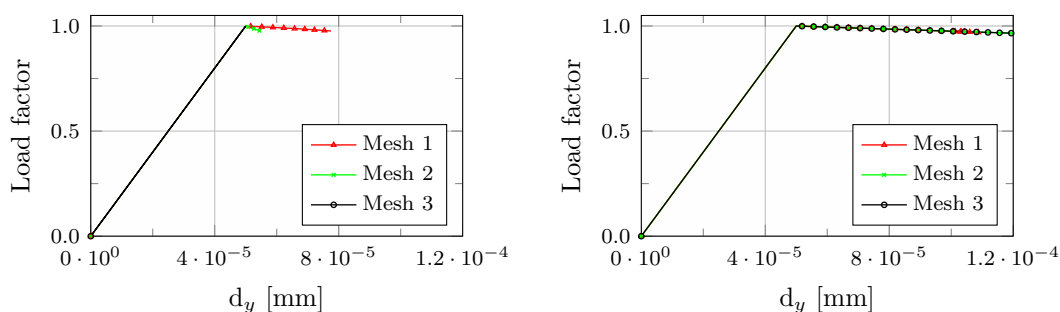
(a) ES-RPIM T4   (b) ES-RPIM T12/4

Figure 6.41: Induced localization - ES-RPIM - Equilibrium paths

These results are better illustrated by the contour plots of the scalar damage variable. In Fig. 6.42 it can be observed that the analyses performed with the T4 scheme led to different damaged configurations for the three meshes. The coarser mesh exhibited a damage configuration that, up step 100, was similar to the one obtained with the

intermediate finite element mesh with the classic medium (Fig. 6.30); after step 100, the scalar damage variable abruptly growed to 1 within a single step. The intermediate mesh manifested an asymmetric configuration, where the damage concentrated in a single inclined band soon after damage initiation, and convergence was lost a few steps after the onset of damage. In the finer mesh instead, the damage abruptly growed to 1 in the step after the onset of damage. The analyses performed with the T12/4 scheme (Fig. 6.41(b)) resulted in similar damaged configurations for the three meshes, at least in the first steps. Indeed, it can be observed that already at the step 15 the coarser mesh presented some irregularities in the damage distribution, which tended to grow in the subsequent steps.

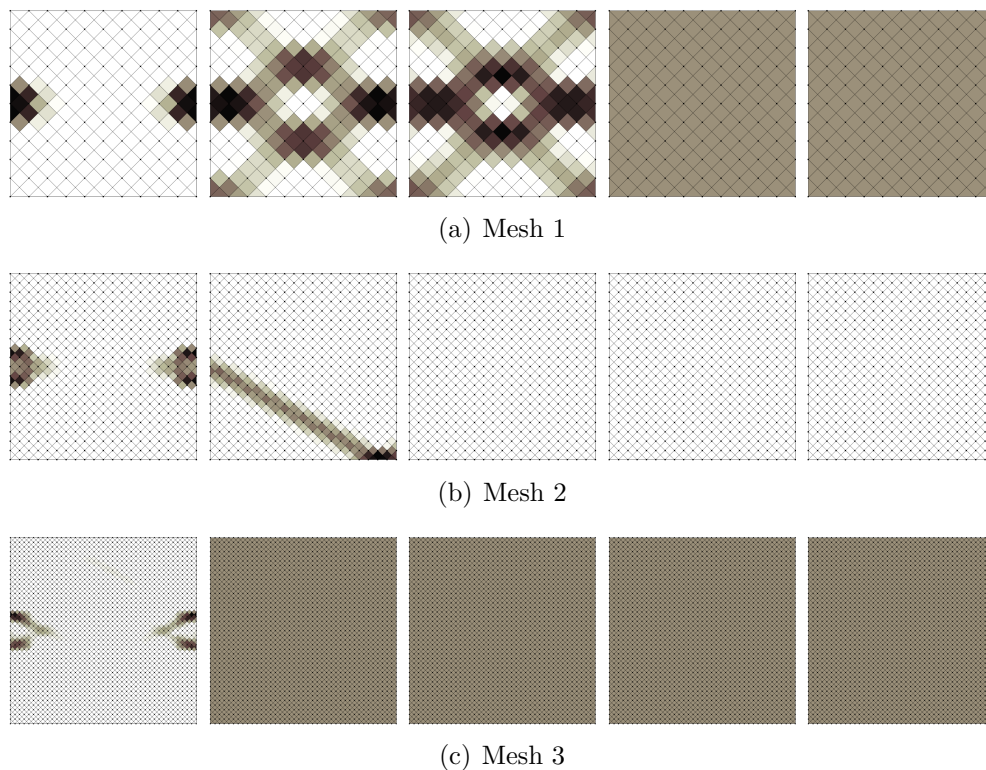(a) Mesh 1

(b) Mesh 2

(c) Mesh 3

Figure 6.42: Induced localization - ES-RPIM T4 - Damaged configurations

It is interesting to observe that the analyses performed with the intermediate and finer meshes with the ES-RPIM T12/4 resulted in damage distributions that are quite similar to the one obtained with the micropolar finite element analysis with $G_c = 2500$ N/mm^2, for a large part of the loading process. However, upon comparison of Figs. 6.33 and 6.43, it can be observed that the solutions started to diverge in the final steps of the loading process. In the finite element analyses, the damaged zone tended first to extend, and then to concentrate in the central band of elements. In the analyses with the smoothed meshfree method on the contrary, the higher values of the scalar damage variable remained mostly confined in the weakened zones.
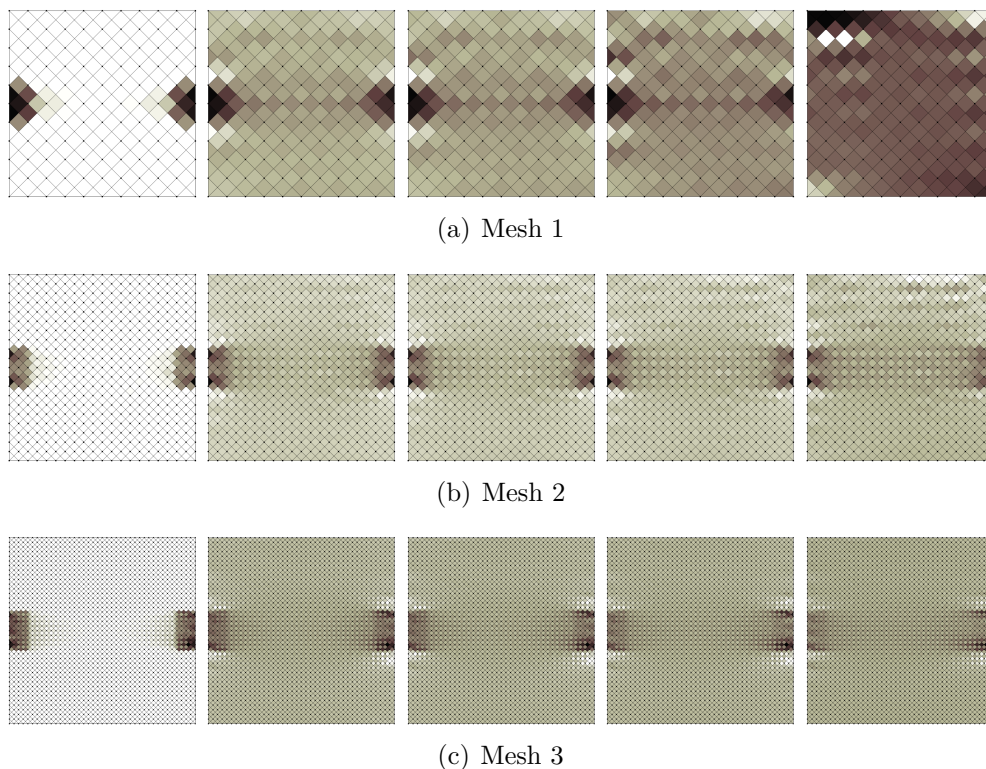
(a) Mesh 1

(b) Mesh 2

(c) Mesh 3

Figure 6.43: Induced localization - ES-RPIM T12/4 - Damaged configurations

6.4.4　Micropolar NS-PIM and ES-PIM

Like in the case of the finite element method, the micropolar formulation was able to improve also the results obtained with smoothed meshfree methods in the example considered in the present section, when the values $G_c = 2500$ N/mm^2 was adopted for the Cosserat's shear modulus. While it wasn't possible to perform the analysis with the NS-RPIM using the classic continuum formulation, the micropolar model allowed to describe, at least partially, the loading process. As it can be observed in Figs. 6.44(a) and 6.45, the results obtained with the NS-RPIM T4 with the three meshes were coincident up to a certain point of the loading processes, in terms of both equilibrium path and damage distribution. Then, the analyses with the meshes 2 and 3 lost convergence and arrested, while the one with the coarser mesh started to diverge from the expected equilibrium path. Regarding the T12/4 scheme (Figs. 6.44(b) and 6.46), it is interesting to observe how it provided significantly worst results than the T4 scheme, both in terms of equilibrium paths and damage distributions, on the contrary of what could be expected from the results obtained in the previous numerical localization example (Section 6.3).

Regarding the ES-RPIM T4 (Figs. 6.47(a) and 6.48), the use of the micropolar formulation led to a slight improvement with respect to the classic continuum model. The analyses were able to represent correctly the damage evolution up to a certain point of the loading process, with results in terms of damage contour plots similar to the ones exhibited by the FEM simulations (Fig. 6.33). The behaviour exhibited by the analyses
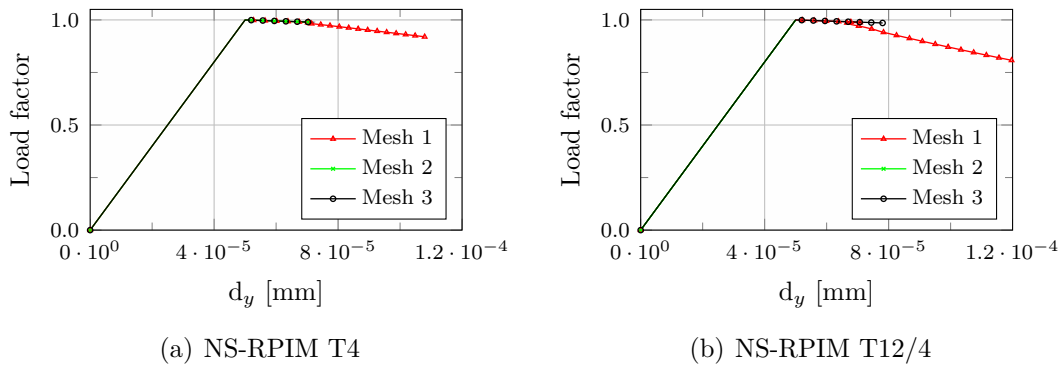
(a) NS-RPIM T4

(b) NS-RPIM T12/4

Figure 6.44: Induced localization - Micropolar NS-RPIM - $G_c = 2500$ N/mm^2 - Equilibrium paths

(a) Mesh 1

(b) Mesh 2

(c) Mesh 3
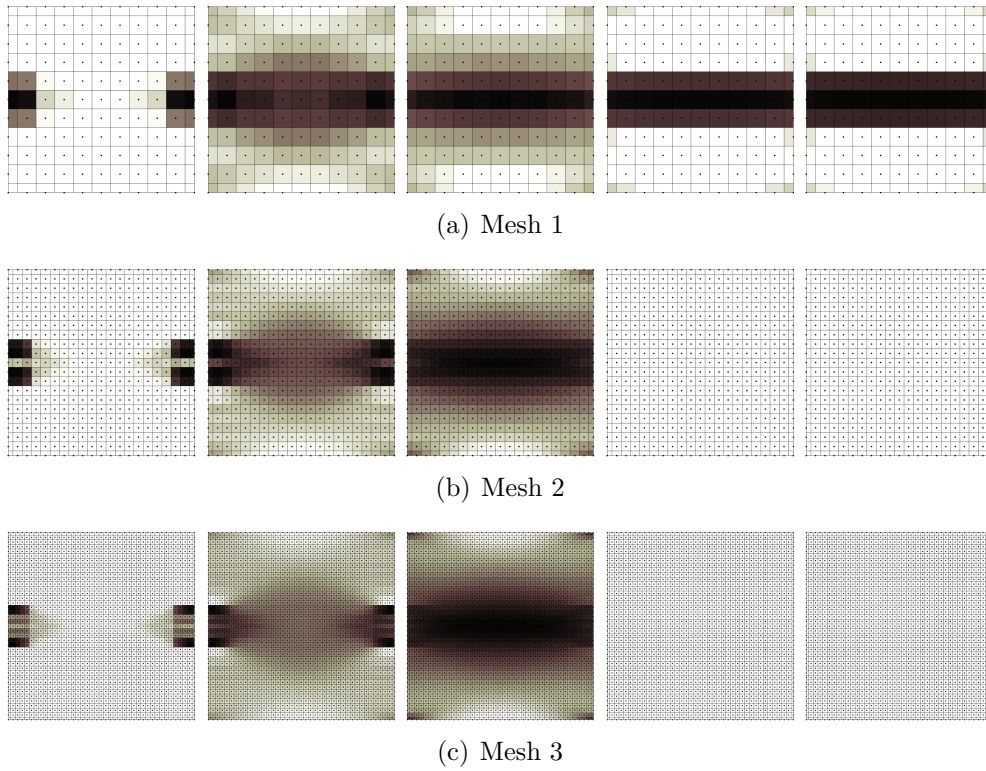
Figure 6.45: Induced localization - Micropolar NS-RPIM T4 - Damage - $G_c = 2500$ N/mm^2
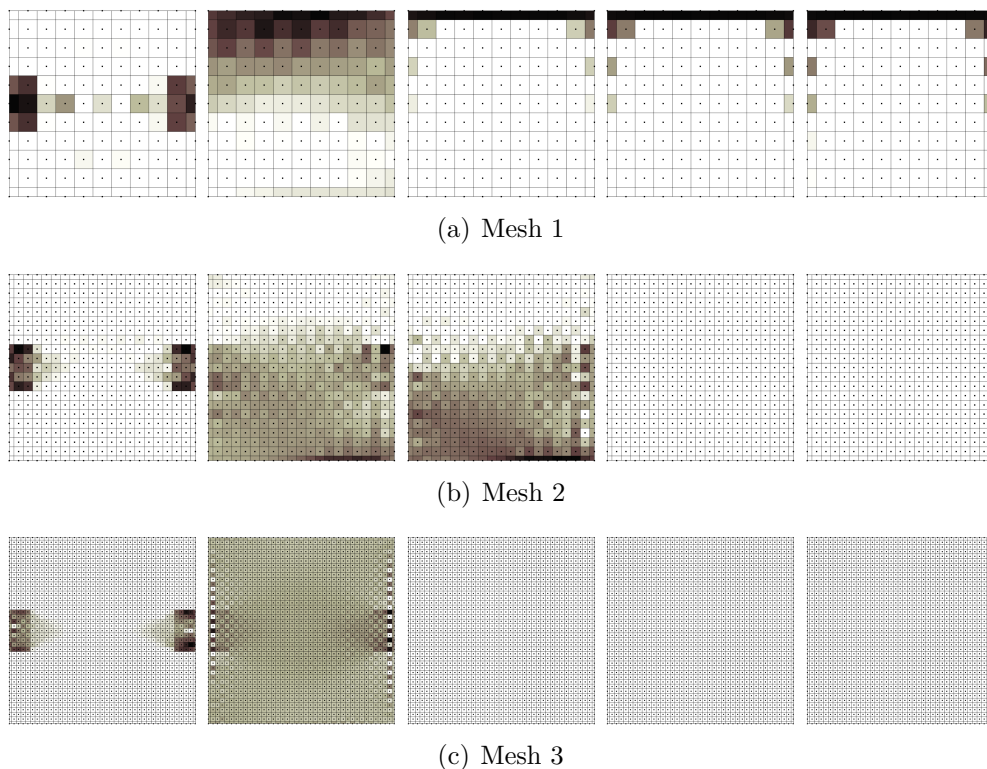
(a) Mesh 1

(b) Mesh 2

(c) Mesh 3

Figure 6.46: Induced localization - Micropolar NS-RPIM T12/4 - Damage - $G_c = 2500$ N/mm^2

with the T12/4 scheme (Figs. 6.47(b) and 6.49) was similar to the one obtained with the classic medium. There was however an improvement regarding the simulations with the mesh 1 that, despite still presenting some irregularities in the damage distribution, exhibited a more regular behaviour which didn't tend to degenerate as in the case of the classic model (Fig. 6.43).
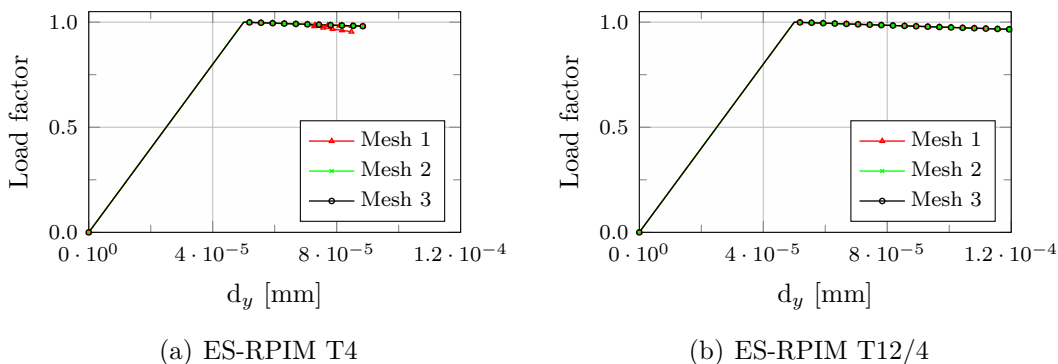

(a) ES-RPIM T4

(b) ES-RPIM T12/4

Figure 6.47: Induced localization - Micropolar ES-RPIM - $G_c = 2500$ N/mm^2 - Equilibrium paths

(a) Mesh 1

(b) Mesh 2

(c) Mesh 3
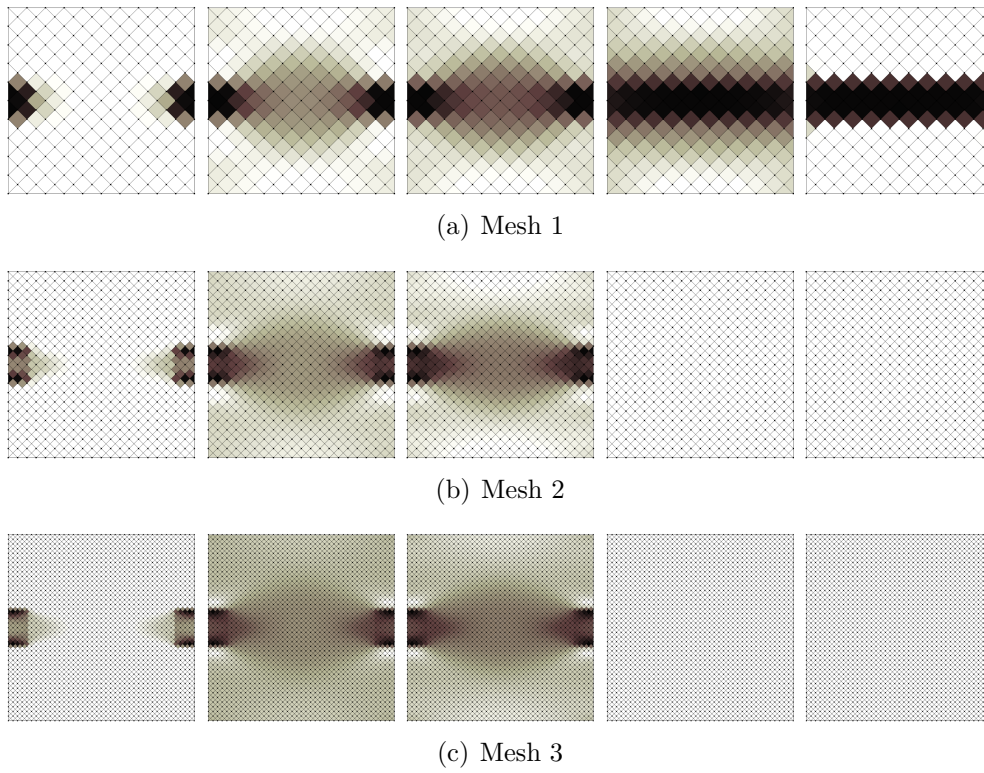
Figure 6.48: Induced localization - Micropolar ES-RPIM T4 - Damage - $G_c = 2500$ N/mm^2
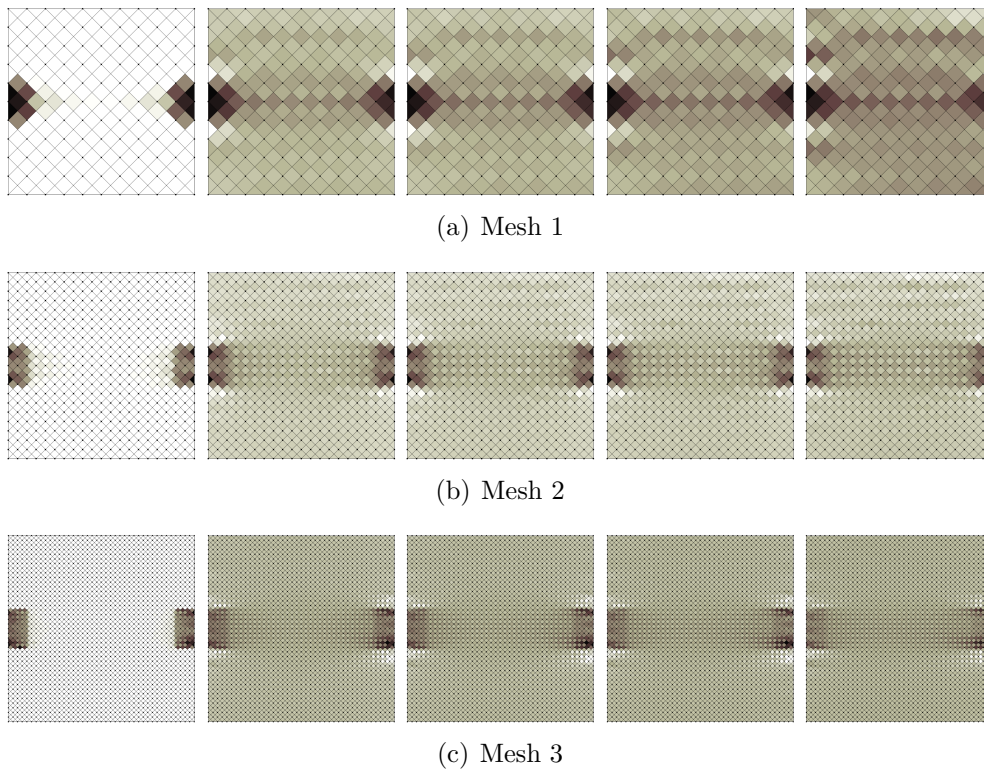

(a) Mesh 1

(b) Mesh 2

(c) Mesh 3

Figure 6.49: Induced localization - Micropolar ES-RPIM T12/4 - Damage - $G_c = 2500$ N/mm^2

Chapter 7

Simulation of experimental tests

The present chapter presents two examples, based on real experimental tests of plain concrete samples. They aim to point out the advantages of the micropolar and smoothed point interpolation strategies; specifically, the more stable solutions exhibited by the micropolar formulation, and a certain mesh-objective behaviour presented by the smoothed point interpolation methods.

7.1   A preface

The following two examples are based on real experimental tests of plain concrete samples, a *four-point shear test* (Section 7.2), and the test of an *L-shaped panel* (Section 7.3), widely adopted in the literature as benchmark tests for constitutive models and numerical procedures. In this case they were choosen in order to emphasize some of the qualities of both the proposed micropolar damage models and the smoothed point interpolation methods. The first one, the four-point shear test, allowed to show how a simple micropolar scalar damage model was able to correctly reproduce the complex behaviour of this test, where scalar damage models based on the classic continuum usually fail, due to the peculiar *mixed-mode* loading with high shear gradients that appears near the notch of the beam. Both this test and the second one, the L-shaped panel, allowed to point out the capability of smoothed point interpolation methods to provide a certain mesh-objectivity in the results, if compared to the standard FEM. Before proceeding to the presentation of the examples, it is necessary to remark that the reason for their inclusion in this manuscript has been to emphasize the aforementioned characteristics of the adopted regularization strategies. When plotting the equilibrium paths obtained in the different simulations the experimental results have also been represented, in order to illustate the capability of the adopted strategies to reproduce the general behaviour of the experimental tests due to their regularization properties. It is remarked however, that the aim wasn't to exactly reproduce the experimental results, since this would have required accurate

calibrations of the damage laws and, possibly, the use of micropolar damage models more complex than the simple scalar one, able to better capture the physical behaviour of the samples.

7.2 Four-point shear test

The four-point shear test of the plain concrete beam depicted in Fig. 7.1 was peformed by Arrea and Ingraffea (Arrea and Ingraffea, 1982), and has been widely used in the literature as a benchmark test for numerical investigations on concrete behaviour (see, e.g., Oliver et al. (2002), Rabczuk and Belytschko (2004), de Borst, Gutiérrez, Wells, Remmers and Askes (2004), Rabczuk and Belytschko (2007), Jirásek (2007b), Fang et al. (2008), Matallah and La Borderie (2009), Rajagopal and Gupta (2011), Ghosh and Chaudhuri (2013) and Chaudhuri (2013)). The beam is characterized by a mixed-mode loading, with an high shear gradient between the fixed constraint and the applied load P. The failure corresponds to a curved crack path, going from the top of the notch to the point which the load P is applied to. Due to its characteristics, the simulation of such test is difficult with scalar-isotropic damage models, and usually requires more complex approaches, like discrete cracking methods (see, e.g., Oliver et al. (2002), Rabczuk and Belytschko (2004), de Borst, Gutiérrez, Wells, Remmers and Askes (2004) and Fang et al. (2008)), or special treatments for scalar damage models like the non-local approach (see, e.g., Jirásek (2007b)), for example. As it will be shown in the present section, analyses performed with classic scalar damage models were not able to reproduce the experimental results of the four-point shear test, due to instabilities in the loading branch of the equilibrium paths. On the other hand, the micropolar approach to scalar damage proposed in Chapter 3 was able to simulate the behaviour of such test. This result was expected for this peculiar loading condition, since in presence of high values of shear stresses couple-stresses usually arise, leading to the activation of the internal bending length, and to the regularization effects of the micropolar formulation.
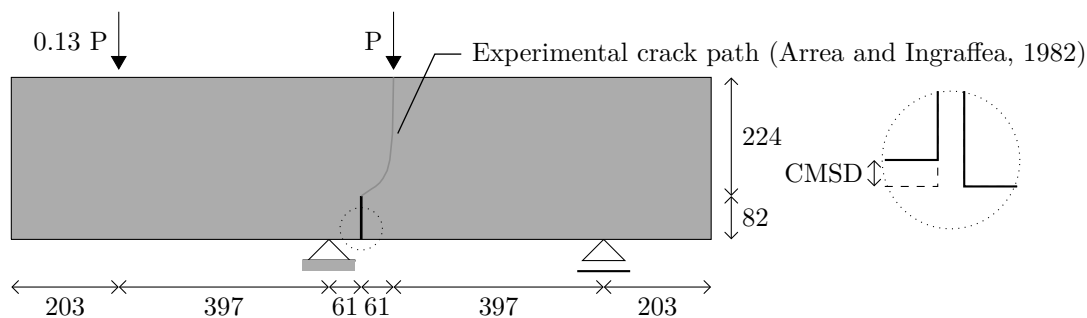

Figure 7.1: Four-point shear test - Geometry (measures in mm)

The concrete investigated by Arrea and Ingraffea (Arrea and Ingraffea, 1982) was characterized by a Young's modulus E = 24800 N/mm^2, Poisson's ratio $\nu = 0.20$, tensile

uniaxial strength between 2.8 N/mm² and 4.0 N/mm², and fracture enegy between 0.10 N/mm² and 0.14 N/mm²; in the following simulations its behaviour was reproduced adopting the *Mazars*[1] scalar damage model (Eq. (2.34)), with the following parameters for the exponential damage law, $\alpha = 0.950$, $\beta = 1000$ and $K_0 = 1.6 \times 10^{-4}$.

7.2.1 FEM simulations

The analyses with the finite element method were performed considering meshes composed by three-node triangular elements in a plane-stress state, with a thickness of 156 mm. Three discretizations were adopted (Fig. 7.2), with mean nodal spacing of 30 mm, 20 mm, and 10 mm between the notch and the point of application of the load P, and 70 mm elsewhere. The notch was represented as sharp, with an initial opening of 5 mm.

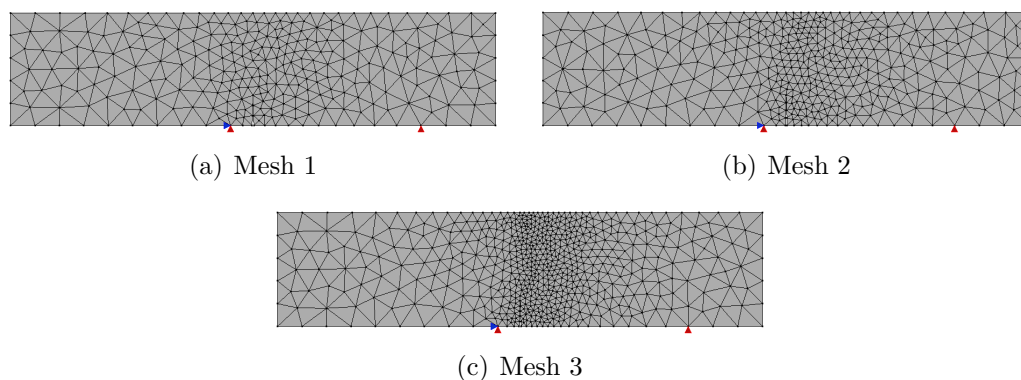

(a) Mesh 1

(b) Mesh 2

(c) Mesh 3

Figure 7.2: Four-point shear test - FEM meshes

The FEM analyses were performed adopting a loading process driven by a *cylindrical arc length* control method, assuming a reference load P = 130000 N, an initial loading factor increment of 0.0125, and a tollerance for convergence in relative displacement of 1×10^{-4}. All the simulations presented in this section were performed considering the tangent approximation of the constitutive operator. The results of the analyses performed with the classic medium, in terms of *crack mouth sliding displacement* (CMSD) plotted against the load factor are illustrated in Fig. 7.3, together with the experimental results obtained by Arrea and Ingraffea (Arrea and Ingraffea, 1982). As it can be observed, no one of the three meshes was able to describe the behaviour of the beam; the meshes 1 and 2 exhibited an elastic unloading once the peak value of the load factor was reached, while the third mesh lost convergence before the maximum load factor value.

The analysis of the four-point shear test was repeated for the three discretizations using the micropolar medium, with six different combinations of the additional material parameters, adopting the values 500 N/mm², 2500 N/mm², and 3500 N/mm² for the Cosserat's shear modulus G_c, and the values 5.0 mm and 10.0 mm for the internal bending

---

[1] For the micropolar strategy, the Mazars equivalent deformation of Eq. (3.146) was adopted.
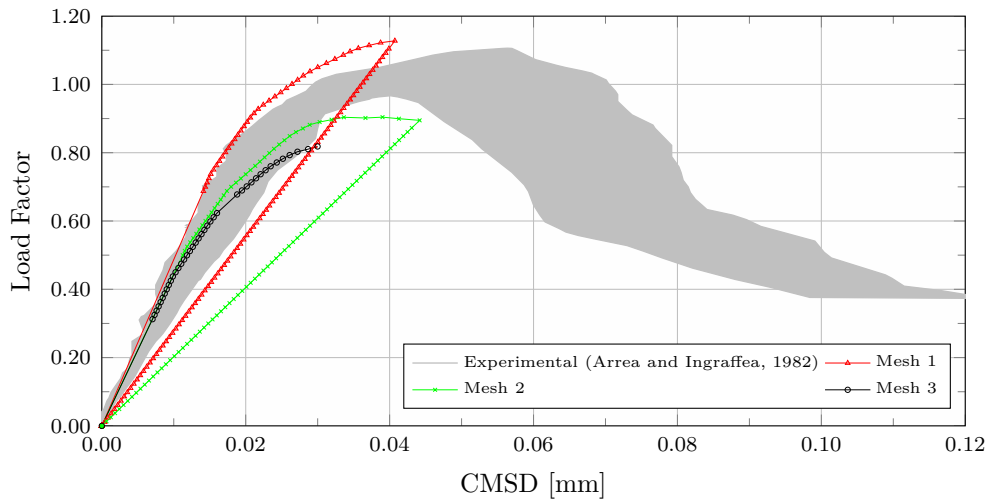
Figure 7.3: Four-point shear test - FEM - Equilibrium paths

length L_b. The results are collected in the plots of Fig. 7.4. As it can be observed, the use of the micropolar medium with a simple scalar damage model allowed to investigate also the post-peak branch of the equilibrium paths, which were affected by both the additional material parameters; specifically, to higher values of G_c and L_b corresponded higher peak values of the load factor. Despite the fact that, on the contrary of the classic medium, the micropolar one allowed to reproduce the softening phase of the loading process, it can be observed that the solutions depicted in Fig. 7.4 strongly depended on the discretization, with lower peak values obtained with the most refined meshes. This fact is emphasized also by the damaged configurations illustrated in Fig. 7.5. The damaged zones obtained with the three meshes were compatible with the expected cracking path (Fig. 7.1); however, it can be observed that to a finer mesh corresponded a narrow damaged zone, pointing out the mesh dependency of the problem, which wasn't mitigated by the micropolar formulation.

7.2.2 ES-RPIM simulations

The beam of Fig. 7.1 was investigated using also the ES-RPIM, with the discretizations depicted in Fig. 7.6, each one obtained constructing the edge-based smoothing domains using as background cells the triangular finite elements of Fig. 7.2, hence maintaining the same nodal distributions of the finite element meshes[2].

Regarding the generation of the support domains, both the T3 and the T6/3 schemes were adopted. The shape functions were constructed with the *radial point interpolation*

---

[2] The simulation of the four-point shear test was performed using also node-based smoothing domains. Both polynomial and radial basis functions were tested, as well as both the selection schemes T3 and T6/3. However, neither with the classic nor with the micropolar medium it was possible to obtain satisfactory results, since damage initiated long before the expected threshold and the analyses arrested soon after the onset of damage. Hence, only the results obtained with the edge-based method are presented in this section.
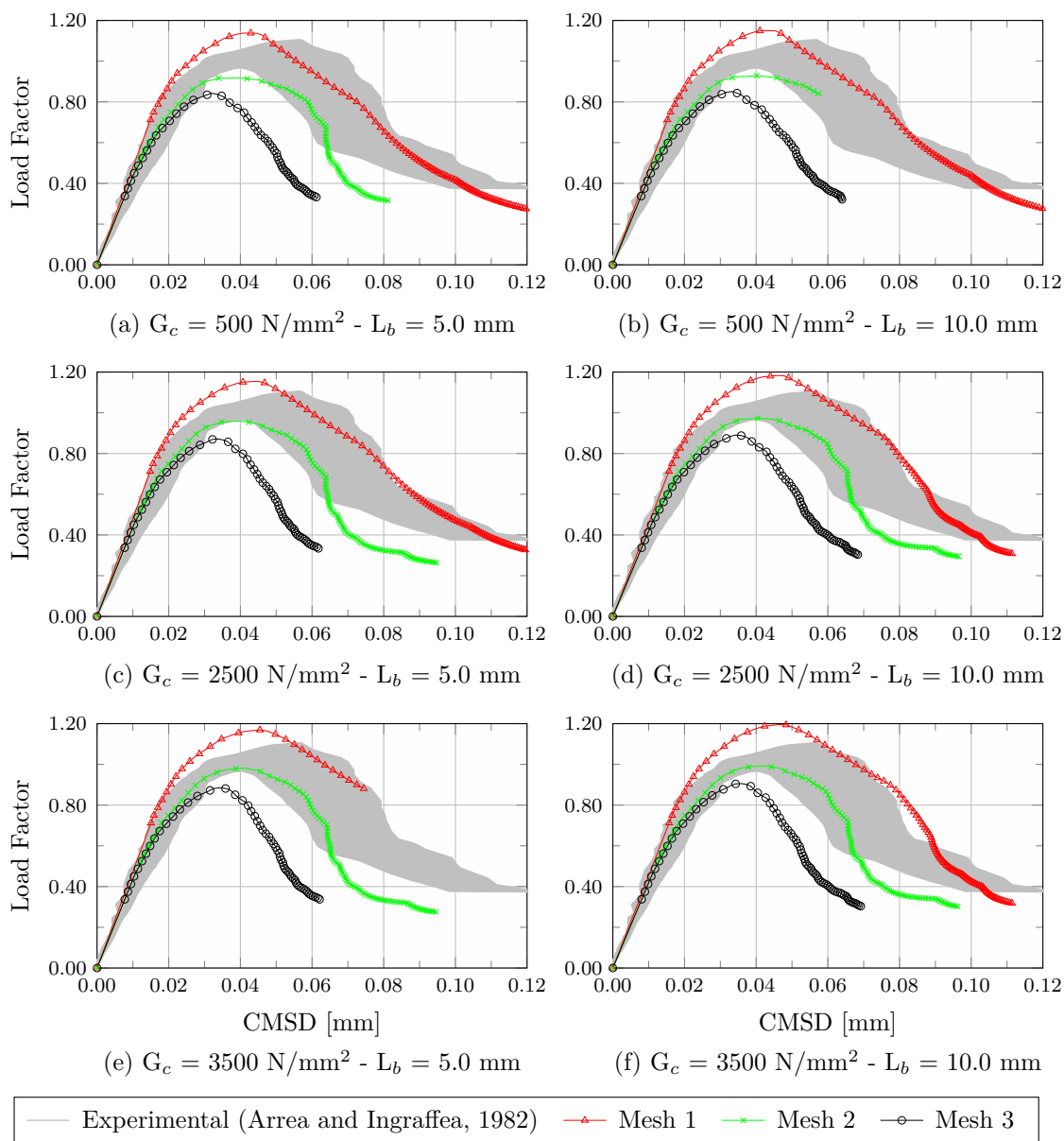
(a) $G_c = 500$ N/mm^2 - $L_b = 5.0$ mm

(b) $G_c = 500$ N/mm^2 - $L_b = 10.0$ mm

(c) $G_c = 2500$ N/mm^2 - $L_b = 5.0$ mm

(d) $G_c = 2500$ N/mm^2 - $L_b = 10.0$ mm

(e) $G_c = 3500$ N/mm^2 - $L_b = 5.0$ mm

(f) $G_c = 3500$ N/mm^2 - $L_b = 10.0$ mm

Figure 7.4: Four-point shear test - Micropolar FEM - Equilibrium paths

(a) Mesh 1

(b) Mesh 2

(c) Mesh 3
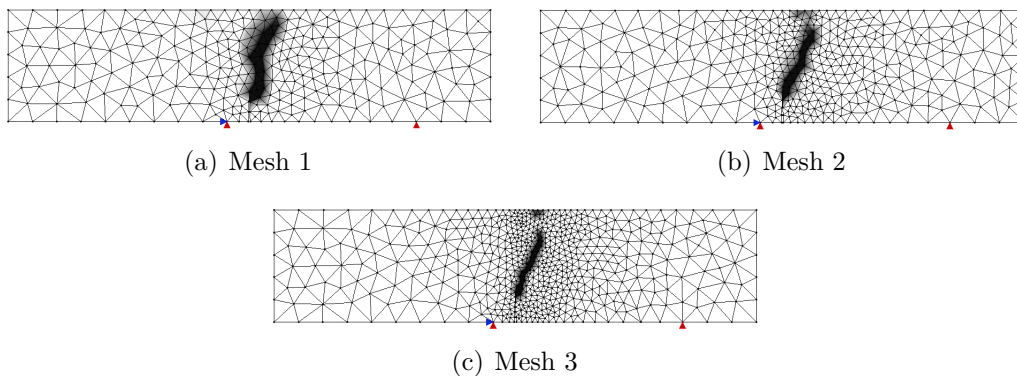
Figure 7.5: Four-point shear test - Micropolar FEM - $G_c = 2500$ N/mm^2 - $L_b = 10.0$ mm - Damaged configuration

(a) Mesh 1   (b) Mesh 2
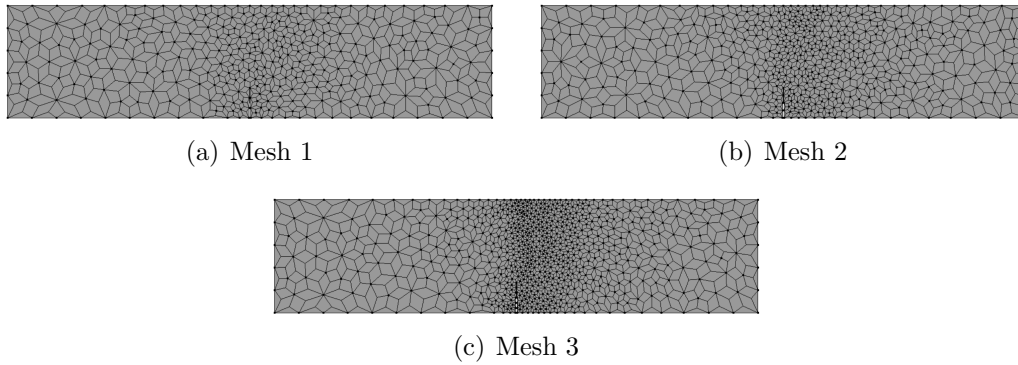

(c) Mesh 3

Figure 7.6: Four-point shear test - ESRPIM meshes

method with polynomial reproduction, using the exponential radial function (Eq. (4.22)) with c = 0.002, and adopting 3 polynomial terms. As for the finite element analyses, the non-linear simulations were performed adopting a loading process driven by a *cylindrical arc length* control method, assuming a reference load P = 130000 N, an initial loading factor increment of 0.0125, and a tollerance for convergence in relative displacement of 1 $\times$ 10^{-4}, considering the tangent approximation of the constitutive operator. The results of the analyses performed with the classic medium are illustrated in Fig. 7.7. As it can be noted, in this case the behaviour of the ES-RPIM was similar to the finite element method (Fig. 7.3); in all the simulations the models lost convergence already in the loading path, except for the mesh 1 with the T3 scheme, which manifested an elastic unloading along the original loading path once the peak value was attained.

(a) T3   (b) T6/3

Experimental (Arrea and Ingraffea, 1982)   —▲— Mesh 1   —✕— Mesh 2   —○— Mesh 3
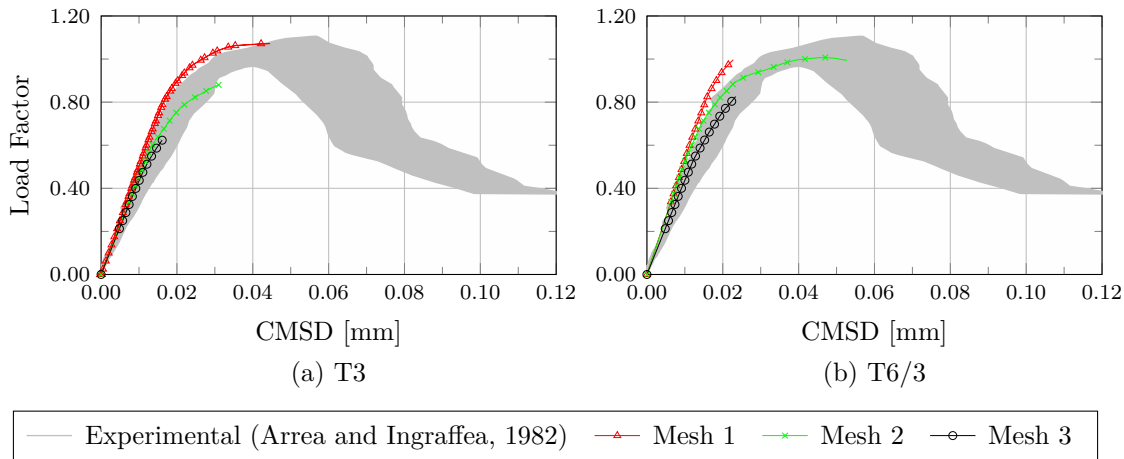
Figure 7.7: Four-point shear test - ES-RPIM - Equilibrium paths

Like in the case of the finite element method, the analyses with the micropolar medium gave significantly better results. Adopting the T3 scheme it was possible to investigate the softening phase of the loading process, except for the combinations with G_c = 500 N/mm^2, which exhibited instabilities with the meshes 1 and 3, and for the mesh 3 with the combination G_c = 2500 N/mm^2 and L_b = 10.0 mm, which also lost convegence in

the loading phase, as it can be observed in Fig. 7.8. Fig. 7.9 illustrates the damaged configurations obtained for the three discretizations with the combination $G_c = 3500$ N/mm^2 and $L_b = 10.0$ mm, showing damaged zones compatible with the expected crack path depicted in Fig. 7.1. However, observing the results illustrated in Figs. 7.8 and 7.9 it is worth to note that also in this case, as previously observed for the finite element method, the analyses were strongly dependent on the discretization, with lower peak values and narrower damaged zones in the finest meshes.
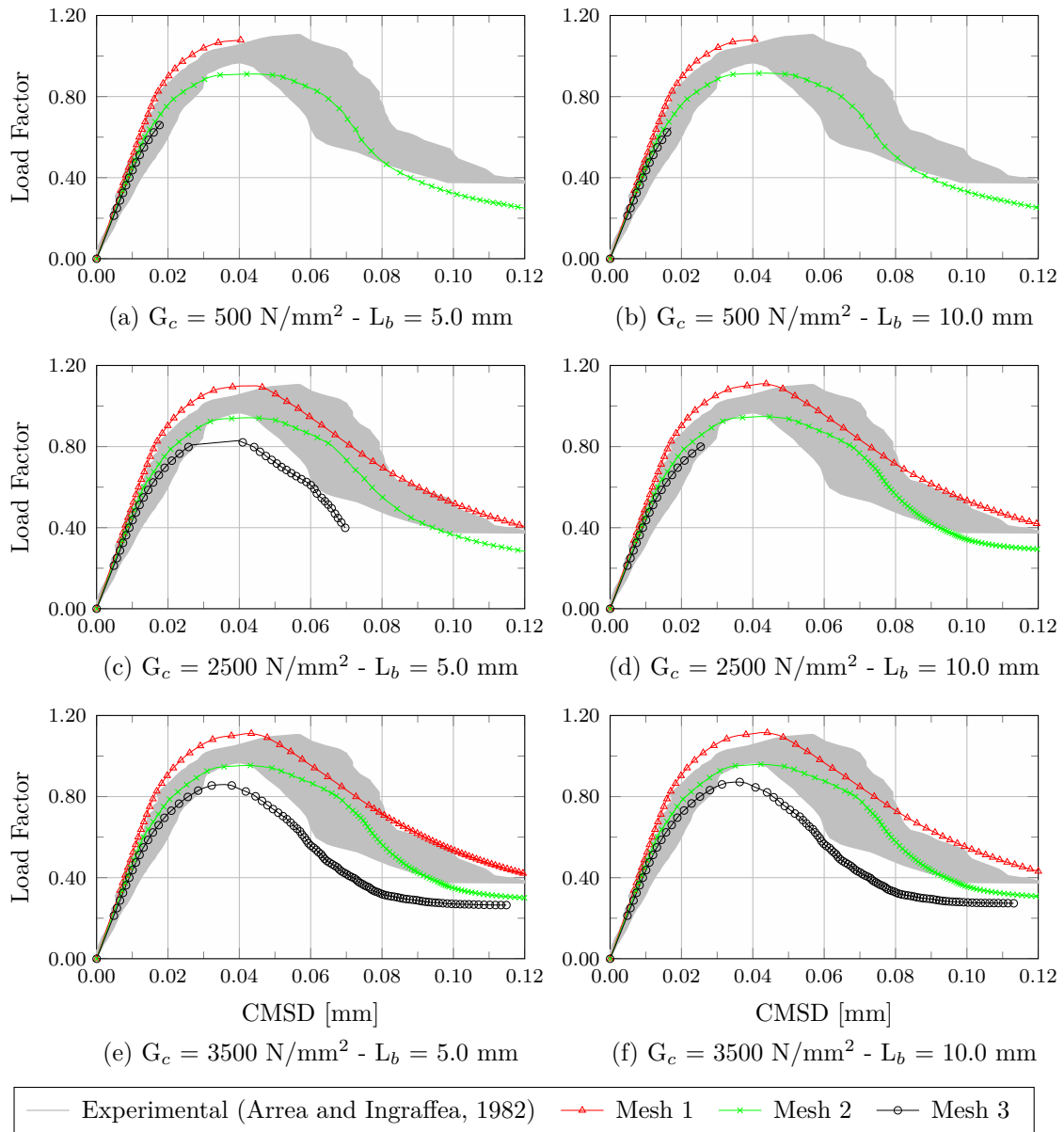

Figure 7.8: Four-point shear test - Micropolar ES-RPIM T3

The adoption of the T6/3 selection scheme in the ES-RPIM simulations led to an improvement of the results. Observing the equilibrium paths of Fig. 7.10 it can be noted that more stable analyses were obtained, also with the combinations with $G_c = 500$ N/mm^2, which were characterized by instabilities in the case of the T3 scheme. Furthermore, while
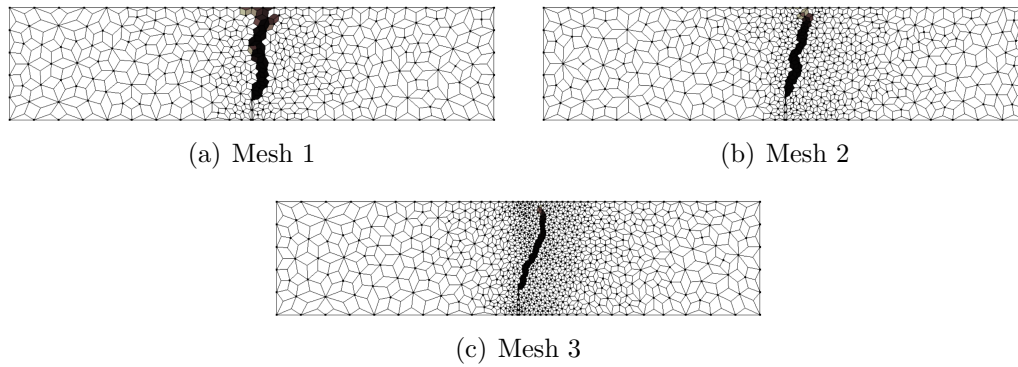
(a) Mesh 1   (b) Mesh 2

(c) Mesh 3

Figure 7.9: Four-point shear test - Micropolar ESRPIM-T3 - $G_c = 3500$ N/mm^2 - $L_b = 10.0$ mm - Damaged configuration

the simulations with the coarsest discretization led to results well above the experimental ones, both the meshes 2 and 3 produced results that fell in the experimental rage. The most interesting result however, is that a certain mesh objectivity was observed adopting this scheme. Indeed, observing the equilibrium paths of the meshes 2 and 3 it can be noted that they exhibited similar results in terms of peak value, and were almost coincident in the final part of the softening branch, especially for the combinations with $G_c = 3500$ N/mm^2, with some discrepancies in the middle of the post peak branch. This result is emphasized also by the contour plots of the scalar damage variable depicted in Fig. 7.11. Comparing Fig. 7.11(b) with Fig. 7.11(c) it can be observed that the two discretizations with the T6/3 scheme produced damaged zones with a similar width, while with the T3 scheme the difference in width was considerably higher (see Figs. 7.9(b) and 7.9(c)).

Remark 7.1: Intrinsic non-local nature of meshfree approximations

The results discussed in Chapter 6 have pointed out the regularization properties of the smoothed point interpolation approximation in problems characterized by numerical or induced localization. The example of the four-point shear test presented in this section instead, allowed to emphasize the capability of such methods to bring a certain degree of *mesh objectivity*, at least in the considered case. As it can be observed, both these characteristics are ascribable to the use of the T6/3 scheme for the selection of support nodes (the T12/4 scheme in case of quadrilateral cells as in Section 6.4), which, as observed in Chapter 4, leads to larger support domains than the T3 scheme; the approximation at each integration point indeed, is constructed using six nodes (three nodes for the integration points along the boundary), on the contrary of the T3 scheme and of the FEM with three-node triangular element, which rely on approximations constructed with only three nodes at each integration point. These properties of regularization and mesh objectivity are analogous to the ones that
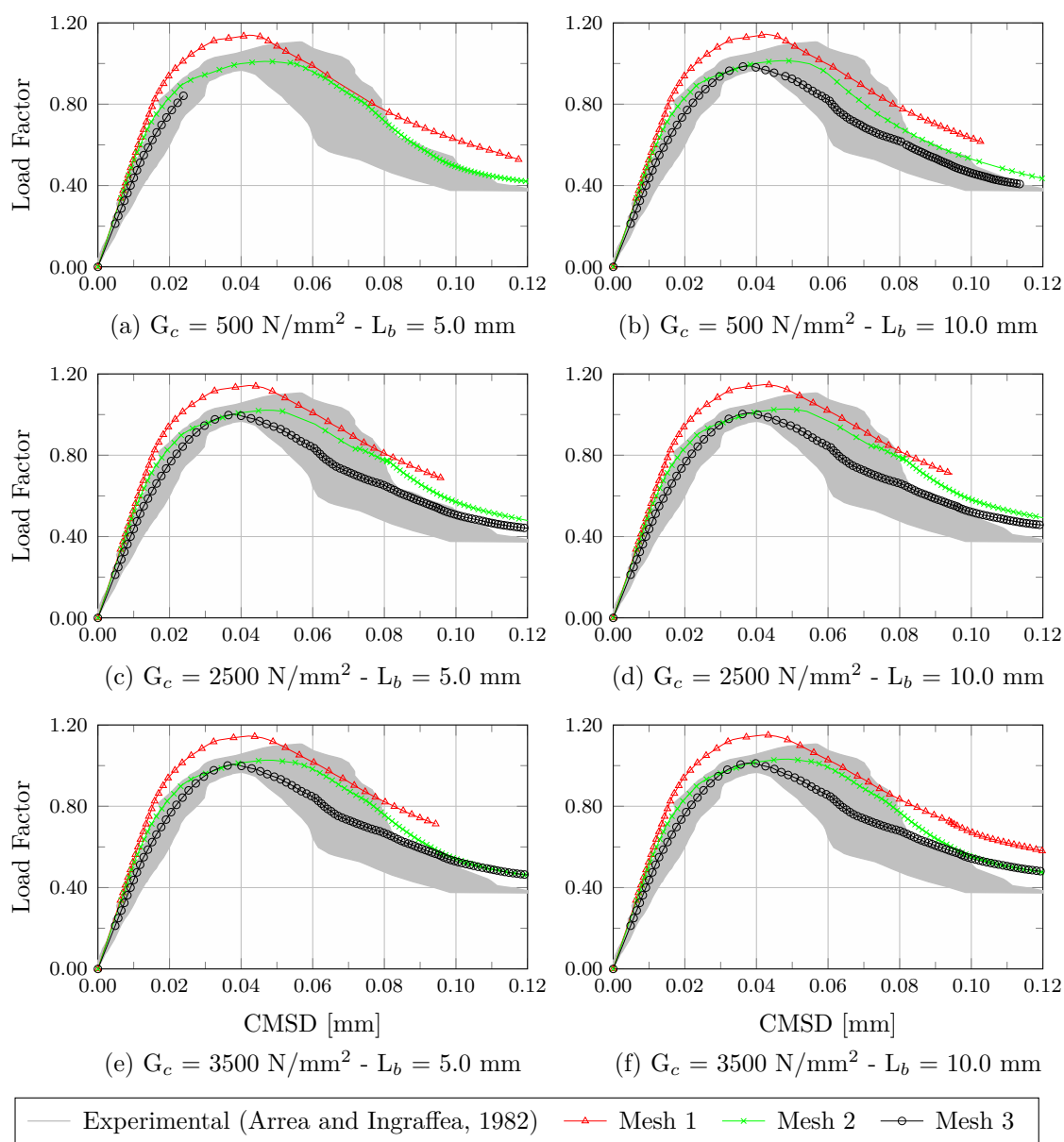
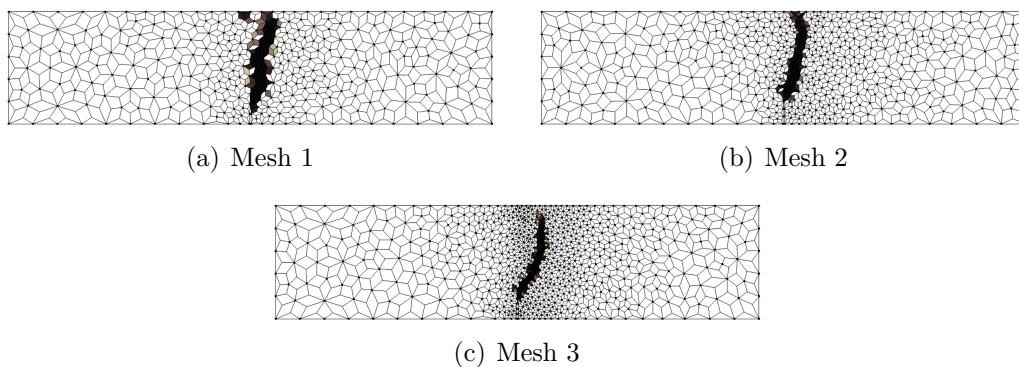Figure 7.10: Four-point shear test - Micropolar ESRPIM-T6/3

Figure 7.11: Four-point shear test - Micropolar ESRPIM-T6/3 - $G_c = 3500$ N/mm^2 - $L_b = 10.0$ mm - Damaged configuration

could be obtained using *non-local* continuum formulations and, since they were exhibited only when larger support domains were adopted, with support nodes beyond the limits of the triangular background cell/finite element, they seems to corroborate the hypothesis discussed in Chapter 4 (as also noted in Remark 6.5) that point interpolation methods are characterized by an *intrinsic non-local nature* that makes them well suited to correctly represent strain-softening problems (as also pointed out in Chen et al. (2000) in case of *reproducing kernel methods*).

7.3 L-shaped panel

The plain concrete L-shaped panel depicted in Fig. 7.12 was investigated experimentally by Winkler et al. (2004). As it can be observed in Fig. 7.12, the failure mode found by the authors consisted in a crack initiating at the concave corner of the panel, propagating in the horizontal direction with a slightly curved path. The authors also performed numerical investigations with a smeared-crack approach. As it will be shown in the present section, differently from the four-point shear test, the analysis of this problem performed with simple scalar-isotropic damage models based on the classic continuum formulation didn't present peculiar difficulties, except for the lack of mesh objectivity. Simulations performed with the micropolar medium didn't show significant improvements with respect to the results that will be presented in this section; hence, they will not be considered here, limiting the discussions to the use of the meshfree approach and its effects on the mesh objectivity problem.
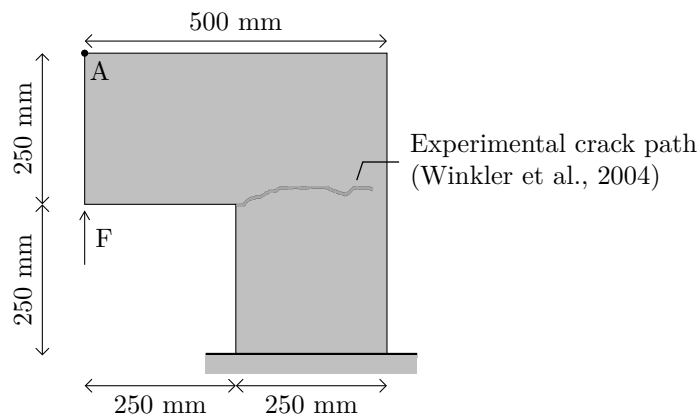
Figure 7.12: L-shaped panel - Geometry

The concrete investigated by Winkler et al. (2004) was characterized by a Young's modulus E = 25850 N/mm^2, a Poisson's ratio $\nu = 0.18$, tensile and compressive uniaxial strengths f$_t$ = 2.7 N/mm^2 and 4.0 N/mm^2, a fracture energy G$_c$ = 0.065 N/mm^2, and a characteristic length of the material h = 28 mm; in the following simulations its behaviour was reproduced adopting the *Mazars* scalar damage model (Eq. (2.34)), with the following parameters for the exponential damage law, $\alpha = 0.950$, $\beta = 1100$ and K$_0$ = 1.12 $\times 10^{-4}$.

7.3.1 FEM simulations

In order to investigate the behaviour of the panel with the finite element method four different discretizations were considered (Fig. 7.13), each one composed by three-node triangular elements in a plane-stress state, with a thickness of 100 mm. The four meshes were characterized by a different mean nodal spacing near the concave corner, equal to 25 mm, 15 mm, 10 mm, and 5 mm, while it was equal to 50 mm elsewhere.

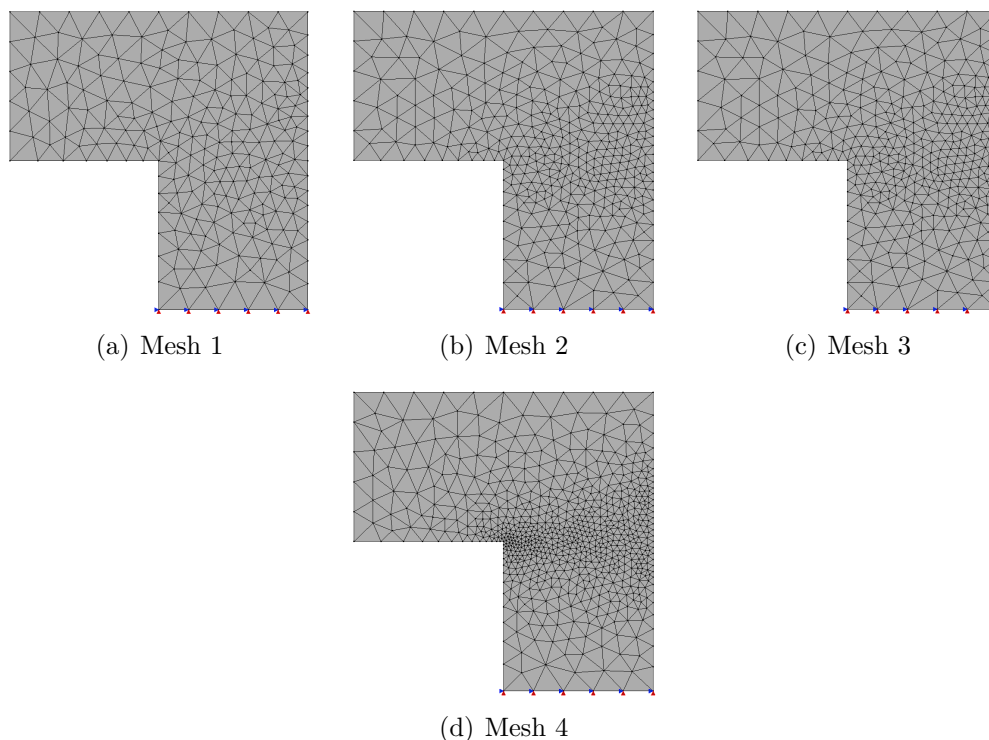(a) Mesh 1   (b) Mesh 2   (c) Mesh 3

(d) Mesh 4

Figure 7.13: L-shaped panel - FEM meshes

The analyses were performed adopting a loading process driven by the *generalized displacement control method* (Yang and Shieh, 1990), assuming a reference load F = 7000 N, an initial loading factor increment of 0.005, and a tollerance for convergence in relative displacement of 1×10^{-4}. All the simulations presented in this section were performed considering the tangent approximation of the constitutive operator, except for some of the simulations discussed in Section 7.3.2.1, which required a secant approximation due to convergence issues. The results of the analyses are illustrated in Fig. 7.14, where the values of the vertical displacement at the point A of Fig. 7.12 are plotted against the load factor, together with the experimental range presented in Winkler et al. (2004). As it can be observed, the results obtained with the coarsest mesh were in good agreement with the experimental results, both in terms of peak value of the load factor and shape of the softening branch, except for an initial stiffness higher than the one observed in the experiment; this issue however, is common to other simulations of such a test that can be found in the literature, and it can be observed also in Winkler et al. (2004).

However, the problem appeared to be strongly dependent on the discretization, since the analyses performed with the other meshes showed lower peak values of the load factor. The presence of mesh dependency is also pointed out by the contour plots of the scalar damage variable illustrated in Fig. 7.15. Indeed, despite their shape was compatible with the experimental cracking path depicted in Fig. 7.12, the damaged zones width varied with the discretization, with narrower widths in the most refined meshes.
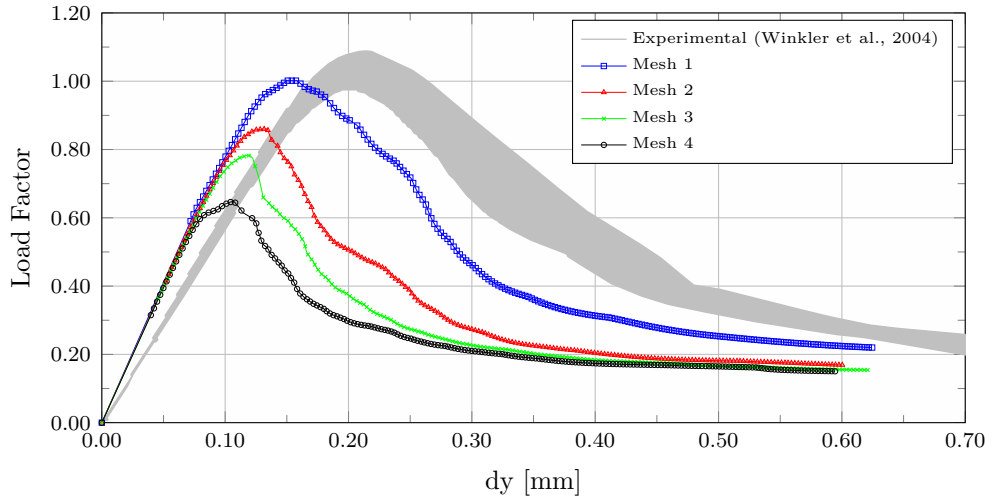

Figure 7.14: L-shaped panel - FEM - Equilibrium paths

As commented in the opening of this section, the FEM simulations of the L-shaped panel were performed also with the micropolar medium. The additional material parameters G_c and L_b exhibited a certain influence on the results of the analyses, since the peak values tended to grow as the values of G_c and L_b were increased. However, they had no effect on the mesh dependency of the problem. Since the use of the micropolar formulation didn't bring any improvement regarding this problem, the corresponding results will not be exposed in the present section.

7.3.2 NS-RPIM and ES-RPIM simulations

The L-shape panel was investigated also with smoothed point interpolation methods, with the discretizations illustrated in Fig. 7.16 for the NS-RPIM and the ones depicted in Fig. 7.17 for the ES-RPIM. Following the same procedure already discussed in the previous examples, node- and edge-based smoothing domains were constructed adopting as background cells the triangular finite elements of the meshes illustrated in Fig. 7.13, in order to maintain the same nodal distributions adopted in the FEM simulations.

At each integration point, the support domain was generated using both the T3 and the T6/3 schemes. The shape functions were constructed with the *radial point interpolation method with polynomial reproduction*, using the exponential radial function (Eq. (4.22)) with c = 0.002, and adopting 3 polynomial terms.
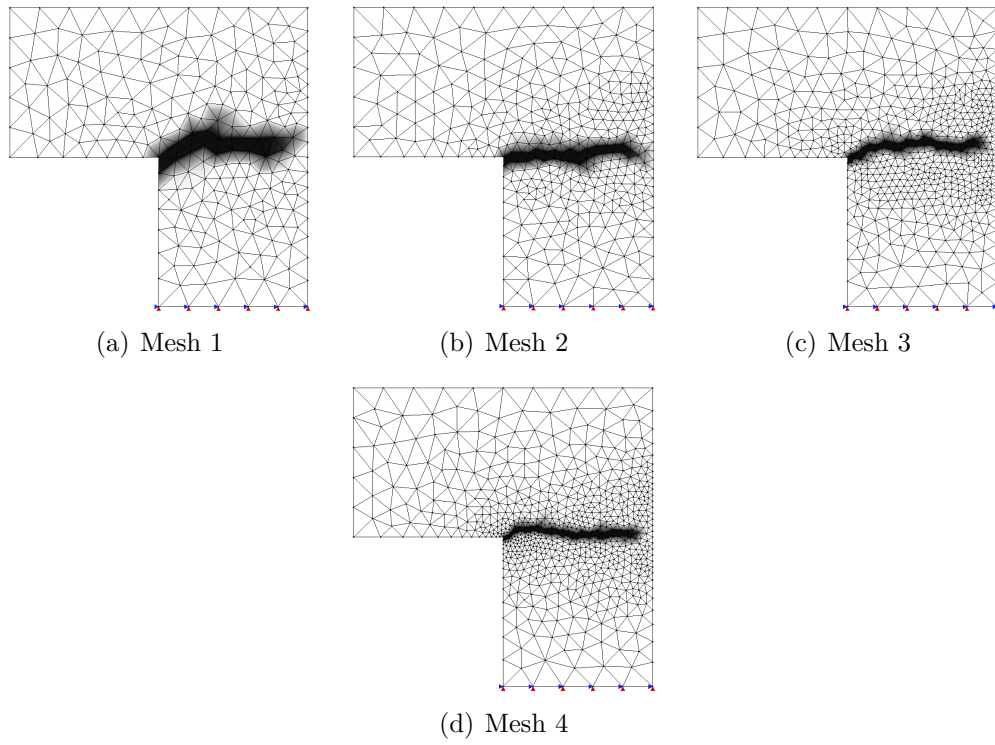
(a) Mesh 1   (b) Mesh 2   (c) Mesh 3

(d) Mesh 4

Figure 7.15: L-shaped panel - FEM - Damaged configurations

(a) Mesh 1   (b) Mesh 2   (c) Mesh 3

(d) Mesh 4
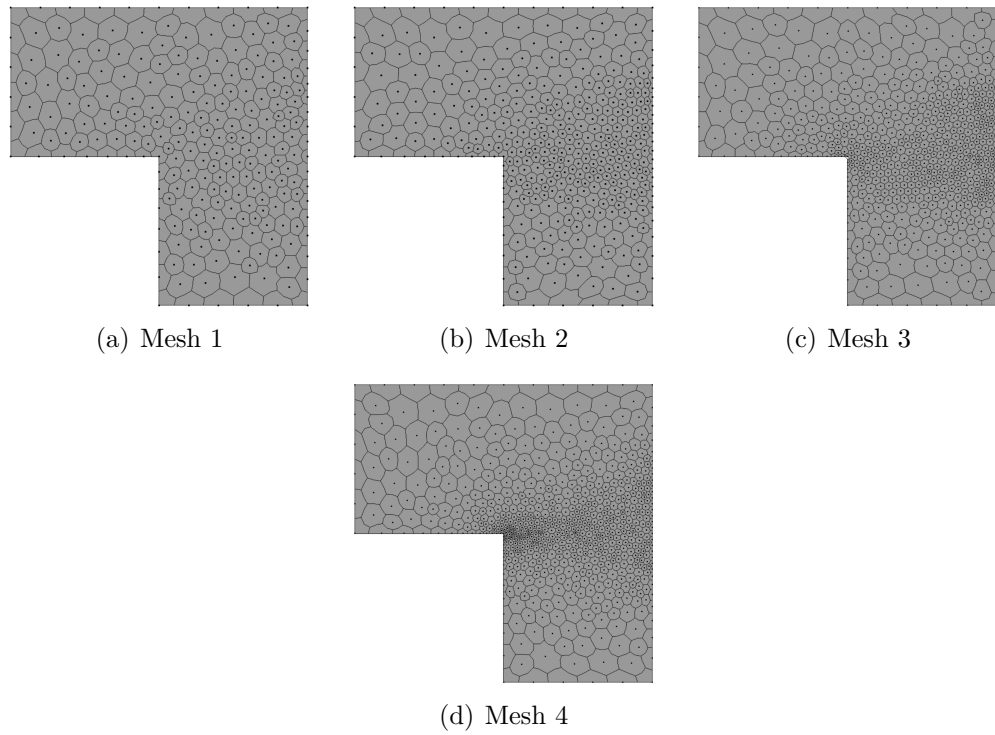
Figure 7.16: L-shaped panel - NS-RPIM meshes

(a) Mesh 1   (b) Mesh 2   (c) Mesh 3
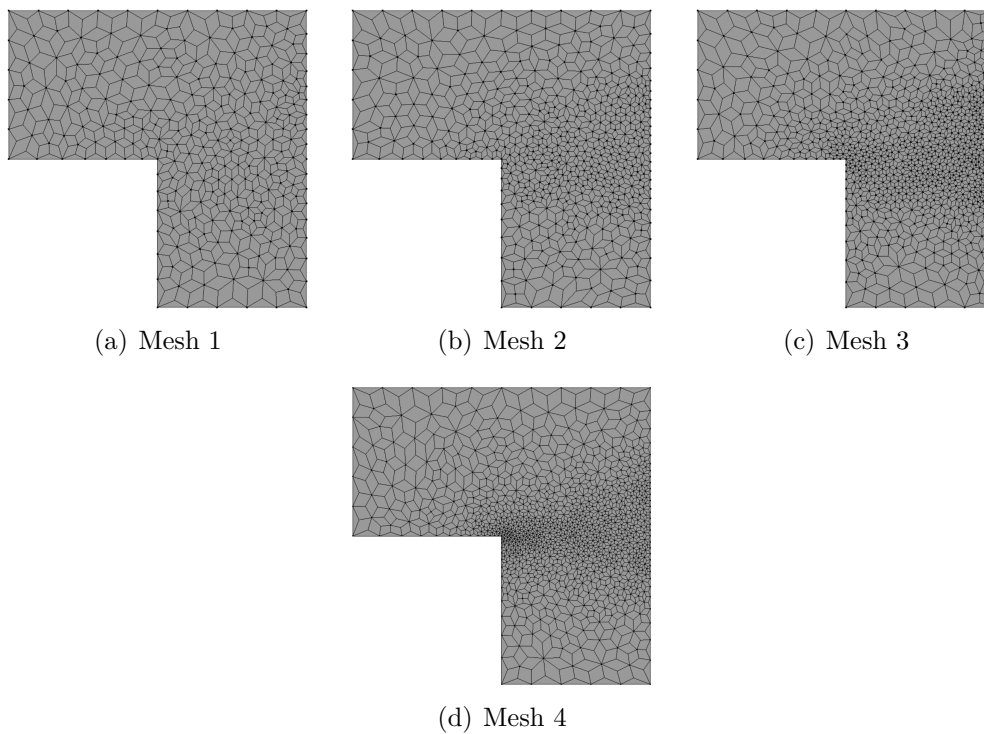

(d) Mesh 4

Figure 7.17: L-shaped panel - ES-RPIM meshes

Remark 7.2: Calibration of the radial functions

The present remark is devoted to the exposition of the guidelines that were followed
in order to calibrate the radial functions adopted in the simulations discussed in the
present volume. As pointed out in Chapter 4, shape functions constructed with the
radial point interpolation method depend on the choice of a peculiar radial function
and its parameters. Optimal values of the radial functions parameters are usually
problem dependent. In Wang and Liu (2002b) the authors investigated some linear
elastic problems with the radial point interpolation method (without smoothing oper-
ation) in order to define ranges of optimal values for the parameters of the MQ radial
function (Eq. (4.21)) and the dimensionless exponential radial function, different from
the one of Eq. (4.22). Regarding the simulations presented in this volume, the calibra-
tion of the radial functions parameters was performed, in general, starting from the
optimal values discussed in Wang and Liu (2002b), eventually adjusting them to the
needs of the specific problems. The final verification of the choosen parameters was
made considering the results of the non-linear analyses; however, the first evaluation
was performed with linear elastic analyses, comparing the results obtained with the
smoothed meshfree methods with the ones of the finite element method.

Regarding the specific problem of the L-shaped panel, the results of the linear
elastic analyses are illustrated in Figs. 7.18 and 7.19, where the values of the vertical

displacement of the point A of Fig. 7.12 are plotted against the mean nodal spacing. Fig. 7.18 illustrates the results obtained with the MQ radial function with C = 1.42, q = 1.03, where these parameters are the ones that resulted to be optimal in the problems investigated in Wang and Liu (2002b). As it can be observed, the analyses with the NS-RPIM, both with the T3 and the T6/3 selection schemes, showed convergence upon mesh refinement. As expected (Liu, 2009), while the convergence of the FEM is "from below" (lower bound solution), the one of the NS-RPIM is "from above" (upper bound solution). The results obtained with the ES-RPIM are intermediate between the ones of the FEM and the one of the NS-RPIM. While the analyses with the selection scheme T6/3 exhibited convergence, this wasn't true for the T3 scheme, which solution started to diverge with in the discretizations with h $\simeq$ 10 mm and h $\simeq$ 5 mm.
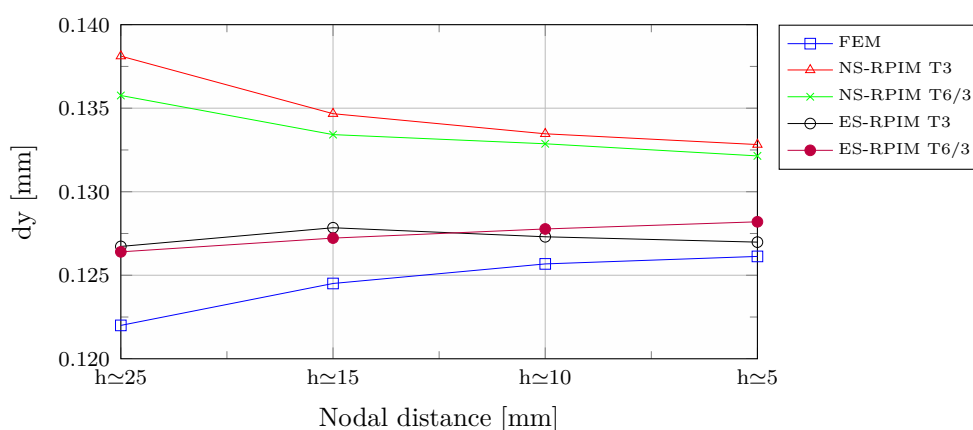
Figure 7.18: L-shaped panel - Convergence - MQ radial function (Eq. (4.21)) with C = 1.42 and q = 1.03

Better results were obtained adopting the exponential radial function with c = 0.002. As it can be observed in Fig. 7.19, the results obtained with the NS-RPIM T3 were almost the same, with slight variations in the results with the NS-RPIM T6/3. The analyses with the ES-RPIM T3, on the contrary of the previous case, exhibited convergence, while the displacements calculated with the ES-RPIM T6/3 were nearer to the ones obtained with the finite element method.
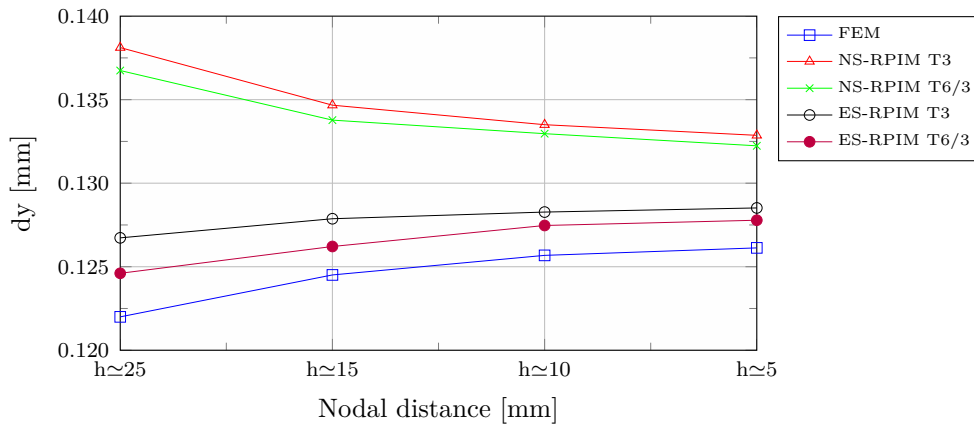
Figure 7.19: L-shaped panel - Convergence - Exponential radial function (Eq. (4.22)) with c = 0.002

It is worth to note that in all the examples based on radial functions presented in this manuscript, for a certain discrete model the parameters of the radial function were assumed to be the same at each point of the model. It is pointed out that better results could have been obtained assuming different values of that parameters from point to point, especially performing a calibration based on the mean nodal distance in the neighbor of each point.

Like for the FEM analyses, the simulations were performed adopting a loading process driven by the *generalized displacement control method* (Yang and Shieh, 1990), assuming a reference load F = 7000 N, an initial loading factor increment of 0.005, and a tollerance for convergence in relative displacement of 1×10^{-4}. The results of the analyses performed with the NS-RPIM in terms of equilibrium paths are illustrated in Fig. 7.20, while the contour plots of the damaged configurations are depicted in Figs. 7.21 and 7.22. As it can be observed, due to the upper bound approximation, the NS-RPIM produced solutions with peak values higher than the ones obtained with the FEM. However, they exhibited the same mesh dependency issues of the finite element solutions. It is interesting to note that both the T3 and the T6/3 schemes produced almost the same results, both in terms of equilibrium paths and damage distributions.

As expected from the linear elastic results depicted in Fig. 7.19, the equilibrium paths obtained with the ES-RPIM (Fig. 7.23) exhibited values that were intermediate between the ones of the FEM and the ones of the NS-RPIM. Regarding the equilibrium paths obtained with the T6/3 scheme it is interesting to note that while they still presented different peak values depending on the discretization, they were characterized by less dispersed results with respect to the ones obtained with the T3 scheme. The effect of the T6/3 scheme was more evident in the meshes 2, 3, and 4, which exhibited a considerable growth of the peak values; the coarsest mesh instead, manifested almost the same peak values with the two schemes, though the post-peak branch presented a reduced

(a) T3   (b) T6/3
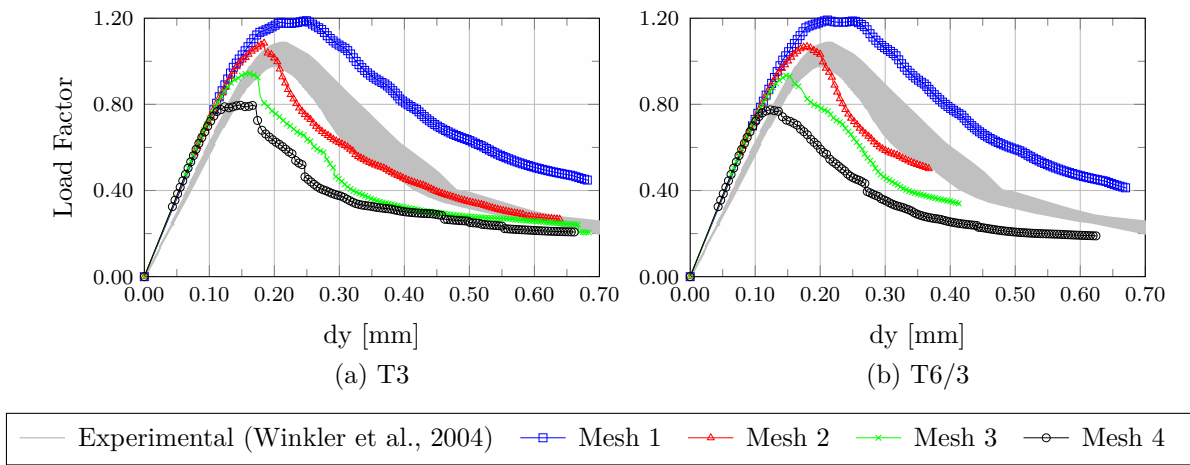
Figure 7.20: L-shaped panel - NS-RPIM - Equilibrium paths

(a) Mesh 1   (b) Mesh 2   (c) Mesh 3

(d) Mesh 4
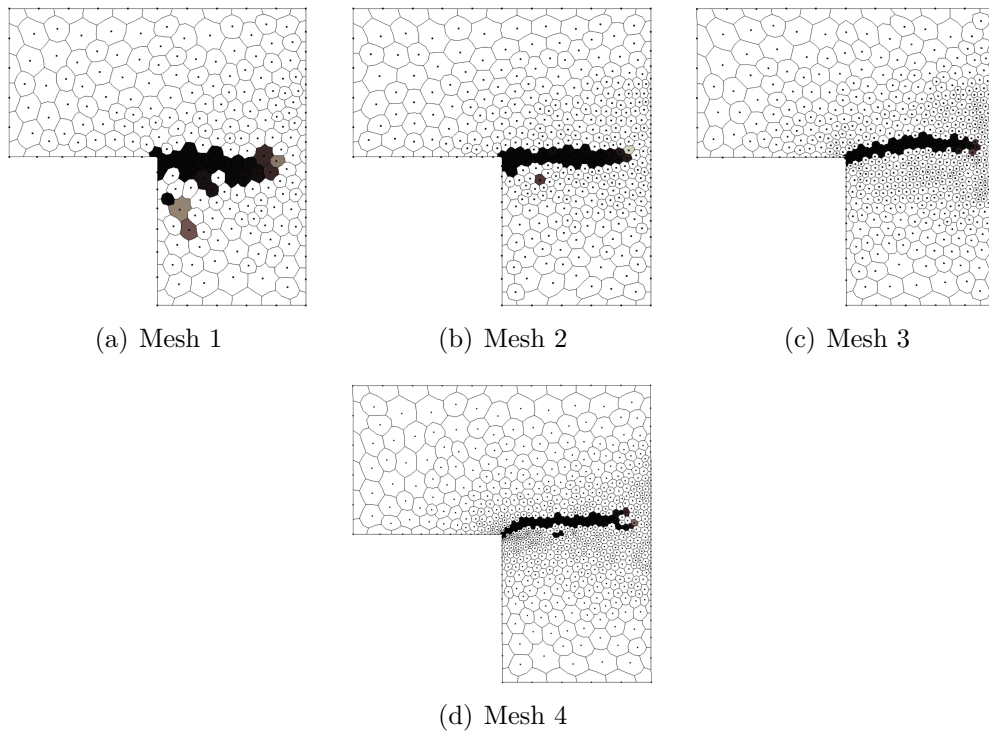
Figure 7.21: L-shaped panel - NS-RPIM T3 - Damaged configurations

(a) Mesh 1   (b) Mesh 2   (c) Mesh 3

(d) Mesh 4
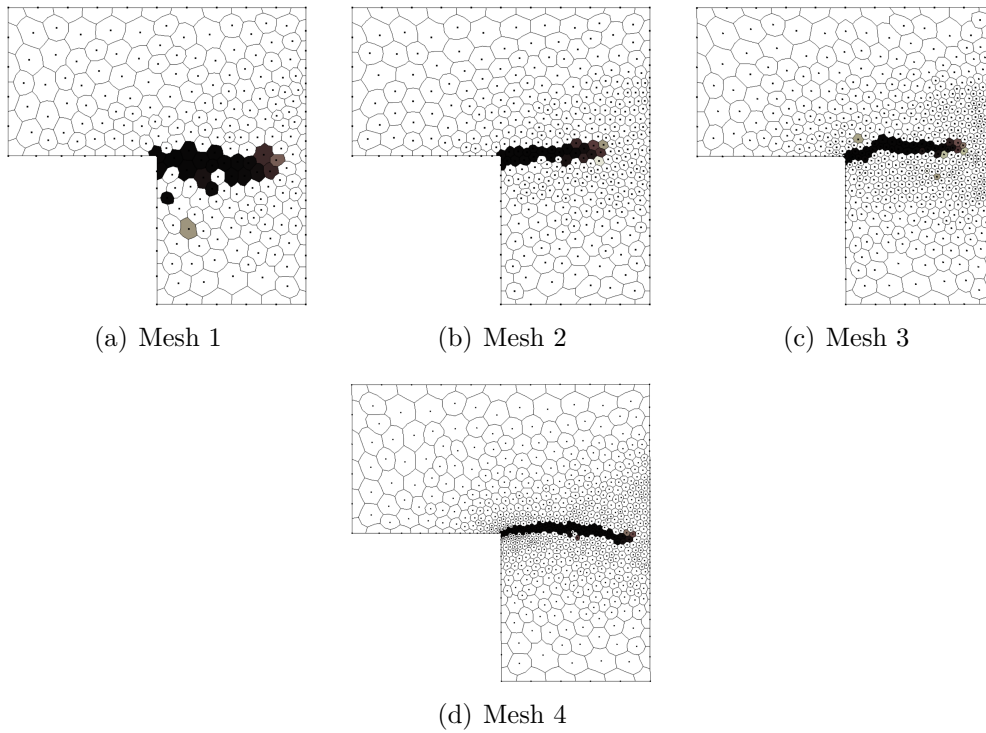
Figure 7.22: L-shaped panel - NS-RPIM T6/3 - Damaged configurations

decay with the T6/3 approach. The fact that the results obtained with the T6/3 scheme were less dispersed is also emphasized by the contour plots of the scalar damage variable depicted in Figs. 7.24 and 7.25. While the damaged zones obtained with the T3 scheme Fig. 7.24 presented a considerably narrower width as the discretization was refined, the ones obtained with the T6/3 scheme appeared to be more uniform.

(a) T3   (b) T6/3

Experimental (Winkler et al., 2004)   Mesh 1   Mesh 2   Mesh 3   Mesh 4
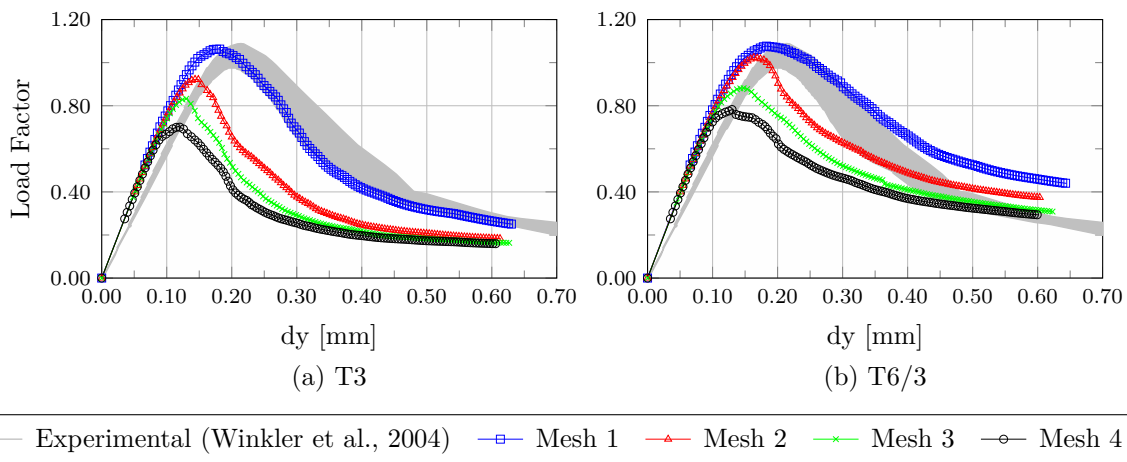
Figure 7.23: L-shaped panel - ES-RPIM - Equilibrium paths

(a) Mesh 1   (b) Mesh 2   (c) Mesh 3

(d) Mesh 4
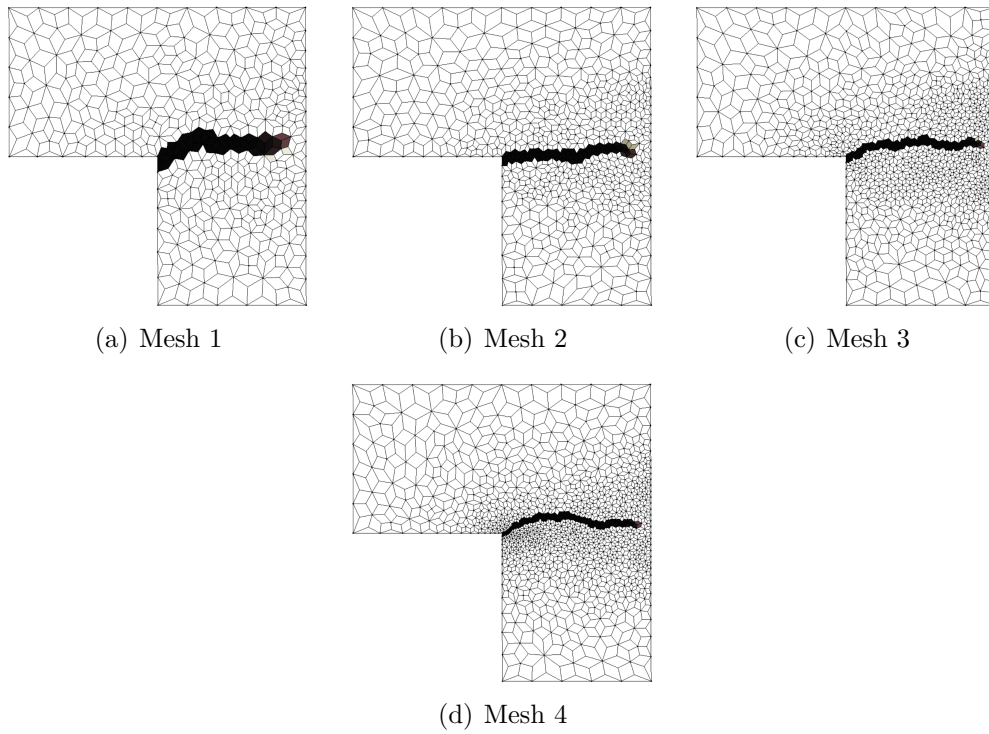
Figure 7.24: L-shaped panel - ES-RPIM T3 - Damaged configurations

(a) Mesh 1   (b) Mesh 2   (c) Mesh 3

(d) Mesh 4
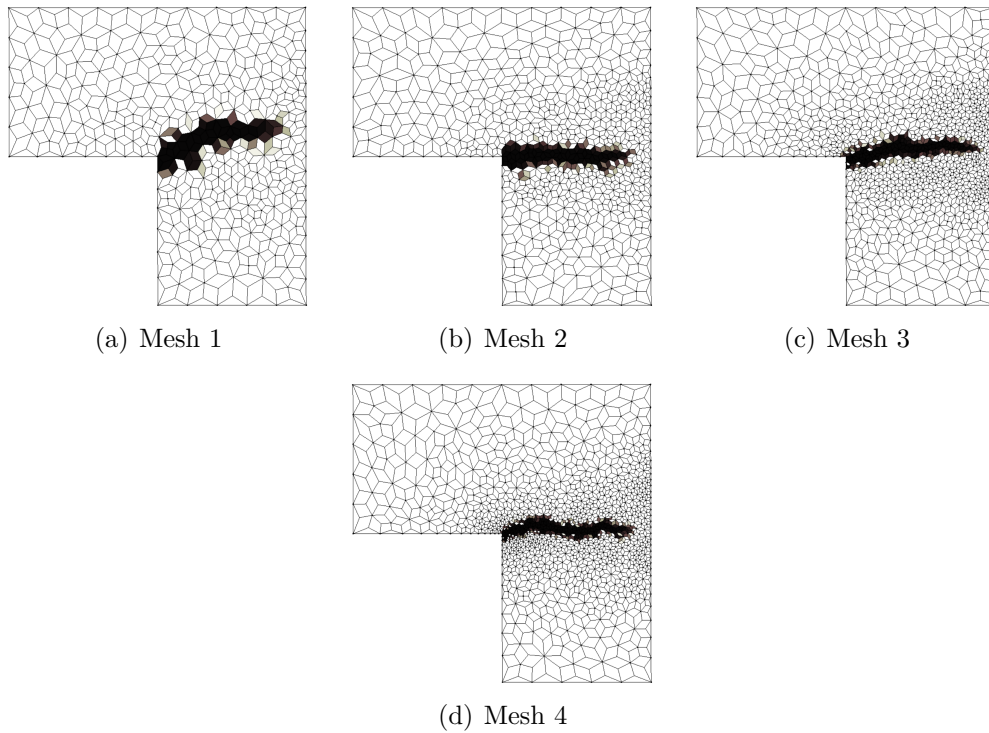
Figure 7.25: L-shaped panel - ES-RPIM T6/3 - Damaged configurations

7.3.2.1 Influence domains

The results discussed in Section 7.2 have pointed out that the ES-RPIM with T6/3 scheme was able, in that specific example, to provide mesh objective solutions. This effect of the T6/3 scheme has been partially observed also in the problem of the L-shaped panel, where it was able to produce less dispersed results with respect to the other approximation methods. As discussed in Remark 7.1, these effects are due to the intrinsic non-local nature of the smoothed point interpolation methods.

Since the T6/3 scheme wasn't sufficient to attain mesh objectivity for the L-shaped panel problem, the analyses were repeated assuming a different approach for the support nodes selection: in the zone near the concave corner (the hatched area in Fig. 7.26), the support domains were constructed using the *influence domains strategy* (Section 4.2.1.3), while in the other parts of the problem domain the T3 scheme was maintained. The adopted influence domains were circular, and the analyses were performed with three different values for their radius, 20 mm, 25 mm, and 30 mm. This approach was applied only to the meshes 2, 3, and 4, while for the mesh 1 the results obtained with the T3 scheme were maintained. As discussed in details in the following Remark 7.3, the idea of this approach was to try to amplify the non-locality of the method by using support domains larger than the ones obtainable with the sole T6/3 scheme.
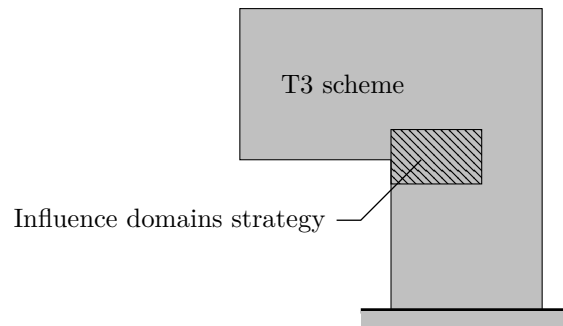
Figure 7.26: L-shaped panel - Area with support nodes selection via influence domains

---

Remark 7.3: Influence domains and non-local effect

As discussed in Section 4.2, support domains in smoothed point interpolation methods are usually constructed using T-schemes since they:
- overcome the singular moment matrix issue
- generate compact support domains, enhancing the efficiency of the method

However, as pointed out by the results exposed in Chapter 6 and in the present chapter, when dealing with strain-softening problems the presence of larger support domains seems to be beneficial in order to achieve mesh objectivity. It is important to emphasize that in the previous period, the term *larger* referred not to the number of

nodes in a support domain, but rather to its size in space. As discussed in Section 4.2 and observed also by other authors (see, e.g., Chen et al. (2000)) it is the contruction of the approximation at each integration point, made using nodes beyond the ones of the background cell which the point belong to, that provide a non-local character to a meshfree method.

The T6/3 scheme is able to provide larger support domains with respect to the T3 scheme, and the associated non-local effects was pointed out by the examples discussed in this volume. However, it is worth to note that the spatial size of the support domains generated by such scheme is still dependent on the mean nodal distance (Fig. 7.27). In order to overcome this limitation, and to improve the non-locality of the method, the use of influence domains for support domains generation was considered. The reason is due to the fact that the spatial size of such support domains (and then their non-local effect) is no longer dependent on the nodes spacing, and can be controlled by the size of the influence domains. This can be observed in Fig. 7.27, where the different support domains for a certain integration point obtained both with T-schemes and the influence domains strategy are depicted for two different discretizations. Like in a non-local continuum formulation, where the use of an intrinsic length may induce a mesh objective behaviour, it seemed reasonable to assume that analyses performed with different discretizations but adopting the same support domain size should have led to the same results; hence the reason for the application of this strategy to the example presented in this section.
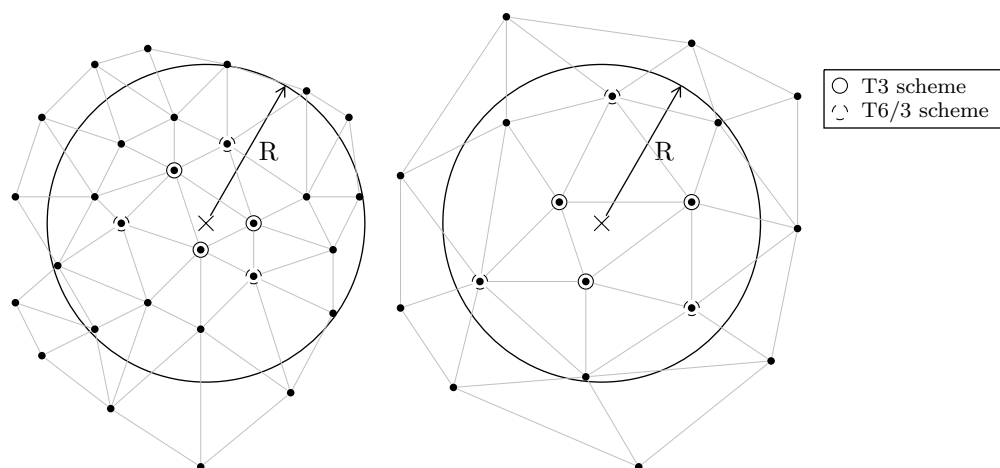
Figure 7.27: Support nodes selection via influence domains and T-schemes

Having discussed the quality of this approach, it is necessary to point out its main drawbacks. The first one is related to the efficiency of the numerical method. Larger influence domains tend to generate support domains with a large number of nodes, destroying the *sparseness* of the stiffness matrix of the discrete model, making more difficult its solution. The effects of this issue however, may be reduced by limiting

the application of such strategy to specific parts of the problem domain, as done in Fig. 7.26 where it was applied in the area interested by damage propagation (or using a KNN approach for support nodes selection, as discussed briefly in Section 4.2.1.3). The second issue is related to the moment matrix. It was observed indeed, that to a large number of nodes corresponded a bad conditioned matrix. The solution used when applying such strategy to the L-shaped panel was to limit the difference between the radius of the circular influence domains and the mean nodes spacing. A further issue regards the boundary integrals performed to evaluate the smoothed shape functions (Eq. (4.58)). When the support nodes selection is performed via T-schemes, it is known that the boundaries of the background cells may be zones of discontinuity for the shape functions, and then they are avoided when choosing the position of the integrations points along the smoothing domains boundary. However, when influence domains are adopted, the position of such discontinuity zones isn't known a priori, and there is the risk for integration points to be placed on them, affecting the quality of the results.

As it can be observed in Fig. 7.28, when circular influence domains with radius R = 20 mm were adopted, the meshes 3 and 4 exhibited almost the same equilibrium path, with a slight discrepancy in the softening branch. For the values R = 25 mm and R = 30 mm the two discretizations still manifested the same peak value, though with larger differences in the post-peak branch. Furthermore, it should be noted that to higher radii corresponded higher peak values. Considering the results obtained for the mesh 2, it is interesting to observe that as the radius of the influence domains was increased, the difference in terms of peak-values between the mesh 2 and the meshes 3 and 4 tended to decrease, emphasizing the behaviour obtained with the T6/3 scheme and observed in Fig. 7.23.

On the other hand, despite a better agreement on the value of the peak load factor, the softening branches still presented different paths. This behaviour can be ascribed, at least partially to the fact that, as pointed out by Fig. 7.26, the influence domains stategy was applied only near the damage initiation zone. In the other zones interested by damage propagation, that have an influence on the shape of the post-peak branch, the approximation was constructed using the T3 scheme, without the introduction of non-local effects. This fact seems to be confirmed also by the contour plots illustrated in Figs. 7.29 to 7.31. Indeed, as it can be observed, as long as the damage developed in the area subjected to nodes selection by influence domains, the width of the damaged zones was almost the same among the three discretizations. As it started to grow outside of that area, the damaged zones become mesh dependent again.

(a) R = 20 mm

(b) R = 25 mm

(c) R = 30 mm
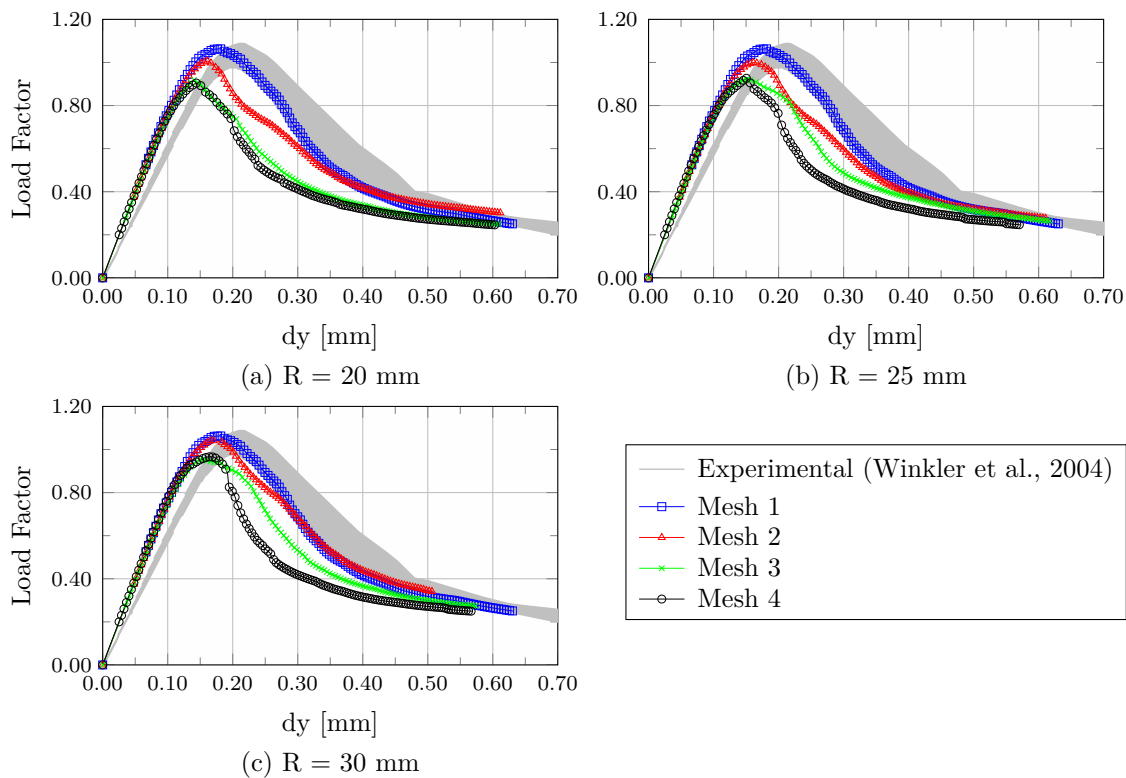
Figure 7.28: L-shaped panel - ES-RPIM with influence domains strategy - Equilibrium paths

(a) Mesh 2

(b) Mesh 3

(c) Mesh 4
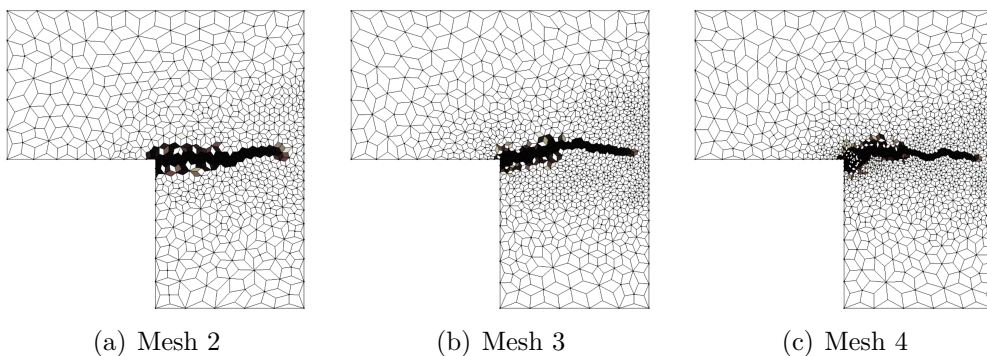
Figure 7.29: L-shaped panel - ES-RPIM with influence domains strategy - R = 20 mm - Damaged configurations

(a) Mesh 2

(b) Mesh 3

(c) Mesh 4
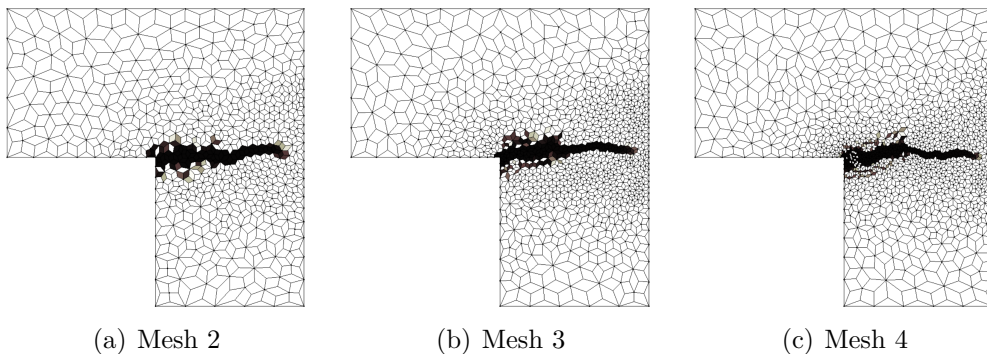
Figure 7.30: L-shaped panel - ES-RPIM with influence domains strategy - R = 25 mm - Damaged configurations

(a) Mesh 2   (b) Mesh 3   (c) Mesh 4
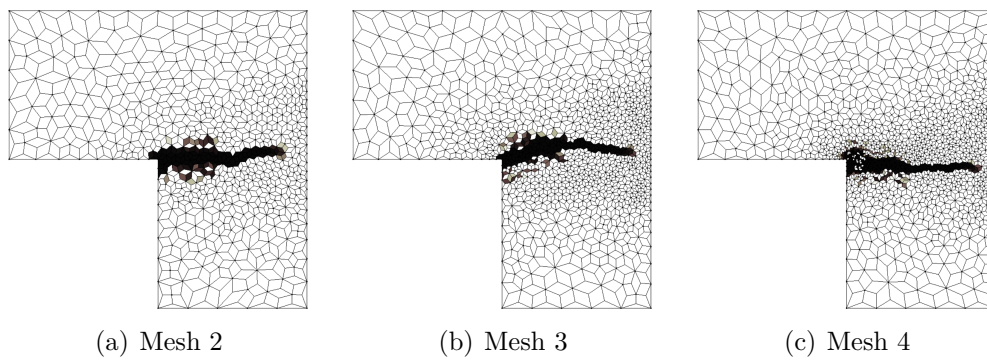
Figure 7.31: L-shaped panel - ES-RPIM with influence domains strategy - R = 30 mm - Damaged configurations

Chapter 8

Conclusions

The main aim of the present thesis was to propose a novel approach to the problem of *localization* in the modelling of *quasi-brittle* media. This task was accomplished adopting two different *regularization strategies*: the *micropolar continuum*, at the *formulation* level, and *smoothed point interpolation meshfree methods*, at the *numerical* level. Both of them, when applied individually (i.e., micropolar damage models + finite element method, and smoothed point interpolation methods + classic damage models), were capable to regularize certain classes of problems characterized by numerical and induced localization. The coupling of the two strategies (i.e., micropolar damage models + smoothed point interpolation methods) allowed to significantly improve the quality of the results in some of the cases where the individual use of one of the strategies wasn't sufficient to regularize the behaviour of the simulation. Interesting results were also obtained using the two stragies to analyze discrete models created using real experimental tests of plain concrete samples as a basis. This last set of simulations allowed to emphasize both the capability of the micropolar model to better represent certain behaviours if compared to the classic theory, and the capability of the smoothed point interpolation methods to provide mesh objective results in physically non-linear analyses. Due to the multiple topics treated in this thesis, the ones that in the author opinion were the more significant and novel contributions will be discussed in the following sections. The last section of this chapter will be devoted instead, to a survey on possible future research trends that could expand the achievements of this thesis.

8.1 Micropolar media

Regarding the field of micropolar media, this thesis provided three significant contributions to the topics listed below:

- modelling of quasi-brittle materials as micropolar elastic-degrading media;
- localization analysis;
- numerical implementation (addressed in Section 8.3).

As pointed out in Section 3.3, in the existent literature there are many applications of the micropolar continuum to problems in elasto-plasticity, with limited applications to damage models. In order to allow the use of the micropolar model to the analysis of quasi-brittle media, one of the first tasks the author dealt with was then the combination of the micropolar theory with damage models (or, more in general, with elastic-degrading models). The realization of this task pointed out a significant differece between existing micropolar physically non-linear models and analogous models based on the classic continuum theory. While the latter had been object of many investigations in the past, which allowed to obtain the so-called *unified formulations* for both elastic-degradation and elasto-plasticity (see, e.g., de Borst (1987), Carol et al. (1994), Rizzi (1995), Carol and Willam (1996), Carol (1996), de Borst and Gutiérrez (1999), Armero and Oller (2000*a,b*), Carol et al. (2001*a,b*) and Hansen et al. (2001)), the contributions in the former focused mainly on elasto-plasticity, with a certain lack of generality if compared to existent classic unified formulations, except for an attempt made in Forest and Sievert (2003) in case of micropolar elasto-plasticity. Taking into account the advantages offered by the aforementioned unified formulations for contitutive models and by their tensorial formalism, the author proposed a novel unified formulation for micropolar media able to represent a large number of elasto-plastic and elastic-degrading micropolar models (Section 3.3), inspired on the *single-criterion Cosserat's plasticity* approach discussed in Forest and Sievert (2003). Of fundamental importance for this formulation was the adoption of a peculiar *compact tensorial representation* of the constitutive equations of the micropolar model, inspired in the symbolism adopted by Eremeyev in his paper on acceleration waves in micropolar elastic media (Eremeyev, 2005).

Regarding the second topic mentioned in the list above, localization analysis, the same issues pointed out for the unified formulation apply also in this case. Indeed, the existent literature contains many investigations regarding localization analysis in classic media, considering both elasto-plasticity and elastic degradation (see the papers cited in Section 2.3), with limited contributions regarding the micropolar continuum. The ones that to the author knowledge are main contributions based on the micropolar continuum available in the literature have been pointed out in Sections 2.3 and 5.1; among them there are:

- the numerical investigations on regularization effects in micropolar elasto-plasticity by de Borst (1991), de Borst and Sluys (1991) and Sluys (1992),

- the extension to micropolar elasto-plasticity of the classic *Maxwell compatibility condition* by Dietsche et al. (1993) and Iordache and Willam (1998), together with analytical and numerical analyses on the regularization effects of the additional material parameters,

- the extension of the classic *Fresnel-Hadamard propagation condition* to visco-elastic micropolar media by Grioli (1980) and to geometrically exact elastic micropolar

media by Eremeyev (2005),

- the evaluation of the effects of the Cosserat's shear modulus on localization with numerical investigations based on an extension of the *Maxwell compatibility condition* for micropolar media with scalar damage[1] by Xotta et al. (2016).

Taking into account the lack of contributions in the field of localization analysis for elastic-degrading micropolar media, one of the main contributions of this thesis has been the extension of the concept of localization analysis to the unified formulation for micropolar elastic-degrading models discussed above. Chapter 5 presented the localization analysis of micropolar elastic-degrading models within the theory of acceleration waves propagation. The main result has been the derivation of a *localization indicator* for micropolar media, analogous to the one for classic media. Using this tool it has been possible to evaluate the effects of two of the micropolar material parameters on the onset of localization, the *Cosserat's shear modulus* and the *internal bending length* (the ones appearing in plane problems), through analytical investigations on two different stress states. The same localization indicator was also adopted to perform numerical localization analyses, using the output data of finite element and meshfree simulations, as done in Xotta et al. (2016).

The contributions by the author concerning the first two topics in the list above resulted in a number of publications in peer-reviewed journals (Gori et al., 2017*c,b*) and conference proceedings (Gori et al., 2015*a,b,c*, 2016, 2017*d*). The contributions on the other topic, the numerical implementation, will be addressed in Section 8.3.

8.2   Smoothed point interpolation methods

As pointed out in Chapter 4, the smoothed point interpolation methods were originally proposed by Liu and his co-authors for problems in classic elasticity (see, e.g., Liu (2008, 2009, 2010*a,b*)), and were also applied to elasto-plasticity (Zhang et al., 2015). The main contributions of this thesis consist in the extension of smoothed point interpolation methods to:

- elastic degradation and damage in classic media;
- micropolar elasticity;
- elastic degradation and damage in micropolar media.

These methods are based on a peculiar *weakened-weak form*, which differs from the standard one for the reduced order of continuity required for the approximation functions. The approximation functions adopted in these methods belong to the so-called *G-spaces* (Liu, 2010*a*), which properties guarantee the existence and uniqueness of the solution of the weakened-weak form. While the application to classic elastic degradation was straightfor-

---

[1]In this case the authors applied the scalar damage only to the Cauchy-like part of the constitutive operator, without affecting the couple-stresses. Hence, only the effect of the Cosserat's shear modulus was evaluated.

ward, consisting just in a proper linearization of the weakened-weak form, the use of these methods in micropolar media required greater efforts. First, a new version of the G-space theory and of the weakened-weak form were introduced, in order to take into account the different formulation with respect to a classic medium. Then, new proofs for existence and uniqueness of solutions of this modified weakened-weak form were provided. As for classic media, the application to physically non-linear models, also required the linearization of this new weakened-weak form. While these new contents were provided for the general framework of smoothed point interpolation methods, the numerical simulations presented in Chapters 6 and 7 focused on two specific strategies, the *node-based smoothed point interpolation method* (NS-PIM) and the *edge-based smoothed point interpolation method* (ES-PIM).

8.3   Numerical implementations

The realization of the numerical simulations presented in Chapters 6 and 7 required the implementation of both the unified formulation for micropolar elastic-degrading models and the node- and edge-based smoothed point interpolation methods, which was performed in the software **INSANE** (Appendix C). Regarding the implementation of the micropolar models, the major result has been the introduction of a peculiar *compact tensor-based format* for the representation of the micropolar constitutive equations, which allowed to obtain a formal compatibility with the equations based on classic media, as pointed out in Section 3.3.3. In virtue of this compatibility it has been possible to implement the micropolar elastic-degrading models in the existent *object-oriented* framework for computational models of the software **INSANE** (Penna, 2011, Gori et al., 2017a) with minimum efforts, reusing large part of the existent code. The main characteristics of this implementation has been presented in Appendix C, and has been included in a paper recently submitted by the author (Gori et al., 2018).

The object-oriented implementation of the smoothed point interpolation methods in the **INSANE** system was more challenging than the one of the constitutive models. Before the contributions of this thesis, the code structure of the **INSANE** was well-suited for the finite element method; other methods like the generalized/extended finite element method and the boundary element method, due to their FEM-like formulation, had been implemented taking advantage of the existent FEM structure. Despite the fact that it had been possible to implement also the Element-Free Galerkin method using the same class structure of the FEM, as done in Silva (2012)[2], the author observed that the same couldn't have been possible for the meshfree methods considered in this treatise. Hence, an important contribution of this thesis has been the introduction in the **INSANE** software

---

[2] The existent implementation of the Element-Free Galerkin method was extended by the author to the case of micropolar media in Gori et al. (2016).

of a new structure, well-suited for the implementation of smoothed point interpolation methods, which partially relies on existent classes used by the other methods. This new object-oriented structure has been kept quite general and, in the author opinion, it should allow for a straightforward implementation of other meshfree methods.

8.4   Future research topics

This manuscript is the final product of a four years research. While the author feel to have given a certain, though limited, contribution on the topics investigated, he recognizes that many questions have been left open, and that many paths and new ideas that arose during this research have not been followed, in favor of the contents of this manuscript. The present section is then thought as a memorandum, regarding the possible future research topics that could give continuity to the work presented in this treatise. These suggestions are collected in the three areas listed below, and exposed in the following:

- localization analysis for the micropolar continuum and other generalized continua;
- regularization effects of meshfree methods;
- modelling of quasi-brittle media as generalized continua.

8.4.1   Localization analysis for the micropolar continuum and other generalized continua

- The present research pointed out some of the regularization properties of the micropolar continuum in elastic-degrading constitutive models, confirming results that had been found previously in the field of micropolar elasto-plasticity. Taking in mind that the localization analysis (or discontinuous failure) is only one of the possible *failure indicators* (see, e.g., Neilsen and Schreyer (1993) and de Borst et al. (1993)), efforts should be made to apply the other indicators, such as the *loss of material stability* and *loss of uniqueness* to constitutive models based on the micropolar theory.
- The investigations presented here, as well as the ones available in the literature regarding localization in micropolar elasto-plasticity, focused on plane-states, where only the Cosserat's shear modulus and the internal bending length appear. Hence, it would be interesting to investigate three-dimensional stress states, evaluating the effects on the onset of localization of the 4 remaining micropolar material parameters.
- The analytical investigations performed in Section 5.4 and the numerical analyses in Chapter 6, took into account a single constitutive model, an associated scalar-isotropic damage model. Further efforts should be focused on the extension of such localization analyses to other micropolar constitutive models, considering also *non-*

associated models where there is a distinction between the *loss of ellipticity* and *loss of strong ellipticity* conditions.

- The *numerical* localization analyses performed in Chapter 6 (and in Xotta et al. (2016)) are an intersting tool for the evaluation of the localized state of a sample during a simulation, but their applicability is limited due their computational cost. Hence, efforts should be made in order to optimize such evaluations, to make them available for a real time use during the simulations.

8.4.2   Regularization effects of meshfree methods

- Regarding the investigation of the regularization effects in meshfree methods, this work focused only on two strategies, the NS-PIM and ES-PIM, both of them applied to the plane-stress state. Further investigations should consider both the application to other stress states and the use of other methods of the smoothed point interpolation family.

- The regularization properties of meshfree methods were first pointed out in Chen et al. (2000) for the Element-Free Galerkin and Reproducing Kernel methods, and the present work pointed out their presence also in two of the smoothing point interpolation methods. It would be interesting then to investigate the presence of such properties also in other common meshfree methods, like the Meshless Local Petrov-Galerkin for example.

- Regarding the physically non-linear simulations peformed in Chapters 6 and 7 with the NS-PIM and ES-PIM, it would be interesting to investigate in details the eventual effects on the onset of localization of the kind of radial functions and of their parameters.

- Furthermore, taking into account the results obtained in Chapter 7 with the use of the influence domains strategy, further investigations should be devoted to overcome the issues related to the use of this method, in order to make it an available regularization tool. As mentioned in Section 4.2.1.3, interesting results could be obtained using support nodes selection strategies via *K-Nearest Neighbor* (KNN) algorithms, for example.

8.4.3   Modelling of quasi-brittle media as generalized continua

- Besides its regularization effects, the micropolar model has been also shown to be useful for the representation of the behaviour of quasi-brittle media in cases where the classic continuum was not sufficient, using simple scalar-isotropic damage models (see, e.g., the four point shear test in Section 7.2). In order to provide an even better representation of experimental results, efforts should be made to obtain further micropolar models capable to take into account more complex phenomena,

like different behaviours in tension and compression, anisotropic damage evolution, and microcracks closure-reopening effect, for example.

- The micropolar elastic-degrading models presented in Section 3.3 are *phenomenological*. Another interesting approach consists in the use of models based on *micromechanics*, i.e., models derived taking into account the peculiar microstructure of a material. In Section 3.2.3.2, some strategies regarding the characterization of the *elastic* material parameters of the micropolar medium have been presented. In the author opinion, a promising path for the derivation of micromechanics-based models could be the use of the analytical and numerical homogenization techniques presented in Section 3.2.3.2, properly improved for the application to physical nonlinearities.

- As pointed out in Section 3.1, the micropolar continuum is only one of the possible *multifield continua*. A better representation of the degrading phenomena in quasi-brittle media could be given by the use of different multifield strategies, more advanced than the micropolar one, especially the ones that combine the use of additional kinematical variables with the inclusion of the degrading phenomena among the field variables of the problem.

Bibliography

Addessi, D., De Bellis, M. L. and Sacco, E. (2016), 'A micromechanical approach for the Cosserat modeling of composites', *Meccanica* vol. 51, 569–592.

Adomeit, G. (1968), Determination of Elastic Constants of a Structured Material, *in* E. Kröner, ed., 'Mechanics of Generalized Continua', Springer Berlin Heidelberg, Berlin, Heidelberg, pp. 80–82.

Armero, F. and Oller, S. (2000*a*), 'A general framework for continuum damage models. I. Infinitesimal plastic damage models in stress space', *International Journal of Solids and Structures* vol. 37(48–50), 7409–7436.

Armero, F. and Oller, S. (2000*b*), 'A general framework for continuum damage models. II. Integration algorithms, with applications to the numerical simulation of porous metals', *International Journal of Solids and Structures* vol. 37, 7437–7464.

Arrea, M. and Ingraffea, A. R. (1982), Mixed mode crack propagation in mortar and concrete, Technical report, Departement of Structural Engineering, Cornell University, Ithaca, USA.

Arriaga, M., McAuliffe, C. and Waisman, H. (2015), 'Onset of shear band localization by a local generalized eigenvalue analysis', *Computer Methods in Applied Mechanics and Engineering* vol. 289, 179–208.

Asaro, R. J. (1983), Micromechanics of Crystals and Polycrystals, *in* 'Advances in Applied Mechanics', Vol. 23, pp. 1–115.

Askar, A. and Cakmak, A. (1968), 'A structural model of a micropolar continuum', *International Journal of Engineering Science* vol. 6, 583–589.

Atluri, S. N. and Zhu, T. (1998), 'A new meshless Local Petrov-Galerkin (MLPG) approach in computational mechanics', *Computational Mechanics* vol. 22(2), 117–127.

Badnava, H., Mashayekhi, M. and Kadkhodaei, M. (2016), 'An anisotropic gradient damage model based on microplane theory', *International Journal of Damage Mechanics* vol. 25(3), 336–357.

Banks, C. B. and Sokolowski, M. (1968), 'On certain two-dimensional applications of the couple stress theory', *International Journal of Solids and Structures* vol. 4, 15–29.

Barenblatt, G. I. (1962), 'The mathematical theory of equilibrium of crack in brittle fracture', *Advances in Applied Mechanics* vol. 7, 55–129.

Bathe, K. J. (1996), *Finite element procedures*, Prentice Hall, New Jersey.

Batoz, J.-L. and Dhatt, G. (1979), 'Incremental displacement algorithms for nonlinear problems', *International Journal for Numerical Methods in Engineering* vol. 14(8), 1262–1267.

Bažant, Z. P. (1991), 'Why continuum damage is nonlocal: Micromechanics arguments', *Journal of Engineering Mechanics* vol. 117(5), 1070–1087.

Bažant, Z. P. and Christensen, M. (1972), 'Analogy between micropolar continuum and grid frameworks under initial stress', *International Journal of Solids and Structures* vol. 8, 327–346.

Bažant, Z. P. and Jirásek, M. (2002), 'Nonlocal integral formulations of plasticity and damage: Survey of progress', *Journal of Engineering Mechanics* vol. 128(11), 1119–1149.

Bažant, Z. P. and Lin, F.-B. (1988), 'Non-local yield limit degradation', *International Journal for Numerical Methods in Engineering* vol. 26(8), 1805–1823.

Bažant, Z. P. and Oh, B. H. (1983), 'Crack band for fracture of concrete', *Matériaux et Constructions* vol. 16, 155–177.

Belytschko, T. and Black, T. (1999), 'Elastic crack growth in finite elements with minimal remeshing', *International Journal for Numerical Methods in Engineering* vol. 45, 601–620.

Belytschko, T., Fish, J. and Engelmann, B. E. (1988), 'A finite element with embedded localization zones', *Computer Methods in Applied Mechanics and Engineering* vol. 70, 59–89.

Belytschko, T., Lu, Y. Y. and Gu, L. (1994), 'Element-free Galerkin methods', *International Journal for Numerical Methods in Engineering* vol. 37(2), 229–256.

Benzerga, A. A. and Leblond, J. B. (2010), 'Ductile Fracture by Void Growth to Coalescence', *Advances in Applied Mechanics* vol. 44, 169–305.

Berglund, K. (1982), *Structural models of micropolar media*, World scientific, pp. 35–86.

Bigoni, D. (2014), *Nonlinear Solid Mechanics: Bifurcation Theory and Material Instability*, Cambridge University Press.

Bigoni, D. and Drugan, W. J. (2007), 'Analytical derivation of Cosserat moduli via homogenization of heterogeneous elastic materials', *Journal of Applied Mechanics* vol. 74, 741–753.

Bigoni, D. and Hueckel, T. (1991*a*), 'Uniqueness and localization—I. Associative and non-associative elastoplasticity', *International Journal of Solids and Structures* vol. 28(2), 197–213.

Bigoni, D. and Hueckel, T. (1991*b*), 'Uniqueness and localization—II. Coupled elastoplasticity', *International Journal of Solids and Structures* vol. 28(2), 215–224.

Bigoni, D. and Zaccaria, D. (1992), 'Loss of strong ellipticity in non-associative elastoplasticity', *Journal of the Mechanics and Physics of Solids* vol. 40(6), 1313–1331.

Bigoni, D. and Zaccaria, D. (1994), 'On the eigenvalues of the acustic tensor in elastoplasticity', *European Journal of Mechanics, A/Solids* vol. 13(5), 621–638.

Borré, G. and Maier, G. (1989), 'On linear versus nonlinear flow rules in strain localization analysis', *Meccanica* vol. 24, 36–41.

Brenner, S. C. and Scott, L. R. (2008), *The mathematical theory of finite elements methods*, 3 edn, Springer.

Carol, I. (1996), Elastic degradation and damage: plasticity-like formulation, stiffness recovery and localization, *in* 'Mecánica Computacional, Volume XVII. Number 4. Solid Mechanics (A)', Tucumán, Argentina.

Carol, I., Rizzi, E. and Willam, K. (2001*a*), 'On the formulation of anisotropic elastic degradation. I. Theory based on a pseudo-logarithmic damage tensor rate', *International Journal of Solids and Structures* vol. 38(4), 491–518.

Carol, I., Rizzi, E. and Willam, K. (2001*b*), 'On the formulation of anisotropic elastic degradation. II. Generalized peudo-Rankine model for tensile damage', *International Journal of Solids and Structures* vol. 38(4), 519–546.

Carol, I., Rizzi, E. and Willam, K. J. (1994), 'A unified theory of elastic degradation and damage based on a loading surface', *International Journal of Solids and Structures* vol. 31(20), 2836–2865.

Carol, I. and Willam, K. (1996), 'Spurious energy dissipation/generation in stiffness recovery models for elastic degradation and damage', *International Journal of Solids and Structures* vol. 33(20-22), 2939–2957.

Cedolin, L., Dei Poli, S. and Iori, I. (1987), 'Tensile behavior of concrete', *Journal of Engineering Mechanics (ASCE)* vol. 113(3), 431–449.

Cervera, M. and Tesei, C. (2017), 'An energy-equivalent d^+/d^- damage model with enhanced microcrack closure-reopening capabilities for cohesive-frictional materials', *Materials* vol. 10.

Chang, C. S. and Liao, C. L. (1990), 'Constitutive relation for a particulate medium with the effect of particle rotation', *International Journal of Solids and Structures* vol. 26(4), 437–453.

Chang, C. S. and Ma, L. (1991), 'A micromechanical-based micropolar theory for deformation of granular solids', *International Journal of Solids and Structures* vol. 28(1), 67–86.

Chang, C. S. and Ma, L. (1992), 'Elastic material constants for isotropic granular solids with particle rotation', *International Journal of Solids and Structures* vol. 29(8), 1001–1018.

Chaudhuri, P. (2013), 'Multi-scale modeling of fracture in concrete composites', *Composites Part B: Engineering* vol. 47, 162–172.

Chen, J. S., Hu, W., Puso, M. and Zhang, X. (2007), Strain smoothing for stabilization and regularization of Galerkin meshfree, *in* M. Griebel and M. A. Schweitzer, eds, 'Meshfree Methods for Partial Differential Equations III', Vol. 57, Springer Berlin Heidelberg, Berlin, Germany, pp. 57–75.

Chen, J.-S., Wu, C.-T., Yoon, S. and You, Y. (2001), 'A stabilized conforming nodal integration for Galerkin mesh-free methods', *International Journal for Numerical Methods in Engineering* vol. 50, 435–466.

Chen, J. S., Wu, T. C., Belytschko, T., Wu, C. and Belytschko, T. (2000), 'Regularization of material instabilities by meshfree approximations with intrinsic length scales', *International Journal for Numerical Methods in Engineering* vol. 47, 1303–1322.

Chen, J.-S., Yoon, S. and Wu, C.-T. (2002), 'Non-linear version of stabilized conforming nodal integration for Galerkin mesh-free methods', *International Journal for Numerical Methods in Engineering* vol. 53, 2587–2615.

Chen, J. S., Zhang, X. and Belytschko, T. (2004), 'An implicit gradient model by a reproducing kernel strain regularization in strain localization problems', *Computer Methods in Applied Mechanics and Engineering* vol. 193, 2827–2844.

Chen, Z. and Butcher, C. (2013), *Micromechanics Modelling of Ductile Fracture*, Vol. 195.

Chung, J. and Waas, A. M. (2009), 'The micropolar elasticity constants of circular cell honeycombs', *Proceedings of the Royal Society A: Mathematical, Physical and Engineering Sciences* vol. 465, 25–39.

Coleman, B. D. and Gurtin, M. E. (1967), 'Thermodynamics with internal state variables', *The Journal of Chemical Physics* vol. 47(2), 597–613.

Collins, I. F. and Houlsby, G. T. (1997), 'Application of thermomechanical principles to the modelling of geotechnical materials', *Proceedings of the Royal Society A: Mathematical, Physical and Engineering Sciences* vol. 453, 1975–2001.

Comi, C. and Perego, U. (2001), 'Fracture energy based bi-dissipative damage model for concrete', *International Journal of Solids and Structures* vol. 38, 6427–6454.

Cosserat, E. and Cosserat, F. (1909), *Théorie des corps déformables*, Hermann et fils, Paris. (in french).

Crisfield, M. (1981), 'A fast incremental/iterative solution procedure that handles "snap-through"', *Computers and Structures* vol. 13(1), 55 – 62.

Crisfield, M. A. (1983), 'An arc-length method including line searches and accelerations', *International Journal for Numerical Methods in Engineering* vol. 19(9), 1269–1289.

Daxini, S. D. and Prajapati, J. M. (2014), 'A review on recent contribution of meshfree methods to structure and fracture mechanics applications', *The Scientific World Journal* vol. 2014, 1–13.

De Bellis, M. L. and Addessi, D. (2014), 'A micromechanical approach for the micropolar modeling of heterogeneous periodic media', *Fracture and Structural Integrity* vol. 29, 37–48.

de Borst, R. (1987), 'Smeared cracking, plasticity, creep and thermal loading - A unified approach', *Computer Methods in Applied Mechanics and Engineering* vol. 62, 89–110.

de Borst, R. (1991), 'Simulation of strain localization: a reappraisal of the Cosserat continuum', *Engineering Computations* vol. 8, 317–332.

de Borst, R. (1993), 'A generalisation of J2-flow theory for polar continua', *Computer Methods in Applied Mechanics and Engineering* vol. 103, 347–362.

de Borst, R. (2002), 'Fracture in quasi-brittle materials: a review of continuum damage-based approaches', *Engineering Fracture Mechanics* vol. 69(2), 95–112.

de Borst, R. and Abellan, M. A. (2002), 'A numerical framework for continuum-discontinuum transition', *Archive of Applied Mechanics* vol. 54(5-6), 377–387.

de Borst, R. and Gutiérrez, M. A. (1999), 'A unified framework for concrete damage and fracture models including size effects', *International Journal of Fracture* vol. 95(1-4), 261–277.

de Borst, R., Gutiérrez, M. a., Wells, G. N., Remmers, J. J. C. and Askes, H. (2004), 'Cohesive-zone models, higher-order continuum theories and reliability methods for computational failure analysis', *International Journal for Numerical Methods in Engineering* vol. 60, 289–315.

de Borst, R. and Mühlhaus, H.-B. (1992), 'Gradient dependent plasticity: Formulation and algorithmic aspects', *International Journal for Numerical Methods in Engineering* vol. 35, 521–539.

de Borst, R., Remmers, J. J. C., Needleman, A. and Abellan, M.-A. (2004), 'Discrete vs smeared crack models for concrete fracture: bridging the gap', *International Journal for Numerical and Analytical Methods in Geomechanics* vol. 28(78), 583–607.

de Borst, R. and Sluys, L. (1991), 'Localization in a Cosserat continuum under static and dynamic loading conditions', *Computer Methods in Applied Mechanics and Engineering* vol. 90, 805–827.

de Borst, R., Sluys, L., Mühlhaus, H.-B. and Pamin, J. (1993), 'Fundamental issues in finite element analyses of localization of deformation', *Engineering Computations* vol. 10, 99–121.

de Vree, J. H. P., Brekelmans, W. A. M. and van Gils, M. A. J. (1995), 'Comparison of nonlocal approaches in continuum damage mechanics', *Computer and Structures* vol. 55(4), 581–588.

Desoyer, T. and Cormery, F. (1994), 'On uniqueness and localization in elastic-damage materials', *International Journal of Solids and Structures* vol. 31(5), 733–744.

Di Prisco, C., Mariotti, R. and Nova, R. (1992), A mathematical model of grouted sand allowing for strength degradation, *in* 'Numerical Models in Geomechanics, Proceedings of the NUMOG IV Conference', Swansea, UK.

Dietsche, A., Steinmann, P. and Willam, K. (1993), 'Micropolar elastoplasticity and its role in localization', *International Journal of Plasticity* vol. 9, 813–831.

Ding, J. and Zhou, A. (2007), 'Eigenvalues of rank-one updated matrices with some applications', *Applied Mathematics Letters* vol. 20, 1223–1226.

Dos Reis, F. and Ganghoffer, J. F. (2011), Construction of micropolar continua from the homogenization of repetitive planar lattices, *in* 'Mechanics of Generalized Continua', Springer-Verlag, Berlin, Germany, pp. 193–217.

Dos Reis, F. and Ganghoffer, J. F. (2012), 'Construction of micropolar continua from the asymptotic homogenization of beam lattices', *Computers and Structures* vol. 112-113, 354–363.

Drucker, D. C. (1964), 'On the postulate of stability of materials in the mechanics of continua', *Journal de Mécanique* vol. 3(2), 235–249.

Dugdale, D. S. (1960), 'Yielding of steel sheets containing slits', *Journal of the Mechanics and Physics of Solids* vol. 8, 100–104.

Eremeyev, V. A. (2005), 'Acceleration waves in micropolar elastic media', *Doklady Physics* vol. 50(4), 204–206.

Eremeyev, V. A., Lebedev, L. P. and Altenbach, H. (2013), *Foundations of Micropolar Mechanics*, 1 edn, Springer-Verlag Berlin Heidelberg.

Eringen, A. C. (1999), *Microcontinuum Field Theories - I: Fundations and Solids*, Springer-Verlag, New York.

Eringen, A. C. and Edelen, D. G. B. (1972), 'On nonlocal elasticity', *International Journal of Engineering Science* vol. 10, 233–248.

Fang, X.-J., Jin, F. and Yang, Q.-D. (2008), 'Extended finite-element analysis of fractures in concrete', *Engineering and Computational Mechanics* vol. 161(EM4), 187–197.

Feng, Y., Perić, D. and Owen, D. (1996), 'A new criterion for determination of initial loading parameter in arc-length methods', *Computer and Structures* vol. 58(3), 479 – 485.

Forest, S. (2009), 'Micromorphic approach for gradient elasticity, viscoplasticity, and damage', *Journal of Engineering Mechanics* vol. 135(3), 117–131.

Forest, S., Blazy, J.-S., Chastel, Y. and Moussy, F. (2005), 'Continuum modeling of strain localization phenomena in metallic foams', *Journal of Materials Science* vol. 40(22), 5903–5910.

Forest, S. and Sievert, R. (2003), 'Elastoviscoplastic constitutive frameworks for generalized continua', *Acta Mechanica* vol. 160, 71–111.

Frémond, M. and Nedjar, B. (1996), 'Damage, gradient of damage and principle of virtual power', *International Journal of Solids and Structures* vol. 33(8), 1083–1103.

Fuina, J. S. (2009), Formulações de modelos constitutívos de microplanos para contínuos generalizados, Phd thesis, Universidade Federal de Minas Gerais (UFMG), Belo Horizonte, Brazil. (in portuguese).

Gauthier, R. and Jahsman, W. E. (1975), 'A quest for micropolar elastic constants', *Journal of Applied Mechanics* vol. 42(2), 369–374.

Geuzaine, C. and Remacle, J. (2009), 'Gmsh: A 3D finite element mesh generator with builtin pre and postprocessing facilities', *International Journal for Numerical Methods in Engineering* vol. 79(11), 1309–1331.

Ghosh, A. and Chaudhuri, P. (2013), 'Computational modeling of fracture in concrete using a meshfree meso-macro-multiscale method', *Computational Materials Science* vol. 69, 204–215.

Gimp (n.d.), https://www.gimp.org/.

Gingold, R. A. and Monaghan, J. J. (1977), 'Smoothed particle hydrodynamics: theory and applications to non-spherical stars', *Monthly Notics of the Royal Astronomical Society* vol. 181, 375–389.

Goda, I., Assidi, M., Belouettar, S. and Ganghoffer, J. F. (2012), 'A micropolar anisotropic constitutive model of cancellous bone from discrete homogenization', *Journal of the Mechanical Behavior of Biomedical Materials* vol. 16, 87–108.

Goda, I., Assidi, M. and Ganghoffer, J. F. (2012), 'Cosserat 3D anisotropic models of trabecular bone from the homogenisation of the trabecular structure', *Computer Methods in Biomechanics and Biomedical Engineering* vol. 15(sup1), 288–290.

Goda, I., Assidi, M. and Ganghoffer, J. F. (2014), 'A 3D elastic micropolar model of vertebral trabecular bone from lattice homogenization of the bone microstructure', *Biomechanics and Modeling in Mechanobiology* vol. 13, 53–83.

Golberg, M., Chen, C. and Bowman, H. (1999), 'Some recent results and proposals for the use of radial basis functions in the BEM', *Engineering Analysis with Boundary Elements* vol. 23, 285–296.

Gori, L., Andrade, M. P., da Silva, R. P., Penna, S. S. and Pitangueira, R. L. d. S. (2016), Scalar damage based on micropolar continua – Mesh-free approximation, *in* S. M. Ávila, ed., 'Proceedings of the XXXVII Iberian Latin-American Congress on Computational Methods in Engineering', Brasília, DF, Brazil.

Gori, L., Penna, S. S. and Pitangueira, R. L. d. S. (2017*a*), 'A computational framework for constitutive modelling', *Computers and Structures* vol. 187, 1–23.

Gori, L., Penna, S. S. and Pitangueira, R. L. d. S. (2017*b*), 'Discontinuous failure in micropolar elastic-degrading models', *International Journal of Damage Mechanics* vol. 0(0).

Gori, L., Penna, S. S. and Pitangueira, R. L. d. S. (2017*c*), 'An enhanced tensorial formulation for elastic degradation in micropolar continua', *Applied Mathematical Modelling* vol. 41, 299–315.

Gori, L., Penna, S. S. and Pitangueira, R. L. d. S. (2017*d*), Micropolar formulation for regularization of material instabilities in scalar damage models, *in* P. Faria, R. Lopez, L. Miguel, W. Gomes and M. Noronha, eds, 'Proceedings of the XXXVIII Iberian Latin-American Congress on Computational Methods in Engineering', Florianópolis, SC, Brazil.

Gori, L., Penna, S. S. and Pitangueira, R. L. d. S. (2018), 'A computational framework for the constitutive modelling of non-linear micropolar media', *European Journal of Computacional Mechanics* vol. 0(0). (submitted).

Gori, L., Pitangueira, R. L. d. S., Penna, S. S. and Fuina, J. S. (2015*a*), 'A generalized elasto-plastic micro-polar constitutive model', *Applied Mechanics and Materials* vol. 798, 505–509.

Gori, L., Pitangueira, R. L. d. S., Penna, S. S. and Fuina, J. S. (2015*b*), Isotropic damage models based on a generalized micro-polar continuum theory, *in* 'Anais do 57º Congresso Brasileiro do Concreto', Bonito, MS, Brazil, pp. 1–14.

Gori, L., Pitangueira, R. L. d. S., Penna, S. S. and Fuina, J. S. (2015*c*), A theoretical and computational framework for isotropic damage models based on a generalized micro-polar continuum theory, *in* N. A. Dumont, ed., 'XXXVI Ibero-Latin American Congress on Computational Methods in Engineering', Rio de Janeiro, RJ, Brazil, pp. 1–15.

Griffith, A. (1921), 'The phenomena of rupture and flow in solids', *Philosophical Transactions of the Royal Society A: Mathematical, Physical and Engineering Sciences* vol. 221(582-593), 163–198.

Grioli, A. C. (1980), 'Propagazione di onde di accelerazione in un solido viscoelastico di Cosserat', *Rendiconti del Seminario Matematico della Università di Padova* vol. 64, 25–37. (in italian).

Hadamard, J. (1903), *Leçons sur la Propagation des Ondes et les Equations de l'Hydrodynamique*, A. Hermann, France. (in french).

Hansen, E., Willam, K. and Carol, I. (2001), A two-surface anisotropic damage/plasticity model for plain concrete, *in* R. de Borst and A. A. Balkema, eds, 'Proceedings of the Fracture Mechanics of Concrete Materials Conference (Framcos-4)', Paris, France, pp. 549–556.

Hassanpour, S. and Heppler, G. R. (2015), 'Micropolar elasticity theory: a survey of linear isotropic equations, representative notations, and experimental investigations', *Mathematics and Mechanics of Solids* pp. 1–19.

Havner, K. S. (1992), *Finite Plastic Deformation of Crystalline Solids*, Cambridge University Press, Cambridge, UK.

Herrmann, G. and Achenbach, J. D. (1968), Applications of theories of generalized Cosserat continua to the dynamics of composite materials, *in* E. Kröner, ed., 'Mechanics of Generalized Continua', Springer Berlin Heidelberg, Berlin, Heidelberg, pp. 69–79.

Hill, R. (1958), 'A general theory of uniqueness and stability in elastic-plastic solids', *Journal of the Mechanics and Physics of Solids* vol. 6(3), 236–249.

Hill, R. (1962), 'Acceleration waves in solids', *Journal of the Mechanics and Physics of Solids* vol. 10, 1–16.

Hill, R. (1963), 'Elastic properties of reinforced solids: Some theoretical principles', *Journal of the Mechanics and Physics of Solids* vol. 11(5), 357–372.

Hill, R. (1998), *The Mathematical Theory of Plasticity*, Oxford classic texts in the physical sciences, Clarendon Press.

Hillerborg, A., Modéer, M. and Petersson, P.-E. (1976), 'Analysis of crack formation and crack growth in concrete by means of fracture mechanics and finite elements', *Cement and Concrete Research* vol. 6, 773–781.

Hlaváček, I. and Hlaváček, M. (1969), 'On the existence and uniqueness of solution and some variational principles in linear theories of elasticity with couple-stresses. I: Cosserat continuum', *Aplikace matematiky* vol. 14(5), 387–410.

Horgan, C. O. (1995), 'Korn's inequalities and their applications in continuum mechanics', *SIAM Review* vol. 37(4), 491–511.

Huang, W. and Bauer, E. (2003), 'Numerical investigations of shear localization in a micro-polar hypoplastic material', *International Journal for Numerical and Analytical Methods in Geomechanics* vol. 27, 325–352.

Huang, W. and Xu, K. (2015), 'Characteristic lengths in Cosserat continuum modeling of granular materials', *Engineering Computations* vol. 32(4), 973–984.

Hunter, J. D. (2007), 'Matplotlib: A 2D graphics environment', *Computing In Science & Engineering* vol. 9(3), 90–95.

Ingraffea, A. R. and Saouma, V. (1987), Numerical modelling of discrete crack propagation in reinforced and plain concrete, *in* 'Fracture Mechanics of Concrete', Martinus Nijhoff Publishers, Dordrecht, pp. 171–225.

Inkscape (n.d.), `https://inkscape.org/`.

INSANE - INteractive Structural ANalysis Environment (n.d.), `https://www.insane.dees.ufmg.br/`.

Iordache, M.-M. M. and Willam, K. (1998), 'Localized failure analysis in elastoplastic Cosserat continua', *Computer Methods in Applied Mechanics and Engineering* vol. 151, 559–586.

Jeong, J. and Neff, P. (2015), 'Existence, uniqueness and stability in linear Cosserat elasticity for weakest curvature conditions', *Mathematics and Mechanics of Solids* vol. 15, 78–95.

Jeremić, B., Runesson, K. and Sture, S. (1999), 'Object-oriented approach to hyperelasticity', *Engineering with Computers* vol. 15, 2–11.

Jeremić, B. and Sture, S. (1998), 'Tensor objects in finite element programming', *International Journal for Numerical Methods in Engineering* vol. 41, 113–126.

Jeremić, B. and Yang, Z. (2002), 'Template elastic-plastic computations in geomechanics', *International Journal for Numerical and Analytical Methods in Geomechanics* vol. 26, 1407–1427.

Jirásek, M. (2007*a*), 'Mathematical analysis of strain localization', *Revue Européenne de Génie Civil* vol. 11(7-8), 977–991.

Jirásek, M. (2007*b*), 'Nonlocal damage mechanics', *Revue Européenne de Génie Civil* vol. 11(7-8), 993–1021.

Joumaa, H. and Ostoja-Starzewski, M. (2011), 'Stress and couple-stress invariance in non-centrosymmetric micropolar planar elasticity', *Proceedings of the Royal Society A: Mathematical, Physical and Engineering Sciences* vol. 467, 2896–2911.

Ju, J. W. (1989), 'On energy-based coupled elastoplastic damage theories: Constitutive modeling and computational aspects', *International Journal of Solids and Structures* vol. 25(7), 803–833.

Ju, J. W. (1990), 'Isotropic and anisotropic damage variables in continuum damage mechanics', *Journal of Engineering Mechanics* vol. 116(12), 2764–2770.

Kachanov, L. (1958), 'Time rupture process under creep conditions', *Izvestiya Academii Nauk SSSR Otdeleine Tekhnicheskikh Nauk* vol. 8, 26–31.

Kaloni, P. N. and Ariman, T. (1967), 'Stress concentration effect in micropolar elasticity', *Journal of Applied Mathematics and Physics* vol. 18, 136–141.

Kanatani, K.-I. (1979), 'A micropolar continuum model for vibrating grid frameworks', *International Journal of Engineering Science* vol. 17, 409–418.

Kile (n.d.), `https://kile.sourceforge.io/`.

Krajcinovic, D. (1996), *Damage Mechanics*, 1st edn, North-Holland, Amsterdam, The Netherlands.

Kupfer, H., Hilsdorf, H. K. and Rusch, H. (1969), 'Behavior of concrete under compressive loadings', *Journal ACI* vol. 66(8), 656–666.

Ladevèze, P. (1983), Sur une théorie de l'endommagement anisotrope, Technical report, Laboratoire de Mécanique et Technologie, Cachan, France. (in french).

Lakes, R. (1995), Experimental methods for study of Cosserat elastic solids and other generalized elastic continua, *in* H.-B. Mühlhaus, ed., 'Continuum models for materials with micro-structure', Wiley, pp. 1–22.

Lemaitre, J. and Desmorat, R. (2005), *Engineering damage mechanics: Ductile, creep, fatigue and brittle failures.*

Lemaitre, J. and Dufailly, J. (1987), 'Damage measurements', *Engineering Fracture Mechanics* vol. 28(5-6), 643–661.

Li, S., Hao, W. and Liu, W. K. (2000*a*), 'Mesh-free simulations of shear banding in large deformation', *International Journal of Solids and Structures* vol. 37, 7185–7206.

Li, S., Hao, W. and Liu, W. K. (2000*b*), 'Numerical simulations of large deformation of thin shell structures using meshfree methods', *Computational Mechanics* vol. 25, 102–116.

Liu, G. (2008), 'A generalized gradient smoothing technique and the smoothed bilinear form for Galerkin formulation of a wide class of computational methods', *International Journal of Computational Methods* vol. 5(2), 199–236.

Liu, G. (2009), *Meshfree Methods: Moving Beyond the Finite Element Method*, CRC Press - Taylor & Francis Group, New York, USA.

Liu, G. (2010*a*), 'A G space theory and a weakened weak (W^2) form for a unified formulation of compatible and incompatible methods: Part I theory', *International Journal for Numerical Mehods in Engineering* vol. 81, 1093–1126.

Liu, G. (2010*b*), 'A G space theory and a weakened weak (W^2) form for a unified formulation of compatible and incompatible methods: Part II applications to solid mechanics problems', *International Journal for Numerical Methods in Engineering* vol. 81, 1127–1156.

Liu, G., Dai, K. Y. and Nguyen, T. T. (2007), 'A smoothed finite element method for mechanics problems', *Computational Mechanics* vol. 39, 859–877.

Liu, G. and Gu, Y. T. (2001), 'A point interpolation method for two-dimensional solids', *International Journal for Numerical Methods in Engineering* vol. 50, 937–951.

Liu, G. and Liu, M. B. (2003), *Smoothed Particle Hydrodynamics - A mesh free particle method*, World Scientific, Singapore.

Liu, G., Nguyen-Thoi, T., Nguyen-Xuan, H. and Lam, K. (2009), 'A node-based smoothed finite element method (NS-FEM) for upper bound solutions to solid mechanics problems', *Computers and Structures* vol. 87, 14–26.

Liu, G. and Zhang, G. (2009), 'A normed G space and weakened weak (W^2) formulation of a cell-based smoothed point interpolation method', *International Journal of Computational Methods* vol. 6(1), 147–179.

Liu, G. and Zhang, G. Y. (2007), 'Upper bound solution to elasticity problems: A unique property of the linearly conforming point interpolation method (LCPIM)', *International Journal for Numerical Mehods in Engineering* vol. 74, 1128–1161.

Liu, G. and Zhang, G. Y. (2008), 'Edge-based smoothed point interpolation methods', *International Journal of Computational Methods* vol. 5(4), 621–646.

Liu, G. and Zhang, G. Y. (2013), *Smoothed Point Interpolation Methods - G Space Theory and Weakened Weak Forms*, World Scientific.

Liu, G., Zhang, G. Y. and Dai, K. Y. (2005), 'A linearly conforming point interpolation method (LC-PIM) for 2D solid mechanics problems', *International Journal of Computational Methods* vol. 2(4), 645–665.

Liu, M. B., Liu, G. R. and Zong, Z. (2008), 'An overview on smoothed particle hydrodynamics', *International Journal of Computational Methods* vol. 5(1), 135–188.

Liu, W. K., Hao, S., Belytschko, T., Li, S. F. and Chang, C. T. (1999), 'Multiple scale meshfree methods for damage fracture and localization', *Computational Materials Science* vol. 16, 197–205.

Liu, W. K., Jun, S. and Zhang, Y. F. (1995), 'Reproducing kernel particle methods', *International Journal for Numerical Methods in Fluids* vol. 20(8-9), 1081–1106.

Liu, X. and Hu, G. (2005), 'A continuum micromechanical theory of overall plasticity for particulate composites including particle size effect', *International Journal of Plasticity* vol. 21, 777–799.

Liu, X., Scarpas, A. and Kasbergen, C. (2007), 'A micropolar formulation of the Desai hierarchical model for elastoplastic porous media', *International Journal of Solids and Structures* vol. 44, 2695–2714.

Lubliner, J. (2008), *Plasticity Theory*, Dover Pubblications.

Lucy, L. B. (1977), 'A numerical approach to the testing of the fission hypothesis', *The Astronomical Journal* vol. 82(12), 1013–1024.

Maier, G. and Hueckel, T. (1979), 'Nonassociated ad coupled flow rules of elastoplasticity for rock-like materials', *International Journal of Rock Mechanics and Mining Sciences* vol. 16, 77–92.

Mariano, P. M. (1999), 'Some remarks on the variational description of microcracked bodies', *International Journal of Non-Linear Mechanics* vol. 34, 633–642.

Mariano, P. M. (2002), Multifield theories in mechanics of solids, Vol. 38 of *Advances in Applied Mechanics*, Elsevier, pp. 1 – 93.

Mariano, P. M. (2016), 'Trends and challenges in the mechanics of complex materials: a view', *Philosophical Transactions of the Royal Society A: Mathematical, Physical and Engineering Sciences* vol. 374(2015034), 1–31.

Mariano, P. M., Gioffrè, M., Stazi, F. L. and Augusti, G. (2002), 'Microcracked bodies with random properties : a preliminary investigation on localization phenomena', *Composite Structures* vol. 80, 1027–1047.

Mariano, P. M., Gioffrè, M., Stazi, F. L. and Augusti, G. (2004), 'Elastic microcracked bodies with random properties', *Probabilistic Engineering Mechanics* vol. 19(1-2), 127–143.

Mariano, P. M. and Stazi, F. L. (2005), 'Computational aspects of the mechanics of complex materials', *Archives of Computational Methods in Engineering* vol. 12(4), 391–478.

Marigo, J. J. (1985), 'Modelling of brittle and fatigue damage for elastic material by growth of microvoids', *Engineering Fracture Mechanics* vol. 21(4), 861–874.

Markov, K. Z. (1995), 'On a microstructural model of damage in solids', *International Journal of Engineering Science* vol. 33(1), 139–150.

Marsden, J. E. and Hughes, T. J. (1994), *Mathematical foundations of elasticity*, Dover Pubblications, New York, USA.

Matallah, M. and La Borderie, C. (2009), 'Inelasticity-damage-based model for numerical modeling of concrete cracking', *Engineering Fracture Mechanics* vol. 76, 1087–1108.

Mazars, J. (1984), Application de le Mécanique de l'endommagement au comportement non lineaire et à la rupture du béton de Structure, PhD thesis, Université Pierre et Marie Curie - Laboratoire de Mécanique et Technologie, Paris, France. (in french).

Mazars, J., Berthaud, Y. and Ramtani, S. (1990), 'The unilateral behaviour of damaged concrete', *Engineering Fracture Mechanics* vol. 35(4-5), 629–635.

Mazars, J. and Lemaitre, J. (1984), Application of continuous damage mechanics to strain and fracture behavior of concrete, *in* S. P. Shah, ed., 'Application Of Fracture Mechanics to Cementitious Composites', Vol. 94 of *NATO ASI Series*, Springer Netherlands, pp. 507–520.

Mazars, J. and Pijaudier-Cabot, G. (1989), 'Continuum damage theory — Application to concrete', *Journal of Engineering Mechanics* vol. 115(2), 345–365.

Menétrey, P. and Zimmermann, T. (1993), 'Object-oriented non-linear finite element analysis: Application to J2 plasticity', *Computers and Structures* vol. 49(5), 767 – 777.

Miehe, C., Teichtmeister, S. and Aldakheel, F. (2016), 'Phase-field modelling of ductile fracture: a variational gradient-extended plasticity-damage theory and its micromorphic regularization', *Philosophical Transactions of the Royal Society A: Mathematical, Physical and Engineering Sciences* vol. 374(20150170).

Miehe, C., Welschinger, F. and Hofacker, M. (2010), 'Thermodynamically consistent phase-field models of fracture: Variational principles and multi-field FE implementations', *International Journal for Numerical Mehods in Engineering* vol. 83, 1273–1311.

Moes, N., Dolbow, J. and Belytschko, T. (1999), 'A finite element method for crack growth without remeshing', *International Journal for Numerical Methods in Engineering* vol. 46, 131–150.

Monaghan, J. (1982), 'Why particle methods work', *Journal on Scientific and Statistical Computing* vol. 3(4), 422–433.

Mora, R. J. and Waas, A. M. (2007), 'Evaluation of the Micropolar elasticity constants for honeycombs', *Acta Mechanica* vol. 192, 1–16.

Mühlhaus, H.-B. and Vardoulakis, I. (1987), 'The thickness of shear hands in granular materials', *Géotechnique* vol. 37(3), 271–283.

Nadai, A. (1931), *Plasticity*, McGraw-Hill, New York.

Nayroles, B., Touzot, G. and Villon, P. (1992), 'Generalizing the finite element method: Diffuse approximation and diffuse elements', *Computational Mechanics* vol. 10(5), 307–318.

Needleman, A. (1987), 'A continuum model for void nucleation by inclusion debonding', *Advances in Applied Mechanics* vol. 54, 525–531.

Needleman, A. (1988), 'Material rate dependence and mesh sensitivity in localization problems', *Computer Methods in Applied Mechanics and Engineering* vol. 67, 69–85.

Neff, P. (2006), 'The cosserat couple modulus for continuous solids is zero viz the linearized Cauchy-stress tensor is symmetric', *ZAMM Zeitschrift fur Angewandte Mathematik und Mechanik* vol. 86(11), 892–912.

Neff, P. and Jeong, J. (2009), 'A new paradigm: the linear isotropic Cosserat model with conformally invariant curvature energy', *ZAMM Zeitschrift fur Angewandte Mathematik und Mechanik* vol. 89(2), 107–122.

Neff, P., Jeong, J. and Fischle, A. (2010), 'Stable identification of linear isotropic Cosserat parameters: bounded stiffness in bending and torsion implies conformal invariance of curvature', *Acta Mechanica* vol. 211, 237–249.

Neilsen, M. and Schreyer, H. (1993), 'Bifurcations in elastic-plastic materials', *International Journal of Solids and Structures* vol. 30(4), 521–544.

Nemat-Nasser, S. and Chang, S. N. (1990), 'Compression-induced high strain rate void collapse, tensile cracking, and recrystallization in ductile single and polycrystals', *Mechanics of Materials* vol. 10(1-2), 1–17.

Ngo, D. and Scordelis, A. C. (1967), 'Finite element analysis of reinforced concrete beams', *Journal of the American Concrete Institute* vol. 64, 152–163.

Noll, W. (1958), 'A mathematical theory of the mechanical behavior of continuous media', *Archive for Rational Mechanics and Analysis* vol. 2, 197–226.

Noor, A. K. and Nemeth, M. P. (1980*a*), 'Analysis of spatial beamlike lattices with rigid joints', *Computer Methods in Applied Mechanics and Engineering* vol. 24, 35–59.

Noor, A. K. and Nemeth, M. P. (1980*b*), 'Micropolar beam models for lattice grids with rigid joints', *Computer Methods in Applied Mechanics and Engineering* vol. 21, 249–263.

Nowacki, W. (1986), *Theory of asymmetric elasticity*, Pergamon Press, Oxford, UK.

Oliver, J., Huespe, a. E., Pulido, M. D. G. and Chaves, E. (2002), 'From continuum mechanics to fracture mechanics: The strong discontinuity approach', *Engineering Fracture Mechanics* vol. 69, 113–136.

Oliver, J., Mora, D. F., Huespe, A. E. and Weyler, R. (2012), 'A micromorphic model for steel fiber reinforced concrete.', *International journal of solids and structures* vol. 49, 2990–3007.

Ord, A., Vardoulakis, I. and Kajewsky, R. (1991), 'Shear band formation in gasford sandstone', *International Journal of Rock Mechanics and Mining Sciences* vol. 42(4), 697–709.

Ortiz, M. (1985), 'A constitutive theory for the inelastic behavior of concrete', *Mechanics of Materials* vol. 4, 67–93.

Ortiz, M. (1987), 'An analytical study of the localized failure modes of concrete', *Mechanics of Materials* vol. 6, 159–174.

Ortiz, M., Leroy, Y. and Needleman, A. (1987), 'A finite element method for localized failure analysis', *Computer Methods in Applied Mechanics and Engineering* vol. 61(2), 189–214.

Ostoja-Starzewski, M. (2002), 'Lattice models in micromechanics', *Applied Mechanics Reviews* vol. 55(1), 35–60.

Ostoja-Starzewski, M., Boccara, S. D. and Jasiuk, I. (1999), 'Couple stress moduli and characteristic length of a two-phase compoiste', *Mechanical Research Communications* vol. 26(4), 387–396.

Ottosen, N. S. and Runesson, K. (1991*a*), 'Acceleration waves in elasto-plasticity', *International Journal of Solids and Structures* vol. 28(2), 135–159.

Ottosen, N. S. and Runesson, K. (1991*b*), 'Properties of discontinuous bifurcation solutions in elasto-plasticity', *International Journal of Solids and Structures* vol. 27(4), 401–421.

Park, H. and Lakes, R. (1987), 'Torsion of a micropolar elastic prism of square cross-section', *International Journal of Solids and Structures* vol. 23(4), 485–503.

Peerlings, R. (1999), Enhanced damage modelling for fracture and fatigue, PhD thesis, Technische Universiteit Eindhoven.

Peerlings, R. H. J., Borst, R. D., Brekelmans, W. A. M. and de Vree, J. H. P. (1996), 'Gradient enhanced damage for quasi-brittle materials', *International Journal for Numerical Methods in Engineering* vol. 39, 3391–3403.

Peerlings, R. H. J., De Borst, R., Brekelmans, W. A. M. and Geers, M. G. D. (2002), 'Localisation issues in local and nonlocal continuum approaches to fracture', *European Journal of Mechanics, A/Solids* vol. 21, 175–189.

Peerlings, R. H. J., Geers, M. G. D., De Borst, R. and Brekelmans, W. A. M. (2001), 'A critical comparison of nonlocal and gradient-enhanced softening continua', *International Journal of Solids and Structures* vol. 38, 7723–7746.

Penna, S. S. (2011), Formulação multipotencial para modelos de degradação elástica: unificação teórica, proposta de novo modelo, implementação computacional e modelagem de estruturas de concreto, Phd thesis, Universidade Federal de Minas Gerais (UFMG). (in portuguese).

Pgfplots (n.d.), `http://pgfplots.sourceforge.net/`.

Pietruszczak, S. and Mróz, Z. (1981), 'Finite element analysis of deformation of strain-softening materials', *International Journal for Numerical Methods in Engineering* vol. 17, 327–334.

Pijaudier-Cabot, G. and Bažant, Z. P. (1987), 'Nonlocal damage theory', *Journal of Engineering Mechanics* vol. 113(10), 1512–1533.

Pozo, P. L., Campos, A., Lascano, S., Oller, S. and Rodriguez-Ferran, A. (2014), 'A finite points method approach for strain localization using the gradient plasticity formulation', *Mathematical Problems in Engineering* vol. 2014.

Puttick, K. E. (1959), 'Ductile fracture in metals', *Philosophical Magazine* vol. 4(44), 964–969.

Quarteroni, A. and Valli, A. (1994), *Numerical Approximation of Partial Differential Equations*, Springer-Verlag Berlin Heidelberg.

Rabczuk, T. (2013), 'Computational methods for fracture in brittle and quasi-brittle solids: State-of-the-art review and future perspectives', *ISRN Applied Mathematics* vol. 2013, 1–38.

Rabczuk, T. and Belytschko, T. (2004), 'Cracking particles: a simplified meshfree method for arbitrary evolving cracks', *International Journal for Numerical Methods in Engineering* vol. 61, 2316–2343.

Rabczuk, T. and Belytschko, T. (2007), 'A three-dimensional large deformation meshfree method for arbitrary evolving cracks', *Computer Methods in Applied Mechanics and Engineering* vol. 196, 2777–2799.

Rabotnov, Y. (1968), Creep rupture, *in* M. Hetényi and W. Vincenti, eds, 'Applied Mechanics - Proceedings of the twelfth international congress of applied mechanics', Springer-Verlag Berlin Heidelberg, pp. 342–349.

Rajagopal, S. and Gupta, N. (2011), 'Meshfree modelling of fracture — A comparative study of different methods', *Meccanica* vol. 46, 1145–1158.

Ramm, E. (1981), Strategies for tracing the nonlinear response near limit points, *in* W. Wunderlich, E. Stein and K. J. Bathe, eds, 'Nonlinear Finite Element Analysis in Structural Mechanics', Springer-Verlag Berlin Heidelberg.

Rashid, Y. R. (1968), 'Analysis of reinforced concrete pressure vessels', *Nuclear Engineering and Design* vol. 7, 334–344.

Reddys, G. V. K. and Venkatasubramaniano, N. K. (1979), 'On the flexural rigidity of a micropolar elastic circular cylindrical tube', *International Journal of Engineering Science* vol. 17(9), 1015–1021.

Rezakhani, R. and Cusatis, G. (2014), 'Asymptotic expansion homogenization of discrete fine-scale models with rotational degrees of freedom for the simulation of quasi-brittle materials', *Journal of the Mechanics and Physics of Solids* vol. 88, 320–345.

Rice, J. R. (1976), The localization of plastic deformation, *in* 'Proceedings of the14th International Congress on Theoratical and Applied Mechanics', pp. 207–220.

Rice, J. R. (1992), 'Dislocation nucleation from a crack tip: An analysis based on the peierls concept', *Journal of the Mechanics and Physics of Solids* vol. 40(2), 239–271.

Rice, J. R. J. and Rudnicki, J. W. (1980), 'A note on some features of the theory of localization of deformation', *International Journal of Solids and Structures* vol. 16, 597–605.

Rice, J. R. and Thomson, R. (1974), 'Ductile versus brittle behaviour of crystals', *Philosophical Magazine* vol. 29(1), 73–97.

Riks, E. (1979), 'An incremental approach to the solution of snapping and buckling problems', *International Journal of Solids and Structures* vol. 15(7), 529 – 551.

Rizzi, E. (1995), Sulla localizzazione delle deformazioni in materiali e strutture, Phd thesis, Politecnico di Milano. (in italian).

Rizzi, E. and Carol, I. (2001), 'A formulation of anisotropic elastic damage using compact tensor formalism', *Journal of Elasticity* vol. 64(2), 85–109.

Rizzi, E., Carol, I. and Willam, K. (1995), 'Localization analysis of elastic degradation with application to scalar damage', *Journal of Engineering Mechanics* vol. 121(4), 541–554.

Rizzi, E., Maier, G. and Willam, K. (1996), 'On failure indicators in multidissipative materials', *International Journal of Solids and Structures* vol. 33(20-22), 3187–3214.

Rots, J. G. and Blaauwendraad, J. (1989), 'Crack models for concrete: Discrete or smeared? Fixed, multi-directional or rotating?', *Heron* vol. 34(1), 1–59.

Rots, J. G., Nauta, P., Kusters, G. M. and Blaauwendraad, J. (1985), 'Smeared crack approach and fracture localization in concrete', *HERON* vol. 30(1), 1–48.

Rudnicki, J. W. and Rice, J. R. (1975), 'Conditions for the localization of deformation in pressure-sensitive dilatant materials', *Journal of Mechanics and Physics of Solids* vol. 23, 371–394.

Runesson, K. and Mróz, Z. (1989), 'A note on nonassociated plastic flow rules', vol. 5, 639–658.

Salehian, A. (2008), Micropolar continuum modeling of large space structures with flexible joints and thermal effects: theory and experiment, PhD thesis, Virginia Polytechnic Institute and State University.

Seppecher, P., Alibert, J. J. and Isola, F. D. (2011), 'Linear elastic trusses leading to continua with exotic mechanical interactions', *Journal of Physics: Conference Series* vol. 319, 1–13.

Silva, R. P. (2012), Análise não-linear de estruturas de concreto por meio do método Element Free Galerkin, Phd thesis, Universidade Federal de Minas Gerais (UFMG), Belo Horizonte, Brazil. (in portuguese).

Simo, J. C. and Hughes, T. J. R. (1998), *Computational Inelasticity*, Springer-Verlag, New York.

Simo, J. C. and Ju, J. W. (1987), 'Strain- and stress-based continuum damage models-I. Formulation', *International Journal of Solids and Structures* vol. 23(7), 821–840.

Sluys, L. J. (1992), Wave propagation, localization and dispersion in softening solids, PhD thesis, Technische Universiteit Delft, Delft, The Nederlands.

Steinmann, P. (1995), 'Theory and numerics of ductile micropolar elastoplastic damage', *International Journal for Numerical Methods in Engineering* vol. 38, 583–606.

Suidan, M. and Schnobrich, W. C. (1973), 'Finite element analysis of reinforced concrete', *Journal of the Structural Division, ASCE* pp. 2109–2121.

Suiker, A. S. J., De Borst, R. and Chang, C. S. (2001), 'Micro-mechanical modelling of granular material. Part 1: Derivation of a second-gradient micro-polar constitutive theory', *Acta Mechanica* vol. 149, 161–180.

Szabó, L. (1998), 'On the eigenvalues of the fourth-order constitutive tensor and loss of strong ellipticity in elastoplasticity', *International Journal of Plasticity* vol. 13(10), 809–835.

Szabó, L. (2000), 'Comments on loss of stong ellipticity in elastoplasticity', *International Journal of Solids and Structures* vol. 37, 3775–3806.

Tantau, T. (2013), Graph drawing in tikz, *in* W. Didimo and M. Patrignani, eds, 'Graph Drawing', Springer Berlin Heidelberg, Berlin, Heidelberg, pp. 517–528.

Tejchman, J. (1997), Modelling of shear localisation and autogeneous dynamic effects in granular bodies, PhD thesis, Universität Karlsruhe.

TekogLu, C. (2007), Size effects in cellular solids, PhD thesis, University of Groningen.

Tekoglu, C., Gibson, L. J., Pardoen, T. and Onck, P. R. (2011), 'Size effects in foams: Experiments and modeling', *Progress in Materials Science* vol. 56, 109–138.

Tekoglu, C. and Onck, P. R. (2008), 'Size effects in two-dimensional Voronoi foams: A comparison between generalized continua and discrete models', *Journal of the Mechanics and Physics of Solids* vol. 56, 3541–3564.

Thomas, T. Y. (1961), *Plastic flow and fracture of solids*, Accademic Press, London.

Tootoonchi, A. and Khoshghalb, A. (2016), A cell-based smoothed point interpolation method for flow-deformation analysis of saturated porous media, *in* 'VII European Congress on Computational Methods in Applied Sciences and Engineering', Crete Island, Greece.

Trovalusci, P., De Bellis, M. L. and Masiani, R. (2017), 'A multiscale description of particle composites: From lattice microstructures to micropolar continua', *Composites Part B: Engineering* vol. 128, 164–173.

Trovalusci, P., Ostoja-Starzewski, M., De Bellis, M. L. and Murrali, A. (2015), 'Scale-dependent homogenization of random composites as micropolar continua', *European Journal of Mechanics, A/Solids* vol. 49, 396–407.

Voigt, W. (1887), 'Theoretische studien über die elasticitätsverhältnisse der krystalle', *Abhandlungen der Königlichen Gesellschaft der Wissenschaften in Göttingen* vol. 34, 3–52.

Wang, D. and Li, Z. (2012), 'A two-level strain smoothing regularized meshfree approach with stabilized conforming nodal integration for elastic damage analysis', *International Journal of Damage Mechanics* vol. 22(3), 440–459.

Wang, J. G. and Liu, G. R. (2002*a*), 'A point interpolation meshless method based on radial basis functions', *International Journal for Numerical Methods in Engineering* vol. 54, 1623–1648.

Wang, J. and Liu, G. (2002*b*), 'On the optimal shape parameters of radial basis functions used for 2-d meshless methods', *Computer Methods in Applied Mechanics and Engineering* vol. 191, 2611–2630.

Wang, L. and Stronge, W. J. (1999), 'Micropolar Theory for Two-Dimensional Stresses in Elastic Honeycomb', *Proceedings of the Royal Society A: Mathematical, Physical and Engineering Sciences* vol. 455, 2091–2116.

Weller, H. G., Tabor, G., Jasak, H. and Fureby, C. (1998), 'A tensorial approach to computational continuum mechanics using object-oriented techniques', *Computers in Physics* vol. 12(6), 620 – 631.

Willoughby, N., Parnell, W. J., Hazel, A. L. and Abrahams, I. D. (2012), 'Homogenization methods to approximate the effective response of random fibre-reinforced Composites', *International Journal of Solids and Structures* vol. 49, 1421–1433.

Winkler, B., Hofstetter, G. and Lehar, H. (2004), 'Application of a constitutive model for concrete to the analysis of a precast segmental tunnel lining', *International Journal for Numerical and Analytical Methods in Geomechanics* vol. 28, 797–819.

Wriggers, P. (2008), *Nonlinear Finite Element Methods*, Springer-Verlag Berlin Heidelberg.

Xotta, G., Beizaee, S. and Willam, K. J. (2016), 'Bifurcation investigation of coupled damage-plasticity models for concrete materials', *Computer Methods in Applied Mechanics and Engineering* vol. 298, 428–452.

Xue, L. and Belytschko, T. (2010), 'Fast methods for determining instabilities of elastic-plastic damage models through closed-form expressions', *International Journal for Numerical Methods in Engineering* vol. 84, 1490–1518.

Yang, Y.-B. and Shieh, M.-S. (1990), 'Solution method for nonlinear problems with multiple critical points', *AIAA Journal* vol. 28(12), 2110–2116.

Zhang, G. Y., Li, Y., Gao, X. X., Hui, D., Wang, S. Q. and Zong, Z. (2015), 'Smoothed point interpolation method for elastoplastic analysis', *International Journal of Computational Methods* vol. 12(4).

Zhang, G. Y., Liu, G. R., Wang, Y. Y., Huang, H. T., Zhong, Z. H., Li, G. Y. and Han, X. (2007), 'A linearly conforming point interpolation method (LC-PIM) for three-dimensional elasticity problems', *International Journal for Numerical Mehods in Engineering* vol. 72, 1524–1543.

Zhang, Y. Q., Liu, G. R. and Han, X. (2006), 'Effect of small length scale on elastic buckling of multi-walled carbon nanotubes under radial pressure', *Physics Letters A* vol. 349, 370–376.

Zienkiewicz, O. C. and Taylor, R. L. (2000), *The finite element method - Volume 1*, Butterworth Heinemann, Oxford.

Appendices

Appendix A

Micropolar scalar-isotropic damage models

In Section 3.3.4 two specific scalar-isotropic damage models that can be derived within the general formulation discussed in Section 3.3 have been presented. This appendix is devoted to further models that were implemented in the framework discussed in Appendix C, but that weren't used in the numerical simulations discussed in Chapters 6 and 7.

A.1   Associated models in strain space

As stated in Section 3.3.4, models associated in strain space are characterized by a gradient of the loading function in the form

$$\underline{n}^* = \tau\ \underline{\Sigma}^0 \tag{A.1}$$

In addition to the Marigo's model of Eq. (3.141), the framework of the software **INSANE** contains two other models of this kind, that are extensions to the micropolar theory of the classic *Simo-Ju* model (Simo and Ju, 1987) and *Ju* model (Ju, 1989), and are expressed by the equivalent deformations

$$\Gamma_{eq} = \begin{cases} \sqrt{2\psi^0} & \text{(Simo-Ju)} \\ \psi^0 & \text{(Ju)} \end{cases} \tag{A.2}$$

where ψ^0 is the same as in Eq. (3.141), corresponding to the values

$$\tau = \begin{cases} 1/\Gamma_{eq} & \text{(Simo-Ju)} \\ 1 & \text{(Ju)} \end{cases} \tag{A.3}$$

A.2   Mazars-Lemaitre model

This model was adopted by the author in two conference papers, Gori et al. (2015b) and Gori et al. (2015c); it is an extension to the micropolar formulation of the classic Mazars-Lemitre model (Mazars and Lemaitre, 1984), and is expressed by equivalent deformation

$$\Gamma^{eq} = \sqrt{\underline{\Gamma} \cdot \underline{\Gamma}} = \sqrt{\underline{\gamma} \cdot \underline{\gamma} + \underline{\kappa} \cdot \underline{\kappa}} \tag{A.4}$$

to which corresponds the following gradient of the loading function

$$\underline{n}^* = \begin{pmatrix} \frac{\underline{\gamma}}{\Gamma^{eq}} & \underline{0} \\ \underline{0} & \frac{\underline{\kappa}}{\Gamma^{eq}} \end{pmatrix} \tag{A.5}$$

A.3   De Vree model

This model was adopted by the author in Gori et al. (2015c), and was obtained as an extension to the micropolar theory of the classic *de Vree's* model (de Vree et al., 1995). Such model is characterized by the following equivalent deformation

$$\Gamma^{eq} = \frac{k-1}{2k(1-2\,\nu)}\, \mathrm{I}_1^{\Gamma} + \frac{1}{2k}\sqrt{\left(\frac{k-1}{1-2\,\nu}\, \mathrm{I}_1^{\Gamma}\right)^2 + \frac{12\,k}{(1+\nu)^2}\, \mathrm{J}_2^{\Gamma}} \tag{A.6}$$

where the parameter k allows to take into account the different behaviour of the material for a compression and a tension state. Such parameter is assumed to be equal to the ratio of the compressive uniaxial strength and the tensile uniaxial strength, $k = f_c/f_t$. In Equation A.6, the first and second invariants of the generalized strain operator are represented by

$$\mathrm{I}_1^{\Gamma} = \mathrm{I}_1^{\gamma} + \mathrm{I}_1^{\kappa} \tag{A.7}$$

$$\mathrm{J}_2^{\Gamma} = \mathrm{J}_2^{\gamma} + \mathrm{J}_2^{\kappa} \tag{A.8}$$

Such quantities can be calculated, for a micropolar model in a plane state, as

$$\mathrm{I}_1^{\gamma} = \mathrm{tr}(\underline{\gamma}) \tag{A.9}$$

$$\mathrm{I}_1^{\kappa} = \mathrm{tr}(\underline{\kappa}) \tag{A.10}$$

$$\mathrm{J}_2^{\gamma} = \frac{1}{4}\left(\underline{\gamma}^{dev} \cdot \underline{\gamma}^{dev} + \underline{\gamma}^{dev} \cdot \underline{\gamma}^{devT}\right) \tag{A.11}$$

$$\mathrm{J}_2^{\kappa} = \frac{1}{2}\left(\underline{\kappa}^{dev} \cdot \underline{\kappa}^{dev}\right) \tag{A.12}$$

where with the superscript *dev* the *deviatoric* part of a tensor is indicated. The gradients of the loading function result in

$$\underline{n}_A^* = \frac{k-1}{2k(1-2\nu)} \frac{\partial \mathrm{I}_1^\Gamma}{\partial \underline{\gamma}} + \frac{1}{4k} \frac{2\left(\frac{k-1}{1-2\nu}\right)^2 \mathrm{I}_1^\Gamma \frac{\partial \mathrm{I}_1^\Gamma}{\partial \underline{\gamma}} + \frac{12\,k}{(1+\nu)^2} \frac{\partial \mathrm{J}_2^\Gamma}{\partial \underline{\gamma}}}{\sqrt{\left(\frac{k-1}{1-2\nu}\, \mathrm{I}_1^\Gamma\right)^2 + \frac{12\,k}{(1+\nu)^2}\, \mathrm{J}_2^\Gamma}} \tag{A.13}$$

$$\underline{n}_C^* = \frac{k-1}{2k(1-2\nu)} \frac{\partial \mathrm{I}_1^\Gamma}{\partial \underline{\kappa}} + \frac{1}{4k} \frac{2\left(\frac{k-1}{1-2\nu}\right)^2 \mathrm{I}_1^\Gamma \frac{\partial \mathrm{I}_1^\Gamma}{\partial \underline{\kappa}} + \frac{12\,k}{(1+\nu)^2} \frac{\partial \mathrm{J}_2^\Gamma}{\partial \underline{\kappa}}}{\sqrt{\left(\frac{k-1}{1-2\nu}\, \mathrm{I}_1^\Gamma\right)^2 + \frac{12\,k}{(1+\nu)^2}\, \mathrm{J}_2^\Gamma}} \tag{A.14}$$

Taking into account Eq. (A.7), the derivatives of the first invariant are represented by

$$\frac{\partial \mathrm{I}_1^\Gamma}{\partial \underline{\gamma}} = \frac{\partial \mathrm{I}_1^\gamma}{\partial \underline{\gamma}} = \frac{\partial \mathrm{tr}(\underline{\gamma})}{\partial \underline{\gamma}} = \underline{id} \tag{A.15}$$

$$\frac{\partial \mathrm{I}_1^\Gamma}{\partial \underline{\kappa}} = \frac{\partial \mathrm{I}_1^\kappa}{\partial \underline{\kappa}} = \frac{\partial \mathrm{tr}(\underline{\kappa})}{\partial \underline{\kappa}} = \underline{id} \tag{A.16}$$

while taking into account Eq. (A.8), the derivatives of the second invariant, for a micropolar model in a plane state, are represented by

$$\frac{\partial \mathrm{J}_2^\Gamma}{\partial \underline{\gamma}} = \frac{\partial \mathrm{J}_2^\gamma}{\partial \underline{\gamma}} = \frac{1}{2}\left(\underline{\gamma}^{dev} + \underline{\gamma}^{devT}\right) \tag{A.17}$$

$$\frac{\partial \mathrm{J}_2^\Gamma}{\partial \underline{\kappa}} = \frac{\partial \mathrm{J}_2^\kappa}{\partial \underline{\kappa}} = \underline{\kappa}^{dev} \tag{A.18}$$

A.4 Mazars model

In Section 3.3.4, a simplied version of the micropolar Mazars model have been presented. In Gori et al. (2017*c*) the author discussed an extension to the micropolar theory of the original treatment of the scalar damage variable proposed in Mazars (1984), which is illustrated below.

As in the orginal work of Mazars, the damage variable is obtained as a combination of two different traction and compression damage variables

$$D := \alpha_t\, D_t + \alpha_c\, D_c \tag{A.19}$$

Such damage variables are defined as the following functions of the equivalent deformation

$$D_t(\Gamma_{eq}) := 1 - \frac{1}{\Gamma_{eq}}\,(1 - A_t)K_0 - \frac{1}{e^{B_t(\Gamma_{eq}-K_0)}}A_t \tag{A.20}$$

$$D_c(\Gamma_{eq}) := 1 - \frac{1}{\Gamma_{eq}}\,(1 - A_c)K_0 - \frac{1}{e^{B_c(\Gamma_{eq}-K_0)}}A_c \tag{A.21}$$

where K_0 is a threshold value for the equivalent deformation, representing the onset

of damage, and where the parameters A_t, A_c, B_t and B_c assume the role of material parameters. The weighting functions α_t and α_c are evaluated as

$$\alpha_t := \sum_{k=1}^{3} H_k \frac{\varepsilon_{(k)}^t \left(\varepsilon_{(k)}^t + \varepsilon_{(k)}^c \right)}{\Gamma_{eq}^2}, \qquad \alpha_c := \sum_{k=1}^{3} H_k \frac{\varepsilon_{(k)}^c \left(\varepsilon_{(k)}^t + \varepsilon_{(k)}^c \right)}{\Gamma_{eq}^2} \qquad \text{(A.22)}$$

where the terms $\varepsilon_{(k)}^t$ and $\varepsilon_{(k)}^c$ represents, respectively, the eigenvalues of the strain tensors $\underline{\varepsilon}^t$ and $\underline{\varepsilon}^c$ obtained using the positive and negative parts of the stress tensor $\underline{\sigma}^0 = \hat{\mathbf{A}} \cdot \underline{\varepsilon}$, represented in its principal system

$$\underline{\sigma}^0 = <\underline{\sigma}^0>_+ + <\underline{\sigma}^0>_-, \quad \underline{\varepsilon}^t := \left(\hat{\mathbf{A}} \right)^{-1} \cdot <\underline{\sigma}^0>_+, \quad \underline{\varepsilon}^c := \left(\hat{\mathbf{A}} \right)^{-1} \cdot <\underline{\sigma}^0>_- \qquad \text{(A.23)}$$

and where the parameters H_k are given by

$$H_k := \begin{cases} 1 & \text{if } \varepsilon_{(k)}^t + \varepsilon_{(k)}^c \geq 0 \\ 0 & \text{if } \varepsilon_{(k)}^t + \varepsilon_{(k)}^c < 0 \end{cases} \qquad \text{(A.24)}$$

Appendix B

Acceleration waves and localization in micropolar media

B.1 Stress and couple-stress: Maxwell compatibility condition

The expressions in Eq. (5.10) are obtained starting from Eqs. (5.7) and (5.8), replacing $\dot{\bar{u}}$ and $\dot{\bar{\varphi}}$ with the vectors $\underline{\sigma} \cdot \bar{v}$ and $\underline{\mu} \cdot \bar{v}$, respectively, where, as already stated, $\bar{v}$ is an arbitrary constant vector, resulting in

$$[\![\mathrm{grad}(\underline{\sigma} \cdot \bar{v})]\!] \cdot \bar{n} = -\frac{1}{c} \, [\![\widetilde{\underline{\sigma} \cdot \bar{v}}]\!] = -\frac{1}{c} \, [\![\dot{\underline{\sigma}}]\!] \cdot \bar{v} \tag{B.1}$$

$$[\![\mathrm{grad}(\underline{\mu} \cdot \bar{v})]\!] \cdot \bar{n} = -\frac{1}{c} \, [\![\widetilde{\underline{\mu} \cdot \bar{v}}]\!] = -\frac{1}{c} \, [\![\dot{\underline{\mu}}]\!] \cdot \bar{v} \tag{B.2}$$

and then in

$$[\![\mathrm{grad}(\underline{\sigma} \cdot \bar{v})]\!] = -\frac{1}{c} \left([\![\dot{\underline{\sigma}}]\!] \cdot \bar{v} \right) \otimes \bar{n}, \quad [\![\mathrm{grad}(\underline{\mu} \cdot \bar{v})]\!] = -\frac{1}{c} \left([\![\dot{\underline{\mu}}]\!] \cdot \bar{v} \right) \otimes \bar{n} \tag{B.3}$$

The expressions in Eq. (5.11) are instead obtained considering the trace of the two previous equations. Focusing on the first one, associated to the stress tensor $\underline{\sigma}$, the left side is expressed in components as $(\sigma_{ij} \, v_j)_{,k} = \sigma_{ij,k} \, v_j$; its trace $\sigma_{ij,i} \, v_j$ results in $\mathrm{div}^{\mathrm{T}}(\underline{\sigma}) \cdot \bar{v}$. The right side is instead expressed by $-1/c \, [\![\dot{\sigma}_{ij}]\!] \, v_j \, n_k$; its trace $-1/c \, [\![\dot{\sigma}_{ij}]\!] \, v_j \, n_i$ results in $-1/c \, \bar{n} \cdot ([\![\dot{\underline{\sigma}}]\!] \cdot \bar{v})$. Repeating for the second expression leads to the searched equations

$$[\![\mathrm{div}^{\mathrm{T}}(\underline{\sigma})]\!] = -\frac{1}{c} \, \bar{n} \cdot [\![\dot{\underline{\sigma}}]\!], \quad [\![\mathrm{div}^{\mathrm{T}}(\underline{\mu})]\!] = -\frac{1}{c} \, \bar{n} \cdot [\![\dot{\underline{\mu}}]\!] \tag{B.4}$$

B.2 Micropolar elastic acceleration waves propagation

The condition for elastic acceleration waves propagation is briefly analyzed in this appendix. The results presented here are analogous to the one obtained by Grioli (1980), Eremeyev (2005). The Fresnel-Hadamard propagation condition, for an initially isotropic micropolar medium results in the following uncoupled eigenvalues problems

$$(A_2 - \rho c^2)\,\bar{g}_A + (A_1 + A_3)\,(\bar{n} \cdot \bar{g}_A)\,\bar{n} = 0 \tag{B.5}$$

$$(C_2 - \rho\theta c^2)\,\bar{g}_C + (C_1 + C_3)\,(\bar{n} \cdot \bar{g}_C)\,\bar{n} = 0 \tag{B.6}$$

The first equation results in the eigenvalue $c = \sqrt{(A_1 + A_2 + A_3)/\rho}$ with multiplicity 1, correspondent to an eigenvector $\bar{g}_A \parallel \bar{n}$ (longitudinal wave), and in the eigenvalue $c = \sqrt{A_2/\rho}$ with multiplicity 2, correspondent to eigenvectors $\bar{g}_A \perp \bar{n}$ (transversal waves). In an analogous way, the second equation results in the eigenvalue $c = \sqrt{(C_1 + C_2 + C_3)/\rho\theta}$ with multiplicity 1, correspondent to an eigenvector $\bar{g}_C \parallel \bar{n}$ (longitudinal wave), and in the eigenvalue $c = \sqrt{C_2/\rho\theta}$ with multiplicity 2, correspondent to eigenvectors $\bar{g}_C \perp \bar{n}$ (transversal waves).

As pointed out by Grioli (1980), a micropolar elastic acceleration wave transports, in general, a second-order discontinuity in the field $\bar{u}$ or in the field $\bar{\varphi}$. A wave transporting discontinuities in both the field should be regarded as a special case, and may verify only for specific values of the material moduli. There are four special cases, represented by *longitudinal waves*

$$\bar{g}_A \parallel \bar{n}, \quad \bar{g}_C \parallel \bar{n}, \qquad A_1 + A_2 + A_3 = \frac{C_1 + C_2 + C_3}{\theta} \tag{B.7}$$

transversal waves

$$\bar{g}_A \perp \bar{n}, \quad \bar{g}_C \perp \bar{n}, \qquad A_2 = \frac{C_2}{\theta} \tag{B.8}$$

and *mixed waves*, defined by

$$\bar{g}_A \parallel \bar{n}, \quad \bar{g}_C \perp \bar{n}, \qquad A_1 + A_2 + A_3 = \frac{C_2}{\theta} \tag{B.9}$$

or by

$$\bar{g}_A \perp \bar{n}, \quad \bar{g}_C \parallel \bar{n}, \qquad A_2 = \frac{C_1 + C_2 + C_3}{\theta} \tag{B.10}$$

B.3 Special cases for localization conditions

Among the proposed localization conditions, as already stated, the most general one is represented by the stationarity of a wave transporting a second-order discontinuity in

both the fields $\bar{u}$ and $\bar{\varphi}$; in this case, the localization condition $\tilde{\underline{Q}}^t \cdot \bar{g} = \bar{0}$ may have a non-trivial solution only if $\det\left(\tilde{\underline{Q}}^t\right) = 0$. It is now showed how the special cases regarding the discontinuity of the sole field $\bar{u}$ or of the sole field $\bar{\varphi}$ can be derived from the general one. Assuming first a discontinuity in the field $\bar{u}$ ($[\![\ddot{u}]\!] \neq 0$ and $[\![\ddot{\varphi}]\!] = 0$), the propagation condition reduces to

$$
\begin{cases}
\underline{Q}^t_{AA} \cdot \bar{g}_A = \rho c^2\, \bar{g}_A \\
\underline{Q}^t_{CA} \cdot \bar{g}_A = 0
\end{cases}
\Rightarrow
\begin{cases}
\underline{Q}^S_{AA} \cdot \bar{g}_A - \frac{1}{H}\left(\bar{a}_A \cdot \bar{g}_A\right) \bar{b}_A = \rho c^2\, \bar{g}_A \\
-\frac{1}{H}\left(\bar{a}_A \cdot \bar{g}_A\right) \bar{b}_C = 0
\end{cases}
\tag{B.11}
$$

The second equation is satisfied only when $\bar{a}_A \cdot \bar{g}_A = 0$ or $\bar{b}_C = \bar{0}$. If the former condition is verified, the first equation reduces to $\underline{Q}^S_{AA} \cdot \bar{g}_A = \rho c^2\, \bar{g}_A$, analogous to the one of elastic waves, with $\underline{Q}_{AA}$ replaced by $\underline{Q}^S_{AA}$. Recalling the equations of Appendix B, it follow that the localization condition ($c \to 0$) is attained only for vanishing material parameters, i.e., when the medium is *completely damaged*; such extreme condition is not considered in this work. Attention is then focused on the condition $\bar{b}_C = 0$. In this case the localization condition reduces to $\underline{Q}^t_{AA} \cdot \bar{g}_A = 0$, and a non-trivial solution is possible only if $\det\left(\underline{Q}^t_{AA}\right) = 0$. The same considerations apply if the discontinuity in the field $\bar{\varphi}$ ($[\![\ddot{u}]\!] = 0$ and $[\![\ddot{\varphi}]\!] \neq 0$) is accounted for. In this case, the localization in the micro-rotation field is possible if both $\bar{b}_A = \bar{0}$ and $\det\left(\underline{Q}^t_{CC}\right) = 0$ are verified.

Appendix C

INSANE: INteractive Structural ANalysis Environment

The **INSANE** system (*INSANE - INteractive Structural ANalysis Environment*, n.d.) is an open source software for computational mechanics, developed at the Structural Engineering Department (DEES) of the Federal University of Minas Gerais. It is based on the *Java* language, and relies on the object-oriented programming (OOP). This, results in a robust software composed by a set of classes that interacts between them, and that are able to represent the different aspects of a numerical simulation with an high level of generalization. The high abstraction of the parts of the software eases the maintenance of the code, and its expansion, resulting in a system well-suited for the simultaneous collaboration of different researchers. The software is composed by a set of interactive graphical applications allowing the operations of pre- and post-processing, and by a numerical core responsible for the analysis of discrete models, which will be discussed in the following sections. The current organization of the software is the results of a large number of contributions by different researchers[1]; the ones that are more strictly related to this thesis are: Fuina (2009), which implemented the micropolar model for elasticity and elasto-plasticity, Penna (2011), which proposed the implementation of the constitutive models formulation discussed in Section 2.2.2, and Silva (2012), which implemented the Element-Free Galerkin (EFG) method.

In the following, the details of the parts of the numerical core which are related to the presente thesis are presented, together with the author's contributions. The structure of the **INSANE** system is presented with the help of *UML* (*Unified Modelling Language*) diagrams, allowing a concise representation of complex aspects of the software. In order to emphasize the author's contributions to the software, the colours illustrated in Fig. C.1 are adopted in the UML diagrams.

---

[1] All the papers, conference proceedings, master and doctoral thesis related to the **INSANE** system are listed in the website of the project, `https://www.insane.dees.ufmg.br/`. The reader should refer to this list of works for all the classes and parts of the code not described in this manuscript.

Figure C.1: UML colors legend

C.1 Numerical core

The main components of the numerical core of the **INSANE** system are the interfaces `Assembler`, `Model` and `Persistence`, and the abstract class `Solution` (Fig. C.2). These objects represent the principal resources that allow the numerical simulation of different problems with different numerical methods.
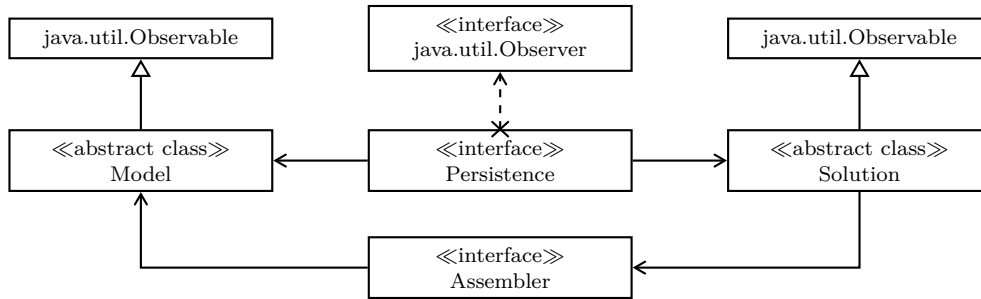

Figure C.2: Numerical core

The task of the `Assembler` (Appendix C.5) is to mount the matricial system of the model, as the one of Eq. (3.177), returning the stiffness matrix and its partitions related to free and constrained degrees of freedom, and the vector of nodal dual parameters. Depending on the kind of approximation considered in the non-linear analysis, the stiffness matrix can be elastic (`getC()`), secant (`getTotalC()`) and tangent (`getIncrementalC()`)[2]. In returning the vector $\{R\}$ (Eq. (3.177)), the main task of the assembler is to mount the vector of nodal forces equivalent to internal stresses (`getFp()`). The abstract class `Solution` (Appendix C.4) provides a set of methods devoted to the solution of the matricial system expressed in Eq. (3.177). Different inherited classes allow the solution of linear and non-linear problems, both for static and dynamic analyses. The abstract class `Model` (Appendix C.3) allows the representation of a generic discrete model in the numerical core of the software. It is composed by several lists of objects, each one representing a peculiar component of a discrete model, like nodes, elements, type of problem, type of analysis model and materials, for example. The interface `Persistence` is responsible for the processing of input and output data, which are persisted as XML (*eXtensible Markup Language*) files. Such class also guarantees the consistency of the data between the different components of the discrete model, applying the *Observer-Observable* de-

---

[2] It is worth to note that in the described methods the symbol C is used to indicate the stiffness matrix, instead of K as in Eq. (3.177). This is justified by the fact that for a more general problem than the quasi-static one adopted here, Eq. (3.177) should account for additional terms, as $[A]\{\ddot{X}\}+[B]\{\dot{X}\}+[C]\{X\} = \{R\}$, where $\{\dot{X}\}$ and $\{\ddot{X}\}$ represent, respectively, the first and second time derivatives of the nodal parameters. However, in the analytical expressions, the symbol K is maintained since it is traditionally adopted in the field of mechanics.

sign pattern. When an alteration in the state of an observed object (i.e., an object that extends the class `java.util.observable`) occours, the propagation mechanism of the alteration is triggered, and the observers (i.e., the objects implementing the interface `java.util.observer`) are notified to update themselves. In the **INSANE** system, as illustrated in Fig. C.2, the role of observer is assumed by the interface `Persistence`, while the observed objects are the abstract classes `Model` and `Solution`.

The components of the numerical core listed here will be discussed in details in the following, together with : data structures for tensors and arrays, meshfree models generation strategies, and constitutive models framework.

C.2   Data structures for tensors and arrays

The Voigt expressions adopted in the manuscript for the representation of discretized equations in both classic and micropolar media contain *vector*, i.e., mono-dimensional arrays indicated as $\{\cdot\}$, and *matrices*, i.e., two-dimensional arrays indicated as $[\cdot]$, while the constitutive expressions presented in Sections 2.2.2 and 3.3 works with *tensors*. The correct handling of such objects is an important aspect for the efficiency of a simulation code, and it can take advantage of the OOP (Jeremić and Sture, 1998). Especially the use of tensor objects in object-oriented software has been treated by a number of authors in the past (see, e.g., Jeremić and Sture (1998) and Weller et al. (1998)), usually for the representation of constitutive models as in Jeremić et al. (1999) and Jeremić and Yang (2002). Tensor objects were also used by Penna (Penna (2011) and Gori et al. (2017*a*)) for the creation of the constitutive models framework for classic media of the software **INSANE** (Appendix C.6), which was later expandend to introduce also physically non-linear micropolar models (Gori et al., 2018). As pointed out in the cited works, the main advantage in the use of tensor objects in a code is that they allow to express the constitutive equations depicted in Sections 2.2.2 and 3.3 in a form that is as close as possible to their mathematical representation, resulting in a more clear and simple code.

In the **INSANE** system, vectors, matrices, and tensors are represented, respectively, by the classes `IVector`, `IMatrix`, and `Tensor`. The class `IVector` (Fig. C.3(a)) possesses two attributes; an integer defining its size, and an *array* containing the vector components in double precision. In an analogous way, the class `IMatrix` (Fig. C.3(b)) is characterized by three attributes: two integers defining the number of rows and columns, and a two-dimensional array containing the matrix components in double precision. For both the `IVector` and `IMatrix` classes, the numbering of the elements begins with zero. Some of the methods of these two classes are exposed in Fig. C.3; there, different constructors for their initialization, as well as different methods to get and set their components are represented. Despite they are not explicitly exposed here, both the classes posses proper methods for the definition of standard algebraic operations like as sum and multiplication.
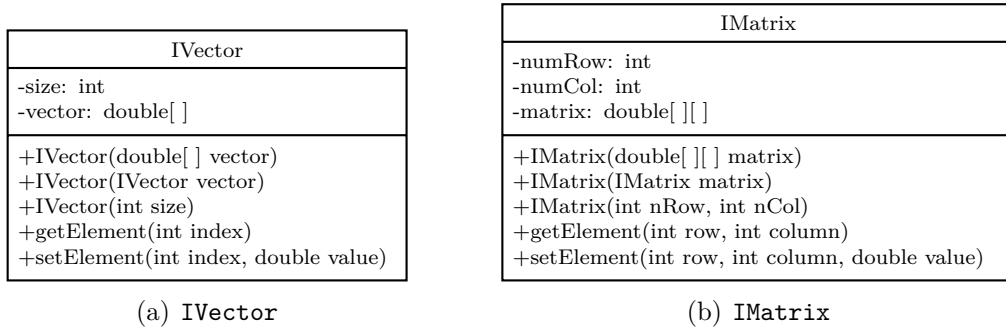
IVector
-size: int
-vector: double[ ]
+IVector(double[ ] vector)
+IVector(IVector vector)
+IVector(int size)
+getElement(int index)
+setElement(int index, double value)

(a) `IVector`

IMatrix
-numRow: int
-numCol: int
-matrix: double[ ][ ]
+IMatrix(double[ ][ ] matrix)
+IMatrix(IMatrix matrix)
+IMatrix(int nRow, int nCol)
+getElement(int row, int column)
+setElement(int row, int column, double value)

(b) `IMatrix`

Figure C.3: Classes `IVector` and `IMatrix`

The class `Tensor` (Fig. C.4) possesses three attributes: an integer defining the *order* of the tensor, an array of integers that indicates the *dimension* of each index of the tensor, and an instance of the class `IMatrix`, that stores the elements of the tensor. With respect to the original implementation, which only allowed three-dimensional tensors (i.e., with each index with dimension equal to 3), this class was updated by the author in order to allow the use of indexes with mixed dimensions. This was necessary for the implementation of the compact tensor-based expressions of the micropolar models discussed in Section 3.3.3. This characteristic is also important for the representation of constitutive equations in multidissipative models; for example, the third-order tensor $\mathbf{\check{m}} = m_{\beta ij}\, \bar{r}_\beta \otimes \bar{e}_i \otimes \bar{e}_j$, appearing in Eq. (2.12), that contains the *N directions of degradation* $\underline{m}^{(\beta)}$ of the strain degrading rate in the stress-based representation (Section 2.2.2), is characterized by the indexes i and j run from 1 to 3, and by the index β that depends on the number of adopted directions of degradation. Furthermore, this property could be used, in future applications of the same constitutive models framework, for the representation of other generalized continua (e.g., the microstretch or the micromorphic models), where the generalized tensors may not be represented as a composition of blocks with the same dimensions as the ones of Section 3.3.3.
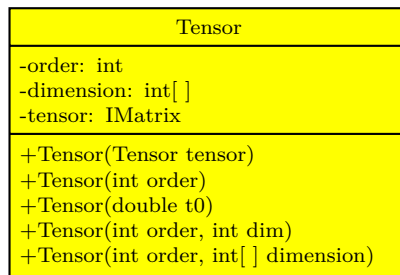
Tensor
-order: int
-dimension: int[ ]
-tensor: IMatrix
+Tensor(Tensor tensor)
+Tensor(int order)
+Tensor(double t0)
+Tensor(int order, int dim)
+Tensor(int order, int[ ] dimension)

Figure C.4: Class `Tensor`

In Fig. C.4, the constructors of the class `Tensor` are also represented; they allow to initialize a tensor as a copy of an existing one (`Tensor(Tensor tensor)`), as an empy three-dimensional tensor with the specified order (`Tensor(int order)`), as a zeroth-order tensor with the specified value (`Tensor(double t0)`), and as a tensor with specified order

and dimensions[3], with the same dimension for all the indexes (`Tensor(int order, int dim)`) or with different dimensions for each index (`Tensor(int order, int[] dim)`).

The internal representation of a tensor is obtained by *composition* using an instance of the class `IMatrix`; for example, a third-order tensor $\check{\mathbf{t}}$ with indexes dimension equal to three, is represented as the matrix

$$[\check{\mathbf{t}}] = \begin{pmatrix} t_{111} & t_{112} & t_{113} & t_{211} & t_{212} & t_{213} & t_{311} & t_{312} & t_{313} \\ t_{121} & t_{122} & t_{123} & t_{221} & t_{222} & t_{223} & t_{321} & t_{322} & t_{323} \\ t_{131} & t_{132} & t_{133} & t_{231} & t_{232} & t_{233} & t_{331} & t_{332} & t_{333} \end{pmatrix} \tag{C.1}$$

This strategy allows to access the components of a tensor and to perform operations like sum, subtaction, and multiplication by a scalar, using the analogous operations already defined for the class `IMatrix`. Since the matrix object is not directly accessible by the user, the aforementioned operations are filtered by proper methods defined in the class `Tensor` (Table C.1), that work with the mathematical syntax of the tensorial equations (i.e., with indexes starting from 1 instead than 0 as in the class `IMatrix`).

Method	Description
`getValue()`	Get the value of a 0th order tensor
`setValue(double v)`	Set the value of a 0th order tensor
`getValue(int i)`	Get the $i - th$ component of a 1st order tensor
`setValue(int i, double v)`	Set the $i - th$ component of a 1st order tensor
`getValue(int i, int j)`	Get the component i, j of a 2nd order tensor
`setValue(int i, int j, double v)`	Set the component i, j of a 2nd order tensor
`add(Tensor t1, Tensor t2)`	Return the sum of t1 and t2
`add2(Tensor t2)`	Set this tensor to the sum of itself and t2
`add3(Tensor t2)`	Return the sum of this tensor and t2
`sub(Tensor t1, Tensor t2)`	Return the difference of t1 and t2
`sub2(Tensor t2)`	Set this tensor to the difference of itself and t2
`sub3(Tensor t2)`	Return the difference of this tensor and t2
`scale(double s)`	Return this tensor multiplied by the scalar s

Table C.1: Access, sum, subtraction, and scaling methods of the class `Tensor`

In order to represent the constitutive equations discussed in Sections 2.2.2 and 3.3, the implementation of operations like the *contraction* between tensors and the *tensorial product* is of fundamental importance. Some of the methods that allow to perform such operations between tensors of different order are illustrated in Table C.2.

Using the methods discussed in this section, the equation representing the secant relation between the generalized stress and the generalized strain operators (Eq. (3.120)), $\Sigma_{ij} = \mathcal{E}^S_{ijk\ell} \, \Gamma_{k\ell}$, can be expressed in the code as `stress = secantOperator.ijklDOTkl(strain)`. The contraction operation $\mathcal{E}^S_{ijk\ell} \, \Gamma_{k\ell}$ is illustrated in the code block of Fig. C.5; as it can be

---

[3] Such class is structured to ideally accomodate tensors of the desired order and dimensions; however, at the current stage of implementation, only tensors of order from 0 to 6 are supported.

Method	Mathematical operation
`iDOTi(Tensor b)`	$c = \bar{a} \cdot \bar{b} = a_i\ b_i$
`ijDOTj(Tensor b)`	$\bar{c} = \underline{a} \cdot \bar{b} = a_{ij}\ b_j\ \bar{e}_i$
`ijklDOTkl(Tensor b)`	$\underline{c} = \hat{\mathbf{a}} \cdot \underline{b} = a_{ijk\ell}\ b_{k\ell}\ \bar{e}_i \otimes \bar{e}_j$
`ijVECkl(Tensor b)`	$\hat{\mathbf{c}} = \underline{a} \otimes \underline{b} = a_{ij}\ b_{k\ell}\ \bar{e}_i \otimes \bar{e}_j \otimes \bar{e}_k \otimes \bar{e}_\ell$

Table C.2: Tensors contraction and tensorial product

observed in the code, the method `ijklDOTkl(Tensor b)` performs such operation making use of the access methods of the class.

```java
public Tensor ijklDOTkl(Tensor b) {
  int dimI = a.getDimension()[0];
  int dimJ = a.getDimension()[1];
  int dimK = a.getDimension()[2];
  int dimL = a.getDimension()[3];
  int[] dim = { dimI, dimJ };
  Tensor t = new Tensor(2, dim);
  for (int i = 1; i < dimI + 1; i++) {
    for (int j = 1; j < dimJ + 1; j++) {
      double c = 0;
      for (int k = 1; k < dimK + 1; k++) {
        for (int l = 1; l < dimL + 1; l++) {
          c += a.getValue(i, j, k, l) * b.getValue(k, l);
        }
      }
      t.setValue(i, j, c);
    }
  }
  return t;
}
```

Figure C.5: Tensor contraction $c_{ij} = a_{ijk\ell}\ b_{k\ell}$

Another important equation that has to be represented in the numerical framework is the one defining the generalized tangent operator (Eq. (3.118)), $\mathcal{E}^t_{ijk\ell} = \mathcal{E}^S_{ijk\ell} - 1/z\ (X_{ij}\ Y_{k\ell})$; using the methods of the class `Tensor` such equation can be expressed as `tangentOp = secantOp.sub3((x.ijVECkl(y)).scale(1/z))`, where the method `ijVECkl(Tensor b)` for the tensorial product is illustrated in the block code of Fig. C.6.

C.3   Discrete models representation

Discrete models are represented within the **INSANE** software by the abstract class `Model` and its subclasses. A partial representation of this organization of classes is represented in Fig. C.7. The class `Model` was originally conceived for element-based methods relying on the standard weak form, like the finite element method, the generalized/extended finite element method, and the boundary element method. It contains different lists of objects which allow the representation of a discrete model and which are shared by the aforementioned numerical methods; each peculiar method is then represented by a specific class which inherits from `Model`. Among these objects, it is pointed out the presence of a

```java
public Tensor ijVECkl(Tensor b) {
    int dimI = this.getDimension()[0];
    int dimJ = this.getDimension()[1];
    int dimK = b.getDimension()[0];
    int dimL = b.getDimension()[1];
    int[] dim = { dimI, dimJ, dimK, dimL };
    Tensor t = new Tensor(4, dim);
    for (int i = 1; i < dimI + 1; i++) {
        for (int j = 1; j < dimJ + 1; j++) {
            for (int k = 1; k < dimK + 1; k++) {
                for (int l = 1; l < dimL + 1; l++) {
                    t.setValue(i, j, k, l, this.getValue(i, j) * b.getValue(k, l));
                }
            }
        }
    }
    return t;
}
```

Figure C.6: Tensorial product $c_{ijk\ell} = a_{ij}\ b_{k\ell}$

list of *nodes* and a list of *elements*. Each node is represented as an instance of the class Node, containing informations on the position of the discrete point and of the values of the field variable at that point, while each element is represented by an instance of the class Element. Briefly, the class Element is composed by a list os nodes, the *incidence* of the element, and by a list of integration points, which allow a generic representation of the components of the aforementioned methods. The specific objects of each numerical method are then obtained extending such class. Within this organization of classes it was also possible to implement the EFG meshfree method (Silva, 2012).
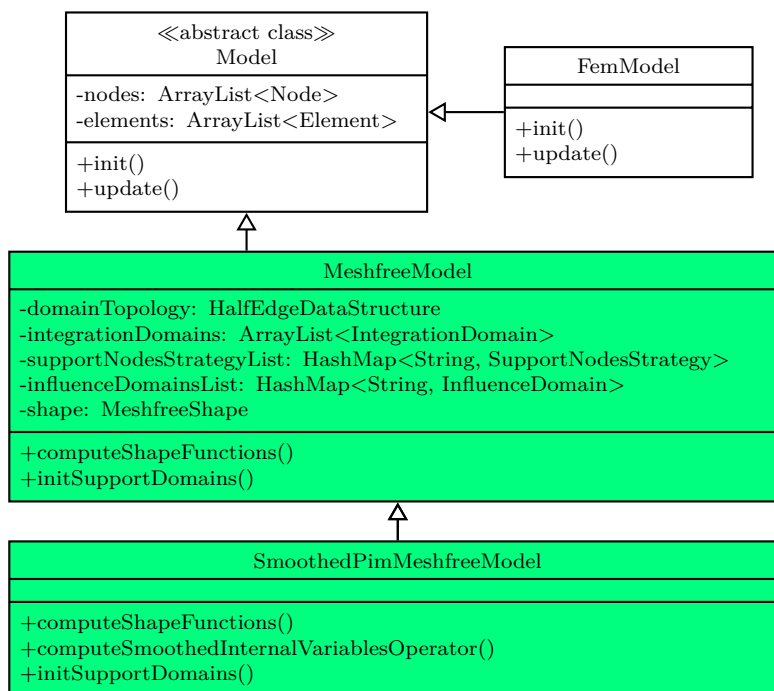
Figure C.7: Class Model

The main characteristic of a finite element is that it embeds two roles in the same

objects; indeed, it is both a set of nodes for which it is possible to generate a stiffness matrix and an integration cell, i.e., an object allowing to perform the numerical integration for the evaluation of the stiffness matrix associated to the nodes. In a meshfree method however, these two roles are in general well separated: the numerical integration is performed over *integration domains*, which can be a tasselation of the whole domain or a set of overlapping regions (as in the Meshless Local Petrov-Galerkin method), while the set of nodes for which a stiffness matrix is generated is the *support domain*, that is characteristic of each integration point. While it was possible to implement the EFG with the existent element-based strategy, the author observed that the implementation of the smoothed point interpolation methods discussed in Chapter 4 would have been impossible within the existent framework. In order to allow the inclusion of these methods, as well as to guarantee the possibility of future implementations of different meshfree methods, it was necessary to create two new entities, the classes `SupportDomain` and `IntegrationDomain` (and the inherited class `SmoothingDomain`), discussed in the following section. Hence, as it can be observed in Fig. C.7, a meshfree model within the **INSANE** is represented by a list of integration domains, as well as a list of nodes inherited from the class `Model`. It also posseses an instance of the class `MeshfreeShape` which indicates the kind of shape function used for the approximation, and informations regarding the geometry of the domain (an instance of the class `HalfEdgeDataStructure`) which, together with the lists of objects of the type `SupportNodesStrategy` and `InfluenceDomain`, are necessary for the search of support nodes with defined strategies.

While the class `MeshfreeModel`[4] is devoted to the representation of meshfree models based on the standard Gauss integration, the class `SmoothedPimMeshfreeModel` allows to represent the methods discussed in Chapter 4, and differs from its superclass for the different implementation of the methods devoted to the evaluation of the shape functions, allowing the evaluation of the smoothed shape functions.

C.3.1   `SupportDomain`, `IntegrationDomain` and `SmoothingDomain`

As discussed before, the class `SupportDomain` is used to represent the support domain at each integration point, and has a role that is analogous to the one of the incidence nodes of a finite element. The main attributes and methods of this class are illustrated in Fig. C.8. Like a finite element it is characterized by a label, a set of nodes (not strictly ordered as the incidence nodes of a finite element), and other informations regarding the kind of analysis models (`AnalysisModel`), the kind of problem (`ProblemDriver`), and the constitutive model of the material (`ConstitutiveModel`). Different from a finite element

---

[4] Despite being quite comprehensive, the structure proposed in this appendix should be improved in the future in order to guarantee the representation of further models, like the Meshless Local Petrov-Galerkin method which is based on different approximations for the trial and test functions, and methods based on the strong form of a problem.

it doesn't posses a set of integration points that, as it will be pointed out below, belong to the integration domain. However, the class `SupportDomain` keeps a reference of the integration point which is associated to (the attribute *degeneration*, an instance of the class `Degeneration`).

As it will be discussed in Appendix C.5, the main task of a support domain, in a meshfree method based on the standard Gauss integration, is to provide the stiffness matrix associated to its nodes, which will be used to compose the global matrix of the model (see, Fig. C.31). This task is executed by the methods `getC()`, `getTotalC()`, and `getIncrementalC()`, which provide the initial, secant and tangent stiffness matrix, respectively. In a physically non-linear problem also the method `getF()` is adopted, in order to obtain the vector of nodal forces equivalent to internal stresses. The further methods illustrated in Fig. C.8 are called in different parts of the code, and are used to evaluate the nodal forces equivalent to applied loads (`getE()`), to evaluate the coordinates of the support nodes (`getGlobalCartesianNodalCoordsMatrix()`), to get the values of the state variables for the nodes of the support domain (`getStateVariables()`), to get the vector containing the values of the dual internal variables (e.g., the stresses) at the degeneration associated to the support domain (`getDegenerationDualInternalVariables()`), and to get the vector of internal variables (e.g., the strains) at the degeneration associated to the support domain (`getPointInternalVariables()`).

Figure C.8: Class `SupportDomain`

The class `IntegrationDomain` (Fig. C.9) is used to represent the integration regions that allow to perform the numerical integration of the equations of meshfree models. In this sense it is similar to a finite element, since also the finite elements can be viewed as a tasselation of a domain used to perform the numerical integration. The inherited class `SmoothingDomain` is (Fig. C.9) used in case of smoothed methods. As it can be seen in Fig. C.9, the class `IntegrationDomain` is not a proper region of the domain where to perform the numerical integration; this role is attributed to the objects of the type `IntegrationCell`, a list of which is contained in the class `IntegrationDomain`. Each

`IntegrationCell` is composed by a list of points (instances of the class `IPoint3d` which represent a geometrical point in the **INSANE**) defining its geometry (the attribute *incidence*), a list of integration points (the attribute *degenerations*), and a shape function (an instance of the class `Shape`) which is used for interpolation operations regarding the cell geometry. It also posseses a reference to the integration domain which it belongs to, the kind of analysis model, material and constitutive model associated to that region of the domain, and a map used to eventually store different values in the cell. Its methods are mostly devoted to the purpose of numerical integration, and are analogous to the ones that could be found in a class representing a finite element; among them ther are methods devoted to the evaluation of the jacobian transformation, (`getJacobianTransformation(Degeneration dg)`), and to the evaluation of the integration factor associated to the kind of natural coordinats system (`getCoordIntegrationFactor()`), for example. `IntegrationCell` is an abstract class; its methods devoted to the generation and initialization of the shape function and of the integration points are defined by its subclasses that represent specific geometries.
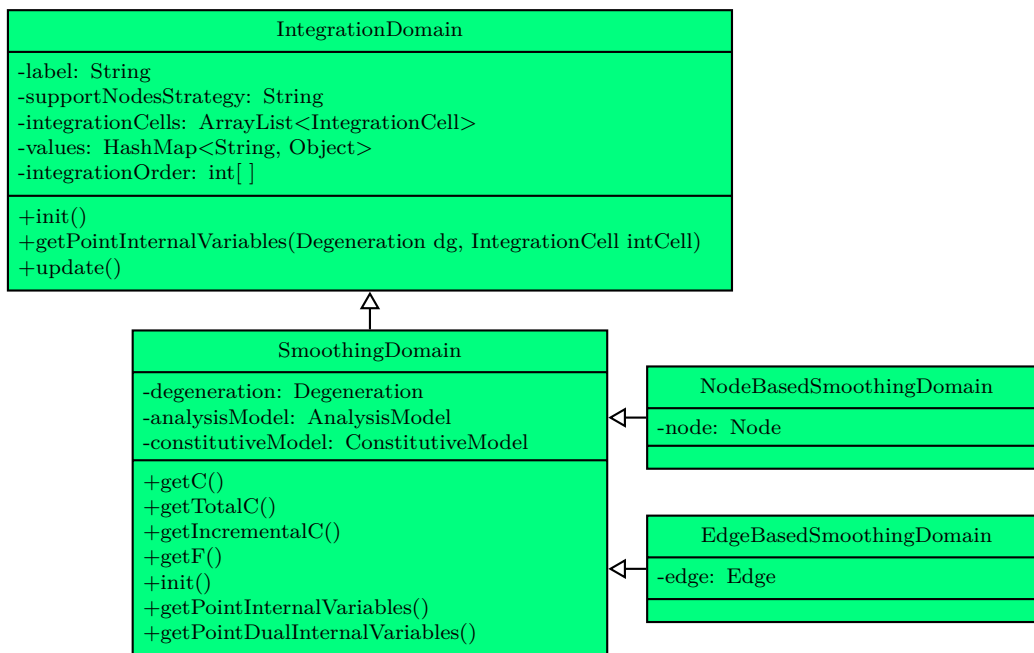
Figure C.9: Classes `IntegrationDomain` and `SmoothingDomain`

The reason for the definition of an integration domain object as a list of integration cells is evident for the smoothed point interpolation methods presented in Sections 4.2.3 and 4.2.4. From Fig. 4.4 it can be observed that a smoothing domain, a specific kind of integration domain, is characterized by a polygonal boundary, along which the numerical integration is performed. As discussed in Section 4.2.3 the numerical integration is performed considering each segment composing the smoothing domain boundary as an integration cell, justifying the choice made in the design of the classes `IntegrationDomain` and `IntegrationCell`. This choice should be also valid in case of MLPG models where,

in general, due to precision issues in the numerical integration, each local integration region is further divided in integration cells.
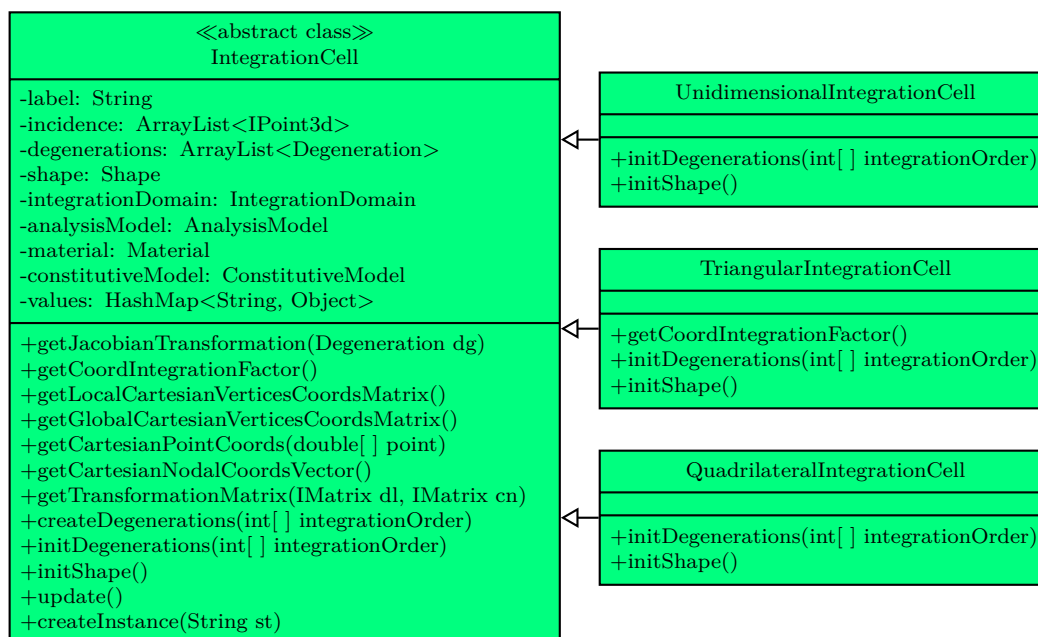

Figure C.10: Class `IntegrationCell`

It is interesting to note that a standard finite element could be easily characterized in terms of the aforementioned objects, using an integration domain composed by a single integration cell with the same geometry of the finite element, with vertices coincident with the incidence nodes of the element, adopting the same support domain for all the integration points of the cells, composed by the incidence of the element.

The class `SmoothingDomain`, which inherits from `IntegrationDomain`, was introduced in order to allow the representation of the smoothed methods presented in Chapter 4. As it will be discussed in Appendix C.5 indeed, standard and smoothed methods require a different approach for the generation of the global stiffness matrix. In case of methods based on the standard integration this matrix is assembled using the contribution of each support domain, which is responsible to provide the stiffness matrix associated to its nodes. On the other hand, the smoothed domains are required to directly provide the stiffness matrix for all the support nodes associated to its integration points distributed on the boundary. Hence, as it can be seen in Fig. C.9, such class posseses the same methods that can be found in the class `SupportDomain` (Fig. C.8). Like its super class, also `SmoothingDomain` uses a list of integration cells, each one endowed with a certain number of integration points. However, such integration points are used with the only purpose to evaluate the smoothed shape functions; in order to keep track of the evolution of the constitutive parameters it is used another integration point, the attribute `degeneration` (`Degeneration`). The class `SmoothingDomain` is extended by two classes, `NodeBasedSmoothingDomain` and `EdgeBasedSmoothingDomain`, devoted to the represen-

tation of the peculiar smoothing domain presented in Sections 4.2.3 and 4.2.4. These subclasses endow the represented smoothing domain with an instance of the object which it is associated to: a *node* of the discrete model (`Node`), or an edge (`Edge`) of the domain topology represented by the background cells expressed in terms of an half-edge data structure (`HalfEdgeDataStructure`).

C.3.2 Support domains and shape functions evaluation

Meshfree models are loaded in the **INSANE** from input files containing all the informations of a discrete model (Section C.3.4), like nodes list and integration domains list. The support domains are generated once the model is loaded with the method `initSupportDomains()` of the class `MeshfreeModel` (Fig. C.7), before its processing. As it can be observed in Fig. C.9, the class `IntegrationDomain` posseses the attribute *supportNodesStrategy*, which defined the strategy that must be adopted for the generation of the support domains associated to the integration points of the integration cells of that integration domain, which is selected from a list in an instance of the class `MeshfreeModel` (the attribute *supportNodesStrategyList*). The strategies for the support nodes selection have been presented in Section 4.2.1.3, and are represented by subclasses of the abstract class `SupportNodesStrategy` (Fig. C.11). Each one of this subclasses contain a different implementation of the method that performs the support nodes search. At this point it is worth to note the presence of the model topology in the call of the method `findSupportDomain(...)`, represented by the background cell with vertices on the nodes expressed by an instance of the class `HalfEdgeDataStructure`.
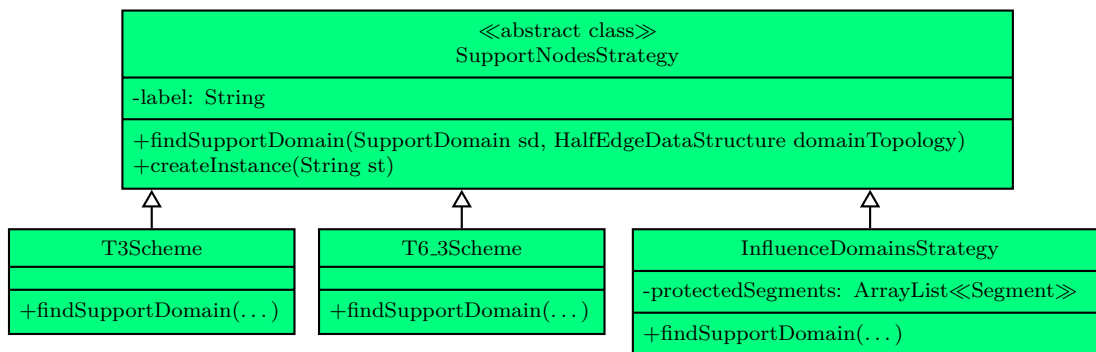

Figure C.11: Class `SupportNodesStrategy`

The class defining the strategy that relies on the use of influence domains (`InfluenceDomainsStrategy`) contains an additional attribute, representing a list of *protected* segments. The influence domains strategy indeed is based at the moment on the *visibility* method, with influence domains of different shapes and sizes defined at each node (instances of the abstract class `InfluenceDomain`).

Since for a large number of integration points this procedure can be very time consuming, the method `initSupportDomains()` make use of the Java *multithreading* strategy, as

pointed out in Fig. C.12, where the implementation in the class `MeshfreeModel` is illus-
trated. The class `SmoothedPimMeshfreeModel` (Fig. C.7) has its own implementation of
the method `initSupportDomains()`; it first call the analogous method of its superclass
in order to fill the support domains of the integration points on the smoothing domains
boundaries, and then it fills the support domain associated to the central point of each
smoothing domain, as illustrated in Fig. C.13.

```java
public void initSupportDomains() {

 ExecutorService executor = Executors.newFixedThreadPool(5);
 ListIterator<IntegrationDomain> intDoms = this.integrationDomains.listIterator();
 while (intDoms.hasNext()) {
  IntegrationDomain intDom = intDoms.next();
  Runnable runnable = new Runnable() {
   private IntegrationDomain integrationDomain;
   private MeshfreeModel model;
   @Override
   public void run() {
    ListIterator<IntegrationCell> intCells = intDom.getIntegrationCells().listIterator();
    while (intCells.hasNext()) {
     IntegrationCell intCell = intCells.next();
     ListIterator<Degeneration> dgs = intCell.getDegenerations().listIterator();
     while (dgs.hasNext()) {
      Degeneration dg = dgs.next();
      SupportDomain sd = new SupportDomain();
      sd.setAnalysisModel(intCell.getAnalysisModel());
      sd.setGlobalAnalysisModel(this.model.getGlobalAnalysisModel());
      sd.setProblemDriver(this.model.getProblemDriver());
      sd.setConstitutiveModel(intCell.getConstitutiveModel());
      sd.setDegeneration(dg);
      dg.addMeshFreeValue(Degeneration.SUPPORT_DOMAIN, sd);
      this.model.getSupportNodesStrategy(intDom.getSupportNodesStrategy())
          .findSupportDomain(sd, this.model.domainTopology);
      sd.init();
     }
    }
   }
   private Runnable setAttributes(IntegrationDomain integrationDomain,
       MeshfreeModel model) {
    this.integrationDomain = integrationDomain;
    this.model = model;
    return this;
   }
  }.setAttributes(intDom, this);
  executor.execute(runnable);
 }
 executor.shutdown();
 try {
  executor.awaitTermination(20, TimeUnit.MINUTES);
 } catch (InterruptedException e) {
   e.printStackTrace();
 }
}
```

Figure C.12: The method `initSupportDomains()` (`MeshfreeModel`)

Once the support domains have been generated, it is necessary to evaluate the shape
functions at each integration point. In the **INSANE**, the values of the FEM shape
functions are calculated each time that they are needed. However, since the operations
involved in the evaluation of meshfree shape functions have a greater computational cost,
it is preferred to evaluate them before the processing, and store them inside each in-
stance of the class `Degeneration`. The evaluation of the shape functions is performed

```
1  @Override
2  public void initSupportDomains() {
3   super.initSupportDomains();
4   ListIterator<IntegrationDomain> smoothDoms = this.getIntegrationDomains()
5      .listIterator();
6   SmoothingDomain smoothDom;
7   while (smoothDoms.hasNext()) {
8    smoothDom = (SmoothingDomain) smoothDoms.next();
9    SupportDomain sd = new SupportDomain();
10   sd.setAnalysisModel(smoothDom.getAnalysisModel());
11   sd.setGlobalAnalysisModel(this.getGlobalAnalysisModel());
12   sd.setProblemDriver(this.getProblemDriver());
13   sd.setConstitutiveModel(smoothDom.getConstitutiveModel());
14   ListIterator<IntegrationCell> integratinCells = smoothDom.getIntegrationCells()
15      .listIterator();
16   while (integratinCells.hasNext()) {
17    IntegrationCell integrationCell = integratinCells.next();
18    ListIterator<Degeneration> degenerations = integrationCell.getDegenerations()
19       .listIterator();
20    while (degenerations.hasNext()) {
21     Degeneration degeneration = degenerations.next();
22     ListIterator<MeshfreeNode> nodes = ((SupportDomain) degeneration.getMeshFreeValues()
23        .get(Degeneration.SUPPORT_DOMAIN)).getNodesList().listIterator();
24     while (nodes.hasNext()) {
25      MeshfreeNode node = nodes.next();
26      if (!(sd.getNodesList().contains(node))) {
27       sd.addNode(node);
28      }
29     }
30    }
31   }
32   sd.setDegeneration(smoothDom.getDg());
33   smoothDom.getDg().addMeshFreeValue(Degeneration.SUPPORT_DOMAIN, sd);
34   sd.init();
35  }
36 }
```

Figure C.13: The method initSupportDomains() (SmoothedPimMeshfreeModel)

within the method `computeShapeFunctions()` of the class `MeshfreeModel`, illustrated in Fig. C.14. The class `SmoothedPimMeshfreeModel` has its own implementation of this method (Fig. C.15), which differs from the one of the superclass for the use of the method `getShapeFunction(...)` instead of the method `getShapeFunctionAndDerivative(...)`, both of them of the class `MeshfreeShape` (Section C.3.3); the former provide only the values of the shape functions, while the latter also of their derivatives. The method in the class `SmoothedPimMeshfreeModel` posseses also a call to the private method `compute-SmoothedInternalVariablesOperators()`, which performs the evaluation of the smoothed shape functions and of the smoothed kinematical operators.

```
 1 public void computeShapeFunctions() {
 2  ListIterator<IntegrationDomain> integrationDomains = this.getIntegrationDomains()
 3     .listIterator();
 4  Degeneration dg;
 5  while (integrationDomains.hasNext()) {
 6   IntegrationDomain intDom = integrationDomains.next();
 7   ListIterator<IntegrationCell> intCells = intDom.getIntegrationCells()
 8      .listIterator();
 9   while (intCells.hasNext()) {
10    ListIterator<Degeneration> dgs = intCells.next().getDegenerations()
11       .listIterator();
12    while (dgs.hasNext()) {
13     dg = dgs.next();
14     IMatrix shapes = this.getShape().getShapeFunctionAndDerivative(dg
15        .getRepresentation().getCartesianCoords(),
16       ((SupportDomain) dg.getMeshFreeValues().get(Degeneration.SUPPORT_DOMAIN))
17          .getNodesList());
18     dg.addMeshFreeValue(Degeneration.MESHFREE_SHAPE_FUNCTIONS, shapes);
19    }
20   }
21  }
22 }
```

Figure C.14: The method `computeShapeFunctions()` (`MeshfreeModel`)

```
 1 public void computeShapeFunctions() {
 2  ListIterator<IntegrationDomain> integrationDomains = this.getIntegrationDomains()
 3     .listIterator();
 4  Degeneration dg;
 5  while (integrationDomains.hasNext()) {
 6   IntegrationDomain intDom = integrationDomains.next();
 7   ListIterator<IntegrationCell> intCells = intDom.getIntegrationCells()
 8      .listIterator();
 9   while (intCells.hasNext()) {
10    ListIterator<Degeneration> dgs = intCells.next().getDegenerations()
11       .listIterator();
12    while (dgs.hasNext()) {
13     dg = dgs.next();
14     IMatrix shapes = this.getShape().getShapeFunction(dg
15        .getRepresentation().getCartesianCoords(),
16       ((SupportDomain) dg.getMeshFreeValues()
17           .get(Degeneration.SUPPORT_DOMAIN)).getNodesList());
18     dg.addMeshFreeValue(Degeneration.MESHFREE_SHAPE_FUNCTIONS, shapes);
19    }
20   }
21  }
22  this.computeSmoothedInternalVariablesOperators();
23 }
```

Figure C.15: The method `computeShapeFunctions()` (`SmoothedPimMeshfreeModel`)

C.3.3 Shape functions

The FEM shape functions are generated using the existent classes that inherit from the abstract class `Shape`. Since the mechanisms for the generation of meshfree approximation functions are quite different, it was necessary to introduce another set of classes, which inherit from the abstract class `MeshfreeShape` (Fig. C.16). This class, an instance of which is possessed by the class `MeshfreeModel` (Fig. C.7), has two attributes, a label and an instance of the class `BasisFunctions` representing the kind of basis function which the shape functions are based on. It also define two abstract methods, `getShapeFunction()` and `getShapeFunctionAndDerivative()`, which returns a matrix containing the values of the shape functions and the values of the shape functions and of their first derivative, respectively, evaluated at the informed point for the support nodes passed as an argument (Fig. C.16). Such methods are then implemented by the inherited classes. At the moment, the implemented classes allow to represent PIM shape functions (`PimShape`), RPIM shape functions (`RPimShape`), and RPIM shape functions with polynomial reproduction (`RPimPolyReproductionShape`). The implementation of the mentioned methods in the class `PimShape` is illustrated in Fig. C.17 as an example.
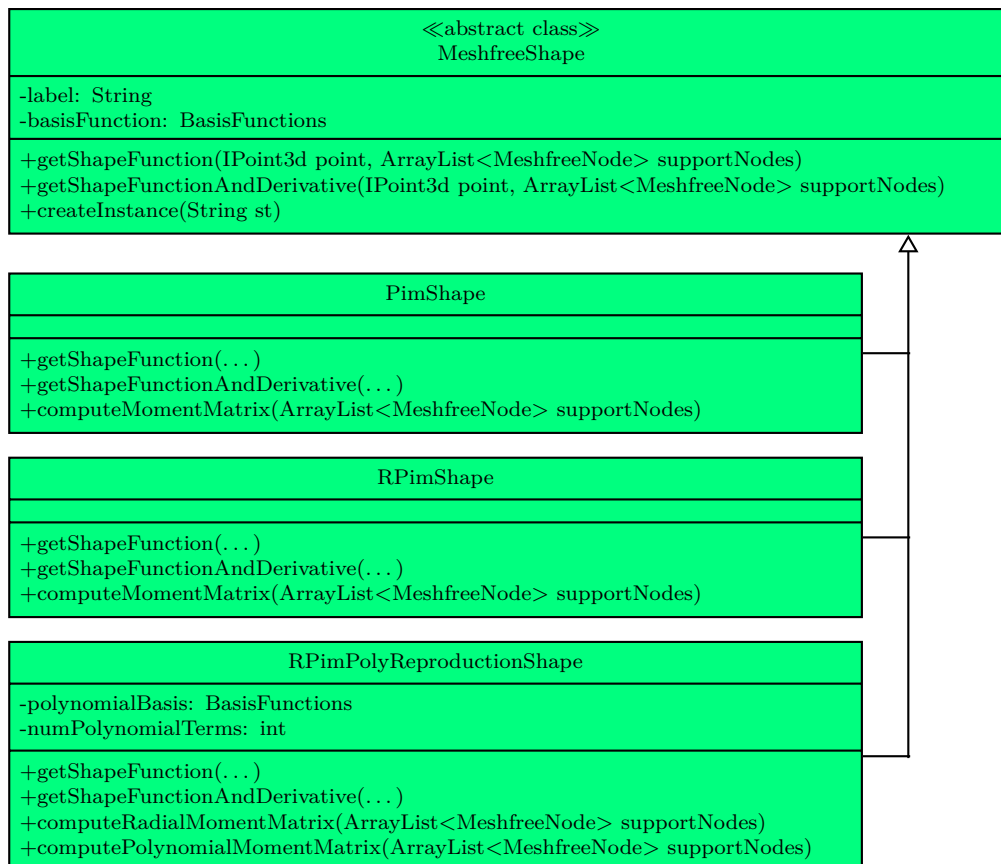

Figure C.16: Class `MeshfreeShape`

The basis functions are represented by the subclasses of the abstract class `BasisFunctions` (Fig. C.18). This class posseses a single attribute defining the number of functions of

```java
public IMatrix getShapeFunction(IPoint3d point, ArrayList<MeshfreeNode> supportNodes) {
 IMatrix sf = new IMatrix(1, supportNodes.size());
 this.getBasisFunction().setnBasisFunctions(supportNodes.size());
 IVector aux = new IVector(supportNodes.size());
 IMatrix pqInv = this.computeMomentMatrix(supportNodes).pseudoInverse();
 IVector p = this.getBasisFunction().getBasisFunctions(point);
 aux.mul(p, pqInv);
 sf.setRow(0, aux);
 return sf;
}

public IMatrix getShapeFunctionAndDerivative(IPoint3d point,
    ArrayList<MeshfreeNode> supportNodes) {
 this.getBasisFunction().setnBasisFunctions(supportNodes.size());
 IMatrix pqInv = this.computeMomentMatrix(supportNodes).pseudoInverse();
 IVector aux = this.getBasisFunction().getBasisFunctions(point);
 IVector aux2 = new IVector(aux.getSize());
 aux2.mul(aux, pqInv);
 IMatrix aux3 = this.getBasisFunction().getDerivedBasisFunctions(point);
 aux3.transpose();
 aux3.mul(pqInv);
 IMatrix sf = new IMatrix(aux3.getNumRow() + 1, supportNodes.size());
 sf.setRow(0, aux2);
 aux3.copySubMatrix(0, 0, aux3.getNumRow(), supportNodes.size(), 1, 0, sf);
 return sf;
}

protected IMatrix computeMomentMatrix(ArrayList<MeshfreeNode> supportNodes) {
 IMatrix pq = new IMatrix(supportNodes.size(), this.getBasisFunction()
    .getnBasisFunctions());
 ListIterator<MeshfreeNode> nodes = supportNodes.listIterator();
 int counter = 0;
 while (nodes.hasNext()) {
  IPoint3d point = nodes.next().getPoint();
  IVector aux = this.getBasisFunction().getBasisFunctions(point);
  pq.setRow(counter, aux);
  counter++;
 }
 return pq;
}
```

Figure C.17: Methods of the class `PimShape`

the basis, and define two abstract methods, which return the value of the basis function (`getBasisFunctions(...)`) and of its derivative (`getDerivedBasisFunctions(...)`) at the specified point. Polynomial basis functions are defined by the abstract class `PolynomialBasisFunctions`, which adds a further attribute, the maximum order of the basis. The methods which allow to calculate the value of the basis and its derivative are implemented by its subclasses defined for specific dimensions.

Radial basis functions instead, are defined by the abstract class `RadialBasisFunctions`, which posseses an instance of the class `RadialFunction` and a list of nodes as attributes. This list of nodes corresponds to the support nodes of the point at which the radial basis is calculated. The class `RadialBasisFunctions` already implements the method `getBasisFunctions(...)`, since for a radial basis is independent on the dimension of the domain. The method `getDerivedBasisFunctions(...)` is instead implemented by its subclasses.
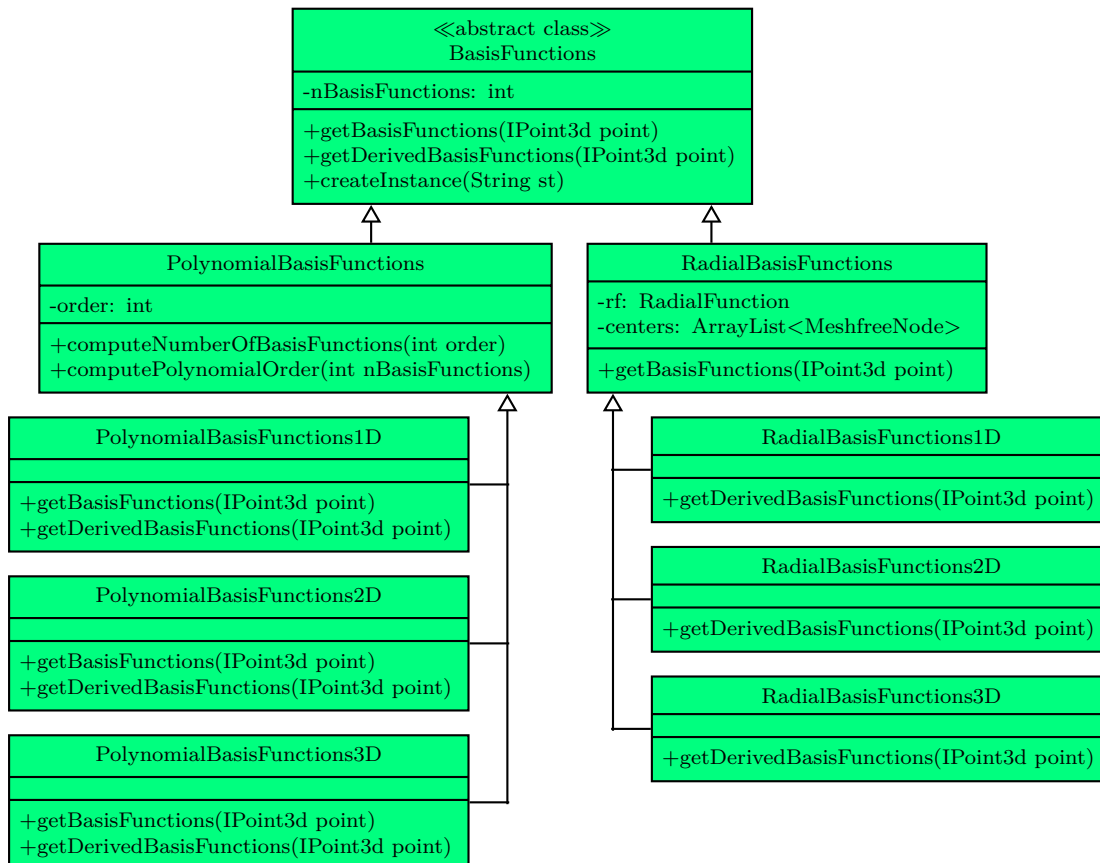

Figure C.18: Class `BasisFunctions`

`RadialFunction` is the abstract class that allows to represent radial functions in the **INSANE**. It defines two methods, `getRadialFunction(double radius)` and `getDerivedRadialFunction(double radius)`, which return the value of a radial function and of its derivative for the informed radius. It is important to note that this derivative is *with respect to the radius*; the correction performed in order to obtain the derivative

with respect to the coordinates system of the model is performed in the inherited classes of `RadialBasisFunctions`. The multiquadric function of Eq. (4.21) is represented by the class `MultiquadricRf`, where the attributes *sharpness* and *exp* correspond, respectively, to the parameters C and q appearing in Eq. (4.21), while the *exponential* function of Eq. (4.22) is represented by the class `ExponentialRf`, where the attribute *cParameter* is the exponent c appearing in Eq. (4.22).
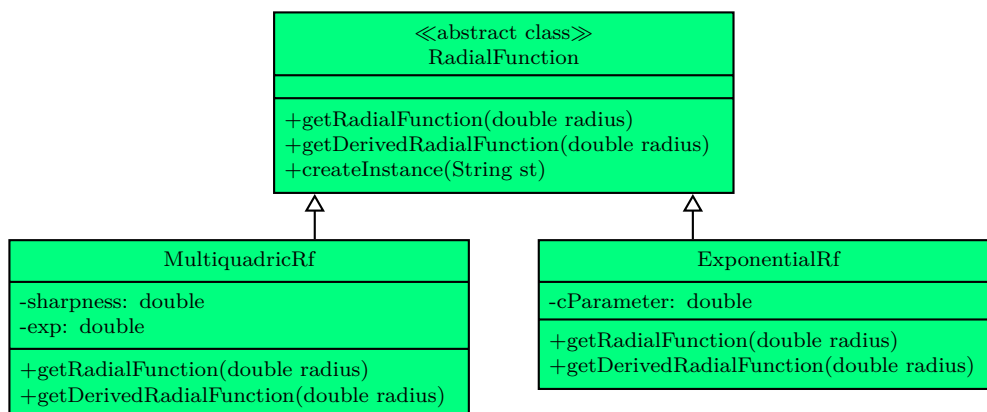

Figure C.19: Class `RadialFunction`

C.3.4   Meshfree models generation

The **INSANE** has a pre-processor that is capable to generate a finite element model and persist it in an XML file, containing all the informations of the discrete model, like nodes, elements, materials, and shape functions, for example. Such file can be modified with a text editor to obtain other methods and functions of the software that are not yet implemented in its graphical user interface (GUI), such as the existent implementation of the EFG. However, since this new implementation for meshfree methods is based on different objects with respect to the currently implemented methods, it is not possible to use the FEM input file generated by the pre-processor to create input files for these meshfree methods.

The initial idea was to generate a discrete meshfree model starting from a model described from a *geometrical* point of view, that is, defined in terms of the geometry of its domain, and by informations regarding loadings and constraints directly applied on the geometry, instead that on discrete objects like nodes, for example. The classes that will be described in the following were designed for this purpose, though the original objective has not been completely implemented yet.

The class that manages the generation of meshfree discrete models is called `Mesh-freeModelGenerator` (Fig. C.20). This class, together with its inherited class `PimModel-Generator`, was designed to have as attributes an instance of the class `DataModel` and an instance of the class `MeshfreeModel`. The method `generateDiscreteModel()`, through

the call to different protected methods that can be overriden by subclasses of `Meshfree-ModelGenerator`, performs all the necessary operations that allow to obtain an object of the kind `MeshfreeModel` from one of the kind `DataModel`.
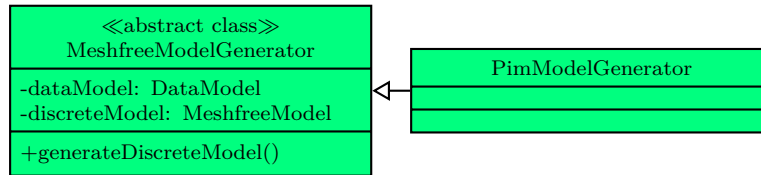

Figure C.20: Class `MeshfreeModelGenerator`

The latter (Fig. C.21), is characterized by the following attributes: an instance of the class `PhysicalModel` (Fig. C.21), containing informations of the problem geometry and boundary conditions applied on the geometry itself, an instance of the class `NodalDistributionStrategy`, which is responsible for the generation of the scattered nodes over the domain, an instance of the class `IntegrationDomainStrategy`, that defines different strategies for the generation of the integration domains of the model, and two maps containing informations regarding the discrete model that must be generated.
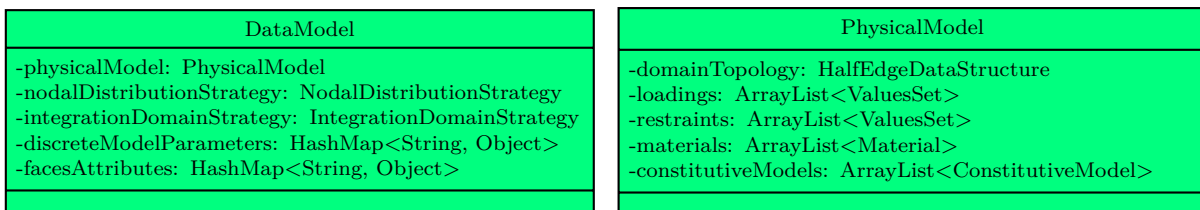

Figure C.21: The classes `DataModel` and `PhysicalModel`

As already stated, the original objective has not been completely implemented yet. Currently, the smoothed PIM and RPIM models described in Chapter 4 (as well as PIM and RPIM methods based on the standard Gauss integration, not discussed in this manuscript) are constructed starting from an existent set of triangular or quadrilateral background cells, which can be generated with **INSANE** pre-processor or with other tools (like **Gmsh**, as in the S-PIM examples presented in Chapters 6 and 7), which vertices are directly converted in nodes (instances of the class `MeshfreeNode`) by the `PimModelGenerator`. The integration and the smoothing domains are generated from these background cells by the classes that inherit from the abstract class `IntegrationDomainStrategy` illustrated in Fig. C.22, an instance of which is contained in the `DataModel`. The class `TriangularCellBased2D`, though not used in this work, allows to generates integration domains for two-dimensional meshfree models based on the standard Gauss integration, with triangular integration cells obtained as different subdivisions of the triangular background cells (the attribute *numberOfCells* indeed, indicates the number of integration cells that should be placed inside a background cell).

The smoothing domains of the NS-PIM and ES-PIM methods based on both triangu-
lar and quadrilateral background cells are generated by the classes `NsPimTriangular-`
`2dStrategy`, `NsPimQuadrilateral2dStrategy`, `EsPimTriangular2dStrategy`, and `Es-`
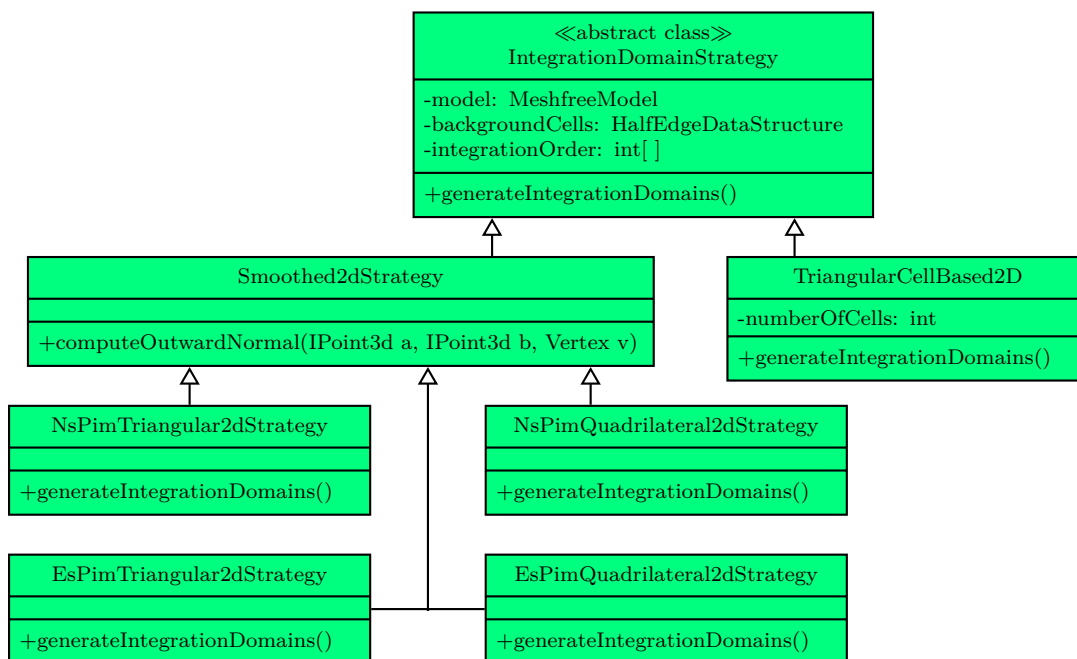`PimQuadrilateral2dStrategy`.

Figure C.22: Classe `IntegrationDomainStrategy`

Once the meshfree model has been generated it is persisted in an XML file, which
contains all the informations of the discrete model, such as nodes list and integration
domains list, for example. This file can then be loaded for the analysis process. In-
put and output files are managed by the new classes `DataModelPersistenceAsXml` and
`DiscreteModelPersistenceAsXml`, analogous to the class `PersistenceAsXml` appearing
in Fig. C.2. At the moment, the results of the analyses are not persisted in XML files as for
FEM models, since the **INSANE** post-processor has not be adapted to meshfree methods
yet. Instead, the results are persisted in CSV (Comma-Separated Values) files, which are
then converted by a third application in files compatible with **Gmsh**, the software used
to generate the S-PIM contour plots in Chapters 6 and 7.

C.4   Non-linear problems solving

The class `Solution` and the other associated classes, are devoted to the solution of linear
systems in the form of Eq. (3.177) (here recalled)

$$[K]\{X\} = \{R\} \qquad\qquad (C.2)$$

and non-linear systems, where the stiffness matrix may vary during the analysis. As discussed in Remark 4.8, such non-linear systems, once linearized, may be solved with an incremental-iterative method, where the pseudo-time, that parametrizes the equilibrium configurations in a quasi-static context, is replaced by a finite discretization, by means of a set of *increments* (or *steps*); inside each step an iterative procedure is performed (predictor-corrector method). The resulting incremental equilibrium equation at the iteration n of the step k is then represented by

$$[K^t]_{n-1}^k \, \{\Delta X\}_n^k = \Delta\lambda_n^k \, \{P\} + \{Q\}_{n-1}^k \tag{C.3}$$

where $[K^t]_{n-1}^k$ is the tangent stiffness matrix at the iteration $n-1$ of the step k, depending in general on the current values of the field variables, $\{\Delta X\}_n^k$ is the vector of incremental nodal parameters at the iteration n of the step k, $\Delta\lambda_n^k$ is the increment of the load multiplier at the iteration n of the step k, $\{P\}$ the vector of the nodal reference loads, and $\{Q\}_{n-1}^k$ the vector of the residual forces at the iteration $n-1$ of the step k, given by $\{Q\}_{n-1}^k = \lambda_{n-1}^k \, \{P\} - \{F\}_{n-1}^k$, where $\{F\}_{n-1}^k$ is the vector of nodal forces equivalent to internal stresses. In case of physical non-linearities, the stiffness matrix $[K^t]$ and the vector $\{F\}$ are assembled considering the contributions of each "element" composing the discrete model, given by

$$[K^t]_{el} = \int_{\mathbf{D}_{el}} [B]^T [\hat{\mathbf{E}}^t][B] \, \mathrm{d}\mathcal{V} \tag{C.4}$$

$$\{F\}_{el} = \int_{\mathbf{D}_{el}} [B]^T \{\underline{\sigma}\} \, \mathrm{d}\mathcal{V} \tag{C.5}$$

for a classic medium, or by

$$[K^t]_{el} = \int_{\mathbf{D}_{el}} [B]^T [\hat{\mathcal{E}}^t][B] \, \mathrm{d}\mathcal{V} \tag{C.6}$$

$$\{F\}_{el} = \int_{\mathbf{D}_{el}} [B]^T \{\underline{\Sigma}\} \, \mathrm{d}\mathcal{V} \tag{C.7}$$

for a micropolar medium, where, depending on the considered problem, $\int_{\mathbf{D}_{el}}$ may represent a line, surface or volume integral over the "element". It is necessary to emphasize that in the present appendix the term "element" will be used in a broad sense, with no restriction to FEM elements. Indeed, since in the **INSANE** system different numerical methods coexist, the term "element", as adopted in this appendix, may refer to the elements of the finite element method, the boundary elements and internal cells of the boundary element method, the quadrature cells of the Element-Free Galerkin metod, or the smoothing domains of the smoothed point interpolation methods. In the above equations, when the smoothed point interpolation methods of Chapter 4 are taken into account, the kinematical operator $[B]$ is replaced by its smoothed version $[\widetilde{B}]$.

Following a standard methodology (Batoz and Dhatt, 1979), non-linear systems in

the form of Eq. (C.3) are analyzed decomposing additively the vector of incremental nodal parameters into two components as $\{\Delta X\}_n^k = \Delta\lambda_n^k \{\Delta X^P\}_n^k + \{\Delta X^Q\}_n^k$, such that $[K^t]_{n-1}^k \{\Delta X^P\}_n^k = \{P\}$ and $[K^t]_{n-1}^k \{\Delta X^Q\}_n^k = \{Q\}_{n-1}^k$. The different phases of the solution procedure adopted in the software are resumed by the pseudo-code of Fig. C.23 (Yang and Shieh, 1990).

1 begin
2   Assemble the vector of nodal reference loads $\{P\}$;
3   **foreach** *iteration n and step k* **do**
4   **repeat**
5   Mount the global tangent stiffness matrix $[K^t]_{n-1}^k$;
6   Compute the incremental nodal parameters $\{\Delta X^P\}_n^k$ and $\{\Delta X^Q\}_n^k$;
7   Compute the load factor increment $\Delta\lambda_n^k$;
8   Update the nodal parameter vector
                $\{X\}_n^k = \{X\}_{n-1}^k + \Delta\lambda_n^k \{\Delta X^P\}_n^k + \{\Delta X^Q\}_n^k$;
9   Update the load factor $\lambda_n^k = \lambda_{n-1}^k + \Delta\lambda_n^k$;
10   Mount the the vector of nodal forces equivalent to internal stresses $\{F\}_n^k$;
11   Update the vector of residual forces $\{Q\}_n^k = \lambda_n^k \{P\} - \{F\}_n^k$;
12   **until** *convergence*;
13   **end**
14 end

Figure C.23: Solution algorithm (Yang and Shieh, 1990)

The part of the **INSANE** system devoted to the solution of linear and non-linear equations is composed by the abstract class `Solution`, as already stated, and by the interfaces `Step` and `IterativeStrategy`. The class `Solution` (Fig. C.24) is responsible for the representation inside the software of different solution procedures that can be adopted depending on the considered problem.
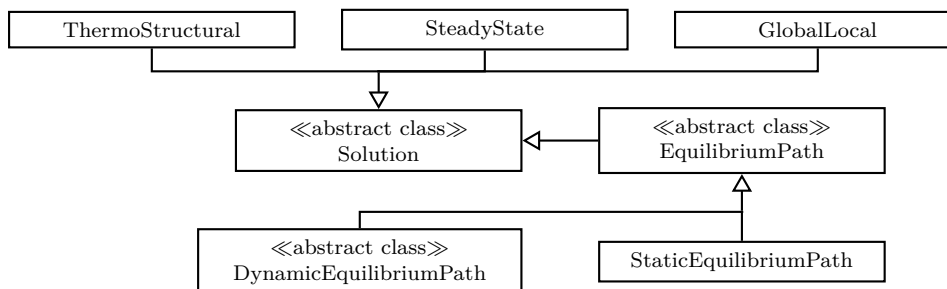

Figure C.24: Abstract class `Solution`

Attention is here devoted to the class `StaticEquilibriumPath`, responsible for the solution of *static non-linear problems*. The method `execute()` implemented in such class triggers the solution algorithm represented in Fig. C.23. Its attribute *step*, an instance of the interface `Step`, contains all the methods that are necessary to the execution of an incremental step of the non-linear analysis; the class `StandardNewtonRaphson`, detailed in Fig. C.26, manages the solution with the *Newton-Raphson* method.
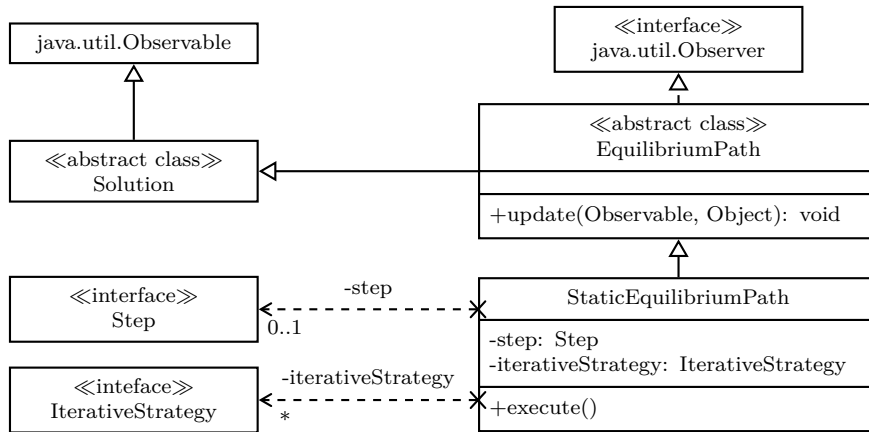
Figure C.25: Class `StaticEquilibriumPath`

The method `execute()` of this class is responsible for the activation of the iterative process inside each step. The attribute *iterativeStrategy*, an instance of the interface `IterativeStrategy`, specifies the control method adopted in the solution, and is responsible for the iterative predictor-corrector strategy defined in the algorithm of Fig. C.23. Among the implemented control methods there are the *load control*, *displacement control* (Batoz and Dhatt, 1979), different *arc-length controls* (Feng et al. (1996), Riks (1979), Ramm (1981), Crisfield (1981) and Crisfield (1983)), and the *generalized displacement control* (Yang and Shieh, 1990).
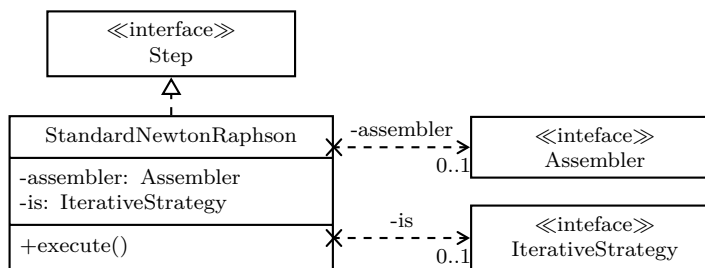
Figure C.26: Class `StandardNewtonRaphson`

The implementation of the solution process for non-linear problems described in Fig. C.23 is resumed by the sequence diagram of Fig. C.27. The class `Solution` (i.e., the inherited class `StaticEquilibriumPath` in case of a static non-linear problem) initiates a loop over the steps of the incremental process while the method `execute()` triggers the iterative process for each step. The tangent stiffness matrix is provided[5] by the `Assembler`, an instance of which is contained in the class `StandardNewtonRaphson` (Fig. C.26). Once the tangent stiffness matrix has been obtained, the method `getXPandXQ()` allows to evaluate the incremental values $\{\Delta X^P\}_n^k$ and $\{\Delta X^Q\}_n^k$ of the state variable; the `IterativeStrategy` is then solicited to return the predicted value of the load factor increment at the first iteration (`getPredictor()`), or its correction for the other iterations (`getCorrector()`).

---

[5] This procedure, and the one for the evaluation of the vector of nodal forces equivalent to internal stresses, will be discussed in details in Appendix C.5.

The updating of both the load factor and the nodal parameters vector is performed by the method `assignStepState(...)`, that receives as an input the evaluated load factor increment. Finally, the vector of residual forces is calculated using the vector of nodal forces equivalent to internal stresses, and the convergence is checked.
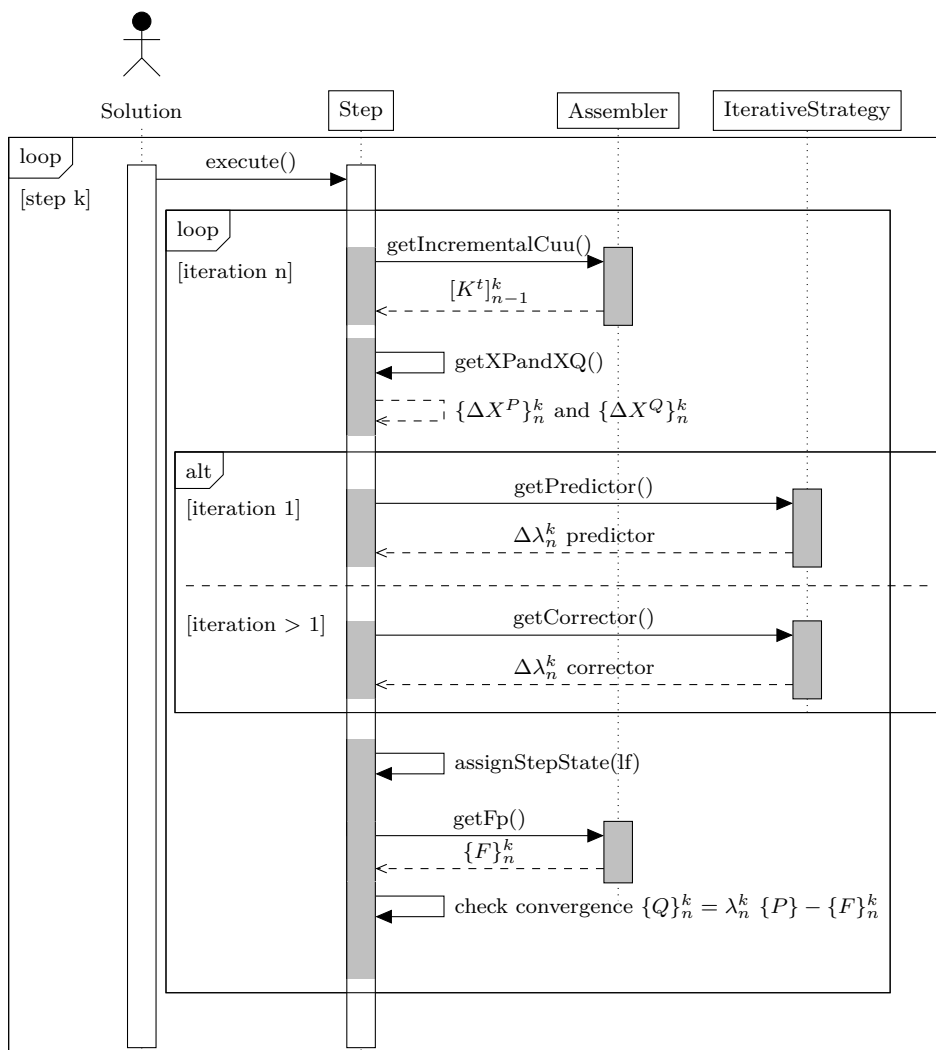

Figure C.27: Non-linear solution sequence diagram

As it can be observed in the class and sequence diagrams exposed in this section, the module `Solution` implemented in the software is highly modular, allowing an easy combination between different incremental methods and iterative strategies for the solution of various kind of static, dynamic, linear and non-linear problems. Furthermore, it is emphasized that this module exhibits no direct connection with a peculiar numerical method or constitutive model, since the only contact with the other parts of the software is through the methods `getIncrementalCuu()` and `getFp()` of the interface `Assembler`. This aspect allows the use of this module for the solution of different problems independently on the peculiar numerical methods and constitutive models adopted in the analysis.

C.5 Assembly of the tangent stiffness matrix and of the internal forces vector

The procedure allowing to mount the tangent stiffness matrix and the vector of internal forces appearing in Eq. (C.3) is managed by the classes that implement the interface `Assembler`. In the **INSANE** system each numerical method is characterized by a class that implement `Assembler`. Here attention is focused on the classes `FemAssembler`, for the finite element method, `MeshfreeAssembler`, for meshfree methods based on the standard Gauss integration, and `SmoothedMeshfreeAssembler`, for the smoothed point interpolation methods (Fig. C.28).
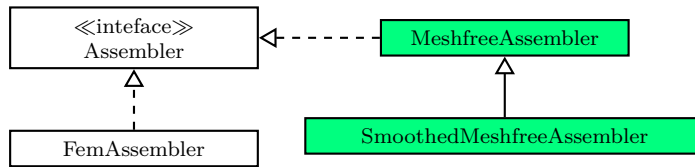

Figure C.28: Interface `Assembler`

This procedure is resumed in the following sequence diagrams, for a finite element model (Fig. C.29), for a meshfree model based on the standard Gauss integration (Fig. C.31), and for a smoothed point interpolation model (Fig. C.32) As pointed out by the diagrams, the entire process is triggered in the three cases by the class `Solution`; as already discussed for the diagram of Fig. C.27, the class `Solution` initiates a loop over the steps of the incremental process, while its method `execute()` triggers the iterative process for each step. For each iteration n and each step k, the implementation of the interface `Assembler` is solicited to provide the tangent stiffness matrix $[K^t]_{n-1}^k$ (`getIncrementalCuu()`). Each one of the classes `FemAssembler`, `MeshfreeAssembler`, and `SmoothedMeshfreeAssembler` (as well as the classes representing the further numerical methods not listed here), contain methods that allow to assemble the global stiffness matrix, making use of the contributions of the "elements" composing the discrete model (Eq. (C.4)). As discussed before, here the term element is used in a wide sense, since it may refer to the finite elements of a finite element model, to the quadrature cells of a meshfree method, the boundary elements and internal cells of a boundary element model, or the smoothing domains of a smoothed point interpolation meshfree method.

In case of a finite element model (Fig. C.29), the class `FemAssembler` initiates a loop over the finite elements composing the discrete model, i.e., the instances of the class `Elements`, asking the stiffness matrix of each one of them with the call `getIncrementalCuu()`. Such object is evaluated by the numerical integration of Eq. (C.4), that can be expressed schematically as the following sum over the *integration points*

$$[K^t]_{el} = \sum_{ip} W_{ip} \left([B]^T [\hat{\mathbf{E}}^t][B] \right)_{ip} J_{ip} \ g_{ip} \tag{C.8}$$
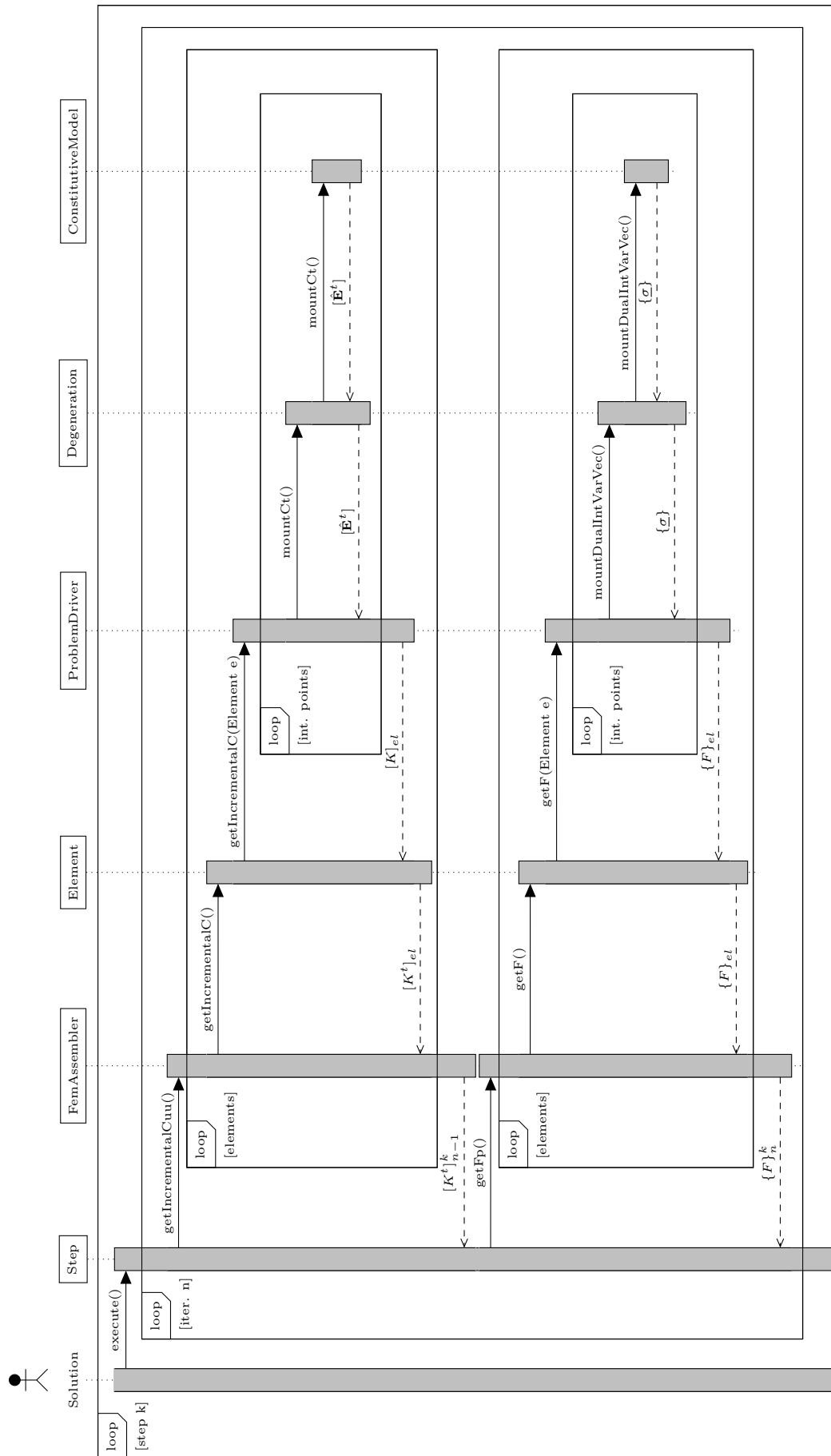
Figure C.29: Tangent stiffness matrix and internal forces vector assembly sequence diagram - FEM

where W_{ip} is a weighting factor, J_{ip} the *Jacobian* representing the integration domain transformation, and g_{ip} a certain geometrical property evaluated at the integration point. The abstract class `ProblemDriver` (called by the method `getIncrementalC(Element e)`) manages the integration procedure, through the subclass `PhysicallyNonLinear` (Section C.5.1). A basic sketch of the integration procedure for a physically non-linear problem is represented in Fig. C.30. In order to perform the numerical integration illustrated in Fig. C.30, the class `PhysicallyNonLinear` solicitates each integration point, represented by an instance of the abstract class `Degeneration` (Section C.5.2), to return the value of the tangent constitutive operator, through the method `mountCt()`.

1	**begin**
2	Initialize the element tangent stiffness matrix $[K^t]_{el}$;
3	**foreach** *integration point ip* **do**
4	Mount the kinematical operator $[B]_{ip}$;
5	Mount the tangent constitutive operator $[\hat{\mathbf{E}}^t]_{ip}$;
6	Evaluate the weighting factor W_{ip} ;
7	Evaluate the Jacobian of the element transformation J_{ip} ;
8	Evaluate the geometrical properties g_{ip};
9	Perform the product $W_{ip} \left([B]^T [\hat{\mathbf{E}}^t][B] \right)_{ip} J_{ip}\ g_{ip}$;
10	Add its value to the element tangent stiffness matrix;
11	**end**
12	**end**

Figure C.30: Integration algorithm for physically non-linear problems - FEM

As illustrated in Fig. C.29, an analogous procedure is repeated in order to mount the vector $\{F\}_n^k$ of nodal forces equivalent to internal stresses, for each step k and iteration n. As for the tangent stiffness matrix, also this object is evaluated considering the contribution of the list of "elements" composing the discrete model, each one calculating numerically the integral of Eq. (C.5) as

$$\{F\}_{el} = \sum_{ip} W_{ip} \left([B]^T \{\underline{\sigma}\} \right)_{ip} J_{ip}\ g_{ip} \tag{C.9}$$

For a meshfree method based on the standard Gauss integration the procedure for the assembly of the stiffness matrix and the vector of nodal forces equivalent to internal stresses is depicted in Fig. C.31. As it can be observed, these objects are mounted using the contribution of each *support domain.* The class `MeshfreeAssembler` executes three nested loops, over each integration domain (instance of class `IntegrationDomain`, described in Appendix C.3), over each integration cell belonging to the selected integration domain (instance of class `IntegrationCell`, described in Appendix C.3), and finally over each integration point contained in the selected integration cell (as for the FEM, each integration point is an instance of the class `Degeneration`). The object `Degeneration`

contains an instance of the class `SupportDomain` (Appendix C.3), representing the support domain at that integration point, which provides to the assembler the tangent stiffness matrix for the set of support nodes through the method `getIncrementalC()`. The integration strategy is different with respect to the one of the standard FEM depicted in Eq. (C.8). In this case the contributions to the global stiffness matrix are evaluated for each integration point individually, using the following equation

$$[K^t]_{S_d}^{ip} = W_{ip} \left([B]^T[\hat{\mathbf{E}}^t][B]\right)_{ip} J_{ip} \; g_{ip} \tag{C.10}$$

Each term $[K^t]_{S_d}^{ip}$ embeds the coefficients for the numerical integration, depending on the characteristics of the integration cell; the summation over the integration points belonging to the same cell is then implicit, and is performed as the support domain matrix is mounted in the global one. Making an analogy with the FEM, each support domain can be considered as a finite element, i.e., a set of nodes for which the stiffness matrix is evaluated. The operation depicted in Eq. (C.10) is performed by an inherited class of `ProblemDriver`, `MeshfreeSolidMech` for a linear elastic problem or `PhysicallyNonlinear-MeshfreeSolidMech` for a physically non-linear problem, through the method `getIncrementalC(SupportDomain sd, IntegrationCell intCell)`. At this point the procedure is analogous to the one depicted in Fig. C.30, except for the absence of the loop over the integration points.

In case of a smoothed point integration method, the procedure for the assembly of the stiffness matrix and the vector of nodal forces equivalent to internal stresses is depicted in Fig. C.32, and is more similar to the one of the standard FEM than to the one described above for a meshfree method with standard Gauss integration. In this case the class `SmoothedMeshfreeAssembler` perform a single loop over the smoothing domains, instances of the class `SmoothingDomain` (inherited from `IntegrationDomain`), each one provides its stiffness matrix $[K(p_k)]_{Sd}$ expressed in Eq. (4.57), according to the following expression

$$[K(p_k)]_{Sd} = A_k[\widetilde{B}(p_k)]^T[\hat{\mathbf{E}}(p_k)][\widetilde{B}(p_k)] \; g_{p_k} \tag{C.11}$$

where, with respect to the expression of Eq. (4.57), the presence of a factor g_{p_k} containing geometrical informations of the smoothing domain (the thickness, for example) is made explicit, since this objects is not embedded in the others depicted in Eq. (C.11). The operation depicted in Eq. (C.11) is performed by an inherited class of `ProblemDriver`, `SmoothedPim` for a linear elastic problem or `PhysicallyNonlinearSmoothedPim` for a physically non-linear problem, through the method `getIncrementalC(SupportDomain sd)`. The operation perfomed for the evaluation of Eq. (C.11) is simpler than the one depicted in Fig. C.30, since there in no need for a loop over the integration points, and since the smoothed kinematical operator has been already evaluated during the initialization phase of the discrete model (Appendix C.3).
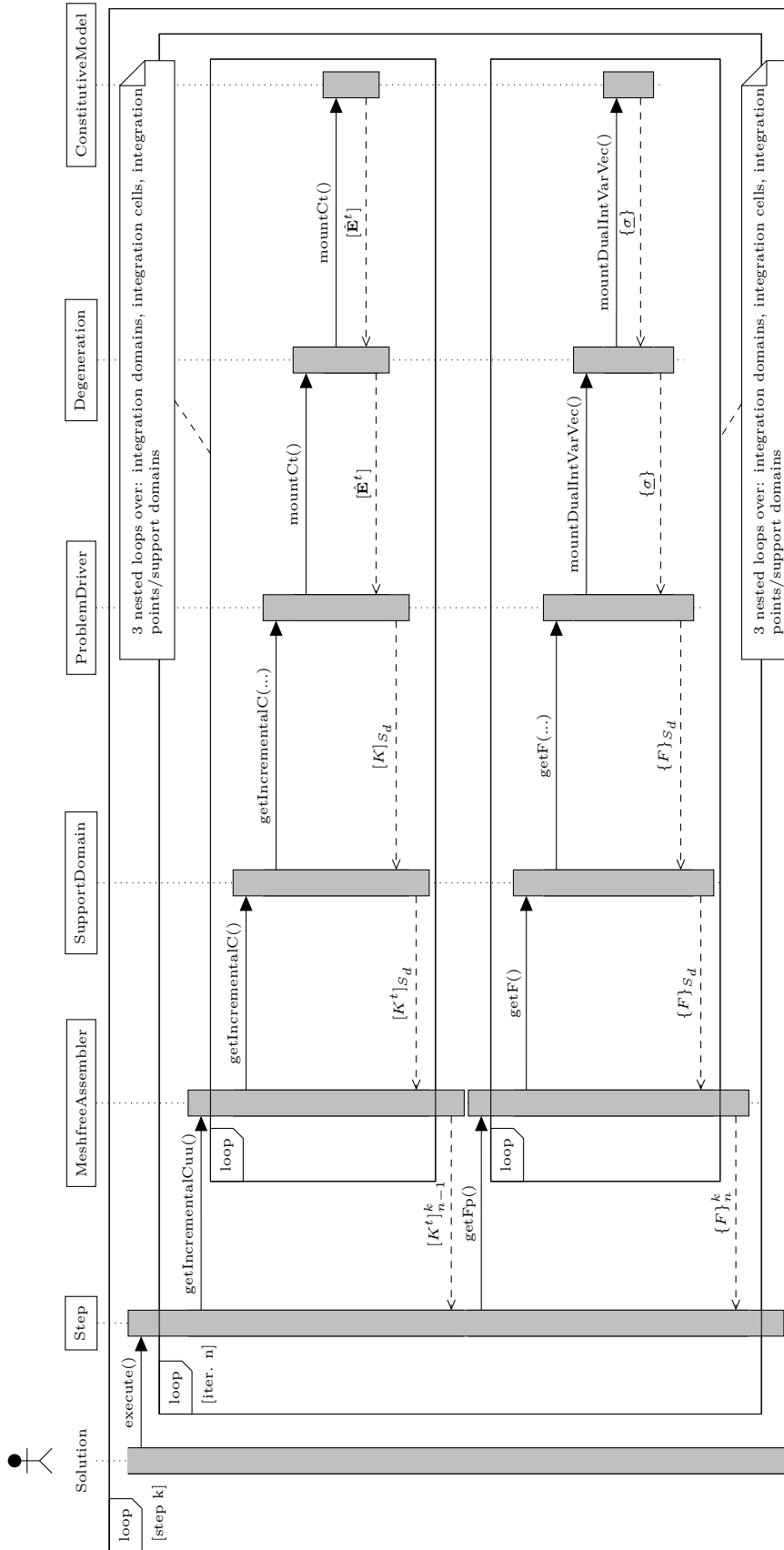
Figure C.31: Tangent stiffness matrix and internal forces vector assembly sequence diagram - Meshfree
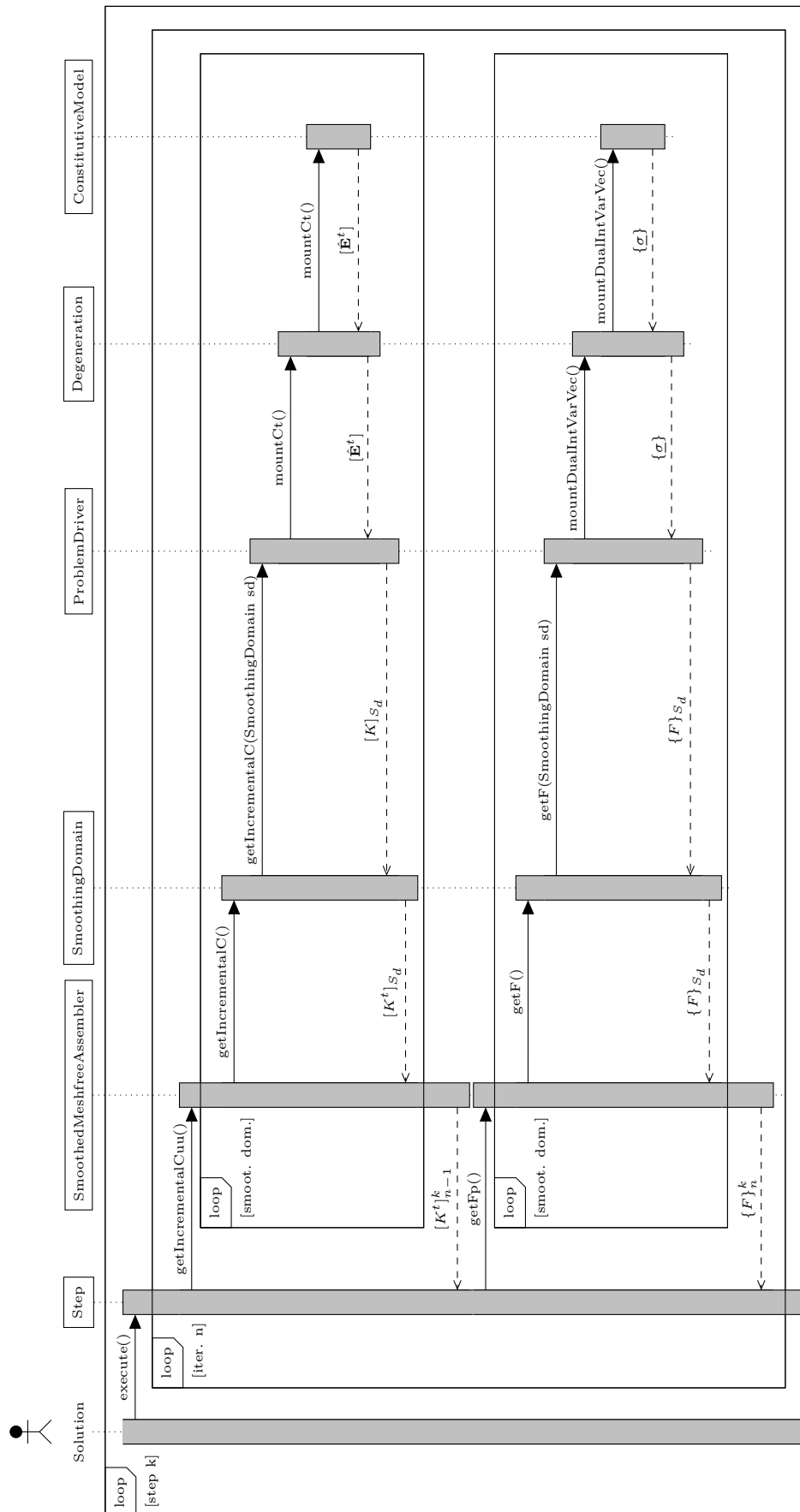
Figure C.32: Tangent stiffness matrix and internal forces vector assembly sequence diagram - Smoothed PIM/RPIM

C.5.1   The abstract class `ProblemDriver`

The partial structure of subclasses of `ProblemDriver` is depicted in Fig. C.33, where the methods used in the previous section are also represented. The existent classes `Parametric` and `PhysicallyNonLinear` were originally implemented in order to represent the numerical integration procedures for parametric finite elements, in linear elasticity and in physically non-linear problems, respectively. Further problems are managed by other subclasses, devoted to the evaluation of the *geometrical* tangent stiffness in a geometrically non-linear problem, or the *load* tangent stiffness matrix in a problem with non-conservative loads (the so-called *follower* loads), for example. The existent classes devoted to the representation of the EFG are not illustrated in Fig. C.33, however, they are an extention of the class `Parametric`. In order to allow the use of the smoothed point interpolation methods treated in this manuscript, as well as other meshfree methods, it was necessary to expand the structure of the `ProblemDriver` class, adding the classes `MeshfreeSolidMech` and `PhysicallyNonlinearMeshfreeSolidMech` devoted to the representation of linear elastic and physically non-linear meshfree methods based on the standard Gauss integration, and the classes `SmoothedPim` and `PhysicallyNonlinear-SmoothedPim` devoted to the representation of linear elastic and physically non-linear smoothed point interpolation methods.
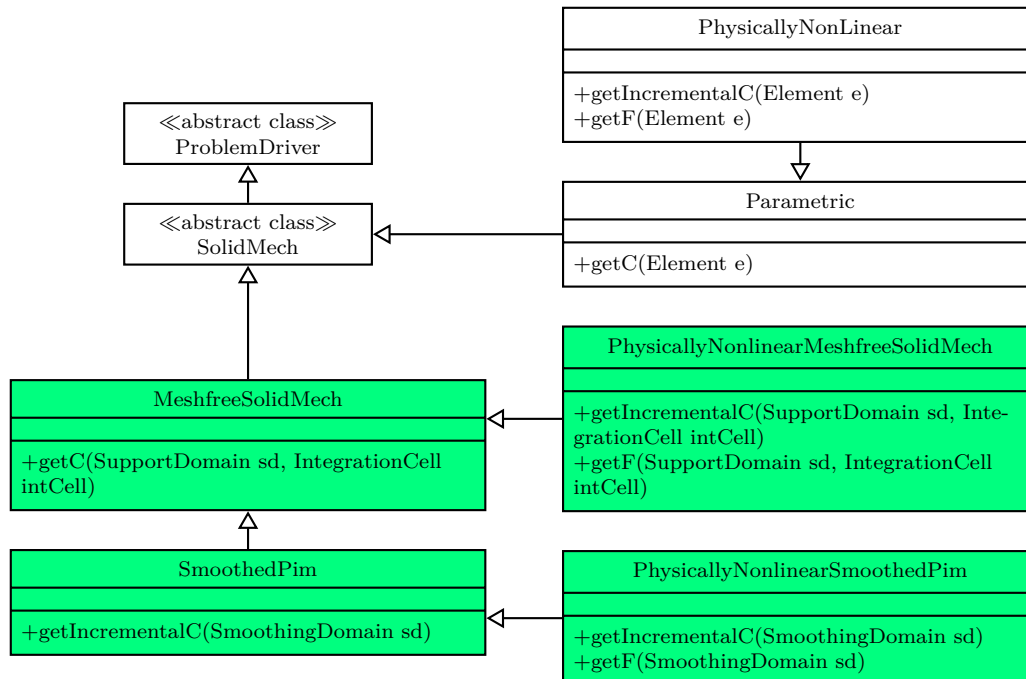

Figure C.33: The `ProblemDriver` class

C.5.2   The abstract class `Degeneration`

The abstract class `Degeneration` (similar to the class `GaussPoint` originally defined by Menétrey and Zimmermann (1993)) represents the degeneration of a certain solid model into a point. Each object of the class `Degeneration` is composed by a list of material points (instances of the class `MaterialPoint`, that represent, for example, a certain number of points discretizing a beam cross section) and by a `Representation`, that represents the integration point itself (with coordinates and weighting factor W_{ip}). Among the different kinds of degenerations, it is pointed out the presence of the class `PrescribedDegeneration`, which geometrical characteristics are explicitly specified (e.g., the thickness for a plane problem), and the class `CrossSection`, which characteristics depend on the set of material points discretizing the section of a beam.
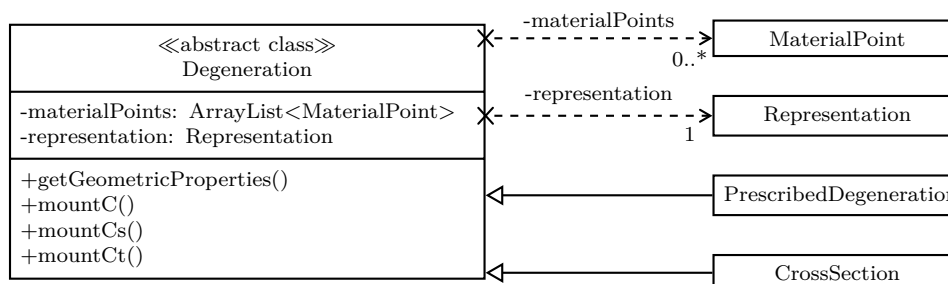

Figure C.34: The `Degeneration` class

The object `Degeneration` is responsible for returning to the `ProblemDriver` its contribution to the numerical integration expressed in Eq. (C.8). To do this, it is asked to mount the constitutive operator (initial, by the method `mountC()`, secant, by the method `mountCs()` or tangent, by the method `mountCt()`) evaluated at the integration point, which value is solicitated to an instance of the class `ConstitutiveModel`, illustrated in the following section.

C.6   Constitutive models framework

As pointed out by the sequence diagrams of Figs. C.29, C.31 and C.32, the main role of the constitutive models framework is to provide the expressions of the constitutive operator (initial $\hat{\mathbf{E}}$ or $\hat{\mathcal{E}}$, secant $\hat{\mathbf{E}}^S$ or $\hat{\mathcal{E}}^S$, tangent $\hat{\mathbf{E}}^t$ or $\hat{\mathcal{E}}^t$) and of the vector of internal stresses ($\underline{\sigma}$ or $\underline{\Sigma}$). Before proceeding with the description of the implementation strategy adopted for the micropolar models of Chapter 3, the main characteristics of the original framework for classic media implemented by Penna (see, e.g., Penna (2011) or Gori et al. (2017a)) are briefly recalled.

The root structure of the original framework is depicted in Fig. C.35. Once all the necessary informations like kind of analysis and material properties, for example,

have been provided, the abstract class `ConstitutiveModel` is able to return the constitutive operator (in all its different approximations) and the internal stresses, through the methods `mountC()` (initial operator), `mountCs()` (secant operator), `mountCt()` (tangent operator), and `mountDualInternalVariableVector()`. Different classes may extend the `ConstitutiveModel`, overriding the aforementioned methods in order to obtain a proper constitutive model (like the class `LinearElasticConstitutiveModel` for linear elastic constitutive models depicted in Fig. C.35). The focus here is on the class `UnifiedConstitutiveModel` and on the inherited classes `UCMMultipleLoadingFunction` and `UCMSingleLoadingFunction`. The first one extends the methods of the class `ConstitutiveModel` devoted to mount the initial and secant constitutive operators and the vector of internal stresses. The class `UCMMultipleLoadingFunction` extends the method `mountCt()` in order to represent *multidissipative* models (i.e., the ones that can be represent in terms of Eq. (2.12)), while the class `UCMSingleLoadingFunction` focuses on *monodissipative* models (i.e., the ones that can be represent in terms of Eq. (2.13)). Details regarding these classes, together with explicative code blocks, have been provided by the authors in Gori et al. (2017*a*) and will not be repeated here.
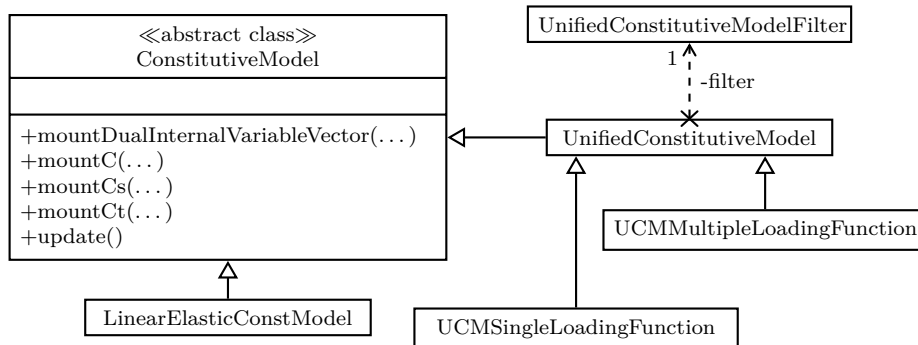

Figure C.35: Abstract Class `ConstitutiveModel`

As it can be observed in Fig. C.35, the class `UnifiedConstitutiveModel` possesses an instance of the class `UnifiedConstitutiveModelFilter`. This is the superclass of a family of classes called *filters*, each one devoted to the representation of a peculiar constitutive model. Indeed, while the objects `UCMMultipleLoadingFunction` and `UCMSingleLoadingFunction` define the structure of constitutive operator equation (Eq. (2.12) and Eq. (2.13)), the elements that allow to mount the tangent operator are provided by the class `UnifiedConstitutiveModelFilter`. Such class possesses methods that define the loading functions and their gradients (`getLoadingFunctionPotential()` and `getHardeningSofteningPotential()`), the directions of degradation (`getInelasticPotential()`), as well as the expressions of the secant constitutive operator (`getSecantTensor()`), as it can be observed in Fig. C.36.

The properties of the framework that has been briefly exposed here, have been widely discussed by the author in Gori et al. (2017*a*). In that publication specific emphasis has

```
┌─────────────────────────────────────────┐
│      UnifiedConstitutiveModelFilter      │
├─────────────────────────────────────────┤
│                                          │
├─────────────────────────────────────────┤
│ +getSecantTensor(. . . )                 │
│ +getInelasticPotential(. . . )           │
│ +getLoadingFunctionPotential(. . . )     │
│ +getHardeningSofteningPotential(. . . )  │
│ +update()                                │
└─────────────────────────────────────────┘
```

Figure C.36: Class `UnifiedConstitutiveModelFilter`

been given to the fact that the use of tensor objects for the representation of constitutive models allowed to obtain a framework for constitutive model that is highly modular and easy to expand, independent on the adopted numerical method, and independent on the peculiar analysis model. The modularity and the expandability can be easily understood considering the underlying theory discussed in Section 2.2.2, that is exactly reproduced with the classes `UnifiedConstitutiveModel` and `UnifiedConstitutiveModelFilter`. The independence on the numerical method and on the analysis model are due to the use of tensor-objects; the result is a set of constitutive models that can be used with different methods (like as the *finite element method*, the *boundary element method*, or different *meshfree methods*) and analysis models (like as *plane-stress* or *plane-strain*) without requiring any modification of the framework. The objective of this section is to show that such framework can be also made *independent on the adopted continuum model*. More specifically, it will be shown that the peculiar structure of the framework allows to introduce different continuum models (in this case the micropolar model) with minimum implementation efforts.

In this section it has been stated that the class `UCMSingleLoadingFunction` is able to represent the tangent constitutive operator for monodissipative classic media, the one expressed in Eq. (2.13). It has been also stated that such equation is represented in the code with tensor objects, in a form that is close to its mathematical expression. Since the tangent constitutive operator for monodissipative micropolar media ($\mathcal{E}^t_{ijk\ell} = \mathcal{E}^S_{ijk\ell} - 1/z \, (X_{ij} \, Y_{k\ell})$, Eq. (3.118)) presents a tensorial expression that is formally identical to the one of the tangent operator for classic media ($E^t_{ijk\ell} = E^S_{ijk\ell} - 1/z \, (x_{ij} \, y_{k\ell})$, Eq. (2.13)), also this expression can be represented by the class `UCMSingleLoadingFunction` with the same code line `tangentOp = secantOp.sub3((x.ijVECkl(y)).scale(1/z))`, without requiring any modification. The only difference between these two equations is the dimension of the involved tensors. However, since the methods of the class `UCMSingleLoadingFunction` depend only on the order of the tensors and not on their size, such class is able to represent both the continuum models. Though this case is not investigated here, the same code could be used also for other continuum models, as long as their tangent constitutive operator can be expressed in a form analogous to the one of Eq. (3.118). The compatibility between Eqs. (2.12) and (3.118) is guaranteed by the compact tensorial representation for micropolar media discussed in Section 3.3.3. Without this representation, the structure

of the classes `ConstitutiveModel` and `UnifiedConstitutiveModel` originally conceived for classic media, couldn't have been used to include micropolar models. A specific set of classes should have been created for each different continuum model undermining the modularity and expandability of the framework. Since the class `UCMSingleLoadingFunction` is able to deal also with the micropolar formulation, the definition of proper constitutive models for micropolar media is a task of the class `UnifiedConstitutiveModelFilter` and its inherited classes.

A partial structure of the filters classes is illustrated in Fig. C.37. As for the class `UnifiedConstitutiveModel`, also in this case a distinction is made between multidissipative and monodissipative models, represented by the classes `MLFConstitutiveModelFilter` and `SLFConstitutiveModelFilter`, respectively; as in Section 3.3 the sole monodissipative micropolar models have been accounted for, attention will be focused only on the latter. Such class is extended by the class `ElastoPlasticConstitutiveModelFilter`, devoted to the representation of elasto-plastic models, and by the class `IsotropicConstitutiveModelFilter`, devoted instead to the representation of scalar-isotropic damage models, as the ones presented in Section 2.2.2.1. These two classes have been illustrated in Gori et al. (2017a) and, since there has been no need to modify them in order to include micropolar models, they will not be discussed here.
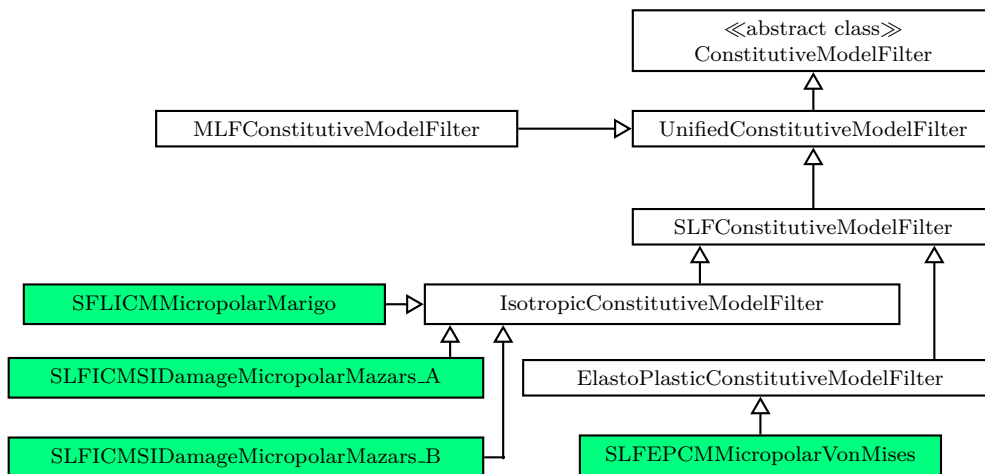

Figure C.37: Class organization of the micropolar filters

Three specific micropolar models can be found in Fig. C.37: the classic J2 elasto-plastic micropolar model proposed by de Borst (1993), represented by the class `SLFEPCMMicropolarVonMises`, and two scalar damage models proposed by the author in Gori et al. (2017c,b) and expressed in Eqs. (3.141), (3.143) and (3.146), represented, respectively, by the classes `SLFICMMicropolarMarigo`, `SLFICMSIDamageMicropolarMazars_B` and `SLFICMSIDamageMicropolarMazars_A`. In order to expose some implementation details, attention is focused on the classes that allow to represent the extention to the micropolar theory of the classic *Marigo* model discussed in Section 3.3.4. These classes allow to compose the

expression

$$\hat{\mathcal{E}}^t = (1 - D)\,\hat{\mathcal{E}} - \frac{1}{H^*}\,(\underline{X} \otimes \underline{Y}) \tag{C.12}$$

where the direction of degradation $\underline{X}$ and the gradient of the loading function $\underline{Y}$ are expressed by

$$\underline{X} = -\hat{\mathcal{E}} \cdot \underline{\Gamma}, \qquad \underline{Y} = \frac{\partial \Gamma_{eq}}{\partial \underline{\Gamma}} \tag{C.13}$$

The secant constitutive operator $\hat{\mathcal{E}}^S = (1 - D)\,\hat{\mathcal{E}}$ is provided by the method `getSecant-Tensor(...)` of the class `IsotropicConstitutiveModelFilter`, using the same code block developed for classic media already discussed in Gori et al. (2017a). The other terms appearing in Eq. (C.12) can be obtained with the methods of the class `SLFICM-MicropolarMarigo`, a part of which is reported in Fig. C.38. The method `getInelas-ticPotential(...)` returns the direction of degradation $\underline{X} = -\hat{\mathcal{E}} \cdot \underline{\Gamma}$, `getLoading-FunctionPotential(...)` returns the gradient of the loading function $\underline{Y} = \partial \Gamma_{eq}/\partial \underline{\Gamma}$, that for the micropolar Marigo model is expressed by $\underline{Y} = (\hat{\mathcal{E}} \cdot \underline{\Gamma})/(\Gamma_{eq}\,E)$, and `get-HardeningSofteningPotential(...)` returns the derivative of the damage law $1/H^* = \partial D(\Gamma_{eq})/\partial \Gamma_{eq}$. The definition of the equivalent deformation measure is also a fundamental operation for the formation of the tangent constitutive operator (its use can be seen at line 16 of Fig. C.38). Such quantity is provided by the method `getEquivalentStrain(...)`. For the considered model, the evaluation of the strain measure $\Gamma_{eq} = \sqrt{2\psi^0/E}$ (Eq. (3.141)), with $2\psi^0 = \underline{\gamma} \cdot (\hat{\mathbf{A}} \cdot \underline{\gamma}) + \underline{\kappa} \cdot (\hat{\mathbf{C}} \cdot \underline{\kappa})$, is illustrated in the code block of Fig. C.39.

The class `SLFICMMicropolarMarigo`, as well as the other filters classes, possesses a number of further methods for its internal operations, like a method for the updating of the constitutive variables during the analysis (`updateConstitutivesVariables(...)`), or a method for the evaluation of the state of the loading function (`unLoadLaw(...)`), which have been discussed in the suggested references, together with the other classes appearing in the code blocks of Figs. C.38 and C.39, like `Material` and `AnalysisModel`.

The operations that allow to mount the vector of internal stresses $\{\underline{\Sigma}\}$ have not been described here, since there haven't been any modifications with respect to the existent implementation for classic media. This emphasize again the generality of a framework based on tensor object. The class responsible for the assembly of the internal stresses is the `UnifiedConstitutiveModel` class. In case of models with elastic degradation, such class provide the internal stresses through the code line `stress = (this.mountCs(...)).mul(strain)`, which is able to represent both the expressions for classic ($\underline{\sigma} = \hat{\mathbf{E}}^S \cdot \underline{\varepsilon}$) and micropolar media ($\underline{\Sigma} = \hat{\mathcal{E}}^S \cdot \underline{\Gamma}$).

The procedures described in this section have shown a strategy for the implementation of micropolar models in an existing framework for classic media. It has been emphasized that the use of tensor objects for the representation of constitutive models originally adopted by the authors in Gori et al. (2017a) has been fundamental for the inclusion of micropolar models with minimum implementation efforts. The adoption of

```
1   public Tensor getInelasticPotential(AnalysisModel am, Material mat,
2       HashMap<Object, Object> cv) {
3     Tensor generalizedElasticTensor = new Tensor(am
4       .getDualInternalVariablesOperatorTensor(mat.getPs()));
5     Tensor generalizedStrainTensor = new Tensor(((Tensor) cv
6       .get(SLFICMMicropolarLemaitreChaboche.GENERALIZED_STRAIN_TENSOR)));
7     Tensor m = new Tensor(generalizedElasticTensor
8       .ijkldotkl(generalizedStrainTensor));
9     m.scale(-1.0);
10    return m;
11  }
12
13  public Tensor getLoadingFunctionPotential(AnalysisModel am, Material mat,
14      HashMap<Object, Object> cv) {
15    Tensor generalizedElasticTensor = am.
16       getDualInternalVariablesOperatorTensor(mat.getPs());
17    Tensor generalizedStrainTensor = ((Tensor) cv
18      .get(SLFICMMicropolarLemaitreChaboche.GENERALIZED_STRAIN_TENSOR));
19    Tensor generalizedStressTensor = generalizedElasticTensor
20      .ijkldotkl(generalizedStrainTensor);
21    double eqvs = (Double) cv.get(SLFICMMicropolarLemaitreChaboche
22      .EQUIVALENT_STRAIN);
23    double e0 = ((LemaitreChabocheMicropolarMaterial) mat)
24      .getMaterialValues(Material.ELASTICITY);
25    Tensor n;
26    if (eqvs > 0) {
27      n = new Tensor(generalizedStressTensor);
28      n.scale(1.0 / (eqvs * e0));
29    } else {
30      n = new Tensor(2, 6);
31    }
32    return n;
33  }
34
35  public Tensor getHardeningSofteningPotential(AnalysisModel am,
36       Material mat, HashMap<Object,
37     Object> cv) {
38    Tensor h = new Tensor(0);
39    double dwdk = ((Double) cv
40      .get(SLFICMMicropolarLemaitreChaboche.TDAMAGE));
41    h.setElement(0, 0, dwdk);
42    return h;
43  }
```

Figure C.38: Methods of the class `SLFICMMicropolarMarigo`

```
1   protected double getEquivalentStrain(Tensor generalizedStrainTensor,
2       AnalysisModel am, Material mat) {
3     Tensor generalizedElasticTensor = new Tensor(am
4       .getDualInternalVariablesOperatorTensor(mat.getPs()));
5     double e0 = ((LemaitreChabocheMicropolarMaterial) mat)
6       .getMaterialValues(Material.ELASTICITY);
7     Tensor aux = generalizedStrainTensor.ijdotij(generalizedElasticTensor
8       .ijkldotkl(generalizedStrainTensor));
9     double value = Math.sqrt(aux.getTensor().getElement(0, 0) / e0);
10    return value;
11  }
```

Figure C.39: Method `getEquivalentStrain(...)` of `SLFICMMicropolarMarigo`

a compact representation for micropolar models as the one described in Section 3.3.3 allowed to obtain constitutive equations formally identical to the ones for the classic media, resulting in the use of the same numerical structure for both the kind of continuum models. As it has been shown, only a few classes are needed to define a peculiar model; for example, if a developer had to implement a new micropolar scalar damage model, with its own equivalent deformation measure, he should only need to extend the class `IsotropicConstitutiveModelFilter` with a new class overriding the methods of the superclass in order to characterize the new constitutive model. A practical application of the framework will be shown in the following section, using two numerical simulations.

In the following two sections the classes `AnalysisModel` and `Material` are presented, since they have a strong relation with the constitutive models framework.

C.6.1   The `AnalysisModel` class

The abstract class `AnalysisModel` is devoted to the representation inside the code of the different problems that can be analized, i.e., three-dimensional, plane-stress, plane-strain, etc. Its inherited classes characterize each problem in terms of number of degrees of freedom, kind and number of internal variables (i.e., strains) and dual internal variables (i.e., stresses). In this context, it is emphasized only its role in relation to the constitutive models framework. As already discussed in the previous sections, a difference exists in the representation of objects inside the proposed constitutive models framework and outside of it. The constitutive relations are expressed in the framework by means of tensor objects, with the advantages in terms of modularity and generalization discussed in the previous section. Outside the framework, as in conventional FEM codes, a matricial representation is adopted, for operations like numerical integration and assembly of stiffness matrices.

The exchange of informations between the framework, that works with tensorial quantities, and the other parts of the code, that work with matricial objects, is guaranteed by the classes that inherit from `AnalysisModel`. Such classes indeed, are able to convert the tensorial representation of an operator into its Voigt expression, and vice-versa. The method `getActiveDualInternalVariablesVector(...)`, for example, is able to convert the second-order stress tensor to its Voigt expression; for a plane-stress analysis model this results in the conversion

$$\underline{\sigma} = \begin{pmatrix} \sigma_{xx} & \sigma_{xy} & 0 \\ \sigma_{yx} & \sigma_{yy} & 0 \\ 0 & 0 & 0 \end{pmatrix} \rightarrow \{\underline{\sigma}\} = \begin{pmatrix} \sigma_{xx} \\ \sigma_{yy} \\ \sigma_{xy} \end{pmatrix} \tag{C.14}$$

In an analogous way, the method `reduceToMatrix(...)`, converts the fourth-order constitutive operator tensor into its Voigt expression; again, for a plane-stress problem, this

results in a 3×3 matrix as

$$\hat{\mathbf{E}} \rightarrow [\hat{\mathbf{E}}] = \frac{E}{1-\nu^2} \begin{pmatrix} 1 & \nu & 0 \\ \nu & 1 & 0 \\ 0 & 0 & 1-\nu \end{pmatrix} \tag{C.15}$$

Among its different tasks, the `AnalysisModel` is also responsible for the generation of the matrix containing the approximation functions of the state variable of the problem and of the matrix representing the kinematical operator, both in its standard and smoothed version, which are created according to the specified model.

A partial structure of this system of classes is represented in Fig. C.40. The original implementation in the **INSANE** system of the micropolar continuum (Fuina, 2009) was made before the introduction of the tensor-based constitutive models framework; hence, a new set of classes have been introduced, in order to guarantee the compatibility with the new strategy for constitutive modelling. In order to allow the use of the new meshfree models implemented in this work, a new class for classic media in plane stress has been introduced, which inherits from the existing `PlaneStress` class.
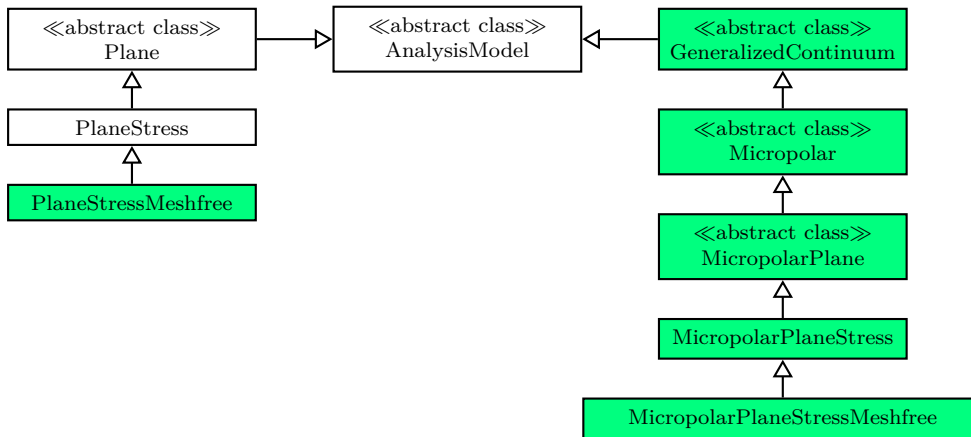

Figure C.40: Class `AnalysisModel`

C.6.2   The `Material` class

The classes that inherit from the superclass `Material` are responsible for the representation of different materials inside the software; as it can be observed in Fig. C.39, one of the roles of such class is to provide the values of the material moduli, through the method `getPs()`, that can be used, for example, by an instance of the class `AnalysisModel` to mount a constitutive operator. Elasto-plastic materials and materials with damage must implement the interfaces `Hardenable` and `Damageable`, respectively. Focusing on the latter, such interface forces a class to implement the methods `getDamage(...)`, that should return the damage level for a certain deformation, and `getInelasticModulus(...)`,

that should return instead the variation of the damage for a certain deformation; as pointed out in Gori et al. (2017a), both methods are called within the inherited classes of `ConstitutiveModelFilter`. Such methods call analogous methods contained in the abstract class `InelasticLaw`, an instance of which may be contained in an class that inherits from `Material`. An exponential damage law like the one of Eq. (2.33), for example, is represented inside the code by the class `DamageLawExponential`, that inherits from `InelasticLaw`. In this case, the evaluation of the damage level with the method `getDamage(...)` is exposed in Fig. C.41.

```java
 1 public double getDamage (double eps) {
 2  double w = 0.0;
 3  if (eps > 0.0) {
 4   if (eps <= kappa) {
 5    w = 0.0;
 6   }
 7   if (eps > kappa) {
 8    w = 1 - (kappa / eps) * (1.0 - alpha + alpha * (Math.exp(-betha * (eps - kappa))));
 9   }
10  }
11  if (eps <= 0.0) {
12   w = 0.0;
13  }
14  if (this.getDamageThreshold() < w) {
15   this.setRateThreshold(this.getRateThreshold() / w);
16   w = this.getDamageThreshold();
17  }
18 return w;
19 }
```

Figure C.41: Method `getDamage(...)` of `DamageLawExponential`

In order to allow the use of the new elastic-degrading micropolar model (Section 3.3) and of the new meshfree methods (Chapter 4), there has been no need to modify the original implementation for micropolar models of the class `Material` ((Fuina, 2009)).